Functionalized Silica Nanoparticles and Coated Cotton Fabrics for Medical and Catalytic Applications

Ming Liu

Universitat Autònoma de Barcelona

Doctoral School

Faculty of Science

Department of Chemistry

Functionalized Silica Nanoparticles and Coated Cotton Fabrics for Medical and Catalytic Applications

Ming Liu

Supervisors:

Prof. Roser Pleixats Rovira

Prof. Adelina Vallribera Massó

PhD in Chemistry

Doctoral Thesis, 2024

Universitat Autònoma de Barcelona

Doctoral School

Faculty of Science

Department of Chemistry

Functionalized Silica Nanoparticles and Coated Cotton Fabrics for Medical and Catalytic Applications

Dissertation submitted for the degree of Doctor

Ming Liu

Supervisors:

Prof. Roser Pleixats Rovira

Prof. Adelina Vallribera Massó

Cerdanyola del Vallès, Bellaterra. 10th, July, 2024

Table of Contents

Table of Contents

Financial and Technical Support

We gratefully acknowledge China Scholarship Council for the predoctoral scholarship (CSC scholarship, No. 202006560005), and the financial support for the research project of Ministerio de Ciencia, Innovación y Universidades (MICINN) of Spain (Projects RTI2018-097853-B-I00, PID2021-124916NB-I00, RED2022-134287-T, RYC2019-027423-I, and PID2021-128496OB-I00) and AGAUR-Generalitat de Catalunya (Projects SGR20170465 and SGR2021-00064).

We acknowledge as well the technical support from *Servei d'Anàlisi Química de la UAB*, *Servei de Ressonància Magnètica Nuclear de la UAB*, *Servei de Microscòpia de la UAB*, *Servei de Difracció de Raigs X de la UAB*, *Institut de Ciència dels Materials de Barcelona (ICMAB-CSIC)*, *Centres Científics i Tecnològics de la Universitat de Barcelona*, *Universidad de Burgos, Servei de Llengües de la UAB*, *Doctoral School of UAB*, *Department of Chemistry of UAB*, *Department of Sanitat i Anatomia Animals of UAB, Servicio de Resonancia Magnética Nuclear de Sólidos del Instituto de Ciencia de Materiales de Madrid – CSIC*, *Departament de Biologia Cel·lular, Fisiologia i Immunologia of UAB*.

Publications

The results obtained in this Thesis have been reported in the following publications:

- Liu, M.; Granados, A.; Reyes-Mesa, D.; Arosemena-Angulo, E. L.; Calvo-Torras, M. Á.; Pleixats, R.; Vallribera, A. Silica nanostructures against fungal growth: design and preparation of antifungal cotton fabrics. *Cellulose* **2022**, *29* (16), 8889-8905.

- Liu, M.; Guinart, A.; Granados, A.; Gimbert-Suriñach, C.; Fernández, E.; Pleixats, R.; Vallribera, A. Coated Cotton Fabrics with Antibacterial and Anti-Inflammatory Silica Nanoparticles for Improving Wound Healing. *ACS Applied Materials & Interfaces* **2024**, *16* (12), 14595-14604.

Abstract

Silica nanoparticles have gained considerable attention, and they have various applications owing to numerous significant properties such as easy synthesis procedure, tunable particle sizes and pores, the versatile surface chemistry and high biocompatibility. This thesis is focused on the preparation and characterization of different kinds of functionalized silica nanoparticles, as well as on some of their biomedical and catalytic applications.

Novel mesoporous or dense silica nanoparticles derived from silylated derivatives of miconazole were prepared and characterized. Further coating of cotton fabrics with these nanoparticles was achieved. The antifungal activity of the modified fabrics was successfully tested. Topical cutaneous applications in antifungal dressings are expected (**Chapter 2**).

Both an anti-inflammatory drug (ibuprofen) and an antibiotic (levofloxacin or norfloxacin) were grafted on silica nanoparticles through amide functional groups. Furthermore, the coating of cotton fabrics with these nanoparticles was performed. The functionalized nanoparticles and textiles were treated with model proteases to facilitate the drug release through enzymatic cleavage of amide bonds. These modified fabrics have potential topical dermal applications in medical bandages to prevent infection and accelerate cicatrisation of wounds (**Chapter 3**).

A series of mesoporous and dense silica nanoparticles were prepared based on a chiral disilylated bis(oxazoline) precursor. These nanomaterials were evaluated as chiral supported bis(oxazoline) ligands in the asymmetric difluoroalkylation reaction of a *β*-ketoester by cooperative photoredox/Ni(II) catalysis. However, moderate yields and no chiral induction was observed (**Chapter 4**).

Abstract

CHAPTER 1

GENERAL INTRODUCTION TO SILICA NANOPARTICLES

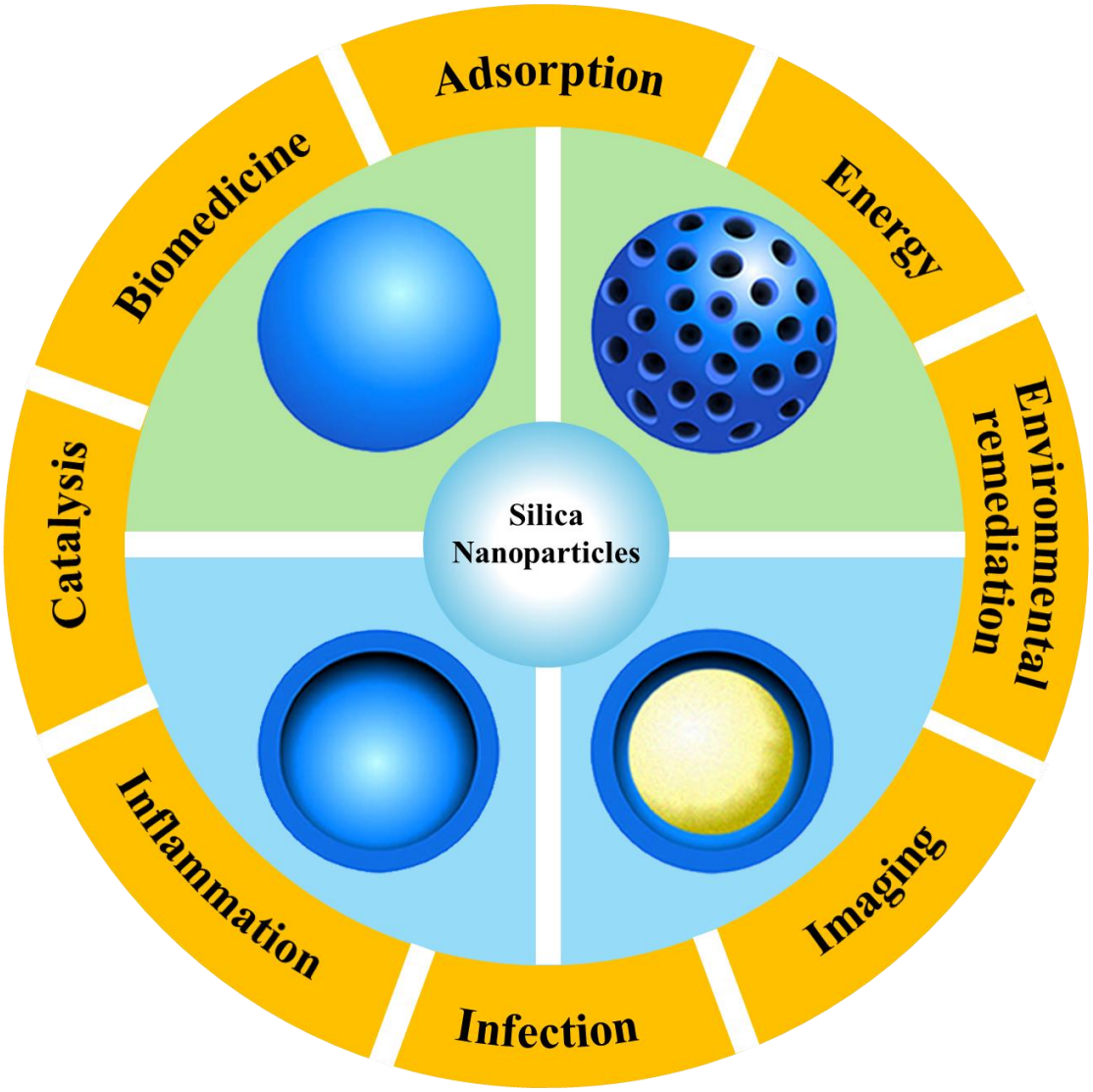

Chapter 1
General Introduction to Silica Nanoparticles

1.1 Introduction

Silicon (Si) is the Earth's second most abundant element within its crust, and the natural or synthetic derivatives containing silicon include a vast array of compounds and materials such as silica, silicates, silicic acids, organosilanes, silicones, ceramics and so on.[1] These materials find widespread utilization across various industrial sectors, including their incorporation as additives within the food and beverage, building and manufacturing industries. Human exposure to silicon occurs through both environmental sources and dietary intake. Orthosilicic acid, deriving from the erosion of rocks and soil minerals are commonly introduced into drinking water/beverages. It's the primary absorbable and available form of silicon to human. Within the human body, silicon holds the third position within the most prevalent trace elements, predominantly localized at active calcification sites within bones. Its presence is crucial for metabolic functions, with deficiencies potentially resulting in impairments to connective and skeletal tissues.[2, 3]

Among various silicon materials, silica, referred to as silicon dioxide (SiO_2), represents the primary component of rock-forming minerals found in magmatic and metamorphic formations. Additionally, it holds significance in sediments and soil compositions. Existing primarily as silicates, it constitutes approximately 75% by weight of the Earth's crust. Free silica is mainly manifested as quartz, comprising 12-14% by weight of the lithosphere. In most instances, the silicon atom in silicon dioxide exhibits tetrahedral coordination, encircled by four oxygen atoms. Each silicon atom shares its four valence electrons with oxygen atoms to form strong covalent bonds. The reactivity of silicas is primarily dictated by their surface characteristics, particularly through the presence of weakly acidic silanol groups. With surface-exposed silanol groups and siloxane bridges as depicted in Figure 1.1, silica exhibits distinct chemical functionalities crucial to define its properties and interactions.[4]

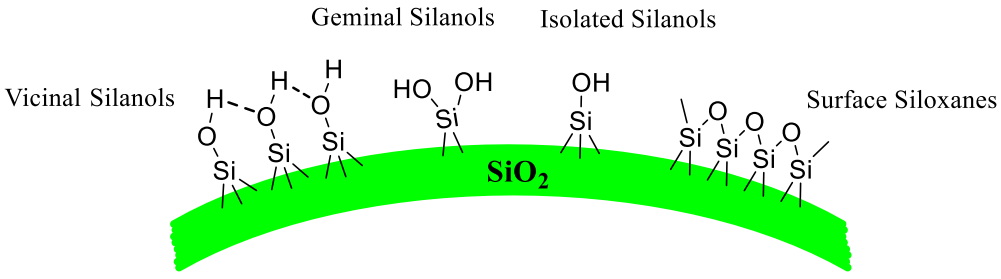

Figure 1.1 The categories of silanol groups and siloxane bridges found on the surface of silica

1.2 Silica nanoparticles

Nanomaterials show properties quite different from those of the bulk materials due to surface effects and quantum size effects.[5] Over the last two decades, considerable advancements have been achieved in nanoscience, enabling scientists to tune the synthesis of different types of nanomaterials exhibiting various structures such as nanospheres,[6] nanowires,[7] nanofibers,[8] nanorods,[9, 10] nanoparticles,[11] hollow nanotubes,[12] core-shell nanomaterials[13] and so on.[14] Different methods to adjust and control the nanostructures developed in fundamental research led to the comprehensive applications in multiple fields such as sensors,[15] energy,[16] catalysis,[17] coating,[18] biomedicine,[19] environment[20] and so on.

Silica nanoparticles (silica NPs) have gained considerable attention owing to numerous significant properties such as easy synthesis procedure, tunable particle sizes and pores, the versatile surface chemistry and high biocompatibility. Numerous methods are employed for the preparation of silica NPs, including plasma manufacturing, chemical vapor deposition, microemulsion synthesis, combustion processing, sol-gel synthesis, and hydrothermal processes. These fabricated silica NPs are categorized into nonporous and mesoporous nanoparticles based on their structural properties.[21] The sol-gel method stands out as one of the most crucial and extensively utilized techniques for silica NPs preparation. This method offers many advantages, including the ability to conduct synthesis at lower temperatures and desired pH levels, resulting in high purity products. Moreover, the kinetics of reactions can be precisely controlled by adjusting the compositions of the reaction mixtures.

1.2.1 The sol-gel chemistry of silica

In general, the sol-gel process for silica materials starts with a monomeric silicon alkoxide precursor $Si(OR)_n$, e.g. tetraethylorthosilicate (TEOS), in an aqueous or alcohol solvent and a suitable catalyst. It is the most common process to synthesize bulk silica (and also silica NPs with some control of the conditions). General hydrolysis and condensation reactions are shown in Scheme 1.1. The hydrolysis reaction involves the substitution of alkoxide groups (-OR) with hydroxyl groups (-OH) and the release of alcohol (ROH). After hydrolysis, condensation reactions occur, wherein silanol groups (Si-OH) react to form siloxane bonds (Si-O-Si), resulting in the production of water (condensation between two Si-OH) and alcohol (condensation between Si-OH and Si-OR) as by-products. In many cases, condensation reactions can start before achieving complete hydrolysis. Factors such as pH, the molar ratio of water to silicon (H_2O/Si), and the presence of catalysts can promote complete hydrolysis before condensation begin. To overcome the immiscibility of the silicon alkoxide and water, a mutual solvent, typically an alcohol, is employed as a homogenizing agent to facilitate the hydrolysis process. Subsequent polymerization process leads to the formation of SiO_2 (nano)materials. In the preparation

of bulk silica, the sol is transformed to a gel in a gelatinization process (formation of tridimensional networks entrapping the solvent), which can then be converted to a powder. In the formation of silica NPs, a gel is not formed but a colloidal solution, from which the NPs can be precipitated and collected upon centrifugation.

The gelation process overall is slow primarily because of the low polarity of the Si-O bond in silicon alkoxides, where the silicon atoms exhibit a low positive charge (δ^+ = 0.32 in TEOS). Therefore, catalysis plays an essential role in accelerating the process. The relative rates of hydrolysis and condensation are highly sensitive to the medium, enabling relatively independent control through acid or base catalysis.[22, 23] The final properties of the silica materials, such as surface area, strongly depend on the experimental parameters used in the sol-gel process. In the case of silica NPs, basic catalysis is mostly used (ammonia, sodium hydroxide) and a cationic surfactant is added if we want to control the porosity, size and monodispersity of the nanomaterial, resulting in mesoporous silica nanoparticles (see section 1.2.3). In the absence of surfactant, non-porous silica NPs are obtained (see section 1.2.2).

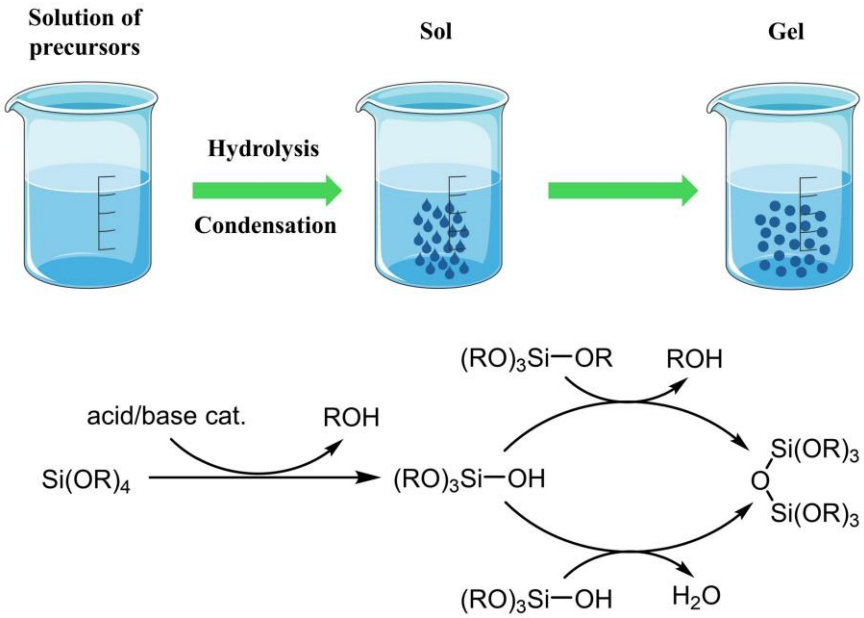

Scheme 1.1 Hydrolysis and condensation stages of sol-gel process

1.2.1.1 Acid catalysis

The mechanisms of the two steps under acidic catalysis are outlined in Scheme 1.2.[24] The alkoxy group of silicon alkoxide is attacked by the proton, leading to a silicon center more electrophilic. The intermediate formed by the nucleophilic attack of water to the silicon center tends to lose an alcohol molecule and the catalyst is recovered. The condensation step starts with the protonation of the oxygen of the silanol group. Then the protonated molecule condenses with the unprotonated one, resulting in the formation of a siloxane bridge (Si-O-Si) and the loss of a hydronium cation, thus forming a water

molecule and recovering the catalyst.

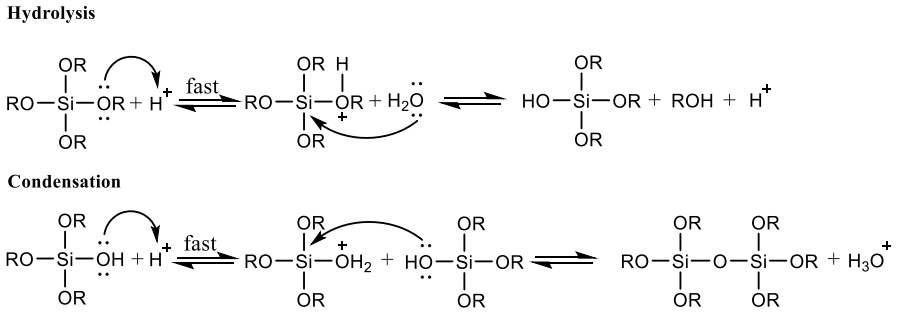

Scheme 1.2 Hydrolysis and condensation of tetraalkoxysilane under acid catalysis

1.2.1.2 Base catalysis

For the basic catalysis process, hydroxide anions initiate a nucleophilic attack on the tetraalkoxysilane, leading to the formation of an anionic pentacoordinate intermediate (Scheme 1.3). An alkoxide group of the intermediate is eliminated, thus forming a molecule of alcohol and recovering the catalyst. Then the condensation process starts with the abstraction of the silanol proton by the hydroxide ion. Finally, the formed siloxide ion attacks the silicon center of the silanol molecule through the S_N2 pathway, resulting in the siloxane linkage (Si-O-Si) and the recovery of the catalyst.

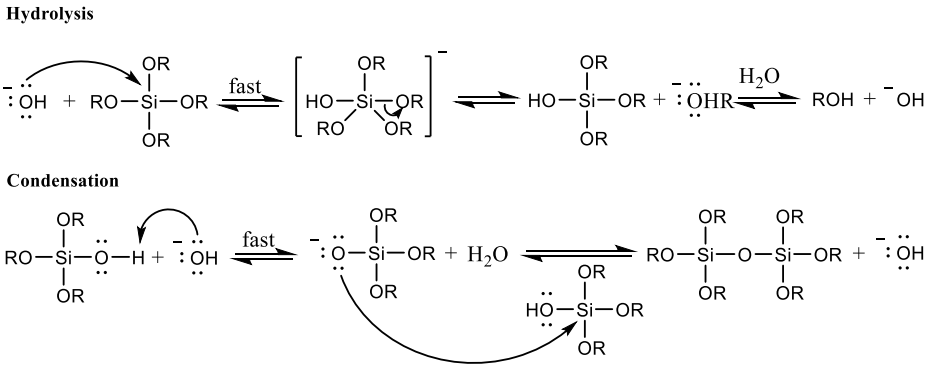

Scheme 1.3 Hydrolysis and condensation of tetraalkoxysilane under base catalysis

Control of silica polymerization can be effectively managed by balancing the rates of precursor hydrolysis and condensation. Both reactions are accelerated by proton-transfer catalysis, involving the above-mentioned acidic or basic catalysis. Consequently, the extent, the timing, and the relative rates of these processes heavily rely on solution reaction conditions during synthesis. A direct method for controlling these processes and subsequent silica formation is by adjusting the pH of the reaction. Near the isoelectric point of silica (approximately pH 2), polymerization is minimal, with rates increasing significantly as the solution becomes either more acidic or more basic. Polymerization rates have a maximum around pH 7, beyond which the negative charge on silica monomers impedes condensation. Moreover, the rates of hydrolysis and condensation are strongly influenced by the presence of inorganic salts (such as alkali metal halides) and the overall ionic strength of the solution. Furthermore, factors including temperature, type of salt species, molar ratio of silicon salt species, solvent dielectric constant,

presence of catalysts, and mixing conditions affect silica polymerization.[25]

The physical and electrochemical characteristics of the resulting materials are heavily influenced by the catalyst type employed in the reaction. Scheme 1.4 depicts a basic illustration of the distinct sol structures generated through either acid or basic catalysis. When silica alkoxides are subjected to acid-catalyzed reactions, the outcome is weakly crosslinked linear oligomers (anisotropic growth). These polymers tend to interweave and generate extra branches. Conversely, in base-catalyzed reactions, rapid hydrolysis and condensation of alkoxide silanes occur, resulting in the formation of highly branched clusters (isotropic growth, spherical form).[26] For this reason, the synthesis of silica nanoparticles typically occurs in a basic or nucleophilic medium, employing substances such as NaOH or NH_3.[27]

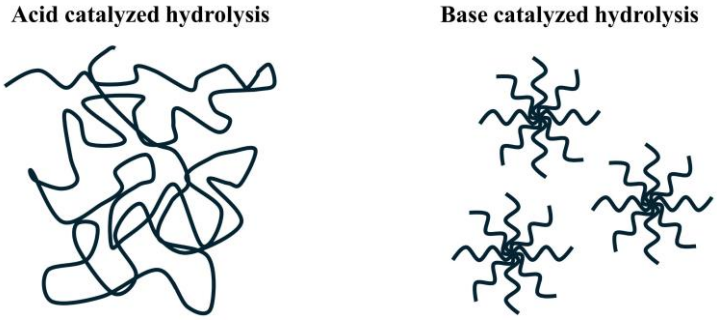

Scheme 1.4 The acid catalyzed linear and base catalyzed branched geometry of the oligomers

Silica NPs can be divided into two categories: nonporous silica NPs and mesoporous silica NPs.

1.2.2 Nonporous silica nanoparticles

Nonporous silica NPs are normally obtained using three main synthetic approaches: Stöber method, reverse microemulsions (water in oil) or direct micelle assisted methods. The Stöber method, established in 1968,[28] represents a typical sol-gel process as discussed above, used first for the preparation on bulk nonporous silica and then adapted to the obtention of nanoparticulated silica. As mentioned before, the absence of surfactant as template is the reason of the non-porosity of the NPs. Nonporous silica NPs can also be produced by the reaction of tetramethylorthosilicate (TMOS) inside the water droplets of a water-in-oil microemulsion, under both acidic (pH 1.05) or basic (pH 10.85) conditions as reported by Kim S. Finnie's group in 2007.[29]

1.2.3 Mesoporous silica nanoparticles (MSN)

Porous nanomaterials consist of materials with micropores (0.2-2 nm), mesopores (2-50 nm) and macropores (50-100 nm).[30] Thus, mesoporous materials refer to a category of materials that possess pores with diameters in the range of 2 to 50 nm, that have advantageous properties due to their ordered

framework, high surface area, tunable particle size, large pore size, and substantial pore volumes, facilitating the easy diffusion of substrate molecules. Consequently, they have found widespread application across diverse fields such as catalysis, drug delivery, membrane separation, biosensing, and sorption analysis. Among the most used mesoporous materials for various applications are alumina, silica, carbon, and transition metal oxides. The mesoporous silica NPs can by prepared by soft template and hard template methods.

In the soft template method, amphiphilic molecules such as surfactants are self-assembled with inorganic precursors The utilized templates are subsequently eliminated through washing or heat treatment under air, resulting in the creation of ordered mesoporous inorganic materials. This process involves two major steps for the silica NPs: the hydrolysis and condensation of silica precursors in the presence of micelle templates and the removal of the surfactant templates through calcination or solvent extraction, thereby forming ordered mesopores within a silica network. The resulting nanomaterials exhibit regular arrays of pores, with pore sizes easily controllable by employing templates of different sizes. In solution synthesis, typically conducted under basic conditions, silanol groups (Si-OH) undergo partial deprotonation to form silanolate ($Si\text{-}O^-$). To counterbalance the negative charge of silica, cationic surfactants are commonly employed, such as cetyltrimethylammonium bromide (CTAB). Consequently, the hydrolysis and condensation rates of silica sources (e.g., TEOS) are highly influenced by the pH of solution.[31, 32]

In the hard template method, inorganic precursors are introduced into pre-synthesized hard template. These templates are then removed through etching with HF or NaOH, or heat treatment under air.[33]

Over the past two decades, notable advancements have been made in the synthesis and modification of mesoporous silica nanomaterials, characterized by well-defined pore geometry and particle morphology. Particularly, considerable efforts have been focused on regulating pore/particle size, enhancing pore connectivity, controlling particle morphology, and facilitating surface functionalization. Their excellent biocompatibility and biodegradation favor their use in biomedicine.[32, 34, 35]

Ordered mesoporous solids such as MCM-41, MCM-48 and SBA-15 bulk silicas, which typically have pores ranging between 2 to 15 nanometers, have been readily prepared some decades ago in aqueous conditions through a combination of templating methods and sol-gel procedures (Table 1.1). Specifically, materials such as MCM-41 and MCM-48 silicas have been easily synthesized under basic aqueous conditions in the presence of surfactants (such as cetyltrimethylammonium bromide, CTAB) and a suitable silica precursor (for instance, tetraethylorthosilicate, TEOS).[36] After template removal,

these materials exhibit high surface area (typically ⩾800 to 1000 m^2/g) and high pore volume (> 0.6 m^3/g) with narrow pore size distribution. On the other side, bulk SBA-15 was firstly reported in 1998 using non-ionic surfactants under acidic aqueous conditions.[37]

Table 1.1 Comparison of various mesoporous silica materials

	Different mesoporous silica			
	SBA-15	SBA-16	MCM-41	MCM-48
Full name	Santa Barbara Amorphous type 15	Santa Barbara Amorphous type 16	Mobil Composition of Matter no. 41	Mobil Composition of Matter no. 48
Structure directing agent (SDA)	Pluronic 123 (non-ionic)	Pluronic F127 (non-ionic)	CTAB (cationic)	CTAB (cationic)
Morphology	large pore hexagonal	large pore cubic	small pore hexagonal	small pore cubic

Along with the development of synthesis strategies, mesoporous materials have also been largely applied to various areas including sensing, cancer therapy, tissue engineering, catalysis, ion batteries and solar cells. The unique porous structures provided by mesoporous materials have revolutionized many research areas in the past decades.

The aforementioned applications for mesoporous silicas were still limited by the lack of control on the morphology and particle size. The ability to control both the size and morphology of the material and to obtain nano-sized silica particles broadens the spectrum of applications of mesoporous silicas and/or improves their performances.[38-40] Mesoporous silica nanoparticles (MSN) can be obtained by similar procedures to that of bulk mesoporous silica. Thus, the MSN of MCM-41 type can be made from tetraethoxysilane (TEOS) by a microemulsion method in alkaline medium using a cationic surfactant (CTAB). The silica nanoparticles are isolated after centrifugation of the colloidal dispersion and the surfactant is removed.[41, 42]

As mesopores typically span between 2 and 50 nm in size, it becomes feasible to attain size-selectivity targeting diverse chemicals by regulating the pore diameters. This regulation permits the passage of chemicals while barring larger interfering compounds. The size-exclusion phenomenon exhibited by mesoporous materials finds extensive application in separation chemicals from intricate sample matrices in analytical chemistry.[43] The pore volume of mesoporous materials determines the loading of significant quantities of molecules into their mesopores.

Mesoporous materials boast abundant surface physicochemical properties, facilitating facile and diverse functionalization with a deal of molecules, which empowers mesoporous materials with functionalities extending beyond their inherent chemical composition and structure.[44] Another most distinctive characteristics of mesoporous materials is their large specific surface area. This remarkable characteristic endows mesoporous materials with abundant active sites.[45] The presence of interconnected (ordered) mesopores provide favorable conditions for the diffusion of molecules within the mesopores, thereby augmenting the contact between guest molecules and binding sites.[46] The pore connectivity becomes particularly crucial in situations where reactions are diffusion-controlled.

For *in vivo* biomedical applications, it is of paramount importance to ensure that nanoparticles effectively carry out their intended function without causing any histopathological lesions or abnormalities. While silica is generally regarded as non-toxic at low doses and has been utilized in the pharmaceutical industry as an excipient for many years,[47, 48] the long-term effects of MSNs *in vivo* must be thoroughly evaluated. The biocompatibility of MSNs is contingent upon various factors including particle size, morphology, structure, surface properties, and dosage.[49, 50] At lower concentrations, MSNs have been found to be non-toxic in numerous cell lines. However, at higher concentrations, they may exhibit inhibitory effects on cells. Therefore, careful consideration and assessment of these factors are essential for the safe and effective utilization of MSNs in biomedical applications.

The surface area of nanoparticles correlates positively with their toxicity. Small-sized nanoparticles with large surface areas and abundant silanol groups have the potential to generate reactive oxygen species (ROS), which contribute to nanoparticle-induced injuries.[51] The pore architecture of silica nanoparticles also significantly influences their biocompatibility. *In vitro* and *in vivo* toxicological investigations on spherical 100 nm MSNs reveal that they do not induce contact hypersensitivity. Additionally, they exhibit lower cytotoxicity and reduced inflammatory responses, which is both time and dose-dependent, compared to their colloidal solid counterparts.[52, 53]

1.3 Organic-inorganic hybrid nanomaterials

Hybrid organic-inorganic nanomaterials represent a burgeoning class of multifunctional nanomaterials that typically incorporate two or more different materials, often combining inorganic and organic components.[54] Inorganic components commonly include materials such as gold or other metals, silica, iron oxide or other metal oxides, quantum dots, among others. Organic components typically encompass ligands, biomolecules, polymers, and similar organic substances. Organic-inorganic nanocomposites

have the capability to integrate the functionalities of both organic and inorganic components, potentially resulting in synergistic effects in various applications.[55]

The hybrid organic-inorganic nanomaterials can inherit the morphology (size and porosity) and the properties (magnetic, optical and chemical properties) from the inorganic component.[56] The organic moieties render the hybrid materials different functional groups and functions. The organic and inorganic components of nanocomposites have the capacity to enhance mutually, leading to the emergence of synergistic properties instead of the simple sum of the two individual contributions. According to the interaction between organic and inorganic parts, these nanomaterials can be categorized into two classes. In the first class of nanomaterial, organic and inorganic components are combined through weak interactions such as hydrogen bond, Van der Waals forces and electrostatic bonds. In the other class of nanomaterial, the two components are linked to each other through strong chemical bonds.[57-59]

Two main families of organic-inorganic hybrid nanomaterials are metal-organic frameworks (MOFs) and organosilica NPs. MOFs are constructed from metal containing nodes (secondary building units, SBUs) and organic linkers.[60] In 1999, Yaghi et al.[61] published findings on MOF-5 (Scheme 1.5), marking the debut of a framework showcasing enduring porosity while evading structural collapse upon the extraction of guest solvent molecules from its pores. The methods for the synthesis, activation, and characterization of MOFs have been sufficiently explored.

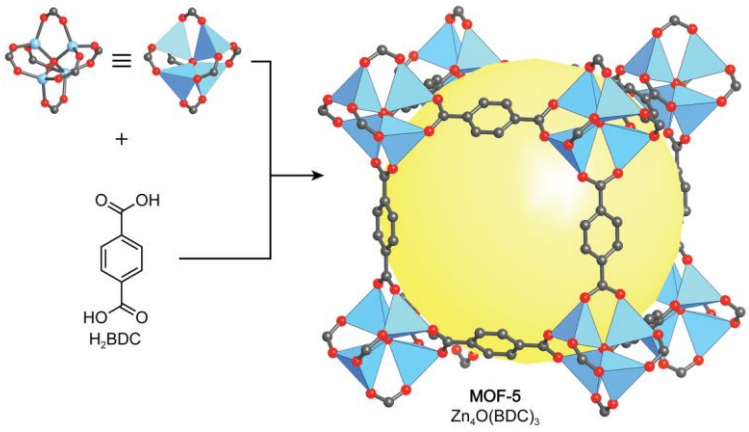

Scheme 1.5 Preparation and structure of MOF-5[61]

The organic constituents of MOFs consist of ditopic or polytopic organic carboxylates (and analogous negatively charged molecules). When these units are connected to metal-containing entities, they produce structurally resilient crystalline MOF frameworks characterized by a typical porosity exceeding 50% of the MOF crystal volume. The surface area measurements of such MOFs usually fall within the range of 1000 to 10,000 m^2/g, surpassing those of conventional porous materials like zeolites and

carbons.[62]

The other main class of hybrid organic-inorganic nanomaterials mentioned above are organosilica nanoparticles, which will be discussed in the next sections as they constitute the object of this thesis.

1.4 Organosilica nanoparticles and functionalized MSNs

Silica-based organic-inorganic hybrids are highly appealing materials due to their ability to amalgamate the properties of a rigid three-dimensional silica network with the distinctive chemical reactivity of the organic component(s) within a single solid structure. While tetraalkoxysilane does contain carbon, the resulting silica particles do not retain any carbon due to the hydrolysis process. Hence, they are termed "inorganosilica" particles. On the other hand, "organosilica" particles refer to silica particles containing carbon, typically accompanied by organic or functional groups.

The preparation of organosilicas is based on the sol-gel process of tetraalkoxysilanes with the addition of organosilanes during or after the procedure. The majority of organosilanes utilized for the functionalization are trialkoxysilanes, characterized by the general formula R-Si(OR')$_3$, where R represents an organic substituent and OR' denotes a hydrolyzable substituent. Similarly, organosilica nanoparticles can be synthesized through the co-condensation of a tetraalkoxysilane, typically tetraethyl orthosilicate (TEOS), and a trialkoxysilane precursor in an ethanol/water mixture or pure water media. Alternatively, they can be prepared via post-grafting of silica nanoparticles with an organosilane in a dried organic solvent.

1.4.1 Nonporous organosilica nanoparticles

Nonporous organosilica nanoparticles are prepared without template. The co-condensation and post-grafting methods for the preparation of these NPs are explained here.

1.4.1.1 Co-condensation

Organosilica nanoparticles can be synthesized similarly to pure silica nanoparticles through sol-gel methods. The process involves the co-condensation of silica precursors (such as tetraalkoxysilanes) with organo(alkoxy)silanes (bearing R-Si(OR')$_3$ environments) usually under basic conditions in the absence of surfactant. This process facilitates the incorporation of organic functionalities into the silica matrix, imparting the desired properties to the resulting materials. However, most organic substituents of the organosilane are buried in the nonporous silica matrix.

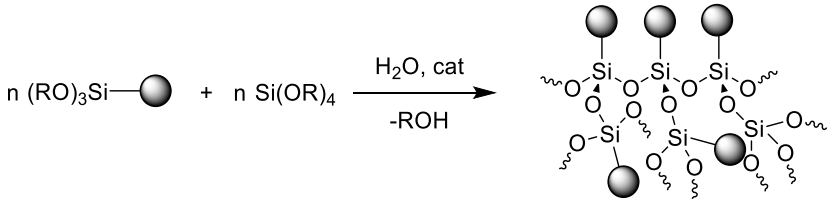

Scheme 1.6 Co-condensation method for the preparation of nonporous organosilica nanoparticles

1.4.1.2 Post-grafting

Some methodologies outlined in existing literature detail the synthesis of silica nanomaterials with adjustable shapes and porosity. Hence, it is alluring to begin with a well-characterized silica nanomaterial, followed by post-functionalization with suitable organosilanes. A typical post-functionalization protocol involves stirring a combination of silica nanomaterial and organo(alkoxy)-silane in refluxing toluene (Scheme 1.7). It's worth noting that drying the silica support and solvents before grafting is frequently considered a necessary step to prevent uncontrolled self-condensation of the organosilane reagent away from the surface, particularly in the presence of residual water molecules.

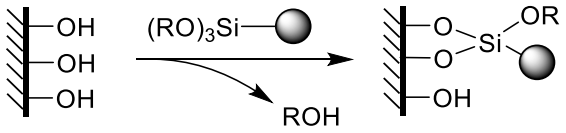

Scheme 1.7 Post-grafting functionalization of nonporous organosilica nanoparticles

1.4.1.3 Organosilanes for the preparation of organosilica nanoparticles

Some common organosilanes such as methyltrimethoxysilane (MTMS), vinyltriethoxysilane (VTES), (3-mercaptopropyl)trimethoxysilane (MPTMS), 3-aminopropyltriethoxysilane (APTES), (3-azidopropyl)triethoxysilane, (3-isocyanatopropyl)triethoxysilane, etc. are shown in Figure 1.2. With these common organosilanes, the silica nanoparticles could be endowed with versatile functional groups. Apart from these commercial organosilanes, various derivatives could be prepared based on aminopropyl or chloropropyl moieties to achieve more complex structures.

The application of (3-azidopropyl)triethoxysilane has garnered significant attention. The compound is increasingly utilized either for the formation of P-N linkages via the Staudinger reaction or for the synthesis of robust triazole linkers through the copper-catalyzed azide-alkyne cycloaddition reaction, commonly known as CuAAC. Also the (3-isocyanatopropyl)triethoxysilane has found extensive use for the formation of silylated carbamate and urea derivatives by reaction with alcohols and amines, respectively. Some other commercially available organo(alkoxy)silanes with functionalities like amino, mercapto, and iso(thio)cyanato are also extensively employed in the production of materials amenable

to post-functionalization. Developing advanced organosilanes necessitates intricate synthesis conditions. Organo(alkoxy)silanes, known for their sensitivity to moisture, demand meticulous preparation and storage under dry and inert environments.

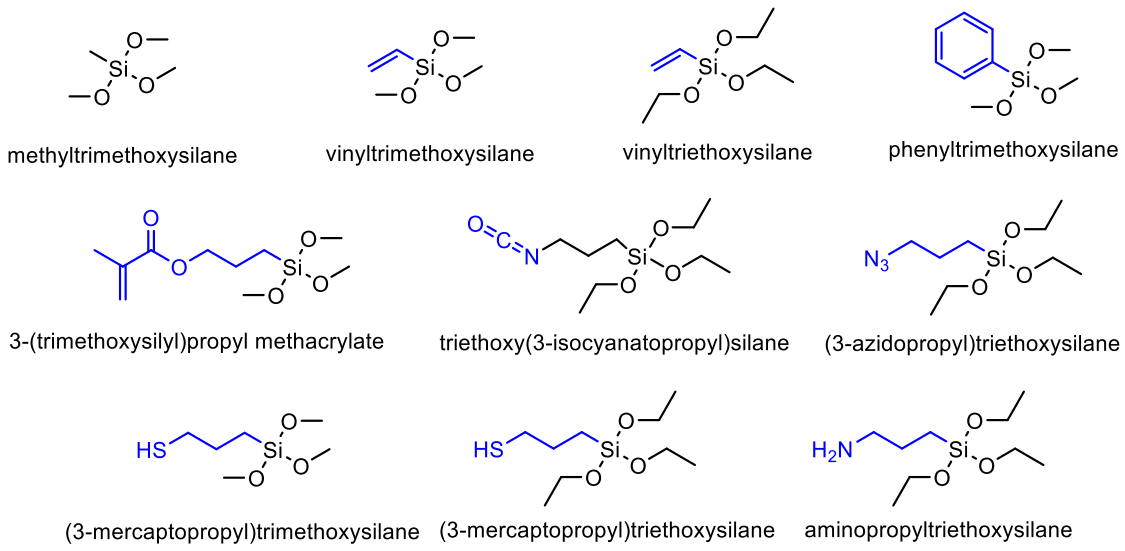

Figure 1.2 Common organosilanes for the preparation of organosilica nanoparticles

1.4.2 Periodic mesoporous organosilica nanoparticles

Since the research groups of Inagaki, Ozin and Stein independently described the first periodic mesoporous organosilica (PMO) materials in 1999,[63-65] many groups have developed versatile bulk PMO materials.[66-68] Then the materials reached nanoscale with different synthesis strategies such as hard and soft templates.[69] The approach leading to periodic mesoporous organosilica NPs involves the utilization of bridged silsesquioxane $(R'O)_3Si\text{-}R\text{-}Si(OR')_3$ precursors, either alone or in conjunction with tetraalkoxysilane. These precursors are co-condensed in the presence of a structure-directing agent, resulting in mesoporous silica nanoparticles with organically modified frameworks (Scheme 1.8). In this method, the organic groups are integrated into the mesopore walls, and the full incorporation of these organic functionalities into the final hybrid material is ensured by the covalent bonding of the silica source to the organic moieties. A vast array of bridged silsesquioxanes bearing 2, 3, or 4 alkoxysilane arms have been employed in this process, and several synthesis strategies have been applied to produce a diverse range of periodic mesoporous organosilica NPs. As in this case the organic units are integrated into the three-dimensional network structure of the silica matrix via two covalent bonds, they are distributed entirely homogeneously throughout the pore walls.[70, 71]

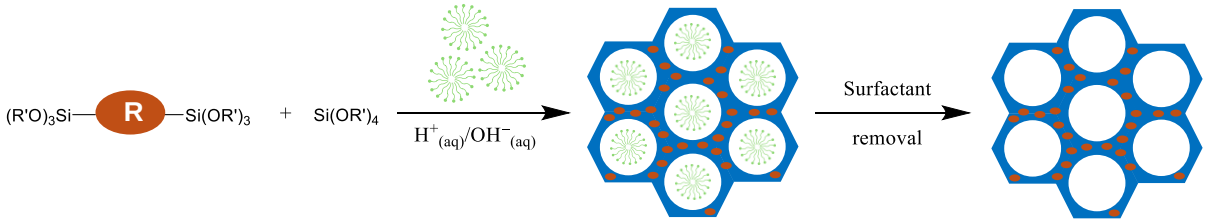

Scheme 1.8 Co-condensation method for the preparation of periodic mesoporous organosilica nanoparticles

1.4.3 Mesoporous organosilica nanoparticles

The advent of organically-functionalized silica-based materials represents a significant breakthrough, greatly expanding the scope of applications for mesoporous silicas by enabling precise control over their structural and, particularly, chemical properties. Mesoporous organosilica nanoparticles can be synthesized through a co-condensation procedure in the presence of a surfactant (structure-directing agent) or by post-grafting methods.

1.4.3.1 Co-condensation

The co-condensation method leverages the versatility of the sol-gel process by facilitating the hydrolysis and co-condensation of tetraalkoxysilane alongside one or more organo-alkoxysilanes in the presence of a template. This results in the formation of organic-inorganic hybrid mesoporous materials characterized by an ordered silica framework, with mesopore walls adorned with pendant organic groups (R in Scheme 1.9). This strategy can be employed to produce mesostructures modified with a diverse array of organo-functional moieties.

The co-condensation route offers several advantages over the post-grafting method, including easier control over the amount of incorporated organo-functional groups, which are typically more uniformly distributed throughout the material. It also tends to induce smaller effects on porosity reduction upon functionalization and requires shorter preparation times. However, exceeding a certain threshold of organosilane content (typically above 20% relative to the total amount of precursors in the starting sol) can lead to a significant decline in the level of mesoporous ordering in the final hybrid material.[72]

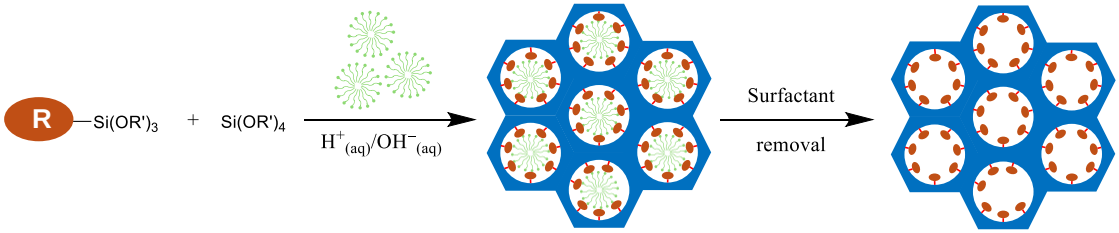

Scheme 1.9 Co-condensation method for the preparation of mesoporous organosilica nanoparticles

1.4.3.2 Post-grafting of MSNs

Achieving precise control over texture poses a significant challenge when employing the sol-gel co-condensation method, particularly for those aiming to engineer materials with meticulously defined pore structure and morphology. Alternatively, MSNs with different porosity could be prepared with the addition of surfactants in advance.[73] Then the organosilanes of the type $(R'O)_3Si$-R react with the free and geminal silanols on the surface and inner wall of MSNs (Scheme 1.10). In principle, functionalization with a variety of organic groups could be achieved by varying the organic residue R in this manner. The modification method offers the advantage that, under the synthetic conditions employed, the mesostructure of the initial silica phase is typically preserved.

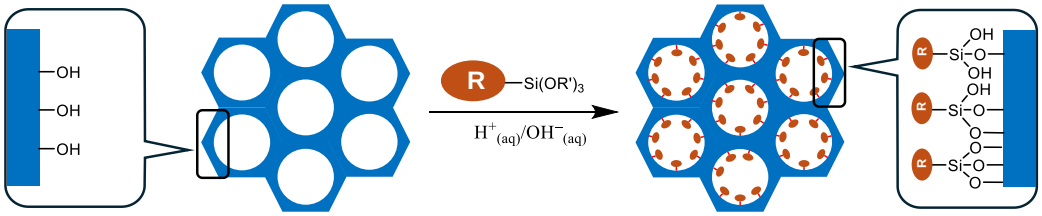

Scheme 1.10 Post-grafting method for mesoporous organosilica nanoparticles

Although quite popular, the grafting methods suffer from several important drawbacks. Indeed, due to diffusion issues, grafting preferentially occurs on the external surface and at pore entrances, before taking place inside the pores. This can even lead to pore-blocking phenomena when voluminous functions are incorporated. Furthermore, the number of grafted functions is not predictable, as this depends on the steric hindrance of the silane used, the solvent and other reaction parameters. Aggregation of the grafted organics can also be observed, when organic groups that are able to self-assemble are used.[74]

1.5 Characterization methods

The methods used to characterize organosilica nanoparticles can be categorized into two primary groups: those aimed at structural, morphological, and textural analyses, and those specifically focused on characterizing the functional groups attached to the silica framework.

The first category encompasses various physicochemical techniques routinely applied to characterize silica nanomaterials. These techniques include electron microscopies, such as scanning electron microscopy (SEM) for morphological information and high-resolution transmission electron microscopy (HRTEM) for visualizing the organized structure at the nanometer scale and evaluating the degree of three-dimensional order. Additionally, powder X-ray diffraction (p-XRD) and/or electron diffraction (ED) techniques are employed to determine the mesostructure types, while gas physisorption porosimetry (BET analysis) is utilized to measure pore volumes, specific surface areas, and pore size distribution. Dynamic light scattering (DLS) is a rapid technique used to measure the mean hydrodynamic diameter and distribution of nanoparticles in solution.

The second category, more specific to organic-inorganic hybrid nanomaterials, comprises various spectroscopic techniques aimed at providing information on the effective incorporation and integrity of organic groups within the silica matrix. Nuclear magnetic resonance (NMR), particularly 29-silicon magic angle spinning nuclear magnetic resonance (^{29}Si MAS-NMR) with proton decoupling, is a highly efficient technique for assessing the degree of condensation through siloxane signals (denoted as Q^n = Si-$(OSi)_n$-$(OH)_{4-n}$, where n = 2-4) and evaluating the effectiveness of covalent bonding of organosilane moieties to the silica framework through organosiloxane signals (denoted as T^m = RSi-$(OSi)_m$-$(OH)_{3-m}$, where m = 1-3) appearing in the spectra. Powder X-ray diffraction is commonly employed to examine any potential structural alterations upon functionalization, while gas physisorption experiments are typically conducted to measure porosity data in materials prepared via one-step co-condensation or post-synthesis grafting. Other spectroscopic techniques such as infrared (IR) and ultraviolet-visible (UV-Vis) spectroscopy can also be utilized to obtain information on the chemical composition of materials, including the nature and chemical form of ligands. Additionally, thermogravimetric measurements (TGA) and elemental chemical analyses (EA) are employed for quantitative analysis of incorporated organic groups.

1.5.1 Electron microscopy

Electron Microscopy serves as a powerful tool for acquiring high-resolution images of micro/nano materials. The morphology of the material can be thoroughly investigated using both Scanning Electron

Microscopy (SEM) and Transmission Electron Microscopy (TEM). Electron microscopy encompasses a versatile array of methodologies for characterizing the microstructural features of a sample across length scales ranging from 100 picometers to 100 millimeters.[75]

Just as the name implies, SEM images the surface of a sample with a focused electron beam scanned across the sample's surface. When the electron beam interacts with the sample, it dissipates energy through various mechanisms. The lost energy is transformed into alternative forms, including heat, emission of low-energy secondary electrons and high-energy backscattered electrons, light emission (cathodoluminescence), or X-ray emission.[76] These signals contain valuable information about the surface properties, such as its topography and composition. To carry out the characterisation, the sample surface must be conductive. Nonconductive samples are typically coated with a layer of conductive material.[75] This instrument can also be paired with other complementary techniques such as energy-dispersive X-ray microanalysis (EDX, EDS, EDAX) to analyse the surface composition. Figure 1.3 shows some examples of silica nanoparticles and corresponding cotton fabrics in the thesis.

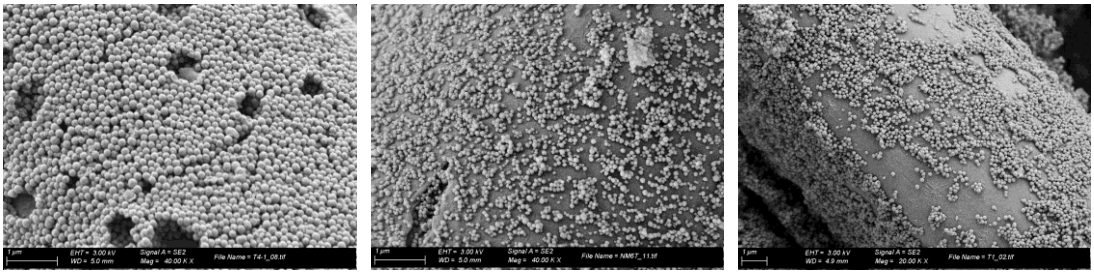

Figure 1.3 SEM images of different silica nanoparticles and coated cotton fabrics

However, SEM microscopes are primarily engineered to scrutinize material surfaces. Conversely, TEM microscopes are predominantly tailored to investigate the internal structure of specimens (porosity), and evaluate nanostructures such as particles, fibers and thin films. Electrons are accelerated through 80-300 kV accelerating voltage to obtain sufficient energy to pass through no more than 1 mm of material. An image is formed by transmitting a beam of electrons through a sample. Typically, the specimen is an ultrathin section less than 100 nanometers or a suspension on a grid. TEM was utilized to characterize the size and porosity of nanosilicas and some images taken in this thesis are shown in Figure 1.4.

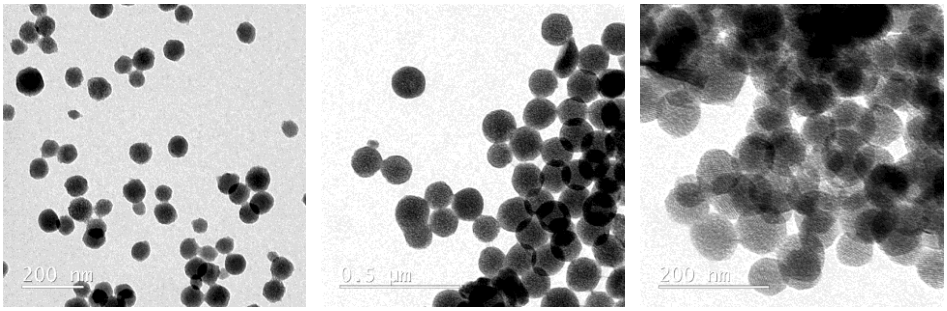

Figure 1.4 TEM images of different silica nanoparticles

1.5.2 Powder X-Ray Diffraction (XRD)

The powder X-Ray diffraction (XRD) technique is commonly employed for the analysis of nanoscale materials. Analysis of a sample via powder XRD yields crucial information about its diffraction pattern, such as phase identification, sample purity, crystallite size. X-ray diffraction techniques hinge upon three primary components: the X-ray source, the sample holder or stage and the detector (Figure 1.5). The characterization method is complementary to various microscopic and spectroscopic techniques. The diffraction of electromagnetic radiation or particles by matter serves as the fundamental principle underlying X-ray diffraction techniques.[77] Leveraging this physical phenomenon enables the extraction of fundamental structural information for solid materials. Whether your sample comprises a pristine single crystal or a polycrystalline array, diffraction data can offer essential insights into the structural characteristics of the sample.[78]

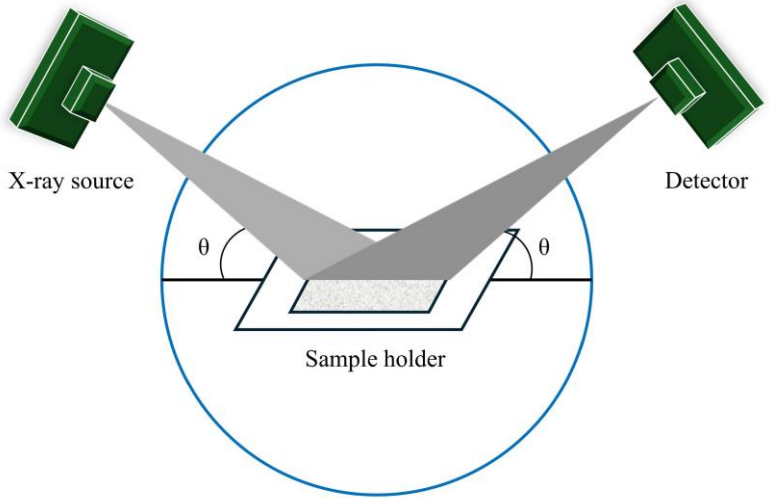

Figure 1.5 Instrument for powder X-ray diffraction

As X-ray photons traverse through the substance, they may undergo scattering or absorption processes, such as ionization or the photoelectric effect. However, it is the analysis of the scattered X-rays that furnishes valuable information regarding the characteristics of the crystallographic lattice. The wavelength of scattering for X-ray photons can either remain constant (coherent) or increase

(incoherent), and it is the coherent interactions that lead to diffraction phenomena. In coherent interactions, the X-ray beam interacts with electrons surrounding the nucleus, inducing oscillations with the same frequency as the electric field component of the electromagnetic wave. Consequently, radiation is emitted in all directions with the same wavelength as the incoming wave. In a periodic arrangement of atoms, such as a crystalline lattice, the X-ray beam can interact with numerous electrons. Coherently scattered waves may then undergo either destructive interference (reducing the wave's amplitude) or constructive interference (increasing magnitude). Constructive interference results in wave fronts that are in phase, leading to a cooperative scattering effect known as diffraction.[79]

Crystal habit serves as a distinguishing characteristic of mineral phases and is closely linked to the atomic arrangement within the material. Typically, the faces observed on highly crystalline specimens align parallel to the planes of atoms containing the highest density of lattice nodes. When an X-ray beam traverses through a crystal, diffraction may manifest as a "reflection", wherein the incident beam reflects out of the crystal from these parallel planes. However, for the diffraction effect to yield measurable intensity, reflections from individual planes must be in phase with each other, facilitating constructive enhancements.

Within the crystalline lattice, a set of parallel atomic planes can be delineated, with each plane separated by a characteristic distance denoted as d (Figure 1.6). X-rays incident upon the first plane undergo reflection at the incident angle, θ. For diffraction to be detectable, these reflections must be reinforced by in-phase reflections from other atomic planes at integral values.

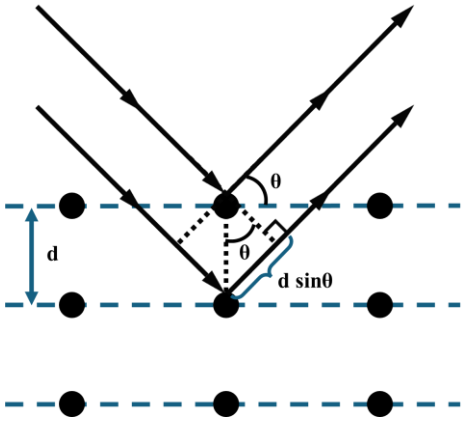

Figure 1.6 Diffraction of the incident X-ray beam by atomic planes

If beams diffracted by two different layers are in phase, constructive interference occurs, leading to the appearance of a peak in the diffraction pattern. Conversely, if they are out of phase, destructive interference occurs, resulting in the absence of a peak. Diffraction peaks only emerge if the conditions for constructive interference are satisfied (Equation 1.1).[80]

$$sin\,\theta = \frac{n\lambda}{2d}$$

Equation 1.1 Bragg's Law, θ: the angle of incidence of the X-ray, n: an integer, λ: the wavelength, d: the interplanar spacing

When a material is structured, well-defined peaks are evident in the plot and from their arrangement, the type of organization (hexagonal, lamellar, cubic, worm-like, etc.) can be discerned. Conversely, amorphous materials do not yield distinct signals. Small-angle X-ray scattering (SAXS) is a method wherein the X-ray scattering arises from the inhomogeneities within the sample on a nanometer scale. SAXS patterns are typically captured at extremely low angles, usually below 10°. Within this range, details regarding the shape, size, and distances of the irregularities, such as clusters or nanoparticles within an organic matrix, can be obtained. The narrower and stronger peaks indicate better pore structure ordering and, inversely, wider and weaker peaks indicate disordered mesostructure.[81]

1.5.3 Dynamic Light Scattering (DLS)

Dynamic light scattering (DLS) is employed to determine the hydrodynamic radius of both the silica nanoparticles and the functionalized nanosilica samples. It is also used to ascertain whether there has been an increase in the particle size following functionalization. Indeed, dynamic light scattering (DLS) measures the temporal fluctuations of light scattered due to the Brownian motion of particles when a solution containing the particles is subjected to a monochromatic beam of light. This technique yields particle size information, typically reported in terms of hydrodynamic diameter, along with the polydispersity index (PDI) of the sample. The PDI is utilized to characterize the particle size distribution. Calculation of the polydispersity index is achieved through the cumulant method. A PDI value below 10% signifies a monodisperse sample, suggesting that all measured particles possess nearly identical sizes.

The fundamental configuration of a DLS apparatus is illustrated in Figure 1.7. A laser emitting at a specific frequency is oriented towards the sample confined within a cuvette. The laser light undergoes scattering in various directions. The scattered light is subsequently captured by the detector at a designated angle over a period, and this data is employed to ascertain both the diffusion coefficient and particle size according to the Stokes-Einstein equation (Equation 1.2).[82]

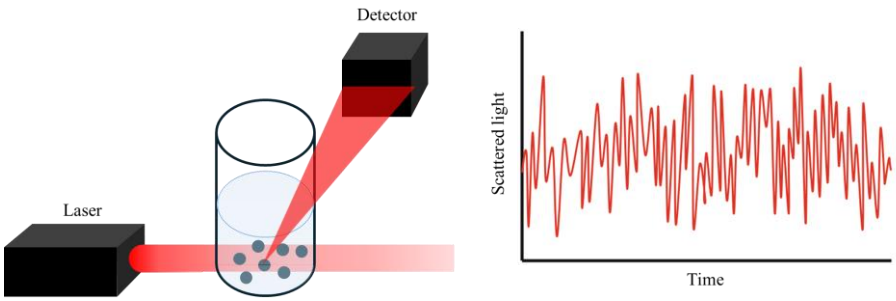

Figure 1.7 The fundamental configuration of a DLS apparatus

The analysis of the autocorrelation derived from temporal fluctuations in scattering intensity enables

the determination of the diffusion coefficient. Under the assumption of spherical and uniform particles, the hydrodynamic radius can then be calculated using the Stokes-Einstein equation.

$$D = \frac{k_B T}{3\pi\eta d}$$

Equation 1.2 Stokes-Einstein equation, D: Diffusion coefficient, k_B: Boltzmann constant, T: Temperature, η: Viscosity, d: Hydrodynamic diameter

1.5.4 Zeta potential

Zeta potential is the surface charge property inherent to the nanoparticles in suspension and this characterization of the nanoparticles is usually utilized with DLS at the same time. The zeta potential serves as a significant and easily measurable indicator of colloidal dispersions' stability.[83] Its magnitude reflects the extent of electrostatic repulsion between surrounding particles that bear similar charges within a dispersion. Table 1.2 shows the relationship between the values of zeta potential and the stability of the colloidal solution. Colloids with high zeta potential, whether negative or positive, are electrically stabilized, whereas colloids with low zeta potentials tend to coagulate or flocculate.

Table 1.2 Stability of a colloid depending on the Zeta potential

Zeta potential (mV)	Stability
0 to ± 5	Rapid coagulation or flocculation
± 10 to ± 30	Incipient instability
± 30 to ± 40	Moderate stability
± 40 to ± 60	Good stability
⩾ ± 60	Excellent stability

Particles dispersed in the liquid typically carry either positive or negative charges. To preserve electrical neutrality, ions with an opposite charge to that of the particles accumulate on the particle surface. When a group of ions envelops the particle surface and gathers in a spherical arrangement, the charged layer is surrounded by a layer bearing the opposite charge (Figure 1.8). This situation is referred to as the formation of an "electrical double layer" (EDL). However, the ionic layer in the liquid is not as straightforward. The distribution of ions is perturbed by thermal motion, leading to a high concentration of ions with an opposite charge in the vicinity of the surface, gradually decreasing as they move away from the surface. Conversely, particles and charged ions exhibit an opposing distribution. At distances far from the particles, the positive and negative ion charges cancel each other out to maintain electrical neutrality. The condenser-type double layer described above manifests as a "diffuse electrical double layer" in the liquid. This term characterizes the gradual blurring of the ion distribution with the opposite

charge as it moves away from the surface.[84]

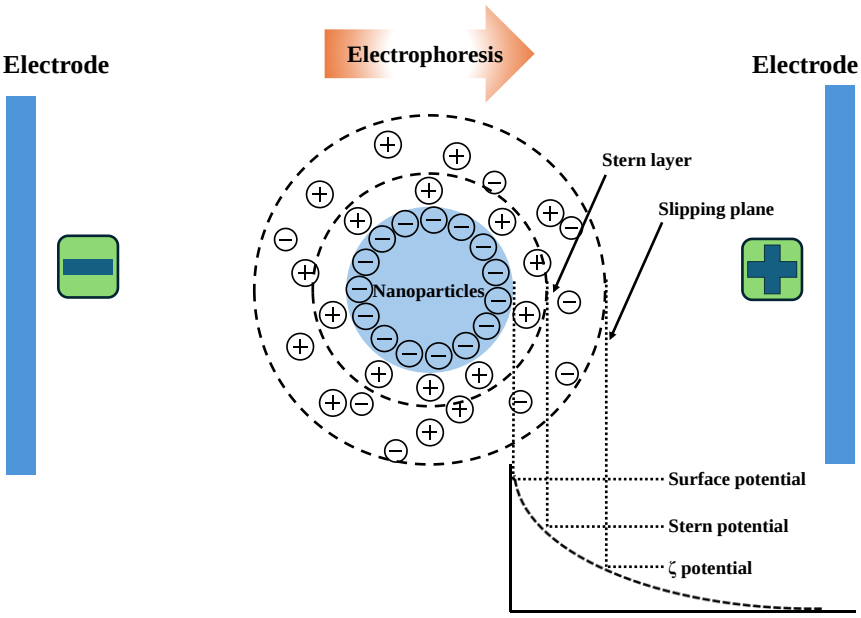

Figure 1.8 The electrical double layer surrounding a negatively charged particle

In contrast to the diffuse ion distribution away from the particle surface, the ion distribution on the inner particle surface remains distinct and unblurred. The diffuse electrical double layer is named with a focus on the diffusion layer. It's important to note that the diffusion layer does not necessarily exist in the immediate vicinity of the surface. Some ions are frequently strongly attracted to the surface and become immobilized. These layers are referred to as fixed layers, sometimes known as the Stern layer (Figure 1.8).

The charge associated with the particles directly influences their behaviours and is measurable. It is understood that particles move along with the fixed layer and an inner portion of the diffuse layer. The surface where this movement occurs is termed the slipping plane. By defining the potential of a region sufficiently electrically neutral away from the particles as zero, the zeta potential is then defined as the potential of the slipping plane relative to this zero-point. In the case of fine particles, a higher absolute value of the zeta potential indicates stronger repulsive forces between the particles and greater dispersion stability. Conversely, when the zeta potential approaches zero, particles are more prone to aggregation. Therefore, zeta potential serves as an indicator of the dispersion stability of dispersed particles.[85]

Zeta potential measurements involve applying an electrical field across the sample and monitoring the movement of nanoparticles (electrophoretic mobility) using laser Doppler velocimetry (LDV). The Henry equation (Equation 1.3) is subsequently employed to determine the zeta potential (ζ). The equation used to calculate the zeta potential includes parameters such as U_e (electrophoretic mobility), ε (dielectric constant), η (absolute zero-shear viscosity of the medium) and $f(\kappa\alpha)$, Henry function, where

κα represents the ratio of the particle radius to the Debye length.[86]

$$U_e = \frac{2\varepsilon\zeta f(\kappa\alpha)}{3\eta}$$

Equation 1.3 Henry equation

1.5.5 Surface area analysis

Surface area analysis serves as a prevalent method for measuring nanoparticle properties, offering insights into a material's adsorption and desorption characteristics. Since solid particles predominantly interact with other media through their surface area, analysing this aspect proves vital. By evaluating the volume of an inert gas that a material can adsorb and the pressure necessary to push the gas into a porous structure, it becomes possible to ascertain various characteristics of the material.[87]

The Langmuir theory, developed by Irving Langmuir in 1916, establishes a connection between the monolayer adsorption of gas molecules (referred to as adsorbates) onto a solid surface and the gas pressure of a medium above the solid surface at a constant temperature, as depicted in Figure 1.9a. This relationship is described by Equation 1.4.[88]

$$\frac{V}{V_m} = \frac{\alpha \cdot P}{1 + \alpha \cdot P}$$

Equation 1.4 Langmuir equation V: the volume of gas adsorbed onto the solid, V_m: the volume of a monolayer of gas molecules covering the whole surface of the solid completely occupied by the adsorbate, P: the gas pressure, α: a constant.

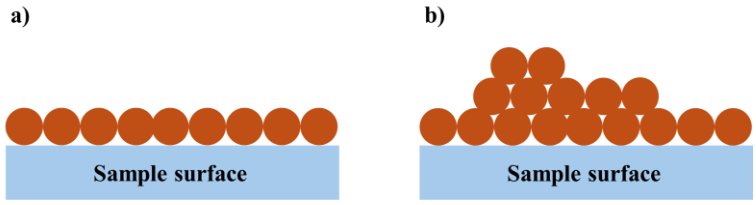

Figure 1.9 Adsorption of gas molecules onto the surface of a sample showing a) the monolayer adsorption model assumed by the Langmuir theory and b) the multilayer adsorption model assumed by the BET theory.

The BET theory was developed by Stephen Brunauer, Paul Emmett, and Edward Teller in 1938, extending the Langmuir theory to multilayer adsorption (Figure 1.9b).[89]

Adsorption is the process whereby atoms or molecules of gas adhere to a surface. The quantity of gas adsorbed relies not only on the exposed surface area but also on factors like temperature, gas pressure, and the strength of interaction between the gas and solid. In BET surface area analysis, nitrogen is commonly utilized due to its high purity and strong interaction with most solids. As the interaction

between gaseous and solid phases tends to be weak, the surface is cooled using liquid nitrogen to facilitate detectable amounts of adsorption. Nitrogen gas is incrementally released into the sample cell in known amounts. By creating conditions of partial vacuum, relative pressures lower than atmospheric pressure are achieved. Once saturation pressure is reached, no further adsorption occurs regardless of any additional pressure increase. Pressure changes during the adsorption process are meticulously monitored by highly precise and accurate pressure transducers. Following the formation of adsorption layers, the sample is removed from the nitrogen atmosphere and heated to release the adsorbed nitrogen from the material, which is then quantified. The data obtained is illustrated in the form of a BET isotherm, plotting the quantity of gas adsorbed against the relative pressure.[90] There are five potential types of adsorption isotherms.[91] In the 1985 IUPAC recommendations physisorption isotherms were grouped into six types. However, over the past 40 years various new characteristic types of isotherms have been identified and shown to be closely related to particular pore structures. The proposed updated classification of physisorption isotherms is shown in Figure 1.10.[92]

Nitrogen and argon adsorption isotherms at 77 K and 87 K typically exhibit Type I (a) isotherms for microporous materials, characterized by predominantly narrow micropores (width < 1 nm). Conversely, Type I (b) isotherms are observed for materials with pore size distributions spanning a broader range, encompassing both wider micropores and potentially narrow mesopores (< 2.5 nm). Reversible Type II isotherms are typically associated with the physisorption of most gases on nonporous or macroporous adsorbents. Type III isotherms indicate relatively weak adsorbent-adsorbate interactions, with the adsorbed molecules clustering around the most favourable sites on the surface of a nonporous or macroporous solid. Type IV isotherms are typically observed with mesoporous adsorbents. Hysteresis accompanies capillary condensation in the case of a Type IV (a) isotherm. Adsorbents with narrower mesopores display fully reversible Type IV (b) isotherms.

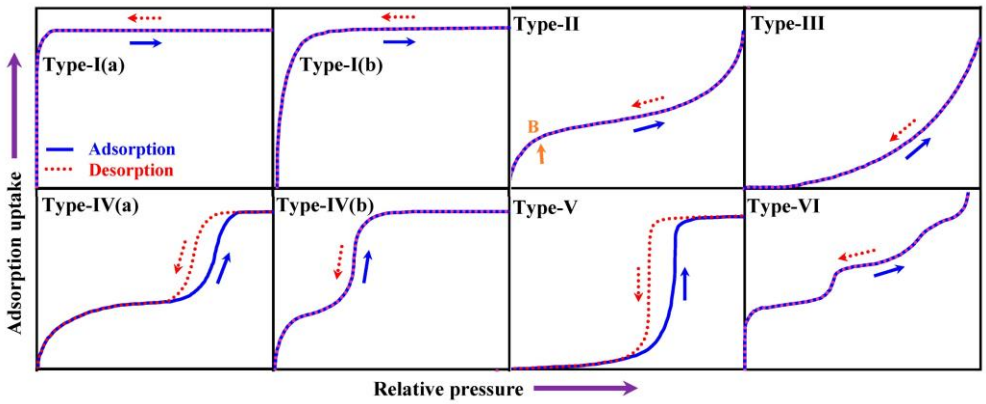

Figure 1.10 Classification of physisorption isotherms

The Type V isotherm shape resembles Type III at low P/P_0 values, indicating relatively weak adsorbent-

adsorbate interactions. At higher P/P_0, molecular clustering occurs before pore filling. The reversible stepwise Type VI isotherm represents layer-by-layer adsorption on a highly uniform nonporous surface.

The BET Equation (Equation 1.5) uses the information from the isotherm to determine the surface area of the sample.[93]

$$\frac{V}{V_m} = \frac{C \cdot \frac{P}{P_0}}{\left(1 - \frac{P}{P_0}\right)\left[1 + (C-1)\frac{P}{P_0}\right]}$$

Equation 1.5 V: the volume of nitrogen adsorbed at P/P_0, V_m: monolayer capacity, which is the volume of gas adsorbed, P: the equilibrium pressure, P_0: the saturation pressure of adsorbates at the temperature of adsorption, C: constant.

1.5.6 Fourier Transform Infrared spectroscopy (FTIR)

Fourier Transform Infrared spectroscopy (FTIR) can be used to identify qualitatively the functional groups of the sample and various chemical bonds by the different molecular vibrations. However, the application of the technique in organosilica materials is limited by the low organic proportion. The vibration signals due to Si-O-Si (around 1000 cm^{-1}) and silanol (Si-OH) species (3500-3200 cm^{-1}) are the principal ones in the IR spectrum.[94]

1.5.7 Elemental analysis

The method involves the combustion of the sample in a high-temperature stream of oxygen and the quantitative analysis of the combustion gases using gas chromatography. The combustion gases generated are directed by a stream of helium (He) towards a reactor containing WO_3 and Cu. This reactor converts the various gases into CO_2, H_2O, N_2, and SO_2, while retaining any excess of oxygen. Subsequently, the helium stream transports the gas mixture to a gas chromatograph where they undergo separation, record (using a thermal conductivity detector), and quantification. By quantitative determination of C, H, N and/or S in substances, the amount of organic portion in samples can be determined. In this thesis, the loading amount of different organic molecules in the nanomaterials was determined by elemental analysis of nitrogen.

1.5.8 Solid-state ^{13}C CP MAS and ^{29}Si CP MAS NMR spectroscopy

The application fields of solid-state NMR are very diverse, including the characterization of polymers, glasses, amorphous material, catalytic material on a solid support, insoluble samples and so on. By combining cross polarization (CP) (to enhance the signal of a dilute nuclei with a low gyromagnetic ratio) and magic angle spinning (MAS) (to generate narrower NMR and more intense NMR lines),[95]

the high-resolution solid-state NMR is obtained, which is also called cross polarization magic angle spinning (CP MAS) nuclear magnetic resonance.

The ^{13}C CP MAS NMR is a spectroscopic method to confirm the presence of the organic moiety in the solid materials, particularly silica in this thesis. The peak position is similar to that of the corresponding pure organic molecule in liquid phase, but the signal is broader. It can only provide qualitative information.

With the ^{29}Si CP MAS NMR, we can differentiate various local silicon environments within a sample and establish correlations with their compositions. The chemical shifts of ^{29}Si NMR spectra are highly responsive to the chemical environment of silicon, particularly the connections with oxygen and carbon nuclei. The signals are divided into four groups: M, D, T and Q, indicating silicon atoms forming one, two, three and four Si-O bonds, respectively. Frequently, a superscript "n" is also denoted; when only silicon, carbon, or proton atoms are found in the second coordination sphere, "n" signifies the count of silicon atoms additionally bonded to the focal Si through Si-O-Si bonds (Figure 1.11).[96]

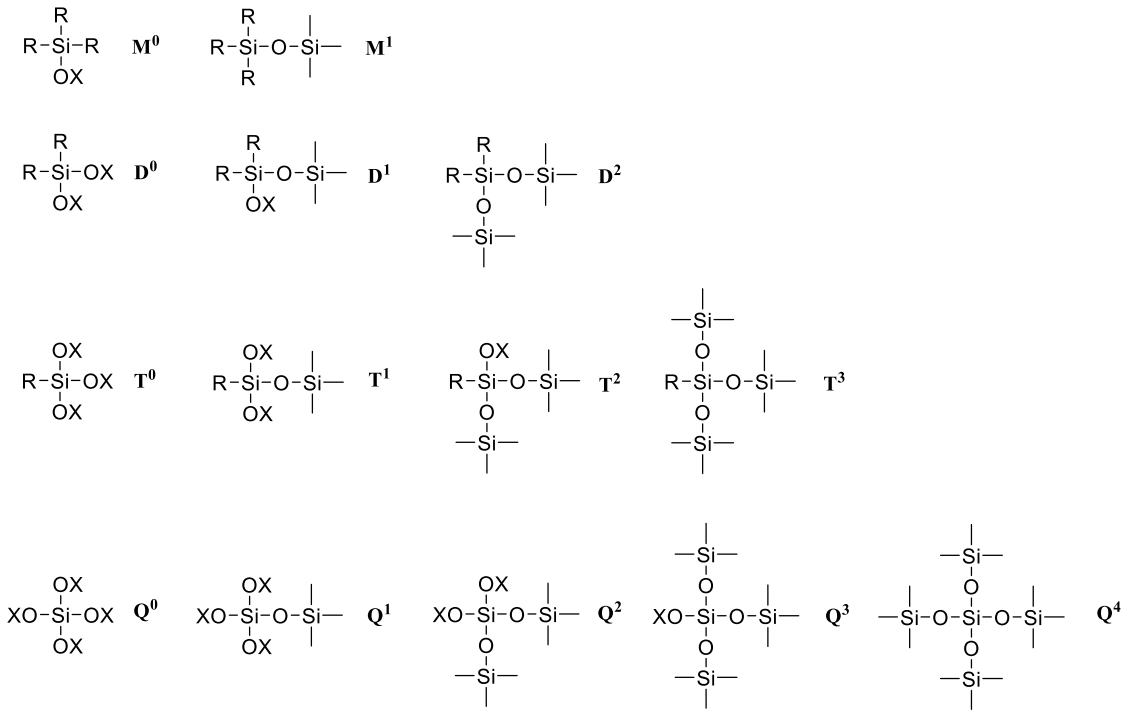

Figure 1.11 Silicon environments and their corresponding label in the ^{29}Si CP MAS NMR spectroscopy

1.6 References

[1] Petkowski, J. J.; Bains, W.; Seager, S. On the Potential of Silicon as a Building Block for Life. *Life* **2020**, *10* (6), 84.
[2] Jugdaohsingh, R. Silicon and bone health. *The journal of nutrition, health & aging* **2007**, *11* (2), 99-110.
[3] Martin, K. R. Silicon: The Health Benefits of a Metalloid. In *Interrelations between Essential Metal Ions and Human Diseases*, Sigel, A., Sigel, H., Sigel, R. K. O. Eds.; Springer Netherlands, 2013; pp 451-473.
[4] Flörke, O. W.; Graetsch, H. A.; Brunk, F.; Benda, L.; Paschen, S.; Bergna, H. E.; Roberts, W. O.; Welsh, W. A.; Libanati, C.; Ettlinger, M.; et al. Silica. In *Ullmann's Encyclopedia of Industrial Chemistry*, 2008; pp 422-507.
[5] Roduner, E. Size matters: why nanomaterials are different. *Chemical Society Reviews* **2006**, *35* (7), 583-592.
[6] Zhang, P.; Qiao, Z.-A.; Dai, S. Recent advances in carbon nanospheres: synthetic routes and applications. *Chemical Communications* **2015**, *51* (45), 9246-9256.
[7] Chen, R.; Lee, J.; Lee, W.; Li, D. Thermoelectrics of Nanowires. *Chemical Reviews* **2019**, *119* (15), 9260-9302.
[8] Xue, J.; Xie, J.; Liu, W.; Xia, Y. Electrospun Nanofibers: New Concepts, Materials, and Applications. *Accounts of Chemical Research* **2017**, *50* (8), 1976-1987.
[9] Aspoukeh, P. K.; Barzinjy, A. A.; Hamad, S. M. Synthesis, properties and uses of ZnO nanorods: a mini review. *International Nano Letters* **2022**, *12* (2), 153-168.
[10] Mosquera, J.; Wang, D.; Bals, S.; Liz-Marzán, L. M. Surfactant Layers on Gold Nanorods. *Accounts of Chemical Research* **2023**, *56* (10), 1204-1212.
[11] Khan, F.; Shariq, M.; Asif, M.; Siddiqui, M. A.; Malan, P.; Ahmad, F. Green Nanotechnology: Plant-Mediated Nanoparticle Synthesis and Application. *Nanomaterials* **2022**, *12* (4), 673.
[12] Yang, M.; Zhang, C. H.; Li, N. W.; Luan, D.; Yu, L.; Lou, X. W. Design and Synthesis of Hollow Nanostructures for Electrochemical Water Splitting. *Advanced Science* **2022**, *9* (9), 2105135.
[13] Zou, H.; Luo, Z.; Yang, X.; Xie, Q.; Zhou, Y. Toward emerging applications using core–shell nanostructured materials: a review. *Journal of Materials Science* **2022**, *57* (24), 10912-10942.
[14] Harish, V.; Ansari, M. M.; Tewari, D.; Gaur, M.; Yadav, A. B.; García-Betancourt, M.-L.; Abdel-Haleem, F. M.; Bechelany, M.; Barhoum, A. Nanoparticle and Nanostructure Synthesis and Controlled Growth Methods. *Nanomaterials* **2022**, *12* (18), 3226.
[15] Du, H.; Xie, Y.; Wang, J. Nanomaterial-sensors for herbicides detection using electrochemical techniques and prospect applications. *TrAC Trends in Analytical Chemistry* **2021**, *135*, 116178.
[16] Wang, H.; Liang, X.; Wang, J.; Jiao, S.; Xue, D. Multifunctional inorganic nanomaterials for energy applications. *Nanoscale* **2020**, *12* (1), 14-42.
[17] Gómez-López, P.; Puente-Santiago, A.; Castro-Beltrán, A.; Santos do Nascimento, L. A.; Balu, A. M.; Luque, R.; Alvarado-Beltrán, C. G. Nanomaterials and catalysis for green chemistry. *Current Opinion in Green and Sustainable Chemistry* **2020**, *24*, 48-55.
[18] Gu, Y.; Xia, K.; Wu, D.; Mou, J.; Zheng, S. Technical Characteristics and Wear-Resistant Mechanism of Nano Coatings: A Review. *Coating* **2020**, *10* (3), 233.
[19] Diez-Pascual, A. M.; Rahdar, A. Functional Nanomaterials in Biomedicine: Current Uses and Potential Applications. *ChemMedChem* **2022**, *17* (16), e202200142.
[20] Singh, B.; Na, J.; Konarova, M.; Wakihara, T.; Yamauchi, Y.; Salomon, C.; Gawande, M. B. Functional Mesoporous Silica Nanomaterials for Catalysis and Environmental Applications. *Bulletin of the Chemical Society of Japan* **2020**, *93* (12), 1459-1496.
[21] Nayl, A. A.; Abd-Elhamid, A. I.; Aly, A. A.; Bräse, S. Recent progress in the applications of silica-based

nanoparticles. *RSC Advances* **2022**, *12* (22), 13706-13726.

[22] Corriu, R. J. P.; Leclercq, D. Recent Developments of Molecular Chemistry for Sol–Gel Processes. *Angewandte Chemie International Edition in English* **1996**, *35* (13-14), 1420-1436.

[23] Ciriminna, R.; Fidalgo, A.; Pandarus, V.; Béland, F.; Ilharco, L. M.; Pagliaro, M. The Sol–Gel Route to Advanced Silica-Based Materials and Recent Applications. *Chemical Reviews* **2013**, *113* (8), 6592-6620.

[24] Buckley, A. M.; Greenblatt, M. The Sol-Gel Preparation of Silica Gels. *Journal of Chemical Education* **1994**, *71* (7), 599.

[25] Manning, J. R. H.; Brambila, C.; Patwardhan, S. V. Unified mechanistic interpretation of amine-assisted silica synthesis methods to enable design of more complex materials. *Molecular Systems Design & Engineering* **2021**, *6* (3), 170-196.

[26] Singh, L. P.; Bhattacharyya, S. K.; Kumar, R.; Mishra, G.; Sharma, U.; Singh, G.; Ahalawat, S. Sol-Gel processing of silica nanoparticles and their applications. *Advances in Colloid and Interface Science* **2014**, *214*, 17-37.

[27] Li, H.; Chen, X.; Shen, D.; Wu, F.; Pleixats, R.; Pan, J. Functionalized silica nanoparticles: classification, synthetic approaches and recent advances in adsorption applications. *Nanoscale* **2021**, *13* (38), 15998-16016.

[28] Stöber, W.; Fink, A.; Bohn, E. Controlled growth of monodisperse silica spheres in the micron size range. *Journal of Colloid and Interface Science* **1968**, *26* (1), 62-69.

[29] Finnie, K. S.; Bartlett, J. R.; Barbé, C. J. A.; Kong, L. Formation of Silica Nanoparticles in Microemulsions. *Langmuir* **2007**, *23* (6), 3017-3024.

[30] Li, S.-R.; Huo, F.-Y.; Wang, H.-Q.; Wang, J.; Xu, C.; Liu, B.; Bu, L.-L. Recent advances in porous nanomaterials-based drug delivery systems for cancer immunotherapy. *Journal of Nanobiotechnology* **2022**, *20* (1), 277.

[31] Brinker, C. J. Hydrolysis and condensation of silicates: Effects on structure. *Journal of Non-Crystalline Solids* **1988**, *100* (1), 31-50.

[32] Croissant, J. G.; Fatieiev, Y.; Almalik, A.; Khashab, N. M. Mesoporous Silica and Organosilica Nanoparticles: Physical Chemistry, Biosafety, Delivery Strategies, and Biomedical Applications. *Advanced Healthcare Materials* **2018**, *7* (4), 1700831.

[33] Steinbach, J. C.; Fait, F.; Mayer, H. A.; Kandelbauer, A. Sol–Gel-Controlled Size and Morphology of Mesoporous Silica Microspheres Using Hard Templates. *ACS Omega* **2023**, *8* (33), 30273-30284.

[34] Zhang, L.; Wang, L.; Yao, H.; Xu, F.; Chen, Y. Biodegradable and biocompatible monodispersed hollow mesoporous organosilica with large pores for delivering biomacromolecules. *Journal of Materials Chemistry B* **2017**, *5* (39), 8013-8025.

[35] Möller, K.; Bein, T. Degradable Drug Carriers: Vanishing Mesoporous Silica Nanoparticles. *Chemistry of Materials* **2019**, *31* (12), 4364-4378.

[36] Kresge, C. T.; Leonowicz, M. E.; Roth, W. J.; Vartuli, J. C.; Beck, J. S. Ordered mesoporous molecular sieves synthesized by a liquid-crystal template mechanism. *Nature* **1992**, *359* (6397), 710-712.

[37] Zhao, D.; Feng, J.; Huo, Q.; Melosh, N.; Fredrickson, G. H.; Chmelka, B. F.; Stucky, G. D. Triblock Copolymer Syntheses of Mesoporous Silica with Periodic 50 to 300 Angstrom Pores. *Science* **1998**, *279* (5350), 548-552.

[38] Ambrogio, M. W.; Thomas, C. R.; Zhao, Y.-L.; Zink, J. I.; Stoddart, J. F. Mechanized Silica Nanoparticles: A New Frontier in Theranostic Nanomedicine. *Accounts of Chemical Research* **2011**, *44* (10), 903-913.

[39] Slowing, I. I.; Vivero-Escoto, J. L.; Trewyn, B. G.; Lin, V. S. Y. Mesoporous silica nanoparticles: structural design and applications. *Journal of Materials Chemistry* **2010**, *20* (37), 7924-7937.

[40] Chen, N.-T.; Cheng, S.-H.; Souris, J. S.; Chen, C.-T.; Mou, C.-Y.; Lo, L.-W. Theranostic applications of

mesoporous silica nanoparticles and their organic/inorganic hybrids. *Journal of Materials Chemistry B* **2013**, *1* (25), 3128-3135.

[41] Théron, C.; Gallud, A.; Carcel, C.; Gary-Bobo, M.; Maynadier, M.; Garcia, M.; Lu, J.; Tamanoi, F.; Zink, J. I.; Wong Chi Man, M. Hybrid Mesoporous Silica Nanoparticles with pH-Operated and Complementary H-Bonding Caps as an Autonomous Drug-Delivery System. *Chemistry – A European Journal* **2014**, *20* (30), 9372-9380.

[42] Wu, S.-H.; Mou, C.-Y.; Lin, H.-P. Synthesis of mesoporous silica nanoparticles. *Chemical Society Reviews* **2013**, *42* (9), 3862-3875.

[43] Du, L.; Cheng, Z.; Zhu, P.; Chen, Q.; Wu, Y.; Tan, K. Preparation of mesoporous silica nanoparticles molecularly imprinted polymer for efficient separation and enrichment of perfluorooctane sulfonate. *Journal of Separation Science* **2018**, *41* (23), 4363-4369.

[44] Kankala, R. K.; Han, Y.-H.; Na, J.; Lee, C.-H.; Sun, Z.; Wang, S.-B.; Kimura, T.; Ok, Y. S.; Yamauchi, Y.; Chen, A.-Z.; et al. Nanoarchitectured Structure and Surface Biofunctionality of Mesoporous Silica Nanoparticles. *Advanced Materials* **2020**, *32* (23), 1907035.

[45] Popat, A.; Hartono, S. B.; Stahr, F.; Liu, J.; Qiao, S. Z.; Qing Lu, G. Mesoporous silica nanoparticles for bioadsorption, enzyme immobilisation, and delivery carriers. *Nanoscale* **2011**, *3* (7), 2801-2818.

[46] Wang, Y.; Zhao, Q.; Han, N.; Bai, L.; Li, J.; Liu, J.; Che, E.; Hu, L.; Zhang, Q.; Jiang, T.; et al. Mesoporous silica nanoparticles in drug delivery and biomedical applications. *Nanomedicine: Nanotechnology, Biology and Medicine* **2015**, *11* (2), 313-327.

[47] Mamaeva, V.; Sahlgren, C.; Lindén, M. Mesoporous silica nanoparticles in medicine—Recent advances. *Advanced Drug Delivery Reviews* **2013**, *65* (5), 689-702.

[48] García-Fernández, A.; Sancenón, F.; Martínez-Máñez, R. Mesoporous silica nanoparticles for pulmonary drug delivery. *Advanced Drug Delivery Reviews* **2021**, *177*, 113953.

[49] Shi, Y.; Miller, M. L.; Di Pasqua, A. J. Biocompatibility of Mesoporous Silica Nanoparticles? *Comments on Inorganic Chemistry* **2016**, *36* (2), 61-80.

[50] Farjadian, F.; Roointan, A.; Mohammadi-Samani, S.; Hosseini, M. Mesoporous silica nanoparticles: Synthesis, pharmaceutical applications, biodistribution, and biosafety assessment. *Chemical Engineering Journal* **2019**, *359*, 684-705.

[51] Yu, Z.; Li, Q.; Wang, J.; Yu, Y.; Wang, Y.; Zhou, Q.; Li, P. Reactive Oxygen Species-Related Nanoparticle Toxicity in the Biomedical Field. *Nanoscale Research Letters* **2020**, *15* (1), 115.

[52] Bhavsar, D.; Patel, V.; Sawant, K. Systematic investigation of in vitro and in vivo safety, toxicity and degradation of mesoporous silica nanoparticles synthesized using commercial sodium silicate. *Microporous and Mesoporous Materials* **2019**, *284*, 343-352.

[53] Chou, C.-C.; Chen, W.; Hung, Y.; Mou, C.-Y. Molecular Elucidation of Biological Response to Mesoporous Silica Nanoparticles in Vitro and in Vivo. *ACS Applied Materials & Interfaces* **2017**, *9* (27), 22235-22251.

[54] Sanchez, C.; Belleville, P.; Popall, M.; Nicole, L. Applications of advanced hybrid organic–inorganic nanomaterials: from laboratory to market. *Chemical Society Reviews* **2011**, *40* (2), 696-753.

[55] Park, W.; Shin, H.; Choi, B.; Rhim, W.-K.; Na, K.; Keun Han, D. Advanced hybrid nanomaterials for biomedical applications. *Progress in Materials Science* **2020**, *114*, 100686.

[56] Fan, W.; Jensen, L. R.; Ceccato, M.; Quaade, T. S.; Gurevich, L.; Yu, D.; Smedskjaer, M. M. Flexible inorganic–organic hybrids with dual inorganic components. *Materials Today Chemistry* **2021**, *22*, 100584.

[57] Gomez-Romero, P. Hybrid Organic-Inorganic Materials-In Search of Synergic Activity. *Advanced Materials* **2001**, *13* (3), 163-174.

[58] Parola, S.; Julián-López, B.; Carlos, L. D.; Sanchez, C. Optical Properties of Hybrid Organic-Inorganic

Materials and their Applications. *Advanced Functional Materials* **2016**, *26* (36), 6506-6544.
[59] García-Martínez, J.-M.; Collar, E. P. Organic–Inorganic Hybrid Materials. *Polymers* **2021**, *13* (1), 86.
[60] Zhou, H.-C. J.; Kitagawa, S. Metal–Organic Frameworks (MOFs). *Chemical Society Reviews* **2014**, *43* (16), 5415-5418.
[61] Omar M. Yaghi, M. J. K., Christian S. Diercks. Emergence of Metal-Organic Frameworks. In *Introduction to Reticular Chemistry*, 2019; pp 1-27.
[62] Furukawa, H.; Cordova, K. E.; O'Keeffe, M.; Yaghi, O. M. The Chemistry and Applications of Metal-Organic Frameworks. *Science* **2013**, *341* (6149), 1230444.
[63] Melde, B. J.; Holland, B. T.; Blanford, C. F.; Stein, A. Mesoporous Sieves with Unified Hybrid Inorganic/Organic Frameworks. *Chemistry of Materials* **1999**, *11* (11), 3302-3308.
[64] Inagaki, S.; Guan, S.; Fukushima, Y.; Ohsuna, T.; Terasaki, O. Novel Mesoporous Materials with a Uniform Distribution of Organic Groups and Inorganic Oxide in Their Frameworks. *Journal of the American Chemical Society* **1999**, *121* (41), 9611-9614.
[65] Asefa, T.; MacLachlan, M. J.; Coombs, N.; Ozin, G. A. Periodic mesoporous organosilicas with organic groups inside the channel walls. *Nature* **1999**, *402* (6764), 867-871.
[66] Bao, X. Y.; Zhao, X. S.; Qiao, S. Z.; Bhatia, S. K. Comparative Analysis of Structural and Morphological Properties of Large-Pore Periodic Mesoporous Organosilicas and Pure Silicas. *The Journal of Physical Chemistry B* **2004**, *108* (42), 16441-16450.
[67] Park, S. S.; Santha Moorthy, M.; Ha, C.-S. Periodic mesoporous organosilicas for advanced applications. *NPG Asia Materials* **2014**, *6* (4), e96.
[68] Zhou, X.; Qiao, S.; Hao, N.; Wang, X.; Yu, C.; Wang, L.; Zhao, D.; Lu, G. Q. Synthesis of Ordered Cubic Periodic Mesoporous Organosilicas with Ultra-Large Pores. *Chemistry of Materials* **2007**, *19* (7), 1870-1876.
[69] Croissant, J. G.; Cattoën, X.; Wong Chi Man, M.; Durand, J.-O.; Khashab, N. M. Syntheses and applications of periodic mesoporous organosilica nanoparticles. *Nanoscale* **2015**, *7* (48), 20318-20334.
[70] Croissant, J.; Salles, D.; Maynadier, M.; Mongin, O.; Hugues, V.; Blanchard-Desce, M.; Cattoën, X.; Wong Chi Man, M.; Gallud, A.; Garcia, M.; et al. Mixed Periodic Mesoporous Organosilica Nanoparticles and Core–Shell Systems, Application to in Vitro Two-Photon Imaging, Therapy, and Drug Delivery. *Chemistry of Materials* **2014**, *26* (24), 7214-7220.
[71] Vivero-Escoto, J. L.; Huxford-Phillips, R. C.; Lin, W. Silica-based nanoprobes for biomedical imaging and theranostic applications. *Chemical Society Reviews* **2012**, *41* (7), 2673-2685.
[72] Giret, S.; Wong Chi Man, M.; Carcel, C. Mesoporous-Silica-Functionalized Nanoparticles for Drug Delivery. *Chemistry – A European Journal* **2015**, *21* (40), 13850-13865.
[73] Linares, N.; Serrano, E.; Rico, M.; Mariana Balu, A.; Losada, E.; Luque, R.; García-Martínez, J. Incorporation of chemical functionalities in the framework of mesoporous silica. *Chemical Communications* **2011**, *47* (32), 9024-9035.
[74] Hoffmann, F.; Cornelius, M.; Morell, J.; Fröba, M. Silica-Based Mesoporous Organic–Inorganic Hybrid Materials. *Angewandte Chemie International Edition* **2006**, *45* (20), 3216-3251.
[75] Inkson, B. J. 2 - Scanning electron microscopy (SEM) and transmission electron microscopy (TEM) for materials characterization. In *Materials Characterization Using Nondestructive Evaluation (NDE) Methods*, Hübschen, G., Altpeter, I., Tschuncky, R., Herrmann, H.-G. Eds.; Woodhead Publishing, 2016; pp 17-43.
[76] Zhou, W.; Apkarian, R.; Wang, Z. L.; Joy, D. Fundamentals of Scanning Electron Microscopy (SEM). In *Scanning Microscopy for Nanotechnology: Techniques and Applications*, Zhou, W., Wang, Z. L. Eds.; Springer New York, 2007; pp 1-40.
[77] Unruh, D. K.; Forbes, T. Z. X-ray Diffraction Techniques. In *Analytical Geomicrobiology: A Handbook of*

Instrumental Techniques, Kenney, J. P. L., Veeramani, H., Alessi, D. S. Eds.; Cambridge University Press, 2019; pp 215-237.
[78] Holder, C. F.; Schaak, R. E. Tutorial on Powder X-ray Diffraction for Characterizing Nanoscale Materials. *ACS Nano* **2019**, *13* (7), 7359-7365.
[79] Iwashita, N. Chapter 2 - X-ray Powder Diffraction. In *Materials Science and Engineering of Carbon*, Inagaki, M., Kang, F. Eds.; Butterworth-Heinemann, 2016; pp 7-25.
[80] Pope, C. G. X-Ray Diffraction and the Bragg Equation. *Journal of Chemical Education* **1997**, *74* (1), 129.
[81] Chu, B.; Hsiao, B. S. Small-Angle X-ray Scattering of Polymers. *Chemical Reviews* **2001**, *101* (6), 1727-1762.
[82] Misono, T. Dynamic Light Scattering (DLS). In *Measurement Techniques and Practices of Colloid and Interface Phenomena*, Abe, M. Ed.; Springer Singapore, 2019; pp 65-69.
[83] Kamble, S.; Agrawal, S.; Cherumukkil, S.; Sharma, V.; Jasra, R. V.; Munshi, P. Revisiting Zeta Potential, the Key Feature of Interfacial Phenomena, with Applications and Recent Advancements. *ChemistrySelect* **2022**, *7* (1), e202103084.
[84] Lunardi, C. N.; Gomes, A. J.; Rocha, F. S.; De Tommaso, J.; Patience, G. S. Experimental methods in chemical engineering: Zeta potential. *The Canadian Journal of Chemical Engineering* **2021**, *99* (3), 627-639.
[85] Bhattacharjee, S. DLS and zeta potential – What they are and what they are not? *Journal of Controlled Release* **2016**, *235*, 337-351.
[86] Clogston, J. D.; Patri, A. K. Zeta Potential Measurement. In *Characterization of Nanoparticles Intended for Drug Delivery*, McNeil, S. E. Ed.; Humana Press, 2011; pp 63-70.
[87] Shaji, A.; Zachariah, A. K. Chapter 9 - Surface Area Analysis of Nanomaterials. In *Thermal and Rheological Measurement Techniques for Nanomaterials Characterization*, Thomas, S., Thomas, R., Zachariah, A. K., Mishra, R. K. Eds.; Elsevier, 2017; pp 197-231.
[88] Swenson, H.; Stadie, N. P. Langmuir's Theory of Adsorption: A Centennial Review. *Langmuir* **2019**, *35* (16), 5409-5426.
[89] Brunauer, S.; Emmett, P. H.; Teller, E. Adsorption of Gases in Multimolecular Layers. *Journal of the American Chemical Society* **1938**, *60* (2), 309-319.
[90] Sing, K. The use of nitrogen adsorption for the characterisation of porous materials. *Colloids and Surfaces A: Physicochemical and Engineering Aspects* **2001**, *187-188*, 3-9.
[91] Brunauer, S.; Deming, L. S.; Deming, W. E.; Teller, E. On a Theory of the van der Waals Adsorption of Gases. *Journal of the American Chemical Society* **1940**, *62* (7), 1723-1732.
[92] Thommes, M.; Kaneko, K.; Neimark, A. V.; Olivier, J. P.; Rodriguez-Reinoso, F.; Rouquerol, J.; Sing, K. S. W. Physisorption of gases, with special reference to the evaluation of surface area and pore size distribution (IUPAC Technical Report). **2015**, *87* (9-10), 1051-1069.
[93] Lowell, S.; Shields, J. E.; Thomas, M. A.; Thommes, M. Surface Area Analysis from the Langmuir and BET Theories. In *Characterization of Porous Solids and Powders: Surface Area, Pore Size and Density*, Lowell, S., Shields, J. E., Thomas, M. A., Thommes, M. Eds.; Springer Netherlands, 2004; pp 58-81.
[94] Sassi, Z.; Bureau, J. C.; Bakkali, A. Structural characterization of the organic/inorganic networks in the hybrid material (TMOS–TMSM–MMA). *Vibrational Spectroscopy* **2002**, *28* (2), 251-262.
[95] Polenova, T.; Gupta, R.; Goldbourt, A. Magic Angle Spinning NMR Spectroscopy: A Versatile Technique for Structural and Dynamic Analysis of Solid-Phase Systems. *Analytical Chemistry* **2015**, *87* (11), 5458-5469.
[96] Geppi, M.; Borsacchi, S.; Mollica, G.; Veracini, C. A. Applications of Solid-State NMR to the Study of Organic/Inorganic Multicomponent Materials. *Applied Spectroscopy Reviews* **2008**, *44* (1), 1-89.

CHAPTER 2

Antifungal Silica Nanoparticles and Cotton Fabrics for Topical Medical Application

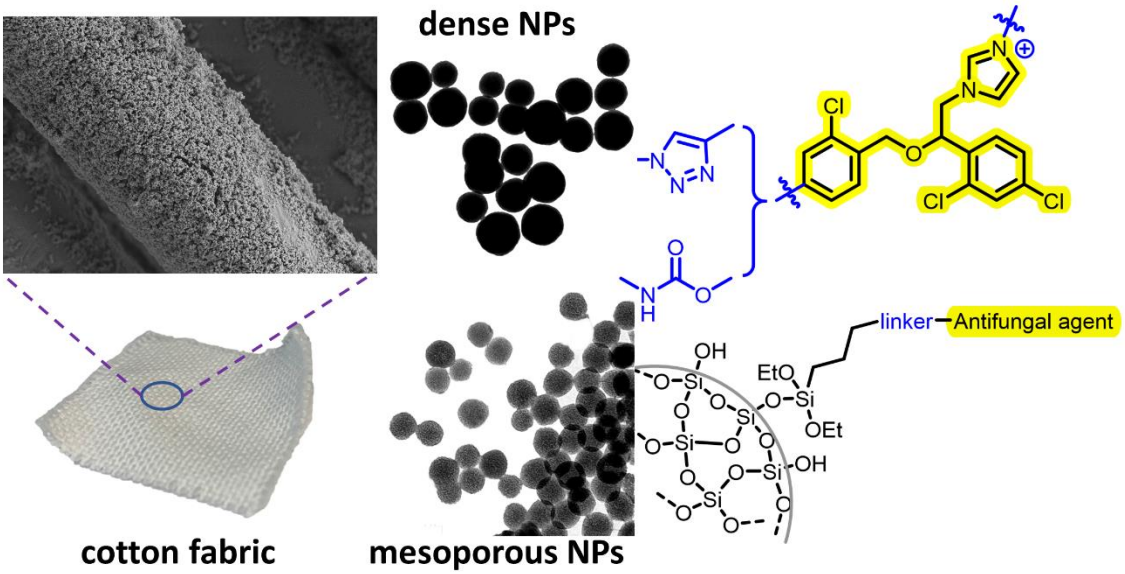

Chapter 2
Antifungal Silica Nanoparticles and Cotton Fabrics for Topical Medical Application

2.1 Introduction

Human body harbors various microbes including bacteria, eukaryotes and viruses. All the microbes constitute our microbiota associated with overall health.[1] The environmental microorganism is much more diverse than that in human body. In our daily life, it is inevitable to encounter a variety of microorganisms, which grow rapidly and may cause damage to people's health. Although the existence of fungi dates back a million years, the history of medicinal mycology and human mycoses began in the early 19th century with the discovery of tinea favosa.[2] David Gruby, in 19th century, discovered and isolated fungal pathogens and proved them to be the cause of fungal infections. Gilchrist reported a human case of blastomycosis in 1894.[3] Over the next 60 years landmarked in the field included the recognition of fungi as human pathogens capable of causing systemic diseases. Therapies were limited to the use of large doses of potassium iodide, phenol and methyl violets. The initial breakthroughs in the development of safe antifungal agents occurred with the discovery of griseofulvin (see Figure 2.1) by Oxford in 1939[4] and the pioneering synthesis of the first benzimidazole by Wooley in 1944.[5] Griseofulvin, derived from *Penicillium griseofulvin*, exhibits a narrow spectrum of activity and poses hepatotoxic risks. The advent of topical chlormidazole (Figure 2.1) in 1958, followed by the introduction of amphotericin B (AmB, Figure 2.1) in 1960,[6] marked the inception of the modern era of antifungal therapy.

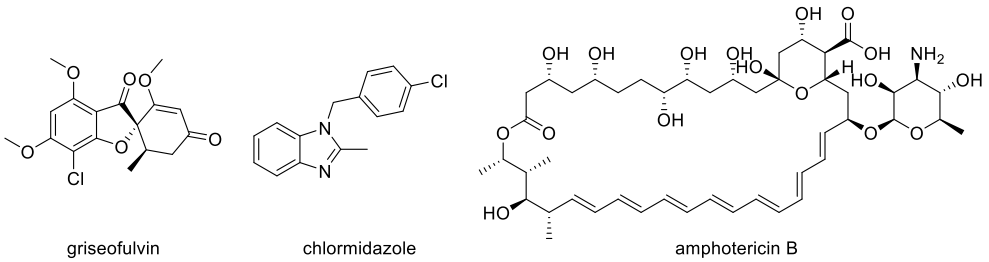

Figure 2.1. Structure of griseofulvin, chlormidazole and amphotericin B (AmB)

In the 1970s, imidazole antifungals were developed, exhibiting broad-spectrum activity against dermatophytes, *Candida*, and various fungi. Notably, the topical agent econazole (Figure 2.2) was synthesized in 1974 and remains in use today. The milestone of discovering ketoconazole in 1981 marked a significant advancement in the quest for safer and more effective agents. The 1990s proved to be a particularly prolific era in antifungal drug development. The advent of fluconazole (Figure 2.2),

the inaugural broad-spectrum triazole, effectively addressed the primary limitations of the imidazoles. In 1992, itraconazole was introduced, broadening the spectrum of activity of the triazole class to encompass various filamentous fungi in addition to *Candida* spp. Concurrently, safer lipid-based formulations of the polyenes AmB and nystatin were also introduced. Antifungal development saw further expansion into the new millennium with the emergence of the echinocandins, marking the introduction of the first new class of antifungal agents in nearly four decades, notably caspofungin in 2001 (Figure 2.2). Since 2001, the echinocandin class has continued to expand with the addition of micafungin and anidulafungin. Simultaneously, the triazole class has broadened with the inclusion of voriconazole and posaconazole, both demonstrating enhanced activity against fluconazole-resistant *Candida* spp. and filamentous molds.

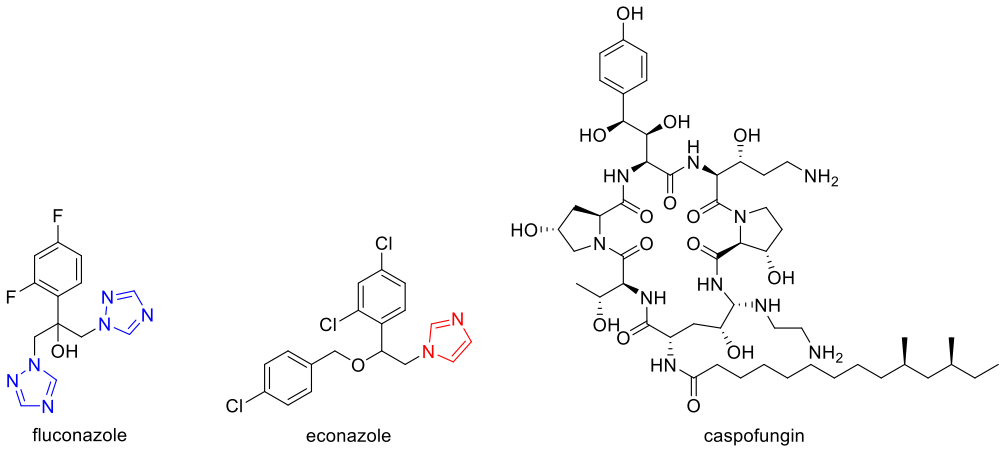

Figure 2.2. Structure of fluconazole, econazole and caspofungin

Systemic fungal infections usually originate in the lungs (aspergillosis and other mould infections as a result of inhalation) or from endogenous flora (candidemia as a result of infected lines or leakage from the gastrointestinal tract) and can spread to many other organs. Systemic antifungal drugs are used to treat these systemic fungal infections affecting internal organs.[7] They are either fungicidal (kill the fungus) or fungistatic (inhibit fungal growth) and they can be administered orally or intravenously. On the other hand, topical antifungals are products that treat superficial fungal infections that affect most frequently the skin, hair, and nails of humans.[8] Consequently, they are applied directly to the skin, nails, and hair. They are available as creams, gels, lotions, nail lacquers, ointments, powders, and sprays.

Compared to bacterial and viral diseases of human beings, fungal diseases are not epidemic and most of the mycoses are not so severe to be lethal. Superficial fungal infections are the most common but hard to treat in human beings. Due to the eukaryotic cellular functions, fungi are more similar than bacteria to mammalian cells. Hence, the diagnosis and treatment of fungal diseases could be difficult, especially for those with immune deficiency. In fact, fungal infections represent a huge global problem resulting in over 1.7 million of deaths every year in humans and over one billion people suffer from

severe fungal diseases.[9] Some hosts for the fungi proliferation are food crops, animal species and textiles. Focusing in the last one, textiles are excellent substrates for microbial proliferation under appropriate moisture, nutrients, and temperature conditions.[10] In the hospital environment, contaminated cotton based materials can infect patients and professionals. Moreover, contamination of these textiles in clinical atmospheres can contribute to the spread of airborne pathogens, which then fall by gravity and infect the environment.

Besides, in 2020 the World Health Organization (WHO) developed the first meeting of the WHO antifungal expert group for the identification of priority fungal pathogens to develop a priority pathogens list for fungal infections of public health importance and to define the R&D priorities.[11] So, this global problem has been overlooked and belittled for a long time. Additionally, in this complex scenario, global warming and accompanying climate changes have resulted in an increased incidence of many fungal diseases.[12] Thus, in this context, the development of new drugs to treat fungal diseases is mandatory. This rapidly growing area of research will continue to be important as the need for potent, less toxic antifungal agents continues to increase.

2.1.1 Pharmacology of antifungal agents

Unlike the development of antibacterial agents, to date relatively few drug targets in fungi have been exploited in the development of currently available antifungal agents. Fungi have similarities to mammalian cells, and this fact has made the search for antifungal drug targets difficult. To date, three targets have been exploited: plasma membrane sterols; nucleic acid synthesis and cell wall constituents (Figure 2.3).[13]

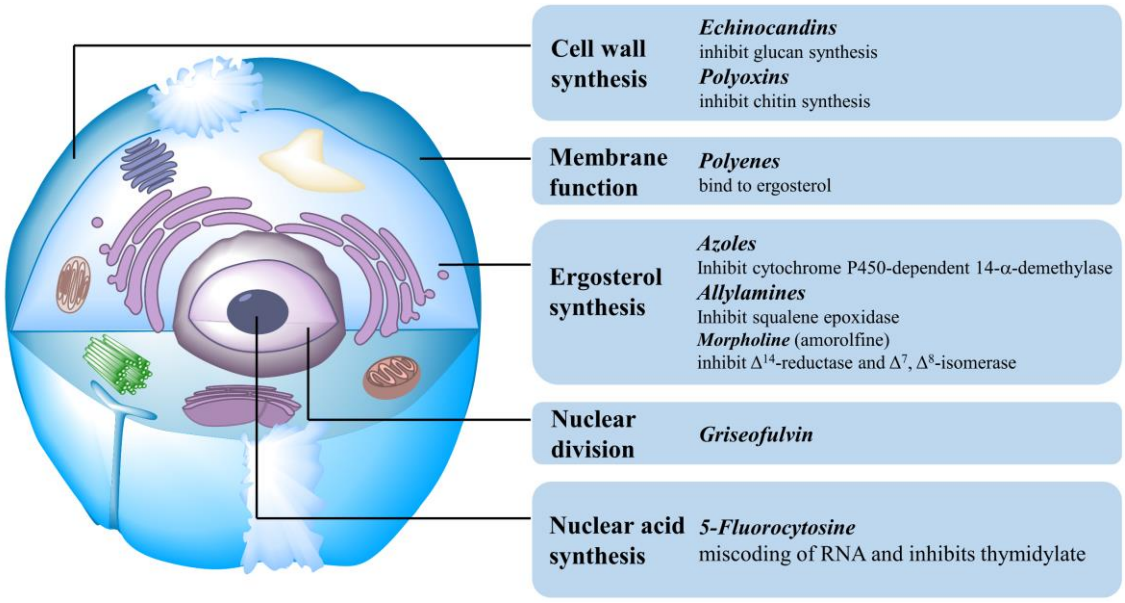

Figure 2.3 Sites of action of antifungals[14]

2.1.1.1 Plasma membrane sterols

Most of the current antifungal agents available for systemic use rely on the direct (the polyenes) or indirect (the azoles) interaction with the plasma membrane sterol ergosterol.[15] Ergosterol, a key component of the fungal cell membrane, is critical for the integrity of the membrane and its functions, by regulating membrane fluidity and asymmetry. This sterol is not present in mammalian cells and thus is ideal to be a target. Moreover, indirectly, ergosterol is targeted by a variety of antifungal agents that act at one or more steps in the biosynthesis of ergosterol.

One target in the ergosterol biosynthesis pathway is cytochrome P450 (CYP)-dependent 14α-demethylase, which catalyzes the demethylation of ergosterol precursors.[16] Inhibition of 14α-demethylase ultimately causes the depletion of ergosterol and the accumulation of sterol precursors, including 14α methylated sterols (Figure 2.4). Squalene epoxidase is another target in the ergosterol biosynthesis pathway, inhibition of which can lead to fungicidal effects. Amorolfine, a topical antifungal agent of the morpholine family for the treatment of onychomycosis, which is not available in the US, acts via inhibition of Δ^{14}-reductase and Δ^{7}, Δ^{8}-isomerase, which are also enzymes involved in ergosterol synthesis. Undoubtedly, many more clinically useful antifungal agents will be discovered as the search for newer, more potent ergosterol synthesis inhibitors continues.

As already mentioned, other antifungals interfere in the nucleic acid synthesis or in the synthesis of the cell wall.[13]

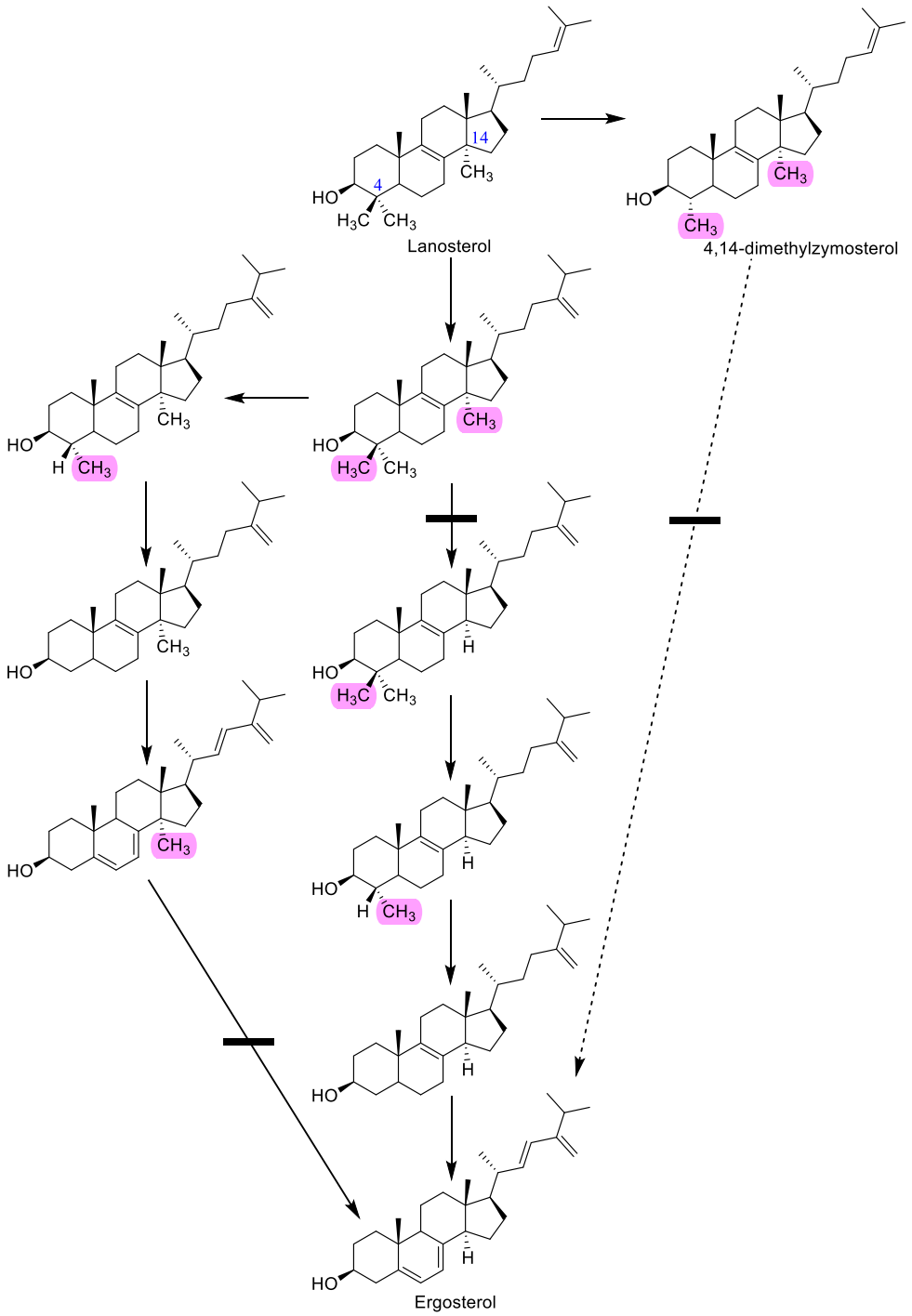

Figure 2.4 Pathway for ergosterol biosynthesis blocked by azoles[14]

2.1.2 Classification of antifungal agents

The dominating antifungal agents can be classified into four groups, namely, polyene macrolides, allylamines, echinocandins and azoles.

2.1.2.1 Polyene macrolides

The first polyene macrolide antifungal, nystatin (Figure 2.5), was discovered by Hazen and Brown in

1950.[17] Then another polyene antifungal, amphotericin B (AmB) (see Figure 2.1) was discovered and used to treat blastomycosis in 1957.[18] These polyenes (AmB, nystatin, and also natamycin) are large (molecules with 26-28 carbon atoms) macrolides. In the large ring, there are a series of conjugated carbon-carbon double bonds on one side, and many hydroxyl groups on the other side, which afford the amphipathic property of the molecules (Figure 2.1 and Figure 2.5).[19]

The amphipathic or amphiphilic property helps in binding with ergosterol incorporated in the cell membranes forming ionic transmembrane channels, leading to the leakage of potassium and sodium ions and the fungal cell death.[20] Amphotericin B (Figure 2.1) is amphiphilic and acts by binding through both hydrophilic hydrogen bonds and hydrophobic, non-specific van de Waals forces to ergosterol in fungal cell membranes. Amphotericin B has a greater affinity to bind ergosterol and ergosterol-containing membranes (present in fungi) than cholesterol or cholesterol-containing membranes (present in humans). The polyenes could be used in the treatment of superficial fungal infections.

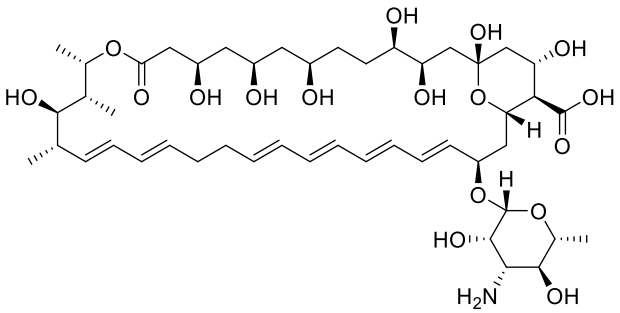

Figure 2.5 Structure of nystatin

2.1.2.2 Allylamines

The allylamines were introduced in 1980s as antifungal agents. As we have mentioned, squalene epoxidase catalyzes the conversion of squalene into 2,3-squalene epoxide, which is one step in the ergosterol biosynthesis pathway. Allylamines can inhibit the enzyme involved in the process and lead to the permeability change of fungal cell membrane.[21] The main members of this family are naftifine, terbinafine and butenafine (Figure 2.6).

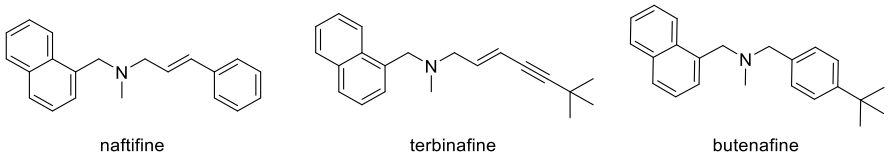

Figure 2.6 Structure of naftifine, terbinafine and butenafine

2.1.2.3 Echinocandins

The echinocandins consist of a cyclic synthetic hexapeptide with different side chains. These lipopeptides derive from fungi natural products and inhibit the β-(1,3)-D-glucan synthase, blocking the synthesis of β-(1,3)-glucan. β-(1,3)-D-Glucan is the main component of cell wall, which is not present

in mammalian cells. This lessens cellular structural integrity and morphology and ultimately results in osmotic lysis of the cell.[22] These cell wall-acting echinocandin class of antifungal agents was the first major class of systemically acting antifungals to exploit a unique target, β-(1,3)-glucan synthase. Examples of echinocandins are caspofungin (see Figure 2.2) and micafungin (Figure 2.7).

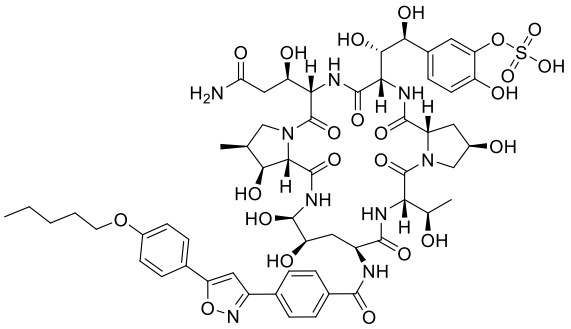

Figure 2.7 Structure of micafungin

2.1.2.4 Importance of azoles as antifungal agents

Azoles are the most used clinical antifungals. They are classified into two groups: those with two nitrogens in the azole ring (imidazoles), and those with three nitrogens in the azole ring (triazoles). As already mentioned, the first azole antifungal agent, benzimidazole, was discovered by Oxford in 1944. It was not until 1958, that the first azole drug, topical chlormidazole (see Figure 2.1), was introduced to the market by Chemie Grünenthal.

The azoles exert a fungistatic effect by dose-dependent inhibition of CYP-dependent 14α-demethylase, which ultimately depletes ergosterol and compromises cell wall integrity.[23] The free nitrogen atoms of the azole ring bind to the iron atom of the haem (or heme) in cytochrome P450 (CYP) enzyme. The interaction with the enzyme disturbs the biosynthesis of ergosterol from lanosterol, inhibiting fungal growth.

Imidazoles are important members of the azole family. The core *N*-heterocyclic aromatic unit make the molecule highly polar. The imidazole antifungal family comprise econazole (Figure 2.2), clotrimazole, miconazole and ketoconazole (Figure 2.8). These early imidazoles were beneficial for topical applications instead of oral therapy because of the poor aqueous solubility. Then the triazole ring was introduced to replace the imidazole ring.[24] The first generation of triazole based antifungals (fluconazole (Figure 2.2) and itraconazole (Figure 2.8)) exhibit a broader antifungal activity spectrum than imidazoles. They also possessed greater water solubility, better bioavailability and selectivity for fungal CYP enzyme over that of mammalian.

Itraconazole is highly lipophilic, and it is moderately to very active against most medically important fluconazole-susceptible and -resistant Candida species. Voriconazole (Figure 2.8) was then developed and became the principal drug for treatment of invasive aspergillosis.

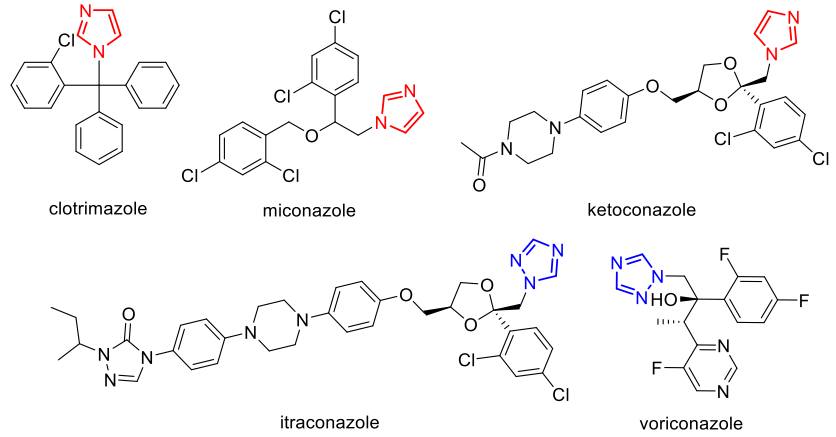

Figure 2.8 Structure of imidazoles: clotrimazole; miconazole; ketoconazole.

Structure of triazoles: itraconazole and voriconazole.

Certain azoles (i.e., ketoconazole, voriconazole) may interact with secondary targets in the ergosterol biosynthesis pathway; 14α-demethylase is the primary target for this class of compounds.

2.1.2.4.1 Miconazole

Like other azole antifungals, miconazole (Figure 2.8) exerts its effect by disrupting the cell membrane of the fungus. It inhibits ergosterol synthesis by interacting with 14-α demethylase, a cytochrome P-450 enzyme that, as we have mentioned before in this introduction, is required for the conversion of lanosterol to ergosterol, an essential membrane component. Inhibition of ergosterol synthesis results in increased cell permeability, causing filtration of cell contents. Miconazole does not have the same effect on human cholesterol synthesis. Miconazole, marketed under various brand names such as Monistat, serves as an antifungal medication indicated for treating ringworm, pityriasis versicolor, and yeast topical infections.[25] Specifically, miconazole acts as a topical antifungal agent for ringworm affecting the body, groin (jock itch), and feet (athlete's foot). Administered in the form of cream or ointment, miconazole is applied directly to the affected skin area. The compound was patented in 1968 and subsequently approved for medical use in 1971.

2.1.3 Antifungal agents and nanostructures for cotton fabrics coating

On the other side, cotton fabrics are widely used materials in medicine because of their excellent properties including biodegradability, softness, permeability, and hygroscope capacity.[26] However, cotton textiles provide a good living environment for fungi because of massive hydrophilic cellulose and pores. Consequently, much effort has been done in the preparation of functional cotton materials for avoiding the global problem of fungi proliferation on cotton surfaces.

2.1.3.1 Molecular agents

Numerous antifungal molecular agents have been selected for coating cotton fabrics,[27] including quaternary ammonium salts, *N*-halamines, recognized antifungal drugs (ketoconazole) and bioactive dyes. Rosenau's group described the covalent grafting of xanthene-derived photosensitizers onto cellulose sheets that produce single oxygen upon white light illumination having photomicrobicidal activity.[28] Sun *et al.* synthesized cationic and anionic derivatives of polyquaternary ammonium salts based on *N,N*-dimethylaminoethyl methacrylate (cationic polymers) and acrylic acid (anionic polymers) which were deposited onto cotton fabrics through the layer by layer technique after free radical polymerization (Scheme 2.1). After a chlorine bleach the amide groups were transformed into *N*-halamines.[29] Another example was based on the use of β-cyclodextrin and ketoconazole. β-Cyclodextrin with an encapsulated antifungal drug was loaded on the surface of a wound dressing and a controlled release of ketoconazole to skin was achieved.[30] Moreover, application of 1,3-bis[(furan-2-yl)methylene] thiourea[31] and curcuma[32] dyes resulted in excellent finished textiles against some fungi. The uniform dispersion of guanazole-metal complexes on cotton fabrics surface (Ag^{+} and Zn^{2+}) via self-assembly resulted in antifungal and flame retardant materials.[33]

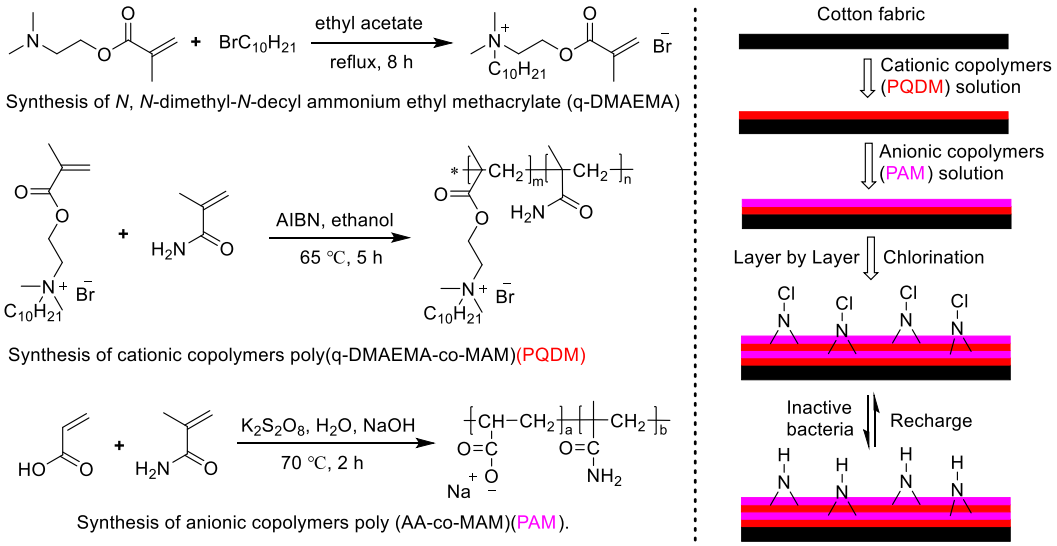

Scheme 2.1 Synthesis of cationic and anionic copolymers (left) and layer-by-layer coating process (right)

2.1.3.2 Nanostructures

Among the antifungal agents, several nanostructures have been intensively studied, including organic molecules-based nanoparticles (NPs), metal NPs and metal oxide NPs. An effective ultrasound assisted deposition of vanillin NPs, raspberry ketone NPs and camphor NPs on textiles was reported by Gedanken's group.[34] These nanomaterials were coated on cotton fabrics and showed excellent antifungal activity on cotton bandages. Recently, carbon quantum dots, nucleated from a pyrimidine-

based compound or from carboxymethyl cellulose, were immobilized within a textile matrix possessing microbial inhibition.[27, 35] Among metals, Ag NPs are the most explored. Most of the recent publications use a green route for their preparation and stabilization. It has been described the biosynthesis of Ag NPs using the corn grain contaminant (*Nigrospora oryzae*),[36] an endophytic actinomycete strain of *Streptomyces laurentii* previously isolated from the roots of the plant *Achillea fragrantissima*,[37] *Ulva lactuca* extracts,[38] *Citrus sinensis* peel juice,[39] *Moringa oleifera* extracts[40] and *Mikania micrantha* leaves extracts.[41] All these Ag NPs were coated onto cotton fabrics by different techniques and then studied with good results against several common fungi strains. Another approach was based on coating, by pad-dry-cure process, Ag NPs previously formed on siliceous matrixes dopped with carbon including a calcination step.[42] Furthermore, bimetallic Ag/Cu NPs exhibited a pronounced antimycotic activity.[43, 44]

Among nanostructures of metal oxides, ZnO and TiO_2 nanoparticles are the most studied. Gafur and co-workers prepared ZnO NPs and coated them on cotton fabrics using the dip coating technique.[45] El-Nahhal's group used ultrasound irradiation for the deposition of ZnO NPs on cotton fibers.[46] Gowri and collaborators described the obtention of antimicrobial TiO_2 nanoparticles from titanium tetraisopropoxide and extracts derived from *Aloe vera* plant, after calcination at 500 °C (Scheme 2.2).[47] In 2019, functional antimicrobial cotton was prepared applying TiO_2 NPs and green walnut shell dye to modify the metal oxide NPs and achieve natural dye coloration.[48] Djamaan and collaborators dispersed TiO_2–SiO_2/chitosan NPs on cotton fabrics surface.[49] The hybrid TiO_2-SiO_2/chitosan (2:1) NPs presented high ability to generate hydroxyl radicals and the superoxide anion, which can destroy the fungi's cell membranes.

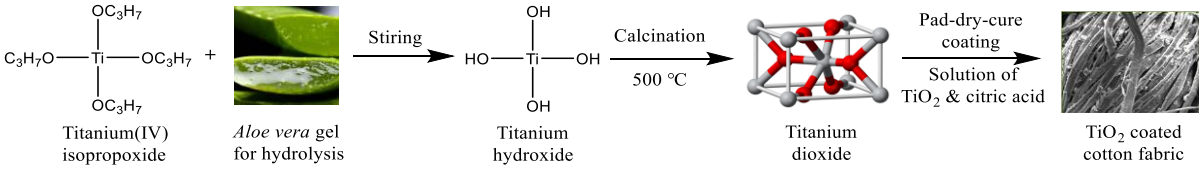

Scheme 2.2 Formation of TiO_2 nanoparticles by Aloe vera extract and coated cotton fabric

In some cases, mixtures of metal and metal oxide NPs have been used for multifunctional thin coating textile finishing. The use of hybrid Al_2O_3/SiO_2 modified with Ag/Cu NPs and TiO_2 P25 was described in 2018.[50] Gao's research group prepared silver/zinc oxide (Ag/ZnO) NPs with different molar ratios by chemical precipitation method observing a synergism between ZnO and Ag NPs in the antimicrobial properties of coated cotton fabrics.[51] As illustrated in Scheme 2.3, Ag/ZnO nanocomposite was prepared through a simple wet chemical method. And then nanoparticles were modified with silane coupling agent KH-570, followed by the addition of diallyl dimethyl ammonium chloride (DMDAAC), allyl

glycidyl ether (AGE) and potassium persulfate at 80 °C. Then cotton fabrics were immersed in the solution of P(DMDAAC-AGE)/Ag/ZnO for padding, dried and cured to obtain coated cotton fabrics.

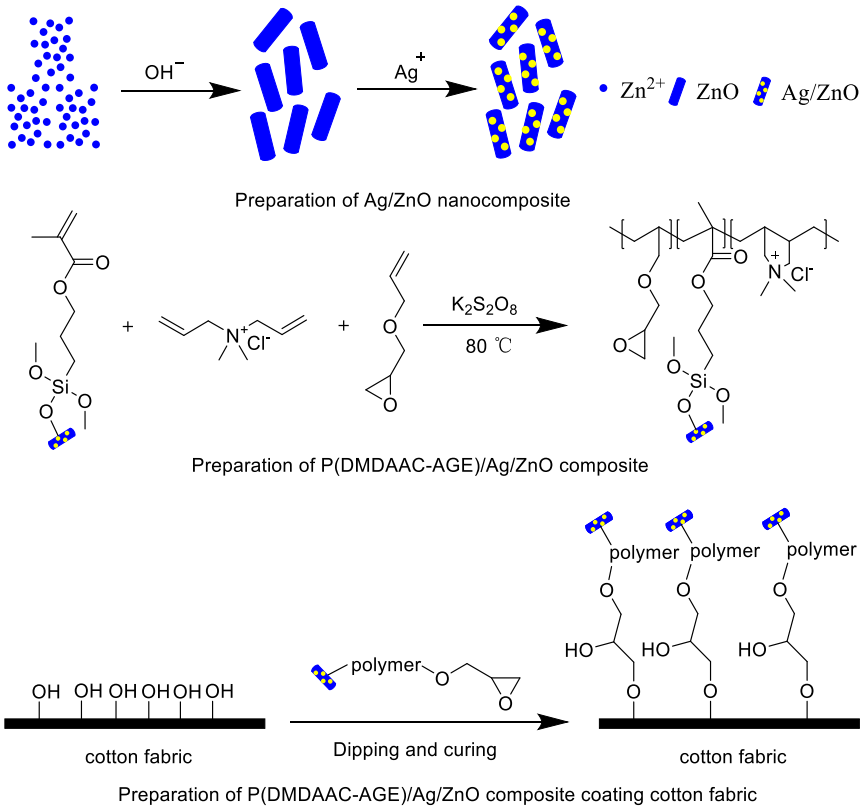

Scheme 2.3 Synthesis of organic-inorganic polymer/Ag/ZnO nanoparticles and coated cotton fabric

Considering the mentioned precedents, we envisaged the development of a different approach to achieve modified cotton fabrics with antifungal properties. Taking advantage of the long experience of the group in carrying out sol-gel processes for the preparation of hybrid silicas[52-57] and in the coating of textiles,[58-63] we envisioned the covalent anchoring of well-known antifungal agents on silica nanoparticles (either dense or mesoporous), which have deserved great attention as a biocompatible form of silica.[64-66] Miconazole core was chosen as a model structure because it has been traditionally used to topically treat superficial infections caused by fungi.

2.2 Objectives

Based on the previous introduction, we intend the development of a different approach to achieve modified cotton fabrics with antifungal properties for topical applications. We choose miconazole as a model structure. For that purpose, our specific objectives of this chapter of the thesis are as follows:

a) The synthesis of silylated antifungal derivatives based on traditional miconazole, using various linkers for the introduction of terminal triethoxysilyl group.

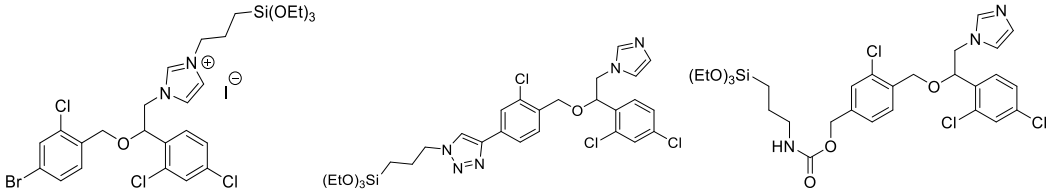

b) The preparation of dense and mesoporous functionalized silica NPs from these silylated precursors and the characterization of all the new nanomaterials with the appropriate techniques in each case, such as infrared spectroscopy, ^{13}C and ^{29}Si CP MAS solid-state NMR, elemental analysis, electron microscopy, nitrogen-sorption measurements, powder X-ray diffraction, dynamic light scattering and zeta-potential.

c) The preparation and characterization of cotton fabrics coated with these antifungal-functionalized silica NPs.

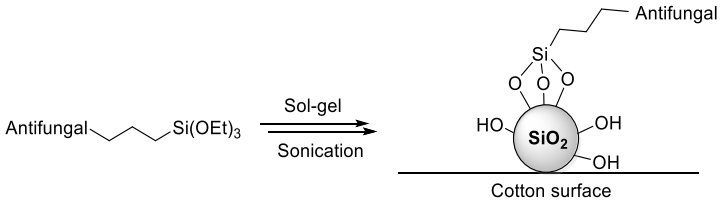

d) The assay of the antifungal activity of the modified cotton textiles towards different microorganisms.

2.3 Results and Discussion

2.3.1 Synthesis of silylated derivatives of antifungals

Miconazole core was chosen as a model structure because it has been traditionally used to topically treat superficial infections caused by fungi. With the purpose to covalently attach the antifungal units onto silica nanoparticles, the presence of a triethoxysilyl moiety on its structure was selected. As miconazole (Figure 2.8) is pharmacologically used as a nitrate salt,[67] the alkylation of the imidazole ring with a silylated alkyl iodide was first considered. Then, different linkers to attach this silylated unit were also evaluated (such as triazole and carbamate).

First, we performed the reaction of the alkoxide generated from the alcohol **1** with the corresponding substituted benzyl bromide to afford the starting materials **2**, **3**, **4** and **5** required for the next steps (Scheme 2.4).[68, 69]

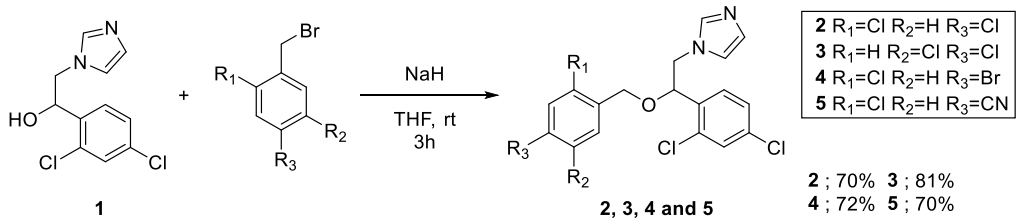

Scheme 2.4 Synthesis of **2**, **3**, **4** and **5** from alcohol **1**

Then, we developed a bimolecular nucleophilic substitution reaction between miconazole **2** and 3-iodopropyltriethoxysilane in dry acetonitrile, yielding the corresponding imidazolium iodide **6** (95% yield). As we also wanted to check the importance of the position of the chlorine atoms in the benzyloxy moiety, we prepared the silylated imidazolium iodide **7** from **3** by an analogous procedure (94% yield) (Scheme 2.5).

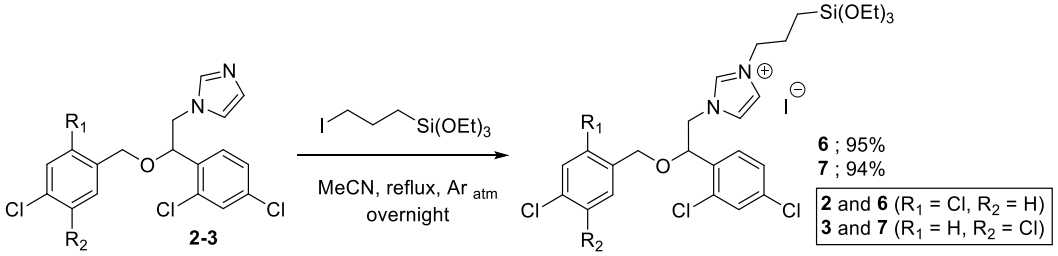

Scheme 2.5 Synthesis of silylated imidazolium iodides **6** and **7** from **2** and **3**

With the purpose to evaluate the effect of the change of the chlorine by a bromine atom, the alkylation of the imidazole ring of compound **4** was performed, affording the silylated imidazolium iodide **8** in 95% (Scheme 2.6).

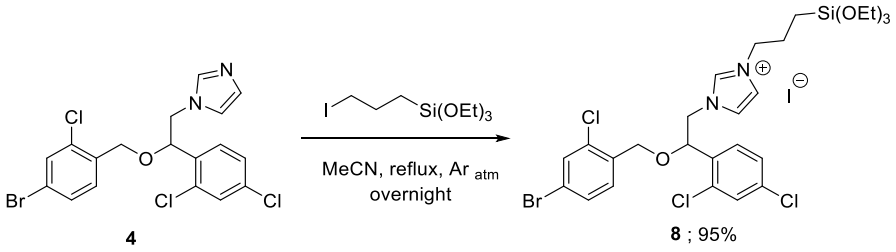

Scheme 2.6 Synthesis of silylated imidazolium iodide **8** from **4**

Then, we moved to different linkers to attach the silylated unit to the miconazole core (such as triazole and carbamate). Thus, the alkyne **9** was synthesized from the bromoarene **4** in 78% yield through a Sonogashira coupling with 2-methylbut-3-yn-2-ol. This alkyne **9** was deprotected under catalytic NaH to afford the corresponding terminal alkyne **10** (92% yield), which was coupled with (3-azidopropyl)triethoxysilane giving **11** (92% yield) through a click reaction, namely a Cu-catalyzed azide-alkyne cycloaddition[70] under microwave and anhydrous conditions.[71] Thus, the silylated triazole derivative **11** was prepared in a 66% global yield in three steps from **4** (Scheme 2.7).

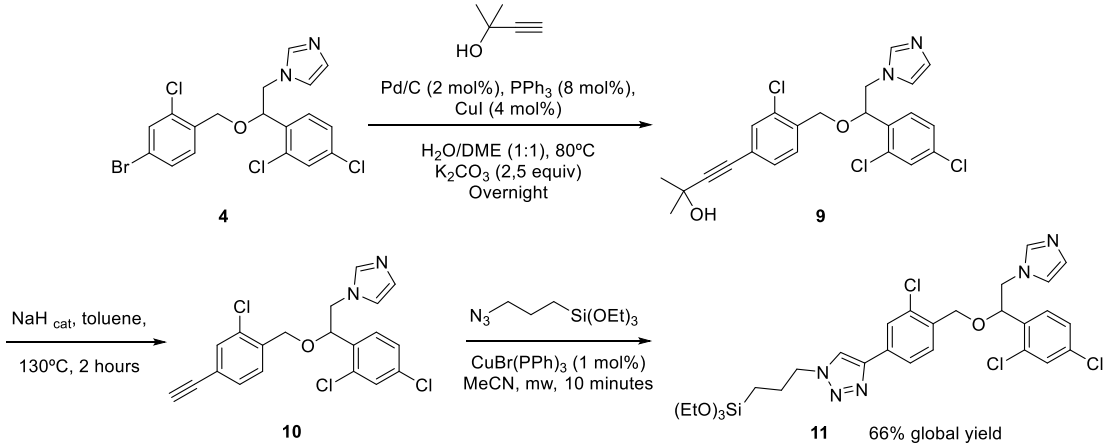

Scheme 2.7 Synthesis of silylated derivative **11** from **4**

The preparation of a silylated carbamate derivative was undertaken from the nitrile **5**. First, the nitrile was reduced to the corresponding aldehyde **12** (69%) by DIBAL at 0 ºC in dry toluene. Then, the carbonyl group was reduced with sodium borohydride to obtain the primary alcohol **13** (81% yield). Finally, the alcohol was efficiently reacted with the commercial silylated isocyanate in refluxing THF, using dibutyltin dilaurate as catalyst, to afford the silylated carbamate **14** (81% yield). Thus, compound **14** was prepared in three steps in 45% overall yield from **5** (Scheme 2.8).

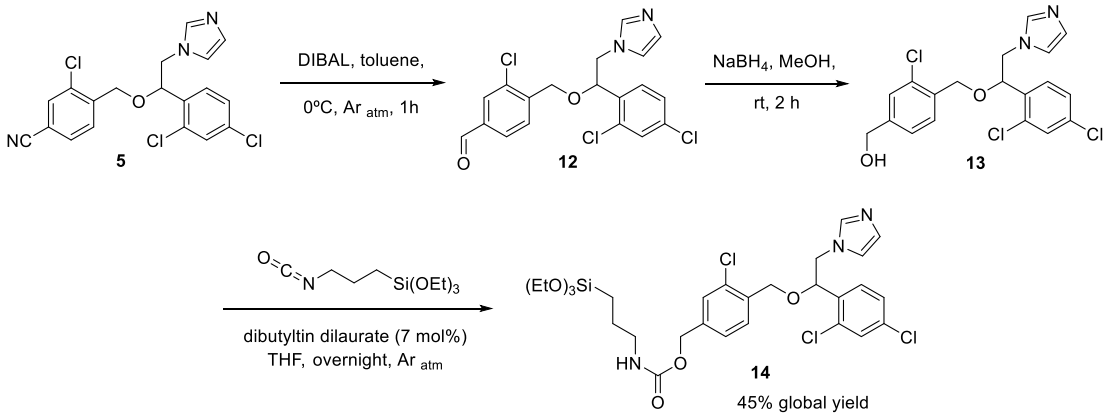

Scheme 2.8 Synthesis of silylated derivative **14** from **5**

2.3.2 Preparation and characterization of antifungal functionalized silica nanoparticles

With the modified silylated antifungal molecules (**6**, **7**, **8**, **11** and **14**; schemes 2.5 to 2.8) in hand, we turned to the covalent anchoring of these drugs to silica nanoparticles. We followed two different approaches, namely co-condensation and grafting.

First, we prepared functionalized dense nanoparticles **dN1-dN5** by co-condensation of silylated precursors (**6**, **7**, **8**, **11** or **14**) with TEOS using a 28% aqueous ammonia solution in ethanol (Scheme 2.9).[63, 72] The mixed solution was stirred at room temperature for 12 h and then the dense nanoparticles were collected by centrifugation (13500 rpm) and washed successively with ethanol, Milli-Q water, and ethanol until neutral pH.

On the other hand, functionalized mesoporous silica nanoparticles **mN6-mN8** (Scheme 2.9) were prepared by grafting the corresponding silylated drug to previously synthesized mesoporous silica nanoparticles of MCM-41 type[73] in refluxing toluene for 24 h. The NPs were collected by centrifugation (13500 rpm) and then washed successively with ethanol, acetone, and dichloromethane.

All these nanomaterials were characterized by elemental analysis, transmission electron microscopy (TEM), dynamic light scattering (DLS), zeta-potential, infrared spectroscopy, powder XRD and nitrogen-sorption measurements when appropriate.

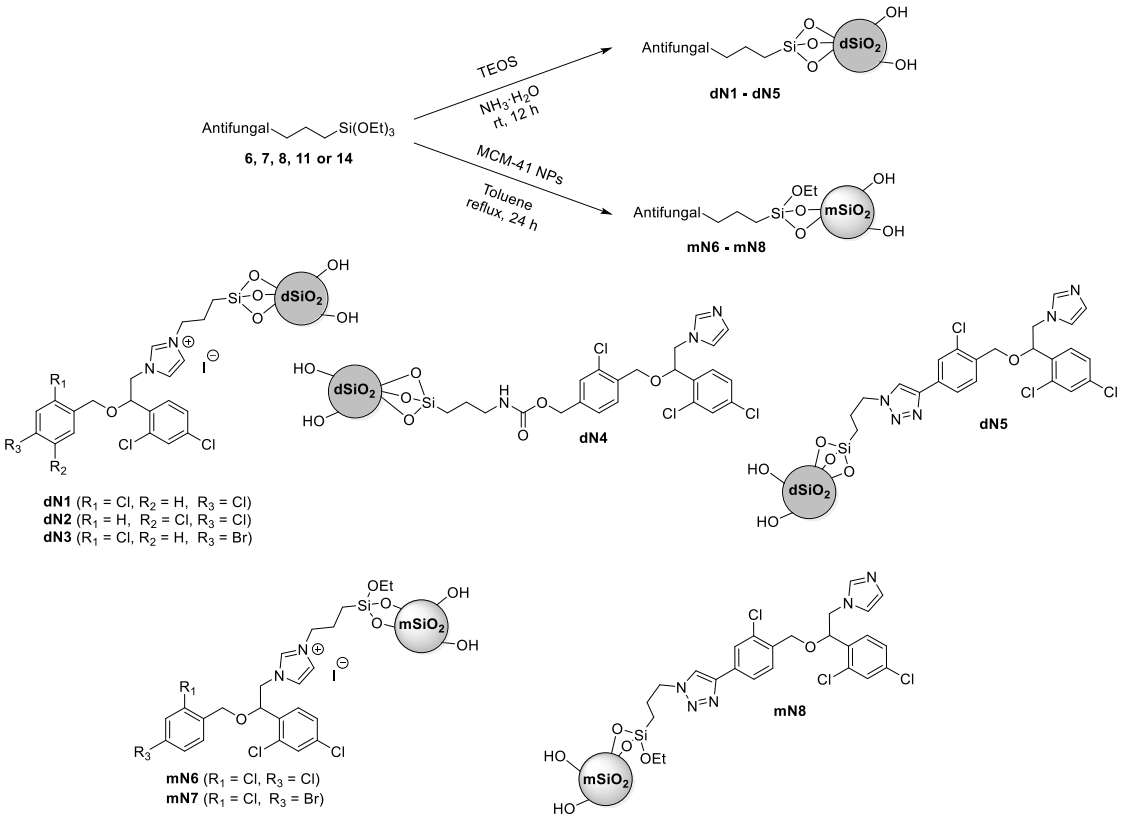

Scheme 2.9 Preparation of antifungal functionalized silica nanoparticles

Some physical data obtained after characterization are summarized in Table 2.1. First, the nanometric size and morphology of these materials were analysed by TEM and DLS. Materials **dN1**, **dN2** and **dN3** prepared by co-condensation of silylated imidazolium iodides **6**, **7** and **8** in basic medium in the absence of template appeared as nonporous dense aggregates and they showed high polydispersity in the dynamic light scattering measurements (Table 2.1).

Table 2.1 Characterization data of **dN1-dN5** and **mN6-mN8**.

Material	Drug loading (mmol·g^{-1})[a]	Particle size (nm)		Z-potential (mV)
		TEM	DLS[b]	
dN1	0.507	nd[c]	nd[c]	+50.2
dN2	0.332	nd[c]	nd[c]	+37.3
dN3	0.360	nd[c]	nd[c]	+37.4
dN4	0.263	136 ± 31	427	-64.7
dN5	0.244	206 ± 45	416	-21.0
mN6	0.514	86 ± 24	120	+37.0
mN7	0.471	140 ± 17	215	+35.6
mN8	0.377	147 ± 31	204	-28.1

[a] Calculated from the N elemental analysis. [b] Hydrodynamic diameters. [c] Not determined, the sample presented high polydispersity index.

Contrarily, **dN4** and **dN5** prepared from neutral silylated precursors **14** and **11** under analogous conditions exhibited spherical morphology, with diameters around 136 ± 31 nm and 206 ± 45 nm (see the TEM image of **dN5** in Figure 2.9 left, and Fig. 2.10 left, as an example) and showed a good polydispersity index in DLS (Table 2.1 and Figure 2.10 right).

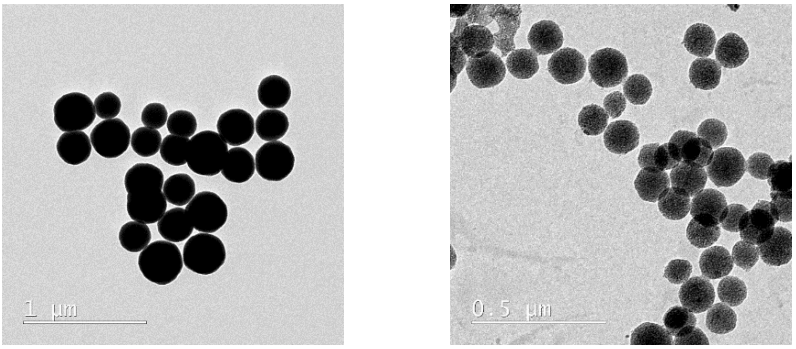

Figure 2.9 Left: TEM image of **dN5**. Right: TEM image of **mN6**

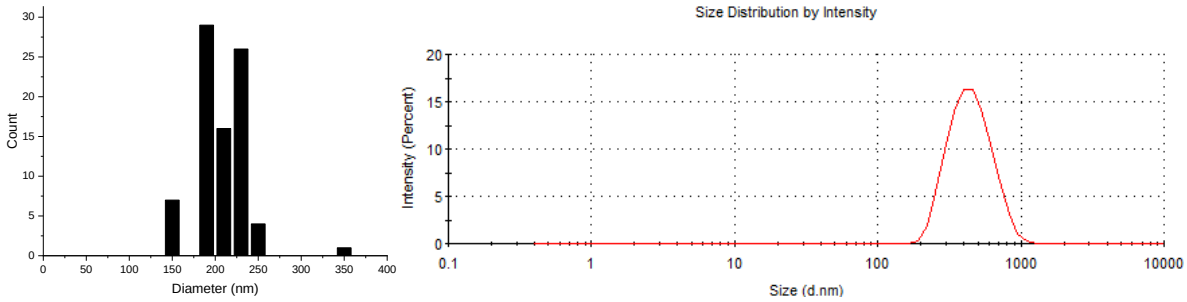

Figure 2.10 Left: TEM size distribution of **dN5**. Right: DLS of **dN5**

Besides, **mN6-mN8** nanomaterials prepared by grafting appeared as mesoporous spherical nanoparticles with average diameters of 86 ± 24, 140 ± 17 and 147 ± 31 nm (see Table 2.1). A selected TEM image of **mN6** is given in Figure 2.9, right). The BET surface area of **mN6** and **mN8** were 313 and 192 $m^2\ g^{-1}$, respectively (see the nitrogen-sorption isotherms in Figure 2.11). The *p*-XRD analyses showed the organized porosity for the MCM-41 materials, typical for a hexagonal 2D symmetry (see Figure 2.12 for the *p*-XRD of **mN6** and **mN8**).

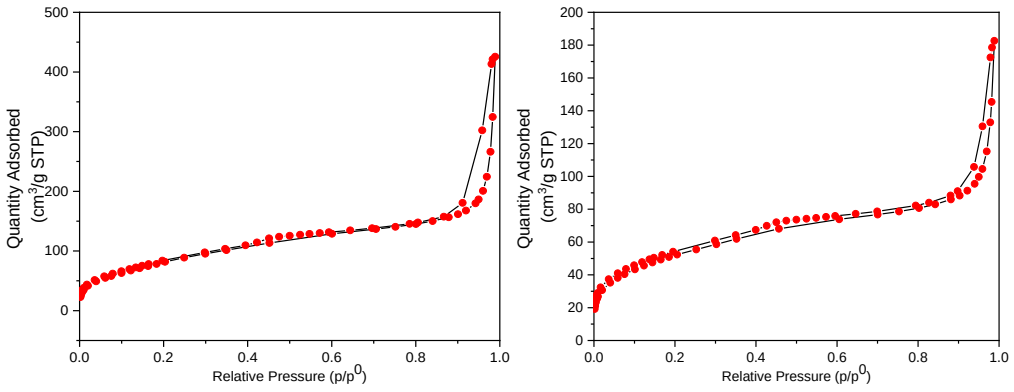

Figure 2.11 N_2-sorption isotherms of **mN6** (left) and **mN8** (right)

In these cases, DLS measurements showed hydrodynamic diameters that are in agreement with the TEM size of the corresponding dried nanoparticles if we consider the likely adsorption of water molecules onto the nanoparticle surface (Table 2.1). The drug loading in the NPs was determined from the nitrogen elemental analysis (Table 2.1).

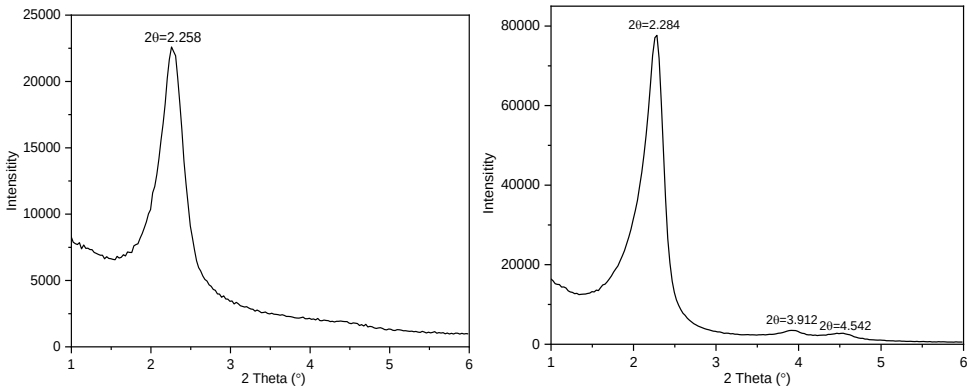

Figure 2.12 p-XRD of **mN6** (left) and **mN8** (right)

The stability of all nanoparticles in milli-Q water suspension (1 mg/mL) was checked by zeta potential. The nanomaterials **dN1**, **dN2**, **dN3, mN6** and **mN7**, prepared from the imidazolium salts, presented positive values from +35.6 to +50.2 mV, which are in good agreement with a good stability in water suspension and the presence of cationic imidazolium moieties on the surface of the particles. On the other hand, the nanoparticles **dN4**, **dN5** and **mN8,** synthesized from neutral silylated derivatives, showed negative zeta potential values (from -21 to -64.7 mV) also indicative of a good stability. The negative sign in these samples is in consonance with the non-protonation of the basic imidazole ring and the residual deprotonated silanol groups (see Figure 2.13 for the DLS of **dN3** and **mN8**).

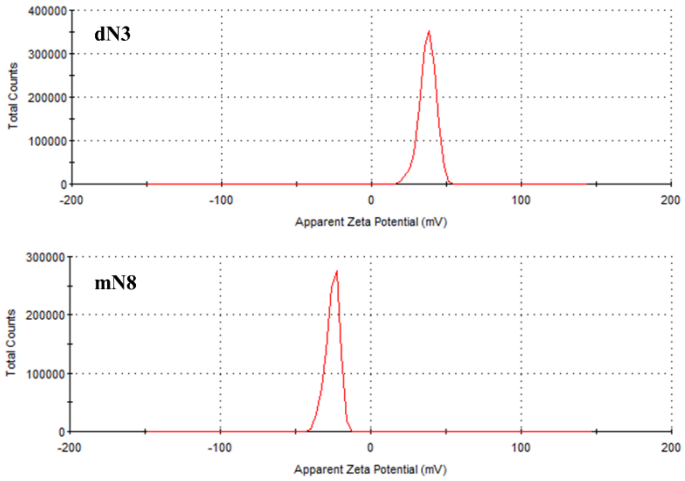

Figure 2.13 Zeta potential of **dN3** and **mN8**

Solid-state ^{29}Si and ^{13}C NMR spectra ensured the presence of the corresponding organic moiety in the nanomaterials. The ^{29}Si CP MAS NMR showed two groups of chemical shifts: T units from -61 to -69 ppm formed from the organosilanes and Q units ranging from -90 to -111 ppm resulting from TEOS.

The presence of T signals suggested that the integrity of the Si-C bond was maintained during the formation of the nanomaterials, which was also confirmed by a signal between 8 and 10 ppm in the solid-state ^{13}C NMR spectra (see Figure 2.14 for ^{29}Si CP MAS NMR and ^{13}C CP MAS NMR spectra of **dN5** as an example).

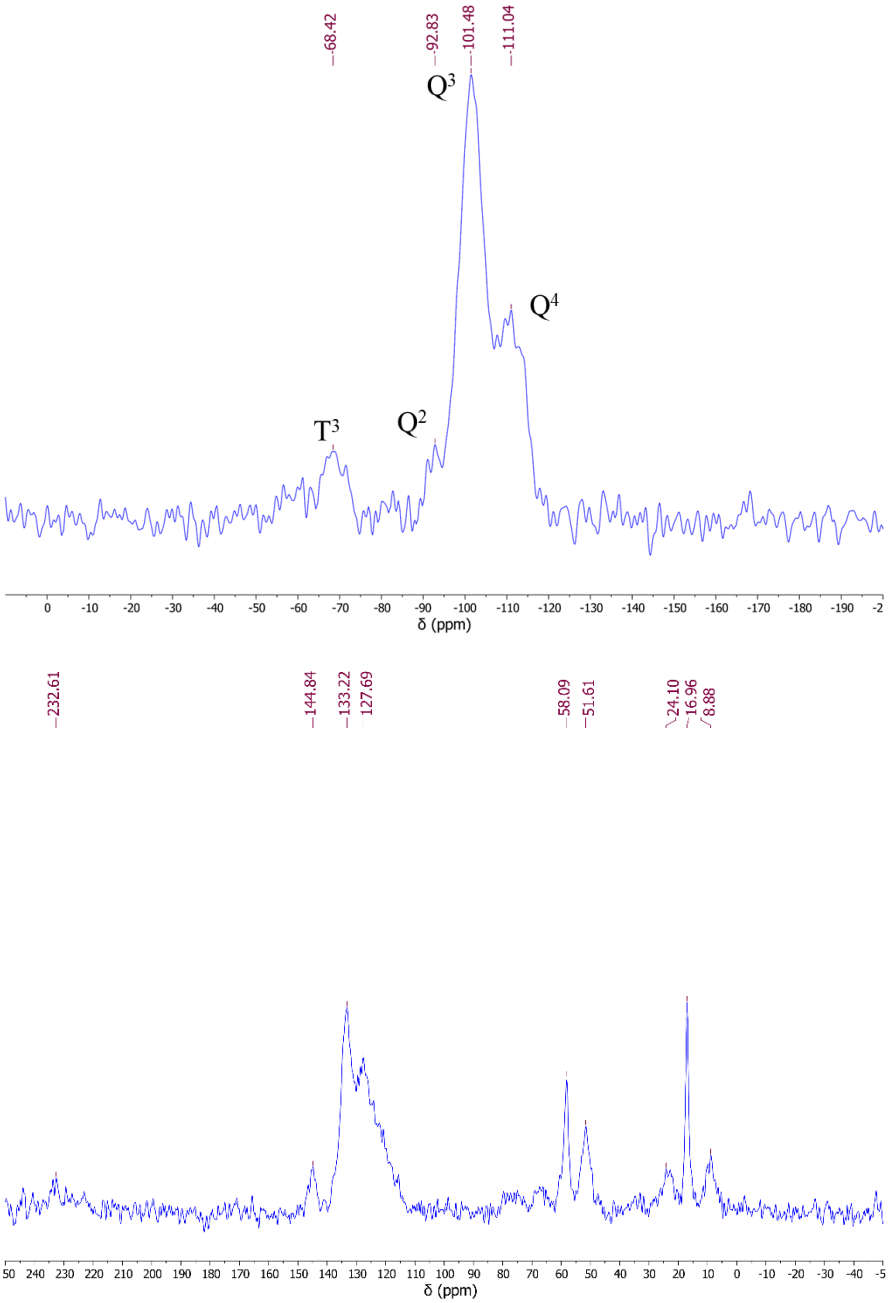

Figure 2.14 ^{29}Si CP MAS NMR (top) and ^{13}C CP MAS NMR (bottom) spectra of **dN5**

2.3.3 Preparation and characterization of cotton fabrics coated with antifungal functionalized silica nanoparticles

The preparation of cotton fabrics coated with antifungal-functionalized silica nanoparticles was

performed as represented in Scheme 2.10. Before coating, the cotton fabrics were washed with liquid soap in a solution of water and K_2CO_3 for one hour, rinsed with distilled water and dried in an oven at 100 °C for one hour. There is a little difference in the dip coating process of cotton fabrics with dense and mesoporous NPs.

On one hand, a piece of 3 x 3 cm of clean cotton fabric was added to a previously sonicated (30 min) milky solution resulting from the co-hydrolysis of TEOS with organosilanes in aqueous ammonia in ethanol, and further sonicated for 30 minutes. Afterwards, the cotton fabric was removed from the solution, washed with distilled water, and then dried under high vacuum at 50 ºC (**Fabric-dN1** to **Fabric-dN5** in Scheme 2.10).

On the other hand, once the grafting procedure for the preparation of mesoporous functionalized nanoparticles was finished, a piece of 3 x 3 cm of clean cotton fabric was immersed into the previously sonicated solution (30 min) and further sonicated for 30 minutes. After this time, the cellulose material was removed, washed with toluene, and dried under high vacuum at 50 ºC (**Fabric-mN6** to **Fabric-mN8** in Scheme 2.10).

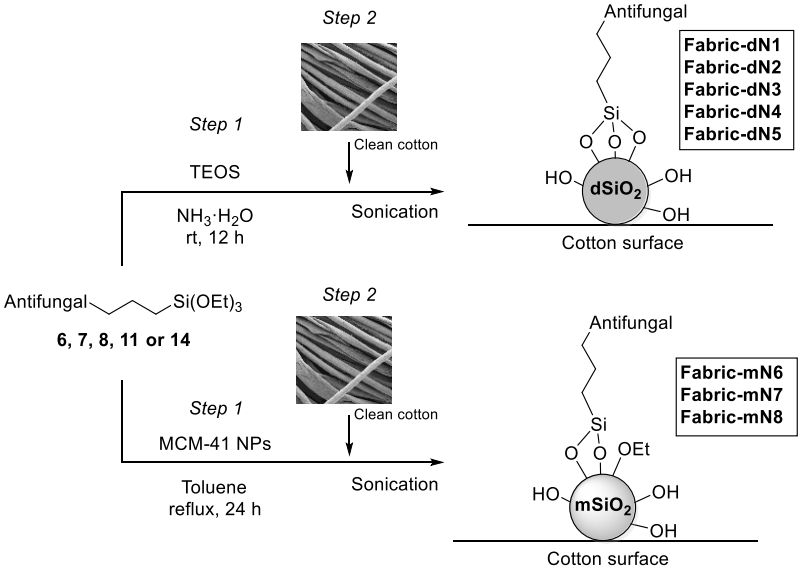

Scheme 2.10 Preparation of cotton fabrics coated with antifungal-functionalized silica nanoparticles

The cotton textiles coated with the nanostructures were analysed by scanning electron microscopy (SEM). In Figure 2.15 we present the SEM images of **Fabric-dN1** to **Fabric-dN5**. The cotton fabrics (**Fabric-dN1** – **Fabric-dN3**) coated with dense nonporous nanoparticles prepared from silylated imidazolium iodides presented cauliflower like structures, in agreement with the high polydispersity index observed in the DLS measurements of the corresponding nanoparticles (**dN1**-**dN3**). On the contrary, cotton fabrics (**Fabric-dN4** and **Fabric-dN5**) coated with dense nanoparticles prepared from the non-charged imidazole-containing organosilanes presented high homogeneity regarding the

particles size. This last feature was also observed in cotton fabrics (**Fabric-mN6** – **Fabric-mN8**) coated with functionalized mesoporous nanoparticles, regardless of the chemical nature of the employed organosilanes. Thus, in Figure 2.16 we can observe the SEM images of **Fabric-mN6**, **Fabric-mN7**, and **Fabric-mN8** in which the NPs are distributed uniformly on the surface of cotton fabrics.

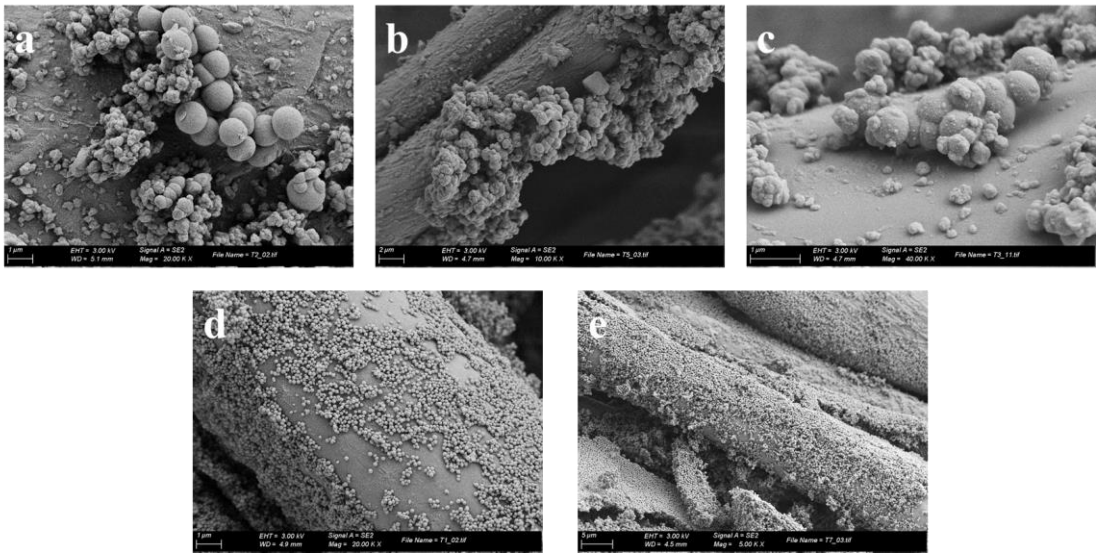

Figure 2.15 SEM images of coated cotton fabrics: a) **Fabric-dN1**, b) **Fabric-dN2**, c) **Fabric-dN3**, d) **Fabric-dN4** and e) **Fabric-dN5**

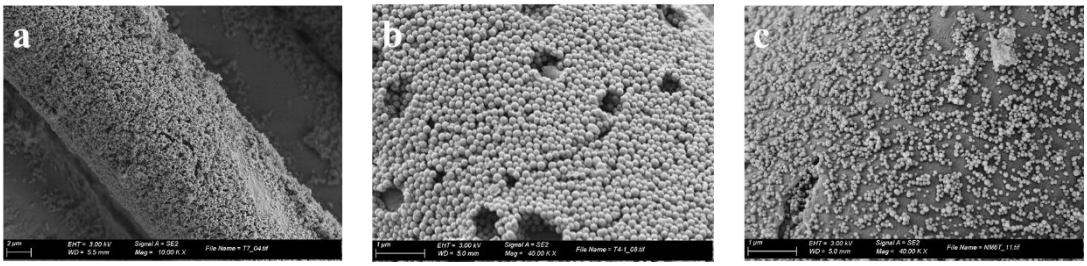

Figure 2.16 SEM images of coated cotton fabrics: a) **Fabric-mN6**, b) **Fabric-mN7** and c) **Fabric-mN8**

The surface composition was checked by energy dispersive X-ray spectroscopy (EDX) and element mapping. The presence of Si, C, O, N and, in some cases, Cl and Br atoms, were clearly observed (see Figure 2.17 for the element mapping of **Fabric-dN5** as an example).

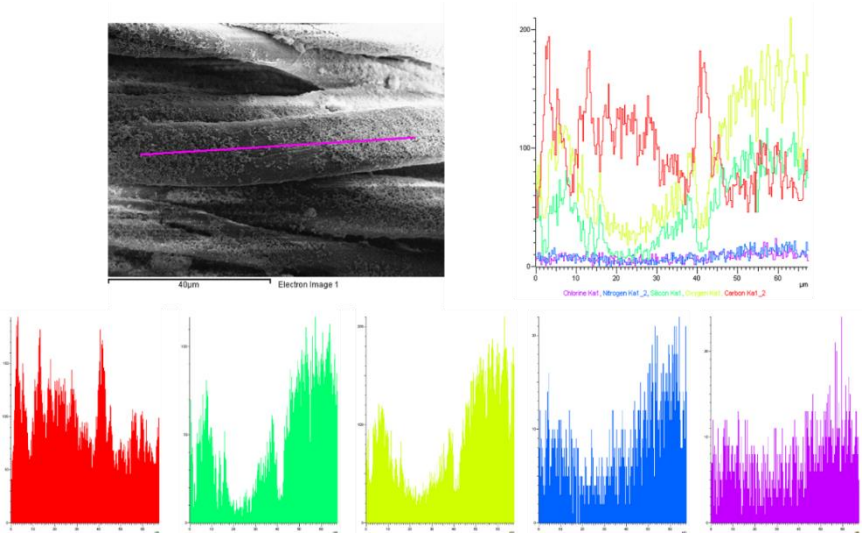

Figure 2.17 EDX linear scanning and element mapping of **Fabric-dN5**

The measured contact angle for **Fabric-dN3** and **Fabric-dN5** were 131º and 148º, respectively (Figure 2.18), indicative of hydrophobic surfaces. Contrarily, **Fabric-mN7** and **Fabric-mN8** were not hydrophobic as the modified fabrics absorbed the water drop after a few seconds.

Figure 2.18 Contact angle of **Fabric-dN3** (left) and **Fabric-dN5** (right)

2.3.4 Antifungal activity of the fabrics coated with antifungal-functionalized silica nanoparticles

This part of the work has been undertaken in collaboration with the group of Professor Maria Angeles Calvo-Torras of the Department of *Sanitat i Anatomia Animals* of the *Universitat Autònoma de Barcelona*, and E. Leonardo Arosemena-Angulo performed the experiments.

The antifungal activity of all the fabrics coated with antifungal-functionalized silica nanoparticles was tested against four different microorganisms, three filamentous fungi and a yeast (*Trichophyton mentagrophytes CECT 2783*, *Aspergillus brasiliensis CECT 2091*, *Penicillium chrysogenum CECT 2307* and *Candida albicans CECT 1001*). *Trichophyton mentagrophytes* is a fungus which causes ringworm in companion animals, tinea infections in humans and one of the most common fungi that cause zoonotic skin disease. *Aspergillus brasiliensis* is a major environmental pollutant. *Penicillium chrysogenum* can induce respiratory allergic symptoms such as allergic rhinitis, asthma, and allergic broncho-pulmonary mycosis. *Candida albicans* is an opportunistic pathogenic yeast that is a common member of the human gut flora but can cause infections in humans and animals such as candidiasis and onychomycosis.

Preliminary experiments were carried out following the antibiogram technique (antifungigram)[74-78] to study the production of inhibition halos using fragments of the impregnated cotton fabrics (**Fabric-dN3**) and confronting them with the fungal strains. Small pieces of the cotton fabrics were deposited on the surface's plate and inoculated with each of the microorganisms. They were incubated for 24–48 h and the inhibition halos were observed (see Table 2.2).

Table 2.2. Inhibition halos for the impregnated cotton fabric (**fabric-dN3**) that were confronted with the fungal strains following the antibiogram technique

Material	Strain			
	Penicillium rugulosum	*Aspergillus brasiliensis*	*Trichophyton mentagrohytes*	*Candida albicans*
Fabric-dN3	22 mm	20 mm	3 mm	15 mm

Considering these initial positive results, then we carried out a quantitative study of the activity of these impregnated fabrics, mimicking its application on the surface of the skin of the affected organism. The methodology used was a modification of that indicated in international standards (UNEEN ISO 846:2020 Plastics- Evaluation of the action of microorganisms (ISO 846:2019)) to quantify the capacity to reduce the viability of the fungal strains tested. Thus, the modified fabrics were impregnated with the

corresponding strain and kept in the stove at 25 ºC in aerobiosis for 24 h. The results are shown in Table 2.3. The activity of the modified fabric has been expressed in % effectiveness as $[(CFU_0 - CFU_{24})/CFU_0] \times 100$, where CFU_{24} (CFU = Colony Forming Units) is the number of fungal cells that are viable after the fabric is kept in contact with fungi for 24 h and CFU_0 is the number of viable fungal cells at time 0. To our delight, all the fabrics were found to be moderately (25%) or highly active (90%) against *Trichophyton mentagrophytes*. The effectiveness against the yeast *Candida albicans* varies from 25 to 75%. Whereas **Fabric-dN4** and **Fabric-mN8** were not active against *Aspergillus brasiliensis*, the other modified cotton fabrics exhibited low (10%), moderate (25%) or high (90%) activity. Excellent antifungal properties (90% effectiveness) were found for **Fabric-dN1**, **Fabric-mN6** and **Fabric-mN7** against *Penicillium chrysogenum*, and moderate activity (25%) in the case of **Fabric-dN4** and **Fabric-mN8**. Thus, the antifungal activity of the coated fabrics was found to be highly dependent on the microorganism. That allows specific fungal treatments for each microorganism. Within the same fungal or yeast strain, some influence of the structural features of the organic moiety or the type of nanoparticles was also observed, although no clear general rule can be inferred from the results. Within *Trichophyton mentagrophytes* the higher % effectiveness of **Fabric-mN7** over **Fabric-dN3** and of **Fabric-mN8** over **Fabric-dN5** (see Table 2.3) could be attributed to the differences in the hydrophilicity/hydrophobicity of the corresponding surfaces. As the microorganisms are grown in aqueous medium, a hydrophobic antifungal cotton surface would make more difficult the interaction with the fungus. It is noteworthy that **Fabric-dN1**, **Fabric-mN6** and **Fabric-mN7** are good candidates to be used as topical antifungal agents in cotton medical textiles for the remarkable results.

Table 2.3 Antifungal activity (% effectiveness) of **Fabric-dN1** to **Fabric-dN5** and **Fabric-mN6** to **Fabric-mN8**.

Material	**Strain**			
	Trichophyton mentagrophytes	*Aspergillus brasiliensis*	*Penicillium chrysogenum*	*Candida albicans*
Fabric-dN1	90	10	90	55
Fabric-dN2	25	25	0	25
Fabric-dN3	25	25	0	25
Fabric-dN4	90	0	25	25
Fabric-dN5	25	25	0	25
Fabric-mN6	90	10	90	55
Fabric-mN7	90	90	90	75
Fabric-mN8	90	0	25	25

2.4 Conclusions

a) Several silylated derivatives have been prepared taking the topical antifungal agent miconazole as a model. Different linkers to attach the silylated unit have been employed (carbamate and triazole). Additionally, as miconazole is used as a nitrate salt, the alkylation of the imidazole ring with a silylated alkyl iodide has also been performed.

b) The covalent anchoring of these silylated derivatives to mesoporous or dense silica nanoparticles has been achieved by grafting and co-condensation procedures, respectively. The functionalized nanoparticles were characterized by EA, IR, ^{13}C and ^{29}Si CP MAS solid-state NMR, TEM, p-XRD, DLS and zeta-potential.

c) Cotton textiles have been coated with these antifungal-functionalized silica nanoparticles under ultrasonic conditions. The characterization of the coated cotton fabrics has been carried out by SEM, EDX and element mapping.

d) The antifungal activity of all the modified fabrics has been tested against three filamentous fungi and a yeast (*Trichophyton mentagrophytes* CECT 2783, *Aspergillus brasiliensis* CECT 2091, *Penicillium chrysogenum* CECT 2307 and *Candida albicans* CECT 1001) and has been found to be highly dependent on the microorganism. Some influence of the structural features of the organic moiety, the type of nanoparticles and the hydrophobicity of the cotton surface has also been observed, although no general rule can be deduced. Remarkably, all of them have shown activity against *Candida albicans* and *Trichophyton mentagrop*hytes, with up to 75 and 90% effectiveness, respectively. High expectations arise for topical cutaneous applications in wound dressings (bandages, gauzes, strips).

2.5 Experimental section

2.5.1 General information

The ^{1}H and ^{13}C NMR spectra were recorded at 298.0 K on a Bruker DPX-360 or 400 MHz Bruker Advance-III equipped with a BBFO probe with an automatic tuning. All the spectra were calibrated using the residual solvent signal ($CDCl_3$, δ_H, 7.26 and δ_C, 77.16 ppm and CD_3OD, δ_H, 3.31 and δ_C, 49.0 ppm). Chemical shift data were expressed in ppm and coupling constant (*J*) values in Hz. Multiplicity of peaks was abbreviated as s (singlet), d (doublet), t (triplet), q (quartet), and dd (doublet of doublets). The ^{29}Si and ^{13}C CP-MAS NMR spectra were obtained from a Bruker AV400WB, the repetition time was 5 seconds with contact times of 2 milliseconds and the number of scans acquired was between 800 and 1600. This NMR instrument belongs to the *Servicio de Resonancia Magnética Nuclear de Sólidos del Instituto de Ciencia de Materiales de Madrid - CSIC*. FTIR spectroscopy was recorded with a Bruker Tensor 27 spectrometer using a Golden Gate ATR module with a diamond window. High resolution mass spectra (HRMS) were obtained by direct injection of the sample with electrospray techniques in Hewlett-Packard 5989A and microTOF-Q instruments, respectively. Elemental analysis of C, N, and H were performed using Flash 2000 Organic Elemental analyzer of Thermo Fisher Scientific with BBOT as an internal standard. Transmission electron microscopy (TEM) analyses were performed on a JEM-2011 Electron Microscope at 200 kV. Scanning electron microscopy (SEM), energy-dispersive X-ray spectroscopy (EDX), and element line scans mapping were taken on a SEM Zeiss Merlin with and INCA detector from Oxford Instruments. Thus, microscopic investigations of the specimens were carried out using a ZEISS MERLIN scanning electron microscope (SEM). The specimens were mounted on conductive carbon adhesive tabs and images were taken after the specimens had been sputter-coated (K550X EMITECH) with a very thin layer of gold. For the elemental composition of the fabric surface, an INCA energy dispersive X-ray (EDX) detector from Oxford Instruments was used. Dynamic light scattering (DLS) and zeta potential measurements have been performed using a Zetasizer Nano ZS (Malvern Instruments) with 8 mg of silica NPs in 8 mL of Milli-Q water, and the pH of the solution was measured by CRISON pH meter Basic 20. The surface areas were determined by the Brunauer-Emmett-Teller (BET) method from N_2 adsorption−desorption isotherms obtained with a Micromeritics ASAP2000 analyzer after degassing samples for 55 h at 30°C under vacuum. Powder X-ray diffraction (P-XRD) was performed with X'Pert Power (PANalytical, Almelo, Netherlands), 45Kv/40 mA, Kα radiation (λ=1.5419 Å) with a cooper anode. For contact angle (CA) measurements, the hydrophobic tests performed were the measurement of the contact angle of a water droplet (4 µL) deposited on top of each fabric. These experiments were carried out at ICMAB installations with a Contact Angle Measuring System DSA 100 from KRÜSS, which is located in a physico-chemical laboratory (humidity and temperature control). All chemicals were purchased from Fluorochem and

Merck, and they were used without further purification, unless specified. MCM-41 nanoparticles, (3-iodopropyl)triethoxysilane and (3-azidopropyl)triethoxysilane were prepared as previously reported in our group.[63, 79, 80]

2.5.2 General procedure for the preparation of 4-((1-(2,4-dichlorophenyl)-2-(1*H*-imidazol-1-yl)ethoxy)methyl) arenes

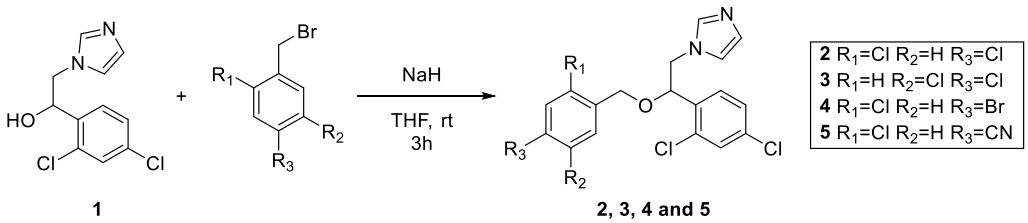

1 **2, 3, 4 and 5**

In a dried Schlenk the benzylic alcohol derivative **1** (1 equiv) was dissolved in 10 mL of anhydrous THF under argon atmosphere. Then, sodium hydride (60% in mineral oil, 4 equiv) was added to the solution and the mixture was stirred at rt for 15 minutes. Then, the corresponding benzylic bromide (1.23 equiv) was added and the mixture was stirred at rt until completion of the reaction (3 hours). When the reaction was over, 10 mL of cold water was added, followed by the addition of 20 mL of dichloromethane. The organic phase was separated, and the aqueous layer was extracted with more dichloromethane. The organics were combined, dried over anhydrous sodium sulphate and evaporated under reduced pressure. The products were purified by flash column chromatography (hexane : AcOEt 1:4).

1-(2-((2,4-dichlorobenzyl)oxy)-2-(2,4-dichlorophenyl)ethyl)-1*H*-imidazole (2)[68]

White solid, 70% yield (566 mg, 1.36 mmol) from 500 mg (1.95 mmol) of starting material **1**. **M.P.**: 160-163 ºC. **^{1}H NMR** (360 MHz, $CDCl_3$) δ (ppm): 4.08 (dd, *J* = 7.4 Hz, *J* = 14.5 Hz, 1H), 4.25 (dd, *J* = 2.5 Hz, *J* = 14.5 Hz, 1H), 4.36 (d, *J* = 14.5 Hz, 1H), 4.50 (d, *J* = 14.5 Hz, 1H), 5.03 (dd, *J* = 2.5 Hz, *J* = 7.4 Hz, 1H), 6.92 (s, 1H), 7.03 (s, 1H), 7.20 (d, *J* = 8.4 Hz, 1H), 7.25(dd, *J* = 7.7 Hz, *J* = 8.4 Hz, 1H), 7.38 (m, 3H) and 7.47 (bs, 2H). **^{13}C NMR** (91 MHz, $CDCl_3$) δ (ppm): 51.3, 68.2, 77.6, 119.8, 127.4, 128.0, 128.4, 129.3, 129.4, 129.7, 130.0, 132.3, 133.3, 133.7, 133.7, 134.4, 135.1, 138.0.

1-(2-((3,4-dichlorobenzyl)oxy)-2-(2,4-dichlorophenyl)ethyl)-1H-imidazole (3)[69]

White solid, 81% yield (337 mg, 0.81 mmol) from 257 mg (1.0 mmol) of starting material **1**. **M.P.**: 155-157 ºC. **^{1}H NMR** (360 MHz, $CDCl_3$,) δ (ppm): 4.05 (dd, *J* = 7.4 Hz, *J* = 14.5 Hz, 1H), 4.19 (m, 2H), 4.36 (d, *J* = 14.5 Hz, 1H), 4.41 (d, *J* = 14.5 Hz, 1H), 4.96 (dd, *J* = 2.5 Hz, *J* = 7.4 Hz, 1H), 6.93 (m, 2H), 7.05 (s, 1H), 7.23 (bs, 1H), 7.31 (bs, 2H), 7.35 (d, *J* = 8.4 Hz, 1H), 7.45 (m, 2H). **^{13}C NMR** (91 MHz, $CDCl_3$): δ (ppm) = 51.3, 70.1, 77.1, 119.7, 126.8, 128.1, 128.4, 129.4, 129.5, 129.7, 130.6, 132.1, 132.7, 133.4, 133.7, 135.1, 137.1, 137.9.

1-(2-((4-bromo-2-chlorobenzyl)oxy)-2-(2,4-dichlorophenyl)ethyl)-1H-imidazole (4)

White solid, 70% yield (290 mg, 0.63 mmol) from 231 mg (0.90 mmol) of starting material **1**. **M.P.**: 82-84 ºC. **^{1}H NMR** (360 MHz, $CDCl_3$) δ (ppm): 4.08 (dd, *J* = 7.4 Hz, *J* = 14.5 Hz, 1H), 4.25 (dd, *J* = 2.5 Hz, *J* = 14.5 Hz, 1H), 4.34 (d, *J* = 14.5 Hz, 1H), 4.49 (d, *J* = 14.5 Hz, 1H), 5.04 (dd, *J* = 2.5 Hz, *J* = 7.4 Hz, 1H), 6.91 (s, 1H), 7.04 (s, 1H), 7.14 (d, *J* = 8.4 Hz, 1H), 7.30 (m, 2H), 7.40 (dd, *J* = 2.0 Hz, *J* = 8.2 Hz, 1H), 7.49 (m, 2H). **^{13}C NMR** (91 MHz, $CDCl_3$,) δ (ppm): 51.7, 68.7, 77.6, 78.0, 120.1, 122.5, 128.3, 128.8, 129.8, 130.1, 130.7, 132.4, 133.7, 134.1, 134.2, 134.3, 134.5, 138.3. **IR** (ATR) ν (cm^{-1}): 3059, 2896, 1580, 1073. **EA** Calcd for $C_{18}H_{14}BrCl_3N_2O$: C, 46.94; H, 3.06; N, 6.08. Found: C, 46.99, H, 3.14, N, 5.90.

3-chloro-4-((1-(2,4-dichlorophenyl)-2-(1*H*-imidazol-1-yl)ethoxy)methyl)benzonitrile (5)

White solid, 72% yield (293 mg, 0.72 mmol) from 257 mg (1.0 mmol) of starting material 1. **M.P.**: 79-82 ºC. **^{1}H NMR** (360 MHz, $CDCl_3$) δ (ppm): 4.14 (dd, *J* = 7.5 Hz, *J* = 14.6 Hz, 1H), 4.29 (dd, *J* = 2.7 Hz, *J* = 14.6 Hz, 1H), 4.43 (d, *J* = 14.0 Hz, 1H), 4.57 (d, *J* = 14.0 Hz, 1H), 5.07 (dd, *J* = 7.5 Hz, *J* = 2.7 Hz, 1H), 6.93 (s, 1H), 7,06 (s, 1H), 7.31 (bs, 2H), 7.41 (d, *J* = 8.0 Hz, 1H), 7.49 (m, 2H), 7.57 (dd, *J* = 8.0 Hz, *J* = 1.2 Hz, 1H), 7.63 (d, *J* = 1.2 Hz, 1H). **^{13}CNMR** (101 MHz, $CDCl_3$,) δ (ppm): 51.2, 68.1, 77.3, 78.1, 112.8, 117.3, 119.7, 128.1, 128.2, 128.9, 129.4, 129.8, 130.7, 132.4, 133.2, 133.3, 135.3, 137.5, 140.5. **IR** (ATR) ν (cm^{-1}): 3073, 2931, 2231, 1470, 1095, 788. **HRMS** (ESI) m/z: $[M+H]^+$ Calcd for $C_{19}H_{15}Cl_3N_3O$ 406.0275; found 406.0271.

2.5.3 General procedure for the preparation of imidazolium iodides (6, 7 and 8)

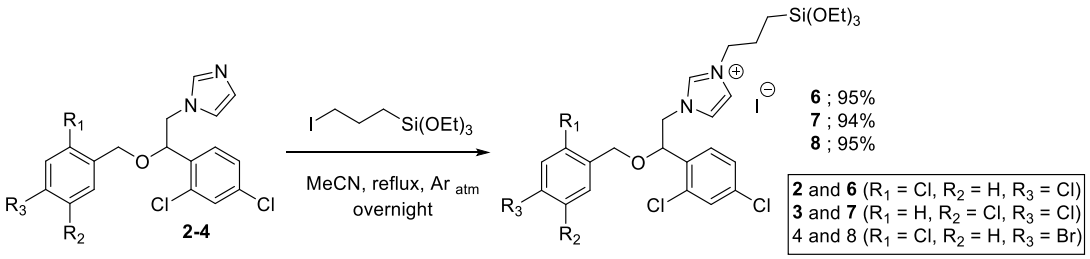

A solution of the corresponding imidazole derivative (1 equiv) and triethoxy(3-iodopropyl)silane (1 equiv) in dry acetonitrile (20 mL) was refluxed under argon overnight. After completion of the reaction, the solvent was removed under high vacuum. The final oil was washed with anhydrous pentane, affording the corresponding imidazolium iodide in excellent yield.

1-(2-((2,4-dichlorobenzyl)oxy)-2-(2,4-dichlorophenyl)ethyl)-3-(3-(triethoxysilyl)propyl)-1*H*-imidazol-3-ium iodide (6)

Yellowish oil, 95% yield (512 mg, 0.68 mmol) from 300 mg (0.72 mmol) of starting material **2**. **^{1}H NMR** (360 MHz, $CDCl_3$) δ (ppm): 0.56 (t, *J* = 7.2 Hz, 2H), 1.19 (t, *J* = 7.0 Hz, 9H), 2.01 (quint, *J* = 7.3 Hz, 2H), 3.80 (q, *J* = 7.0 Hz, 6H), 4.38 (m, 2H), 4.45 (d, *J* = 12.0 Hz, 1H), 4.51 (d, *J* = 12.0 Hz, 1H), 4.64 (m, 2H), 5.22 (t, *J* = 5.5 Hz, 1H), 7.25 (m, 1H), 7.3 (m, 1H), 7.39 (m, 5H), 9.85 (s, 1H). **^{13}C NMR** (91 MHz, $CDCl_3$) δ (ppm): 7.1, 18.3, 24.3, 51.9, 53.3, 58.7, 68.3, 75.8, 121.9, 123.0, 127.3, 127.9, 128.2, 128.4, 129.2, 129.9, 131.3, 132.1, 133.3, 133.6, 134.7, 135.7, 137.8. **IR** (ATR) ν (cm^{-1}): 3362, 2971, 1589, 1043. **HRMS** (ESI) m/z: $[M]^+$ Calcd for $C_{27}H_{35}Cl_4N_2O_4Si$ 619.1115; found 619.1102.

1-(2-((3,4-dichlorobenzyl)oxy)-2-(2,4-dichlorophenyl)ethyl)-3-(3-(triethoxysilyl)propyl)-1*H*-imidazol-3-ium iodide (7)

Yellowish oil, 94% yield (507 mg, 0.67 mmol) from 300 mg (0.72 mmol) of starting material **3**. **^{1}H NMR** (360 MHz, $CDCl_3$) δ (ppm): 0.63 (t, *J* = 7.2 Hz, 2H), 1.25 (t, *J* = 7.1 Hz, 9H), 2.05 (quint, *J* = 7.2 Hz, 2H), 3.83 (q, *J* = 7.1 Hz, 6H), 4.39 (m, 2H), 4.42 (d, *J* = 12.0 Hz, 1H), 4.54 (d, *J* = 12.0 Hz, 1H), 4.68 (d, *J* = 5.5 Hz, 1H), 5.25 (t, *J* = 5.5 Hz, 1H), 7.13 (m, 2H), 7.29 (m, 3H), 7.36 (d, *J* = 7.0 Hz, 1 H), 7.49 (m, 2H), 10.19 (s, 1H). **^{13}C NMR** (91 MHz, $CDCl_3$) δ (ppm): 7.1, 18.4, 24.4, 51.9, 53.3, 58.7, 68.3, 75.8, 121.9, 123.1, 127.3, 128.2, 129.1, 129.2, 130.0, 131.3, 132.1, 132.7, 133.7, 134.1, 134.8, 135.7, 137.2. **IR** (ATR) ν (cm^{-1}): 3346, 2969, 1588, 1075. **HRMS** (ESI) m/z: $[M]^+$ Calcd for $C_{27}H_{35}Cl_4N_2O_4Si$ 619.1115; found 619.1109.

1-(2-((4-bromo-2-chlorobenzyl)oxy)-2-(2,4-dichlorophenyl)ethyl)-3-(3-(triethoxysilyl)propyl)-1*H*-imidazol-3-ium iodide (8)

Yellowish oil, 95% yield (613 mg, 0.77 mmol) from 375 mg (0.81 mmol) of starting material **4**. **^{1}H NMR** (360 MHz, $CDCl_3$) δ (ppm): 0.60 (t, *J* = 7.2 Hz, 2H), 1.23 (t, *J* = 7.1 Hz, 9H), 2.01 (quint, *J* = 7.2 Hz, 2H), 3.83 (q, *J* = 7.1 Hz, 6H), 4.36 (m, 2H), 4.43 (d, *J* = 12.0 Hz, 1H), 4.52 (d, *J* = 12.0 Hz, 1H), 4.64 (d, *J* = 5.5 Hz, 1H), 5.24 (t, *J* = 5.5 Hz, 1H), 7.31 (m, 3H), 7.40 (d, *J* = 7.0 Hz, 1H), 7.47 (m, 4H), 10.0 (s, 1H). **^{13}C NMR** (91 MHz, $CDCl_3$) δ (ppm): 7.0, 18.4, 24.3, 51.9, 53.3, 58.7, 68.4, 75.9, 121.6, 122.7, 128.6, 129.1, 129.7, 130.0, 130.6, 131.7, 132.0, 132.1, 133.2, 133.6, 134.4, 135.8, 137.6. **IR** (ATR) ν (cm^{-1}): 3371, 2971, 1585, 1043. **HRMS** (ESI) m/z: $[M]^+$ Calcd for $C_{27}H_{35}BrCl_3N_2O_4Si$ 663.0610; found 663.0598.

2.5.4 Synthesis of 4-(3-chloro-4-((1-(2,4-dichlorophenyl)-2-(1*H*-imidazol-1-yl)ethoxy)methyl)phenyl)-2-methylbut-3-yn-2-ol (9)

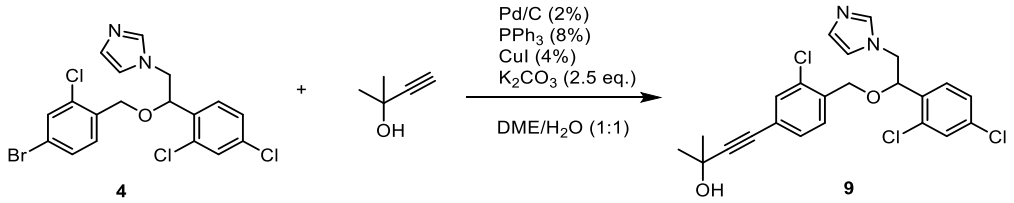

Compound **4** (0.50 g, 1.08 mmol) was dissolved in a degassed mixture of 3 mL of water and 3 mL of 1,2-dimethoxyethane under nitrogen atmosphere. To the solution were added K_2CO_3 (375 mg, 2.71 mmol), CuI (8.3 mg, 0.04 mmol), PPh_3 (23 mg, 0.08 mmol) and Pd/C (23 mg, 0.02 mmol). The mixture was stirred for 30 minutes at rt and then the alcoholic alkyne was added through syringe (0.26 mL, 2.74 mmol). The reaction was stirred overnight at 80 ºC under inert atmosphere, then the mixture was cooled to room temperature, filtered through Celite® and extracted with dichloromethane three times. The organics were washed with water, dried, and concentrated in vacuo. The residue was purified by flash column chromatography (AcOEt 100%) to afford **9**. White solid, 78% yield (393 mg, 0.84 mmol). **M.p.**: 122-125 ºC. **^{1}H NMR** (360 MHz, MeOD) δ (ppm): 1.63 (s, 6H), 2.54 (bs, 1H), 4.09 (dd, *J* = 7.5 Hz, ^2J = 14.6 Hz, 1H), 4.25 (dd, *J* = 2.7 Hz, *J* = 14.6 Hz, 1H), 4.37 (d, *J* = 14.0 Hz, 1H), 4.52 (d, *J* = 14.0 Hz, 1H), 5.03 (dd, *J* = 2.7 Hz, *J* = 7.5 Hz, 1H), 6.94 (s, 1H), 7.06 (s, 1H), 7.20 (d, *J* = 8.1 Hz, 1H), 7.32 (m, 3H), 7.46 (m, 3H). **^{13}C NMR** (91 MHz, MeOD) δ (ppm): 30.2, 64.4, 68.0, 95.6, 124.3, 127.6, 128.8, 129.1, 129.3, 129.8, 132.8, 133.4, 134.2, 136.6, 134.9. **IR** (ATR) ν (cm^{-1}): 3200, 3082, 2925, 1488, 1040. **EA** Calcd for $C_{23}H_{21}Cl_3N_2O_2$ C: 59.57%, H: 4.56%, N: 6.04%; found C: 59.48%, H: 4.61%, N: 5.83%.

2.5.5 Synthesis of 1-(2-((2-chloro-4-ethynylbenzyl)oxy)-2-(2,4-dichlorophenyl)eth-yl)-1*H*-imidazole (10)

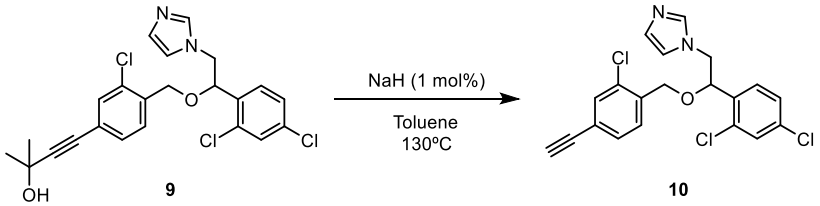

The alcohol **9** (720 mg, 1.44 mmol) was dissolved in dry toluene (30 mL) in a round-bottom flask. Then NaH (60% in mineral oil, 0.6 mg, 0.014 mmol) was added and a distillation system was adapted. The system was heated at 130 ºC for 2 hours. After this time, the TLC showed full conversion and most of the toluene has been distilled. The crude mixture was directly poured into a flash silica gel column chromatography and eluted with pure AcOEt. Terminal alkyne **10** was obtained as a colorless solid in 93% yield (586 mg, 1.33 mmol). **M.p.**: 95-97 ºC. **^{1}H NMR** (360 MHz, $CDCl_3$): δ = 3.13 (s, 1H), 4.09 (dd, *J* = 7.5 Hz, *J* = 14.6 Hz, 1H), 4.24 (dd, *J* = 2.7 Hz, *J* = 14.6 Hz, 1H), 4.39 (d, *J* = 14.0 Hz, 1H),

4.52 (d, *J* = 14.0 Hz, 1H), 5.04 (dd, *J* = 2.7 Hz, *J* = 7.5 Hz, 1H), 6.90 (s, 1H), 7.03 (s, 1H), 7.29 m, (3H), 7.55 (m, 4H). **^{13}C NMR** (91 MHz, $CDCl_3$) δ (ppm): 52.0, 68.5, 77.6, 78.8, 82.0, 123.2, 128.0, 128.3, 128.6, 128.8, 129.7, 130.6, 132.0, 132.1, 132.6, 132.7, 133.2, 133.7, 135.0, 135.6. **IR** (ATR) ν (cm^{-1}): 3293, 2924, 1505, 1076, 790. **HRMS** (ESI) m/z: $[M+H]^+$ Calcd for $C_{20}H_{15}Cl_3N_2O$+H 405.0323; found 405.0314.

2.5.6 Synthesis of 4-(3-chloro-4-((1-(2,4-dichlorophenyl)-2-(1H-imidazol-1-yl) ethoxy)methyl)phenyl)-1-(3-(triethoxysilyl)propyl)-1H-1,2,3-triazole (11)

The alkyne **10** (400 mg, 1.0 mmol) and 3-(azidopropyl)triethoxysilane (0.246 g, 1 mmol) were dissolved in dry acetonitrile (4 mL) in a microwave tube. Then $CuBr(PPh_3)_3$ (9.2 mg, 0.01 mmol) was added and the system was closed. The tube was introduced in the microwave apparatus and the reaction was led to proceed at 120ºC and 200 W for 10 minutes. Afterwards, the solution was filtered through Celite® and then the solvent was evaporated. The residue was gently washed with dry pentane. The final compound **11** was obtained as a colorless oil in 92% yield (601 mg, 0.92 mmol).

^{1}H NMR (360 MHz, $CDCl_3$) δ (ppm): 0.65 (t, *J* = 7.2 Hz, 2H), 1.24 (t, *J* = 7.1 Hz, 9H), 2.09 (quint, *J* = 7.2 Hz, 2H), 3.84 (q, *J* = 7.1 Hz, 6H), 4.12 (bs, 1H), 4.25 (bs, 1H), 4.43 (m, 3H), 4.56 (d, *J* = 14.0 Hz, 1H), 5.06 (bs, 1H), 7.06 (bs, 2H), 7.32 (m, 3H), 7.56 (m, 3H), 7.84 (m, 2H). **^{13}C NMR** (91 MHz, $CDCl_3$) δ (ppm): 7.5, 18.3, 24.3, 52.6, 58.6, 68.6, 77.3, 120.2, 124.1, 126.4, 128.0, 128.4, 128.5, 128.6, 129.6, 131.9, 132.0, 132.1, 132.2, 133.2, 133.7, 134.0, 134.1, 134.9, 146.0. **IR** (ATR) ν (cm^{-1}): 3107, 2927, 1616, 1590, 1040. **HRMS** (ESI) m/z: $[M+H]^+$ Calcd for $C_{29}H_{36}Cl_3N_5O_4Si$+H 652.1675; found 652.1666.

2.5.7 Synthesis of 3-chloro-4-((1-(2,4-dichlorophenyl)-2-(1*H*-imidazol-1-yl)ethoxy) methyl)benzaldehyde (12)

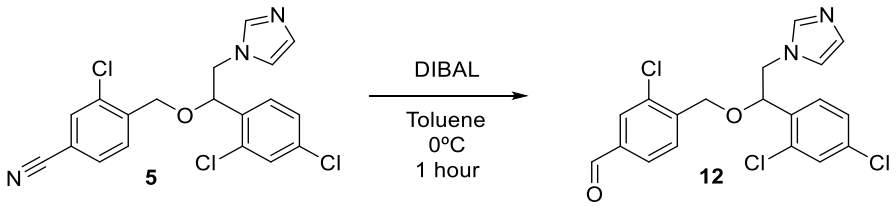

To a stirred solution of compound **5** (1 mmol, 0.41 g) in dry toluene at 0ºC was added 1.5 mL of a DIBAL solution in toluene (1 M). The reaction was stirred at 0ºC for 60 minutes. Afterwards, hydrochloric acid 10 M (10 mL) was added to the mixture, and when the solution turned a white slurry, 20 mL of HCl 1 M was added. Then, a solution of 5% $NaHCO_3$ was added until the pH of the aqueous

solution was 10. The organic phase was separated, and the aqueous phase was further extracted with dichloromethane. The organics were combined, dried over anhydrous Na_2SO_4 and the solvent removed under high vacuum. The titled compound **12** was purified from the crude by flash column chromatography using hexane:ethyl acetate (1:9) as eluent. Oil, 69% yield (285 mg, 0.69 mmol). **^{1}H NMR** (360 MHz, $CDCl_3$) δ (ppm): 4.13 (dd, *J* = 7.5 Hz, *J* = 14.6 Hz, 1H), 4.28 (dd, *J* = 2.7 Hz, *J* = 14.6 Hz, 1H), 4.46 (d, *J* = 14.0 Hz, 1H), 4.58 (d, *J* = 14.0 Hz, 1H), 5.08 (dd, *J* = 7.5 Hz, *J* = 2.7 Hz, 1H), 6.93 (s, 1H), 7.06 (s, 1H), 7.33 (m, 2H), 7.49 (m, 3H), 7.77 (dd, *J* = 8.0 Hz, *J* = 1.2 Hz, 1H), 7.85 (d, *J* = 1.2 Hz, 1H), 9.97 (s, 1H). **^{13}C NMR** (91 MHz, $CDCl_3$) δ (ppm): 51.3, 68.4, 78.0, 119.8, 128.1, 128.2, 128.5, 128.9, 129.3, 129.8, 132.5, 133.3, 134.4, 133.5, 135.2, 136.9, 137.9, 141.4, 190.5. **IR** (ATR) ν (cm^{-1}): 2849, 1730, 1375, 1184. **HRMS** (ESI) m/z: $[M+H]^+$ Calcd for $C_{19}H_{16}Cl_3N_2O_2$ 409.0272; found 409.0263.

2.5.8 Synthesis of (3-chloro-4-((1-(2,4-dichlorophenyl)-2-(1*H*-imidazol-1-yl)ethoxy) methyl)phenyl)methanol (13)

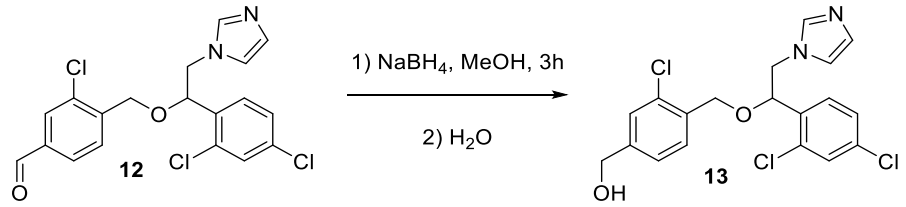

To a stirred solution of aldehyde **12** (2.9 mmol, 1.2 g) in methanol (20 mL) at rt was added in one portion 0.22 g (5.8 mmol) of $NaBH_4$. After 3 hours, the methanolic solution was poured into 100 mL of water. The solution was transferred into a separatory funnel, and extractions with dichloromethane were performed. The organics were collected, dried over anhydrous sodium sulphate, and the solvent removed under high vacuum. The titled alcohol **13** (0.96 g, 2.35 mmol, 81% yield) was obtained as oil after purification from the crude by flash column chromatography using ethyl acetate as eluent. **^{1}H NMR** (360 MHz, $CDCl_3$) δ (ppm): 4.03 (dd, *J* = 7.5 Hz, *J* = 14.6 Hz, 1H), 4.20 (dd, *J* = 2.7 Hz, *J* = 14.6 Hz, 1H), 4.35 (d, *J* = 14.0 Hz, 1H), 4.56 (d, *J* = 14.0 Hz, 1H), 4.56 (bs, 1H), 4.67 (s, 2H), 5.02 (dd, *J* = 7.5 Hz, *J* = 2.7 Hz, 1H), 6.90 (s, 1H), 6.95 (s, 1H), 7.22 (m, 2H), 7.29 (dd, *J* = 8.4 Hz, *J* = 1.2 Hz, 1H), 7.39 (dd, *J* = 7.8 Hz, *J* = 2.2 Hz, 1H), 7.45 ppm (d, *J* = 2.2 Hz, 1H). **^{13}C NMR** (91 MHz, $CDCl_3$) δ (ppm): 51.4, 63.5, 68.7, 77.3, 119.9, 125.2, 127.7, 128.0, 128.5, 128.7, 129.5, 129.6, 133.1, 133.2, 133.4, 134.0, 134.9, 137.5, 143.7. **IR** (ATR) ν (cm^{-1}): 3114, 2852, 1558, 1090. **HRMS** (ESI) m/z: $[M+H]^+$ Calcd for $C_{19}H_{18}Cl_3N_2O_2$ 411.0428; found 411.0432.

2.5.9 Synthesis of 3-chloro-4-((1-(2,4-dichlorophenyl)-2-(1H-imidazol-1-yl)ethoxy) methyl)benzyl (3-(triethoxysilyl)propyl)carbamate (14)

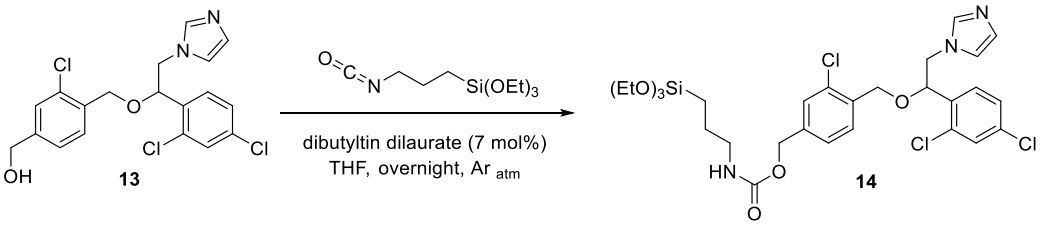

To a stirred solution of alcohol **13** (0.61 mmol, 250 mg) in dry THF (5 mL) was added triethoxy(3-isocyanatopropyl)silane (0.15 mL, 0.24 mmol) and 0.01 mL of dibutyltin dilaurate. The reaction was led to proceed overnight under reflux. Next, the solvent was evaporated under high vacuum. The crude was purified by flash column chromatography using ethyl acetate as eluent to obtain the carbamate **14**. Colorless oil, 81% yield (324 mg, 0.50 mmol). **^{1}H NMR** (360 MHz, $CDCl_3$) δ (ppm): 0.65 (t, *J* = 6.7 Hz, 2H), 1.24 (t, *J* = 7.0 Hz, 9H), 1.66 (quint, *J* = 6.7 Hz, 2H), 3.22 (dd, *J* = 7.0 Hz, *J* = 13.1 Hz, 2H), 3.84 (q, *J* = 7.0 Hz, 6H), 4.09 (dd, *J* = 7.5 Hz, *J* = 14.6 Hz, 1H), 4.25 (dd, *J* = 2.7 Hz, *J* = 14.6 Hz, 1H), 4.39 (d, *J* = 14.0 Hz, 1H), 4.53 (d, *J* = 14.0 Hz, 1H), 5.09 (m, 3H), 6.92 (s, 1H), 7.03 (s, 1H), 7.29 (m, 3H), 7.33 (m, 2H), 7.46 (m, 2H). **^{13}C NMR** (91 MHz, $CDCl_3$) δ (ppm): 7.7, 18.3, 23.2, 43.5, 51.3, 58.5, 65.2, 68.6, 77.6, 119.8, 126.4, 127.9, 128.5, 128.6, 129.2, 129.3, 129.6, 133.2, 133.2, 133.9, 134.3, 135.0, 137.9, 138.4, 156.1. **IR (ATR)** ν (cm^{-1}): 3327, 2972, 1709, 1508, 1243, 1042. **HRMS** (ESI) m/z: $[M+H]^+$ Calcd for $C_{29}H_{39}Cl_3N_3O_6Si$ 658.1674; found 658.1672. **EA** Calcd for $C_{29}H_{38}Cl_3N_3O_6Si$; C: 52.85%, H: 5.81%, N: 6.38%; found C: 52.49%, H: 5.90%, N: 6.48%.

2.5.10 General procedure for the preparation of functionalized silica nanoparticles by co-condensation method (dN1 - dN5)

Tetraethoxysilane (2.08 g, 10.0 mmol) and the corresponding silylated antifungal (**6**, **7**, **8**, **11** or **14**) (0.75 mmol) were dissolved in absolute EtOH (35 mL). Then, an ammonium hydroxide-ethanol solution was added (9 mL of 28% NH_3 H_2O in 35 mL EtOH). The mixture was magnetically stirred intensively (1400 rpm) at room temperature for 12 hours. The functionalized nanoparticles were collected by centrifugation (12000 rpm for 10 minutes) and washed with ethanol until neutral pH was reached. Then, the obtained white solid was washed successively with Mili-Q water and 96% ethanol, and the nanomaterials were dried under high vacuum.

dN1: **EA**: 12.91% C, 1.91% H, 1.42% N (0.507 mmol/g material). **IR** (ATR) ν (cm^{-1}): 3155, 1590, 1474, 1034, 952, 789. **Solid-state ^{13}C-CP-MAS NMR** (100.6 MHz) δ (ppm): 233.85, 227.46, 134.01, 128.23, 80.74, 75.48, 66.71, 52.87, 23.85, 17.30, 8.81. **^{29}Si-CP-MAS NMR** (79.5 MHz) δ (ppm): -61.76 -64.33 (T^3), -90.56 (Q^2), -99.47 (Q^3), -110.09 (Q^4). **DLS** showed high polydispersity, **Zeta Potential**: ζ = 50.2

mV, **pH** = 6.20.

dN2: **EA**: 10.20% C, 1.88% H, 0.93% N (0.332 mmol/g material). **IR** (ATR) ν (cm^{-1}): 3279, 1562, 1472, 1037, 890, 789. **Solid-state ^{13}C-CP-MAS NMR** (100.6 MHz) δ (ppm): 230.03, 131.40, 69.97, 58.40, 52.20, 21.87, 17.04, 8.35. **^{29}Si-CP-MAS NMR** (79.5 MHz) δ (ppm): -63.21, -66.13 (T^3), -90.68, -93.39 (Q^2), -100.96 (Q^3), -109.05 (Q^4). DLS showed high polydispersity, Zeta Potential: ζ = 37.3 mV, pH = 6.15.

dN3: **EA**: 12.04% C, 2.03% H, 1.01% N (0.360 mmol/g material). **IR** (ATR) ν (cm^{-1}): 3159, 1587, 1562, 1471, 1038, 950, 790. **Solid-state ^{13}C-CP-MAS NMR** (100.6 MHz) δ (ppm): 232.20, 227.54, 132.37, 122.47, 76.48, 67.89, 52.48, 24.05, 17.39, 8.84. **^{29}Si-CP-MAS NMR** (79.5 MHz) δ (ppm): -67.06 (T^3), -101.00 (Q^3), -109.66 (Q^4). **DLS** showed high polydispersity, **Zeta Potential**: ζ = 37.4 mV, **pH** = 6.22.

dN4: **EA**: 9.27% C, 1.95% H, 1.10% N (0.263 mmol/g material). **IR** (ATR) ν (cm^{-1}): 3341, 1060, 950, 791. **Solid-state ^{13}C-CP-MAS NMR** (100.6 MHz) δ (ppm): 157.21, 133.87, 128.37, 77.31, 66.27, 58.63, 51.69, 43.69, 23.59, 17.10, 9.77. **^{29}Si-CP-MAS NMR** (79.5 MHz) δ (ppm): -67.87 (T^3), -101.59 (Q^3), -111.11 (Q^4). **DLS:** 427 nm, **Zeta Potential**: ζ = -64.7 mV, **pH** = 8.80.

dN5: EA: 8.05% C, 1.97% H, 1.71% N (0.244 mmol/g material). **IR** (ATR) ν (cm^{-1}): 3230, 1620, 14533, 1045, 953, 792. **Solid-state ^{13}C-CP-MAS NMR** (100.6 MHz) δ (ppm): 232.61, 144.84, 133.22, 127.69, 58.09, 51.61, 24.10, 16.96, 8.88. **^{29}Si-CP-MAS NMR** (79.5 MHz) δ (ppm): -68.42 (T^3), -92.83 (Q^2), -101.48 (Q^3), -111.04 (Q^4). **DLS**: 416 nm, **Zeta Potential**: ζ = -21.0 mV, **pH** = 9.09.

2.5.11 General procedure for the preparation of functionalized silica nanoparticles by grafting method (mN6 - mN8)

The corresponding silylated antifungal derivative (0.30 mmol) and mesoporous silica nanoparticles of MCM-41 type (360 mg) were refluxed in anhydrous toluene (60 mL) for 24 h in a 250 mL round bottom flask equipped with a Dean-Stark apparatus. Then the suspension was centrifuged (13500 rpm at 25 ºC for 45 min). The solid was washed successively with ethanol (3 × 30 mL), acetone (2 × 30 mL) and dichloromethane (2 × 30 mL) (30 min at 50 ºC under sonication, 30 min for centrifugation), and further dried under high vacuum to give the grafted material as a white solid.

mN6: **EA**: 15.28% C, 1.92% H, 1.44% N (0.514 mmol/g material). **IR** (ATR) ν (cm^{-1}): 3292, 1065, 963, 792. **Solid-state ^{13}C-CP-MAS NMR** (100.6 MHz) δ (ppm): 232.82, 134.23, 128.17, 75.53, 52.47, 29.58, 23.53, 8.46. **^{29}Si-CP-MAS NMR** (79.5 MHz) δ (ppm): -66.58, -68.67 (T^3), -101.39 (Q^3), -111.44

(Q^4). **BET**: S_{BET} = 313 m^2/g, V_{pore} = 0.22 cm^3/g. **DLS**: 120 nm, **Zeta Potential**: ζ = 37.0 mV, **pH** = 6.00.

mN7: **EA**: 13.16% C, 1.69% H, 1.32% N (0.471 mmol/g material). **IR** (ATR) ν (cm^{-1}): 3301, 1050, 961, 791 cm^{-1}. **DLS**: 215 nm, **Zeta Potential**: ζ = 35.6 mV, **pH** = 6.38.

mN8: **EA**: 15.62% C, 2.34% H, 2.64% N (0.377 mmol/g material). **IR** (ATR) ν (cm^{-1}): 3323, 1065, 963, 793. **Solid-state ^{13}C-CP-MAS NMR** (100.6 MHz) δ (ppm): 144.62, 133.82, 68.57, 52.09, 22.90, 9.54. **^{29}Si-CP-MAS NMR** (79.5 MHz) δ (ppm): -69.07 (T^3), -92.18 (Q^2), -101.16 (Q^3), -110.22 (Q^4). **BET**: S_{BET} = 192 m^2/g, V_{pore} = 0.125 cm^3/g. **DLS**: 204 nm, **Zeta Potential**: ζ = -28.1 mV, **pH** = 7.89.

2.5.12 General procedure for the coating of cotton fabrics with functionalized silica nanoparticles (Fabric dN1 - dN5 and Fabric mN6 - mN8)

2.5.12.1 With antifungal nonporous silica nanoparticles (Fabric dN1-dN5)

Tetraethoxysilane (2.08 g, 10.0 mmol) and the corresponding silylated antifungal (0.75 mmol) were dissolved in absolute EtOH (35 mL). Then, an ammonium hydroxide-ethanol solution was added (9 mL of 28% $NH_3\,H_2O$ in 35 mL EtOH). The mixture was magnetically stirred intensively (1400 rpm) at room temperature for 12 hours. The resulting mixture was ultrasonicated for 30 min and then a piece of 3 x 3 cm of clean cotton fabric was added (the cotton fabric was previously washed with 1 mL liquid soap and 20 g sodium carbonate in a solution of 400 mL water for one hour and dried in an oven at 100 °C for one hour as reported in our group).[60] The whole system was further sonicated for 30 minutes. Afterwards, the cotton fabric was removed from the solution, washed with distilled water, and then dried under high vacuum at 50 ºC.

2.5.12.2 With antifungal mesoporous silica nanoparticles (Fabric mN6-mN8)

The corresponding silylated antifungal derivative (0.30 mmol) and mesoporous silica nanoparticles of MCM-41 type (360 mg) were refluxed in anhydrous toluene (60 mL) for 24 h in a 250 mL round bottom flask equipped with a Dean-Stark apparatus. The resulting mixture was ultrasonicated for 30 min and then a piece of clean cotton fabric (3 × 3 cm) was immersed in the prepared coating solution. The whole system was ultrasonicated for 30 min. After this period of time, the cotton fabric was removed from the solution, rinsed with toluene and dried in a vacuum oven at 50 °C for several hours.

2.5.13 Antifungal activity of the modified cotton fabrics

With the coated fabrics with nanoparticles in hand, their effectiveness against four microorganisms

(filamentous fungi and yeast) was measured (*Trichophyton mentagrophytes* CECT 2783, *Aspergillus brasiliensis* CECT 2091, *Penicillium chrysogenum* CECT 2307 and *Candida albicans* CECT 1001). A suspension of known concentration was prepared by titration (by preparation of serial dilutions and seeding) of the order of 106 CFU/mL (Colony Forming Units) of each fungal culture. In addition, two assays were performed where sterile Petri dishes were prepared and fragments of the fabrics were deposited (each containing a different type of nanoparticle) and each type of nanoparticle had four replicated impregnated each with one of the four types of fungus. One of the trials was at time 0 and another with a 24-hour exposure (during this period they were kept at 25 ºC and in aerobiosis). Immediately after impregnating the fabrics, in the time trial 0, the deposited culture was recovered using a sterile swab and reseeded in Petri dishes containing Agar Saboureaud (a suitable culture medium for the correct growth of the fungi). The results of this test correspond to the maximum number of CFU that can be recovered per plate just after the direct contact of the fungi with the studied fabrics. The inoculated plates were kept in an oven for 3 - 5 days at 25 ºC in aerobiosis and then proceed to the reading of CFU developed at time 0 (CFU_0). By contrast, the second group of fabrics was kept in contact with fungi for 24 hours. After this time, the same procedure was done as with time group 0, obtaining in this case the CFU in 24 hours (CFU_{24}). Once the results were obtained, the effectiveness of the antifungal can be expressed in % effectiveness as $[(CFU_0 - CFU_{24})/CFU_0]\times100$.

2.6 References

[1] Xu, X.; Wang, Z.; Zhang, X. The human microbiota associated with overall health. *Critical reviews in biotechnology* **2015**, *35* (1), 129-140.
[2] Ajello, L. Natural history of the dermatophytes and related fungi. *Mycopathologia et mycologia applicata* **1974**, *53* (1), 93-110.
[3] Fathy, C. A.; Jonna, G.; Agarwal, A. Blastomycosis. In *The Uveitis Atlas*, Gupta, V., Nguyen, Q. D., LeHoang, P., Agarwal, A. Eds.; Springer India, 2019; pp 1-4.
[4] Aris, P.; Wei, Y.; Mohamadzadeh, M.; Xia, X. Griseofulvin: An Updated Overview of Old and Current Knowledge. *Molecules* **2022**, *27* (20).
[5] Maertens, J. A. History of the development of azole derivatives. *Clinical Microbiology and Infection* **2004**, *10*, 1-10.
[6] Abu-Salah, K. M. Amphotericin B: an update. *British journal of biomedical science* **1996**, *53* (2), 122-133.
[7] Albengres, E.; Le Louët, H.; Tillement, J. P. Systemic antifungal agents. Drug interactions of clinical significance. *Drug safety* **1998**, *18* (2), 83-97.
[8] Zhang, A. Y.; Camp, W. L.; Elewski, B. E. Advances in Topical and Systemic Antifungals. *Dermatologic Clinics* **2007**, *25* (2), 165-183.
[9] Brown, G. D.; Denning, D. W.; Gow, N. A.; Levitz, S. M.; Netea, M. G.; White, T. C. Hidden killers: human fungal infections. *Science translational medicine* **2012**, *4* (165), 165rv113.
[10] Lim, S.-H.; Hudson, S. M. Application of a fiber-reactive chitosan derivative to cotton fabric as an antimicrobial textile finish. *Carbohydrate Polymers* **2004**, *56* (2), 227-234.
[11] *First meeting of the WHO Antifungal Expert Group on Identifying Priority Fungal Pathogens: meeting report* Geneva: World Health Organization, 2020.
[12] Garcia-Solache Monica, A.; Casadevall, A. Global Warming Will Bring New Fungal Diseases for Mammals. *mBio* **2010**, *1* (1), e00061-00010.
[13] Ivanov, M.; Ćirić, A.; Stojković, D. Emerging Antifungal Targets and Strategies. *International Journal of Molecular Sciences* **2022**, *23* (5), 2756.
[14] Gubbins, P. O.; Anaissie, E. J. CHAPTER 7 - Antifungal therapy. In *Clinical Mycology (Second Edition)*, Anaissie, E. J., McGinnis, M. R., Pfaller, M. A. Eds.; Churchill Livingstone, 2009; pp 161-195.
[15] Suchodolski, J.; Muraszko, J.; Bernat, P.; Krasowska, A. A Crucial Role for Ergosterol in Plasma Membrane Composition, Localisation, and Activity of Cdr1p and H^+-ATPase in *Candida albicans*. *Microorganisms* **2019**, *7* (10), 378.
[16] Lepesheva, G. I.; Waterman, M. R. Sterol 14alpha-demethylase cytochrome P450 (CYP51), a P450 in all biological kingdoms. *Biochimica et biophysica acta* **2007**, *1770* (3), 467-477.
[17] Espinel-Ingroff, A. V. The advent of antifungal and immunosuppressive therapies: 1950 to 1969. In *Medical Mycology in the United States: A Historical Analysis (1894–1996)*, Espinel-Ingroff, A. V. Ed.; Springer Netherlands, 2003; pp 49-78.
[18] Cifani, C.; Costantino, S.; Massi, M.; Berrino, L. Commercially available lipid formulations of amphotericin b: are they bioequivalent and therapeutically equivalent? *Acta bio-medica : Atenei Parmensis* **2012**, *83* (2), 154-163.
[19] Vardanyan, R.; Hruby, V. Chapter 30 - Antibiotics. In *Synthesis of Best-Seller Drugs*, Vardanyan, R., Hruby, V. Eds.; Academic Press, 2016; pp 573-643.
[20] Kristanc, L.; Božič, B.; Jokhadar, Š. Z.; Dolenc, M. S.; Gomišček, G. The pore-forming action of polyenes: From model membranes to living organisms. *Biochimica et Biophysica Acta (BBA) - Biomembranes* **2019**, *1861*

(2), 418-430.
[21] Phillips, R. M.; Rosen, T. 37 - Topical antifungal agents. In *Comprehensive Dermatologic Drug Therapy (Third Edition)*, Wolverton, S. E. Ed.; W.B. Saunders, 2013; pp 460-472.e465.
[22] Curto, M. Á.; Butassi, E.; Ribas, J. C.; Svetaz, L. A.; Cortés, J. C. G. Natural products targeting the synthesis of β(1,3)-D-glucan and chitin of the fungal cell wall. Existing drugs and recent findings. *Phytomedicine* **2021**, *88*, 153556.
[23] Kelly, S. L.; Lamb, D. C.; Kelly, D. E. Inhibitors of CYP51 As Antifungal Agents and Resistance to Azole Antifungals. In *Molecular and Applied Aspects of Oxidative Drug Metabolizing Enzymes*, Arinç, E., Schenkman, J. B., Hodgson, E. Eds.; Springer US, 1999; pp 157-172.
[24] Li, S. R.; Tan, Y. M.; Zhang, L.; Zhou, C. H. Comprehensive Insights into Medicinal Research on Imidazole-Based Supramolecular Complexes. *Pharmaceutics* **2023**, *15* (5), 1348.
[25] Fothergill, A. W. Miconazole: a historical perspective. *Expert Review of Anti-infective Therapy* **2006**, *4* (2), 171-175.
[26] Liu, H.; Guo, L.; Hu, S.; Peng, F.; Zhang, X.; Yang, H.; Sui, X.; Dai, Y.; Zhou, P.; Qi, H. Scalable Fabrication of Highly Breathable Cotton Textiles with Stable Fluorescent, Antibacterial, Hydrophobic, and UV-Blocking Performance. *ACS Applied Materials & Interfaces* **2022**, *14* (29), 34049-34058.
[27] Emam, H. E.; El-Shahat, M.; Hasanin, M. S.; Ahmed, H. B. Potential military cotton textiles composed of carbon quantum dots clustered from 4-(2,4-dichlorophenyl)-6-oxo-2-thioxohexahydropyrimidine-5-carbonitrile. *Cellulose* **2021**, *28* (15), 9991-10011.
[28] Hettegger, H.; Gorfer, M.; Sortino, S.; Fraix, A.; Bandian, D.; Rohrer, C.; Harreither, W.; Potthast, A.; Rosenau, T. Synthesis, characterization and photo-bactericidal activity of silanized xanthene-modified bacterial cellulose membranes. *Cellulose* **2015**, *22* (5), 3291-3304.
[29] Li, L.; Jung, J.; Ma, W.; Wen, J.; Ren, X.; Sun, Y. Enhanced antimicrobial and antifungal property of two-dimensional fibrous material assembled by N-halamine polymeric electrolytes. *Materials Science and Engineering: C* **2020**, *115*, 111122.
[30] Hedayati, N.; Montazer, M.; Mahmoudirad, M.; Toliyat, T. Ketoconazole and Ketoconazole/β-cyclodextrin performance on cotton wound dressing as fungal skin treatment. *Carbohydrate Polymers* **2020**, *240*, 116267.
[31] Jabar, J. M.; Alabi, K. A.; Lawal, A. K. Synthesis, characterization and application of novel 1, 3-bis[(furan-2-l)methylene]thiourea functional dye on wool and cotton fabrics. *SN Applied Sciences* **2020**, *2* (11), 1850.
[32] Gargoubi, S.; Saghrouni, F.; Chevallier, P.; Tolouei, R.; Boudokhane, C.; Ladhari, N.; Mantovani, D. Polydopamine-modified interface improves the immobilization of natural bioactive-dye onto textile and enhances antifungal activity. *Biointerphases* **2020**, *15* (4), 041011.
[33] Nabipour, H.; Wang, X.; Rahman, M. Z.; Song, L.; Hu, Y. An environmentally friendly approach to fabricating flame retardant, antibacterial and antifungal cotton fabrics via self-assembly of guanazole-metal complex. *Journal of Cleaner Production* **2020**, *273*, 122832.
[34] Tzhayik, O.; Lipovsky, A.; Gedanken, A. Sonochemical fabrication of edible fragrant antimicrobial nano coating on textiles and polypropylene cups. *Ultrasonics Sonochemistry* **2017**, *38*, 614-621.
[35] Ahmed, H. B.; Abualnaja, K. M.; Ghareeb, R. Y.; Ibrahim, A. A.; Abdelsalam, N. R.; Emam, H. E. Technical textiles modified with immobilized carbon dots synthesized with infrared assistance. *Journal of Colloid and Interface Science* **2021**, *604*, 15-29.
[36] Dawoud, T. M.; Yassin, M. A.; El-Samawaty, A. R. M.; Elgorban, A. M. Silver nanoparticles synthesized by Nigrospora oryzae showed antifungal activity. *Saudi Journal of Biological Sciences* **2021**, *28* (3), 1847-1852.
[37] Eid, A. M.; Fouda, A.; Niedbała, G.; Hassan, S. E.; Salem, S. S.; Abdo, A. M.; F. Hetta, H.; Shaheen, T. I. Endophytic Streptomyces laurentii Mediated Green Synthesis of Ag-NPs with Antibacterial and Anticancer

Properties for Developing Functional Textile Fabric Properties. *Antibiotics* **2020**, *9* (10), 641.
[38] Sahayaraj, K.; Rajesh, S.; Rathi, J. A. M.; Kumar, V. Green preparation of seaweed-based silver nano-liquid for cotton pathogenic fungi management. *IET Nanobiotechnology* **2019**, *13* (2), 219-225.
[39] Anwar, Y.; Alghamdi, K. M. Imparting antibacterial, antifungal and catalytic properties to cotton cloth surface via green route. *Polymer Testing* **2020**, *81*, 106258.
[40] El-Sayed, A. A.; Amr, A.; Kamel, O. M. H. M.; El-Saidi, M. M. T.; Abdelhamid, A. E. Eco-friendly fabric modification based on AgNPs@Moringa for mosquito repellent applications. *Cellulose* **2020**, *27* (14), 8429-8442.
[41] Ratnasari, A.; Endarko, E.; Syafiuddin, A. A green method for the enhancement of antifungal properties of various textiles functionalized with silver nanoparticles. *Biointerface Research in Applied Chemistry* **2020**, *10*, 7284-7294.
[42] Katerine, I.; Romina A, A.; Jorge E, S.; José R, V.-B.; Carlos, R.-G.; Patricia G, V. Antifungal activity of cotton fabrics finished modified silica-silver-carbon-based hybrid nanoparticles. *Textile Research Journal* **2019**, *89* (5), 825-833.
[43] Paszkiewicz, M.; Gołąbiewska, A.; Rajski, Ł.; Kowal, E.; Sajdak, A.; Zaleska-Medynska, A. The Antibacterial and Antifungal Textile Properties Functionalized by Bimetallic Nanoparticles of Ag/Cu with Different Structures. *Journal of Nanomaterials* **2016**, *2016* (3), 6056980.
[44] Eremenko, A. M.; Petrik, I. S.; Smirnova, N. P.; Rudenko, A. V.; Marikvas, Y. S. Antibacterial and Antimycotic Activity of Cotton Fabrics, Impregnated with Silver and Binary Silver/Copper Nanoparticles. *Nanoscale Research Letters* **2016**, *11* (1), 28.
[45] Roy, T. S.; Shamim, S. U. D.; Rahman, M. K.; Ahmed, F.; Gafur, M.; Applications. The development of ZnO nanoparticle coated cotton fabrics for antifungal and antibacterial applications. *Materials Sciences and Applications* **2020**, *11* (9), 601-610.
[46] El-Nahhal, I. M.; Elmanama, A. A.; El Ashgar, N. M.; Amara, N.; Selmane, M.; Chehimi, M. M. Stabilization of nano-structured ZnO particles onto the surface of cotton fibers using different surfactants and their antimicrobial activity. *Ultrasonics Sonochemistry* **2017**, *38*, 478-487.
[47] Gowri, S.; Rajiv Gandhi, R.; Senthil, S.; Suresh, J.; Sundrarajan, M. Enhancing antimicrobial activity of biotemplated TiO_2 nanoparticles using aloe vera plant extract. *Journal of Bionanoscience* **2016**, *10* (3), 181-190.
[48] Nazari, A. Superior Self-cleaning and Antimicrobial Properties on Cotton Fabrics Using Nano Titanium Dioxide along with Green Walnut Shell Dye. *Fibers and Polymers* **2019**, *20* (12), 2503-2509.
[49] Rilda, Y.; Mahardika, G.; Alif, A.; Agustien, A.; Dachriyanus, D.; Djamaan, A. Antifungal property of cotton fabric textile: Modification of cotton fiber functions by coating compounds of TiO_2-SiO_2/Chitosan. *Der Pharma Chemica* **2016**, *8*, 124-131.
[50] Kowalczyk, D.; Brzeziński, S.; Kamińska, I. Multifunctional nanocoating finishing of polyester/cotton woven fabric by the sol-gel method. *Textile Research Journal* **2018**, *88* (8), 946-956.
[51] Gao, D.; Li, Y.; Lyu, B.; Lyu, L.; Chen, S.; Ma, J. Construction of durable antibacterial and anti-mildew cotton fabric based on P(DMDAAC-AGE)/Ag/ZnO composites. *Carbohydrate Polymers* **2019**, *204*, 161-169.
[52] Fernandez, M.; Ferre, M.; Pla-Quintana, A.; Parella, T.; Pleixats, R.; Roglans, A. Rhodium-NHC Hybrid Silica Materials as Recyclable Catalysts for [2+2+2] Cycloaddition Reactions of Alkynes. *European Journal of Organic Chemistry* **2014**, *2014* (28), 6242-6251.
[53] Borja, G.; Monge-Marcet, A.; Pleixats, R.; Parella, T.; Cattoën, X.; Wong Chi Man, M. Recyclable Hybrid Silica-Based Catalysts Derived from Pd–NHC Complexes for Suzuki, Heck and Sonogashira Reactions. *European Journal of Organic Chemistry* **2012**, *2012* (19), 3625-3635.
[54] Ferré, M.; Cattoën, X.; Wong Chi Man, M.; Pleixats, R. Sol–gel immobilized n-heterocyclic carbene gold complex as a recyclable catalyst for the rearrangement of allylic esters and the cycloisomerization of γ-alkynoic

acids. *ChemCatChem* **2016**, *8* (17), 2824-2831.
[55] Monge-Marcet, A.; Cattoen, X.; Alonso, D. A.; Najera, C.; Man, M. W. C.; Pleixats, R. Recyclable silica-supported prolinamide organocatalysts for direct asymmetric Aldol reaction in water. *Green chemistry* **2012**, *14* (6), 1601-1610.
[56] Boffi, A.; Cacchi, S.; Ceci, P.; Cirilli, R.; Fabrizi, G.; Prastaro, A.; Niembro, S.; Shafir, A.; Vallribera, A. The Heck reaction of allylic alcohols catalyzed by palladium nanoparticles in water: chemoenzymatic synthesis of (R)-(−)-rhododendrol. *ChemCatChem* **2011**, *3* (2), 347-353.
[57] Bernini, R.; Cacchi, S.; Fabrizi, G.; Forte, G.; Petrucci, F.; Prastaro, A.; Niembro, S.; Shafir, A.; Vallribera, A. Perfluoro-tagged, phosphine-free palladium nanoparticles supported on silica gel: application to alkynylation of aryl halides, Suzuki–Miyaura cross-coupling, and Heck reactions under aerobic conditions. *Green Chemistry* **2010**, *12* (1), 150-158.
[58] Soler, R.; Salabert, J.; Sebastián, R. M.; Vallribera, A.; Roma, N.; Ricart, S.; Molins, E. Highly hydrophobic polyfluorinated azo dyes grafted on surfaces. *Chemical Communications* **2011**, *47* (10), 2889-2891.
[59] Montagut, A. M.; Gálvez, E.; Shafir, A.; Sebastián, R. M.; Vallribera, A. Triarylmethane dyes for artificial repellent cotton fibers. *Chemistry–A European Journal* **2017**, *23* (16), 3810-3814.
[60] Salabert, J.; Sebastián, R. M.; Vallribera, A. Anthraquinone dyes for superhydrophobic cotton. *Chemical Communications* **2015**, *51* (75), 14251-14254.
[61] Montagut, A. M.; Granados, A.; Ballesteros, A.; Pleixats, R.; Llagostera, M.; Cortés, P.; Sebastián, R. M.; Vallribera, A. Antibiotic protected silver nanoparticles for microbicidal cotton. *Tetrahedron* **2019**, *75* (1), 102-108.
[62] Montagut, A. M.; Granados, A.; Lazurko, C.; El-Khoury, A.; Suuronen, E. J.; Alarcon, E. I.; Sebastián, R. M.; Vallribera, A. Triazine mediated covalent antibiotic grafting on cotton fabrics as a modular approach for developing antimicrobial barriers. *Cellulose* **2019**, *26*, 7495-7505.
[63] Li, H.; Granados, A.; Fernández, E.; Pleixats, R.; Vallribera, A. Anti-inflammatory Cotton Fabrics and Silica Nanoparticles with Potential Topical Medical Applications. *ACS Applied Materials & Interfaces* **2020**, *12* (23), 25658-25675.
[64] Tarn, D.; Ashley, C. E.; Xue, M.; Carnes, E. C.; Zink, J. I.; Brinker, C. J. Mesoporous silica nanoparticle nanocarriers: biofunctionality and biocompatibility. *Accounts of chemical research* **2013**, *46* (3), 792-801.
[65] Croissant, J. G.; Cattoën, X.; Man, M. W. C.; Durand, J.-O.; Khashab, N. M. Syntheses and applications of periodic mesoporous organosilica nanoparticles. *Nanoscale* **2015**, *7* (48), 20318-20334.
[66] Ni, D.; Jiang, D.; Ehlerding, E. B.; Huang, P.; Cai, W. Radiolabeling silica-based nanoparticles via coordination chemistry: basic principles, strategies, and applications. *Accounts of Chemical Research* **2018**, *51* (3), 778-788.
[67] Al-Badr, A. A. Miconazole Nitrate: Comprehensive Profile. In *Profiles of Drug Substances, Excipients and Related Methodology*, Brittain, H. G. Ed.; Vol. 32; Academic Press, 2005; pp 3-65.
[68] Chevreuil, F.; Landreau, A.; Seraphin, D.; Larcher, G.; Bouchara, J.-P.; Richomme, P. Synthesis and antifungal activity of new thienyl and aryl conazoles. *Journal of Enzyme Inhibition and Medicinal Chemistry* **2006**, *21* (3), 293-303.
[69] Oh, K.; Higashi, M.; Yoshizawa, Y. Biological evaluation of imidazole derivatives as inhibitors of hydroperoxide lyase, a key enzyme in plant volatile biosynthesis. *Journal of Pesticide Science* **2011**, *36* (1), 58-62.
[70] Breugst, M.; Reissig, H.-U. The Huisgen Reaction: Milestones of the 1,3-Dipolar Cycloaddition. *Angewandte Chemie International Edition* **2020**, *59* (30), 12293-12307.
[71] Bürglová, K. n.; Moitra, N.; Hodacova, J.; Cattoën, X.; Wong Chi Man, M. Click approaches to functional water-sensitive organotriethoxysilanes. *The Journal of Organic Chemistry* **2011**, *76* (18), 7326-7333.

[72] Wang, H.; Fang, J.; Cheng, T.; Ding, J.; Qu, L.; Dai, L.; Wang, X.; Lin, T. One-step coating of fluoro-containing silica nanoparticles for universal generation of surface superhydrophobicity. *Chemical Communications* **2008**, (7), 877-879.

[73] Théron, C.; Gallud, A.; Carcel, C.; Gary-Bobo, M.; Maynadier, M.; Garcia, M.; Lu, J.; Tamanoi, F.; Zink, J. I.; Wong Chi Man, M. Hybrid Mesoporous Silica Nanoparticles with pH-Operated and Complementary H-Bonding Caps as an Autonomous Drug-Delivery System. *Chemistry – A European Journal* **2014**, *20* (30), 9372-9380.

[74] Serrano, M. C.; Ramírez, M.; Morilla, D.; Valverde, A.; Chávez, M.; Espinel-Ingroff, A.; Claro, R.; Fernández, A.; Almeida, C.; Martín-Mazuelos, E. A comparative study of the disc diffusion method with the broth microdilution and Etest methods for voriconazole susceptibility testing of Aspergillus spp. *Journal of Antimicrobial Chemotherapy* **2004**, *53* (5), 739-742.

[75] Ramírez, M.; Serrano, M. C.; Castro, C.; López, E.; Almeida, C.; Fernández, A.; Romero, A.; Martín-Mazuelos, E. Comparative study of disc diffusion and microdilution methods in susceptibility testing of micafungin against Candida species. *Journal of Antimicrobial Chemotherapy* **2006**, *58* (4), 861-863.

[76] Espinel-Ingroff, A.; Canton, E.; Gibbs, D.; Wang, A. Correlation of Neo-Sensitabs Tablet Diffusion Assay Results on Three Different Agar Media with CLSI Broth Microdilution M27-A2 and Disk Diffusion M44-A Results for Testing Susceptibilities of *Candida spp*. and *Cryptococcus* neoformans to Amphotericin B, Caspofungin, Fluconazole, Itraconazole, and Voriconazole. *Journal of Clinical Microbiology* **2007**, *45* (3), 858-864.

[77] Colosi, I. A.; Faure, O.; Dessaigne, B.; Bourdon, C.; Lebeau, B.; Colosi, H. A.; Pelloux, H. Susceptibility of 100 filamentous fungi: comparison of two diffusion methods, Neo-Sensitabs and E-test, for amphotericin B, caspofungin, itraconazole, voriconazole and posaconazole. *Medical Mycology* **2012**, *50* (4), 378-385.

[78] Martos, A. I.; Martín-Mazuelos, E.; Romero, A.; Serrano, C.; González, T.; Almeida, C.; Puche, B.; Cantón, E.; Pemán, J.; Espinel-Ingroff, A. Evaluation of disk diffusion method compared to broth microdilution for antifungal susceptibility testing of 3 echinocandins against Aspergillus spp. *Diagnostic Microbiology and Infectious Disease* **2012**, *73* (1), 53-56.

[79] Guo, W.; Monge-Marcet, A.; Cattoën, X.; Shafir, A.; Pleixats, R. Sol–gel immobilized aryl iodides for the catalytic oxidative α-tosyloxylation of ketones. *Reactive and Functional Polymers* **2013**, *73* (1), 192-199.

[80] Li, H.; Pérez-Trujillo, M.; Cattoën, X.; Pleixats, R. Recyclable mesoporous organosilica nanoparticles derived from proline-valinol amides for asymmetric organocatalysis. *ACS Sustainable Chemistry & Engineering* **2019**, *7* (17), 14815-14828.

CHAPTER 3

Antibacterial and Anti-Inflammatory Silica Nanoparticles and Cotton Fabrics for Improving Wound Healing

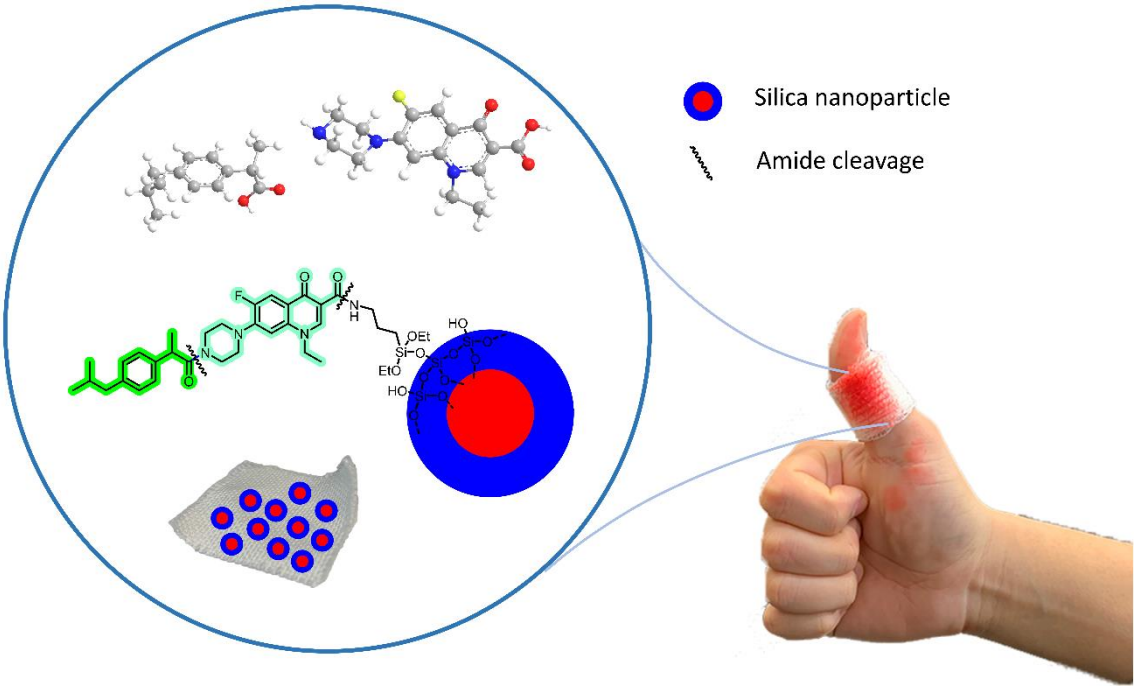

Chapter 3
Antibacterial and Anti-Inflammatory Silica Nanoparticles and Cotton Fabrics for Improving Wound Healing

3.1 Introduction

The skin is the largest human organ, acting as a protective barrier between the body and the external environment by avoiding microbial contamination, the attack of damaging substances and excess of fluid loss.[1] In daily life, trauma, burns, or chronic diseases may cause cutaneous wounds. Wounded skin becomes vulnerable to excessive fluid loss and microbial contamination, so it's necessary to cover skin during the lengthy wound healing process.[2] Skin wounds have always been a major clinical problem because wound healing is a complex physiological process along with a series of interactions between multiple cell types, soluble factors, and extracellular components.[3] Among the healing process, inflammation phase consists of the recruitment of neutrophils, monocytes, and macrophages in the injury site to initiate and sustain an immune response. The objective of this phase is the prevention of contamination and debridement of necrotic tissue.[4]

The microbial infection of wounds not only increases patient discomfort or delay wound healing, but it can also evolve to more complicated and serious infection. The most common treatment for infected wounds is the systemic administration of broad-spectrum antibiotics.[5] However, this indiscriminate use can affect skin microbiota and prompt proliferation of multi-resistant strains. Topical delivery ensures antimicrobial agent release at the infection site, reducing the concentration needed to control the infection and consequently decreasing systemic distribution and toxicity.[6]

On the other hand, the natural low-cost fabric medical cotton gauze is widely used as a dressing material in the clinical treatment of skin wounds because of its excellent mechanical properties, good biocompatibility, soft nature, and moisture absorbing ability.[7] However, due to its porous structure and to the abundance of hydrophilic groups on its surface, it may also create an ideal environment for the survival and growth of many types of bacteria, which usually causes inflammation and excessive immune response and delays wound healing. Therefore, with increasing awareness of healthcare-related infections, there is a strong demand to develop functional medical gauzes with a broad-spectrum of antibacterial and anti-inflammatory activities to prevent wound infection, promote wound healing and

accelerate cicatrisation.[8-10]

3.1.1 Antibiotics

Antibiotics (or antibacterials) have been defined as organic chemicals of natural or synthetic origin that inhibit or kill pathogenic bacteria.[11] Since the discovery and production of antibiotics, the fear of infectious diseases was taken away.

The Nobel Prize in Physiology or Medicine in 1908 was awarded to Ilya I. Mechnikov and Paul Ehrlich for the recognition of their work on immunity. The first synthetic antibiotic, Salvarsan, was discovered by Paul Ehrlich in 1909.[12] The history of this discovery starts with the decision of Ehrlich to seek for a drug that would be effective against the spirochaete that causes syphilis. Among the arsenical drugs already tested for other purposes there was one, the 606th of the series tested, which had been set aside in 1907 as being ineffective. After that, Ehrlich's former colleague, Kitasato, sent his pupil, named Hata, to work at Ehrlich's Institute. Learning that Hata had succeeded in infecting rabbits with syphilis, Ehrlich asked him to test this discarded drug on these rabbits. Hata did so and found that it was very effective. When hundreds of experiments had repeatedly proved its efficacy against syphilis, Ehrlich announced it under the name salvarsan. In 1910 salvarsan was produced for clinical trials and therapy. This drug selectively binds the pathogens, and the arsenate kills them. Subsequently, further work on this subject was done to solve the side effects caused by arsenic poisoning, and eventually it turned out the 914th arsenical substance, named neosalvarsan, with less arsenical content. Although the curative effect of Neosalvarsan was lower, it was more easily manufactured and, being more soluble, it was more easily administered (1914).[13] Salvarsan also known as arsphenamine or compound 606, was the first modern antimicrobial agent that was introduced as effective treatment for syphilis, relapsing fever, and African trypanosomiasis. Arsphenamine's structure was first proposed to be analogous to an azo compound, however findings from mass spectral analysis (2005) indicate that comprises a blend of cyclic structures with three and five As atoms (Figure 3.1).[14]

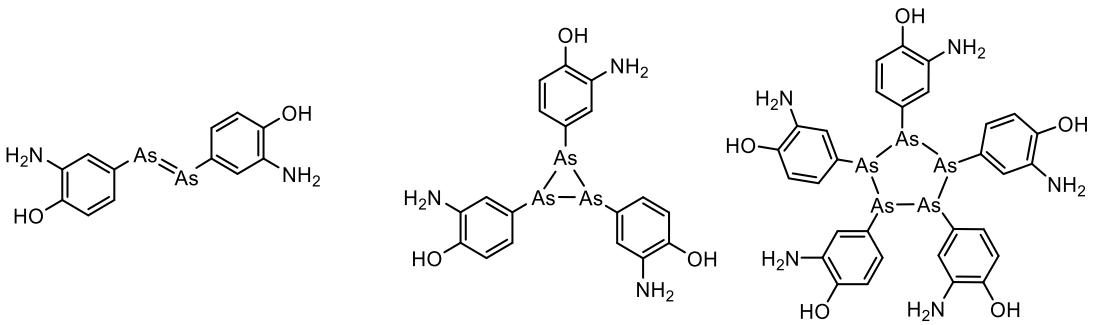

Figure 3.1 Structure of salvarsan

Inspired by Ehrlich's research, Paul Gerhard Domagk tested some azo dyes *in vitro* and *in vivo* but failed to produce a useful antibiotic. Then he turned to test many sulfonamide-containing dyes synthesized by his colleagues in Bayer. In 1932, a red dye, sulfamidochrysoidine, turned out to be effective in infected mice but ineffective in vitro. Later on, Tréfouël and colleagues found that sulfamidochrysoidine was degraded by enzymes to the active drug sulfanilamide. Thousands of derivatives with a sulfanilamide-based structure were developed in the following years.

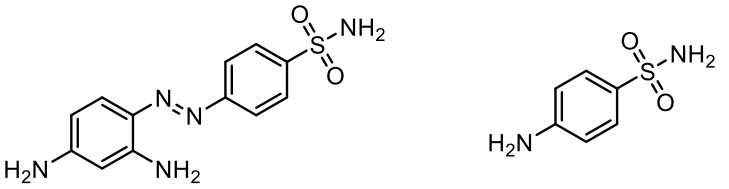

sulfamidochrysoidine active form sulfanilamide

Figure 3.2 Structures of Prontosil and the active form sulfanilamide

Several different classes of antibiotics have been described along the years based on different chemical structures, such as β-lactams, polypeptides, aminoglycosides, tetracyclines, macrolides and quinolones.[15]

3.1.1.1 Penicillin and other β-lactam antibiotics

Sir Alexander Fleming was a Scottish physician and microbiologist, best known for discovering the world's first broadly effective antibiotic substance, which he named penicillin.[16] His discovery in 1928 of what was later named benzylpenicillin (or penicillin G) from the mold *Penicillium chrysogenum*/*rubens* has been described as the "single greatest victory ever achieved over disease". Fleming observed that the staphylococcus colonies around a large colony of a contaminating mold became transparent and were obviously undergoing lysis (1929). Then, in 1940, E. B. Chain purified penicillin and in 1941 penicillin was introduced in therapy. Another contribution of Fleming was that he developed a new screening method for the discovery of new bioactive compounds from microorganisms. The new method was widely used in screening of antibiotics because of the less required resources. For this discovery, Fleming shared the Nobel Prize in Physiology or Medicine in 1945 with H. Florey and E. B. Chain. Fleming noticed the potential resistance of bacteria to penicillin and in 1940 Abraham and Chain published that an extract of *E. coli* can destroy the activity of penicillin. A great number of semisynthetic penicillin-derivates (for example ampicillin and methicillin) were developed to overcome the resistance.[17] Penicillin and derivatives belong to the class of β-lactam antibiotics. Other β-lactam-type antibiotics that have also been developed are cephalosporins and carbapenems (Figure 3.3).

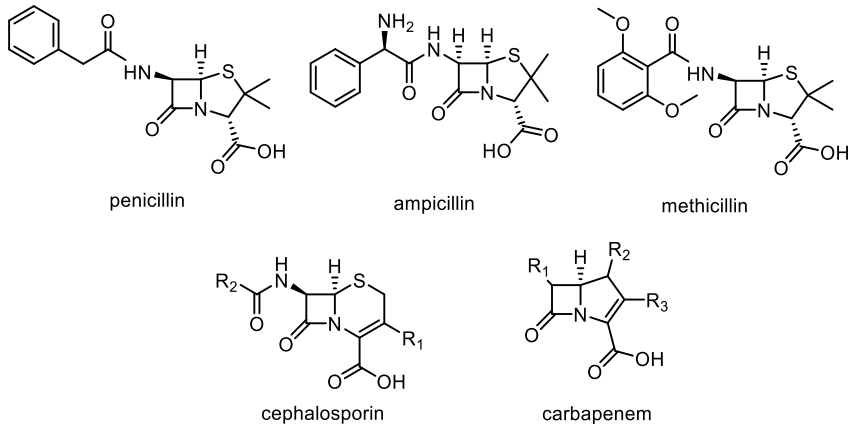

Figure 3.3 Structures of penicillin and other β-lactam antibiotics

3.1.1.2 Polypeptides

To fight against penicillin-resistant *M. tuberculosis*, Waksman and his colleagues searched for soil borne microorganisms to inhibit or kill the bacterium and discovered the genus *Streptomyces* as promising producer of new antibiotics.[18] Based on Fleming's screening method, they selected soil bacteria with bioactivity, searched for the growth inhibition zones surrounding the isolated soil bacteria and tested the inhibition towards pathogenic bacteria. The first promising substance isolated was actinomycin, a polypeptide, isolated from an actinobacterium.[19] Actinomycin showed activity towards a great range of bacteria, but was too toxic for humans as antibiotic. It binds to DNA duplexes, thereby interfering with the action of enzymes engaged in replication and transcription. Then, bacitracin, another polypeptide antibiotic complex, was originally isolated from *Bacillus subtilis* and *Bacillus licheniformis*.[20] Bacitracin inhibits peptidoglycan synthesis by binding to a lipid pyrophosphate carrier that transports cell wall precursors to the growing cell wall.

3.1.1.3 Aminoglycosides

Aminoglycosides are natural or semisynthetic antibiotics derived from actinomycetes. They were among the first antibiotics to be introduced for routine clinical use and several examples have been approved for use in humans. The aminoglycosides are broad-spectrum, bactericidal antibiotics that are commonly prescribed for children, primarily for infections caused by Gram-negative pathogens. Another hit within the program was the first described antibiotic of the aminoglycoside class, the Streptomycin (Figure 3.4) which was first isolated from *Streptomyces griseus* and introduced into clinical use in 1944.[21] Then, several other members of the class were introduced over the intervening years including neomycin (1949, *S. fradiae*),[22] kanamycin (1957, *S. kanamyceticus*),[23] gentamicin (1963, *Micromonospora purpurea*),[24] netilmicin (1967, derived from sisomicin),[25] tobramycin (1967, *S. tenebrarius*),[26] and amikacin (1972, derived from kanamycin).[27] The chemical nature of an

aminoglycoside is based on a glycosyl-modified polypeptide chain. The mechanism of action consists of altering bacterial protein synthesis through binding to the 30S ribosomal subunit.

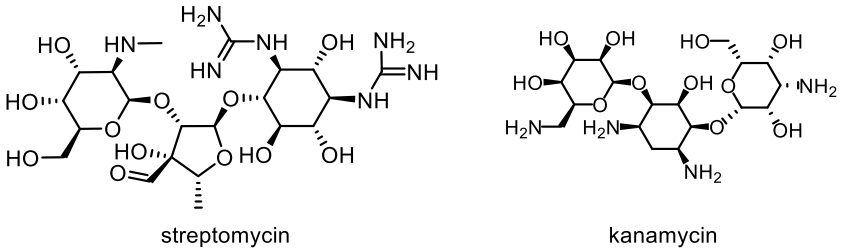

Figure 3.4 Structures of streptomycin and kanamycin

They found widespread use as first-line agents in the early days of antimicrobial chemotherapy, but were eventually replaced in the 1980s with cephalosporins, carbapenems, and fluoroquinolones.[28]

3.1.1.4 Tetracyclines

Another important antibiotic class discovered from *Streptomyces* species are the tetracyclines (Figure 3.5). The first tetracycline, chlortetracycline, was discovered by Duggar in 1948 from the fermenter broth of *Streptomyces aureofaciens*.[29] Then oxytetracycline was discovered by Finlay *et al.* as product of *S. rimosus* in 1950, and its structure was determined subsequently by R. B. Woodward.[30] These antibiotics present a linear fused tetracyclic nucleus to which various functional groups are attached. Tetracyclines were used extensively in human and animal infection therapy because of the availability and lack of side effects, resulting in the emergence of microbial resistance. Other tetracyclines were identified later, either as naturally occurring molecules, e.g., tetracyclines from *S. aureofaciens, S. rimosus*, and *S. viridofaciens*[31] and demethylchlortetracycline from *S. aureofaciens*; or as products of semisynthetic approaches, e.g., methacycline, doxycycline, and minocycline.[32]

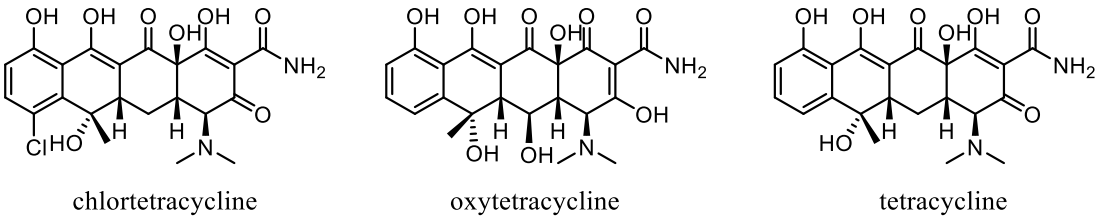

Figure 3.5 Structures of chlortetracycline, oxytetracycline and tetracycline

3.1.1.5 Macrolides

Erythromycin, the first described macrolide, was discovered and isolated from *Streptomyces erythreus* by J. M. McGuire in 1952.[33] The molecular structure of this family of antibiotics consists in a 12-16

macrocyclic lactone ring with a glycosidic linked amino sugar. To overcome the acid instability of erythromycin, azithromycin was developed in 1980.[34] Then, to solve the macrolide resistance, ketolides, semisynthetic derivatives of macrolides, were designed. Telithromycin was the first and the only approved ketolide for human uses.[35]

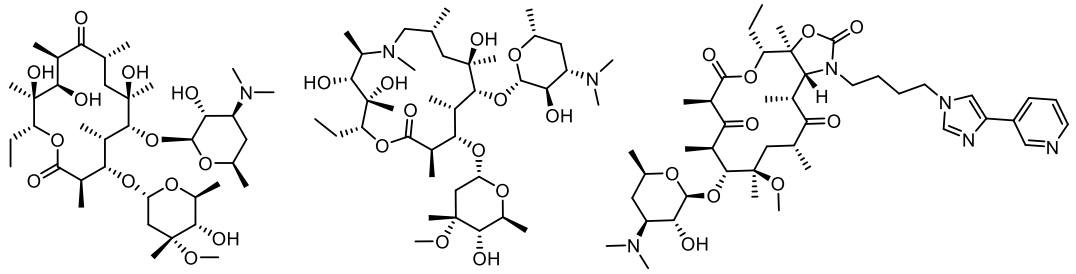

Figure 3.6 Structures of erythromycin, azithromycin and telithromycin

3.1.1.6 Quinolones

Since the discovery of their pharmacological properties in the early 1960s, quinolones have gained increasing importance as key products in therapies to treat both community-acquired and severe hospital-acquired infections. Quinolones are not natural products produced by bacteria but are synthetic products. Nalidixic acid, the first clinical quinolone drug, was discovered by G. Lesher and coworkers as a by-product during the synthesis of the antimalarial drug chloroquine and prepared at the Sterling-Winthrop Research Institute.[36] Nalidixic acid is a narrow-spectrum agent against enteric bacteria used for treating uncomplicated urinary tract infections (UTIs). The molecular structure of quinolones is based on a bicyclic core structure related to 4-quinolone. During the 1970s-1980s, the coverage of the quinolone class was expanded significantly by the breakthrough development of fluoroquinolones, containing a fluorine atom in the structure, which show a much broader spectrum of activity and improved pharmacokinetics compared to the first-generation quinolones. Many clinical quinolones have different substituents at the N-l, C-6, C-7, and C-8 positions. These modifications of key positions have an influence on the antimicrobial activity, pharmacokinetics, and metabolic properties.[37] Ciprofloxacin, the top quinolone product, showed enhanced activity and a broad antibacterial spectrum. Commonly recommended medications of fluoroquinolone antibiotics include ciprofloxacin, levofloxacin and norfloxacin (Figure 3.7).[38]

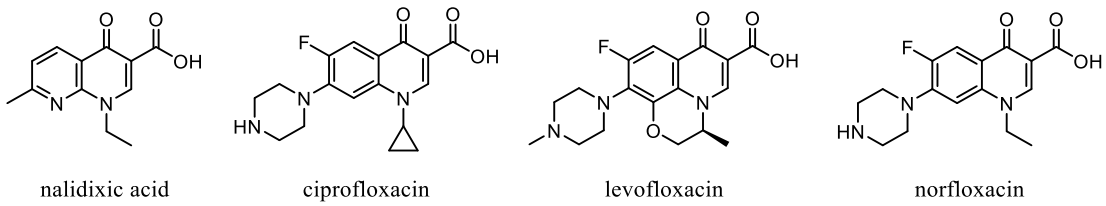

Figure 3.7 Structures of nalidixic acid, ciprofloxacin, levofloxacin and norfloxacin

3.1.1.7 Mechanism of action of antibiotics

Antibiotics have various biological mechanisms according to the action position (Figure 3.8). Bacterial cells possess a cell wall composed of peptidoglycans, consisting of long sugar polymers. The enzymes transglycosidases facilitate the cross-linking of glycan strands in the peptidoglycans, where peptide chains extend from the sugar polymers and establish cross-links between them. Within this process, the D-alanyl-alanine segment of the peptide chain forms cross-links through glycine residues, facilitated by penicillin-binding proteins (PBPs). This cross-linking mechanism contributes to the reinforcement of the cell wall. The synthesis of the cell wall is hindered by β-lactams and polypeptides. Interaction between the β-lactam ring and the PBP make the synthesis of new peptidoglycans impossible. Consequently, the disruption of the peptidoglycan layer induces bacterial lysis.

The information within bacterial DNA is employed to generate messenger RNA (mRNA) in a process recognized as transcription. Then, the ribosome synthesizes proteins present in mRNA, a process called translation. The bacterial 70S ribosome is composed of two ribonucleoprotein subunits, the 30S and 50S subunits. Aminoglycosides are molecules with a positive charge that bind to the negatively charged outer membrane, resulting in the creation of large pores. Then aminoglycosides engage with the 16S rRNA (ribosomal RNA) of the 30S subunit, near the A site, forming hydrogen bonds. This interaction induces misreading and termination of mRNA translation. Tetracyclines target the conserved sequences of the 16S rRNA within the 30S ribosomal subunit. This action prevents the binding of tRNA (transfer RNA) to the A site during protein synthesis. Macrolides affect the translation process by directing their action toward the conserved sequences of the peptidyl transferase center in the 23S rRNA of the 50S ribosomal subunit.

Fluoroquinolones hinder bacterial DNA gyrase, an enzyme that cleaves double-stranded DNA, introduces negative supercoils, and subsequently seals the cleaved ends. This enzymatic process is crucial to prevent excessive positive supercoiling of the strands during their separation, facilitating replication or transcription processes. Fluoroquinolones bind tightly to the A subunit within DNA gyrase and disrupt its ability to cut and reseal strands effectively. Within bacteria, sulfonamides serve as competitive inhibitors targeting the enzyme dihydropteroate synthase (DHPS), a crucial player in folate synthesis. Consequently, these sulfonamides exhibit bacteriostatic effects, impeding the proliferation and multiplication of bacteria.

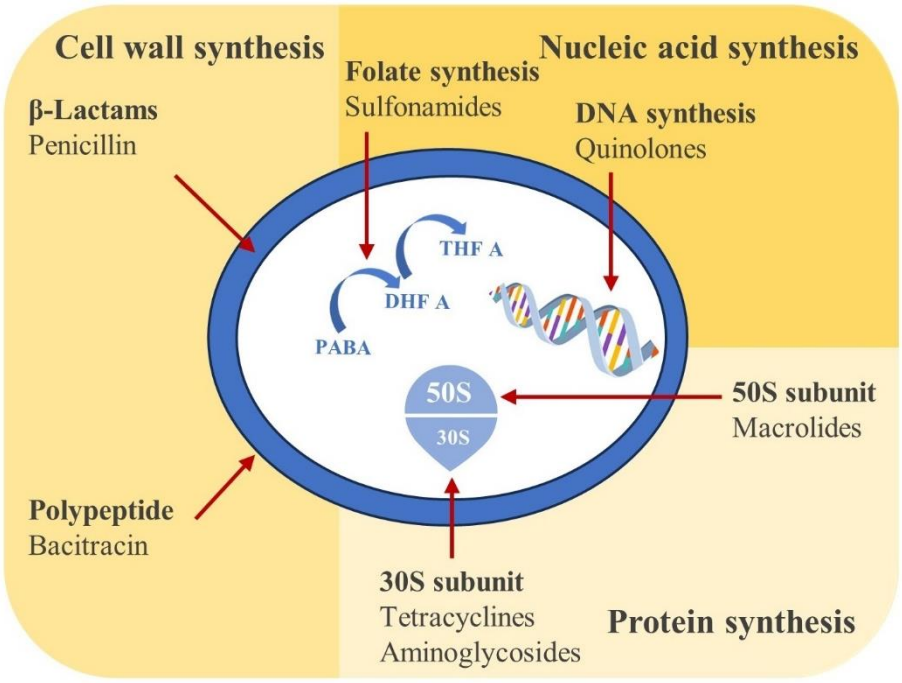

Figure 3.8 Mechanism of action of antibiotics[39]

3.1.2 Anti-inflammatory agents

Inflammation stood as one of the first acknowledged and delineated disease phenomena. Celsus defined the inflammation through the four cardinal manifestations, namely, pain, redness, warmth, and swelling.[40] Galenius (alternatively attributed to Virchow) appended "loss of function" to the description. During 18th century, physicians acknowledged the frequent coexistence of local inflammation with "general inflammation", evidenced by fever and malaise. The bark of the cinchona tree, containing quinine, emerged as one of the earliest known remedies found to be efficacious in combating fever. The effectiveness of willow bark in Europe was then substantiated, leading to the isolation of the natural salicin (a β-D-glucoside of salicyl alcohol, precursor of the salicylic acid) as the active constituent of willow.[41] Subsequently, salicylic acid was isolated independently. Eventually, Kolbe performed the comprehensive synthesis of pure salicylic acid. Chemists in Bayer company carried out the esterification of the phenolic OH of salicylic acid with acetic acid, obtaining the aspirin, a synthetic compound with anti-inflammatory, analgesic and antipyretic properties which had less side-effects than the parent natural salicylic acid. By the end of the 19th century, phenazone (antipyrine) and phenacetin were synthesized by serendipity. Due to the similarity in their therapeutic effects, these medications were often grouped together and commonly referred to as aspirin-like drugs. However, as they were clearly distinct from corticosteroids glucocorticoids, they were also termed "nonsteroidal anti-inflammatory drugs" (NSAIDs) (Figure 3.9).

Ibuprofen and diclofenac represent nonsteroidal anti-inflammatory drugs (NSAIDs) widely employed for alleviating pain, fever, and inflammation (see Figure 3.9). Ibuprofen's discovery dated back to 1961,

credited to S. Adams and J. Nicholson during their tenure at Boots UK Limited, and was initially marketed under the name Brufen. It follows aspirin and paracetamol in over the counter (OTC) usage for managing symptoms of acute pain, inflammation, and fever. However, the utilization patterns of these analgesics vary significantly from country to country. Among them, OTC ibuprofen is presumably the least toxic, with rare associations with fatalities from accidental or intentional ingestion, or severe adverse reactions.[42]

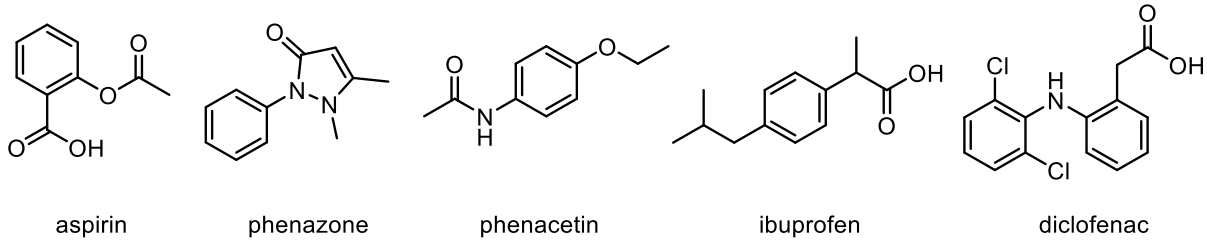

Figure 3.9 Some non-steroidal anti-inflammatory agents

In 1941, H. Selye provided the initial scientific description of corticosteroids. Then, in 1949, corticosteroid treatment was introduced for the first time in medicine for the inflammation. It was arguably a breakthrough in the treatment of rheumatoid arthritis, marking the first anti-rheumatic drug with disease-modifying properties. Steroids were hailed as “a genuine miracle cure”, and Tadeusz Reichstein, Edward Calvin Kendall, and Philip Showalter behind its discovery were honored with the Nobel Prize for Physiology and Medicine in 1950. However, patients realized the side-effects of treatment with these steroids such as the moon face, the perforated and bleeding ulcers, the bruising and crushed vertebrae.[43] By the early 1960s, steroid treatment was completely avoided by the rheumatology community. An anti-steroid sentiment emerged during this period.

These anti-inflammatory drugs act on different pathways of the arachidonic acid cascade.[44] A simplified depiction of the arachidonic acid pathway with a focus on cyclooxygenase (COX)-mediated prostaglandin synthesis is presented in Figure 3.10. Corticosteroids function by impeding the activity of phospholipase enzymes at the onset of the pathway. Nonsteroidal anti-inflammatory drugs (NSAIDs) work by suppressing both COX-1 and COX-2 enzymes, leading to the inhibition of prostaglandin production, which is related to inflammation.

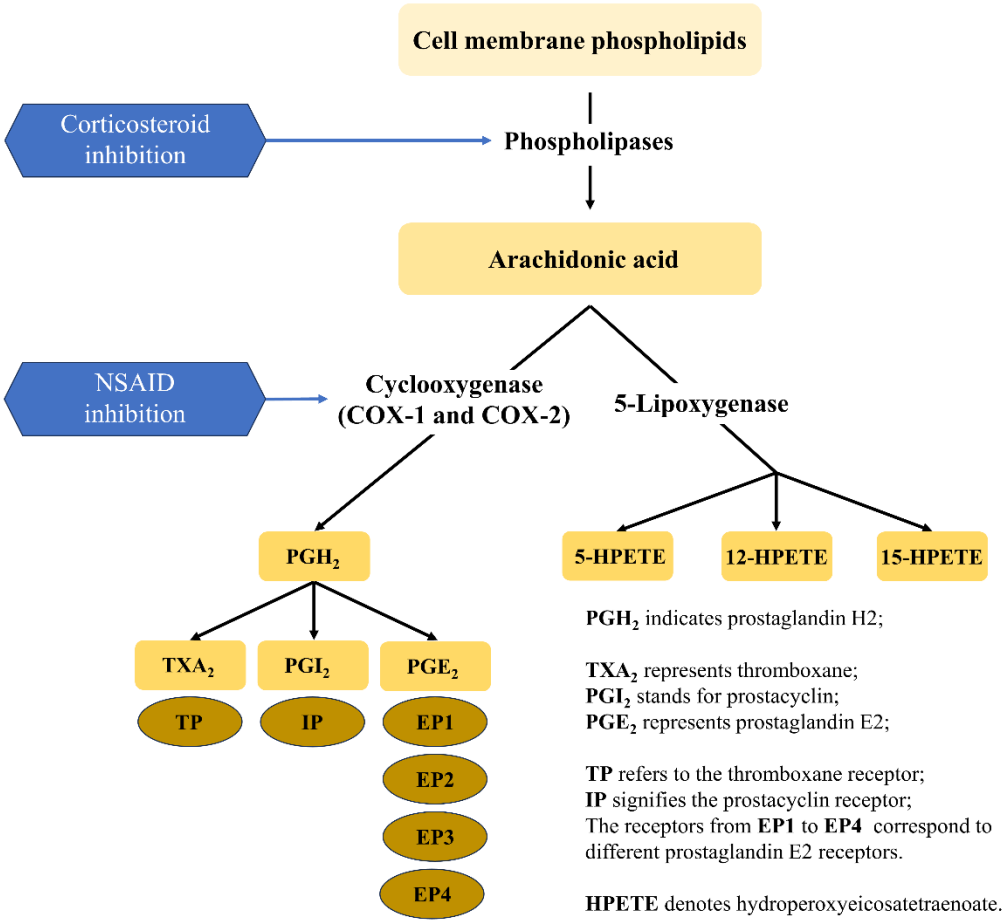

Figure 3.10 Main mechanism of action of anti-inflammatory agents[45]

3.1.3 Antibacterial and anti-inflammatory wound dressing materials

The development of advanced wound dressings to ensure non-fouling, bacteria-free environment and suitable moisture is crucial for chronic wound healing. Recent strategies have focused on anti-inflammatory properties related to the acceleration of wound healing. However, it remains a considerable challenge to simultaneously integrate antibiofouling, antibacterial, anti-inflammation and exudate-managing properties into a single dressing. In fact, wound dressings research has been set by the insights on wound healing process and by patient's demand. As mentioned previously in section 3.1, high expectations arise regarding the modified wound dressings, which must accelerate cicatrisation.

Since the 1990s, natural antibacterial and anti-inflammatory agents extracted from plant products have attracted growing attention in medicine and used in this context. Polyphenolic compounds, including gallic acid, are particularly well known and have been widely used for numerous applications because of their excellent antibacterial, antioxidant, and anti-inflammatory properties. In this context, cotton textiles were functionalized by cross-linking with cyclodextrin-hydroxypropyl methyl cellulose-based hydrogel capable to encapsulate and release gallic acid giving rise to a composite wound dressing with

enhanced biological properties.[46] In addition, Liu's group covalently immobilized plant-derived gallic acids on a pre-modified cotton gauze with abundant amino groups on the surface through reaction with (3-aminopropyl)triethoxysilane (APTES). Then, the amino groups of modified cotton were reacted with phenol groups of gallic acid (GA) derivatives through Schiff's base formation (Figure 3.11).[47] Furthermore, chitosan-based hydrogel, encapsulating Red Cabbage Extract (RCE) was prepared and used in therapeutic pH-sensitive wound dressing. The preparation consisted in the reaction of RCE, methacrylic-chitosan and *N*, *N*-methylene-bis-acrylamide in the presence of potassium persulphate. The mixture was then added to a piece of gauze bandage and left for crosslinking.[48] El-Sayed and coworkers reported the microencapsulation of antimicrobial and anti-inflammatory-rich fractions from marine macroalgae and sea grass in sodium alginate or meypro gum. These extracts were used to finish cotton fabrics by dip coating technique.[49]

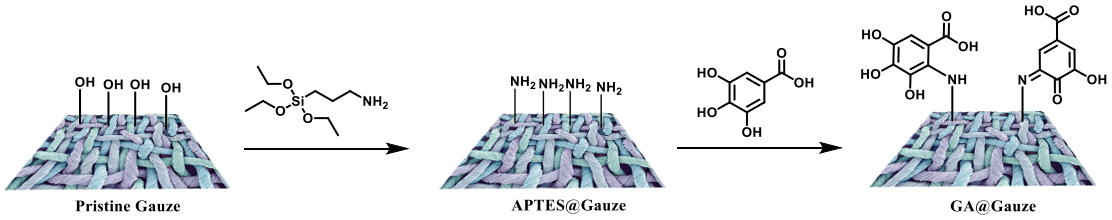

Figure 3.11 Illustration for the fabrication of gallic acid modified gauze

On the other hand, nanoscale materials have also been examined for these applications. Nanomaterials based on the use of abundant natural compounds are appreciated in medicinal applications.[9] Thus, in 2022, mesoporous silica SBA-15 was amine functionalized with 3-aminopropyltrimethoxysilane (APTES@SBA-15) and then added into a solution of poly vinyl alcohol (PVA) and Curcumin. Nanofibers were then fabricated by electrospinning technique and studied for skin wound healing application (Figure 3.12). Curcumin is a plant-derived phytochemical compound, known for its anti-microbial and anti-inflammatory properties, and the amine functionalized mesoporous silica improved the solubility of Curcumin aiding the release of the drug in a sustained manner.[50] In 2022, the keratin of hedgehog spines was extracted and doped with Harmaline and Ginkgo Biloba, and later it was electrospun on the cotton fabric surface to create multifunctional band aid. These nanofibers exhibited anti-inflammatory and bactericidal effects.[51] Moreover, nitric oxide-propelled nanomotors were prepared for bacterial biofilm elimination and endotoxin removal to treat infected burn wounds. First, silica layers were deposited on Fe_3O_4 nanoparticles (Fe_3O_4 NPs) using tetraethyl orthosilicate (TEOS) and 3-aminopropyl triethoxysilane. Then a coupling reaction of residual amino groups with 3-mercaptopropionic acid gave rise to thiolated Fe_3O_4 NPs. These NPs were partially coated with polydopamine (PDA) layers. Polymyxin B (PMB) was conjugated on PDA, and then NO donors were conjugated with –SH groups to construct nitric oxide-propelled nanomotors.[52]

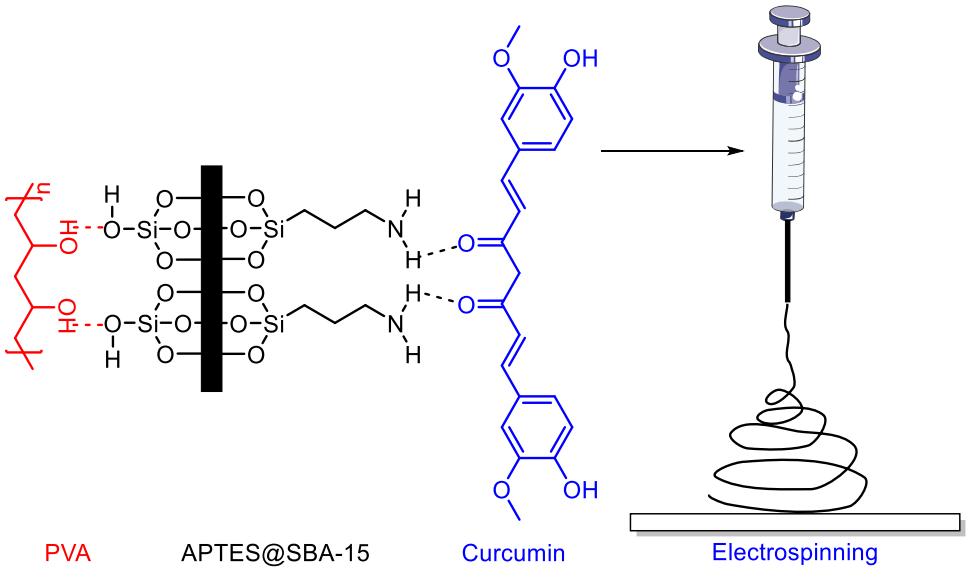

Figure 3.12 Illustration of electrospinning with SBA-15 incorporated in PVA/Curcumin solution

As the most used commercial antibacterial nanomaterials, silver nanoparticles have been extensively adopted in cotton dressings to achieve antiseptic properties. Silver nanoparticles embedded in zwitterionic poly(carboxybetaine-co-dopaminemethacrylamide) copolymer (PCBDA) were anchored onto cotton fabrics (Figure 3.13). The PCBDA copolymer was synthesized via the free radical polymerization using carboxybetaine acrylate (CBA) and dopaminemethacrylamide (DMA) as monomers and AIBN as the initiator. The preparation of PCBDA@AgNPs was performed as a one-step process in the presence of PCBDA copolymer and $AgNO_3$ aqueous solution at pH 11. The catechol groups of dopamine can not only form chelation with Ag ions but also be oxidized to quinone under alkaline condition, providing electrons to reduce Ag ions for in situ formation of silver nanoparticles. Catechol groups can also react with amino groups of the APTES modified cotton gauzes through covalent interaction and hydrogen bonding. *In vivo* wound healing assay confirmed that these Ag nanoparticles could effectively inhibit the wound infection and reduce the inflammatory response.[53] Furthermore, Alisir's group described the fabrication of poly(lactic acid) nanofibers containing the firstly synthesized silver diclofenac complex with 2-methylimidazole. The combination of silver(I), diclofenac (dicl) and 2-methylimidazole (mim) in a single product ($[Ag(mim)_2](dicl)$) could speed up the healing process by providing antibacterial, antifungal and anti-inflammatory protection on the wounded skin.[54]

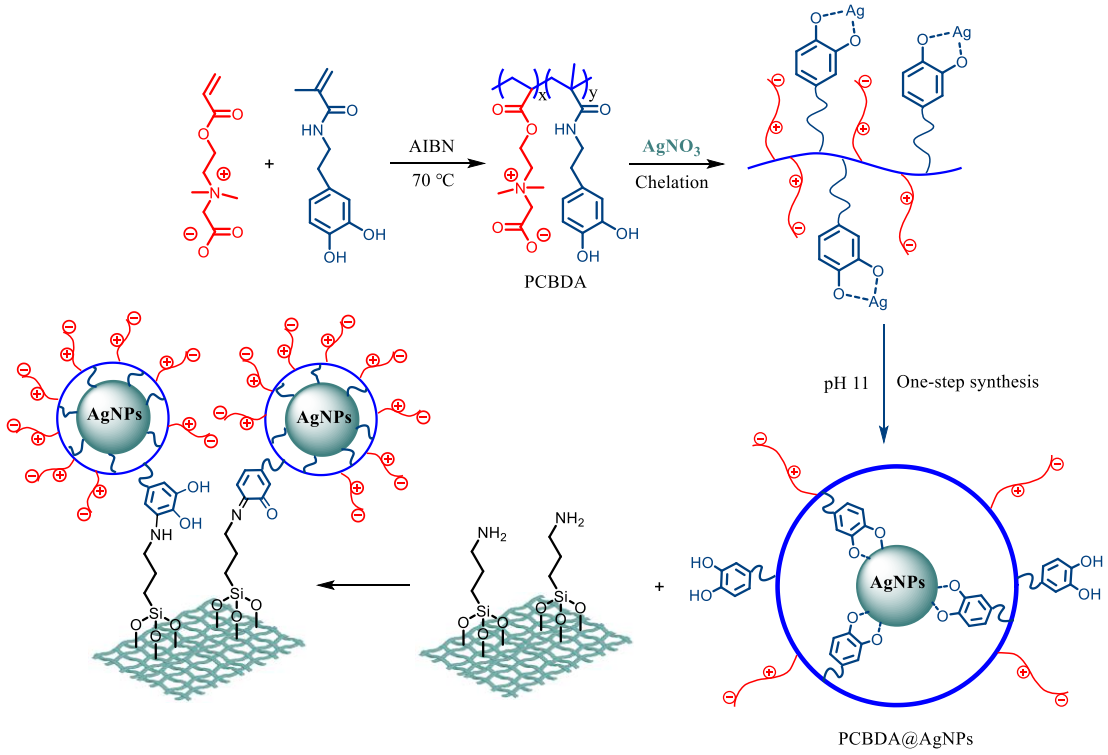

Figure 3.13 Illustration of zwitterionic PCBDA@AgNPs modified cotton gauze

3.1.3.1 Precedents of our group in the preparation of antibacterial and anti-inflammatory wound dressing materials

As part of a research program of our group centered on the design of cotton fabrics for medical applications, in 2019 silver nanoparticles (Ag NPs) with appropriate modified antibiotics were prepared and applied on cotton fabrics (Figure 3.14).[55] Different antimicrobial derivatives were used as stabilizer to protect silver nanoparticles. We modified the original antibiotics to incorporate a thiol group to take profit of the well-known silver-thiol affinity, obtaining thiol-attached eugenol (EuSH), triarylmethane (TAMSH) and fluoroquinolone (FQSH). Fluoroquinolone was also modified with a poly(oxyethylenated) chain, allowing us to have a fluoroquinolone derivate (FQPEG) finally linked to Ag. Silver nanoparticles (Ag@EuSH, Ag@ TAMSH and Ag@FQPEG) were prepared and coated on the cotton surface. The fabric coated with Ag NPs with eugenol derivates in surface, Ag@EuSH) and fabric coated with Ag NPs embedded in PEGfluoroquinolone derivatives in surface, Ag@FQPEG) displayed antibacterial activity for both *Staphylococcus aureus* and *Pseudomonas aeruginosa* strains. These coated antimicrobial cotton fabrics can be applied in different medical textiles.

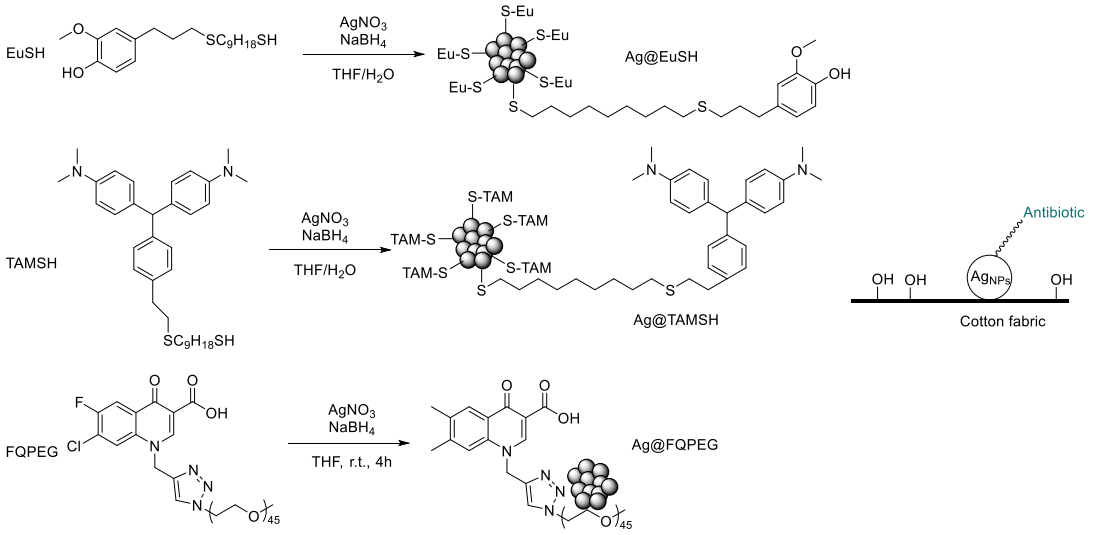

Figure 3.14 Preparation of antimicrobial Ag NPs and coated cotton fabrics

Later, we tethered 1,9-nonandithiol modified eugenol (EuSH) and fluoroquinolone (FQSH) through a triazine moiety onto the surface of cotton fabrics, thus minimizing the leaching of the bioactive molecule (Figure 3.15). The bactericidal activity of the functionalized fabrics was demonstrated, and of note no release of the covalent linked antibiotic was necessary.[56]

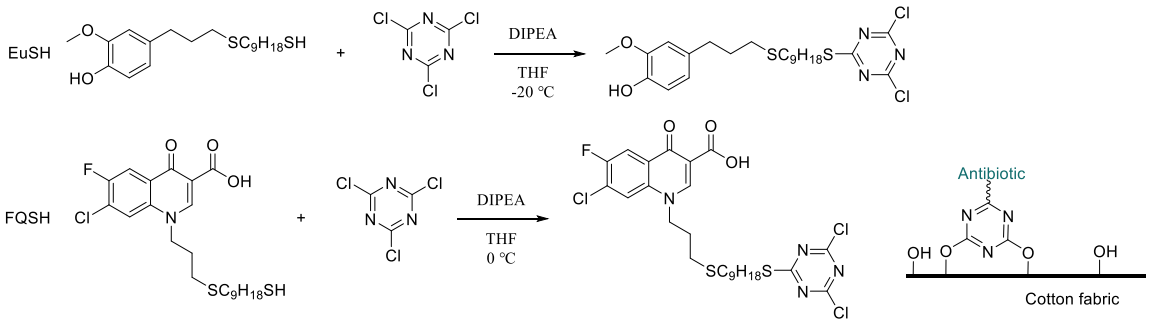

Figure 3.15 Synthesis of functional antimicrobial molecules and coated cotton fabrics

Following with our program, then we prepared anti-inflammatory cotton fabrics by direct covalent attachment of anti-inflammatory (Anti-Inf) silylated drugs derivatives (Salicylic acid, Ibuprofen and Diclofenac) onto the surface of cotton fabrics through an amide group.[57] In addition, as silica nanoparticles present significant advantages in biomedical applications, we synthesized functionalized silica nanoparticles using the same drug derivatives through an amide group and used them for the coating of textiles (Figure 3.16).[57] It should be mentioned that in almost all the numerous published studies for drug delivery the cargo is encapsulated and physically adsorbed into the pores, while the covalent attachment of the drug to the surface of the nanoparticle is a less used strategy. During inflammation, many leukocytes leave the blood vessels and are recruited to the wounded area (chemotaxis).[58] The result is an increased phagocytic activity, a rise in the release of proteases, peroxidases, and oxygen reactive species which contribute to the cleavage and elimination of external agents. Thus, the protease activity in a wound may by high and has been measured using an appropriate

substrate, usually consisting of a peptide linked with a fluorophore or chromophore moiety through an amide bond.[59] The detection of the chromogenic of fluorogenic moiety is thus an evidence supporting that proteases can cleave amide bonds.[60,61] In fact, the treatment of these functionalized nanoparticles and cotton textiles with model proteases and leukocytes from animal origin resulted in an *in situ* release of the drug by the selective enzymatic cleavage of the amide bond. In contrast to the antibiotics case reported previously (can act by contact), the release of the anti-inflammatory is necessary for topical cutaneous applications.[57] Moreover, the coating of cotton fabrics with silica nanoparticles functionalized with antifungal agents has been described in the chapter 2 of this manuscript.[62]

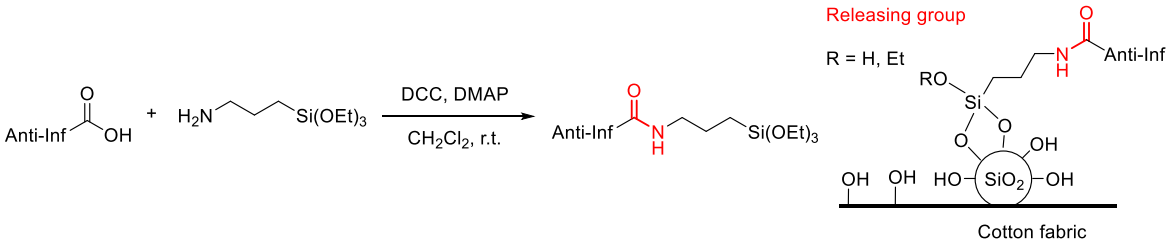

Figure 3.16 Amide-linked silylated Anti-Inf drugs and functionalized silica NPs coated cotton fabrics

Pursuing our interest on the design and application of cotton fabrics for medical applications, we plan to fabricate bifunctional silica nanoparticles with both antibiotic and anti-inflammatory properties that could be used for coating cotton gauzes or strips towards wound healing application. Thus, we pretend to prepare silica nanoparticles covalently functionalized with carboxyl-containing non-steroidal anti-inflammatory drugs and carboxyl-containing antibiotics through amide bonds (see approach A, Figure 3.17). In addition, we plan to prepare silica nanoparticles derived from a silylated monomer with both carboxyl-containing antibiotic and anti-inflammatory moieties in the same organic backbone, previously linked by an amide bond (see approach B, Figure 3.17). Finally, the modification of cotton fabrics with these bifunctional silica nanoparticles will be studied.

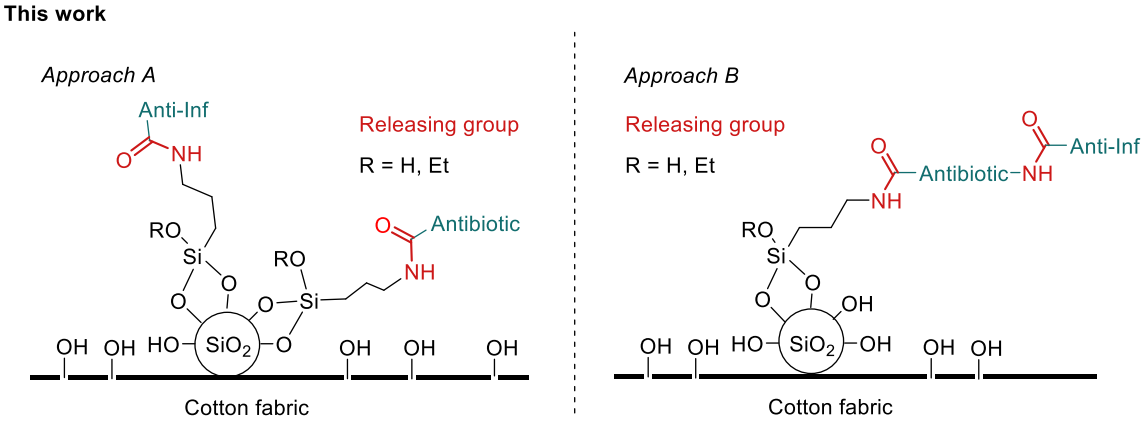

Figure 3.17 Approaches for the coating of cotton fabrics with antibacterial and anti-inflammatory silica nanoparticles

3.2 Objectives

Based on the previous introduction, we intend to prepare silica nanoparticles with both antibiotic and anti-inflammatory properties and the corresponding coated cotton gauzes for wound dressing applications. For that purpose, the specific objectives of this chapter of the thesis are as follows:

a) The synthesis of silylated derivatives based on both carboxyl-containing anti-inflammatory (ibuprofen) and antibiotic (levofloxacin, norfloxacin) compounds in which the drug component is linked to the silyl moiety through a covalent amide bond. This bond should be cleaved by proteases present in the wound to deliver the carboxyl-containing drug *in situ*.

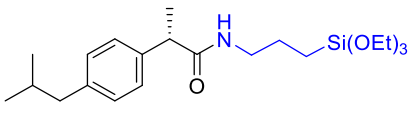

From ibuprofen

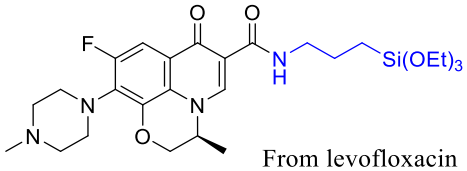

From levofloxacin

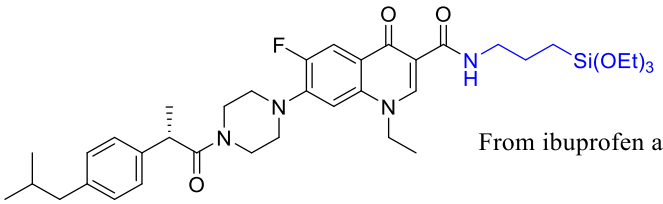

From ibuprofen and norfloxacin

b) The preparation of functionalized silica NPs from these silylated precursors, and the characterization of all the new nanomaterials with the appropriate techniques.

c) The preparation and characterization of cotton fabrics coated with these drug-functionalized silica NPs (Figure 3.14 approaches A and B).

d) The treatment of functionalized silica nanoparticles and coated cotton fabrics with proteases for the cleavage of the amide bond and the detection of released antibiotics and anti-inflammatory drugs.

3.3 Results and Discussion

3.3.1 Synthesis of silylated derivatives of anti-inflammatory and antibiotic drugs

A topical nonsteroidal anti-inflammatory agent Ibuprofen, and common fluoroquinolone antibiotic drugs levofloxacin and norfloxacin were selected as model medicinally-relevant molecules. A carboxylic acid group is the common moiety in all the structures, which is necessary to form a covalent amide bond with the silylated linker. In addition, the covalent grafting onto silica nanoparticles will prevent the leaching of the bioactive molecule. On the other hand, the amide group is crucial for the *in-situ* drug release for cutaneous uses via enzymatic cleavage of the peptide bond by proteases present in the wound.

The synthesis of the silylated derivatives of ibuprofen and levofloxacin was carried out following two different methodologies as indicated in Scheme 3.1. (*S*)-Ibuprofen, **15**, was mixed with *N*,*N*'-dicyclohexylcarbodiimide (DCC), (triethoxysilyl)propylamine, **16**, and a catalytic amount of 4-(dimethy-lamino)pyridine (DMAP) in CH_2Cl_2 at room temperature overnight, affording **17** in 50 % yield after purification by silica gel column chromatography. Levofloxacin, **18**, was first transformed into the corresponding acyl chloride which was then reacted, without purification, with a stoichiometric amount of (triethoxysilyl)propylamine, **16**, in dichloromethane at room temperature to obtain the silylated amide **19** in 99% yield.

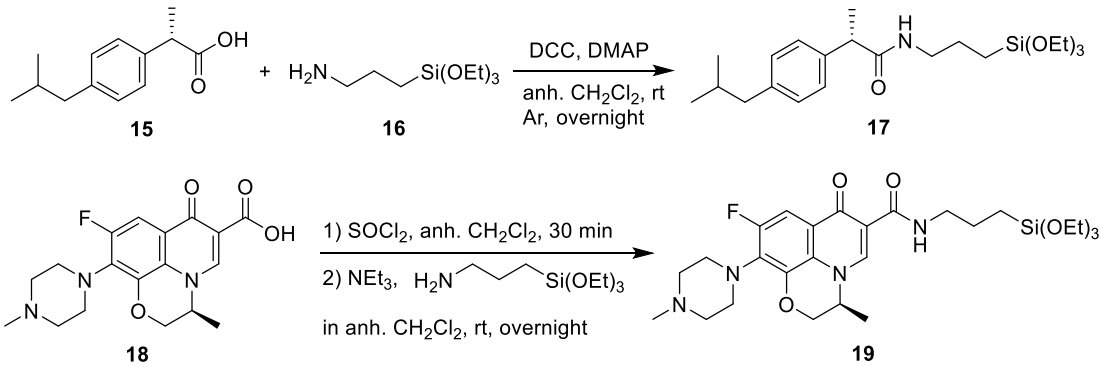

Scheme 3.1 Preparation of silylated derivatives of ibuprofen and levofloxacin **17** and **19**

On the other hand, a monosilylated derivative containing both anti-inflammatory and antibiotic moieties was synthesized following the steps summarized in Scheme 3.2. In this approach, norfloxacin, **20**, was selected due to the nucleophilic secondary amine present in the piperazine ring, which will allow to covalently link it to the anti-inflammatory ibuprofen derivative via an amide bond (step 2, Scheme 3.2). First, the norfloxacin methyl ester **21** was prepared in 79% yield through the treatment of its acyl chloride derivative with MeOH. Then, ibuprofen **15** was tethered to **21** using hexafluorophosphate azabenzotriazole tetramethyl uronium (HATU) as coupling reagent in the presence of triethylamine to

form the amide **22** in 83% yield. After ester hydrolysis under basic conditions, the coupling between the acid **23** and the silylated amine **16** was carried out with HATU as coupling reagent yielding the desired silylated derivative **24** in 71% yield. Thus, compound **24** containing ibuprofen and norfloxacin moieties was synthesized in 4 steps in a 46% overall yield.

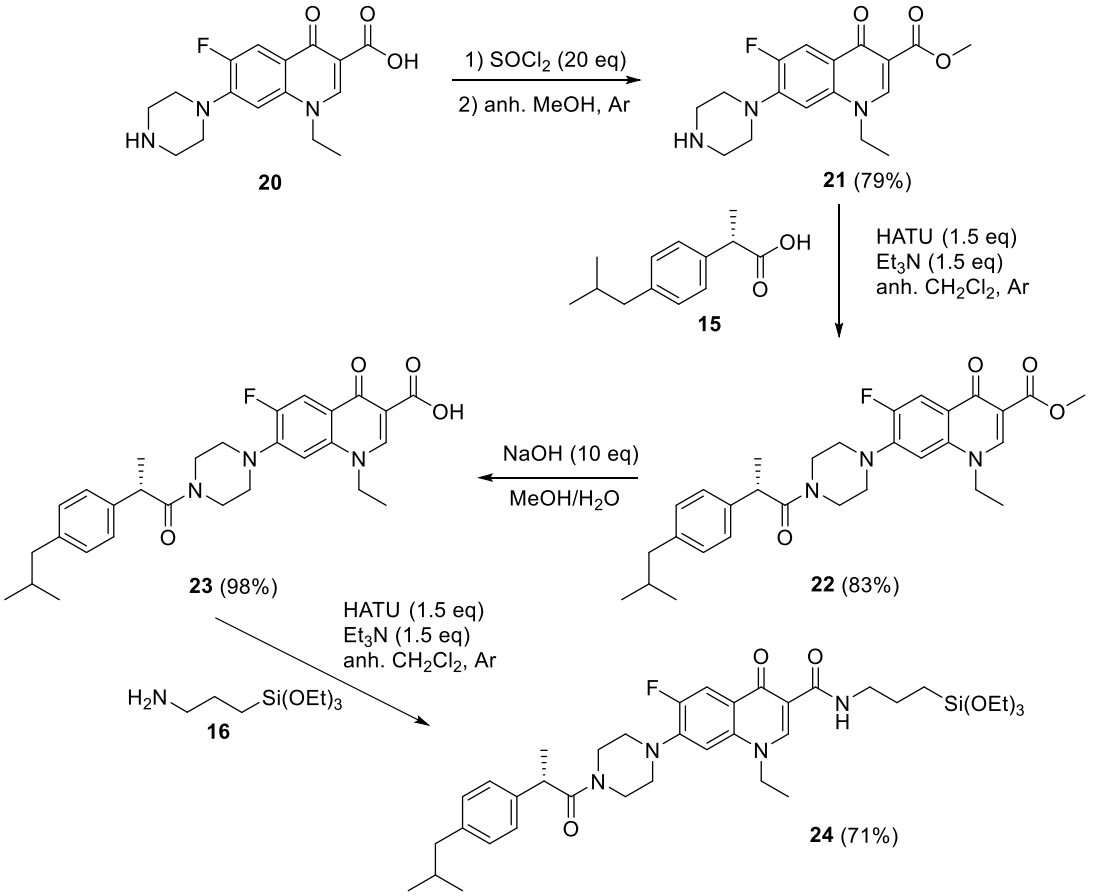

Scheme 3.2 Preparation of silylated derivative **24** from norfloxacin and ibuprofen

The final step is a classic amidation reaction in which HATU is used for the activation of carbonyl providing a better leaving group.[63] The mechanism is as follows (Scheme 3.3). The carboxylate anion (formed by deprotonation by Et_3N) attacks HATU to form the unstable O-acyl(tetramethyl)isouronium salt. The OAt anion (3*H*-1,2,3-triazolo[4,5-b]pyridine, 1-oxide) rapidly attacks the isouronium salt, affording the OAt-active ester and liberating a stoichiometric quantity of tetramethylurea. Then the silylated amine, as a nucleophile, reacts with the ester and results in acylation and releasing of 1-hydroxy-7-azabenzotriazole.

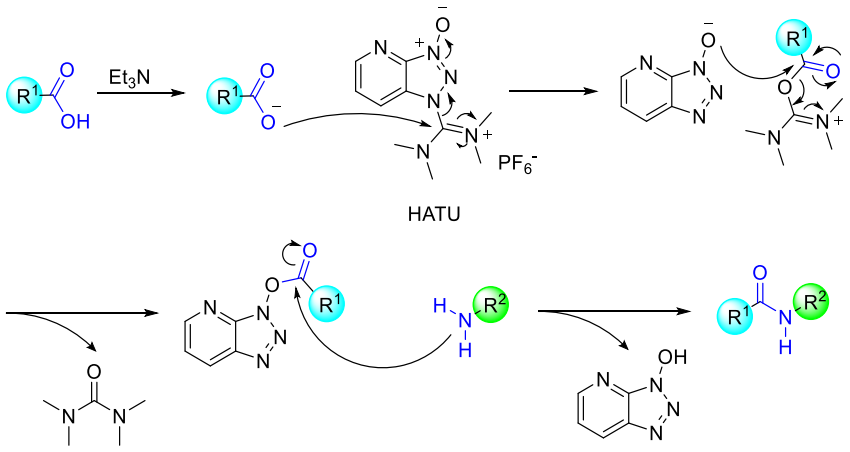

Scheme 3.3 Amide bond formation mechanism mediated by HATU

3.3.2 Preparation and characterization of antibacterial and anti-inflammatory functionalized silica nanoparticles

Then, we turned to the covalent anchoring of the anti-inflammatory and antibiotic drugs to silica nanoparticles by sol-gel condensation methods. Materials **SiO_2@Ibu+Leflox** were obtained by co-condensation of silylated precursors **17** and **19** with TEOS using a 28% ammonium hydroxide-ethanol solution as promoter (Scheme 3.4). For the synthesis of **SiO_2@Ibu+Leflox** different molar ratios TEOS/**17**/**19**/EtOH/NH_3/H_2O were used maintaining a ratio TEOS/**17**+**19** (20:1). First, a 50:50 ratio of silylated drug derivatives **17**:**19** was assayed obtaining modified silica nanoparticles that exhibited a low zeta-potential value which was indicative of low stability (Table 3.1, entry 1). In addition, transmission electron microscopy images (TEM, Figure 3.18 A) showed high level of nanoparticles aggregation. The instability was probably derived from the antibiotic moiety because we know from previous work in our group that silica nanoparticles exclusively using ibuprofen are stable.

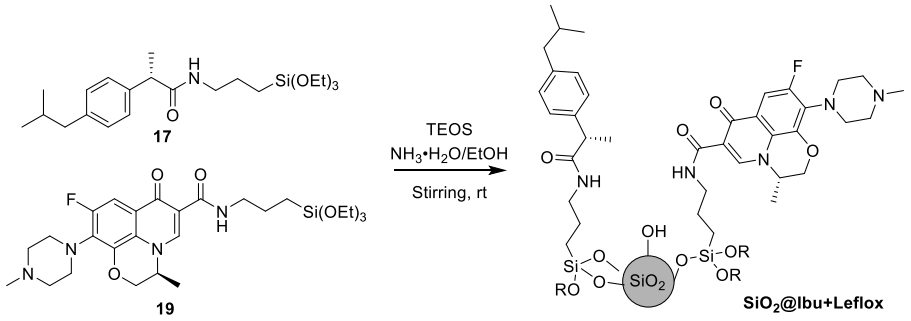

Scheme 3.4 Preparation of functionalized silica nanoparticles **SiO_2@Ibu+Leflox**

Thus, we decided to modify the molar ratio **17**:**19** (75:25). In this case, TEOS (16.97 mmol), the silylated ibuprofen derivative **17** (0.63 mmol) and the silylated levofloxacin derivative **19** (0.21 mmol) were dissolved in absolute EtOH (42 mL). Then, an ammonium hydroxide-ethanol solution (10 mL of 28% $NH_3 \cdot H_2O$ in 42 mL EtOH) was added. The zeta-potential for the pure sample indicated better stability in this case (Table 3.1, entry 2). Transmission electron microscopy image (Figure 3.18 B) also

showed low level of nanoparticles aggregation.

Table 3.1 Characterization data of functionalized silica nanoparticles

Material	Drug loading (mmol/g)[a]	Particle size (nm)		Z-potential (mV)
		TEM	DLS[b]	
SiO_2@Ibu+Leflox (20:0.5:0.5)	0.23 : 0.23	/	2733	5.7
SiO_2@Ibu+Leflox (20:0.75:0.25)	0.075 : 0.025	317±22	426	-41.0
SiO_2@Norflox-Ibu (20:1)	0.15	686±32	836	-65.5
SiO_2@Norflox-Ibu (30:1)	0.13	540±30	658	-69.9
SiO_2@Norflox-Ibu (40:1)	0.15	389±22	486	-72.3

[a] Estimated from the N elemental analysis [b] Hydrodynamic diameters

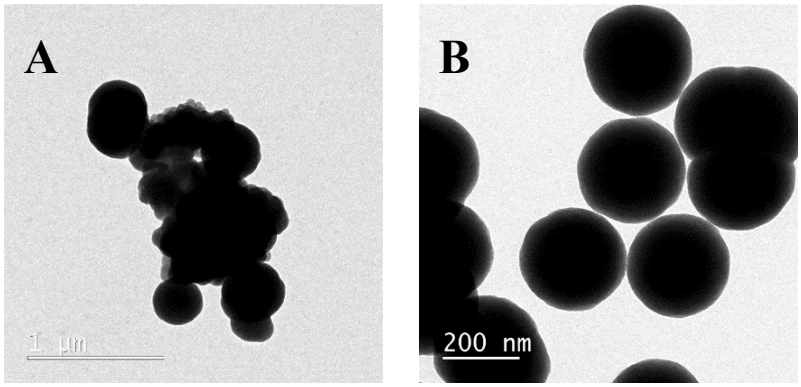

Figure 3.18 TEM image of A) **SiO_2@Ibu+Leflox (20:0.5:0.5)** and B) **SiO_2@Ibu+Leflox (20:0.75:0.25)**.

Then, we centered our attention to another approach (Scheme 3.5) following the same procedure for the sol-gel process but now using the monosilylated monomer **24**. Mixtures of TEOS/**24**/EtOH/NH_3 /H_2O were used and three different ratios TEOS/**24** (20:1, 30:1 and 40:1) were evaluated. The TEM analysis of materials **SiO_2@Norflox-Ibu** confirmed the nanometric size and features of the functionalized nanoparticles showing dense spherical morphologies with sizes from 389 to 686 nm (Table 1 and Figure 3.19).

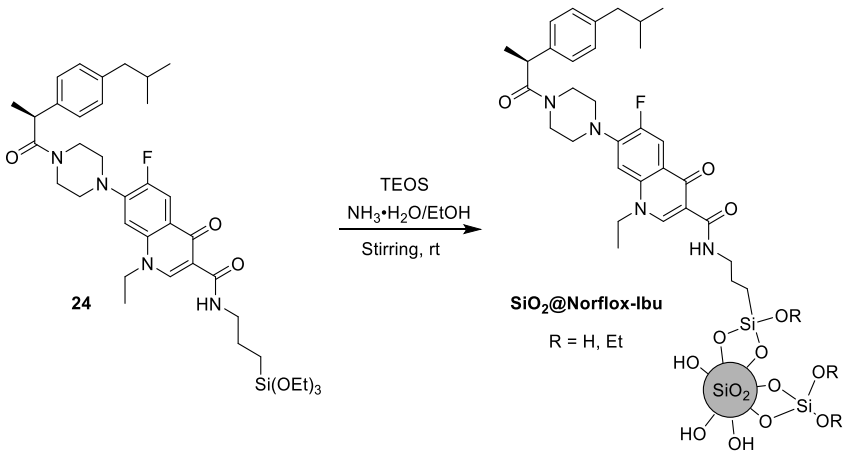

Scheme 3.5 Preparation of functionalized silica nanoparticles **SiO_2@Norflox-Ibu**

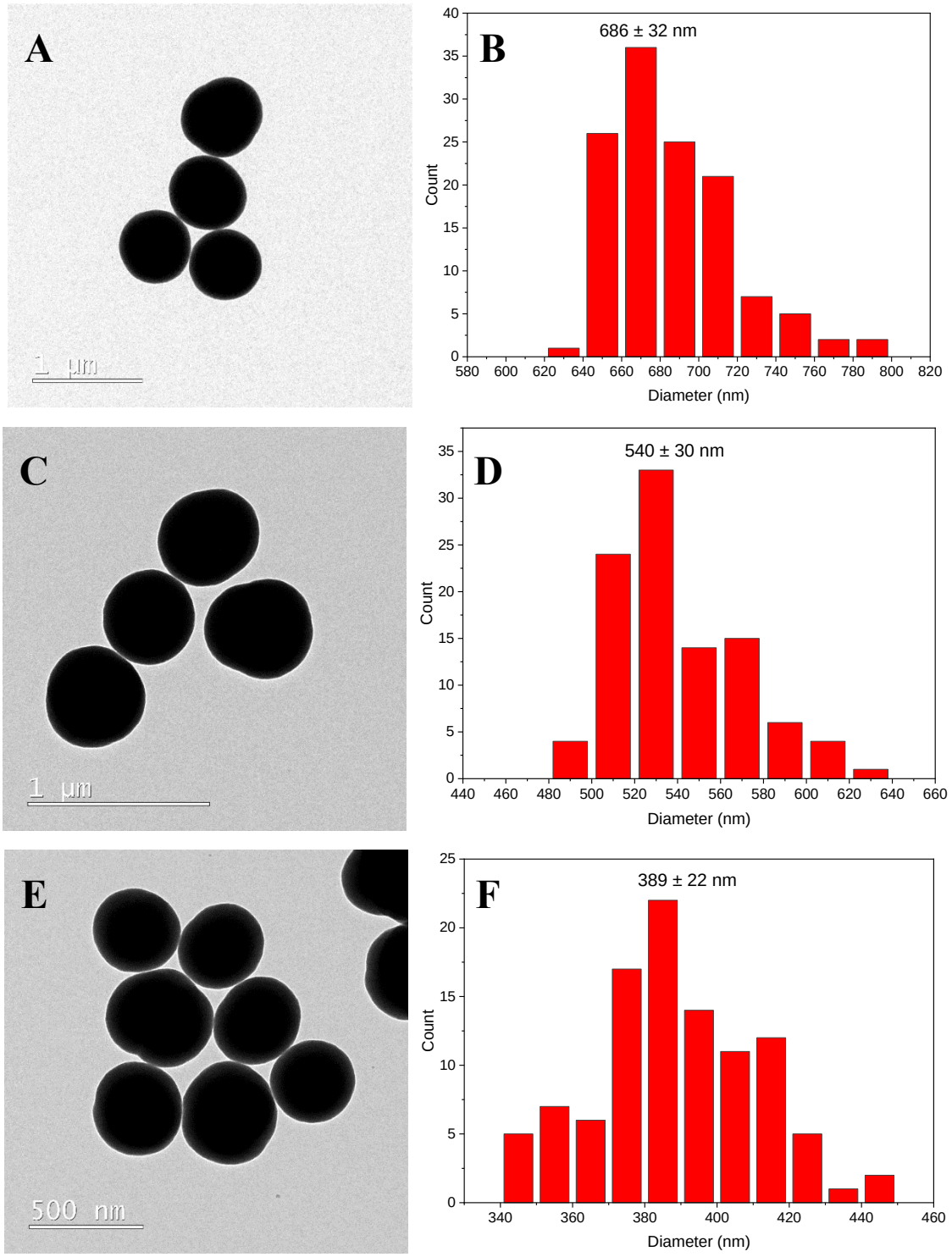

Figure 3.19 TEM image of **SiO_2@Norflox-Ibu** A) (**20:1**), C) (**30:1**) and E) (**40:1**) and size distribution of **SiO_2@Norflox-Ibu** B) (**20:1**), D) (**30:1**) and F) (**40:1**)

The modified silica NPs **SiO_2@Norflox-Ibu** exhibited high negative values of zeta-potential, from -65.5 to -72.3 mV, in agreement with residual deprotonated silanol groups and no protonation of the amino group, and indicative of high stability (Table 3.1, entries 3-5). Dynamic light scattering measurements (DLS) (Figure 3.20) were in accordance with the TEM size of the corresponding dried

nanoparticles if we consider the likely adsorption of water molecules onto the nanoparticle surface (Table 3.1).

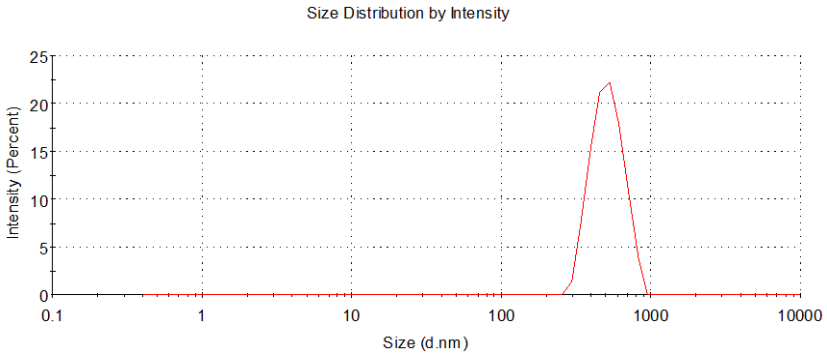

Figure 3.20 DLS of **SiO_2@Norflox-Ibu (TEOS:24 40:1)**

The presence of the organic moiety in the modified NPs **SiO_2@Norflox-Ibu** was ensured by the solid state ^{29}Si and ^{13}C NMR spectra. Thus, the superposition of the ^{13}C NMR spectrum of **24** in solution and that of **SiO_2@Norflox-Ibu** (TEOS:**24** 20:1) in the solid state shows a good similarity between the two spectra, supporting thereby the integrity of the organic framework (Figure 3.21 A). The ^{29}Si CP MAS NMR spectrum of **SiO_2@Norflox-Ibu** (TEOS:**24** 40:1) showed two groups of chemical shifts: T units (-56.5 and -65.4 ppm) derived from organosilane **24** and Q units (-92.4, -101.8 and -112.4 ppm) resulting from TEOS (Figure 3.21 B). The presence of T signals is also an indication that the integrity of the Si-C bond was maintained during the formation of the nanomaterials.

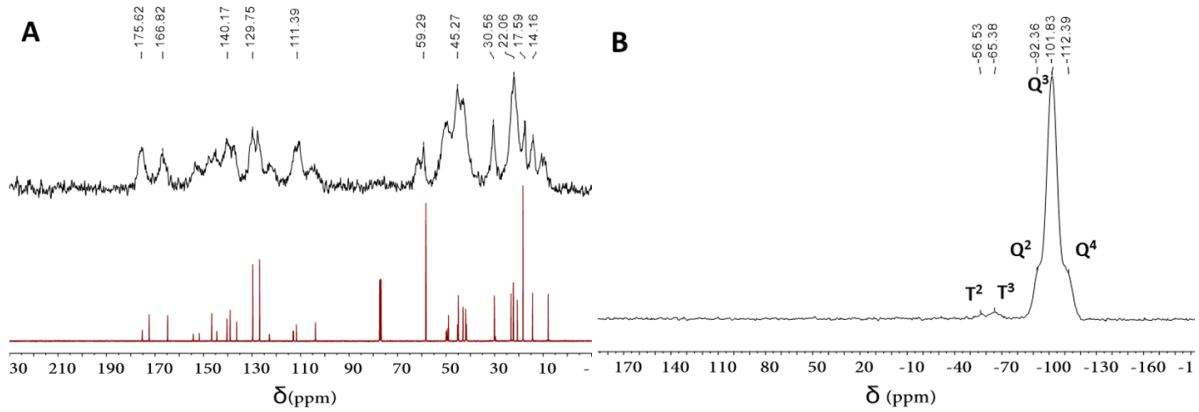

Figure 3.21 A) ^{13}C CP MAS NMR spectrum of **SiO_2@Norflox-Ibu (TEOS:24 20:1)** and ^{13}C NMR spectrum of **24**.

B) ^{29}Si CP MAS NMR spectrum of **SiO_2@Norflox-Ibu (TEOS:24 40:1)**

The drug content in the NPs was determined from the nitrogen elemental analysis (Table 3.1). For the materials **SiO_2@Ibu+Leflox**, the given values are based on the initial amounts of silylated monomers and the estimation that **17** and **19** have the same condensation rate. For the nanomaterial **SiO_2@Ibu+Leflox (20:0.75:0.25)** the drug content found was quite low (Table 3.1, entry 2). The materials **SiO_2@Norflox-Ibu** contain both drug moieties in the molecule **24**, thus, the values

correspond to the whole organic moiety in the materials.

3.3.3 Preparation and characterization of cotton fabrics coated with antibacterial and anti-inflammatory functionalized silica nanoparticles

With the drug-functionalized silica NPs in hand, we turned to the loading of cotton fabrics with these nanoparticles using the one-step coating method. As we have mentioned, for **SiO_2@Ibu+Leflox**, a low proportion of antibiotic (ratio Ibu:Leflox 75:25) was required to afford stable silica nanoparticles and the total amount of drugs in the final nanomaterial was quite low according to the elemental analysis. On the other hand, the precise amount of ibuprofen *vs* levofloxacin in the silica matrix cannot be estimated without assuming the same reactivity in sol-gel process for both **17** and **19**. For these reasons, we decided to perform the coating only with **SiO_2@Norflox-Ibu** materials. As depicted in Table 3.1, the drug loading amount in the nanoparticles did not significantly vary with the molar ratio TEOS:**24**. For that reason, the coating solution was obtained by hydrolysis and co-condensation of TEOS with organosilane **24** (molar ratio 40:1) in aqueous ammonia and ethanol under stirring. Without any further isolation, the resulting milky solution was ultrasonicated for 30 minutes to produce a homogeneous suspension in which a piece of cotton was immersed and the whole system was ultrasonicated for another 30 minutes. Then, the cotton textile was removed from the solution and washed with distilled water, then dried at 120°C for 1 h. The presence of abundant silica nanoparticles on the surface of cotton fabrics loaded with **SiO_2@Norflox-Ibu** (TEOS:**24** 40:1) by one-step coating was clearly observed by SEM (Figure 3.22 A). The textile piece gained 10 mg after coating with NPs according to gravimetric analysis. The chemical composition of the surface of the modified fabrics was analyzed by energy dispersive X-ray spectroscopy (EDX) (Figure 3.22 B and Figure 3.23). As expected, the EDX analysis showed peaks for the elements C, O, N, Si, and F. The peaks corresponding to C, N and F indicate the presence of the organic moiety in modified silica nanoparticles.

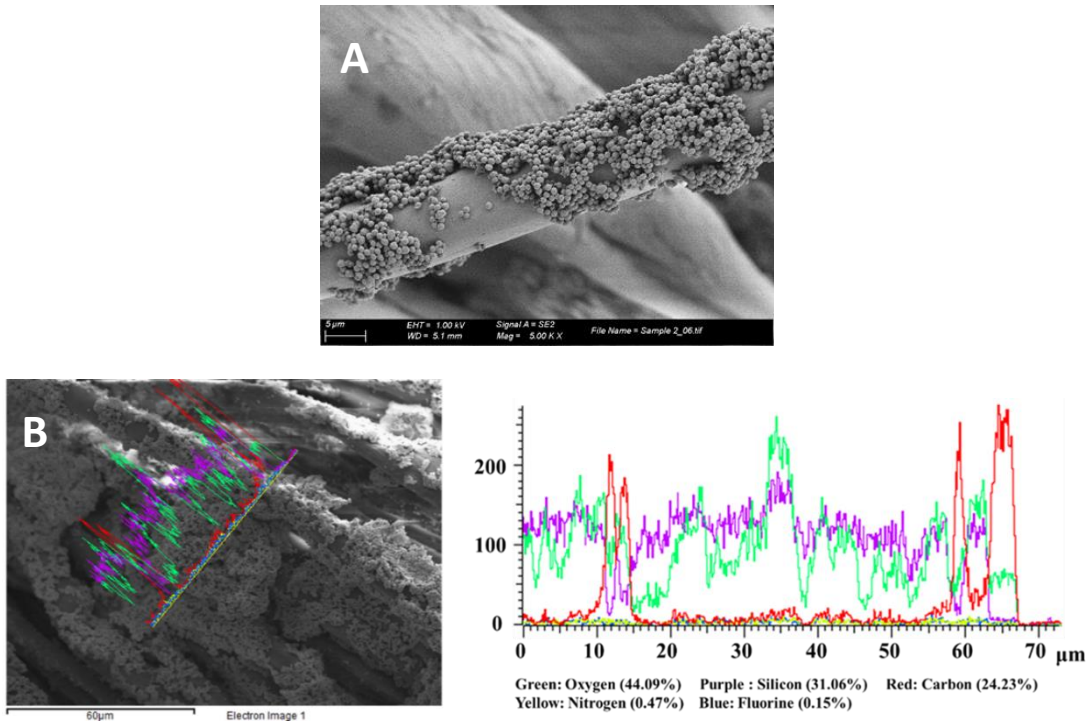

Figure 3.22 A) SEM image and B) EDX spectrum of coated cotton fabrics

Fabric-SiO_2@Norflox-Ibu (TEOS:24 40:1)

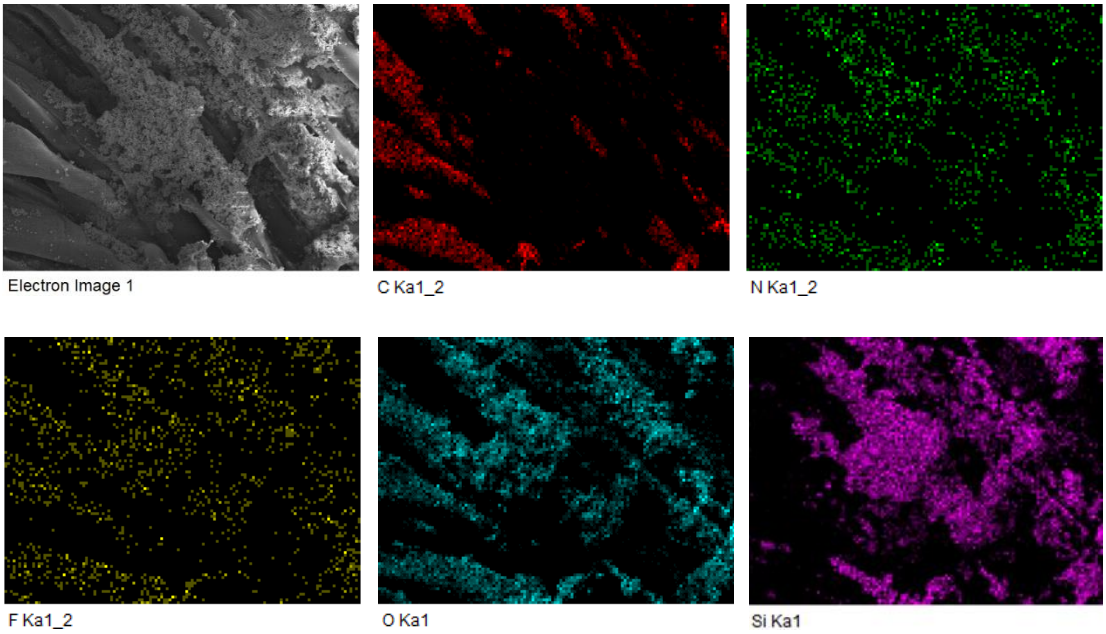

Figure 3.23 EDX element mapping of coated cotton fabrics **Fabric-SiO_2@Norflox-Ibu (TEOS:24 40:1)**

3.3.4 Release of antibacterial and anti-inflammatory drugs from modified cotton fabrics and functionalized silica nanoparticles by selective cleavage of amide bond

The anti-inflammatory drug must be released from the fabric to be in contact with the damaged area and locally modulate the inflammation of the wounds. On the contrary, we have previously demonstrated that some fluoroquinolone derivatives covalently attached on the surface of a cotton fabric presented excellent antimicrobial activity for *S. aureus* being able to reduce preformed *S. aureus* biofilms.[56] Some experiments were carried out to demonstrate that these covalently linked microbicidal fluoroquinolone-based agents do not leach from the fabric surface, and thus they do not contribute to the development of resistance.[56]

With the **SiO_2@Norflox-Ibu (**TEOS:**24** 40:1) and **Fabric-SiO_2@Norflox-Ibu** (TEOS:**24** 40:1) in hand, the next step was to study the release of the bioactive components assaying model proteases such as trypsin, papain, and proteinase K. These enzymes would produce the cleavage of the amide bonds (Figure 3.24) giving rise to Ibuprofen and Norfloxacin release. First, the detachment from nanoparticles **SiO_2@Norflox-Ibu** (TEOS:**24** 40:1, 20 mg) was tested with the aforementioned proteases (Table 3.2, entries 1-3). The experiments were performed in PBS buffer (pH = 7.4, 0.2 M, 2 mL) at 37ºC under stirring for 24 h. After separation of the nanoparticles by centrifugation, the supernatant was extracted with dichloromethane. Then the solvent was removed, and the residue was dissolved in acetonitrile. The solution was analyzed by UV-vis and the amount of released drugs could be quantified by analyzing the intensity of the absorption peaks at λ = 220 nm for Ibuprofen and λ = 285 nm for Norfloxacin according to the corresponding calibration curves.

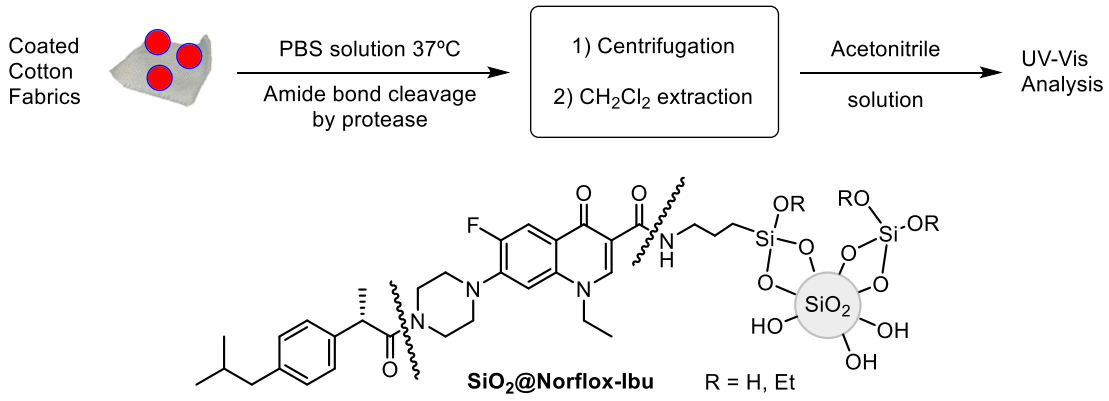

Figure 3.24 Procedure for drug-release experiment of NPs and coated cotton fabrics

The percentage of release was increased by performing a 48 h treatment (Table 3.2, entry 4). Thus, release of Ibuprofen could be clearly observed. However, the low solubility of Norfloxacin in neutral pH made the quantitative measurement inaccurate. As an alternative, we centered our attention to the qualitative detection of Norfloxacin by changing the post-treatment analysis. Thus, 2 mL glacial acetic acid was added to the mixture after protease treatment. After 30 min stirring, the mixture was

centrifugated at 12000 rpm. The supernatant was separated, diluted with water to 10 mL, analyzed by UV-vis and compared with an acidic aqueous solution of commercial Norfloxacin (Figure 3.25). Finally, we treated a 3 x 3 cm cotton piece of **Fabric-SiO_2@Norflox-Ibu (**TEOS:**25** 40:1) with papain in PBS buffer (pH = 7.4, 0.2 M, 5 mL) at 37ºC under stirring for 48 h (Table 3.2, entry 5).

Table 3.2 Release of drugs from nanoparticles and coated fabrics

Entry	Sample	Protease	Time	Release (%)	
				Norfloxacin	Ibuprofen
1[a]	**SiO_2@Norflox-Ibu (**TEOS:**24** 40:1)	Trypsin	24 h	0.12±0.01%	4.5±0.3%
2[a]	**SiO_2@Norflox-Ibu (**TEOS:**24** 40:1)	Papain	24 h	0.26±0.05%	7.1±0.4%
3[a]	**SiO_2@Norflox-Ibu (**TEOS:**24** 40:1)	Proteinase K	24 h	0.15±0.05%	5.8±0.5%
4[a]	**SiO_2@Norflox-Ibu (**TEOS:**24** 40:1)	Papain	48 h	[c]	11.1±0.2%
5[b]	**Fabric-SiO_2@Norflox-Ibu (**TEOS:**24** 40:1)	Papain	48 h	[c]	43.5±2.5%

[a] Experiments with 20 mg of NPs and $4x10^{-4}$ mmol of protease. [b] Experiment with 10 mg of NPs in the coating and $1x10^{-3}$ mmol of papain. [c] Qualitative detection. See text

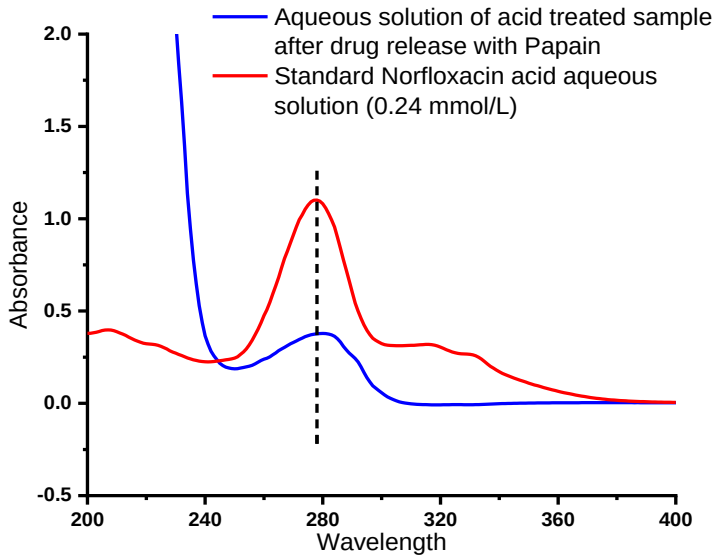

Figure 3.25 Qualitative detection of norfloxacin by UV-Vis after treatment of **SiO_2@Norflox-Ibu** (TEOS:**24** 40:1) with papain for 48 h

Moreover, the supernatants of papain treated **SiO_2@Norflox-Ibu (**TEOS:**24** 40:1) and **Fabric-SiO_2@Norflox-Ibu (**TEOS:**24** 40:1) were used to test the inhibitory effects of the released norfloxacin on the growth of *S. Aureus*. Indeed, a small area of inhibition of bacterial growth (Figure 3.26) could be

observed. Bacterial (*S. Aureus*) growth is inhibited by the supernatants. Thus, this is an indication that norfloxacin has been released from the modified silica nanoparticles and fabrics upon enzymatic hydrolysis of the amide bond. In each Petri plate, we show the inhibition of bacterial growth after 24 h/37 ºC incubation with (+) or without (-) papain. In both cases, digestion with papain enhances the release of norfloxacin resulting in wider growth inhibition halo. This part of the work has been undertaken in collaboration with Professor Ester Fernandez Gimeno of the Departament de Biologia Cel·lular, Fisiologia i Immunologia of the Universitat Autònoma de Barcelona.

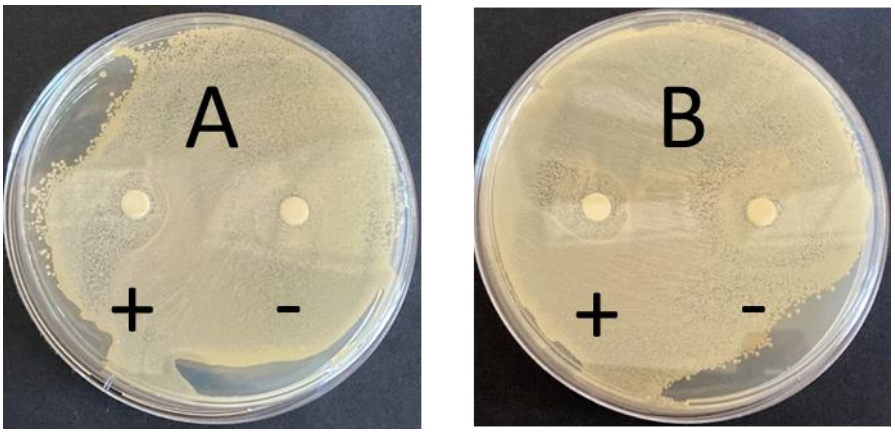

Figure 3.26 The inhibition halo of *S. Aureus* with the supernatants of A) the **Fabric-SiO_2@Norflox-Ibu (**TEOS:**24** 40:1) and B) **SiO_2@Norflox-Ibu (**TEOS:**24** 40:1)

3.4 Conclusion

a) Three silylated derivatives of medicinally relevant molecules have been successfully prepared. Thus, the carboxyl-containing nonsteroidal anti-inflammatory drug ibuprofen and the fluoroquinolone antibiotic levofloxacin were modified to incorporate a terminal triethoxysilyl group through a linker containing an amide bond. In an analogous way, we have obtained a monosilylated monomer bearing both carboxyl-containing antibiotic (norfloxacin) and anti-inflammatory (ibuprofen) moieties in the same molecule, the link between both drug moieties being also an amide bond.

b) We have prepared bifunctionalized silica nanoparticles (**SiO_2@Ibu+Leflox**) by co-condensation of both silylated anti-inflammatory (ibuprofen) and antibiotic (levofloxacin) derivatives with tetraethoxysilane using a 28% ammonium hydroxide-ethanol solution. We have also synthesized silica nanoparticles (**SiO_2@Norflox-Ibu**) derived from the monosilylated monomer bearing both carboxyl-containing antibiotic (norfloxacin) and anti-inflammatory (ibuprofen) moieties in the same molecule using the same method. These dense nanoparticles have been characterized by transmission electron microscopy, dynamic light scattering, Z-potential, solid state ^{29}Si and ^{13}C NMR spectroscopy, and elemental analysis.

c) Of note, cotton fabrics have been coated with drug-functionalized nanoparticles **SiO_2@Norflox-Ibu** by one-step procedure under ultrasonic conditions. The modified textiles **Fabric-SiO_2@Norflox-Ibu** have been characterized by scanning electron microscopy, energy dispersive X-ray spectroscopy and element mapping.

d) The corresponding drugs have been released *in situ* through enzymatic cleavage of the amide bonds in **SiO_2@Norflox-Ibu** and **Fabric-SiO_2@Norflox-Ibu** by treatment with proteases (UV-Vis analysis). The inhibitory effects of the released antibacterial norfloxacin on the growth of *S. Aureus* have also been observed.

e) Topical applications for medical gauzes provided with antibiotic and anti-inflammatory activities to prevent infection and accelerate cicatrisation in cutaneous chronic wounds are expected.

3.5 Experimental section

3.5.1 General information

The information of NMR, IR, MS, elemental analysis, SEM, EDX, elements mapping, TEM, zeta-potential and DLS was given in ***Section* 2.5.1**.

The ^{13}C CP MAS NMR was acquired from a 400 MHz Bruker NEO spectrometer at 10 KHz spinning rate, ns 15360 (18 h), d1 = 2s. Cross-Polarization mixing time was set to 1 ms. Externally calibrated with adamantane sample (29.5 ppm). Spectra processed with a line broadening 20. **The ^{29}Si CP MAS NMR** was obtained from a 400 MHz Bruker NEO spectrometer at 10 KHz spinning rate, ns 15360 (15 h), d1 = 1 s. Cross-Polarization mixing time was set to 1ms. Externally calibrated with DSS sample (0 ppm). Spectra processed with a line broadening 40.

UV-Vis absorption spectroscopy was recorded with Agilent/HP 8453 spectrophotometer or a Varian Cary 60 UV-Vis spectrophotometer operating in a 1 cm pathlength rectangular quartz cuvette.

The proteases used in the experiments were proteinase K (50.7 units/mg), papain (20 units/mg) and trypsin (≥10,000 BAEE units/mg protein). These proteases have similar molecular weight and are active in PBS. They are commonly used for the cleavage of amide bond.

3.5.2 Synthesis of (*S*)-2-(4-isobutylphenyl)-*N*-(3-(triethoxysilyl)propyl)propenami-de (17)

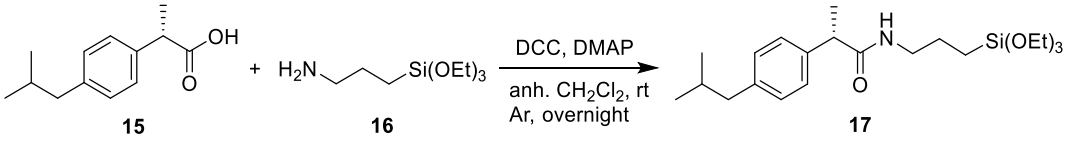

Ibuprofen **15** (206 mg, 1 mmol) was placed in a Schlenk under argon atmosphere. Then, DMAP (6 mg, 5 mol %), DCC (206 mg, 1 mmol, 1 equiv) and dry dichloromethane (5 mL) were added, and the solution was stirred until homogenization. Then 3-(triethoxysilyl)propan-1-amine **16** (266 mg, 1.2 mmol) was introduced by syringe. The reaction was allowed to proceed under stirring at room temperature until completion (TLC monitoring). The crude mixture was poured into water and extracted with dichloromethane. The combined organic phase was washed with brine, dried with anhydrous sodium sulphate, and evaporated under vacuum. The residue was purified by silica gel column chromatography (hexane:ethyl acetate = 3:1) to afford **17** in 50% yield (205 mg, 0.5 mmol). The spectroscopic data matches with those previously reported.[57]

^{1}H NMR (400 MHz, $CDCl_3$) δ (ppm): 7.19 (d, *J* = 7.9 Hz, 2H), 7.10 (d, *J* = 7.9 Hz, 2H), 5.62 (s, 1H), 3.51 (q, *J* = 7.2 Hz, 1H), 3.19 (q, *J* = 6.4 Hz, 2H), 2.45 (d, *J* = 7.2 Hz, 2H), 1.85 (dt, *J* = 13.5, 6.7 Hz, 1H), 1.57 – 1.47 (m, 5H), 1.19 (t, *J* = 7.0 Hz, 9H), 0.90 (d, *J* = 6.6 Hz, 6H), 0.51 (dd, *J* = 9.7, 6.6 Hz, 2H).

3.5.3 Synthesis of (*S*)-9-fluoro-3-methyl-10-(4-methylpiperazin-1-yl)-7-oxo-*N*-(3-(triethoxysilyl)propyl)-2,3-dihydro-7H-[1,4]oxazino[2,3,4-*ij*]quinoline-6-carboxa-mide (19)

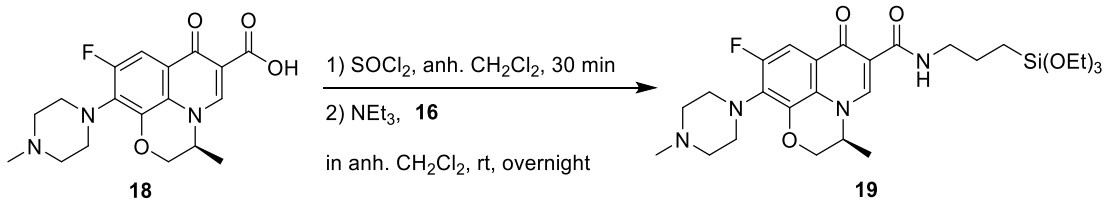

Step 1: Levofloxacin **18** (362 mg, 1.0 mmol, 1 equiv) was introduced in the Schlenk under argon atmosphere in 10 mL of anhydrous CH_2Cl_2. Then, 1.5 equiv of $SOCl_2$ (179 mg, 1.5 mmol, 1.5 equiv) were added and let it react at rt under argon atmosphere for half an hour. Then the solution was evaporated to dryness to remove the solvent and excess of $SOCl_2$. The crude mixture was directly used for the next step.

Step 2: The remaining solid was dissolved in 5 mL of CH_2Cl_2 and triethylamine (5.0 mmol, 5 equiv) was added. Then, a solution of silylated amine **16** (101.2 mg, 1.0 mmol, 1 equiv) in 5 mL of dry CH_2Cl_2 was added and led to react overnight. Distilled water (100 mL) was added and extractions with CH_2Cl_2 (4x20 mL) were carried out. The organic phase was dried over anhydrous Na_2SO_4, filtered, and

evaporated to dryness to afford **19** (563 mg, 0.99 mmol) in 99% yield.

^{1}H NMR (400 MHz, $CDCl_3$) δ (ppm): 10.01 (s, 1H), 8.64 (s, 1H), 7.71 (d, *J* = 12.4 Hz, 1H), 4.46-4.37 (m, 2H), 4.37-4.25 (m, 1H), 3.83 (q, *J* = 6.9 Hz, 6H), 3.52-3.32 (m, 6H), 2.59 (s, 4H), 2.40 (s, 3H), 1.76 (p, *J* = 7.6 Hz, 2H), 1.58 (d, *J* = 6.4 Hz, 3H), 1.23 (t, *J* = 6.9 Hz, 9H), 0.73(t, *J* = 8.2 Hz, 2H). **^{13}C NMR** (91 MHz, $CDCl_3$) δ (ppm):175.3, 164.9, 155.9, 155.7 (d, *J* = 247.5 Hz), 143.8, 139.5 (d, *J* = 6.6 Hz), 131.5 (d, *J* = 14.6 Hz), 124.3, 122.6 (d, *J* = 8.8 Hz), 111.2, 105.1 (d, *J* = 24.1 Hz), 79.0, 68.2, 50.1, 46.0, 45.8, 40.3, 38.8, 28.4, 27.6, 18.3, 8.7. **^{19}F NMR** (376 MHz, $CDCl_3$) δ (ppm): -121.2 (d, *J* = 12.6 Hz). **IR** (ATR) ν (cm^{-1}): 3235, 2930, 2324, 1649, 1600, 1239, 1200, 1046, 1071, 800. **HRMS** (ESI) m/z $[M+H]^+$ calcd for $C_{27}H_{42}FN_4O_6Si$ 565.2852, found: 565.2851.

3.5.4 Synthesis of methyl 1-ethyl-6-fluoro-4-oxo-7-(piperazin-1-yl)-1,4-dihydroquinoline-3-carboxylate (21)

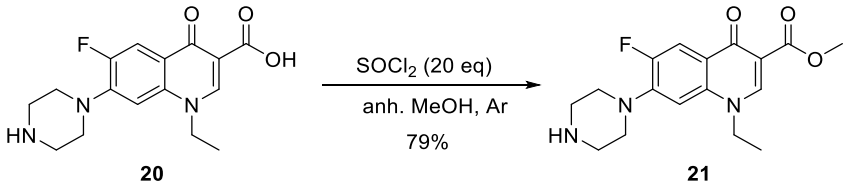

20 **21**

Thionyl chloride (2.7 mL, 28.5 mmol, 20 equiv) was added dropwise into a solution of norfloxacin **20** (451 mg, 1.412 mmol, 1 equiv) in 10 mL of dry methanol at 0 °C. The mixture turned to clear and was heated to reflux for 24 h. The solution was neutralized with 10% Na_2CO_3 aqueous solution. The aqueous phase was extracted with DCM:MeOH (90:10). The organic phase was dried over anhydrous Na_2SO_4, filtered, and concentrated in vacuo affording the ester **21** (371 mg, 1.11 mmol, 79%) as a white powder. The crude was directly used for the next step. The spectroscopic data matches with those previously reported.[64]

^{1}H NMR (400 MHz, $CDCl_3$) δ (ppm): 8.46 (s, 1H), 8.10 (d, *J* = 13.3 Hz, 1H), 6.76 (d, *J* = 6.8 Hz, 1H), 4.23 (q, *J* = 7.2 Hz, 2H), 3.94 (s, 3H), 3.25 (m, 4H), 3.17--3.07 (m, 4H), 2.09 (bs, 1H), 1.56 (t, *J* = 7.2 Hz, 3H).

3.5.5 Synthesis of methyl (*S*)-1-ethyl-6-fluoro-7-(4-(2-(4-isobutylphenyl)propanoyl)piperazin-1-yl)-4-oxo-1,4-dihydroquinoline-3-carboxylate (22)

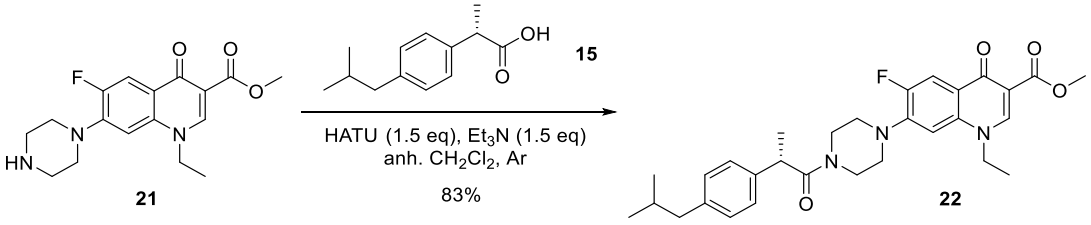

21 **22**

(*S*)-2-(4-Isobutylphenyl)propanoic acid **15** (200 mg, 1 mmol), Et_3N (0.2 mL, 1.4 mmol, 1.4 equiv) and

HATU (0.45 g, 1.18 mmol) were dissolved in anhydrous CH_2Cl_2 (10 mL), the mixture was stirred for 30 minutes under argon atmosphere. Then the mixture was added to a solution of methyl 1-ethyl-6-fluoro-4-oxo-7-(piperazin-1-yl)-1,4-dihydroquinoline-3-carboxylate **21** (323 mg, 0.97 mmol, 0.97 equiv) in dry CH_2Cl_2 (5 mL) at room temperature and refluxed for 48 h. The reaction was monitored by TLC. The reaction mixture was quenched with water, extracted with ethyl acetate, dried over anhydrous Na_2SO_4, and concentrated under reduced pressure. The obtained crude was purified by silica gel column chromatography by using EtOAc:MeOH (90:10) as eluent to afford **22** (0.42 g, 0.805 mmol, 83 %).

M.p.: 96-98 °C; **^{1}H NMR** (400 MHz, $CDCl_3$) δ (ppm): 8.37 (s, 1H), 7.90 (d, *J* = 13.2 Hz, 1H), 7.17 (d, *J* = 7.8 Hz, 2H), 7.08 (d, *J* = 7.9 Hz, 2H), 6.64 (d, *J* = 6.8 Hz, 1H), 4.15 (q, *J* = 7.3 Hz, 2H), 3.91 (m, 2H), 3.83 (s, 3H), 3.75 (s, 1H), 3.65 (s, 1H), 3.52 (s, 1H), 3.11 (s, 3H), 2.68 (s, 1H), 2.42 (d, *J* = 7.1 Hz, 2H), 1.81 (m, 1H), 1.51-1.39 (m, 6H), 0.85 (m, 6H). **^{13}C NMR** (101 MHz, $CDCl_3$) δ (ppm): 173.8 (d, *J* = 2.0 Hz) 172.6, 165.9, 153.0 (d, *J* = 249.5 Hz), 148.2, 144.6 (d, *J* = 10.1 Hz), 140.3, 139.1, 136.1, 129.8, 127.0, 123.4 (d, *J* = 7.1 Hz), 113.4 (d, *J* = 23.2 Hz), 109.3, 104.3, 51.9, 49.8, 49.2, 45.3, 45.0, 42.9, 41.7, 30.2, 22.41, 22.37, 20.7, 14.4. **IR** (ATR) ν (cm^{-1}): 2951, 2866, 1723, 1693, 1617, 1486, 1432, 1315, 1221, 1091, 1019, 840, 803. **HRMS** (ESI) m/z $[M+H]^+$ calcd for $C_{30}H_{37}FN_3O_4$: 522.2763, found: 522.2762.

3.5.6 Synthesis of (*S*)-1-ethyl-6-fluoro-7-(4-(2-(4-isobutylphenyl)propanoyl)piper-azin-1-yl)-4-oxo-1,4-dihydroquinoline-3-carboxylic acid (23)

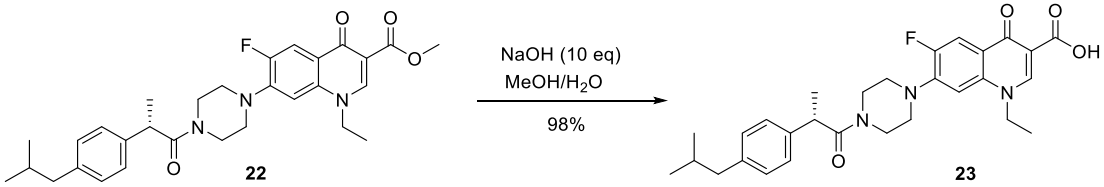

To an ice-cooled solution of ester **22** (522 mg, 1 mmol, 1 equiv) in methanol (5 mL) was added 1 M NaOH aqueous solution (10 mL, 10 mmol, 10 equiv). The mixture was let to stir at rt for 48 hours. Afterwards the solution was brought to pH 2-3 through the addition of 1 M HCl aqueous solution. The resulting solution was extracted with CH_2Cl_2, the organic extract was dried over anhydrous sodium sulfate and the solvent was removed in vacuo to afford a white powder. The product was recrystallized with CH_2Cl_2 and hexane to afford **23** (497.5 mg, 0.98 mmol) in 98 % yield.

M.p.: 182-184 °C. **^{1}H NMR** (400 MHz, $CDCl_3$) δ (ppm): 8.64 (s, 1H), 8.01 (d, *J* = 12.9 Hz, 1H), 7.15 (d, *J* = 7.9 Hz, 2H), 7.09 (d, *J* = 7.8 Hz, 2H), 6.72 (d, *J* = 6.7 Hz, 1H), 4.28 (q, *J* = 7.3 Hz, 2H), 4.06 (m, 1H), 3.88 (app q, *J* = 6.8 Hz, 1H), 3.70 (m, 1H), 3.59 (m, 2H), 3.29 (m, 1H), 3.23-3.05 (m, 2H), 2.66 (m, 1H), 2.43 (d, *J* = 7.2 Hz, 2H), 1.82 (m, 1H), 1.55 (t, *J* = 7.2 Hz, 3H), 1.46 (d, *J* = 6.8 Hz, 3H), 0.85 (m, 6H). **^{13}C NMR** (101 MHz, $CDCl_3$) δ (ppm): 176.9 (d, *J* = 2.0 Hz), 172.6, 167.1, 153.4 (d, *J* = 252.5 Hz), 147.2, 145.7 (d, *J* = 11.1 Hz), 140.5, 139.0, 137.1, 129.9, 127.0, 120.8 (d, *J* = 8.1 Hz), 112.8 (d, *J*

= 23.2 Hz), 108.4, 104.1 (d, *J* = 3.0 Hz), 49.8, 49.5, 45.3, 45.0, 43.1, 41.6, 30.2, 22.43, 22.40, 20.8, 14.5. **IR** (ATR) ν (cm^{-1}): 2953, 2867, 1712, 1625, 1432, 1230, 1018, 805, 747. **HRMS** (ESI) m/z $[M+H]^+$ calcd for $C_{29}H_{35}FN_3O_4$: 508.2606, found: 508.2599. **EA**: calcd: 68.62% C, 6.75% H, 3.74% F, 8.28% N, found 68.56% C, 6.76% H, 8.12% N.

3.5.7 Synthesis of (*S*)-1-ethyl-6-fluoro-7-(4-(2-(4-isobutylphenyl)propanoyl)piper-azin-1-yl)-4-oxo-*N*-(3-(triethoxysilyl)propyl)-1,4-dihydroquinoline-3-carboxamide (24)

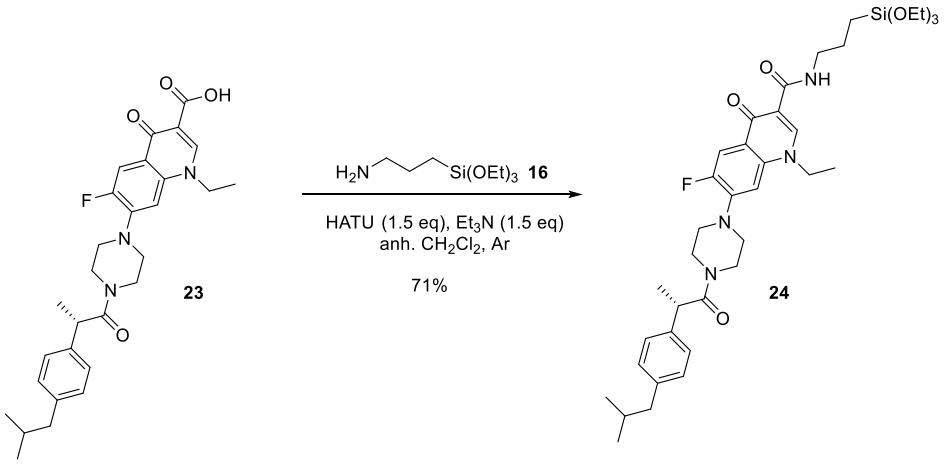

Carboxylic acid **23** (0.35 g, 0.690 mmol, 1 equiv), Et_3N (0.10 mL, 1.00 mmol, 1.4 equiv) and HATU (0.3 g, 0.789 mol, 1.14 equiv) were dissolved in CH_2Cl_2 (10 mL), the mixture was stirred for 30 minutes under argon atmosphere. Then, 3-(triethoxysilyl)propan-1-amine **16** (0.16 g, 0.723 mmol, 1.04 equiv) was added and the solution was refluxed for 48 h. The reaction was monitored by TLC. The reaction mixture was quenched with water, extracted with ethyl acetate, dried over anhydrous sodium sulfate and concentrated under reduced pressure. The obtained residue was purified by silica gel column chromatography by using AcOEt : EtOH (95 : 5) as eluent to afford compound **24** in 71 % yield (0.35 g, 0.493 mmol).

^{1}H NMR (400 MHz, $CDCl_3$) δ (ppm): 9.98 (t, *J* = 5.8 Hz, 1H), 8.65 (s, 1H), 7.97 (d, *J* = 13.1 Hz, 1H), 7.12 (d, *J* = 7.8 Hz, 2H), 7.05 (d, *J* = 7.8 Hz, 2H), 6.63 (d, *J* = 6.7 Hz, 1H), 4.18 (q, *J* = 7.3 Hz, 2H), 4.01 (m, 1H), 3.85 (m 1H), 3.77 (q, *J* = 7.0 Hz, 6H), 3.65 (m, 1H), 3.54 (m, 2H), 3.40 (app q, *J* = 6.8, 2H), 3.19 (m, 1H), 3.07 (m, 2H), 2.56 (m, 1H), 2.38 (d, *J* = 7.2 Hz, 2H), 1.85-1.64 (m, 3H), 1.51-1.37 (m, 6H), 1.17 (t, *J* = 7.0 Hz, 9H), 0.81 (m, 6H), 0.67 (t, *J* = 8.2 Hz, 2H). **^{13}C NMR** (101 MHz, $CDCl_3$) δ (ppm): 175.3, 172.4, 164.8, 153.0 (d, *J* = 249.5 Hz), 146.6, 144.5 (d, *J* = 11.1 Hz), 140.4, 139.0, 136.4, 129.8, 126.92, 122.9 (d, *J* = 7.1 Hz), 113. 0 (d, J = 23.2 Hz), 111.8, 103.9 (d, *J* = 3.0 Hz), 58.4, 50.0, 49.0, 45.3, 45.0, 43.0, 42.0, 41.6, 30.2, 23.3, 22.34, 22.30, 20.7, 18.3, 14.4, 8.0. **IR** (ATR) ν (cm^{-1}): 3240, 2970, 2925, 1650, 1541, 1487, 1229, 1074, 775. **HRMS** (ESI) m/z $[M+H]^+$ calcd for $C_{38}H_{56}FN_4O_6Si$: 711.3948 found: 711.3946.

3.5.8 General procedure for the preparation of functionalized silica nanoparticles SiO_2@Ibu+Leflox

Tetraethoxysilane (2.08 g, 10.0 mmol), the silylated anti-inflammatory ibuprofen **17** (0.25 mmol) and silylated antibiotic levofloxacin **19** (0.25 mmol) were dissolved in absolute EtOH (25 mL). Then, an ammonium hydroxide-ethanol solution (6 mL of 28% $NH_3 \cdot H_2O$ in 25 mL EtOH) was added. The mixture was magnetically stirred (1400 rpm) at room temperature for 12 hours. Then the functionalized nanoparticles were collected by centrifugation (13500 rpm for 10 minutes) and washed with ethanol until neutral pH was reached. Then, the obtained solid was washed successively with Mili-Q water and 96% ethanol, and it was dried under vacuum for several hours. We got functionalized silica nanoparticles **SiO_2@Ibu+Leflox (20:0.5:0.5)**. For the preparation of **SiO_2@Ibu+Leflox (20:0.75:0.25)**, we changed the ratio of TEOS: silylated drugs **17** and **19**.

SiO_2@Ibu+Leflox (20:0.5:0.5): **EA**: 9.26% C, 2.02% H, 1.61% N (**17** 0.23 mmol/g material, **19** 0.23 mmol/g material). **IR** (ATR) ν (cm^{-1}): 3274.8, 1051.1, 948.5, 800.1. **DLS**: 2733 nm, **Zeta-potential**: ζ = 5.7 mV.

SiO_2@Ibu+Leflox (20:0.75: 0.25): **EA**: 4.20% C, 1.83% H, 0.25% N (**17** 0.075 mmol/g material, **19** 0.025 mmol/g material). **IR** (ATR) ν (cm^{-1}): 3302.3, 1054.3, 947.0, 796.1, 545.3. **DLS**: 426 nm, **Zeta-potential**: ζ = -41.0 mV.

3.5.9 General procedure for the preparation of functionalized silica nanoparticles SiO_2@Norflox-Ibu

Tetraethoxysilane (2.08 g, 10.0 mmol) and the silylated derivative **24** (0.5 or 0.33 or 0.25 mmol) were dissolved in absolute EtOH (25 mL). Then, an ammonium hydroxide-ethanol solution was added (6 mL of 28% NH_3 H_2O in 25 mL EtOH). The mixture was magnetically stirred (1400 rpm) at room temperature for 12 hours. The functionalized nanoparticles were collected by centrifugation (13500 rpm for 10 minutes) and washed with ethanol until neutral pH was reached. Then, the obtained white solid was washed successively with Mili-Q water and 96% ethanol, and the nanomaterial was dried under high vacuum. We obtained **SiO_2@Norflox-Ibu** with different ratios of TEOS and silylated drug **24**.

SiO_2@Norflox-Ibu (20:1): **EA**: 1.96% C, 1.52% H, 0.86% N (0.15 mmol/g material). **IR** (ATR) ν (cm^{-1}): 3409.3, 1631.0, 1052.4, 948.1, 794.4, 522.7. **^{13}C-CP-MAS NMR** (100.6 MHz) δ (ppm): 175.6, 166.9, 140.0, 129.8, 111.4, 59.3, 45.3, 30.6, 22.1, 17.6, 14.2. **^{29}Si-CP-MAS NMR** (79.5 MHz) δ (ppm): -58.35 (T^2), -66.77 (T^3), -102.34 (Q^3), -112.08 (Q^4). **DLS**: 836 nm, **Zeta-potential**: ζ = -65.5 mV.

SiO_2@Norflox-Ibu (30:1): **EA**: 2.52% C, 1.69% H, 0.74% N (0.13 mmol/g material). **IR** (ATR) ν (cm^{-1}): 3283.5, 1637.8, 1058.2, 953.5, 795.9, 543.6. **DLS**: 658 nm, **Zeta-potential**: ζ = -69.9 mV.

SiO_2@Norflox-Ibu (40:1): **EA**: 1.61% C, 1.63% H, 0.84% N (0.15 mmol/g material). **IR** (ATR) ν (cm^{-1}): 3374.0, 1630.1, 1053.6, 949.4, 792.7, 565.7. **^{29}Si-CP-MAS NMR** (79.5 MHz) δ (ppm): -56.53 (T^2), -65.38 (T^3), -92.36 (Q^2), -101.83 (Q^3), -112.39 (Q^4). **DLS**: 486 nm, **Zeta-potential**: ζ = -72.3 mV.

3.5.10 Procedure for the preparation of cotton fabrics coated with functionalized silica nanoparticles SiO_2@Norflox-Ibu (40:1)

Tetraethoxysilane (2.08 g, 10.0 mmol) and the corresponding silylated derivative **24** (0.25 mmol) were dissolved in absolute EtOH (25 mL). Then, an ammonium hydroxide-ethanol solution was added (6 mL of 28% $NH_3\,H_2O$ in 25 mL EtOH). The mixture was magnetically stirred intensively (1400 rpm) at room temperature for 12 hours and then ultrasonicated for 30 min. Afterwards, a piece of clean cotton fabric (3 × 3 cm) was immersed in the solution and the solution was ultrasonicated for 30 min. After 30 min, the cotton fabric was removed from the solution, washed with water and ethanol for several times and dried in a vacuum oven at 50 ºC for 12 h.

3.5.11 Treatment of functionalized silica nanoparticle SiO_2@Norflox-Ibu (40:1) with proteases for quantitative analysis by UV-Vis

The functionalized silica nanoparticles (20 mg) were dispersed in phosphate-buffered saline (PBS, pH 7.4) (2 mL) in an Eppendorf tube, the corresponding protease (Table 3.2) was added and the mixture was gently stirred at 37 ºC for the given time (orbital shaker). The concentration of protease was 0.2 mM. Then, after removal of nanoparticles by centrifugation, the supernatant was extracted with dichloromethane (10 × 3 mL). The solvent was removed under vacuum from the combined organic phases. The residue was dissolved in acetonitrile and the solution was analyzed by UV-Vis (ibuprofen 220 nm¸ norfloxacin 285 nm).

3.5.12 Treatment of functionalized silica nanoparticle SiO_2@Norflox-Ibu (40:1) with proteases for qualitative detection of norfloxacin

The functionalized silica nanoparticles (20 mg) were dispersed in phosphate-buffered saline (PBS) (2 mL) in an Eppendorf tube, the corresponding protease was added and the mixture was gently stirred at 37 ºC for 48 h (orbital shaker). The concentration of protease was 0.2 mM. Glacial acetic acid (2 mL) was added and the mixture was stirred for 30 min. Then after removal of nanoparticles by centrifugation,

the supernatant was diluted to 10 mL and the aqueous solution was analyzed by UV-Vis. The commercial norfloxacin aqueous solution (0.24 mmol/L) was prepared with the same amount of glacial acetic acid and was analyzed by UV-Vis (285 nm).

3.5.13 Treatment of cotton fabrics coated with functionalized silica nanoparticles with proteases

A piece of **Fabric-SiO_2@Norflox-Ibu (40:1)** (3 × 3 cm) was cut into small pieces and dispersed in phosphate-buffered saline (PBS) (5 mL) in an Eppendorf tube, the corresponding protease was added and the mixture was gently stirred at 37 ºC for 48 h (orbital shaker). The concentration of protease was 0.2 mM. After the removal of cotton fabrics, the supernatant was extracted with dichloromethane (25 × 3 mL). The solvent was removed under vacuum from the combined organic phases. The residue was dissolved in acetonitrile and the solution was analyzed by UV-Vis.

3.5.14 Inhibitory tests of bacterial growth

The supernatants of papain treated **SiO_2@Norflox-Ibu** (TEOS:**24** 40:1) and **Fabric-SiO_2@Norflox-Ibu** (TEOS:**24** 40:1) were used to test the inhibitory effects of the released norfloxacin on the growth of *S. Aureus.* Pieces of paper were dipped into the supernatants of nanoparticles and cotton fabric with or without papain. Then bacterial growth around papers after 24 h/37 ºC incubation in Petri plates was investigated. Comparing the size of inhibition halo, we can certify the release of norfloxacin.

3.6 References

[1] Walker, M. Human skin through the ages. *International Journal of Pharmaceutics* **2022**, *622*, 121850.
[2] Hernández-Rangel, A.; Martin-Martinez, E. S. Collagen based electrospun materials for skin wounds treatment. *Journal of Biomedical Materials Research Part A* **2021**, *109* (9), 1751-1764.
[3] Rodrigues, M.; Kosaric, N.; Bonham, C. A.; Gurtner, G. C. Wound Healing: A Cellular Perspective. *Physiological Reviews* **2019**, *99* (1), 665-706.
[4] Lu, G.; Ding, Z.; Wei, Y.; Lu, X.; Lu, Q.; Kaplan, D. L. Anisotropic Biomimetic Silk Scaffolds for Improved Cell Migration and Healing of Skin Wounds. *ACS Applied Materials & Interfaces* **2018**, *10* (51), 44314-44323.
[5] Li, S.; Renick, P.; Senkowsky, J.; Nair, A.; Tang, L. Diagnostics for wound infections. *Advances in Wound Care* **2021**, *10* (6), 317-327.
[6] Smith, R.; Russo, J.; Fiegel, J.; Brogden, N. Antibiotic Delivery Strategies to Treat Skin Infections When Innate Antimicrobial Defense Fails. *Antibiotics* **2020**, *9* (2), 56.
[7] Montaser, A. S.; Rehan, M.; El-Senousy, W. M.; Zaghloul, S. Designing strategy for coating cotton gauze fabrics and its application in wound healing. *Carbohydrate Polymers* **2020**, *244*, 116479.
[8] Pierce, P. D., MD, Glenn F; Mustoe, M., Thomas A. Pharmacologic enhancement of wound healing. *Annual Review of Medicine* **1995**, *46* (1), 467-481.
[9] Granados, A.; Pleixats, R.; Vallribera, A. Recent Advances on Antimicrobial and Anti-Inflammatory Cotton Fabrics Containing Nanostructures. *Molecules* **2021**, *26* (10), 3008.
[10] Chen, S.; Li, A.; Wang, Y.; Zhang, Y.; Liu, X.; Ye, Z.; Gao, S.; Xu, H.; Deng, L.; Dong, A. Janus polyurethane sponge as an antibiofouling, antibacterial, and exudate-managing dressing for accelerated wound healing. *Acta Biomaterialia* **2023**, *171*, 428-439.
[11] Davies, J.; Davies, D. Origins and Evolution of Antibiotic Resistance. *Microbiology and Molecular Biology Reviews* **2010**, *74* (3), 417-433.
[12] Nicolaou, K. C.; Rigol, S. A brief history of antibiotics and select advances in their synthesis. *The Journal of Antibiotics* **2018**, *71* (2), 153-184.
[13] Chen, L.; Kumar, S.; Wu, H. A review of current antibiotic resistance and promising antibiotics with novel modes of action to combat antibiotic resistance. *Archives of Microbiology* **2023**, *205* (11), 356.
[14] Lloyd, N. C.; Morgan, H. W.; Nicholson, B. K.; Ronimus, R. S. The Composition of Ehrlich's Salvarsan: Resolution of a Century-Old Debate. *Angewandte Chemie International Edition* **2005**, *44* (6), 941-944.
[15] Pancu, D. F.; Scurtu, A.; Macasoi, I. G.; Marti, D.; Mioc, M.; Soica, C.; Coricovac, D.; Horhat, D.; Poenaru, M.; Dehelean, C. Antibiotics: Conventional Therapy and Natural Compounds with Antibacterial Activity—A Pharmaco-Toxicological Screening. *Antibiotics* **2021**, *10* (4), 401.
[16] Lalchhandama, K. History of penicillin. *WikiJournal of Medicine* **2021**, *8* (1), 1-16.
[17] Miller, E. L. The penicillins: A review and update. *Journal of Midwifery & Women's Health* **2002**, *47* (6), 426-434.
[18] Hutchings, M. I.; Truman, A. W.; Wilkinson, B. Antibiotics: past, present and future. *Current Opinion in Microbiology* **2019**, *51*, 72-80.
[19] Takahashi, Y.; Nakashima, T. Actinomycetes, an Inexhaustible Source of Naturally Occurring Antibiotics. *Antibiotics* **2018**, *7* (2), 45.
[20] Toscano, W. A.; Storm, D. R. Bacitracin. *Pharmacology & Therapeutics* **1982**, *16* (2), 199-210.
[21] Serio, A. W.; Keepers, T.; Andrews, L.; Krause, K. M. Aminoglycoside Revival: Review of a Historically Important Class of Antimicrobials Undergoing Rejuvenation. *EcoSal Plus* **2018**, *8* (1).
[22] Llewellyn, N. M.; Spencer, J. B. Biosynthesis of 2-deoxystreptamine-containing aminoglycoside antibiotics.

Natural Product Reports **2006**, *23* (6), 864-874.
[23] Hotta, K.; Kondo, S. Kanamycin and its derivative, arbekacin: significance and impact. *The Journal of Antibiotics* **2018**, *71* (4), 417-424.
[24] Maxwell, A.; Ghate, V.; Aranjani, J.; Lewis, S. Breaking the barriers for the delivery of amikacin: Challenges, strategies, and opportunities. *Life Sciences* **2021**, *284*, 119883.
[25] Campoli-Richards, D. M.; Chaplin, S.; Sayce, R. H.; Goa, K. L. Netilmicin. *Drugs* **1989**, *38* (5), 703-756.
[26] Neu, H. C. Tobramycin: An Overview. *The Journal of Infectious Diseases* **1976**, *134*, S3-S19.
[27] Ramirez, M. S.; Tolmasky, M. E. Amikacin: Uses, Resistance, and Prospects for Inhibition. *Molecules* **2017**, *22* (12), 2267.
[28] Krause, K. M.; Serio, A. W.; Kane, T. R.; Connolly, L. E. Aminoglycosides: An Overview. *Cold Spring Harbor perspectives in medicine* **2016**, *6* (6), a027029.
[29] Ross, A.; Schügerl, K. Tetracycline production by Streptomyces aureofaciens: the time lag of production. *Applied Microbiology and Biotechnology* **1988**, *29* (2), 174-180.
[30] Petković, H.; Lukežič, T.; Šušković, J. Biosynthesis of Oxytetracycline by Streptomyces rimosus: Past, Present and Future Directions in the Development of Tetracycline Antibiotics. *Food technology and biotechnology* **2017**, *55* (1), 3-13.
[31] Chopra, I.; Roberts, M. Tetracycline Antibiotics: Mode of Action, Applications, Molecular Biology, and Epidemiology of Bacterial Resistance. *Microbiology and Molecular Biology Reviews* **2001**, *65* (2), 232-260.
[32] Minuth, J. N.; Holmes, T. M.; Musher, D. M. Activity of Tetracycline, Doxycycline, and Minocycline Against Methicillin-Susceptible and -Resistant Staphylococci. *Antimicrobial Agents and Chemotherapy* **1974**, *6* (4), 411-414.
[33] Griffith, R. S.; Black, H. R. Erythromycin. *Pediatric Clinics of North America* **1961**, *8* (4), 1115-1131.
[34] Bakheit, A. H. H.; Al-Hadiya, B. M. H.; Abd-Elgalil, A. A. Chapter One - Azithromycin. In *Profiles of Drug Substances, Excipients and Related Methodology*, Brittain, H. G. Ed.; Vol. 39; Academic Press, 2014; pp 1-40.
[35] Shi, J.; Montay, G.; Bhargava, V. O. Clinical Pharmacokinetics of Telithromycin, the First Ketolide Antibacterial. *Clinical Pharmacokinetics* **2005**, *44* (9), 915-934.
[36] Shimizu, M. Quinolone antibacterial agents: Their past, present, future. *Journal of Infection and Chemotherapy* **1995**, *1* (1), 16-29.
[37] Tillotson, G. S. Quinolones: structure-activity relationships and future predictions. *Journal of Medical Microbiology* **1996**, *44* (5), 320-324.
[38] Oliphant, C. M.; Green, G. M. Quinolones: a comprehensive review. *American family physician* **2002**, *65* (3), 455-464.
[39] Kapoor, G.; Saigal, S.; Elongavan, A. Action and resistance mechanisms of antibiotics: A guide for clinicians. *Journal of anaesthesiology, clinical pharmacology* **2017**, *33* (3), 300-305.
[40] Fullerton, J. N.; Gilroy, D. W. Resolution of inflammation: a new therapeutic frontier. *Nature Reviews Drug Discovery* **2016**, *15* (8), 551-567.
[41] Brune, K.; Hinz, B. The discovery and development of antiinflammatory drugs. *Arthritis and rheumatism* **2004**, *50* (8), 2391-2399.
[42] Rainsford, K. D. Ibuprofen: pharmacology, efficacy and safety. *Inflammopharmacology* **2009**, *17* (6), 275-342.
[43] Buchman, A. L. Side Effects of Corticosteroid Therapy. *Journal of Clinical Gastroenterology* **2001**, *33* (4), 289-294.
[44] Sala, A.; Proschak, E.; Steinhilber, D.; Rovati, G. E. Two-pronged approach to anti-inflammatory therapy through the modulation of the arachidonic acid cascade. *Biochemical Pharmacology* **2018**, *158*, 161-173.

[45] Monteiro, B.; Steagall, P. V. Antiinflammatory Drugs. *The Veterinary clinics of North America. Small animal practice* **2019**, *49* (6), 993-1011.
[46] Pinho, E.; Calhelha, R. C.; Ferreira, I. C. F. R.; Soares, G. Cotton-hydrogel composite for improved wound healing: Antimicrobial activity and anti-inflammatory evaluation—Part 2. **2019**, *30* (4), 863-871.
[47] Lang, S.; Chen, C.; Xiang, J.; Liu, Y.; Li, K.; Hu, Q.; Liu, G. Facile and Robust Antibacterial Functionalization of Medical Cotton Gauze with Gallic Acids to Accelerate Wound Healing. *Industrial & Engineering Chemistry Research* **2021**, *60* (28), 10225-10234.
[48] Arafa, A. A.; Nada, A. A.; Ibrahim, A. Y.; Sajkiewicz, P.; Zahran, M. K.; Hakeim, O. A. Preparation and characterization of smart therapeutic pH-sensitive wound dressing from red cabbage extract and chitosan hydrogel. *International Journal of Biological Macromolecules* **2021**, *182*, 1820-1831.
[49] El-Rafie, H. M.; El-Rafie, M. H.; AbdElsalam, H. M.; El-Sayed, W. A. Antibacterial and anti-inflammatory finishing of cotton by microencapsulation using three marine organisms. *International Journal of Biological Macromolecules* **2016**, *86*, 59-64.
[50] Rathinavel, S.; Indrakumar, J.; Korrapati, P. S.; Dharmalingam, S. Synthesis and fabrication of amine functionalized SBA-15 incorporated PVA/Curcumin nanofiber for skin wound healing application. *Colloids and Surfaces A: Physicochemical and Engineering Aspects* **2022**, *637*, 128185.
[51] Monavari, M.; Zohoori, S.; Davodiroknabadi, A. Anti-inflammatory and bactericidal effect of keratin/harmaline/ginkgo biloba electrospun nano fibres as band aid. *Micro & Nano Letters* **2022**, *17* (9), 210-215.
[52] Peng, J.; Xie, S.; Huang, K.; Ran, P.; Wei, J.; Zhang, Z.; Li, X. Nitric oxide-propelled nanomotors for bacterial biofilm elimination and endotoxin removal to treat infected burn wounds. *Journal of Materials Chemistry B* **2022**, *10* (22), 4189-4202.
[53] Xiang, J.; Zhu, R.; Lang, S.; Yan, H.; Liu, G.; Peng, B. Mussel-inspired immobilization of zwitterionic silver nanoparticles toward antibacterial cotton gauze for promoting wound healing. *Chemical Engineering Journal* **2021**, *409*, 128291.
[54] Alisir, S. H.; Ozdemir, N.; Burgaz, E.; Dege, N.; Canavar, Y. E. Fabrication and Antimicrobial Activity of Poly(lactic acid) Nanofibers Containing Firstly Synthesized Silver Diclofenac Complex with (2-methylimidazole) for Wound Dressing Applications. *Fibers and Polymers* **2021**, *22* (10), 2738-2749.
[55] Montagut, A. M.; Granados, A.; Ballesteros, A.; Pleixats, R.; Llagostera, M.; Cortés, P.; Sebastián, R. M.; Vallribera, A. Antibiotic protected silver nanoparticles for microbicidal cotton. *Tetrahedron* **2019**, *75* (1), 102-108.
[56] Montagut, A. M.; Granados, A.; Lazurko, C.; El-Khoury, A.; Suuronen, E. J.; Alarcon, E. I.; Sebastián, R. M.; Vallribera, A. Triazine mediated covalent antibiotic grafting on cotton fabrics as a modular approach for developing antimicrobial barriers. *Cellulose* **2019**, *26*, 7495-7505.
[57] Li, H.; Granados, A.; Fernández, E.; Pleixats, R.; Vallribera, A. Anti-inflammatory Cotton Fabrics and Silica Nanoparticles with Potential Topical Medical Applications. *ACS Applied Materials & Interfaces* **2020**, *12* (23), 25658-25675.
[58] Cañedo-Dorantes, L.; Cañedo-Ayala, M. Skin acute wound healing: a comprehensive review. *International journal of inflammation* **2019**, *2019*.
[59] Cox, S. W.; Cho, K.; Eley, B. M.; Smith, R. E. A simple, combined fluorogenic and chromogenic method for the assay of proteases in gingival crevicular fluid. *Journal of Periodontal Research* **1990**, *25* (3), 164-171.
[60] Bendicho, S.; Martí, G.; Hernández, T.; Martín, O. Determination of proteolytic activity in different milk systems. *Food Chemistry* **2002**, *79* (2), 245-249.
[61] Lottenberg, R.; Christensen, U.; Jackson, C. M.; Coleman, P. L. Assay of coagulation proteases using peptide chromogenic and fluorogenic substrates. *Methods in Enzymology* **1981**, *80*, 341-361.

[62] Liu, M.; Granados, A.; Reyes-Mesa, D.; Arosemena-Angulo, E. L.; Calvo-Torras, M. Á.; Pleixats, R.; Vallribera, A. Silica nanostructures against fungal growth: design and preparation of antifungal cotton fabrics. *Cellulose* **2022**, *29* (16), 8889-8905.
[63] Shome, A.; Jha, K. T.; Chawla, P. A. Hexafluorophosphate Azabenzotriazole Tetramethyl Uronium (HATU): A Unique Cross-Coupling Reagent. *SynOpen* **2023**, *07* (04), 566-569.
[64] Luo, X.; Wang, P. Ynonylation of Acyl Radicals by Electroinduced Homolysis of 4-Acyl-1,4-dihydropyridines. *Organic Letters* **2021**, *23* (13), 4960-4965.

CHAPTER 4

Immobilization of Chiral Box-Ligands on Silica Nanoparticles for the Enantioselective Difluoroalkylation of *β*-Ketoesters by Cooperative Photoredox/Ni (II) Catalysis

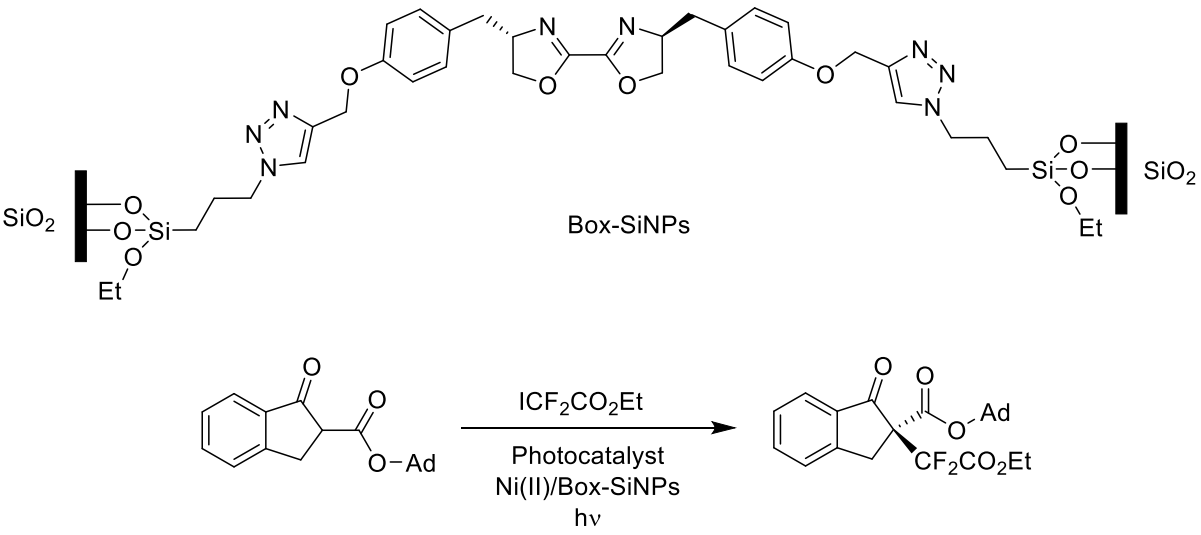

Chapter 4
Immobilization of Chiral Box-Ligands on Silica Nanoparticles for the Enantioselective Difluoroalkylation of *β*-Ketoesters by Cooperative Photoredox/Ni (II) Catalysis

4.1 Introduction

4.1.1 Fluorine and organofluorinated compounds

Fluorine, ranked as the 13th most prevalent element in the Earth's crust (constituting 0.059% by weight), stands as the most abundant halogen present on our planet.[1] Fluorine is the lightest of the halogen group and is the most electronegative element.[2] Over the past 100-150 years, the fluorochemical industry has experienced significant growth due to the pivotal role of numerous fluorinated products across various aspects of our daily life. Chlorofluorocarbons were used as refrigerants and then replaced with hydrochlorofluorocarbons and hydrofluorocarbons because of detrimental effects on the ozone layer.[3] Fluorinated liquid crystal monomers also find extensive applications in LCD devices.[4, 5] The incorporation of fluorine is pivotal in advancing modern pharmaceuticals, as the introduction frequently boosts bioactivity and metabolic stability.[6] Therefore, about half of the best-selling drugs (blockbuster drugs) are fluorine-containing pharmaceuticals.[7] The diseases targeted by FDA-approved pharmaceuticals containing fluorine are illustrated in Fig 4.1. Another significant fluorine trend is evident in the agricultural sector, where "fluorination" allows for the precise adjustment of various physicochemical properties of active ingredients, which includes lipophilicity, water solubility, and metabolic stability.[8] The rationalization behind fluorination of drugs and agrochemicals is well-founded, offering significant benefits such as the development of more potent life-saving medicines and selective crop-protection agents.

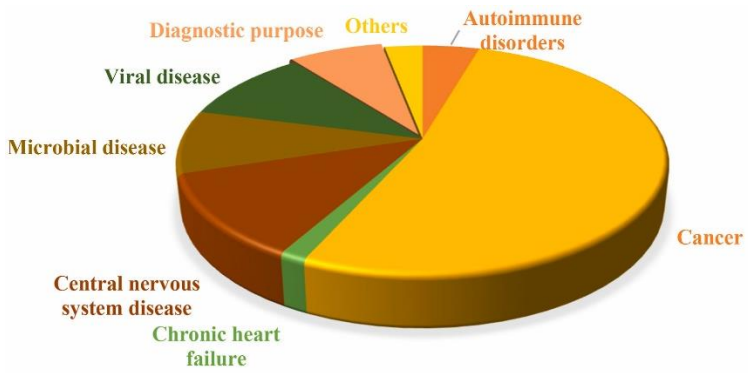

Figure 4.1 The diseases targeted by FDA-approved pharmaceuticals containing fluorine from 2015 to 2022[6]

The small size of the fluorine atom, measuring 1.47 Å, is a unique characteristic. Its van der Waals radius resembles that of hydrogen. Consequently, a fluorine atom can imitate a hydrogen atom (1.2 Å) or a hydroxy group (1.40 Å) in a bioactive compound, which provide the basis for the introduction of fluorine. These isosteric substitutions typically do not significantly change the shape of the molecule. The stereoelectronic effects resulting from fluorine's high electronegativity can cause changes in the preferred molecular conformation following fluorine substitution.

Differing from intravenously administered drugs, the bioavailability of orally administered drugs can decrease due to either poor absorption or first-pass metabolism. For an orally administered drug, it needs to endure the physiological pH in the stomach sufficiently to cross into the bloodstream and reach the site of action in adequate quantities. Subsequently, it should efficiently carry out its intended function and eventually metabolize at a suitable rate into non-toxic substances. The introduction of fluorine in a molecule significantly impacts the acidity or basicity of neighboring functional groups due to fluorine being the most electronegative element. Then, changes in pK_a can increase binding affinity and bioavailability by altering the absorption process.

The common transporting process for an orally administered drug to be absorbed and distributed depends on the permeability of the cell membrane. For a drug molecule to traverse a cell membrane, its lipophilicity must be balanced to allow passage into the lipid core without becoming entrapped within it. Lipophilicity is quantified by the partition coefficient (log P) between octanol and water. Lipinski's rule of five, a set of empirical rules used as a guide to predict good drug candidates states that a log P > 5 will likely result in poor absorption.

After the drug was absorbed, drug molecules undergo metabolism that leads to detoxification and depressed lipophilicity. The primary enzymes involved in drug metabolism are cytochrome P450 monooxygenases, predominantly found in the liver. Enhancing stability against oxidation processes

mediated by P450 enzymes is often necessary during drug development. A well-established approach to achieve this objective is to substitute metabolically labile hydrogen with fluorine.[9] Initially, hydroxylation of C-H bonds can be impeded by fluorination due to the higher bonding energy of the C-F bond (≈441 kJ/mol) compared to the C-H bond (≈414 kJ/mol). The electron-withdrawing property of fluorine also deactivates fluorinated aromatic rings against oxidative metabolism. Hydroxyl and amino groups adjacent to fluorine are also more resistant to oxidation.

4.1.2 Difluoroalkylation

In pharmaceutical research and drug development, there has been significant interest in incorporating fluoroalkyl motifs for use in drug design. As example, some drugs containing fluoroalkyl motifs are described in Figure 4.2. Perfluorohexyloctane was used in ophthalmology as eye drop water-free and single-component, without preservatives, aimed at reducing tear evaporation on the ocular surface. Leniolisib acted as a selective small molecule inhibitor for the treatment of immunodeficiency diseases. Eflornithine was developed as an ornithine decarboxylase inhibitor to lower the relapse risk in both adult and pediatric patients with high-risk neuroblastoma (HRNB), who have shown at least a partial response to previous therapy. Roflumilast was developed as an anti-inflammatory agent and was utilized in the treatment of chronic obstructive pulmonary disease (COPD).[10]

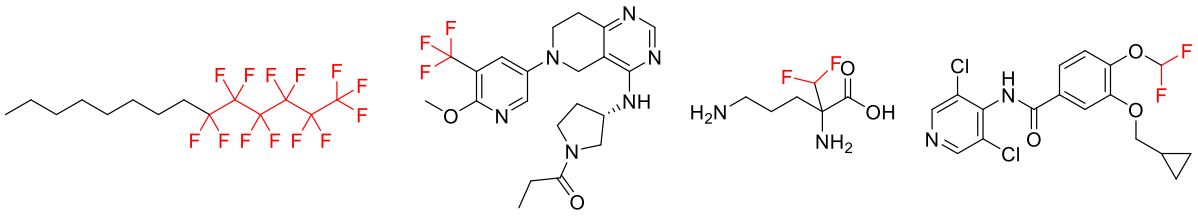

Figure 4.2 Some drugs containing fluoroalkyl motifs

In addition to the considerable progress in developing strategies for C-H functionalization involving fluorination and trifluoromethylation reactions, substantial research efforts have focused on the late-stage introduction of CF_2R (R = a functional group) and CF_2H moieties into organic frameworks through nucleophilic, electrophilic, and radical approaches (Scheme 4.1).[11]

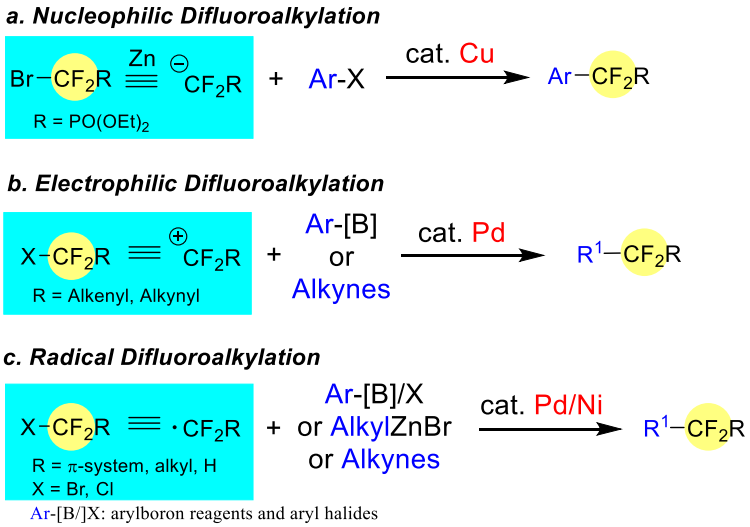

Scheme 4.1 Introduction of CF_2R through nucleophilic, electrophilic, and radical approaches

Among difluoroalkylation reagents (Figure 4.3), significant attention has been focused on two types: HCF_2LG (where LG stands for leaving group) and XCF_2FG (where X represents Br or I, and FG stands for functional group).[12] For XCF_2R (where X = Br, I), the cleavage of C-Br or C-I bonds is favored, preserving the functional groups to yield difluoroalkylated products containing a CF_2R moiety. Conversely, removal of the leaving group led to the attachment of HCF_2 to the substrates. Due to its high reactivity, the CF_2R radical can in fact react with various substrates to construct complex molecules through difluoroalkylation reactions. Both metal-catalyzed difluoroalkylations and visible-light-induced methods have been used with success.[13-15] Additionally, some donor compounds can induce the formation of RCF_2 radicals for difluoroalkylations through the formation of an electron donor-acceptor (EDA) complex.

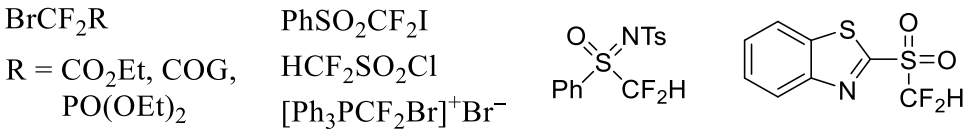

Figure 4.3 Some common difluoroalkylation reagents

4.1.2.1. Metal-catalyzed difluoroalkylations

To illustrate metal-catalyzed difluoroalkylations some important examples have been selected. Various transition metals, including Pd, Ru, Cu, Ni, etc. have been effectively employed in difluoroalkylation reactions.

X. Zhang's group suggested to use inexpensive and readily accessible difluoroalkyl halides as fluoroalkyl sources under transition-metal-catalyzed (Cu, Pd and Ni) difluoroalkylation reactions through cross-coupling.[16] A broad spectrum of difluoroalkyl halides were employed in these reactions. This includes activated difluoroalkyl halides ($Cl/BrCF_2R$, R = π system), unactivated difluoroalkyl halides ($BrCF_2R$, R = alkyl, H), and notably, the inert and cost-effective industrial chemical

chlorodifluoromethane ($ClCF_2H$). These reagents offer straightforward and efficient pathways to synthesize a variety of difluoroalkylated (hetero)arenes. For example, they described a Pd-catalyzed carbonylation of difluoroalkyl bromides with (hetero)arylboronic acids under one atmosphere pressure of CO (Scheme 4.2). This reaction could also be applied to aryl potassium trifluoroborate salts.[17] Moreover, novel palladium-catalyzed difluoroalkylation of aryl boronic acids has been devised by X. Zhang, employing bromodifluoromethylphosphonate, bromodifluoroacetate, and their derivatives.[18] This approach offers a convenient and valuable route to a range of functionalized difluoromethylated arenes, including $ArCF_2PO(OEt)_2$, $ArCF_2CO_2Et$, and $ArCF_2CONR^1R^2$.

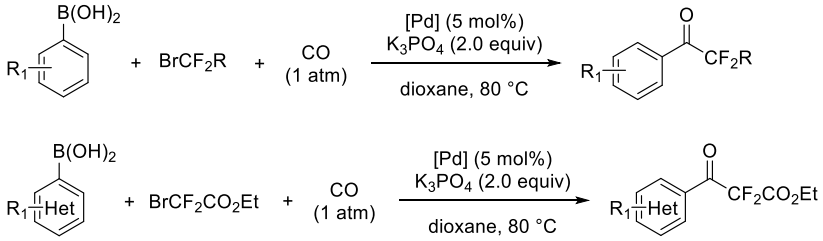

Scheme 4.2 Pd-catalyzed carbonylation of arylboronic acids with difluoroalkyl bromides and bromodifluoroacetate

In addition, a palladium-catalyzed reaction of difluoroalkyl bromides with isocyanides is presented as an efficient and versatile method for synthesizing difluoroalkylated phenanthridine derivatives.[19] This strategy can also be extended to perfluoroalkyl iodides.

Of note, X. Zhang's group reported an effective approach for synthesizing difluoroalkylated alkenes via a Pd-catalyzed Heck-type reaction using functionalized difluoromethyl bromides (Scheme 4.3). This reaction facilitated the difluoroalkylation of numerous alkenes under mild conditions, exhibiting excellent compatibility with various functional groups.[20]

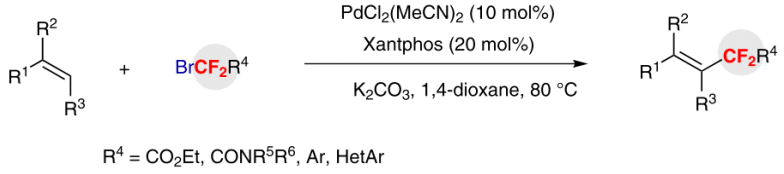

Scheme 4.3 Synthesis of difluoroalkylated alkenes through Pd-catalyzed Heck-type reaction with functionalized difluoromethyl bromides

G. Wang's research team reported a Pd-catalyzed four-component radical carbonylation and difluoroalkylation reaction of alkynes using ethyl difluoroiodoacetate as the CF_2 radical precursor under a balloon pressure of CO in a single step (Scheme 4.4). This method enabled the construction of two new C-C bonds and one C-O (N) bond with high regioselectivity.[21]

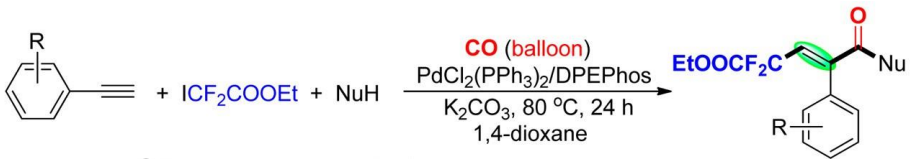

Scheme 4.4 Palladium catalyzed regioselective difluoroalkylation and carbonylation of alkynes

A highly selective difluoromethylation of 8-aminoquinoline amides at the C5 position, catalyzed by ruthenium, has been successfully developed by Y. Zhao (Scheme 4.5).[22] This method is compatible with a wide variety of functional groups, yielding the corresponding difluoromethylated products in moderate to good quantities.

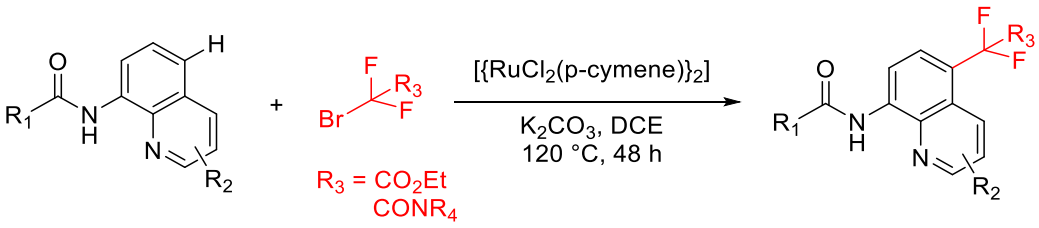

Scheme 4.5 Ruthenium-catalyzed C–H functionalization of 8-aminoquinolines

G. Wang's research team has successfully accomplished direct C-H difluoroalkylations and perfluoroalkylations of alkenes and (hetero)arenes. They used bench-stable cuprous iodide as the catalyst and commercially available fluoroalkyl halides as the fluorinated reagents.[23] A method for the direct difluoroalkylation of aldehyde hydrazones with functionalized difluoromethyl bromides has been developed using copper catalysis (Scheme 4.6).[24] This process affords stereodefined *α*,*α*-difluoro-*β*-keto hydrazones under mild conditions and is amenable to scale-up, facilitating potential practical applications.

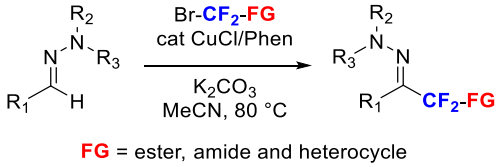

Scheme 4.6 C-H difluoroalkylation of aldehyde hydrazones under copper catalysis

A groundbreaking copper-catalyzed reductive radical difunctionalization reaction has been established, enabling the difluoroalkylation-thiolation of aryl alkenes (Scheme 4.7 a).[25] Crucially, the use of B_2pin_2 as an organic reductant is pivotal to the reaction, circumventing the generation of stoichiometric metallic waste. Q. Song developed an efficient and general method for the C (sp^2)–H difluoroalkylation of aldehyde-derived hydrazones via a Cu^{II}/B_2pin_2-catalyzed reaction between difluoroalkyl bromides and hydrazones (Scheme 4.7 b).[26] This reaction enables the synthesis of both aromatic and aliphatic difluoroalkylated aldehyde-derived hydrazones in good to excellent yields.

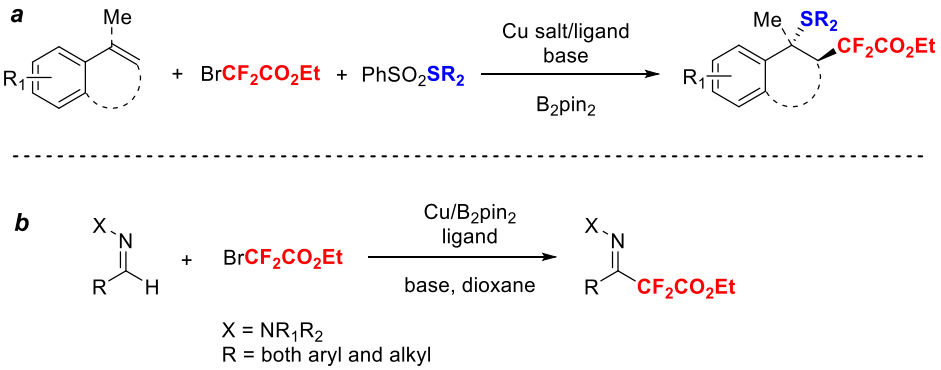

Scheme 4.7 Copper/B_2pin_2 catalyzed difluoroalkylation

Xi-Sheng Wang has pioneered the nickel-catalyzed decarboxylative fluoroalkylation of α,β-unsaturated carboxylic acids using widely accessible fluoroalkyl halides (Scheme 4.8).[27] In addition, X.-S. Wang developed a method for the difluoroalkylation of tertiary C–H bonds through cobalt-catalyzed cross-coupling between aryl ketones (cyclic and acyclic ketones) and fluoroalkyl bromides.[28]

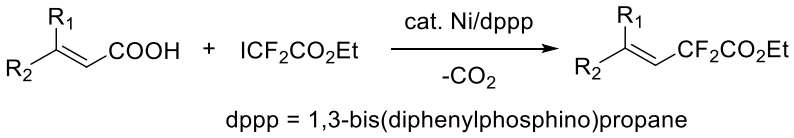

Scheme 4.8 Nickel catalyzed decarboxylative fluoroalkylation

Importantly there have been some groups that have developed enantioselective processes. X. Zhang and colleagues have documented a copper-catalyzed, highly enantioselective difluoroalkylation of secondary propargyl sulfonates utilizing difluoroenoxysilanes. This combination of copper with PyBox demonstrates a remarkable catalytic effect, enabling the enantioselective synthesis of propargylic α,α-difluoroketones (Scheme 4.9). These products serve as versatile building blocks for a wide array of transformations.[29] In addition, Christian Wolf has presented a practical approach for the catalytic enantioselective addition of α,α-difluoroenolates to aldehydes, employing 5 mol% of copper (II) triflate and a novel bisoxazoline ligand, readily prepared in two steps.[30] High yields and ee values were achieved with various prenucleophiles and aldehydes, encompassing aliphatic substrates, under mild conditions and within short reaction times.

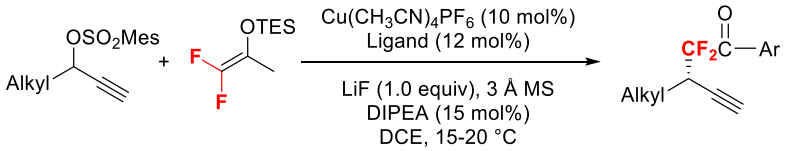

Scheme 4.9 Copper catalyzed enantioselective difluoroalkylation of propargyl sulfonates with difluoroenoxysilane

4.1.2.2. Visible-light-induced difluoroalkylation methods

In recent years, there has been a notable resurgence of interest in photocatalysis within the realm of organic chemistry, spurred by the pioneering research conducted by D. W. C. MacMillan[31] and T. P. Yoon[32] in 2008. As already mentioned, despite the existence of numerous protocols for fluoroalkylation, radical processes have significantly contributed to the synthesis of fluorine-containing molecules due to their high reactivity.[13] Among the methods for generating CF_3 and CF_2R radicals, the photoredox strategy stands out as an efficient approach, offering unique advantages concerning environmental sustainability, energy efficiency and safety considerations. It is notable that these transformations can proceed easily under mild reaction conditions, offering experimental simplicity. Among the reports of fluoroalkylation, the groups of D. W. C. MacMillan and E. J. Cho have described plenty of pioneer works.[33-37]

As said before, the radical-triggered reactions via visible light photoredox catalysis have garnered significant attention for the difluoroalkylation process. Typically, these chemical transformations induced by visible light rely on the capability of photocatalysts, which can be transition metal complexes, organic dyes, or heterogeneous semiconductors, to facilitate single electron transfer (SET) processes with organic molecules upon excitation with visible light. A variety of transition metal photocatalysts, such as iridium, platinum and ruthenium complexes and organic photocatalysts, including *N*-methyl-9-mesitylacridinium perchlorate, Eosin Y and 1,2,3,5-tetrakis(carbazolyl)-4,6-dicyanobenzene have been implemented in photochemistry for the difluoroalkylation of organic substrates.[11]

In some cases, the photocatalytic cycle effectively progresses through a single electron transfer (SET) mechanism (Scheme 4.10). The photocatalyst is initially excited to an activated state by visible light. This activated photocatalyst can donate an electron to the fluorinated reagent, resulting in the release of a CF_2 radical. Then the radical can react with alkenes, alkynes, arenes etc.

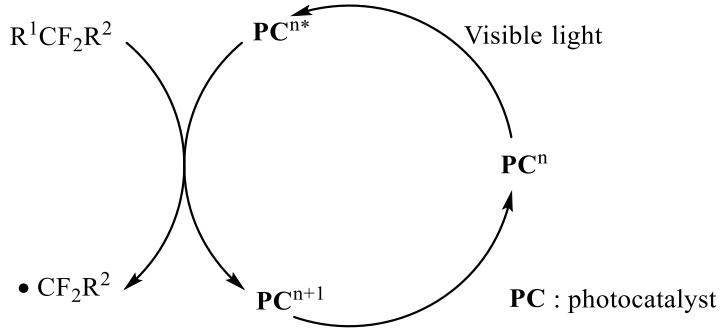

Scheme 4.10 Photoredox radical releasing procedure of difluoroalkylation

A variety of radical-mediated fluoroalkylation reactions have been developed by E. J. Cho's group in 2016.[38] These protocols involve the generation of radicals using polypyridyl-based Ru, Ir, or Pt complexes as photocatalysts, often in combination with additives like tertiary amines. They established

an efficient and selective method for the difluoroalkylation of alkenes (Scheme 4.11). In these reactions, difluoroalkylated alkanes and alkenes are generated using ethyl 2-bromo-2,2-difluoroacetate as the difluoroalkyl donor, fac-Ir(ppy)$_3$ as the photoredox catalyst and under visible light irradiation.[39]

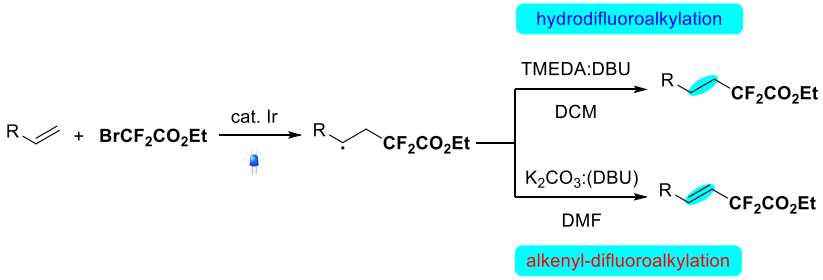

Scheme 4.11 Visible light-induced selective difluoroalkylation of alkenes

S. K. Hashmi in another pioneered work in 2016 described the gold-catalyzed intermolecular photoredox C(sp^2)-H difluoroalkylation and perfluoroalkylation of aromatic aldehyde hydrazones using commercially available fluoroalkyl bromides (Scheme 4.12).[40]

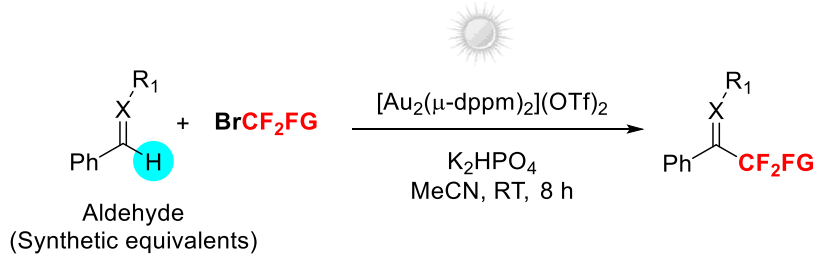

Scheme 4.12 Gold catalyzed difluoroalkylation and perfluoroalkylation of hydrazones

C.-M. Che reported in 2017 the Pt(II)-photocatalyzed, controlled, and selective difluoroalkylation reactions of cinnamic acids and alkynes, resulting in the production of *E*-, *Z*-difluoroalkyl alkenes and difluoroalkyl alkenyl iodides, respectively (Scheme 4.13).[41]

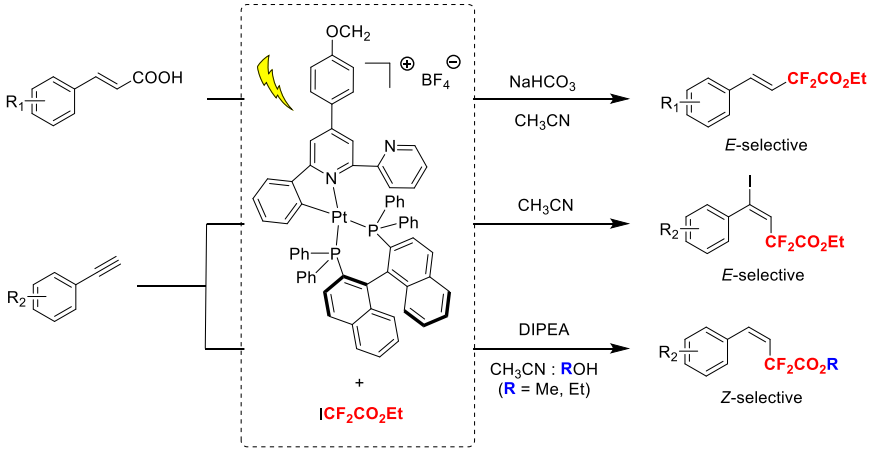

Scheme 4.13 Platinum photocatalyzed selective construction of *E*-, *Z*-difluoroalkyl alkenes and difluoroalkyl alkenyl iodides

C.-Y. He introduced an effective and versatile approach for synthesizing difluoroalkylated uracils, pyridinones, and coumarins in 2017.[42] This method utilizes a visible-light-induced reaction involving

$Ir(ppy)_3$, difluoroalkyl bromides with uracils, pyridinones, and coumarins (Scheme 4.14).

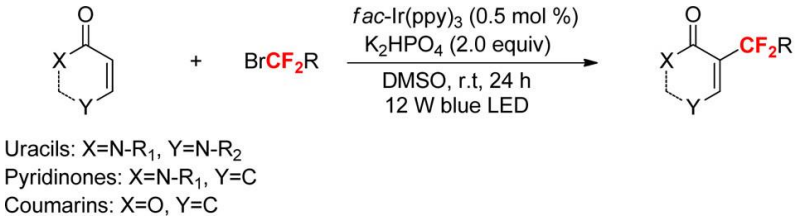

Scheme 4.14 Visible-Light-Induced Direct Difluoroalkylation of Uracils, Pyridinones, and Coumarins

In 2018, D.-G Yu reported an oxy-difluoroalkylation of allylamines with carbon dioxide (CO_2) via visible-light photoredox Ru based catalysis (Scheme 4.15). These multicomponent reactions are efficient to generate a series of important 2-oxazolidinones with functionalized difluoroalkyl groups.[43]

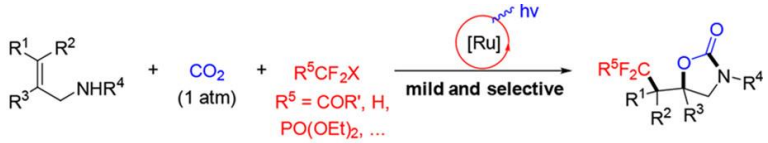

Scheme 4.15 Oxy-difluoroalkylation of allylamines with CO_2 via visible-light photoredox catalysis

Later on, in 2019, B. Fan decribed the difluoroalkylation of alkynes and alkenes by direct photoexcitation of ethyl difluoroiodoacetate (Scheme 4.16).[44] Under catalyst- and oxidant-free conditions, iododifluoroalkylation and hydrodifluoroalkylation products were generated from alkynes, and difluoroalkylation products were prepared from alkenes. This methodology provides a streamlined access to difluoroalkylated organic compounds starting from simple alkynes or alkenes.

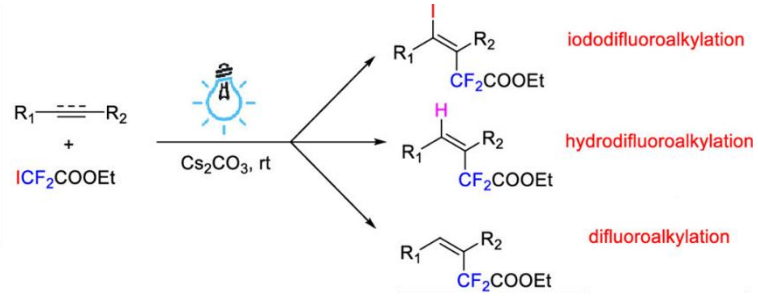

Scheme 4.16 Blue light induced difluoroalkylation of alkynes and alkenes

Visible-light-promoted oxo-difluoroalkylation (acetylation and acetamidation) of alkenes with dimethyl sulfoxide as both the solvent and the oxidant using $Ir(ppy)_3$ as photocatalyst was also developed in 2019 (Scheme 4.17).[45] The method produces the corresponding *α*,*α*-difluoro-*γ*-ketoacetates and acetamides in modest yields, with both terminal and internal alkenes showing good reactivity in the reaction.

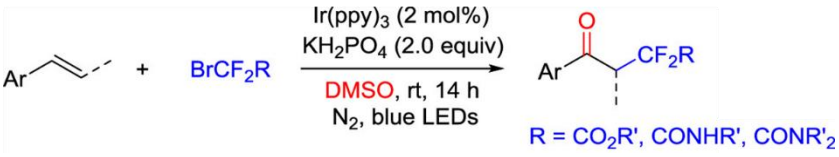

Scheme 4.17 Visible light promoted oxo-difluoroalkylation of alkenes

In our research group we have developed two complementary synthetic methods for the difluoroalkylation of anilines, avoiding the use of transition-metal photocatalysts (Scheme 4.18). Our first protocol promotes the difluoroalkylation using Eosin Y as an organic photocatalyst under very mild conditions. The reaction works well when using electronically rich anilines. The mechanistic findings evidenced the generation of the $\cdot CF_2CO_2Et$ radical as an intermediate. Additionally, we described the formation of a new EDA complex formed by the combination of anilines and ethyl difluoroiodoacetate. The simple photoexcitation of this new molecular aggregate promotes the formation of difluoroalkylated arenes in an efficient manner with chemical yields up to 89%.[46]

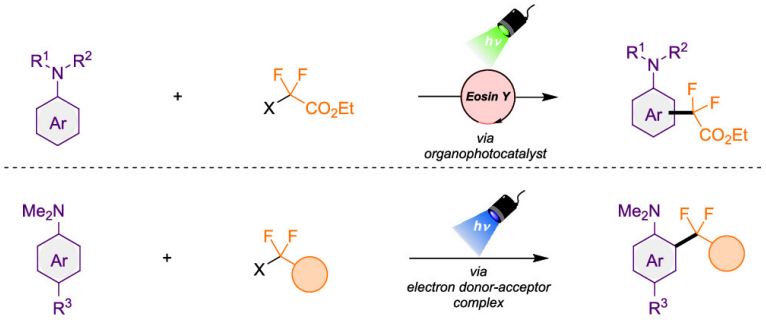

Scheme 4.18 Photoinduced difluoroalkylation of anilines

Recently, in 2024, F.-L. Qing's group incorporated atypical reagents as phosphonium reagents, triflic anhydride, and methyl fluorosulfonyldifluoroacetate with surprising reactivities under photocatalysis conditions.[47] These reagents have significantly broadened the potential for radical difluoromethylation, trifluoromethylation, and difluoroalkylation reactions.

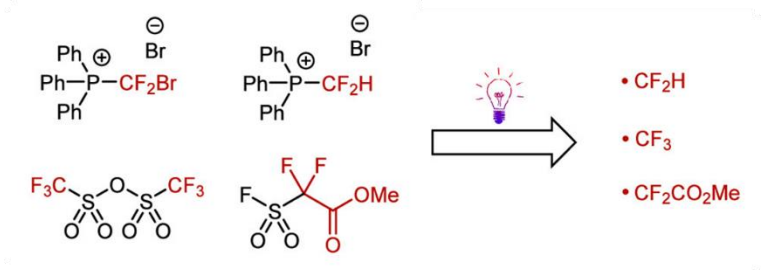

Scheme 4.19 Atypical reagents with surprising reactivities under photocatalysis conditions

4.1.3 Difluoroalkylation of *β*-ketoesters

β-Ketoesters and related *β*-diketo derivatives are of fundamental importance given that they have been used as basic synthons for the synthesis of important natural products, such as mokupalide (a hexaprenoid from a marine sponge), nonactin (an antibiotic), sitophilure (insect pheromone), and kermesic acid (food colorant additive).[48]

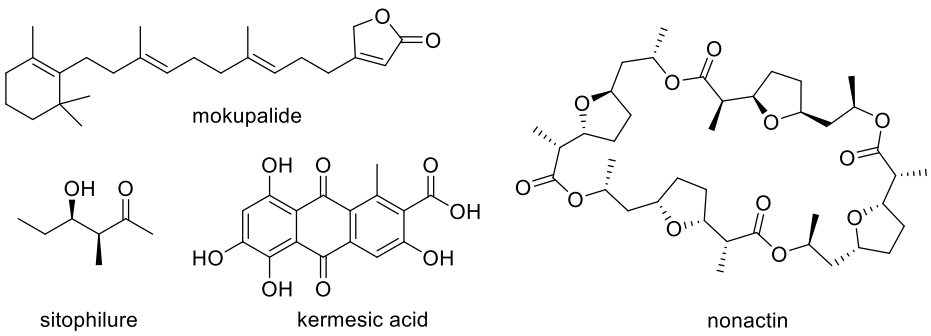

Figure 4.4 Some natural products that have been synthesized from a *β*-ketoester synthon

In view of the common use of *β*-ketoesters in the pharmaceutical, agrochemical, chemical, and polymer industries, considerable interest into the racemic and enantioselective fluoroalkylation methods exist in the scientific community. Fluorination and trifluoromethylation have been explored with success. More recently, di-/perfluoroalkylation methods have been explored.

A straightforward and cost-effective method for preparing fluoroalkylated compounds has been detailed by Kangkui Li. This method involved the direct photoexcitation of halofluoroalkanes with blue light absorptivity, facilitating the difluoroalkylation of aryl ketones.[49] The reaction can be also applied into the racemic difluoroalkylation of *β*-ketoester (Scheme 4.20).

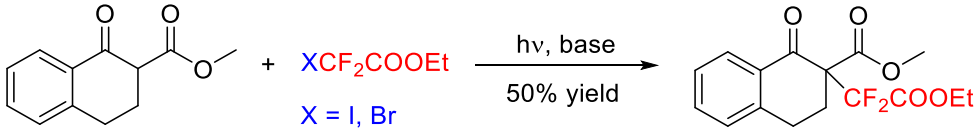

Scheme 4.20 Racemic difluoroalkylation of *β*-ketoesters

A nickel-catalyzed difluoroalkylation of α-C–H bonds in aryl ketones has been developed by Chao Li to produce highly stereo-defined tetrasubstituted monofluoroalkenes from secondary ketones and quaternary alkyl difluorides from tertiary ketones.[50] This reaction can be utilized for the racemic difluoroalkylation of *β*-ketoesters (Scheme 4.21).

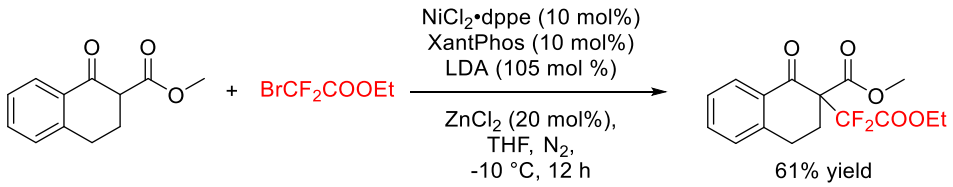

Scheme 4.21 Nickel catalyzed difluoroalkylation of aryl ketones (and *β*-ketoester) to alkyl difluorides

In reference to the enantioselective difluoroalkylation of *β*-ketoesters there are two important reports that we want to comment. One of them was reported in 2018 by the group of W.-J. Xiao describing the enantioselective catalytic di-/perfluoroalkylation of *β*-ketoesters by using Ni(II) together with 2,2'-linked bis(oxazoline) chiral ligand under photoredox conditions (Ir complex as photocatalyst, light).[51] The results in this manuscript are remarkable obtaining the difluoromethylation of 18 different *β*-ketoesters with an enantiomeric relation up to 95:5 under this cooperative photoredox/Nickel catalysis. A plausible radical based reaction mechanism was proposed (Scheme 4.22). Photoexcitation of photocatalyst PC (A) with visible light results in the excited state of photocatalyst (B), which can undergo reductive quenching by the complex Ni/pybox (Ni/L1, D) to give the complex E and Ir(II) photocatalyst C. Subsequent single-electron oxidation of Ir(II) (E[(Ir(III)/Ir(II)] = −1.37 V vs SCE) by haloalkane ICF_2CO_2Et generates electrophilic radical G and regenerates the ground state of photocatalyst A. At the sometime, the *β*-ketoester is activated by the chiral Lewis acid to give nickel-enolate intermediate F, which could be trapped by radical G to afford the unstable intermediate H. Finally, the oxidation of $[Ni/L1]^-$ either by photoexcited state B or oxidation state E reforms the Ni(II) species D ([Ni/L1]) and releases the final product.

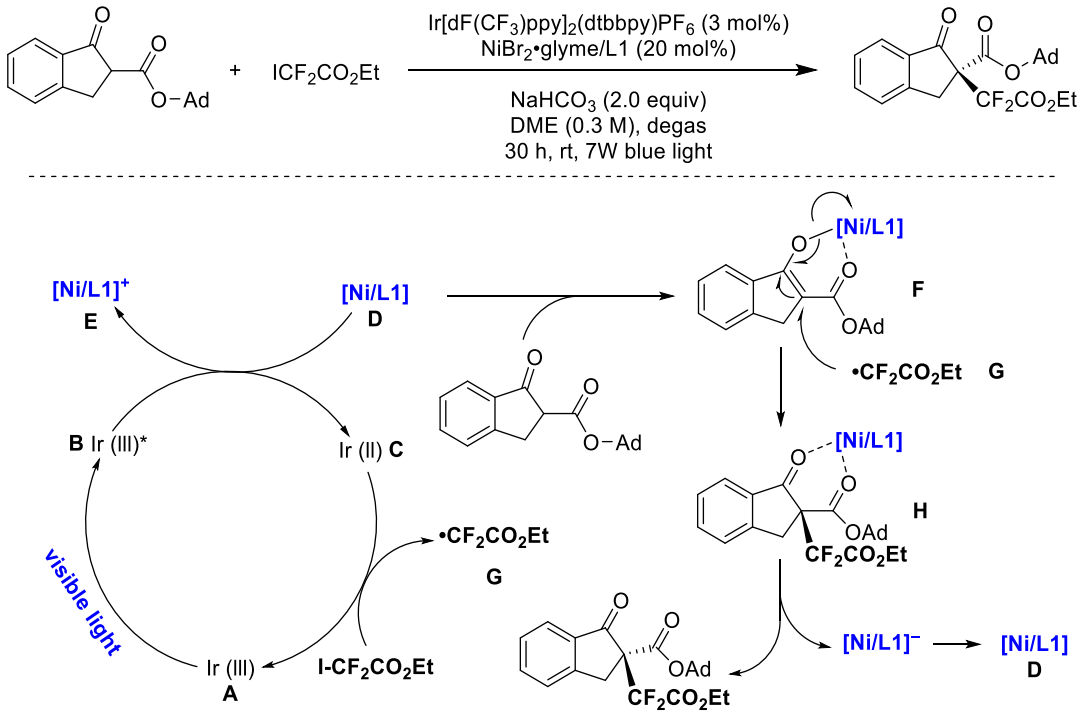

Scheme 4.22 Xiao's difluoroalkylation reaction of *β*-ketoesters

Recently in 2024, C. P. Johnston's group developed a phase-transfer-catalyzed asymmetric α-difluoroalkylation of *β*-ketoesters through visible light-promoted radical generation.[52] They developed a light-initiated asymmetric tertiary α-difluoroalkylation procedure that operates under mild phase-transfer conditions. When using a phase-transfer catalyst (PTC), UV-vis spectroscopic evidence

suggests that a solution-phase visible light-absorbing EDA complex is responsible for radical initiation. However, contributions from other pathways, evident in the absence of a PTC, may also operate alongside to generate the ethyl difluoroacetate radical.

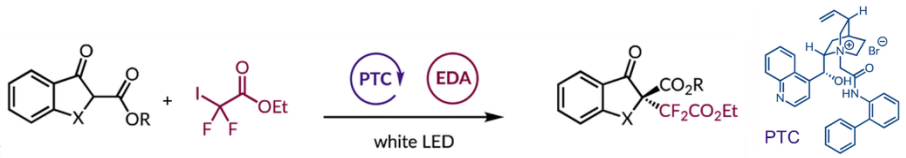

Scheme 4.23 EDA complex driven phase transfer catalyzed difluoroalkylation

4.1.4 Ligand/catalyst immobilization

To further improve the efficiency, stereoselectivity and applicability of perfluoroalkylation in practical applications, ligand/catalyst immobilization system could be considered. Homogeneous catalysts typically exhibit higher activity and selectivity because reactants can more easily access the catalyst's active sites, making them more commonly used. Conversely, heterogeneous catalysts can be more easily recovered from the reaction mixture through straightforward methods like filtration or centrifugation.[53] Catalysts can be immobilized through various techniques, including adsorption, covalent bonding, ionic interaction, entrapment, or encapsulation. Organic catalysts have been supported on organic (COFs, MOFs, acidic alginate gel, resin and so on),[53, 54] inorganic (silica, ionic liquid, aluminas, aluminosilicates, titanium oxides, zirconia, …),[55, 56] and magnetic matrices[57] to facilitate easy separation and recycling.

The discovery of MCM-41 in the 1990s, a member of the M41S family known for its ordered mesoporous structure, introduced a new perspective in the field of heterogeneous catalysis.[58] Our group has a wide experience in the use of hybrid silicas as recyclable catalysts: a) Pd complexes for C-C coupling reactions,[59-61] b) Ru alkylidenes for metathesis reactions,[62, 63] c) Rh-NHC complexes for [2+2+2] cycloaddition reactions of alkynes,[64] d) Au-NHC complexes for rearrangement reactions of allylic esters and cycloisomerization of γ-alkynoic acids,[65] e) imidazolium and dihidroimidazolium salts as organocatalysts for Knoevenagel reactions,[66] f) iodoarene-based organocatalysts for the oxidative α-tosyloxylation of ketones,[67] g) chiral proline-derived organocatalysts for asymmetric aldol reactions.[68] In 2016, Dr. Meritxell Ferré prepared several hybrid silica materials using sol-gel cogelification and grafting methods from chiral mono-silylated proline sulphonamide precursors (Scheme 4.24).[69] The catalytic performances and reusability of these hybrid silica materials were evaluated in direct intermolecular asymmetric aldol reactions between ketones and aromatic aldehydes, as well as in a Robinson annulation, all conducted under simple and green conditions (water, room temperature).

These materials achieved good conversions and recyclability, with moderate to good diastereo- and enantioselectivities.

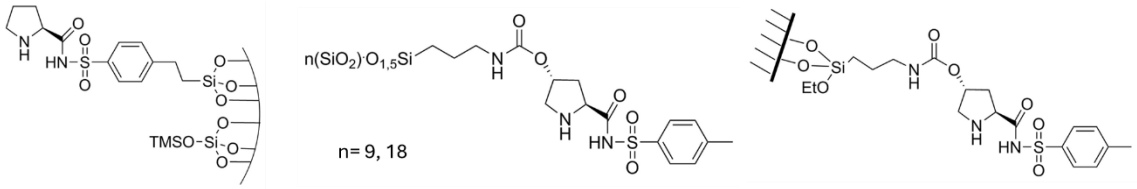

Scheme 4.24 Hybrid silica materials for direct intermolecular asymmetric aldol reactions

Going a step further from bulk organosilicas to nanosized materials, Wenbin Lin chose chiral $RuCl_2$–diphosphine–diamine complexes as model precatalysts to be supported on the mesoporous silica nanospheres.[70] These silica nanospheres were employed in the asymmetric hydrogenation of aromatic ketones to produce chiral secondary alcohols, and in the hydrogenation of racemic aryl aldehydes to yield chiral primary alcohols (Scheme 4.25).

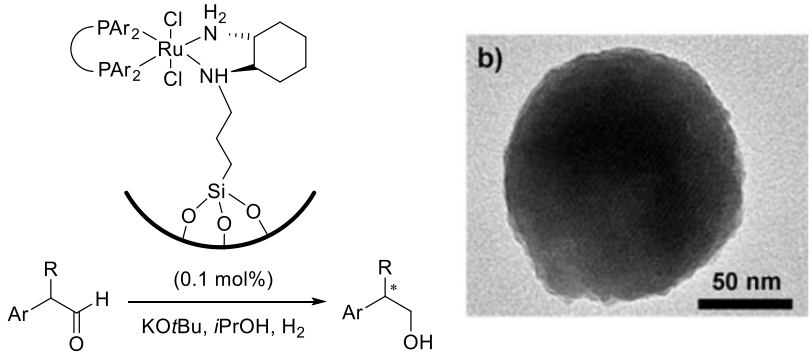

Scheme 4.25 Silica nanosphere supported ruthenium catalysts for asymmetric hydrogenation

Two distinct types of azide-functionalized magnetite@silica nanoparticles have been synthesized.[71] The effectiveness of the immobilized complexes as catalysts was assessed in desymmetrizing racemic 1,2-diols through asymmetric benzoylation (Scheme 4.26).

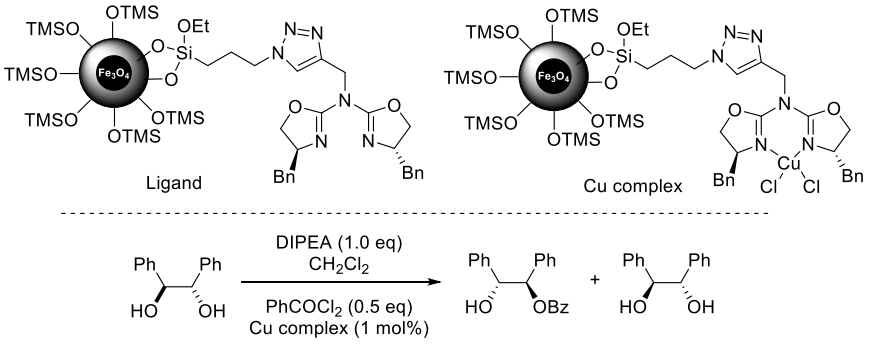

Scheme 4.26 Aza(bisoxazoline)-$CuCl_2$ immobilized on magnetite@silica nanoparticles for benzoylation

Guohua Liu conveniently prepared a chiral cationic rhodium/diamine complex within base-functionalized mesostructured silica nanoparticles, thereby constructing a bifunctional heterogeneous catalyst.[72] The bifunctionality of the silica nanoparticles facilitates two efficient enantioselective

organic transformations with high yields and enantioselectivities (Scheme 4.27). These include the asymmetric transfer hydrogenation of α-haloketones followed by epoxidation to produce diverse chiral aryloxiranes, and the amination of α-haloketones with anilines followed by asymmetric transfer hydrogenation to generate various β-amino alcohols.

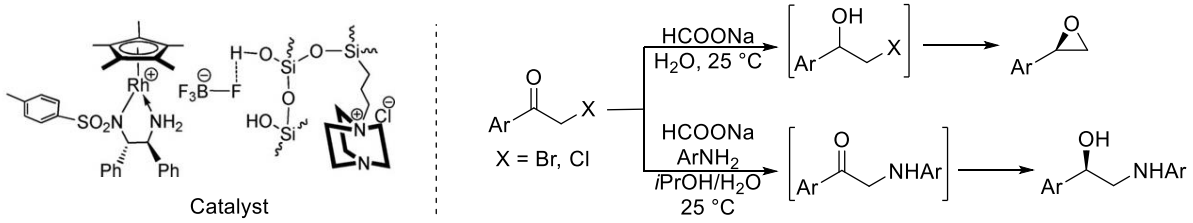

Scheme 4.27 Base-rhodium/diamine-bifunctionalized mesostructured silica nanoparticles

In our group, Hao Li described the preparation of mesoporous organosilica nanoparticles derived from mono- and bis-silylated proline-valinol amides in 2019 (Scheme 4.28).[73] These nanoparticles were synthesized both by grafting onto preformed mesoporous silica nanoparticles (MSN) and by a co-condensation method in a neutral medium using Brij-56/CTAB as templates. The activity of these materials was evaluated as recyclable catalysts in the asymmetric aldol reaction. The best organocatalysts, derived from the monosilylated precursor, exhibited good diastereo- and enantiomeric ratios using a simple and environmentally friendly optimized protocol (water, 0 °C, no co-catalyst). The nanocatalyst was easily recovered by centrifugation and could be recycled for up to five runs without any loss of activity and selectivity.

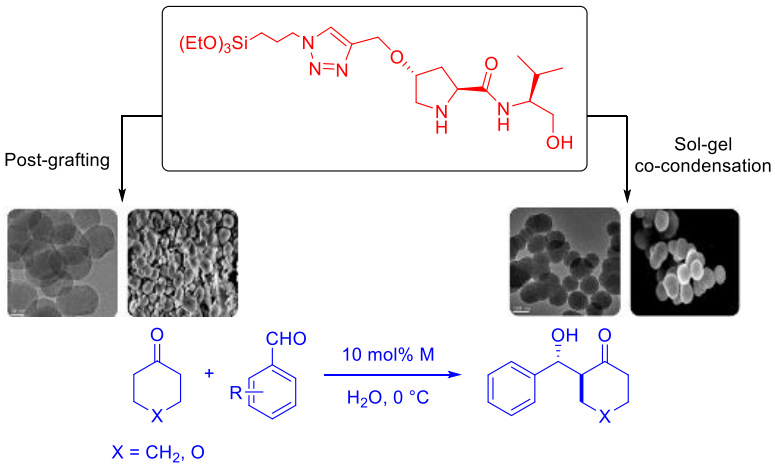

Scheme 4.28 Mesoporous silica nanoparticles derived from proline-valinol amides for asymmetric organocatalysis

Frequently, in asymmetric reactions the chiral ligand is very valuable due to its prize, if commercially available, or to the difficult preparation in the laboratories. The exploration of recyclable chiral ligands for the enantioselective di-/perfluoroalkylation reactions of *β*-ketoesters remains a challenge because, at the best of our knowledge, no precedents exist on the immobilization of chiral systems for the mentioned reactions.

4.2 Objectives

Based on the previous introduction, we plan to synthesize a disilylated bis(oxazoline) chiral ligand for the preparation of functionalized silica nanoparticles with this monomer. The aim is to use the mixture of this supported ligand with a nickel salt and an iridium photosensitizer as catalyst for the enantioselective difluoroalkylation of *β*-ketoesters under photochemical conditions. The chiral ligand would be easily recycled. For that purpose, the specific objectives in this part of the thesis are as follows:

a) The synthesis of a disilylated bis(oxazoline) precursor and the preparation of several functionalized dense and mesoporous silica nanoparticles derived from this chiral monomer by post-grafting and co-condensation methods.

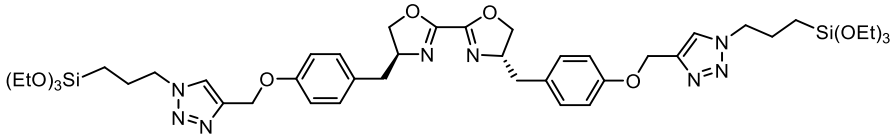

b) The characterization of all the new nanomaterials with the appropriate techniques in each case, such as infrared spectroscopy, ^{13}C and ^{29}Si CP MAS solid-state NMR, elemental analysis, electron microscopy, powder X-ray diffraction, dynamic light scattering and zeta-potential.

c) The assay of these functionalized silica nanoparticles as recyclable chiral ligands in the difluoroalkylation reaction of *β*-ketoesters through photoredox/nickel catalysis. We envisage to test the following benchmark reaction.

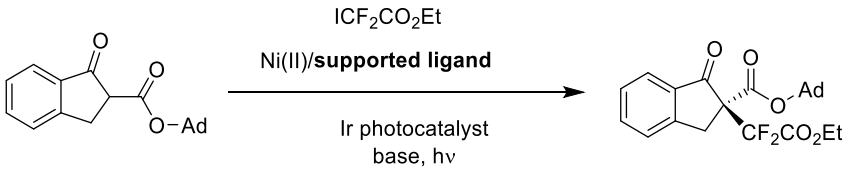

4.3 Results and Discussion

4.3.1 Synthesis of a disilylated derivative of a bis(oxazoline) ligand

The standard synthesis route of a bis(oxazoline) ligand starts from the reaction of an oxalate with an aminoalcohol. Then the hydroxyl groups are replaced by chloro groups by treatment with thionyl chloride and the corresponding intermediate is cyclized under basic conditions, leading to the bis(oxazoline).[74-76] Following previously described methodology, the starting amino alcohol hydrochloride **25** was treated with diethyl oxalate in the presence of triethylamine in refluxing toluene for 12 h, obtaining the diamide **26** (64% yield). The phenolic moiety in the starting aminoalcohol was chosen as a mean to facilitate the posterior introduction of the silylated functionality. However, in the presence of phenolic hydroxyl groups in **26**, the subsequent chlorination reaction failed. To solve this problem, the phenolic hydroxyl groups were protected by methylation to give **27** (66% yield). After the chlorination of **27** (treatment with $SOCl_2$ in anhydrous toluene), we afforded **28** in 97% yield. Then, cyclization of **28** in a methanol solution of KOH gave rise to **29** (95% yield). BBr_3 was added dropwise to a solution of **29** in dichloromethane at -78 ºC to deprotect the O-Me groups,[77] but the oxazoline structure was broken in this basic condition and the desired compound **30** could not be obtained (Scheme 4.29. Route 1). Thus, we tried to deprotect first the O-Me groups of **28** and then perform the cyclization reaction of the dichlorinated **31** to the bis(oxazoline) **30**. However, we could not isolate the bisphenol **30** in pure form (Scheme 4.29. Route 2).

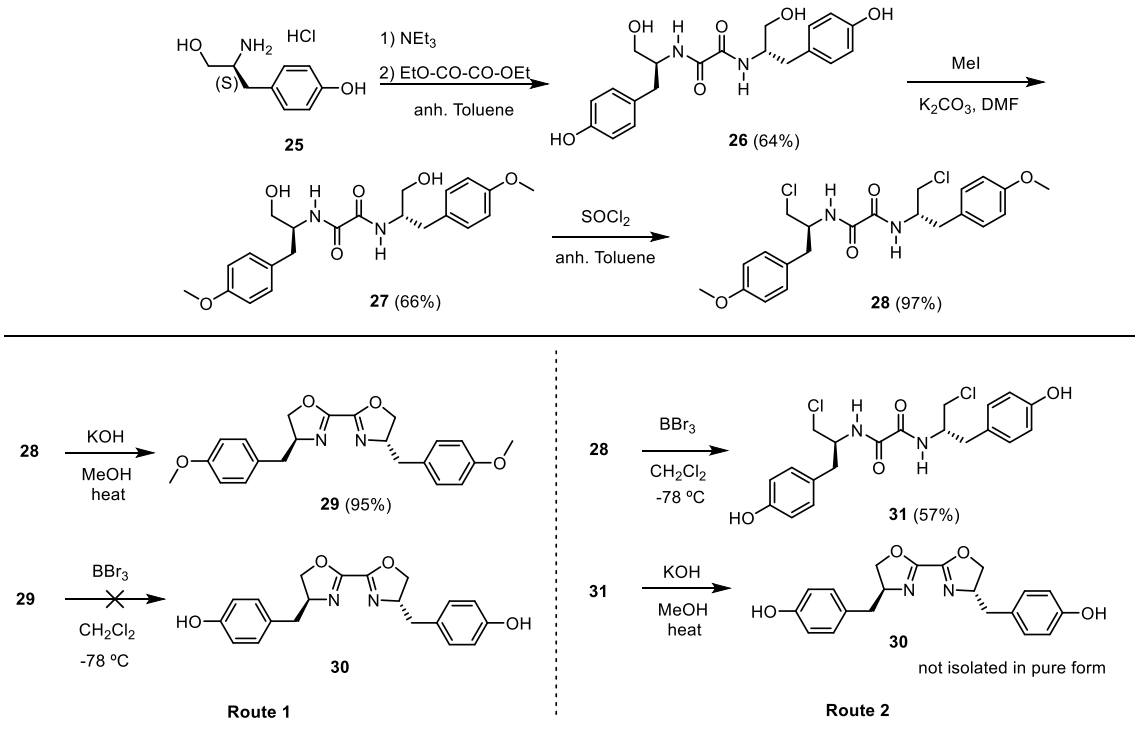

Scheme 4.29 First unsuccessful trials to afford a precursor of the disilylated bis(oxazoline) ligand

After these preliminary experiments, we decided to protect the phenolic hydroxyl groups in the diamide **26** with propargyl instead of methyl groups (Scheme 4.30). This protecting group would allow the further introduction of a silylated moiety by reaction with a silylated azide, thus no deprotection step would be needed. The starting amino alcohol hydrochloride **25** was treated with diethyl oxalate in the presence of triethylamine in refluxing toluene for 12 h, obtaining the diamide **26** in 64 % yield. The reaction of **26** with propargyl bromide in anhydrous dimethylformamide at room temperature in the presence of potassium carbonate afforded **32** in 91% yield. The chlorination reaction of **32** with thionyl chloride in anhydrous toluene gave **33** in 96% yield and the subsequent cyclization was performed with potassium hydroxide in methanol to achieve the bis(oxazoline) **34** in 84% yield. Then, a copper catalyzed alkyne-azide cycloaddition reaction (CuAAC) of the dialkyne **34** with commercial (3-azidopropyl)triethoxy-silane under anhydrous conditions[73] led to the final organosilane **35** in 100% yield. In summary, the precursor **35** was prepared in five steps from **25** with an overall yield of 47%.

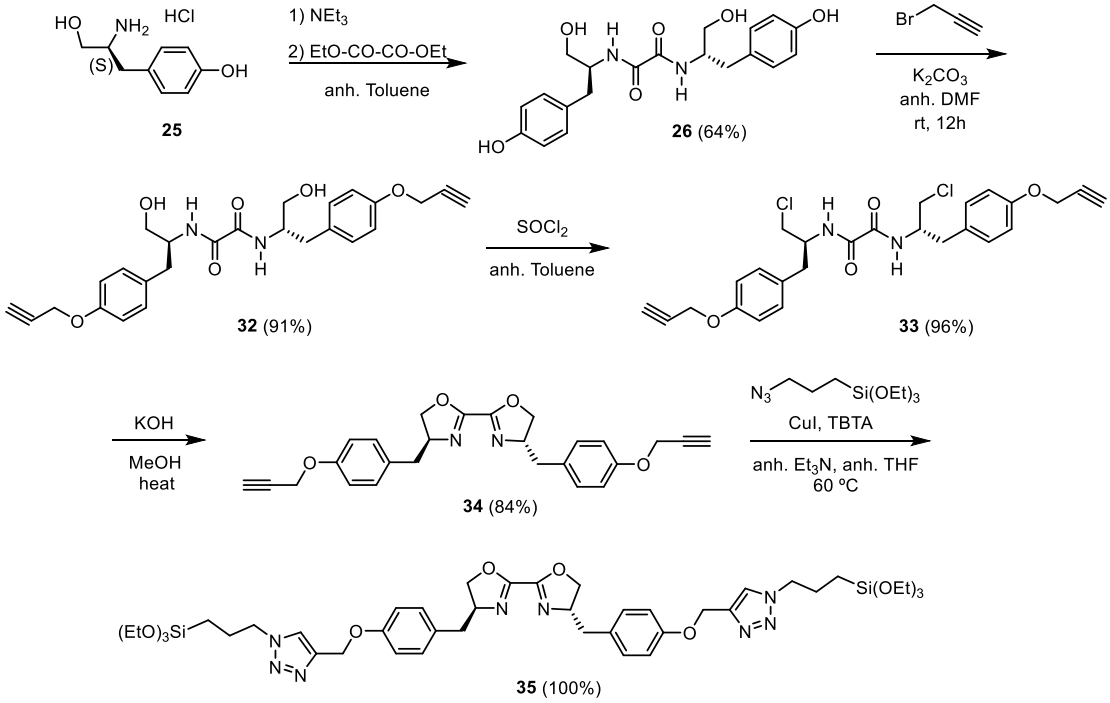

Scheme 4.30 Synthesis of the disilylated bis(oxazoline) derivative **35** from **25**

4.3.2 Preparation and characterization of silica nanoparticles functionalized with a Box ligand

From the organosilane **35**, four different dense or mesoporous silica nanoparticles were prepared by sol-gel co-condensation methodology and by post-grafting on mesoporous silica nanoparticles (Scheme 4.31). The **M0** NPs were obtained in a buffer solution of pH 7 with a mixture of cationic and nonionic surfactants (CTAB and Brij-56) according to a reported procedure.[78] First, we prepared mesoporous silica nanoparticles **mN9** by grafting the organosilane **35** to the previously synthesized **M0** NPs in

refluxing toluene. Then material **mN10** was obtained by co-condensation of precursor **35** with tetraethyl orthosilicate (TEOS) using Brij-56 and hexadecyltrimethylammonium bromide (CTAB) as templates in a buffer solution of pH 7 with the following molar ratios: Brij-56:CTAB:TEOS:**35**:H_2O = 7:20:160:16:120000.[73] After stirring for 8 h at 95 °C, the nanoparticles were collected by centrifugation (12000 rpm). Finally, the surfactants were removed by washing with an ethanol solution of NH_4NO_3 (6 g/L) and the resulting material was washed successively with ethanol, Mili-Q water and ethanol.[73] On the other hand, dense nanoparticles **dN6** and **dN7** were prepared by co-condensation of silylated precursor **35** with TEOS using a 28% aqueous ammonia solution in ethanol.[79] The molar ratio of **35**:TEOS varies from 1:10 to 1:20. The NPs were collected by centrifugation (12000 rpm) and then washed successively with ethanol, acetone, and ethanol (Scheme 4.31).

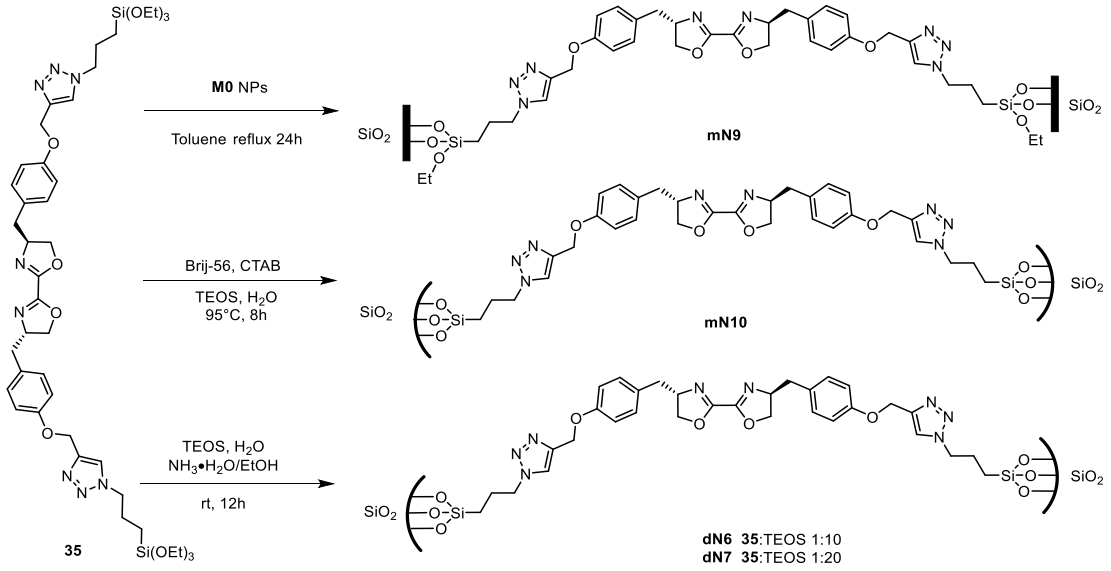

Scheme 4.31 Preparation of functionalized silica nanoparticles

We thought that the hydrophilicity of the nanoparticles surface (plenty of OH groups) could affect the formation of the Ni complex that is relatively oxyphilic. Thus we modify the surface polarity of **mN9**, the remaining OH groups were capped with -$SiMe_3$ groups by reaction with hexamethyldisilazane (HMDS)[80] to obtain **mN11** (Scheme 4.32).

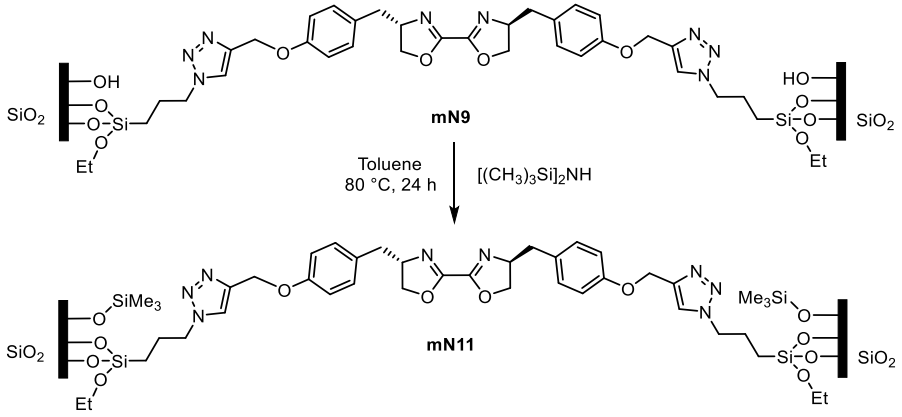

Scheme 4.32 Silylation of **mN9** with HMDS

All nanomaterials were characterized by elemental analysis, scanning electron microscopy (SEM), transmission electron microscopy (TEM), dynamic light scattering (DLS), zeta-potential, infrared spectroscopy, and powder XRD and nitrogen-sorption measurements when appropriate. Some characterization data are summarized in Table 4.1.

Table 4.1 Characterization data of **mN9-mN11** and **dN6-dN7**

Materials	Ligand loading (mmol/g)[a]	Particle size (nm)		Zeta-potential (mV)
		TEM (nm)	DLS[b] (nm)	
mN9	0.87	81 ± 5.5	380	+7.6
mN10	0.59	60 ± 4.0 with aggregates	4191	+5.9
mN11	0.84	--	--	--
dN6	0.51	143 ± 13.8	729	+17.8
dN7	0.33	220 ± 25.8	353	+25.1

[a] Calculated from the N elemental analysis [b] Hydrodynamic diameters

From the perspective of size and morphology (Figure 4.5), **mN9** inherited the spherical structure of **M0** NPs with a mean particle size of 81 nm. From the TEM images, **mN10** contains small nanoparticles (60 ± 4 nm) but also some aggregates, which is consistent with a hydrodynamic diameter of 4191 nm (Figure 4.6). The zeta potential values of both nanomaterials are less than +10 mV, which indicates a trend to flocculation. For the dense nanoparticles, the spherical profile is clearer in the case of **dN7** with a molar ratio of **35**:TEOS of 1:20. The zeta potential of **dN7** is higher than **dN6**, which accounts for the better stability. With more organosilane on the nanomaterial, **dN6** has a higher hydrodynamic diameter than **dN7** (Table 4.1). The TEM images of the nanomaterials are presented in Figure 4.5.

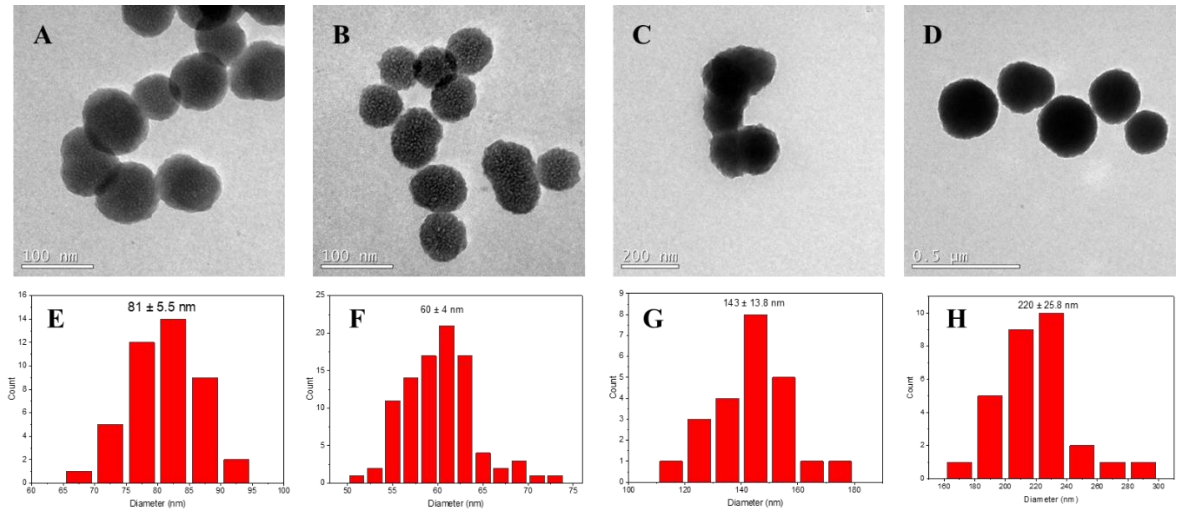

Figure 4.5 TEM images of **mN9** (A), **mN10** (B), **dN6** (C) and **dN7** (D) and size distribution of **mN9** (E), **mN10** (F), **dN6** (G) and **dN7** (H)

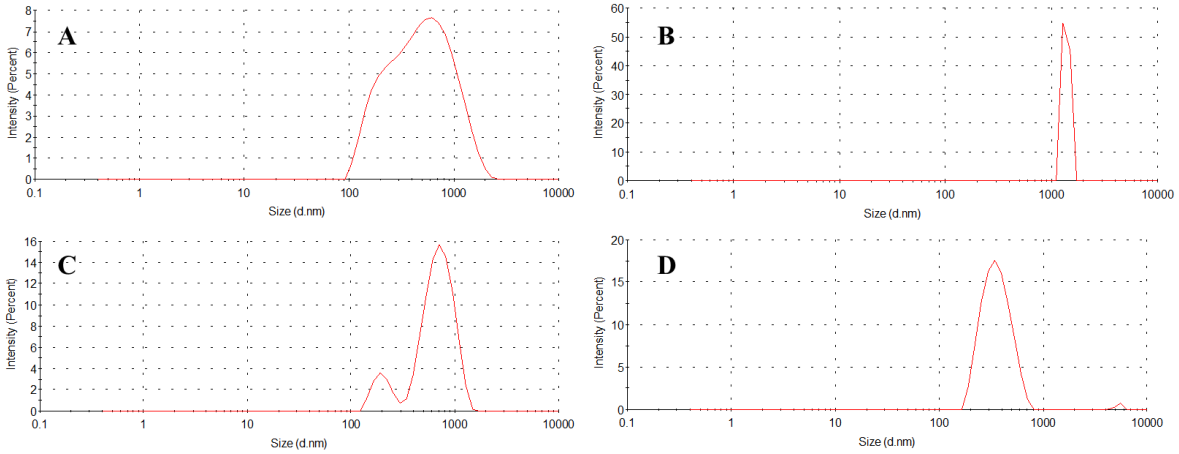

Figure 4.6 DLS of **mN9** (A), **mN10** (B), **dN6** (C) and **dN7** (D)

After the grafting of organosilane **35** to **M0**, the intensity of the peak (2 Theta=2.007 °) in **mN9** decreases, with a little shift in the position, indicative of a certain loss of the wormlike organization (Figure 4.7).

The presence of the organic moiety on **mN9** is also ensured by solid-state ^{13}C and ^{29}Si NMR spectra. The superposition of the ^{13}C NMR spectrum of organosilane **35** in solution and of **mN9** in solid-state shows a good similarity between the two spectra, indicating the integrity of the organic moiety (Figure 4.8 a). The ^{29}Si CP MAS NMR spectrum shows three signals at -92.90, -103.61 and -113.42 ppm, which are assigned to Q^2 geminal silanol, Q^3 free silanol and Q^4 siloxane groups, formed from TEOS. The signals at -59.95 and -68.92 ppm, attributed to T^2 and T^3, arise from the organosilane **35** (Figure 4.8 b).

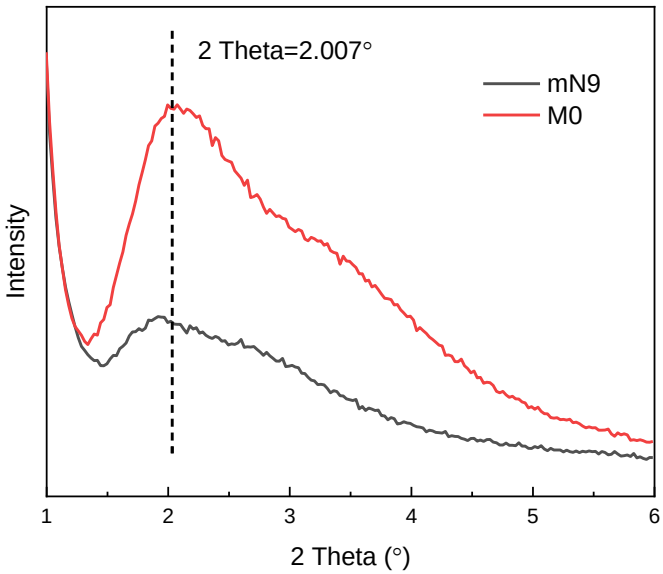

Figure 4.7 *p*-XRD of **M0** and **mN9**

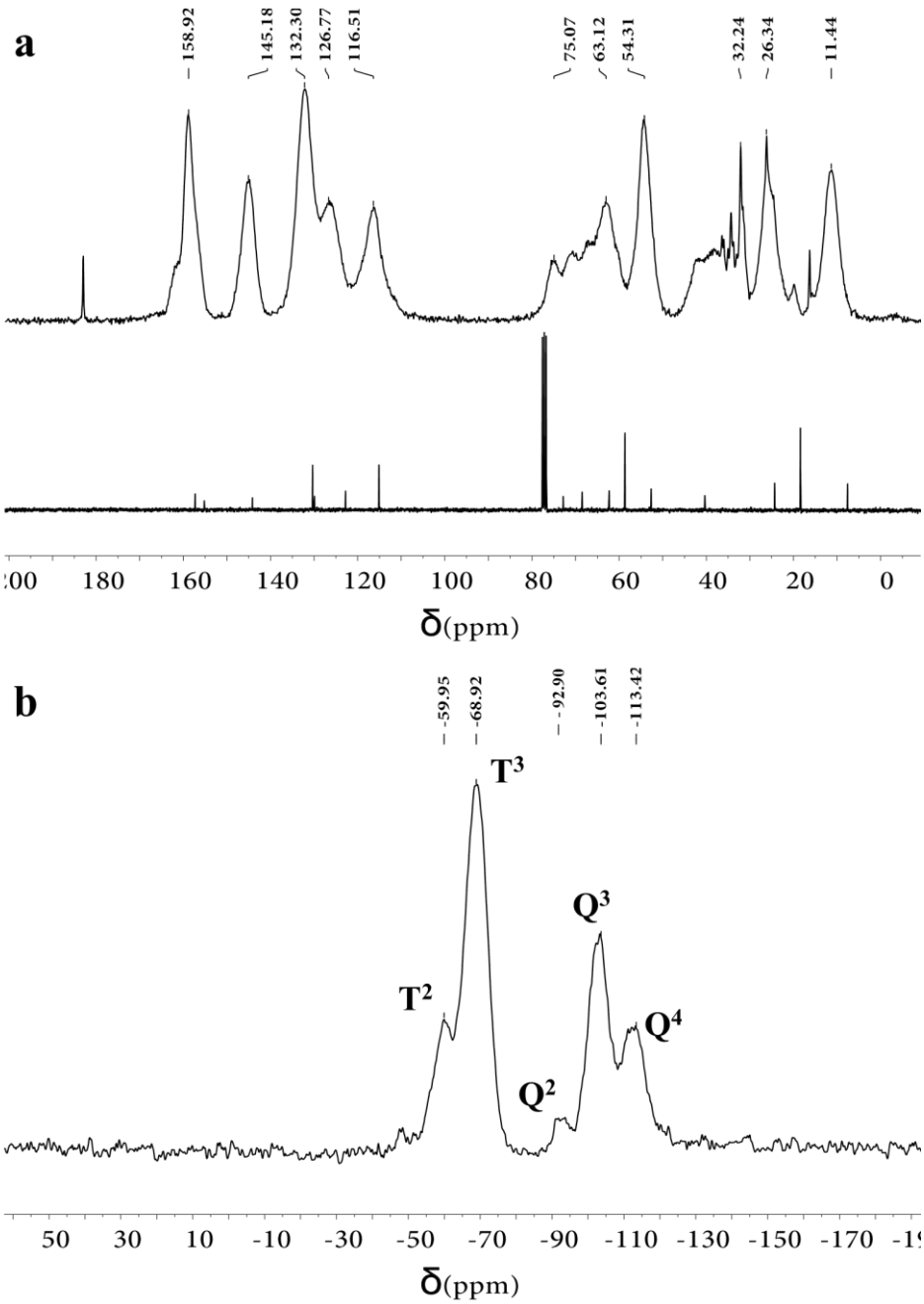

Figure 4.8 ^{13}C CPMAS NMR spectrum of **mN9** and ^{13}C NMR of **35** (a) and ^{29}Si CPMAS NMR spectrum of **mN9** (b)

Finally, the surface composition was checked through energy dispersive X-ray spectroscopy (EDX) element mapping, revealing the presence of Si, C, O, and N elements (see Figure 4.9). The ligand loading content in the NPs was determined from the nitrogen elemental analysis (Table 4.1).

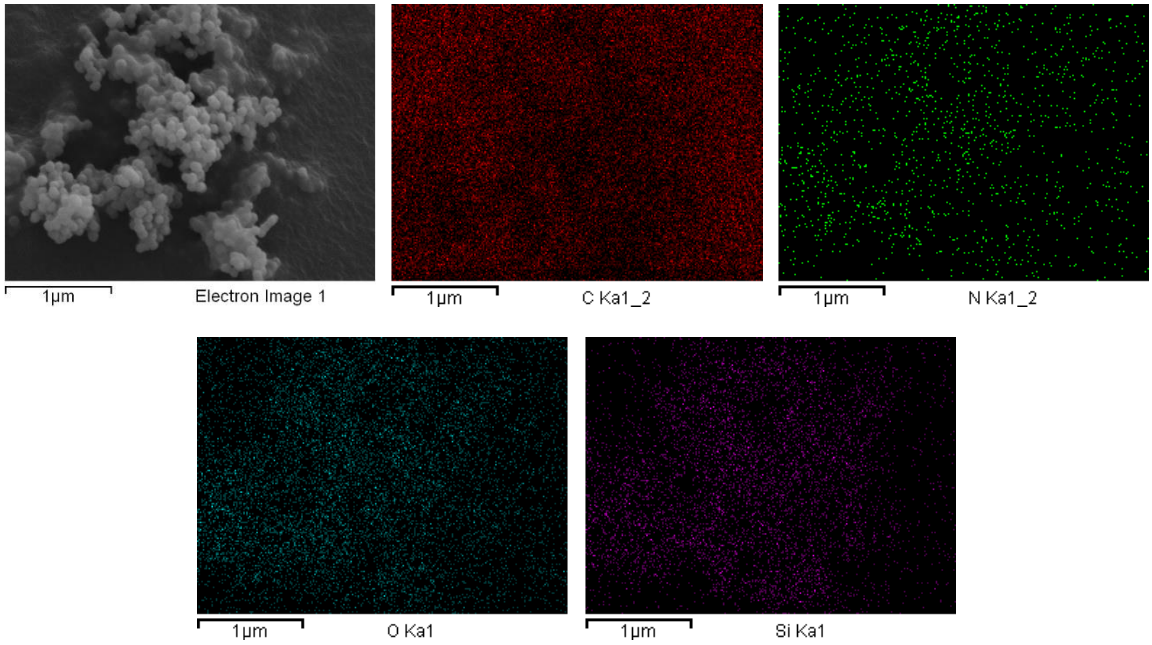

Figure 4.9 EDX element mapping of **mN9**

4.3.3 Catalytic activity of functionalized silica nanoparticles

As already mentioned in the objective, our purpose was to study these materials as recoverable chiral ligands in the previously described difluoroalkylation of *β*-ketoester enabled by cooperative photoredox/Nickel catalysis. First adamantyl-*β*-ketoester was prepared by transesterification from methyl ester as previously reported by our group.[81, 82] Adopting the optimal conditions reported by Xiao's group,[51] we successfully repeated the homogeneous asymmetric difluoroalkylation protocol with the *β*-ketoester **36** and ethyl 2,2-difluoro-2-iodoacetate, obtaining the desired product **37** in 52% yield and 92:8 er (Xiao's research as indicated in Scheme 4.22: 67% yield and 94:6 er). Then, based on Xiao's research,[51] all the functionalized silica nanoparticles were assayed as supported ligands in the enantioselective difluoroalkylation of this *β*-ketoester **36** (Scheme 4.33). We introduced some modifications in the optimal conditions and the general procedure due to the immobilization of the (bis)oxazoline ligand onto silica nanoparticles (Box-SiNPs). We mixed the functionalized silica NPs (20 mol% of ligand) with $NiBr_2$•glyme (15 mol%) in anhydrous DME and the mixture was stirred at room temperature for 12 h to form the chiral metal complex (NiBox-SiNPs). Then the NPs were separated by centrifugation and washed with DME to remove any amount of $NiBr_2$•glyme not coordinated to the ligand. The *β*-ketoester **36** was mixed under stirring with sodium bicarbonate in anhydrous DME for 2 h to form the corresponding salt. Then the supported catalyst (NiBox-SiNPs) was added to this solution to obtain the coordination of the enolate in the Nickel sphere (binary complex,

Scheme 4.33). Finally the photocatalyst Ir[dF(CF_3)ppy]$_2$(dtbbpy)PF_6 (3 mol%) and the alkylating reagent I-CF_2CO_2Et (2 equiv) were added to the mixture. The final concentration was 0.15 M, different from the reported (0.3 M) by Xiao. The stirred solution under argon was irradiated at 456 nm with a 7W blue light lamp at room temperature for 72 h (the lamp was placed at a distance of 5 cm). We followed the evolution of the reaction by TLC.

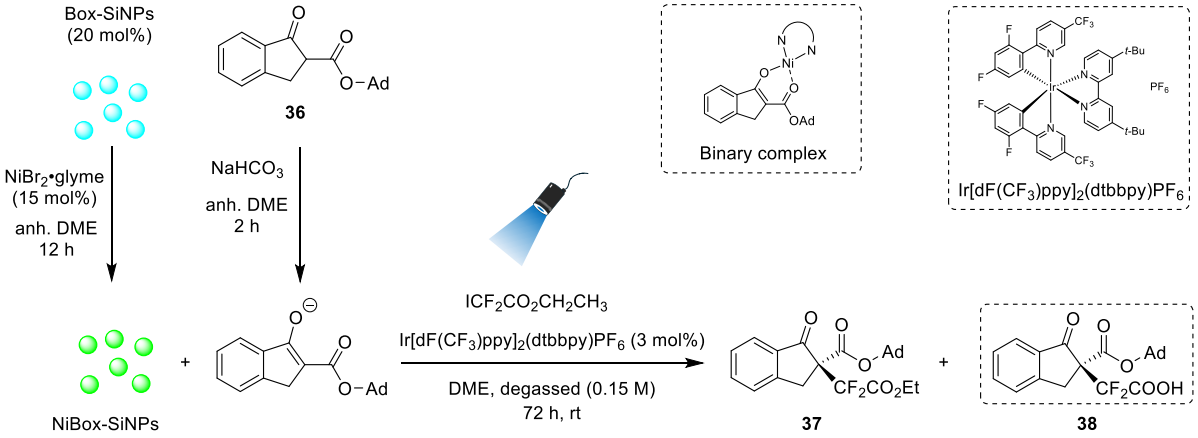

Scheme 4.33 Procedure for the enantioselective difluoroalkylation of *β*-ketoester **36** by cooperative photoredox/Ni(II) catalysis with supported bis(oxazoline) ligand

Then the product was purified through column chromatography and the enantiomeric ratio was determined by HPLC analysis using a chiral column (chiralpak AD-H) with hexane and *i*-PrOH as eluents. Unfortunately, a racemic mixture of **37** was obtained in all the cases (Table 4.2). The isolated yields were low to moderate considering that compound **37** hydrolyzed to acid **38** in the reaction conditions although no water was present.

Table 4.2. Results for the difluoroalkylation of **36** using supported bis(oxazolines)

material	**37** (%)	**38** (%)	er
mN9	22%	23%	50 : 50
mN10	17%	10%	50 : 50
mN11	/	23%	/
dN6	10%	13%	50 : 50
dN7	14%	13%	50 : 50

We do not have a simple and clear explanation for these negative results. As we have explained the reaction takes place, but in in a racemic manner. The stereoselective control can fail in several of the steps of the proposed mechanism. We have no experimental evidence to affirm that the following steps have occurred:

1. Coordination of the Ni to Box chiral ligand (NiBox-SiNPs)

2. Coordination of the enolate to the Nickel (enolate-NiBox-SiNPs)
3. Stereoselective reaction of the radical derived from ICF_2COOEt to the enolate-NiBox-SiNPs

The racemic pathway giving rise to the difluoroalkylated compound can take place in an homogeneous manner. This may be due to the leaching of the Nickel from the coordination complex (NiBox-SiNPs). Moreover, even if the Ni is correctly complexed perhaps the porosity or morphology of the pores prevents the enolate to have access to the metal sphere. Otherwise, if this is not the case, even if the enolate and fluorinated reagent coordinate to the previously formed NiBox-SiNPs the conformation space could not to be adequate to ensure the stereocontrol of the reaction. In fact, we have changed the substituents on the BOX chiral ligand from simple benzyl or isopropyl substituents used by Xiao's group to a completely different chain. After the formation of the nanomaterial the conformational environment is not easily predictable. Moreover, this chain possesses other heteroatoms that can interfere in the coordination of the metal.

In related homogeneous enantioselective catalytic reactions, we have studied the formation of the intermediate complexes by NMR and MS-ESI.[83, 84] However with these materials, these techniques cannot be applied.

Although we know it is a challenging task, we plan to explore other reactions in the future. Perhaps an intramolecular reaction could be easier, thus in this case we avoid the coordination of the second reagent. For instance, we found a nice article of C.R.D Correia[85] describing the enantioselective synthesis of isoindolones via palladium catalyzed intramolecular Heck reaction using the Box ligand shown in Scheme 4.34.

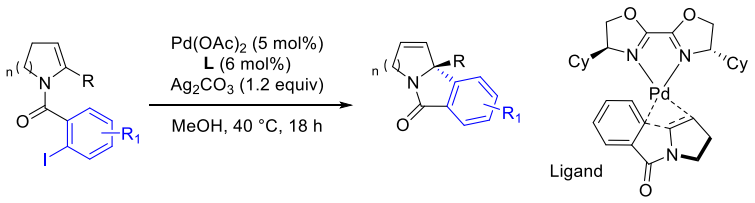

Scheme 4.34. Palladium-bis(oxazoline) catalyzed enantioselective synthesis of isoindolones

In addition, we have interest for different reaction pathways. Of note, Wang's group described the enantioselective construction of C-SCF_3 bonds via nickel catalyzed Negishi coupling reaction using the same *N*, *N*-ligand shown in scheme 4.35. A radical reaction is proposed in their mechanistic studies.

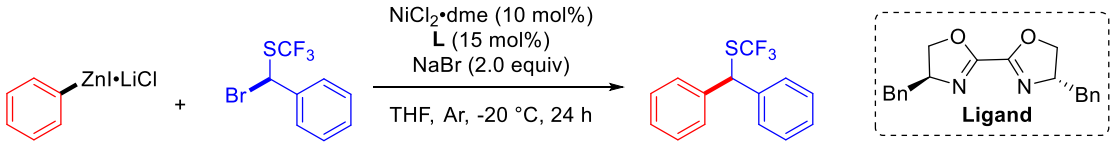

Scheme 4.35. Nickel catalyzed enantioselective construction of C−SCF_3 stereocenters

4.4 Conclusions

a) The disilylated bis(oxazoline) precursor **35** has been prepared from the amino alcohol **25** and diethyl oxalate in five steps with a 47% overall yield. The key step is a copper-catalyzed azide-alkyne cycloaddition (CuAAC) reaction, which allowed the formation of a 1,2,3-triazole ring to link the organic moiety and the triethoxysilyl group.

b) Mesoporous silica nanoparticles (MSNs) functionalized with the disilylated bis(oxazoline) precursor **35** have been prepared by grafting the precursor to previously synthesized MSNs **M0** (nanomaterial **mN9**) and by co-condensation of precursor **35** with TEOS in an aqueous buffered medium (pH 7) with Brij-56/CTAB as templates (nanomaterial **mN10**). Dense silica nanoparticles have also been prepared through co-condensation of precursor **35** and TEOS in ethanol with $NH_3 \bullet H_2O$ (nanomaterials **dN6** and **dN7**).

c) The functionalized mesoporous and dense silica nanoparticles have been fully characterized by infrared spectroscopy, ^{13}C and ^{29}Si CP MAS solid-state NMR, elemental analysis, transmission electron microscopy, dynamic light scattering, zeta-potential, energy dispersive X-ray spectroscopy (EDX) element mapping, and powder X-ray diffraction (when appropriate).

d) These functionalized silica nanoparticles have been evaluated as chiral supported bis(oxazoline) ligands in the difluoroalkylation reaction of β-ketoester **36** with ethyl 2,2-difluoro-2-iodoacetate by cooperative photoredox/Ni(II) catalysis. However, the yields were low and no chiral induction was observed.

4.5 Experimental section

4.5.1 General information

The information of NMR, CP-MAS NMR, IR, MS, elemental analysis, EDX, elements mapping, TEM, zeta-potential and DLS was given in ***Section* 2.5.1** and ***Section* 3.5.1**.

Specific rotation values ($[\alpha]_D$) were obtained at 20 ºC in a JASCO J-175 polarimeter at the *Servei d'Anàlisi Química* (SAQ) of the *Universitat Autònoma de Barcelona* (UAB) at 589.6 nm and they are given in 10^{-1} deg cm^2 g^{-1}.

Some elemental analyses were obtained in an Elemental Analyzer EA 3100 (Eurovector) equipped with Microbalance WXTS3DU (Mettler Toledo) in *Centres Científics i Tecnològics* of the *Universitat de Barcelona.*

Some high-resolution mass spectra (HRMS) were obtained in an Agilent 6545 Q-TOF mass spectrometer of the *Universidad de Burgos*.

Enantiomeric ratios (er) were determined by chiral HPLC with a chiral column (chiralpak AD-H) with hexane and *i*-PrOH as solvents (hexane : *i*-PrOH = 96:4, flow rate: 1 mL/min).

4.5.2 *N, N'*-bis((*S*)-1-hydroxy-3-(4-hydroxyphenyl)propan-2-yl)oxalamide (26)

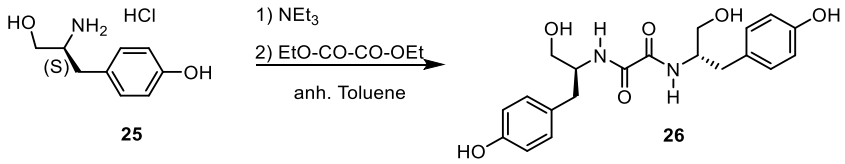

A solution of (*S*)-4-(2-amino-3-hydroxypropyl)phenol hydrochloride, **25** (0.49 g, 2.42 mmol) in anhydrous toluene (10 mL) was placed in a 50 mL Schlenk flask. Triethylamine (0.27 g, 2.67 mmol, 1.1 equiv) was added, and the reaction mixture was kept at 60 ℃ for 1 h. Then diethyl oxalate (0.18 g, 1.23 mmol, 0.5 equiv) was added, and the mixture was heated to reflux for 12 h. The reaction mixture was cooled to rt, water was added the mixture was left under stirring for 24 h. Then it was filtered to obtain **26**[86] as a white solid (0.3 g, 64% yield).

^{1}H NMR (400 MHz, DMSO) δ (ppm): 9.16 (s, 2H, HO-Ph), 8.27 (d, J = 9.1 Hz, 2H, NH), 6.95 (d, J = 8.4 Hz, 4H), 6.65 (d, J = 8.4 Hz, 4H), 4.82 (t, J = 5.6 Hz, 2H, HO-CH_2), 3.85 (m, 2H), 3.42-3.29 (m, 4H), 2.71 (dd, J = 13.8 and 6.1 Hz, 2H), 2.60 (dd, J = 13.8 and 8.0 Hz, 2H). **^{13}C NMR** (101 MHz, DMSO) δ (ppm): 159.50, 155.57, 129.90, 128.77, 115.01, 61.93, 53.30, 35.32.

4.5.3 *N, N'*-bis((*S*)-1-hydroxy-3-(4-methoxyphenyl)propan-2-yl)oxalamide (27)

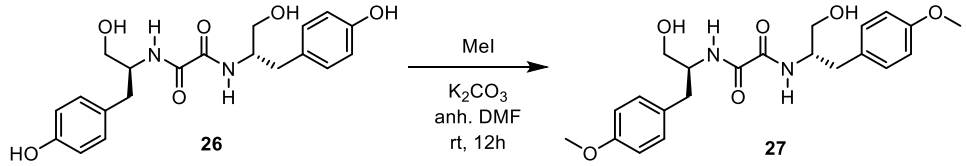

Methyl iodide (0.08 g, 0.56 mmol, 2.2 equiv) was added to a suspension of the amide **26** (0.1 g, 0.26 mmol) in dry DMF (2 mL). Then oven dried K_2CO_3 (10 equiv) was added to the reaction mixture. After stirring for 12 h at room temperature, the mixture was filtered off and the solid washed with AcOEt (3 × 20 mL). Then 1 M NaOH aqueous solution (3 × 20 mL) was added to the filtrate to remove any unreacted **26**. The organic phase was separated and dried over anhydrous sodium sulphate and the solvent was removed under reduced pressure to obtain the protected diamide **27** (0.07 g, 66 %).

^{1}H NMR (300 MHz, DMSO) δ (ppm): 8.28 (d, J = 9.1 Hz, 2H, NH), 7.06 (d, J = 8.6 Hz, 4H), 6.80 (d, J = 8.6 Hz, 4H), 4.83 (t, J = 5.6 Hz, 2H), 3.98-3.80 (m, 2H), 3.71 (s, 6H), 3.38 (dd, J = 5.5 and 2.1 Hz, 4H), 2.78 (dd, J = 13.8 and 5.6 Hz, 2H), 2.65 (dd, J = 13.8 and 8.4 Hz, 2H).

4.5.4 *N, N'*-bis((*S*)-1-chloro-3-(4-methoxyphenyl)propan-2-yl)oxalamide (28)

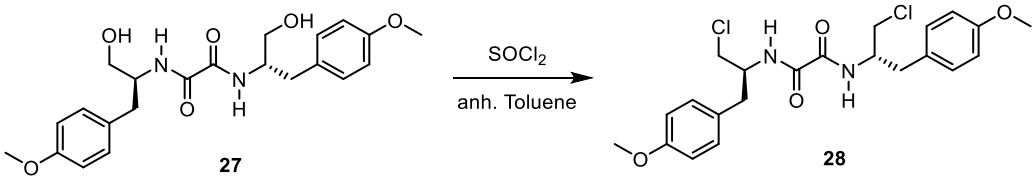

Thionyl chloride (0.2 g, 1.68 mmol, 5 equiv) was added to a suspension of **27** (0.14g, 0.34 mmol) in dry toluene (10 mL). The reaction mixture was maintained at 60 ℃ for 1 h and then heated to 90 ℃ for 12 h. The mixture was cooled to rt. An aqueous solution of 1 M KOH was added until neutral pH and the mixture was extracted with CH_2Cl_2 (3 × 20 mL). The organic extracts were washed with brine (1 × 20 mL), dried with Na_2SO_4, filtered and the solvent removed under vacuum to afford **28** as a white solid (0.148 g, 97%).

^{1}H NMR (400 MHz, $CDCl_3$) δ (ppm): 7.60 (d, J = 8.9 Hz, 2H), 7.16 (d, J = 8.6 Hz, 4H), 6.86 (d, J = 8.6 Hz, 4H), 4.34 (m, 2H), 3.80 (s, 6H), 3.61 (dd, J = 11.4, 4.4 Hz, 2H), 3.52 (dd, J = 11.4, 3.8 Hz, 2H), 2.92 (d, J = 7.2 Hz, 4H).

4.5.5 (4*S*,4'*S*)-4,4'-bis(4-methoxybenzyl)-4,4',5,5'-tetrahydro-2,2'-bioxazole (29)

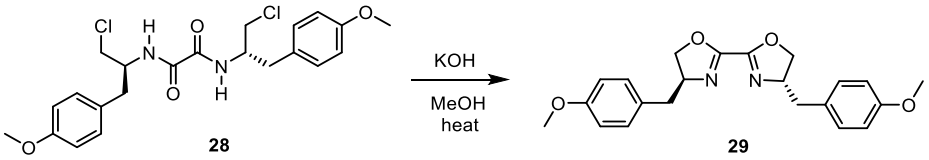

28 **29**

A mixture of potassium hydroxide (0.03 g, 0.53 mmol, 4.85 equiv) and **28** (0.05 g, 0.11 mmol) in methanol (3 mL) was heated to reflux for 12 h. Potassium chloride gradually precipitated as the reaction proceeded. The reaction mixture was cooled to rt, poured into H_2O (20 mL) and extracted with CH_2Cl_2 (3 × 20 mL). The organic extracts were washed with brine (20 mL), dried (Na_2SO_4), filtered and concentrated to dryness to afford **29** (0.04 g, 95%).

^{1}H NMR (400 MHz, $CDCl_3$) δ (ppm): 7.12 (d, J = 8.6 Hz, 4H), 6.84 (d, J = 8.6 Hz, 4H), 4.63-4.50 (m, 2H), 4.36 (dd, J = 9.5, 8.7 Hz, 2H), 4.20-4.10 (m, 2H), 3.79 (s, 6H), 3.19 (dd, J = 13.9, 5.0 Hz, 2H), 2.66 (dd, J = 14.0, 9.0 Hz, 2H).

4.5.5 Attempt to prepare 30 from 29

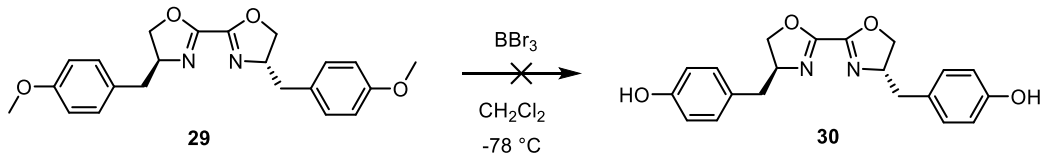

29 **30**

To a solution of **29** (0.04 g, 0.11 mmol) in CH_2Cl_2 (3 mL) was added dropwise a solution of BBr_3 in CH_2Cl_2 (1.0 M, 0.32 mL, 2.96 equiv) under nitrogen at -78 ℃. The reaction mixture was allowed to warm to room temperature and further stirred at room temperature for 24 h. Ice water was added and the solution was extracted with ethyl acetate. The organic layer was washed with water, dried over Na_2SO_4 and the solvent evaporated. The ^{1}H NMR of the crude product showed signals from the broken cycle structure.

4.5.6 Preparation of 31 from 28

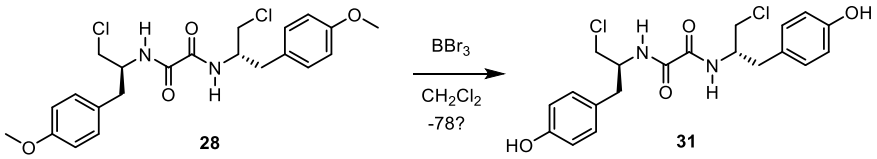

To a solution of **28** (0.066 g, 0.145 mmol) in CH_2Cl_2 (5 mL) was added dropwise a solution of BBr_3 in CH_2Cl_2 (1.0 M, 1.2 mL, 8.2 equiv) under nitrogen at -78 °C. The reaction mixture was allowed to warm to room temperature and further stirred at room temperature for 24 h. Ice water was added and the solution was extracted with ethyl acetate. The organic layer was washed with water and then dried over Na_2SO_4 and the solvent evaporated to afford **31** (0.035 g, 57 %).

^{1}H NMR (300 MHz, DMSO) δ (ppm): 9.20 (s, 2H), 8.69 (d, *J* = 9.1 Hz, 2H), 6.95 (d, *J* = 8.5 Hz, 4H), 6.66 (d, *J* = 8.4 Hz, 4H), 4.07 (dd, *J* = 8.2, 3.9 Hz, 2H), 3.66 (d, *J* = 6.2 Hz, 4H), 2.72 (t, *J* = 7.3 Hz, 4H).

4.5.7 *N*, *N'*-bis((*S*)-1-hydroxy-3-(4-(prop-2-yn-1-yloxy)phenyl)propan-2-yl)oxalamide (32)

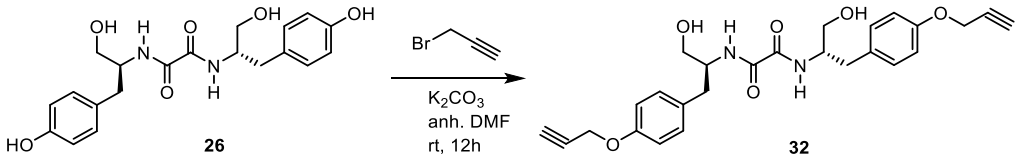

A propargyl bromide solution (0.43 g of 80 wt% in xylene corresponding to 0.34 g of propargyl bromide, 3.49 mmol, 3.5 equiv) was added quickly to a suspension of the diamide **26** (0.32 g, 0.82 mmol) in dry DMF (5 mL). Then oven dried K_2CO_3 (0.97g, 7 mmol, 8.5 equiv) was added to the reaction mixture. After stirring for 12 h at room temperature, the mixture was filtered off and the solid was washed with AcOEt (3 × 20 mL). Then 1 M NaOH aqueous solution (3 × 20 mL) was added to the filtrate to remove any unreacted **26**. The organic phase was separated and dried over anhydrous sodium sulphate and the solvent was removed under reduced pressure to obtain the oxalamide **32** (0.35 g, 91%).

M.p.: 194-195 °C. **^{1}H NMR** (400 MHz, DMSO) *δ* (ppm): 8.31 (d, *J* = 9.1 Hz, 2H, NH), 7.09 (d, *J* = 8.7 Hz, 4H ar), 6.86 (d, *J* = 8.7 Hz, 4H ar), 4.84 (t, *J* = 5.6 Hz, 2H, OH), 4.74 (d, *J* = 2.4 Hz, 4H), 3.89 (m, 2H), 3.53 (t, *J* = 2.4 Hz, 2H), 3.37 (m, 4H), 2.78 (dd, *J* = 13.9 and 5.8 Hz, 2H), 2.66 (dd, *J* = 13.8 and 8.4 Hz, 2H). **^{13}C NMR** (76 MHz, DMSO) *δ* (ppm):159.5, 155.6, 131.5, 129.9, 114.5, 79.4, 78.1, 62.1, 55.3, 53.15, 35.2. **IR** (ATR) ν (cm^{-1}): 3276.5, 1653.3, 1510.4, 1211, 1021.6. **HRMS** (ESI): m/z $[M+H]^+$ calcd for $C_{26}H_{29}N_2O_6$: 465.2026 found: 465.2024 $\mathbf{[\alpha]_D^{20}}$ = -58.15 (c=0.0081 g/mL, DMSO).

4.5.8 *N*, *N'*-bis((*S*)-1-chloro-3-(4-(prop-2-yn-1-yloxy)phenyl)propan-2-yl)oxalamide (33)

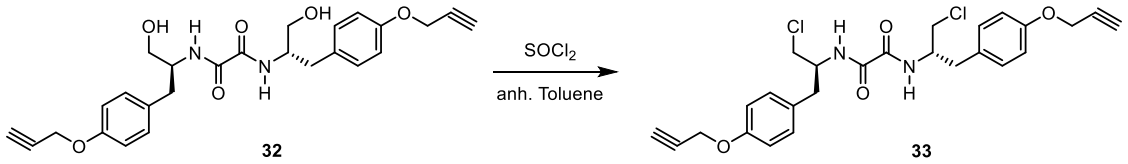

32 33

Thionyl chloride (0.19 g, 1.59 mmol, 5 equiv) was added to a suspension of **32** (0.12 g, 0.26 mmol) in toluene (10 mL). The reaction mixture was maintained at 60 ℃ for 1 h and then heated to 90 ℃ for 12 h. The reaction mixture was cooled to rt. An aqueous solution of 1 M KOH was added to neutral pH and the aqueous phase extracted with CH_2Cl_2 (3 × 20 mL). The organic extracts were washed with brine (1 × 20 mL), dried with Na_2SO_4, filtered and the solvent evaporated to afford **33** as a white solid (0.12 g, 96%).

M.p.: 174-175 ℃. **^{1}H NMR** (400 MHz, $CDCl_3$) δ (ppm): 7.60 (d, J = 9.0 Hz, 2H, NH), 7.18 (d, J = 8.6 Hz, 4H ar), 6.94 (d, J = 8.6 Hz, 4H ar), 4.68 (d, J = 2.4 Hz, 4H), 4.35 (m, 2H), 3.61 (dd, J = 11.4 and 4.3 Hz, 2H), 3.52 (dd, J = 11.4 and 3.7 Hz, 2H), 2.93 (d, J = 7.8 Hz, 4H), 2.52 (t, J = 2.4 Hz, 2H). **^{13}C NMR** (101 MHz, $CDCl_3$) δ (ppm): 159.0, 156.8, 130.4, 129.2, 115.4, 78.6, 75.7, 56.0, 51.7, 45.7, 36.5. **IR** (ATR) ν (cm^{-1}): 3297.9, 3281.3, 1657.8, 1511, 1235, 1036.85, 1020, 824.8, 563.6. **HRMS** (ESI): m/z $[M+H]^+$ calcd for $C_{26}H_{27}Cl_2N_2O_4$: 501.1349 found: 501.1348. $[\alpha]_D^{20}$ = -54 (c = 0.01 g/mL, CH_2Cl_2).

4.5.9 (4*S*,4'*S*)-4,4'-bis(4-(prop-2-yn-1-yloxy)benzyl)-4,4',5,5'-tetrahydro-2,2'-bioxazole (34)

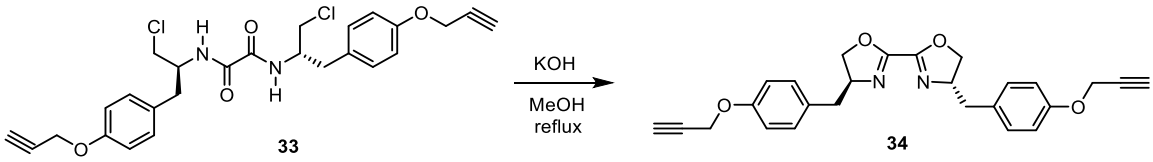

33 34

A mixture of potassium hydroxide (0.3 g, 5.35 mmol, 8.15 equiv) and **33** (0.33 g, 0.66 mmol) in methanol (10 mL) was heated to reflux for 12 h. Potassium chloride gradually precipitated as the reaction proceeded. The reaction mixture was cooled to rt, poured into H_2O (20 mL) and extracted with CH_2Cl_2 (3 × 20 mL). The organic extracts were washed with brine (20 mL), dried (Na_2SO_4), filtered and the solvent evaporated. The product was purified by flash column chromatography through silica gel (hexane:AcOEt 3:7, Rf = 0.58) to afford **34** as a white solid (0.24 g, 84%).

M.p.: 134-135 ℃. **^{1}H NMR** (400 MHz, $CDCl_3$) δ (ppm): 7.14 (d, J = 8.4 Hz, 4H ar), 6.91 (d, J = 8.6 Hz, 4H ar), 4.66 (d, J = 2.5 Hz, 4H), 4.56 (m, 2H), 4.36 (apparent t, J = 9.1 Hz, 2H), 4.14 (apparent t, J=8.3 Hz, 2H), 3.18 (dd, J = 14.0 and 5.1 Hz, 2H), 2.67 (dd, J = 14.0 and 8.9 Hz, 2H), 2.51 (t, J = 2.4 Hz, 2H). **^{13}C NMR** (101 MHz, $CDCl_3$) δ (ppm): 156.5, 155.2, 130.25, 115.2, 78.7, 75.6, 72.8, 68.4, 55.9, 40.3. **IR** (ATR) ν (cm^{-1}): 3247.5, 1620.6, 1509.3, 1227.7, 1122.1, 1024.5, 944.4, 615.8. **HRMS** (ESI): m/z $[M+H]^+$ calcd for $C_{26}H_{25}N_2O_4$: 429.1805 found: 429.1809. $[\alpha]_D^{20}$ = -72.00 (c = 0.01 g/mL,

CH_2Cl_2).

4.5.10 (4*S*,4'*S*)-4,4'-bis(4-((1-(3-(triethoxysilyl)propyl)-1H-1,2,3-triazol-4-yl)methoxy)benzyl)-4,4',5,5'-tetrahydro-2,2'-bioxazole (35)

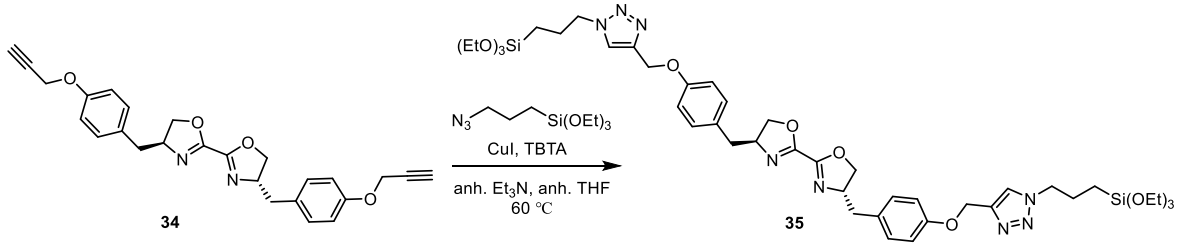

To a dry 10 mL Schlenk flask equipped with a stir bar and under argon atmosphere, **34** (0.053 g, 0.123 mmol), CuI (2 mg, 0.01 mmol, 0.08 equiv), TBTA (2 mg, 0.003 mmol, 0.03 equiv), (3-azidopropyl)triethoxysilane (0.062 g, 0.25 mmol, 2 equiv), anhydrous Et_3N (0.011 mL, 0.73 g/mL, 0.79 mmol, 6.5 equiv) and 5 mL THF were added. The resulting mixture was stirred at 60 °C until **34** was fully consumed. Then the solvent was evaporated and the residue was washed with dry pentane several times to afford **35** as oil (0.114 g, 100 % yield)

^{1}H NMR (300 MHz, $CDCl_3$) δ (ppm): 7.61 (s, 2H), 7.13 (d, J = 8.7 Hz, 4H), 6.93 (d, J = 8.7 Hz, 4H), 5.19 (s, 4H), 4.56 (m, 2H), 4.36 (m, 4H+2H), 4.14 (apparent t, 2H), 3.81 (q, J = 7.0 Hz, 12H), 3.19 (dd, J = 14.0, 5.1 Hz, 2H), 2.66 (dd, J = 14.0, 8.9 Hz, 2H), 2.03 (m, 4H), 1.21 (t, J = 7.0 Hz, 18H), 0.65-0.56 (m, 4H). **^{13}C NMR** (76 MHz, $CDCl_3$) δ (ppm): 157.3, 155.2, 144.2, 130.3, 129.9, 122.8, 115.1, 72.8, 68.5, 62.3, 58.7, 52.7, 40.4, 24.3, 18.1, 7.6. **IR** (ATR) ν (cm^{-1}): 2973.1, 2925.2, 1613.0, 1509.4, 1386.5, 1239.7, 1074.6, 1007.1, 940.9, 860.6, 798.2, 603.6, 558.8, 518.0, 437.3. **HRMS** (ESI): m/z $[M+H]^+$ calcd for $C_{44}H_{67}N_8O_{10}Si_2$: 923.4519 found: 923.4517. $\mathbf{[\alpha]_D^{20}}$ = -24.83 (c = 0.0145 g/mL, CH_2Cl_2).

4.5.11 Preparation of mesoporous M0 silica nanoparticles

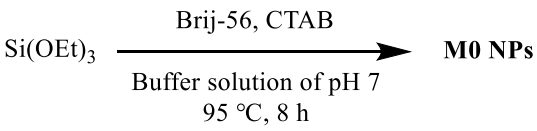

Mesoporous silica nanoparticles **M0** were synthesized in an aqueous buffer solution of pH 7 using a mixture with the following molar ratios: Brij-56:CTAB:TEOS:H_2O = 7:20:160:120,000.[78] Initially, CTAB (911 mg, 2.50 mmol) and Brij-56 (597.6 mg, 0.875 mmol) were dissolved in the buffer solution (prepared from KH_2PO_4 (857.5 mg, 6.3 mmol) and NaOH (145 mg, 3.625 mmol) in H_2O (270 mL, 15000 mmol)), under vigorous stirring and heating at 95 ºC. Upon achieving homogeneity in the solution, TEOS (4.17 g, 20 mmol) was gradually added. The reaction was then maintained for 8 hours under stirring at 95ºC. Subsequently, the suspension was cooled to room temperature while stirring, and

the nanoparticles were collected by centrifugation (12000 rpm at 25 °C for 45 mins). To remove the surfactant, 20 mL of an alcoholic solution of ammonium nitrate (NH_4NO_3, 6 g/L in 96% EtOH) was added to each tube, followed by sonication for 30 min at 50 °C, cooling, and centrifugation (30 min at 12000 rpm at 25 °C). The NH_4NO_3 washing process was repeated 3 times. Each solid in the tubes underwent successive washing with 96% ethanol, Mili-Q water, and 96% ethanol using the same protocol (30 min sonication at 50 °C, centrifugation). Finally, the resulting product was dried for a few hours under vacuum at room temperature, yielding **M0** nanoparticles as a white solid (940 mg).

4.5.12 Preparation of functionalized silica nanoparticles mN9 by post-grafting

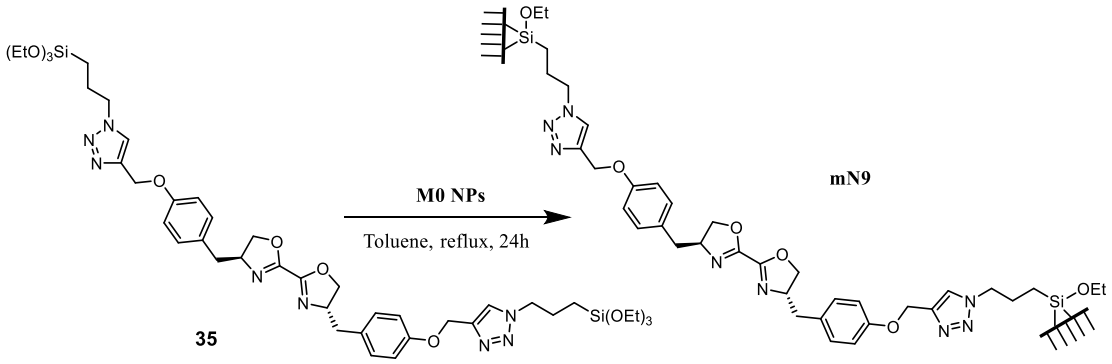

In a 50 mL round bottom flask equipped with a Dean-Stark apparatus, compound **35** (0.25 g, 0.272 mmol) and mesoporous silica nanoparticles **M0** (0.164 g, 2.729 mmol) were refluxed in dry toluene (20 mL) for 24 hours. After this period, the suspension was centrifuged (12000 rpm for 45 min). The solid was washed successively with ethanol (3 × 20 mL) and acetone (2 × 20 mL) (30 min at 50 °C sonication, 30 min for centrifugation at 12000 rpm), then dried under vacuum and finally crushed to yield grafted material **mN9** (0.264 g).

EA: 34.08% C, 4.03% H, 9.71% N (0.87 mmol/g material). **IR** (ATR) ν (cm^{-1}): 3376.9, 1613.7, 1510.3, 1175.7, 1056.5, 804.1, 442.9. **^{13}C-CP-MAS NMR** (100.6 MHz) δ (ppm): 158.9, 145.2, 132.3, 126.8, 116.5, 75.1, 63.1, 54.3, 32.2, 26.3, 11.4. **^{29}Si-CP-MAS NMR** (79.5 MHz) δ (ppm): -60.0 (T^2), -68.9 (T^3), -92.9 (Q^2), -103.6 (Q^3), -113.4 (Q^4). **DLS**: 380 nm, **Zeta-potential**: ζ = +7.6 mV.

4.5.13 Preparation of functionalized silica nanoparticles mN10 by co-condensation

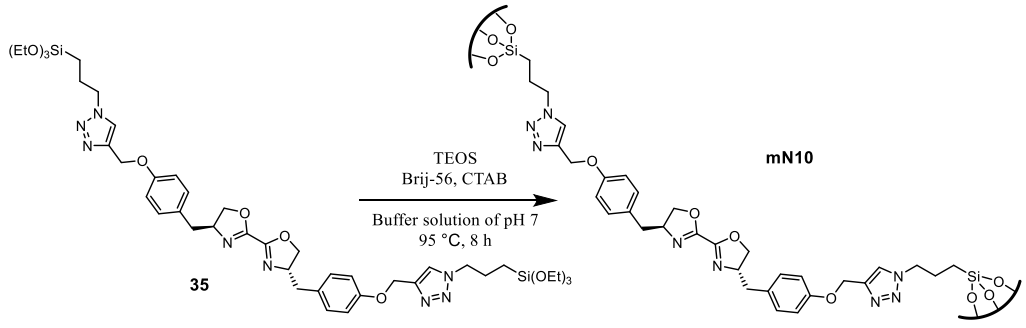

Mesoporous nanoparticles were synthesized in an aqueous buffer solution of pH 7 from a mixture with

the following molar ratio: Brij-56:CTAB:TEOS:**35**:H_2O = 7:20:160:16:120,000. Initially, CTAB (182 mg, 0.499 mmol) and Brij-56 (0.12 g, 0.176 mmol) were dissolved in the buffer solution (prepared from KH_2PO_4 (0.172 g, 1.264 mmol) and NaOH (29.2 mg, 0.73 mmol) in H_2O (54 mL, 2997.5 mmol) under vigorous stirring and heating at 95 ºC. Upon achieving homogeneity in the solution, TEOS (0.84 g, 4 mmol) and **35** (0.37 g, 0.4 mmol) were gradually added. The reaction was maintained stirring at 95ºC for 8 hours. Then the same washing process as for **M0** NPs was conducted. The nanomaterial **mN10** (0.227 g) was obtained as a white solid after drying under vacuum.

EA: 25.89% C, 3.33% H, 6.58% N (0.59 mmol/g material). **IR** (ATR) ν (cm^{-1}): 1614.4, 1510.5, 1065.2, 950.6, 798.7, 445.7. **^{13}C-CP-MAS NMR** (100.6 MHz) δ (ppm): 158.8, 145.2, 132.0, 126.0, 116.5, 75.4, 69.3, 60.4, 55.4, 40.6, 31.7, 26.2, 20.1, 19.5, 11.3. **^{29}Si-CP-MAS NMR** (79.5 MHz) δ (ppm): -47.8 (T^1), -59.8 (T^2), -69.4 (T^3), -92.2 (Q^2), -102.5 (Q^3), -112.8 (Q^4). **DLS**: 4191 nm, **Zeta-potential**: ζ = +5.9 mV.

4.5.14 Preparation of functionalized silica nanoparticles dN6 and dN7 by co-condensation

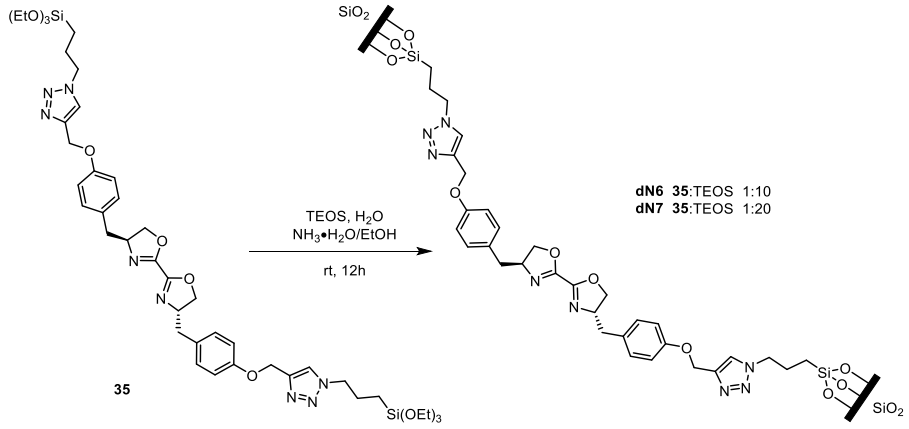

TEOS (0.45 g, 2.16 mmol) and the silylated derivative **35** (0.216 mmol) were dissolved in absolute EtOH (5.5 mL). Then, an ammonium hydroxide-ethanol solution was added (1.3 mL of 28% NH_3 H_2O in 5.5 mL EtOH). The mixture was magnetically stirred (1400 rpm) at room temperature for 12 hours. The functionalized nanoparticles were collected by centrifugation (12000 rpm for 10 minutes) and washed with ethanol until neutral pH was reached. Then, the obtained white solid was washed successively with Mili-Q water and 96% ethanol, and the nanomaterials were dried under high vacuum. We obtained **dN6** (0.236 g). The same procedure was conducted using a ratio of silylated ligand **35**:TEOS of 1:20 and we obtained **dN7 (**0.352 g).

dN6 EA: 20.45% C, 2.87% H, 5.7% N (0.51 mmol/g material). **IR** (ATR) ν (cm^{-1}): 1510.5, 1061.2, 945.2, 800.5, 448. **^{13}C-CP-MAS NMR** (100.6 MHz) δ (ppm): 159.2, 145.4, 132.6, 117.0, 68.5, 63.6, 60.8, 54.6, 42.2, 26.1, 20.4, 12.0. **^{29}Si-CP-MAS NMR** (79.5 MHz) δ (ppm): -48.5 (T^1), -60.3 (T^2), -68.00 (T^3), -93.9 (Q^2), -102.5 (Q^3), -115.5 (Q^4). **DLS**: 729 nm, **Zeta-potential**: ζ = +17.8 mV.

dN7 EA: 13.29% C, 2.29% H, 3.68% N (0.33 mmol/g material). **IR** (ATR) ν (cm^{-1}): 1510.4, 1060.8,

946.7, 797.2, 447. **^{13}C-CP-MAS NMR** (100.6 MHz) δ (ppm): 159.3, 145.7, 132.6, 127.2, 117.1, 63.3, 60.9, 54.9, 39.0, 25.9, 19.5, 11.4. **^{29}Si-CP-MAS NMR** (79.5 MHz) δ (ppm): -59.0 (T^2), -68.6 (T^3), -93.8 (Q^2), -102.1 (Q^3), -112.3 (Q^4). **DLS**: 353 nm, **Zeta-potential**: ζ = +25.1 mV.

4.5.15 Preparation of functionalized silica nanoparticles mN11 by passivation of mN9 with HMDS

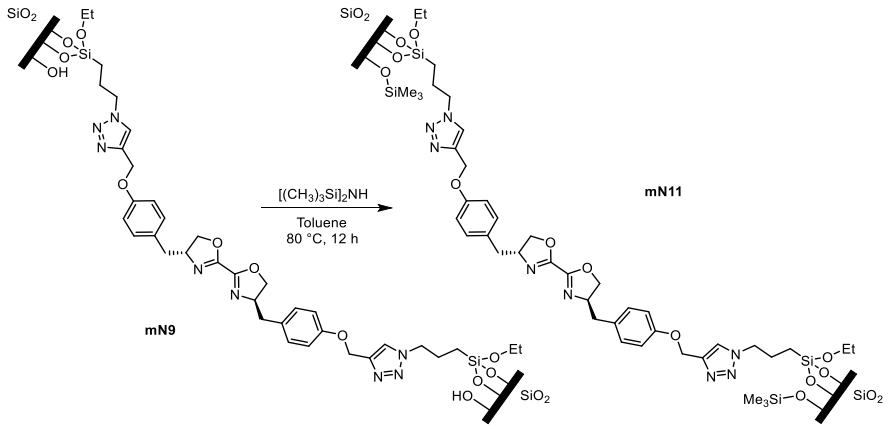

To passivate the surface of **mN9**, 46 mg **mN9** and 3 mL hexamethyldisilazane were added to 3 mL of anhydrous toluene and heated at 80 °C under magnetic stirring for 12 h. The resulting solid was separated by centrifugation (12000 rpm), washed with acetone and dried under vacuum to get 40 mg of **EA**: 35.00% C, 4.37% H, 9.36% N (0.84 mmol/g material).

4.5.16 General procedure for the difluoroalkylation of *β*-ketoester 36 by cooperative photoredox/Ni(II) catalysis with supported bis(oxazoline) ligands

The corresponding nanomaterial (see Table 4.2 in Section 4.3.3) (0.04 mmol ligand) was mixed with $NiBr_2$•glyme (10 mg, 0.03 mmol) in anhydrous DME (0.67 mL) under Ar. The mixture was stirred at room temperature for 12 h to form the chiral metal complex. Then the solid was separated by centrifugation (12000 rpm) and washed with DME to remove the non-coordinated $NiBr_2$•glyme giving a supported Ni(II)/bis(oxazoline). The *β*-ketoester **36** (62 mg, 0.2 mmol) was mixed with sodium bicarbonate (0.033 g, 0.39 mmol) in anhydrous DME (1.3 mL) under stirring at room temperature for 2 h. Then the supported Ni(II)/bis(oxazoline) was added. Finally $Ir[dF(CF_3)ppy]_2(dtbbpy)PF_6$ (7 mg, 0.003 mmol) and $I\text{-}CF_2CO_2Et$ (100 mg, 0.4 mmol) were added to the mixture, followed by degassing under argon. The stirred reaction mixture was irradiated at 456 nm with a 7W blue light lamp at room temperature for 72 h. The lamp was placed at a distance of 5 cm. The evolution of the reaction was controlled by TLC. The solvent was evaporated under reduced pressure and the residue was purified by flash column chromatography on silica gel (hexane : EtOAc = 9 : 1) to obtain **37**. The mobile phase was changed to hexane : EtOAc = 8 : 2 to elute side product **38** out.

37

^{1}H NMR (300 MHz, $CDCl_3$) δ (ppm): 7.80 (d, J = 7.7 Hz, 1H), 7.64 (td, J = 7.4, 1.2 Hz, 1H), 7.49 (d, J = 7.7 Hz, 1H), 7.41 (t, J = 7.4 Hz, 1H), 4.35 (q, J = 7.1 Hz, 2H), 3.73 (q, J = 17.9 Hz, 2H), 2.13 (s, 3H), 2.04 (d, J = 3.5 Hz, 6H), 1.61 (t, J = 3.1 Hz, 6H), 1.35 (t, J = 7.1 Hz, 3H).

38

^{1}H NMR (300 MHz, $CDCl_3$) δ (ppm): 7.79 (d, J = 7.6 Hz, 1H), 7.68-7.60 (m, 1H), 7.47 (d, J = 7.8 Hz, 1H), 7.41 (t, J = 7.6 Hz, 1H), 3.99 (s, 1H), 3.65 (d, J = 17.1 Hz, 1H), 3.21 (d, J = 17.1 Hz, 1H), 2.11 (s, 4H), 1.96 (d, J = 3.0 Hz, 5H), 1.60 (d, J = 2.7 Hz, 6H). **^{13}C NMR** (75 MHz, $CDCl_3$) δ (ppm): 170.4, 152.5, 136.0, 134.2, 128.1, 126.4, 125.2, 84.1, 80.7, 41.1, 39.7, 36.0, 31.0. **^{19}F NMR** (377 MHz, $CDCl_3$) δ (ppm): -108.1 (d, J = 277.7 Hz, 1F), -110.0 (d, J = 277.7 Hz, 1F). **IR** (ATR) ν (cm^{-1}): 2910.3, 2852.3, 1736.2, 1715.7, 1607.5, 1588.2 1456.6, 1246.5, 1194.3, 1043.9, 928.9, 752.9.

4.6 References

[1] Budisa, N.; Kubyshkin, V.; Schulze-Makuch, D. Fluorine-rich planetary environments as possible habitats for life. *Life (Basel, Switzerland)* **2014**, *4* (3), 374-385.

[2] Fuge, R. Fluorine in the environment, a review of its sources and geochemistry. *Applied Geochemistry* **2019**, *100*, 393-406.

[3] Kim, K.-H.; Shon, Z.-H.; Nguyen, H. T.; Jeon, E.-C. A review of major chlorofluorocarbons and their halocarbon alternatives in the air. *Atmospheric Environment* **2011**, *45* (7), 1369-1382.

[4] Babudri, F.; Farinola, G. M.; Naso, F.; Ragni, R. Fluorinated organic materials for electronic and optoelectronic applications: the role of the fluorine atom. *Chemical Communications* **2007**, (10), 1003-1022.

[5] McCormick, D. T.; Fordham, Z. W.; Guymon, C. A. Polymer nanostructure development of fluorinated and aliphatic monoacrylates in smectic liquid crystals via photopolymerization. *Liquid Crystals* **2003**, *30* (1), 49-58.

[6] Henary, E.; Casa, S.; Dost, T. L.; Sloop, J. C.; Henary, M. The Role of Small Molecules Containing Fluorine Atoms in Medicine and Imaging Applications. *Pharmaceuticals* **2024**, *17* (3), 281.

[7] Sheikhi, N.; Bahraminejad, M.; Saeedi, M.; Mirfazli, S. S. A review: FDA-approved fluorine-containing small molecules from 2015 to 2022. *European Journal of Medicinal Chemistry* **2023**, *260*, 115758.

[8] Theodoridis, G. Chapter 4 Fluorine-Containing Agrochemicals: An Overview of Recent Developments. In *Advances in Fluorine Science*, Tressaud, A. Ed.; Vol. 2; Elsevier, 2006; pp 121-175.

[9] Wang, Y.; Liu, A. Carbon–fluorine bond cleavage mediated by metalloenzymes. *Chemical Society Reviews* **2020**, *49* (14), 4906-4925.

[10] Wang, Q.; Bian, Y.; Dhawan, G.; Zhang, W.; Sorochinsky, A. E.; Makarem, A.; Soloshonok, V. A.; Han, J. FDA approved fluorine-containing drugs in 2023. *Chinese Chemical Letters* **2024**, 109780.

[11] Lemos, A.; Lemaire, C.; Luxen, A. Progress in Difluoroalkylation of Organic Substrates by Visible Light Photoredox Catalysis. *Advanced Synthesis & Catalysis* **2019**, *361* (7), 1500-1537.

[12] Dong, D.-Q.; Yang, H.; Shi, J.-L.; Si, W.-J.; Wang, Z.-L.; Xu, X.-M. Promising reagents for difluoroalkylation. *Organic Chemistry Frontiers* **2020**, *7* (17), 2538-2575.

[13] Pan, X.; Xia, H.; Wu, J. Recent advances in photoinduced trifluoromethylation and difluoroalkylation. *Organic Chemistry Frontiers* **2016**, *3* (9), 1163-1185.

[14] Dong, D.-Q.; Yang, S.-H.; Wu, P.; Wang, J.-Z.; Min, L.-H.; Yang, H.; Zhou, M.-Y.; Wei, Z.-H.; Ding, C.-Z.; Wang, Y.-L.; et al. Copper-Catalyzed Difluoroalkylation Reaction. In *Molecules*, 2022; Vol. 27.

[15] Saranya, P. V.; Aneeja, T.; Anilkumar, G. Palladium-catalyzed difluoromethylation and difluoroalkylation reactions: An overview. *Applied Organometallic Chemistry* **2022**, *36* (2), e6503.

[16] Feng, Z.; Xiao, Y.-L.; Zhang, X. Transition-Metal (Cu, Pd, Ni)-Catalyzed Difluoroalkylation via Cross-Coupling with Difluoroalkyl Halides. *Accounts of Chemical Research* **2018**, *51* (9), 2264-2278.

[17] Zhao, H.-Y.; Feng, Z.; Luo, Z.; Zhang, X. Carbonylation of Difluoroalkyl Bromides Catalyzed by Palladium. *Angewandte Chemie International Edition* **2016**, *55* (35), 10401-10405.

[18] Feng, Z.; Min, Q.-Q.; Xiao, Y.-L.; Zhang, B.; Zhang, X. Palladium-Catalyzed Difluoroalkylation of Aryl Boronic Acids: A New Method for the Synthesis of Aryldifluoromethylated Phosphonates and Carboxylic Acid Derivatives. *Angewandte Chemie International Edition* **2014**, *53* (6), 1669-1673.

[19] Gu, J.-W.; Zhang, X. Palladium-Catalyzed Difluoroalkylation of Isocyanides: Access to Difluoroalkylated Phenanthridine Derivatives. *Organic Letters* **2015**, *17* (21), 5384-5387.

[20] Zhang, F.; Min, Q.-Q.; Zhang, X. Palladium-Catalyzed Heck-Type Difluoroalkylation of Alkenes with Functionalized Difluoromethyl Bromides. *Synthesis* **2015**, *47* (19), 2912-2923.

[21] Wang, Q.; He, Y.-T.; Zhao, J.-H.; Qiu, Y.-F.; Zheng, L.; Hu, J.-Y.; Yang, Y.-C.; Liu, X.-Y.; Liang, Y.-M.

Palladium-Catalyzed Regioselective Difluoroalkylation and Carbonylation of Alkynes. *Organic Letters* **2016**, *18* (11), 2664-2667.

[22] Chen, C.; Zeng, R.; Zhang, J.; Zhao, Y. Ruthenium-Catalyzed Difluoroalkylation of 8-Aminoquinoline Amides at the C5-Position. *European Journal of Organic Chemistry* **2017**, *2017* (46), 6947-6950.

[23] Wang, X.; Zhao, S.; Liu, J.; Zhu, D.; Guo, M.; Tang, X.; Wang, G. Copper-Catalyzed C–H Difluoroalkylations and Perfluoroalkylations of Alkenes and (Hetero)arenes. *Organic Letters* **2017**, *19* (16), 4187-4190.

[24] Prieto, A.; Melot, R.; Bouyssi, D.; Monteiro, N. C–H Difluoroalkylation of Aldehyde Hydrazones with Functionalized Difluoromethyl Bromides under Copper Catalysis. *ACS Catalysis* **2016**, *6* (2), 1093-1096.

[25] Kong, W.; Yu, C.; An, H.; Song, Q. Copper-Catalyzed Intermolecular Reductive Radical Difluoroalkylation–Thiolation of Aryl Alkenes. *Organic Letters* **2018**, *20* (16), 4975-4978.

[26] Ke, M.; Song, Q. Copper-Catalyzed C(sp2)–H Difluoroalkylation of Aldehyde Derived Hydrazones with Diboron as Reductant. *The Journal of Organic Chemistry* **2016**, *81* (9), 3654-3664.

[27] Li, G.; Wang, T.; Fei, F.; Su, Y.-M.; Li, Y.; Lan, Q.; Wang, X.-S. Nickel-Catalyzed Decarboxylative Difluoroalkylation of α,β-Unsaturated Carboxylic Acids. *Angewandte Chemie International Edition* **2016**, *55* (10), 3491-3495.

[28] Li, C.; Cao, Y.-X.; Wang, R.; Wang, Y.-N.; Lan, Q.; Wang, X.-S. Cobalt-catalyzed difluoroalkylation of tertiary aryl ketones for facile synthesis of quaternary alkyl difluorides. *Nature Communications* **2018**, *9* (1), 4951.

[29] Gao, X.; Cheng, R.; Xiao, Y.-L.; Wan, X.-L.; Zhang, X. Copper-Catalyzed Highly Enantioselective Difluoroalkylation of Secondary Propargyl Sulfonates with Difluoroenoxysilanes. *Chem* **2019**, *5* (11), 2987-2999.

[30] Zhang, P.; Wolf, C. Catalytic Enantioselective Difluoroalkylation of Aldehydes. *Angewandte Chemie International Edition* **2013**, *52* (30), 7869-7873.

[31] Nicewicz, D. A.; MacMillan, D. W. C. Merging Photoredox Catalysis with Organocatalysis: The Direct Asymmetric Alkylation of Aldehydes. *Science* **2008**, *322* (5898), 77-80.

[32] Ischay, M. A.; Anzovino, M. E.; Du, J.; Yoon, T. P. Efficient Visible Light Photocatalysis of [2+2] Enone Cycloadditions. *Journal of the American Chemical Society* **2008**, *130* (39), 12886-12887.

[33] Iqbal, N.; Choi, S.; Ko, E.; Cho, E. J. Trifluoromethylation of heterocycles via visible light photoredox catalysis. *Tetrahedron Letters* **2012**, *53* (15), 2005-2008.

[34] Pham, P. V.; Nagib, D. A.; MacMillan, D. W. C. Photoredox Catalysis: A Mild, Operationally Simple Approach to the Synthesis of α-Trifluoromethyl Carbonyl Compounds. *Angewandte Chemie International Edition* **2011**, *50* (27), 6119-6122.

[35] Nagib, D. A.; MacMillan, D. W. C. Trifluoromethylation of arenes and heteroarenes by means of photoredox catalysis. *Nature* **2011**, *480* (7376), 224-228.

[36] Allen, A. E.; MacMillan, D. W. C. The Productive Merger of Iodonium Salts and Organocatalysis: A Non-photolytic Approach to the Enantioselective α-Trifluoromethylation of Aldehydes. *Journal of the American Chemical Society* **2010**, *132* (14), 4986-4987.

[37] Nagib, D. A.; Scott, M. E.; MacMillan, D. W. C. Enantioselective α-Trifluoromethylation of Aldehydes via Photoredox Organocatalysis. *Journal of the American Chemical Society* **2009**, *131* (31), 10875-10877.

[38] Cho, E. J. Radical-Mediated Fluoroalkylations. *The Chemical Record* **2016**, *16* (1), 47-63.

[39] Yu, C.; Iqbal, N.; Park, S.; Cho, E. J. Selective difluoroalkylation of alkenes by using visible light photoredox catalysis. *Chemical Communications* **2014**, *50* (85), 12884-12887.

[40] Xie, J.; Zhang, T.; Chen, F.; Mehrkens, N.; Rominger, F.; Rudolph, M.; Hashmi, A. S. K. Gold-Catalyzed Highly Selective Photoredox C(sp2)−H Difluoroalkylation and Perfluoroalkylation of Hydrazones. *Angewandte Chemie International Edition* **2016**, *55* (8), 2934-2938.

[41] Zhong, J.-J.; Yang, C.; Chang, X.-Y.; Zou, C.; Lu, W.; Che, C.-M. Platinum(ii) photo-catalysis for highly

selective difluoroalkylation reactions. *Chemical Communications* **2017**, *53* (64), 8948-8951.

[42] He, C.-Y.; Kong, J.; Li, X.; Li, X.; Yao, Q.; Yuan, F.-M. Visible-Light-Induced Direct Difluoroalkylation of Uracils, Pyridinones, and Coumarins. *The Journal of Organic Chemistry* **2017**, *82* (2), 910-917.

[43] Yin, Z.-B.; Ye, J.-H.; Zhou, W.-J.; Zhang, Y.-H.; Ding, L.; Gui, Y.-Y.; Yan, S.-S.; Li, J.; Yu, D.-G. Oxy-Difluoroalkylation of Allylamines with CO2 via Visible-Light Photoredox Catalysis. *Organic Letters* **2018**, *20* (1), 190-193.

[44] Li, K.; Zhang, X.; Chen, J.; Gao, Y.; Yang, C.; Zhang, K.; Zhou, Y.; Fan, B. Blue Light Induced Difluoroalkylation of Alkynes and Alkenes. *Organic Letters* **2019**, *21* (24), 9914-9918.

[45] Xia, Z.-H.; Gao, Z.-H.; Dai, L.; Ye, S. Visible-Light-Promoted Oxo-difluoroalkylation of Alkenes with DMSO as the Oxidant. *The Journal of Organic Chemistry* **2019**, *84* (11), 7388-7394.

[46] Gallego-Gamo, A.; Granados, A.; Pleixats, R.; Gimbert-Suriñach, C.; Vallribera, A. Difluoroalkylation of Anilines via Photoinduced Methods. *The Journal of Organic Chemistry* **2023**, *88* (17), 12585-12596.

[47] Ouyang, Y.; Qing, F.-L. Photoredox Catalyzed Radical Fluoroalkylation with Non-Classical Fluorinated Reagents. *The Journal of Organic Chemistry* **2024**, *89* (5), 2815-2824.

[48] Govender, T.; Arvidsson, P. I.; Maguire, G. E. M.; Kruger, H. G.; Naicker, T. Enantioselective Organocatalyzed Transformations of β-Ketoesters. *Chemical Reviews* **2016**, *116* (16), 9375-9437.

[49] Li, K.; Chen, J.; Yang, C.; Zhang, K.; Pan, C.; Fan, B. Blue Light Promoted Difluoroalkylation of Aryl Ketones: Synthesis of Quaternary Alkyl Difluorides and Tetrasubstituted Monofluoroalkenes. *Organic Letters* **2020**, *22* (11), 4261-4265.

[50] Li, C.; Cao, Y.-X.; Jin, R.-X.; Bian, K.-J.; Qin, Z.-Y.; Lan, Q.; Wang, X.-S. Highly stereoselective nickel-catalyzed difluoroalkylation of aryl ketones to tetrasubstituted monofluoroalkenes and quaternary alkyl difluorides. *Chemical Science* **2019**, *10* (40), 9285-9291.

[51] Liu, J.; Ding, W.; Zhou, Q.-Q.; Liu, D.; Lu, L.-Q.; Xiao, W.-J. Enantioselective Di-/Perfluoroalkylation of *β*-Ketoesters Enabled by Cooperative Photoredox/Nickel Catalysis. *Organic Letters* **2018**, *20* (2), 461-464.

[52] Adams, C. E.; Johnston, C. P. Light-mediated catalytic enantioselective difluoroalkylation of β-ketoesters via phase-transfer catalysis. *Organic Chemistry Frontiers* **2024**, *11*, 3639-3647.

[53] Fulgheri, T.; Della Penna, F.; Baschieri, A.; Carlone, A. Advancements in the recycling of organocatalysts: From classical to alternative approaches. *Current Opinion in Green and Sustainable Chemistry* **2020**, *25*, 100387.

[54] Zhang, X.; Zhang, Z.; Boissonnault, J.; Cohen, S. M. Design and synthesis of squaramide-based MOFs as efficient MOF-supported hydrogen-bonding organocatalysts. *Chemical Communications* **2016**, *52* (55), 8585-8588.

[55] Kohrt, C.; Werner, T. Recyclable Bifunctional Polystyrene and Silica Gel-Supported Organocatalyst for the Coupling of CO2 with Epoxides. *ChemSusChem* **2015**, *8* (12), 2031-2034.

[56] Großeheilmann, J.; Bandomir, J.; Kragl, U. Preparation of Poly(ionic liquid)s-Supported Recyclable Organocatalysts for the Asymmetric Nitroaldol (Henry) Reaction. *Chemistry – A European Journal* **2015**, *21* (52), 18957-18960.

[57] Dalpozzo, R. Magnetic nanoparticle supports for asymmetric catalysts. *Green Chemistry* **2015**, *17* (7), 3671-3686.

[58] Liang, J.; Liang, Z.; Zou, R.; Zhao, Y. Heterogeneous Catalysis in Zeolites, Mesoporous Silica, and Metal–Organic Frameworks. *Advanced Materials* **2017**, *29* (30), 1701139.

[59] Blanco, B.; Brissart, M.; Moreno-Mañas, M.; Pleixats, R.; Mehdi, A.; Reyé, C.; Bouquillon, S.; Hénin, F.; Muzart, J. Preparation of a hybrid organic–inorganic material containing macrocyclic triolefinic 15-membered palladium(0) complex: Catalytic activity in Suzuki cross-coupling and butadiene telomerization reactions. *Applied Catalysis A: General* **2006**, *297* (2), 117-124.

[60] Trilla, M.; Pleixats, R.; Man, M. W. C.; Bied, C.; Moreau, J. J. E. Hybrid Organic-Inorganic Materials from Di-(2-pyridyl)methylamine-Palladium Dichloride Complex as Recoverable Catalysts for Suzuki, Heck and Sonogashira Reactions. *Advanced Synthesis & Catalysis* **2008**, *350* (4), 577-590.

[61] Borja, G.; Monge-Marcet, A.; Pleixats, R.; Parella, T.; Cattoën, X.; Wong Chi Man, M. Recyclable Hybrid Silica-Based Catalysts Derived from Pd–NHC Complexes for Suzuki, Heck and Sonogashira Reactions. *European Journal of Organic Chemistry* **2012**, *2012* (19), 3625-3635.

[62] Elias, X.; Pleixats, R.; Man, M. W. C.; Moreau, J. J. E. Hybrid Organic-Inorganic Materials Derived from a Monosilylated Hoveyda-type Ligand as Recyclable Diene and Enyne Metathesis Catalysts. *Advanced Synthesis & Catalysis* **2007**, *349* (10), 1701-1713.

[63] Monge-Marcet, A.; Pleixats, R.; Cattoën, X.; Wong Chi Man, M. Sol–gel immobilized Hoveyda–Grubbs complex through the NHC ligand: A recyclable metathesis catalyst. *Journal of Molecular Catalysis A: Chemical* **2012**, *357*, 59-66.

[64] Fernández, M.; Ferré, M.; Pla-Quintana, A.; Parella, T.; Pleixats, R.; Roglans, A. Rhodium-NHC Hybrid Silica Materials as Recyclable Catalysts for [2+2+2] Cycloaddition Reactions of Alkynes. *European Journal of Organic Chemistry* **2014**, *2014* (28), 6242-6251.

[65] Ferré, M.; Cattoën, X.; Wong Chi Man, M.; Pleixats, R. Sol–Gel Immobilized N-Heterocyclic Carbene Gold Complex as a Recyclable Catalyst for the Rearrangement of Allylic Esters and the Cycloisomerization of γ-Alkynoic Acids. *ChemCatChem* **2016**, *8* (17), 2824-2831.

[66] Trilla, M.; Pleixats, R.; Man, M. W. C.; Bied, C. Organic–inorganic hybrid silica materials containing imidazolium and dihydroimidazolium salts as recyclable organocatalysts for Knoevenagel condensations. *Green Chemistry* **2009**, *11* (11), 1815-1820.

[67] Guo, W.; Monge-Marcet, A.; Cattoën, X.; Shafir, A.; Pleixats, R. Sol–gel immobilized aryl iodides for the catalytic oxidative α-tosyloxylation of ketones. *Reactive and Functional Polymers* **2013**, *73* (1), 192-199.

[68] Monge-Marcet, A.; Cattoën, X.; Alonso, D. A.; Nájera, C.; Man, M. W. C.; Pleixats, R. Recyclable silica-supported prolinamide organocatalysts for direct asymmetric Aldol reaction in water. *Green Chemistry* **2012**, *14* (6), 1601-1610.

[69] Ferré, M.; Cattoën, X.; Wong Chi Man, M.; Pleixats, R. Recyclable Silica-Supported Proline Sulphonamide Organocatalysts for Asymmetric Direct Aldol Reaction. *ChemistrySelect* **2016**, *1* (21), 6741-6748.

[70] Mihalcik, D. J.; Lin, W. Mesoporous Silica Nanosphere Supported Ruthenium Catalysts for Asymmetric Hydrogenation. *Angewandte Chemie International Edition* **2008**, *47* (33), 6229-6232.

[71] Schätz, A.; Hager, M.; Reiser, O. Cu(II)-Azabis(oxazoline)-Complexes Immobilized on Superparamagnetic Magnetite@Silica-Nanoparticles: A Highly Selective and Recyclable Catalyst for the Kinetic Resolution of 1,2-Diols. *Advanced Functional Materials* **2009**, *19* (13), 2109-2115.

[72] Liao, H.; Chou, Y.; Wang, Y.; Zhang, H.; Cheng, T.; Liu, G. Multistep Organic Transformations over Base-Rhodium/Diamine-Bifunctionalized Mesostructured Silica Nanoparticles. *ChemCatChem* **2017**, *9* (16), 3197-3202.

[73] Li, H.; Pérez-Trujillo, M.; Cattoën, X.; Pleixats, R. Recyclable Mesoporous Organosilica Nanoparticles Derived from Proline-Valinol Amides for Asymmetric Organocatalysis. *ACS Sustainable Chemistry & Engineering* **2019**, *7* (17), 14815-14828.

[74] Müller, D.; Umbricht, G.; Weber, B.; Pfaltz, A. C2-Symmetric 4,4′,5,5′-Tetrahydrobi(oxazoles) and 4,4′,5,5′-Tetrahydro-2,2′-methylenebis[oxazoles] as Chiral Ligands for Enantioselective Catalysis Preliminary Communication. *Helvetica Chimica Acta* **1991**, *74* (1), 232-240.

[75] Denmark, S. E.; Stavenger, R. A.; Faucher, A.-M.; Edwards, J. P. Cyclopropanation with Diazomethane and Bis(oxazoline)palladium(II) Complexes. *The Journal of Organic Chemistry* **1997**, *62* (10), 3375-3389.

[76] Montgomery, J.; Rand, A. W. Enantioselective alpha-Arylation of Benzamides via Synergistic Nickel and Metallaphotoredox Catalysis. **2019**.

[77] Maeda, K.; Morioka, K.; Yashima, E. Synthesis and Chirality Sensing Properties of Poly[(phenyleneethynylene)-alt-(carboxybiphenyleneethynylene)]s. *Macromolecules* **2007**, *40* (4), 1349-1352.

[78] He, Q.; Cui, X.; Cui, F.; Guo, L.; Shi, J. Size-controlled synthesis of monodispersed mesoporous silica nano-spheres under a neutral condition. *Microporous and Mesoporous Materials* **2009**, *117* (3), 609-616.

[79] Li, H.; Granados, A.; Fernández, E.; Pleixats, R.; Vallribera, A. Anti-inflammatory Cotton Fabrics and Silica Nanoparticles with Potential Topical Medical Applications. *ACS Applied Materials & Interfaces* **2020**, *12* (23), 25658-25675.

[80] Zanatta, L. D.; Barbosa, I. A.; Zanardi, F. B.; de Sousa Filho, P. C.; Bolzon, L. B.; Ramos, A. P.; Serra, O. A.; Iamamoto, Y. Hydrocarbon oxidation by iron-porphyrin immobilized on SBA-15 as biomimetic catalyst: role of silica surface. *RSC Advances* **2016**, *6* (106), 104886-104896.

[81] Pericas, À.; Shafir, A.; Vallribera, A. Zinc(II) oxide: an efficient catalyst for selective transesterification of β-ketoesters. *Tetrahedron* **2008**, *64* (39), 9258-9263.

[82] Granados, A.; Sarró, P.; Vallribera, A. Catalytic Asymmetric Fluorination of Alkyl 1-indanone-2-carboxylates Ruled by Pybox-Eu(III) Combination. In *Molecules*, 2019; Vol. 24.

[83] Comelles, J.; Pericas, À.; Moreno-Mañas, M.; Vallribera, A.; Drudis-Solé, G.; Lledos, A.; Parella, T.; Roglans, A.; García-Granda, S.; Roces-Fernández, L. Highly Enantioselective Electrophilic Amination and Michael Addition of Cyclic β-Ketoesters Induced by Lanthanides and (S,S)-ip-pybox: The Mechanism. *The Journal of Organic Chemistry* **2007**, *72* (6), 2077-2087.

[84] Granados, A.; Rivilla, I.; Cossío, F. P.; Vallribera, A. Lanthanum-Catalyzed Enantioselective Trifluoromethylation by Using an Electrophilic Hypervalent Iodine Reagent. *Chemistry – A European Journal* **2019**, *25* (35), 8214-8218.

[85] Wiethan, C.; Braga, I. B.; Menezes da Silva, V. H.; Batista Jr, J. M.; Correia, C. R. D. Enantioselective Synthesis of Isoindolones via Palladium – Catalyzed Intramolecular Heck-Mizoroki Reactions of Endocyclic Enamides Using N,N-Ligands. *ChemCatChem* **2023**, *15* (12), e202300422.

[86] Makarević, J.; Jokić, M.; Raza, Z.; Čaplar, V.; Katalenić, D.; Štefanić, Z.; Kojić-Prodić, B.; Žinić, M. Chiral bis (tyrosinol) and bis (p-hydroxyphenylglycinol) oxalamide gelators. Influence of aromatic groups and hydrogen bonding on gelation properties. **2004**, *77* (1-2), 403-414.

Formula Index

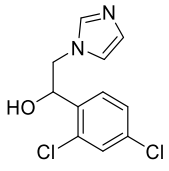

1

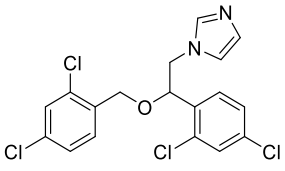

2

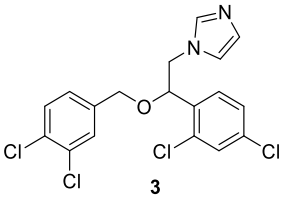

3

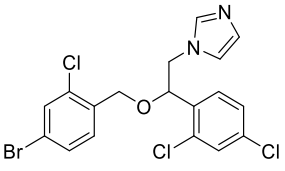

4

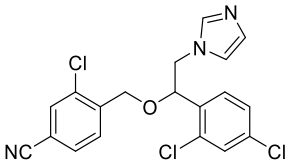

5

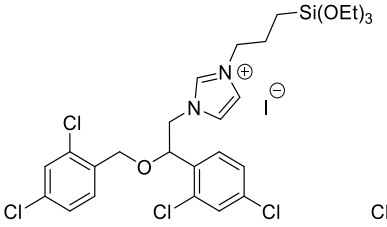

6

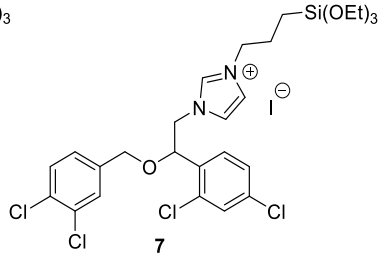

7

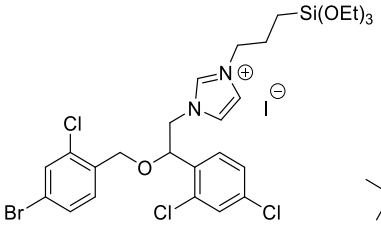

8

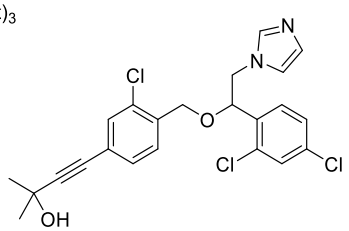

9

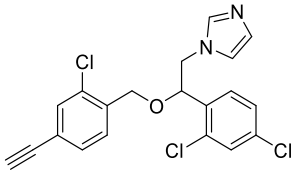

10

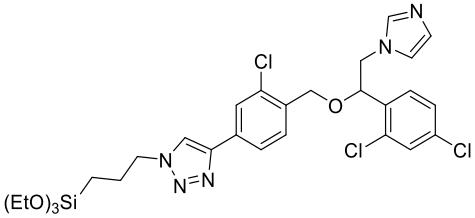

11

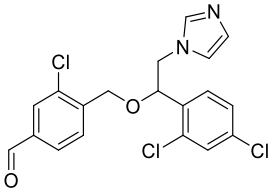

12

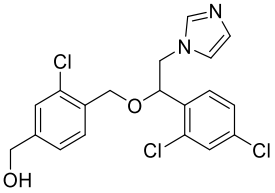

13

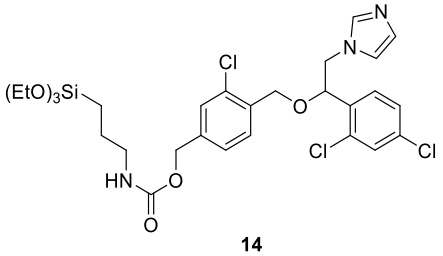

14

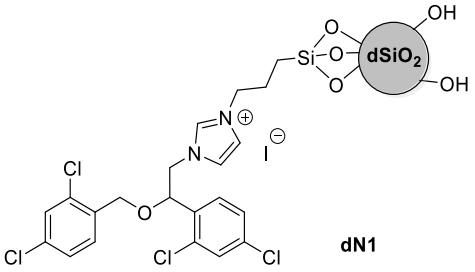

dN1

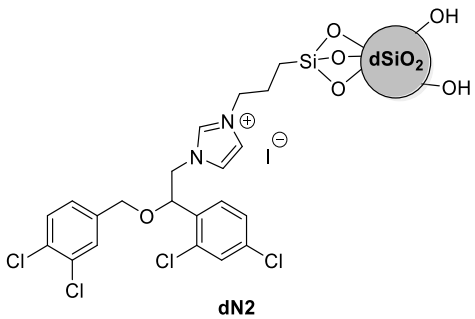

dN2

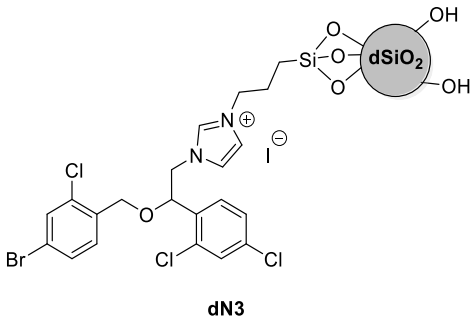

dN3

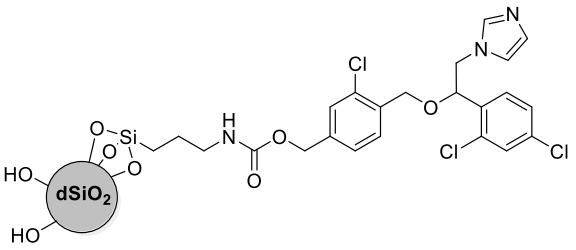

dN4

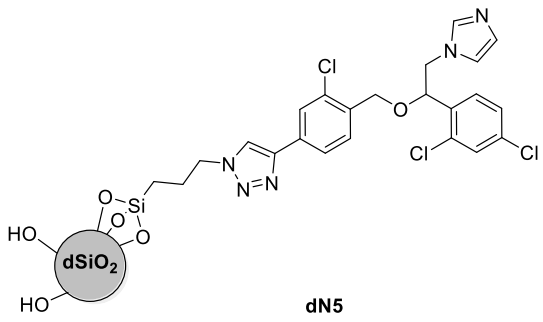

dN5

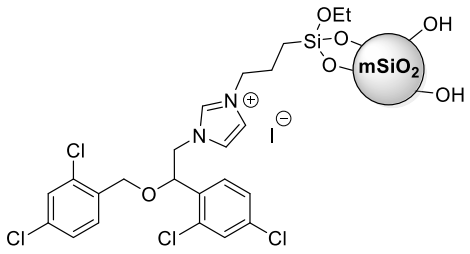

mN6

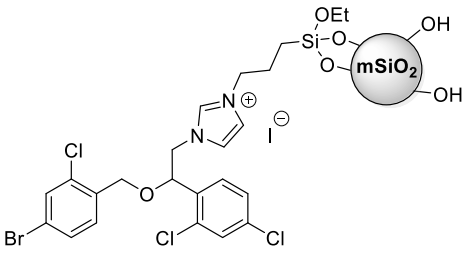

mN7

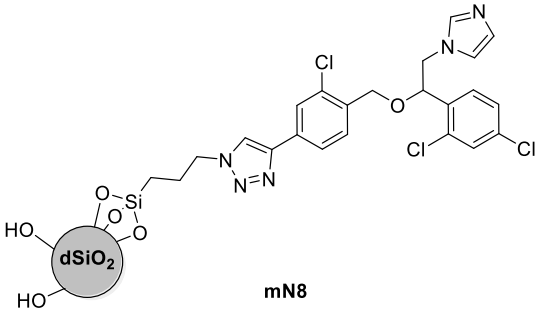

mN8

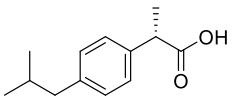

15

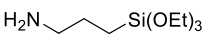

16

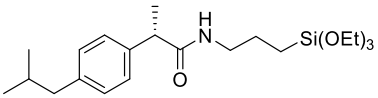

17

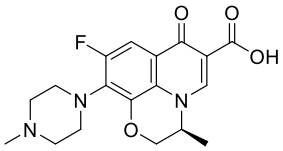

18

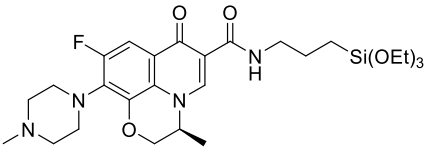

19

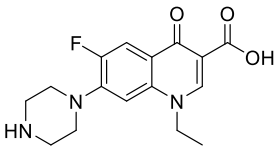

20

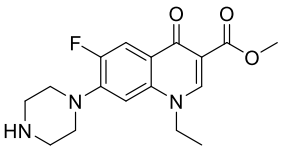

21

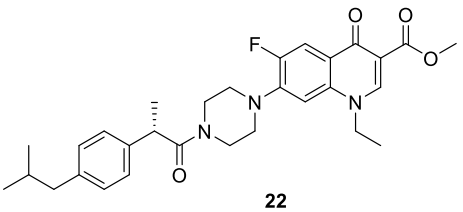

22

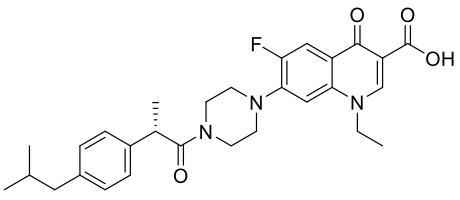

23

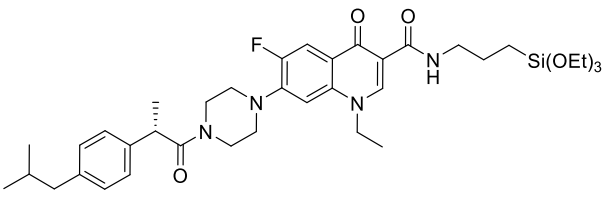

24

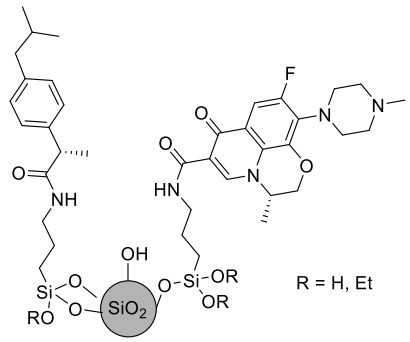

SiO_2@Ibu+Leflox

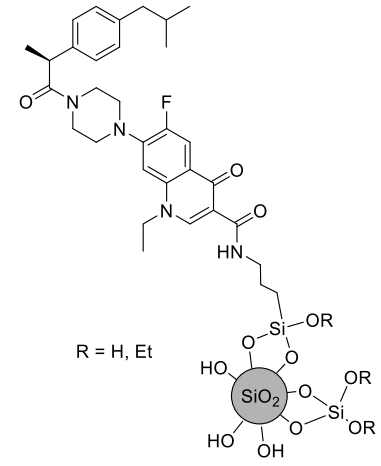

SiO_2@Norflox-Ibu

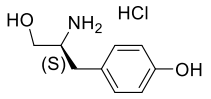

25

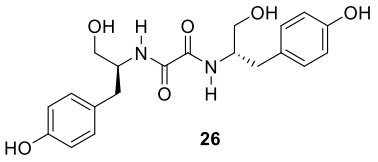

26

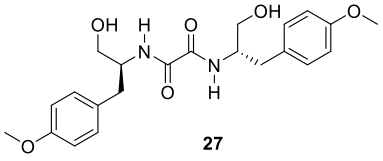

27

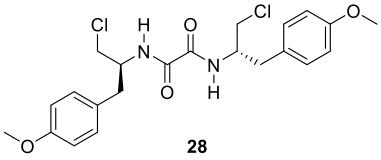

28

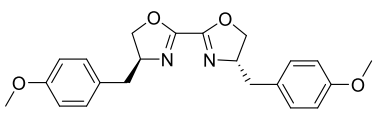

29

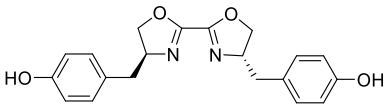

30

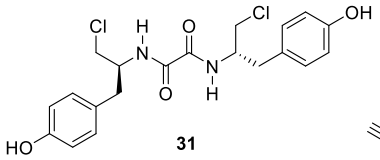

31

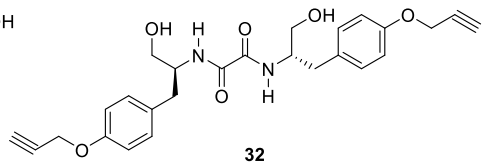

32

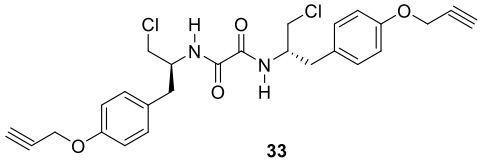

33

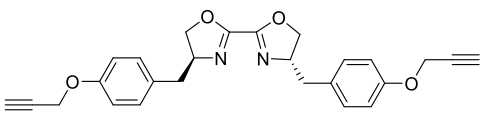

34

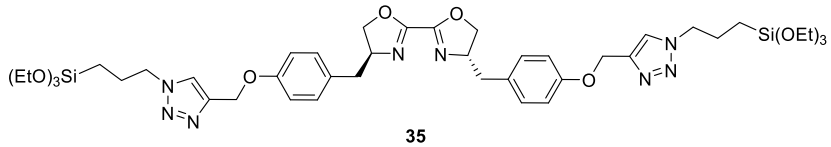

35

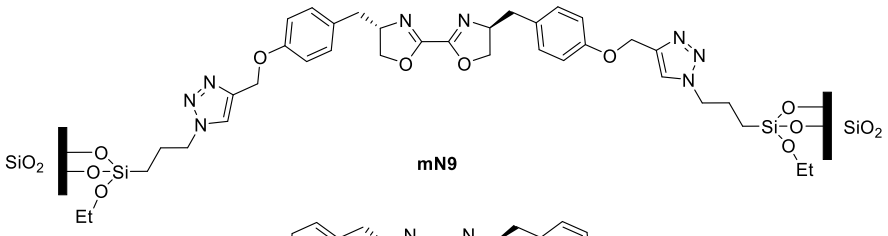

mN9

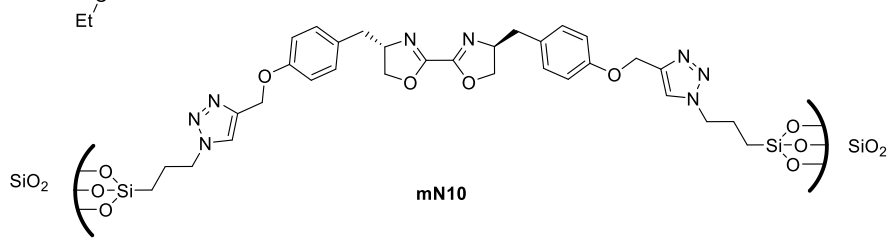

mN10

Formula Index

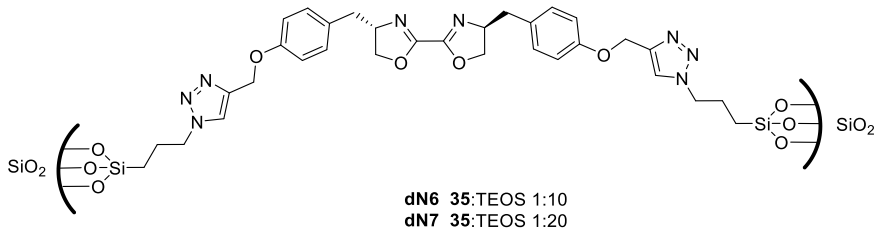

dN6 **35**:TEOS 1:10
dN7 **35**:TEOS 1:20

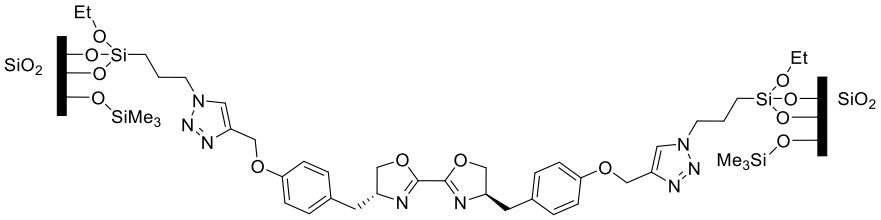

mN11

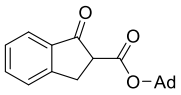

36

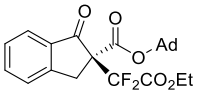

37

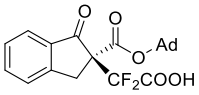

38

Universitat Autònoma de Barcelona

Doctoral School

Faculty of Science

Department of Chemistry

Functionalized Silica Nanoparticles and Coated Cotton Fabrics for Medical and Catalytic Applications

Annex: collection of spectra and characterization data

Ming Liu

Supervisor:

Prof. Roser Pleixats Rovira

Prof. Adelina Vallribera Masso

PhD in Chemistry

Doctoral Thesis, 2024

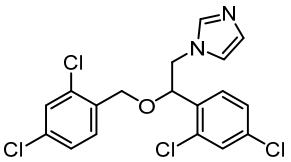

2

^{1}H NMR (360 MHz, $CDCl_3$)

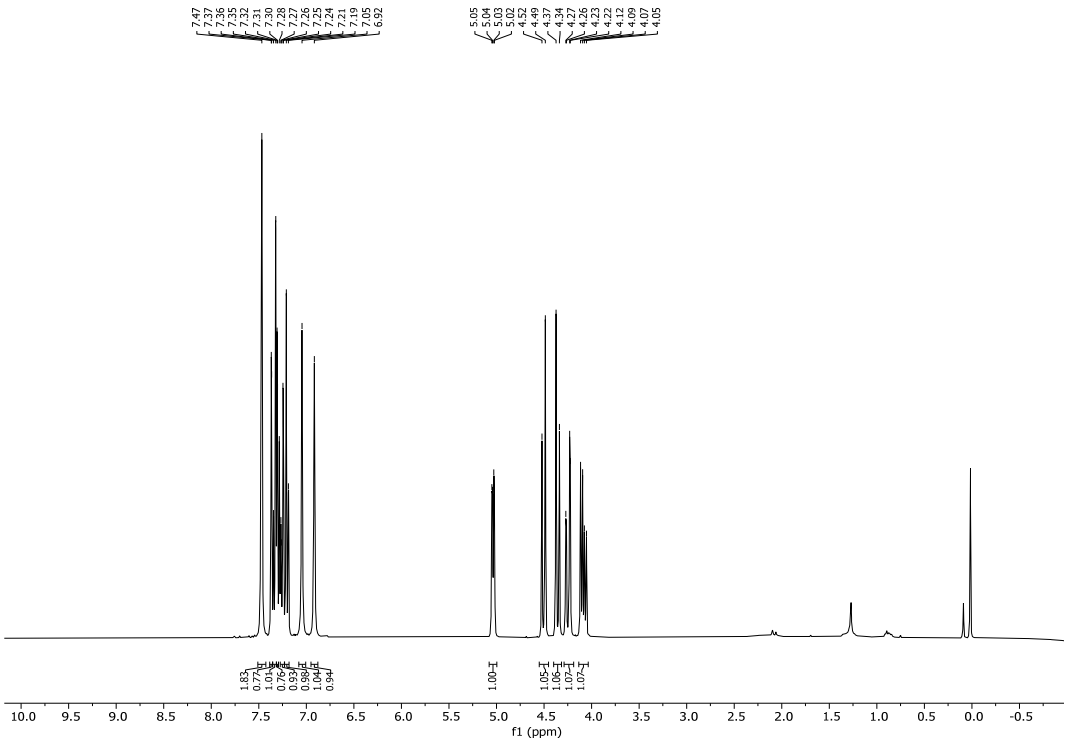

^{13}C NMR (91 MHz, $CDCl_3$)

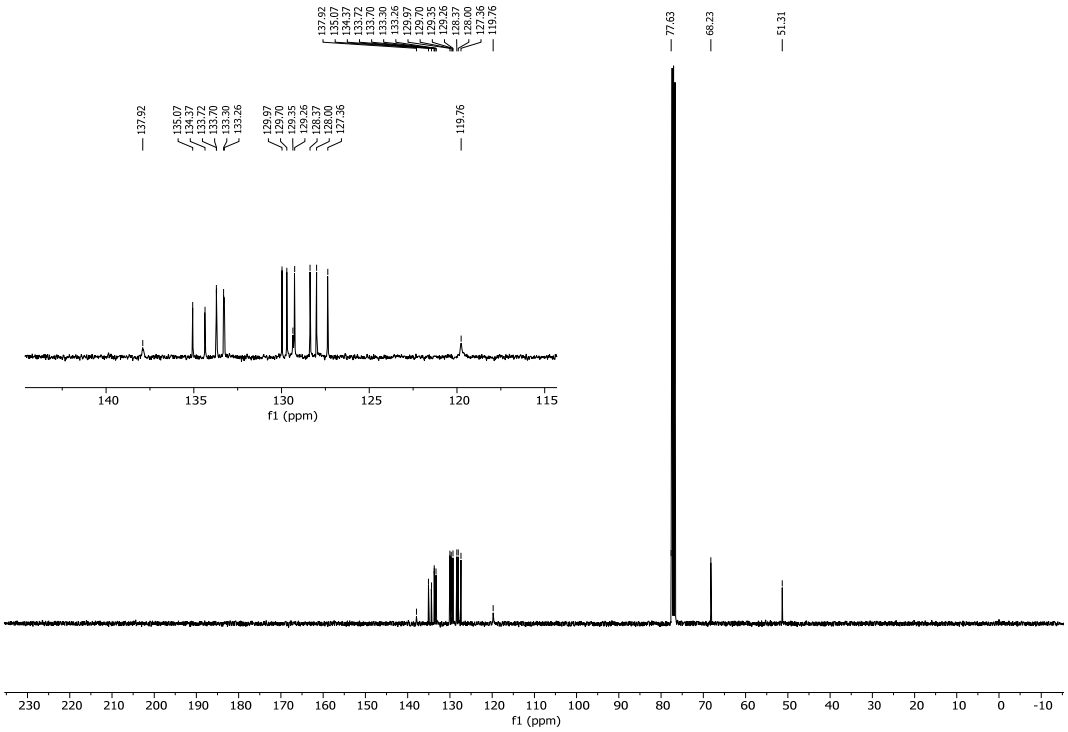

IR (ATR)

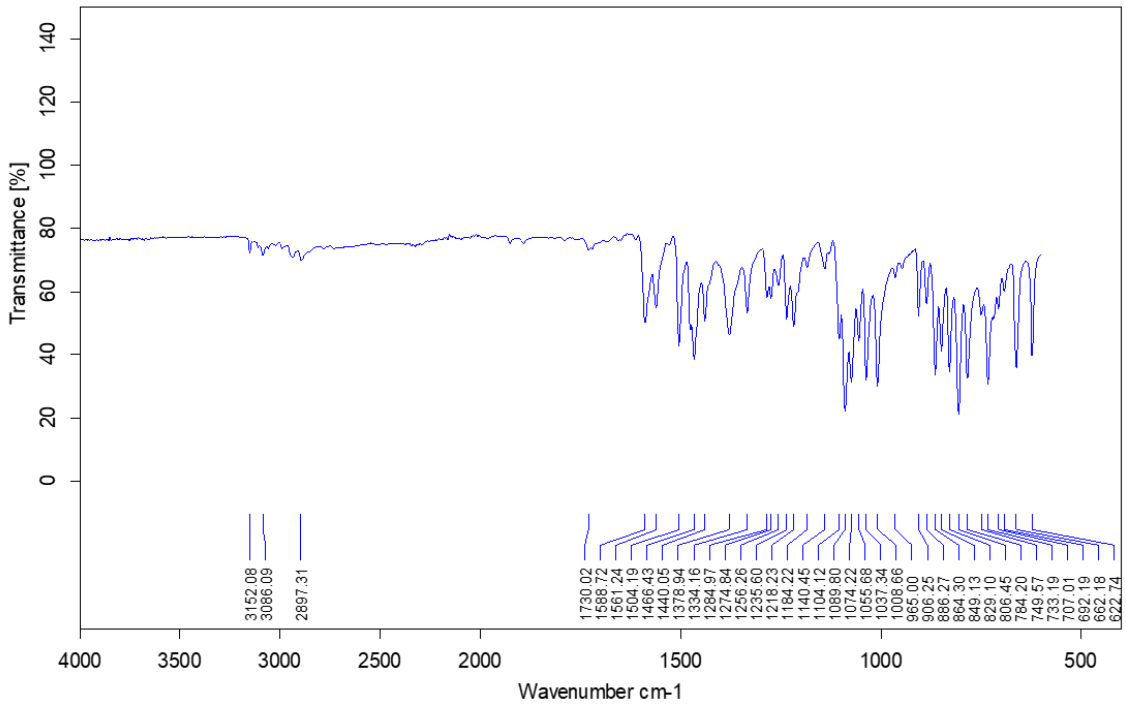
Transmittance [%]
0
20
40
60
80
100
120
140
3152.08
3086.09
2897.31
1730.02
1588.72
1561.24
1504.19
1466.43
1440.05
1378.94
1334.16
1284.97
1274.84
1256.26
1235.60
1218.23
1184.22
1140.45
1104.12
1089.80
1074.22
1055.68
1037.34
1008.66
965.00
906.25
886.27
864.30
849.13
829.10
806.45
784.20
749.57
733.19
707.01
692.19
662.18
622.74
4000
3500
3000
2500
2000
1500
1000
500
Wavenumber cm-1

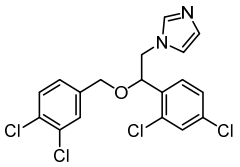

3

^{1}H NMR (360 MHz, $CDCl_3$)

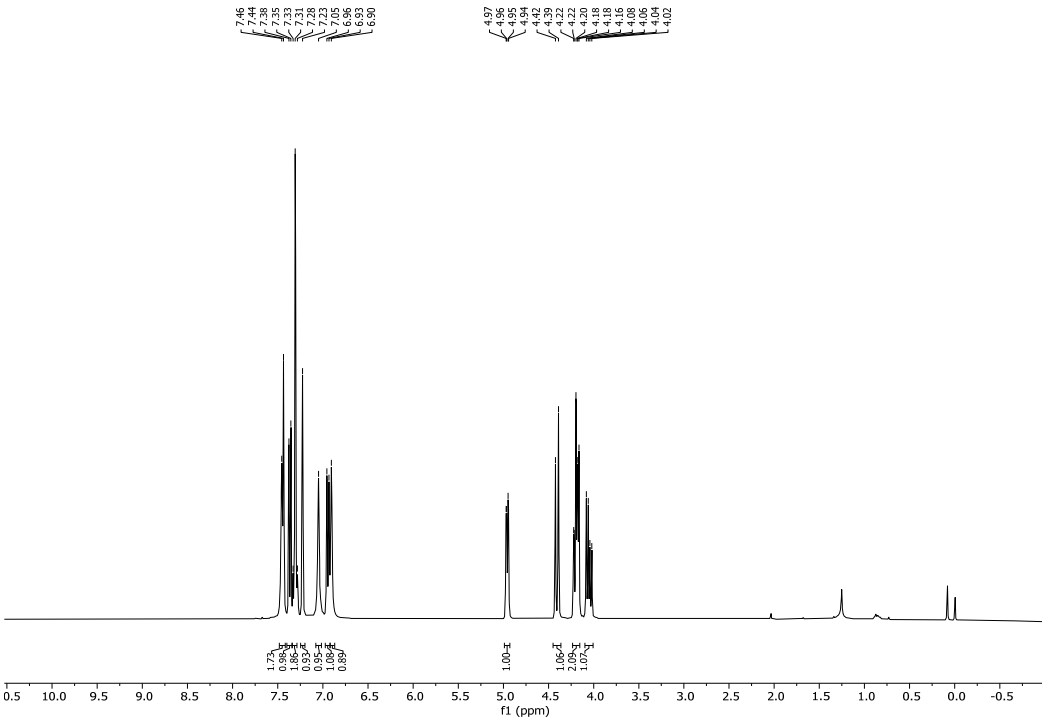

^{13}C NMR (91 MHz, $CDCl_3$)

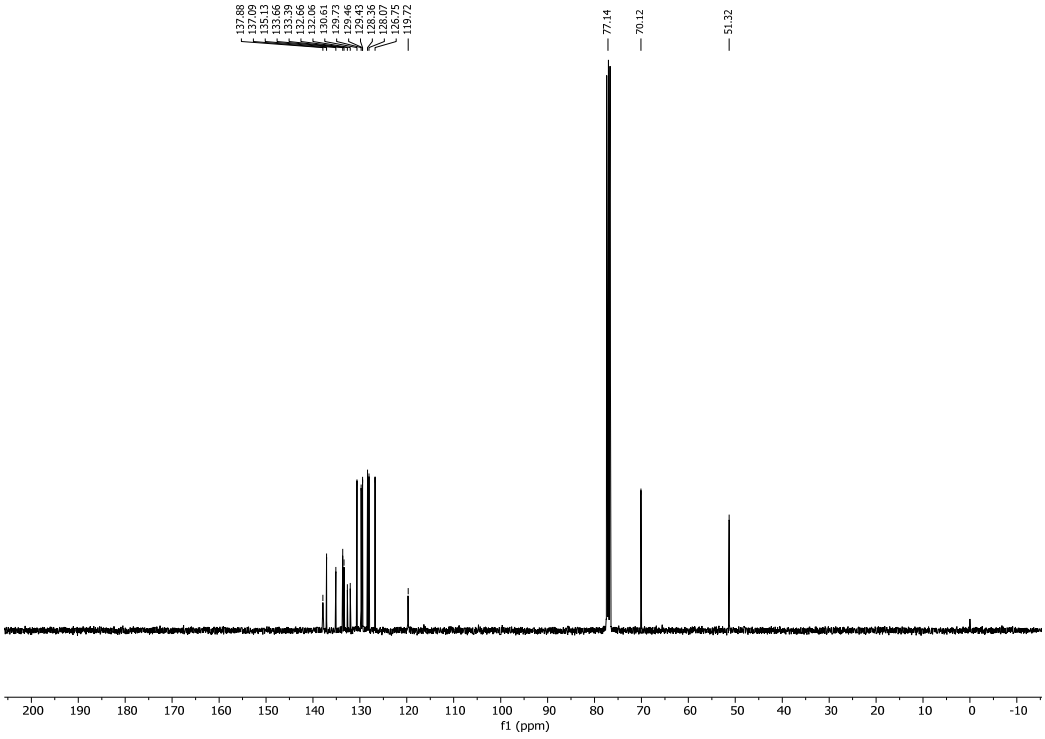

IR (ATR)

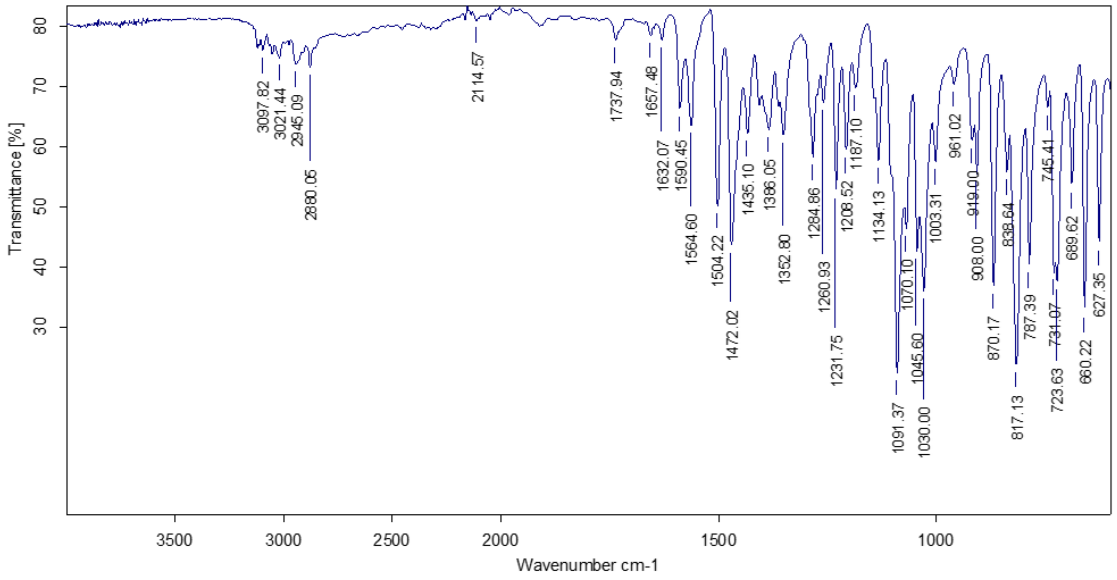
Transmittance [%]
80
70
60
50
40
30
3097.82
3021.44
2945.09
2880.05
2114.57
1737.94
1657.48
1632.07
1590.45
1564.60
1504.22
1472.02
1435.10
1386.05
1352.80
1284.86
1260.93
1231.75
1208.52
1187.10
1134.13
1091.37
1070.10
1045.60
1030.00
1003.31
961.02
919.00
908.00
870.17
838.64
817.13
787.39
745.41
731.07
723.63
689.62
660.22
627.35
3500
3000
2500
2000
1500
1000
Wavenumber cm-1

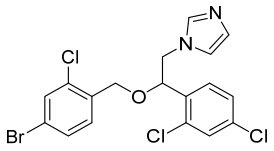

4

^{1}H NMR (360 MHz, $CDCl_3$)

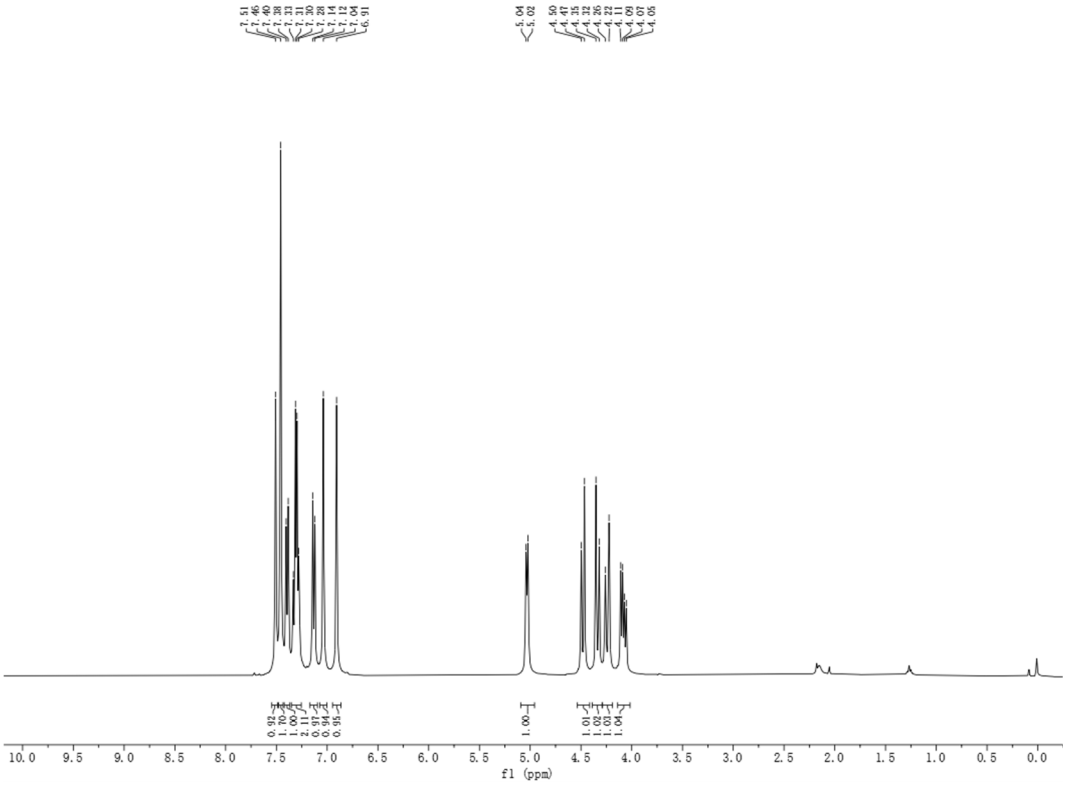

^{13}C NMR (91 MHz, $CDCl_3$)

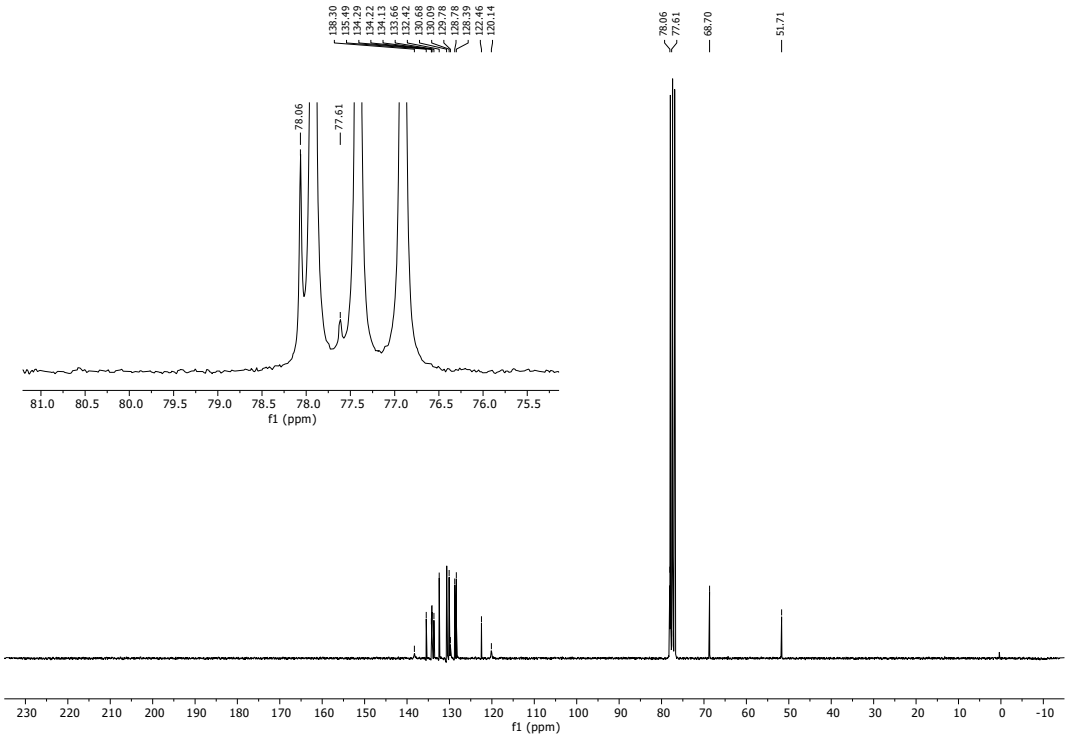

IR (ATR)

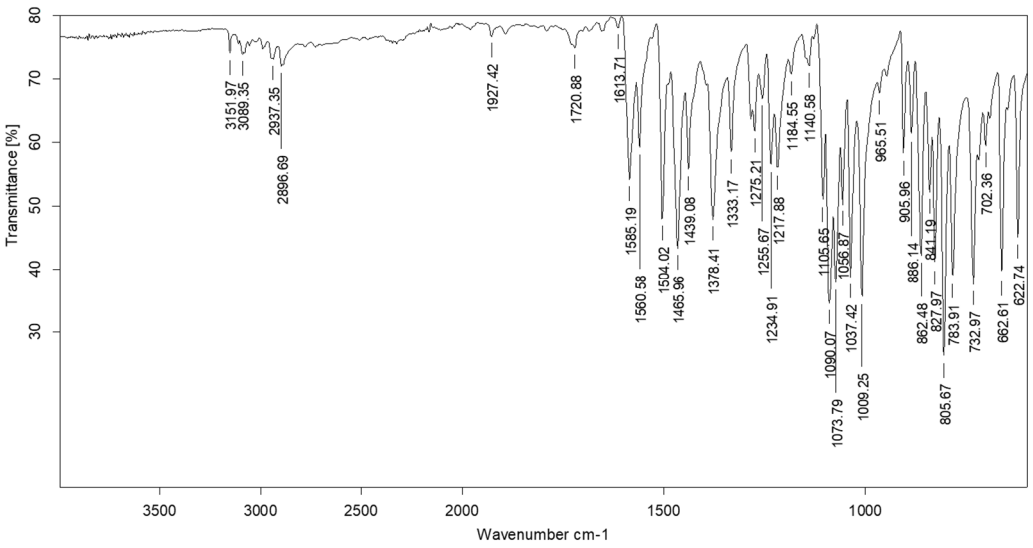
Transmittance [%]
80
70
60
50
40
30
3500
3000
2500
2000
1500
1000
Wavenumber cm-1
3151.97
3089.35
2937.35
2896.69
1927.42
1720.88
1613.71
1585.19
1560.58
1504.02
1465.96
1439.08
1378.41
1333.17
1275.21
1255.67
1234.91
1217.88
1184.55
1140.58
1105.65
1090.07
1073.79
1056.87
1037.42
1009.25
965.51
905.96
886.14
862.48
841.19
827.97
805.67
783.91
732.97
702.36
662.61
622.74

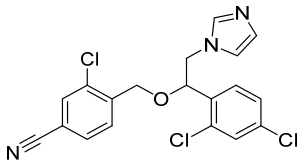

5

^{1}H NMR (360 MHz, $CDCl_3$)

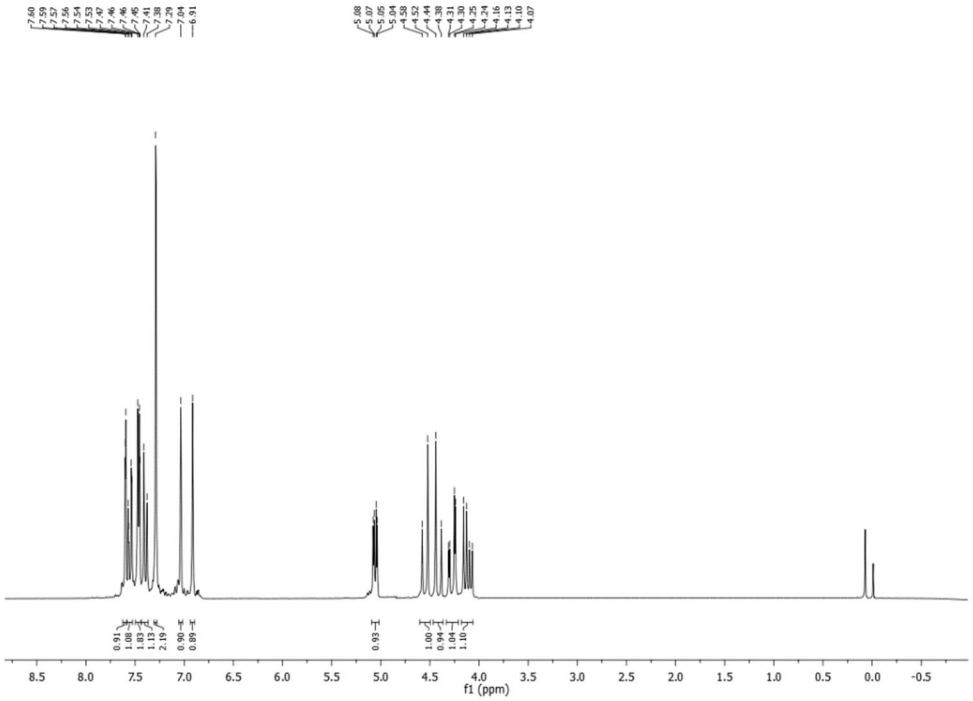

^{13}C NMR (101 MHz, $CDCl_3$)

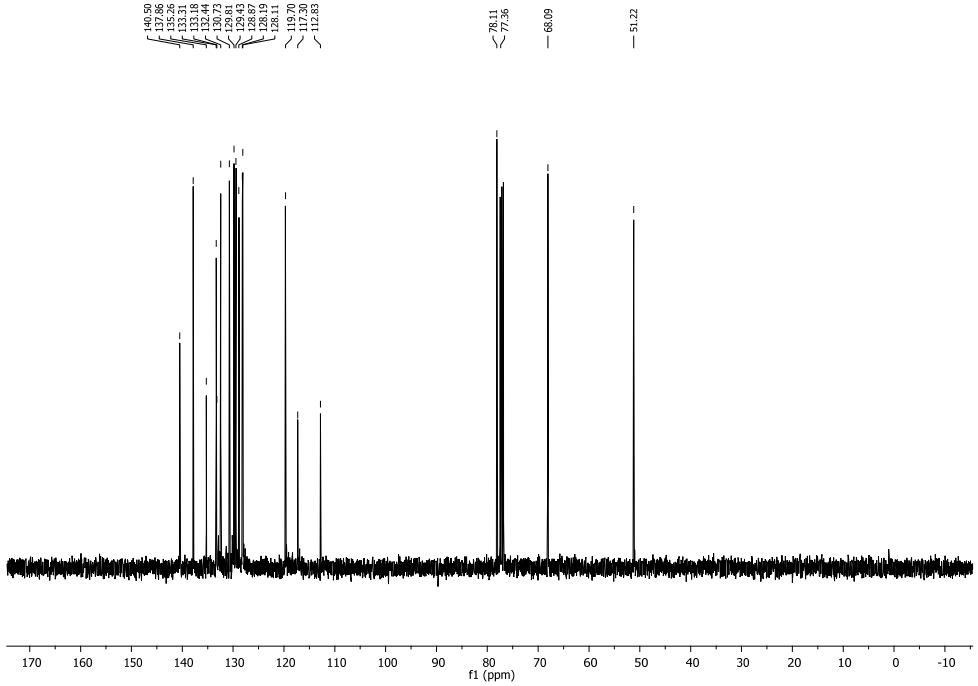

IR (ATR)

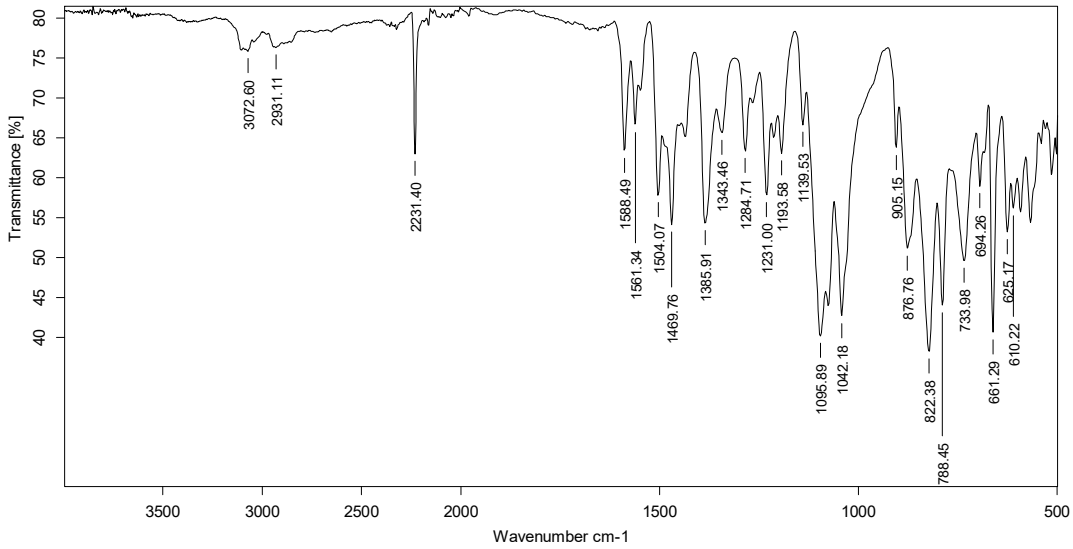
Transmittance [%]
80
75
70
65
60
55
50
45
40
3072.60
2931.11
2231.40
1588.49
1561.34
1504.07
1469.76
1385.91
1343.46
1284.71
1231.00
1193.58
1139.53
1095.89
1042.18
905.15
876.76
822.38
788.45
733.98
694.26
661.29
625.17
610.22
3500
3000
2500
2000
1500
1000
500
Wavenumber cm-1

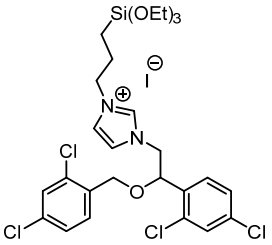

6

^{1}H NMR (360 MHz, $CDCl_3$)

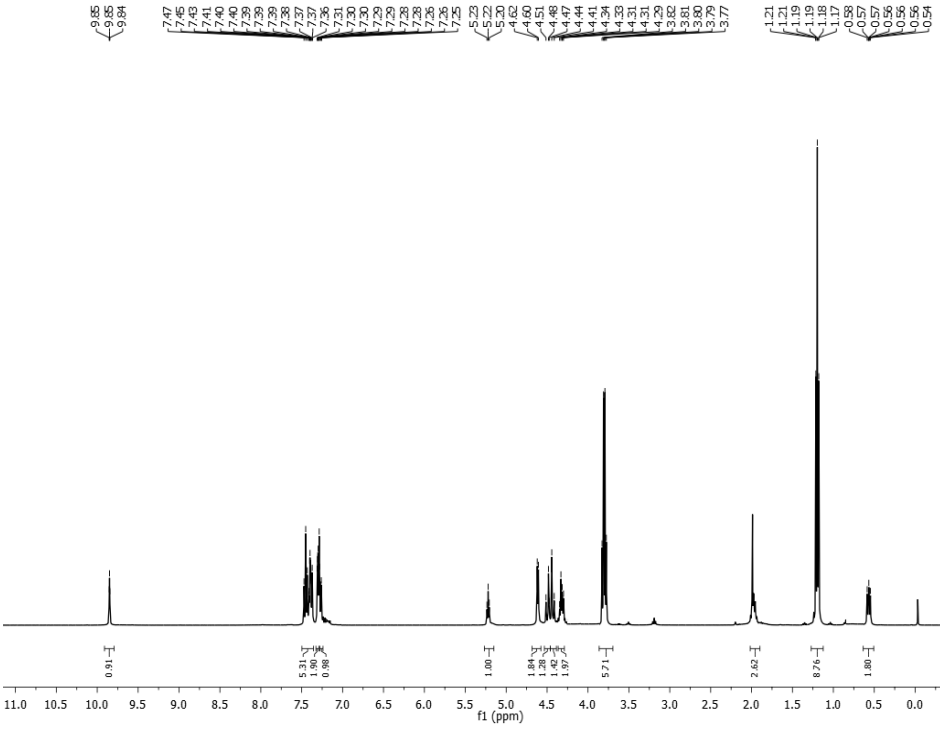

^{13}C NMR (91 MHz, $CDCl_3$)

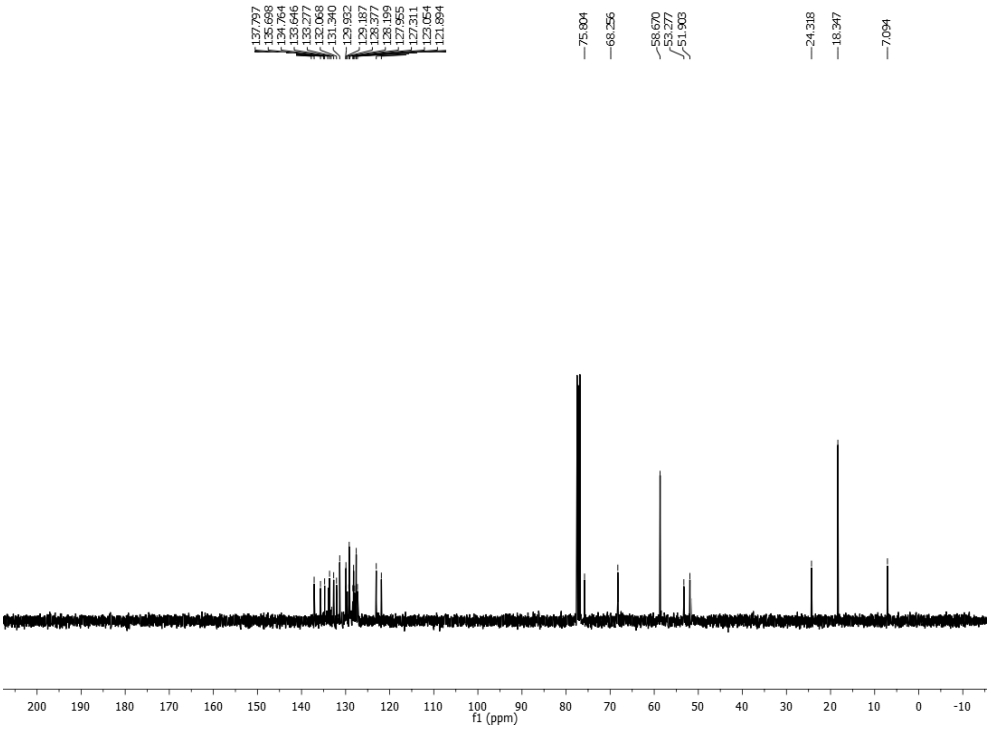

Annex: collection of spectra and characterization data

IR (ATR)

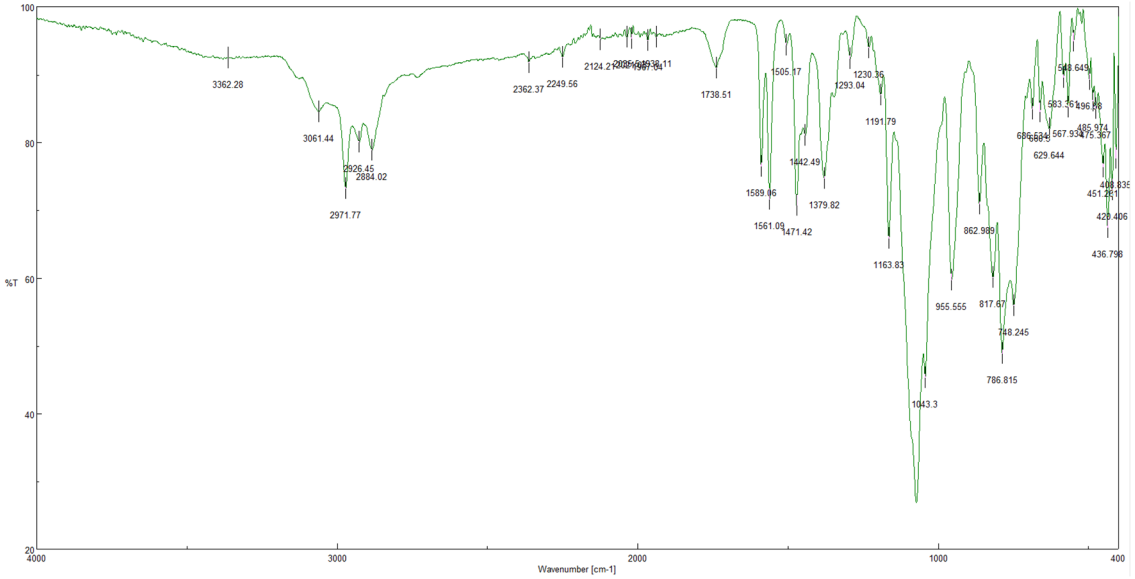

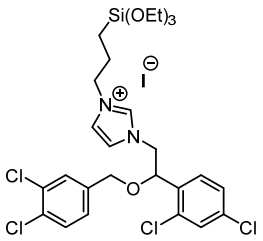

7

^{1}H NMR (360 MHz, $CDCl_3$)

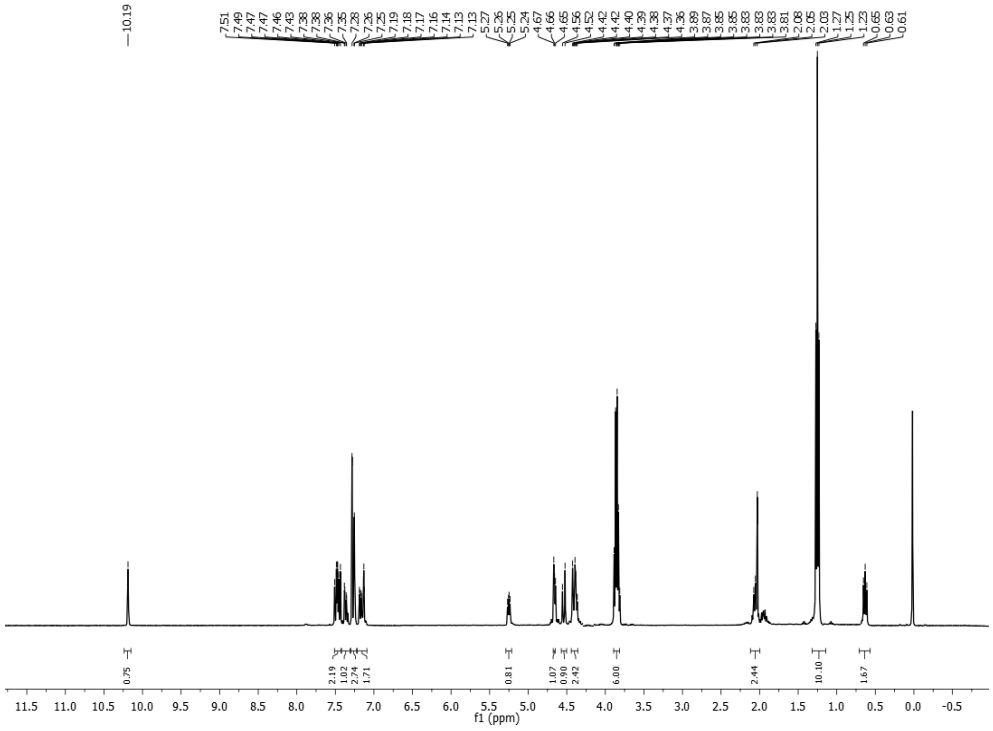

^{13}C NMR (91 MHz, $CDCl_3$)

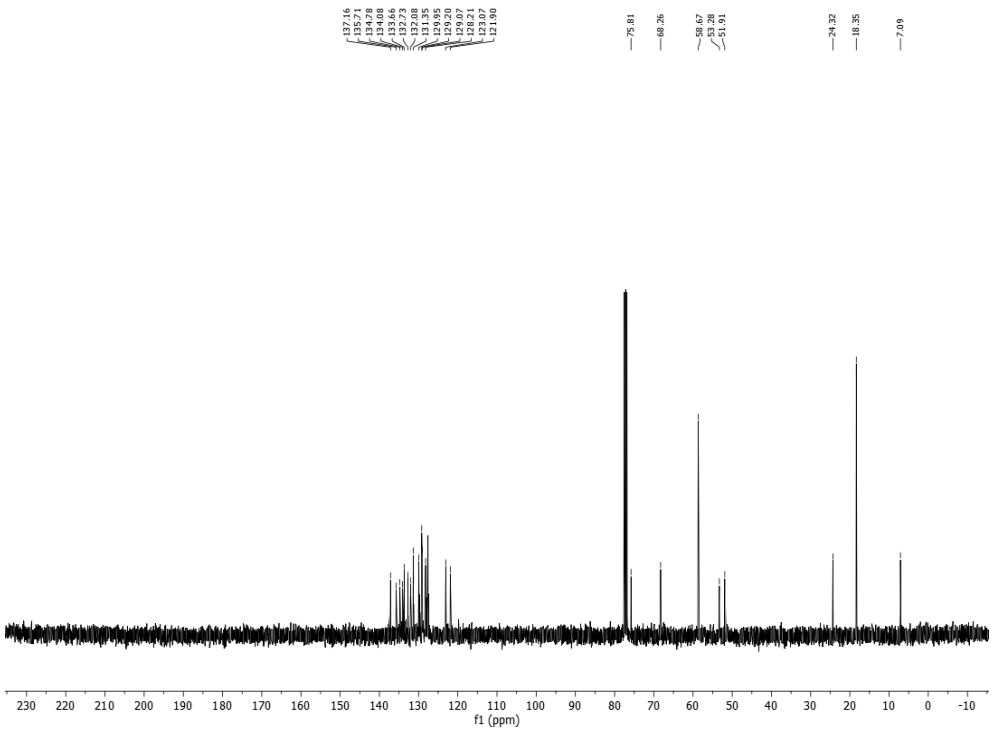

Annex: collection of spectra and characterization data

IR (ATR)

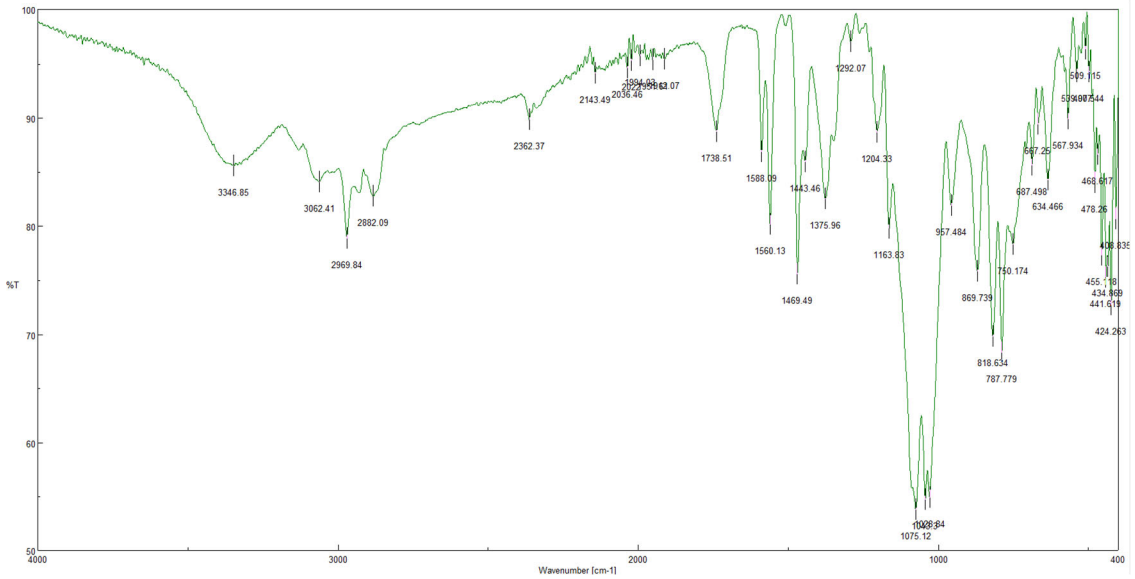

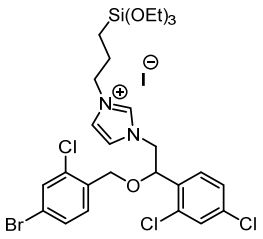

8

^{1}H NMR (360 MHz, $CDCl_3$)

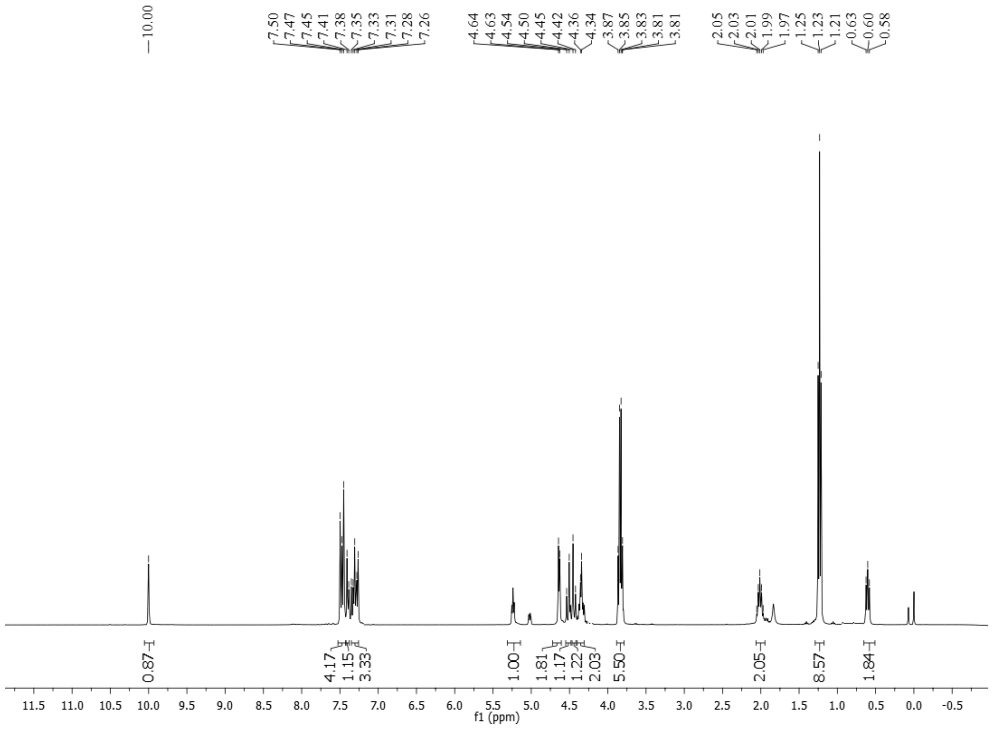

^{13}C NMR (91 MHz, $CDCl_3$)

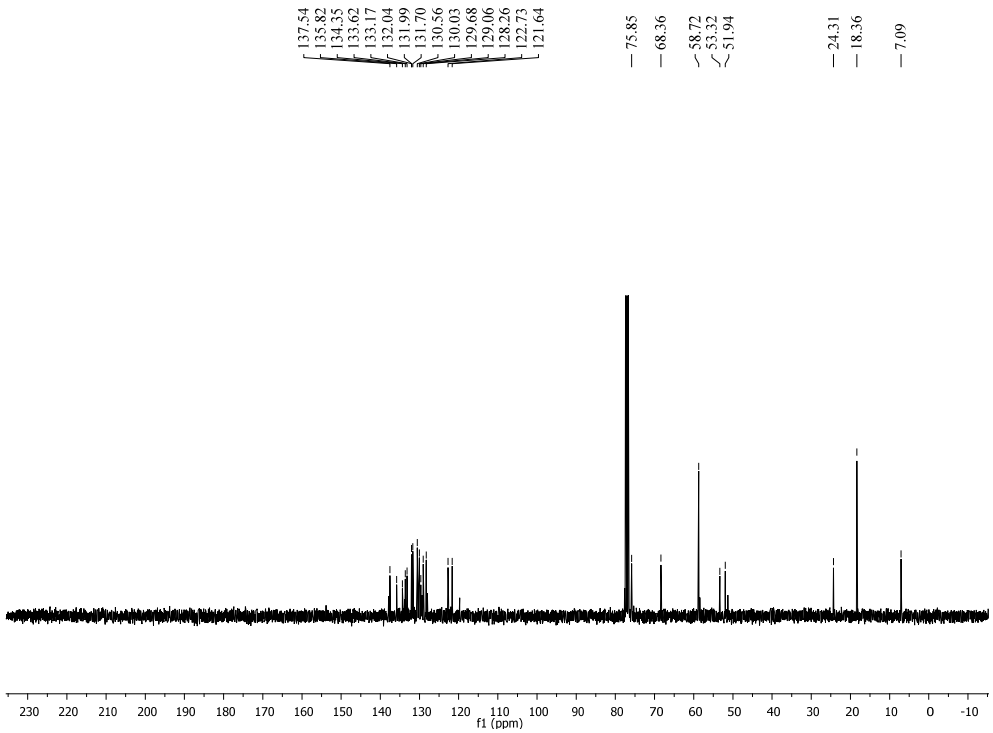

Annex: collection of spectra and characterization data

IR (ATR)

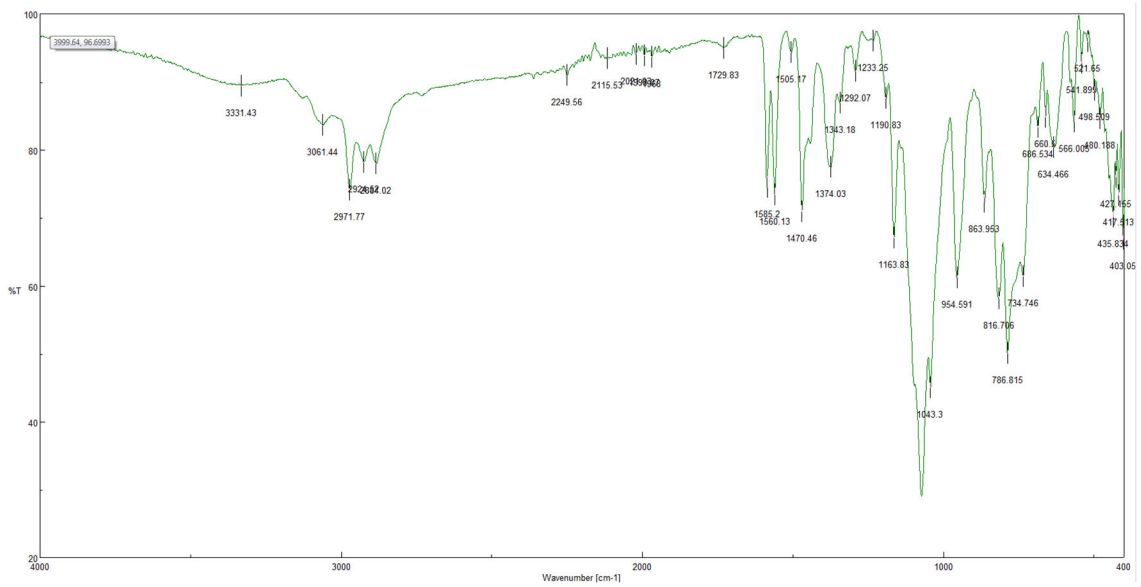

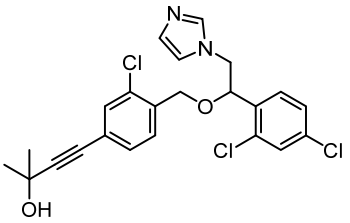

9

^{1}H NMR (360 MHz, MeOD)

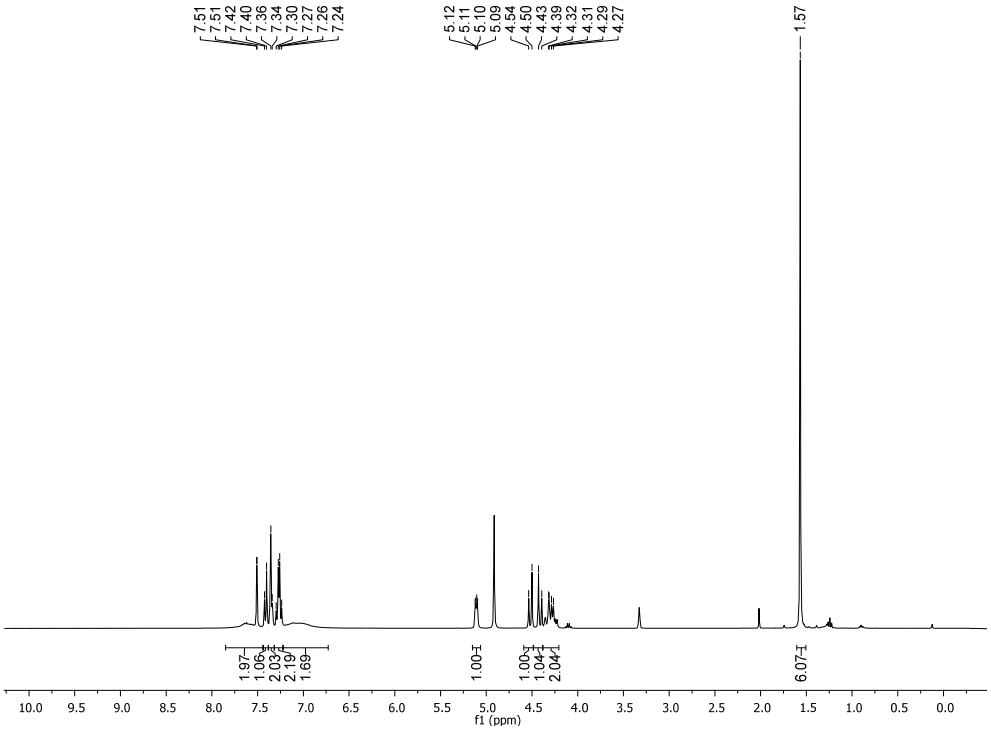

^{13}C NMR (91 MHz, MeOD)

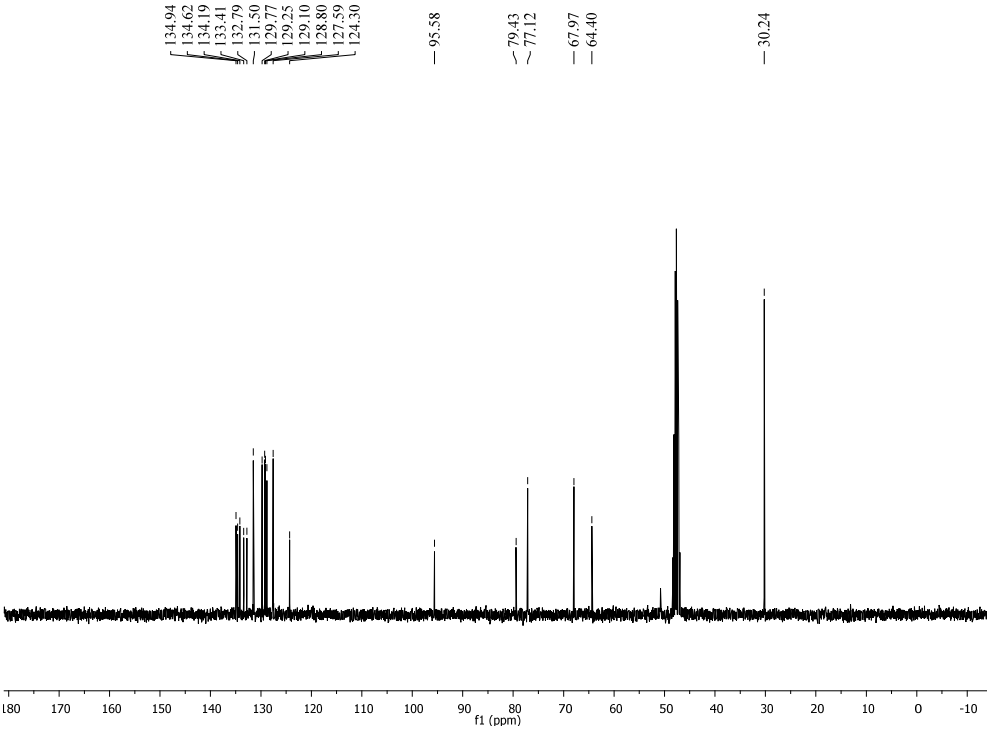

IR (ATR)

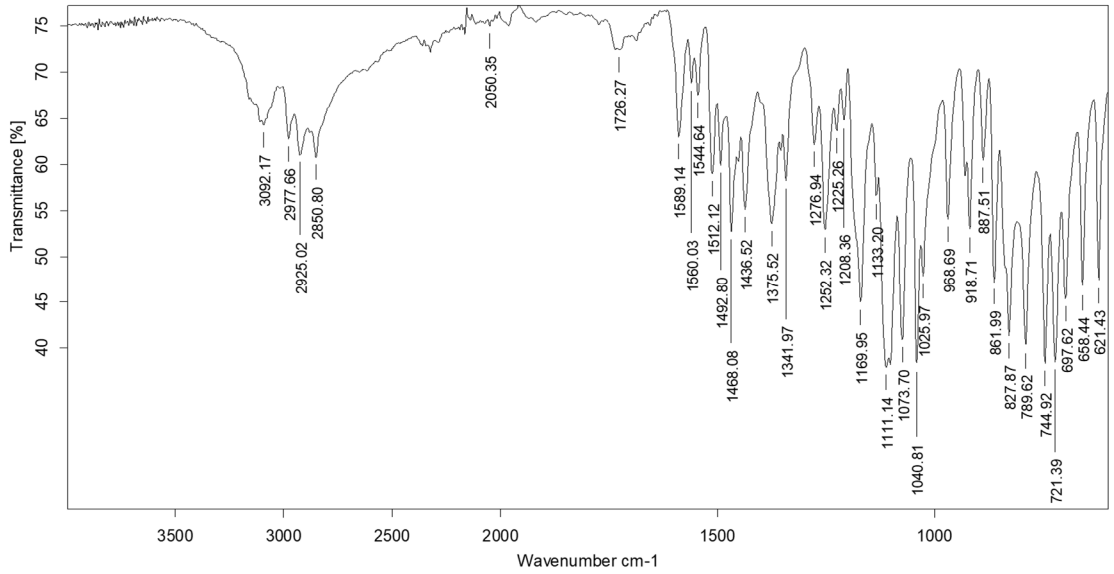
Transmittance [%]
75
70
65
60
55
50
45
40
3092.17
2977.66
2925.02
2850.80
2050.35
1726.27
1589.14
1560.03
1544.64
1512.12
1492.80
1468.08
1436.52
1375.52
1341.97
1276.94
1252.32
1225.26
1208.36
1169.95
1133.20
1111.14
1073.70
1040.81
1025.97
968.69
918.71
887.51
861.99
827.87
789.62
744.92
721.39
697.62
658.44
621.43
3500
3000
2500
2000
1500
1000
Wavenumber cm-1

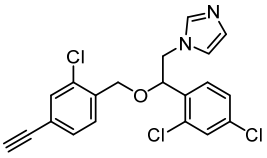

10

^{1}H NMR (360 MHz, $CDCl_3$)

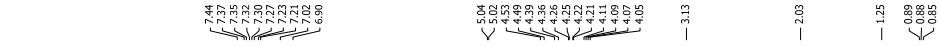

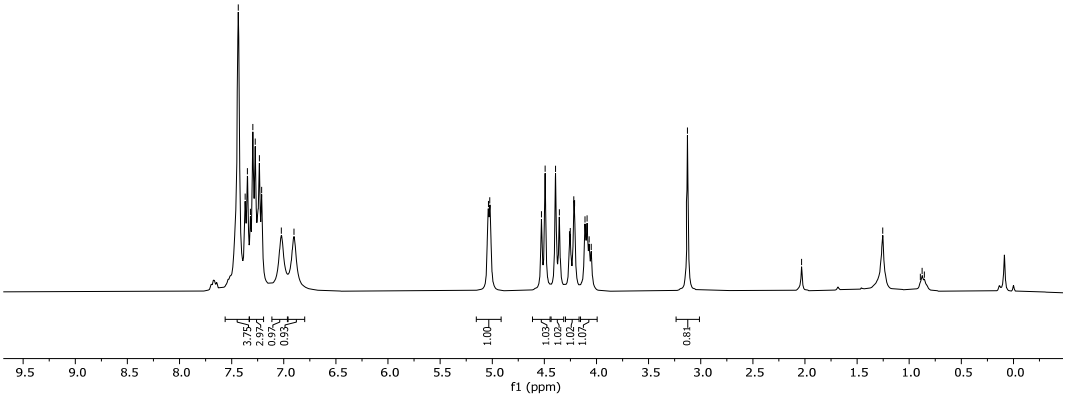

^{13}C NMR (91 MHz, $CDCl_3$)

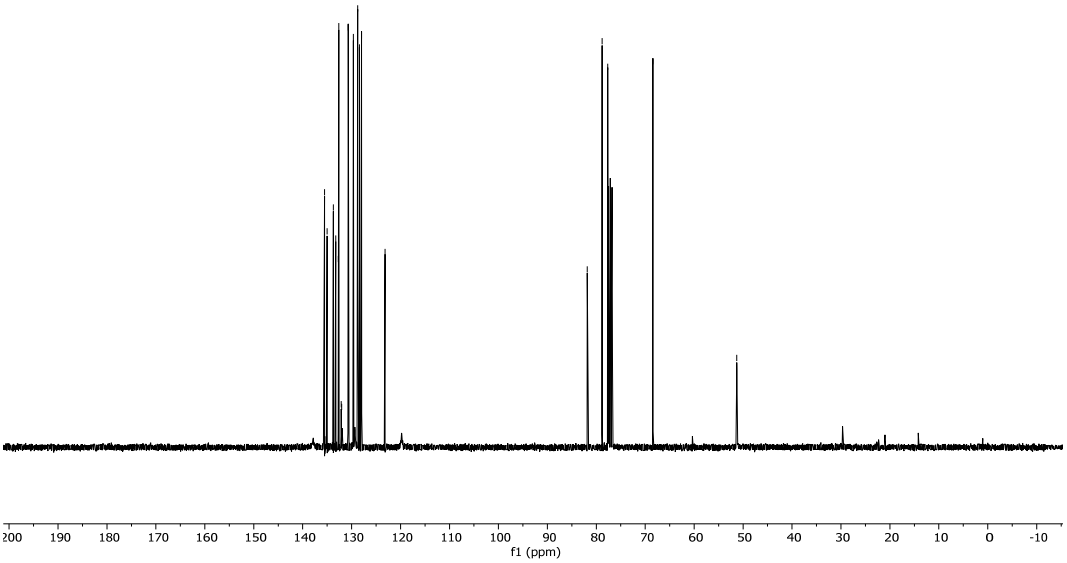

IR (ATR)

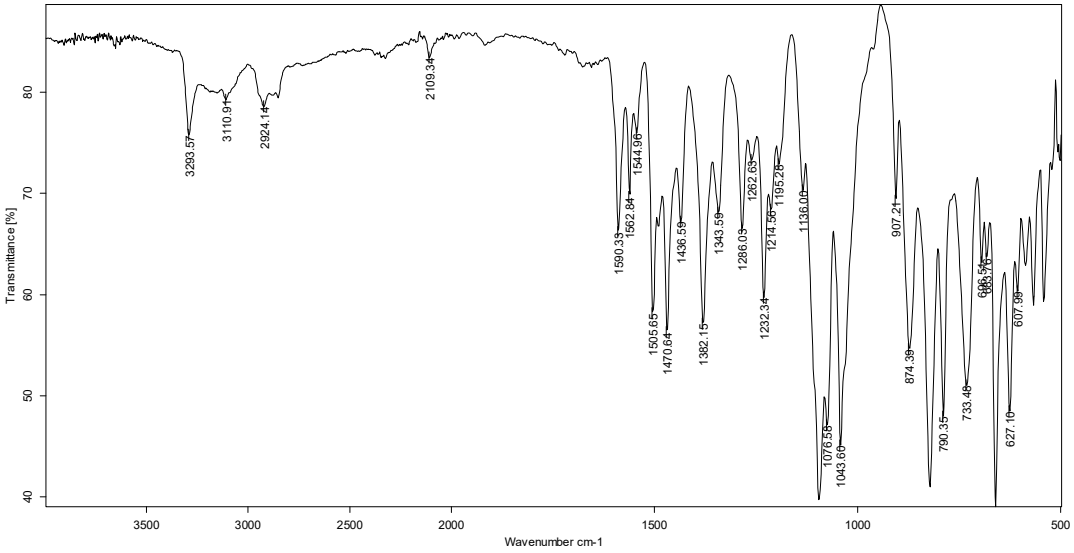
Transmittance [%]
Wavenumber cm-1
3293.57
3110.91
2924.14
2109.34
1590.33
1562.84
1544.96
1505.65
1470.64
1436.59
1382.15
1343.59
1286.03
1262.63
1232.34
1214.55
1195.28
1136.00
1076.58
1043.60
907.21
874.39
790.35
733.48
627.10
607.99

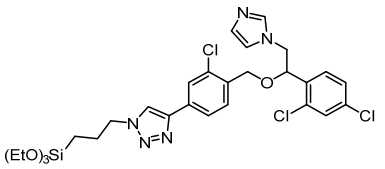

11

^{1}H NMR (360 MHz, $CDCl_3$)

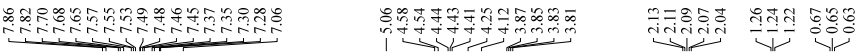

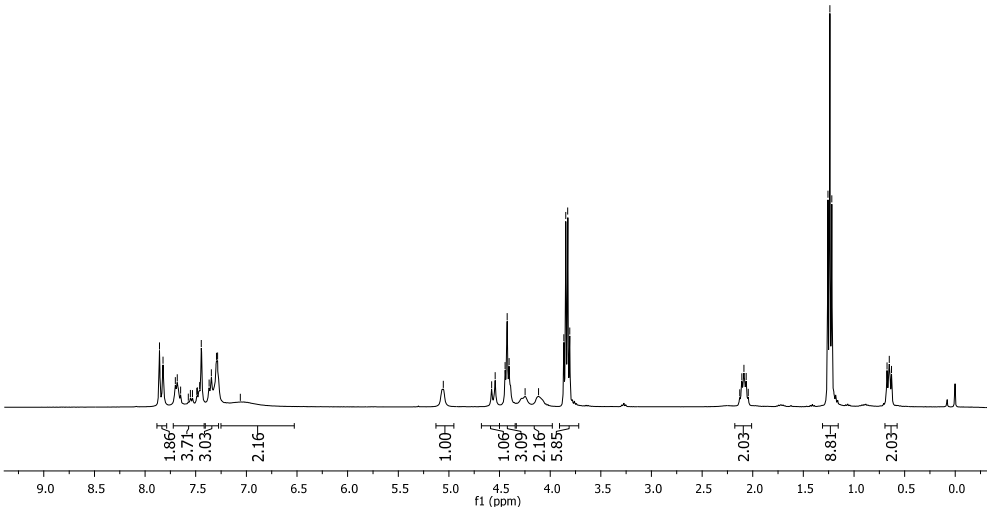

^{13}C NMR (91 MHz, $CDCl_3$)

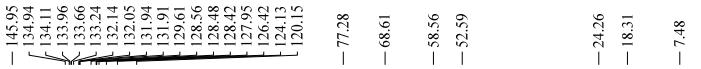

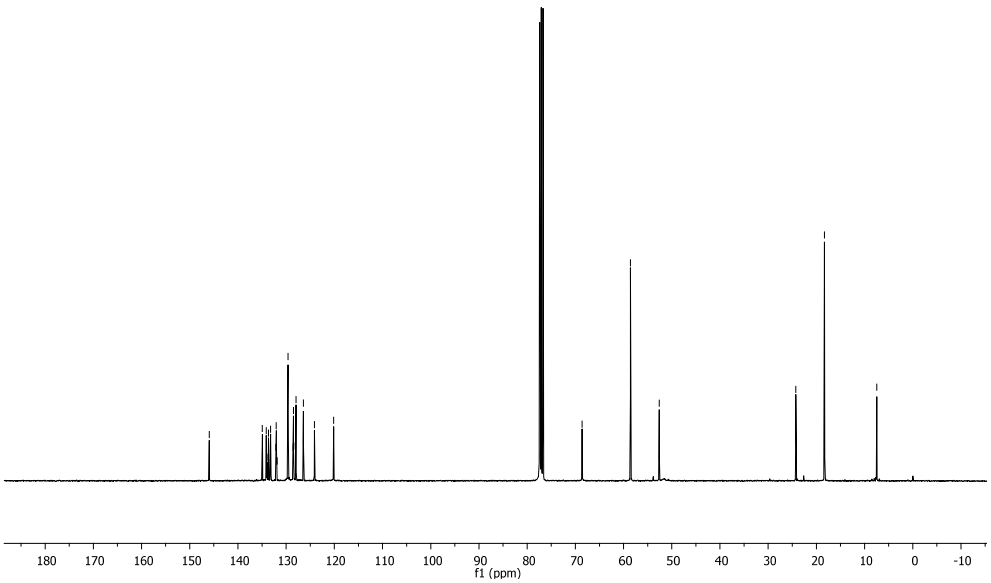

IR (ATR)

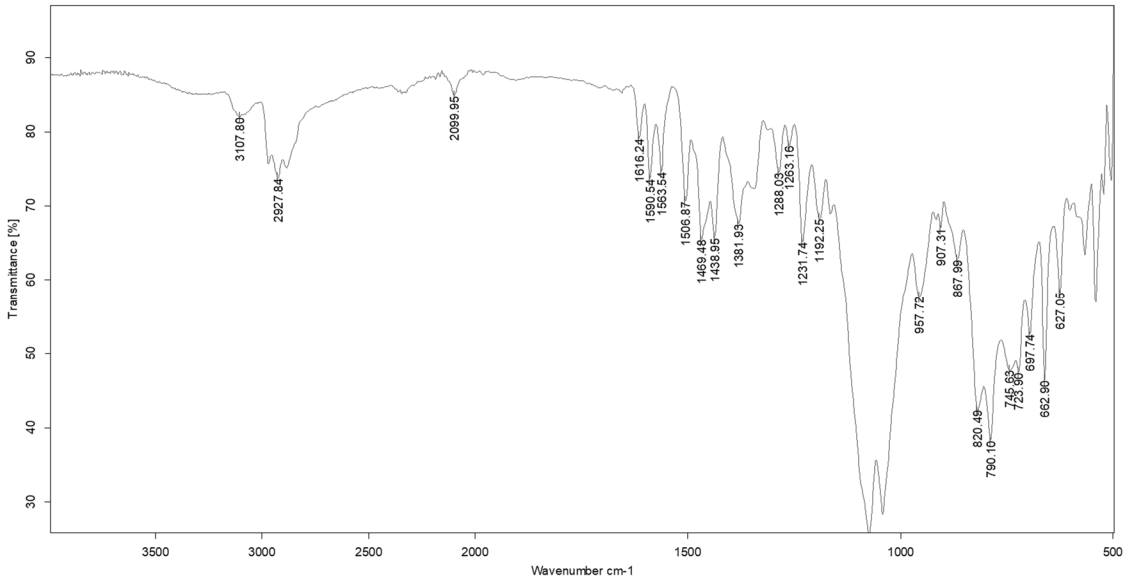
Transmittance [%]
Wavenumber cm-1
3107.80
2927.84
2099.95
1616.24
1590.54
1583.54
1506.87
1469.48
1438.95
1381.99
1288.03
1283.16
1231.74
1192.25
957.72
907.31
867.99
820.49
790.10
745.63
725.96
697.74
662.90
627.05

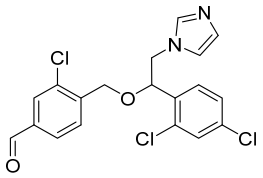

12

^{1}H NMR (360 MHz, $CDCl_3$)

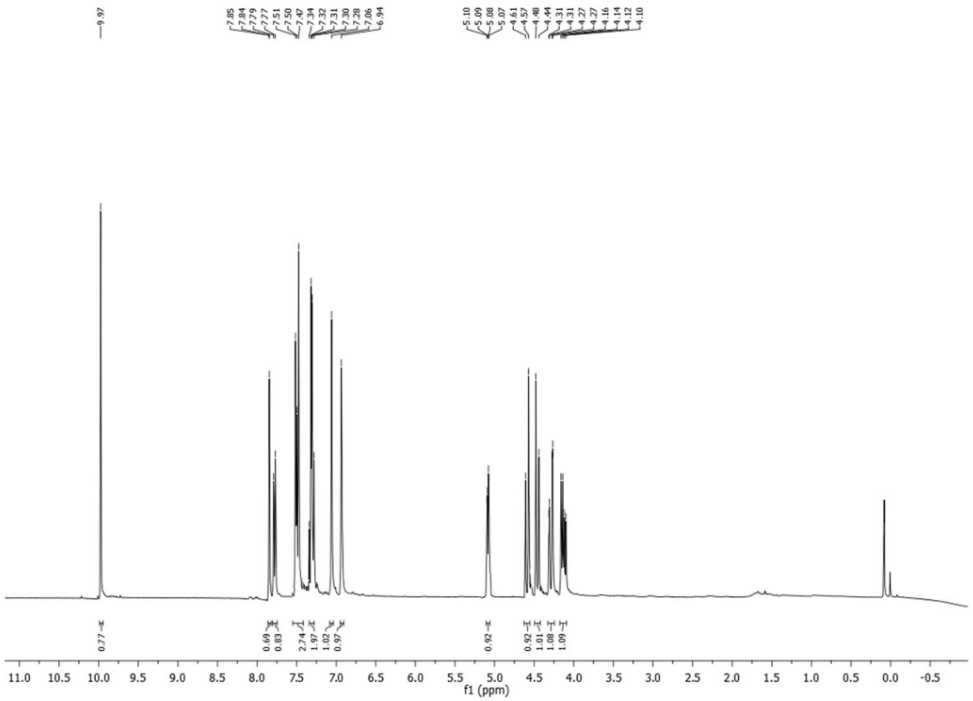

^{13}C NMR (91 MHz, $CDCl_3$)

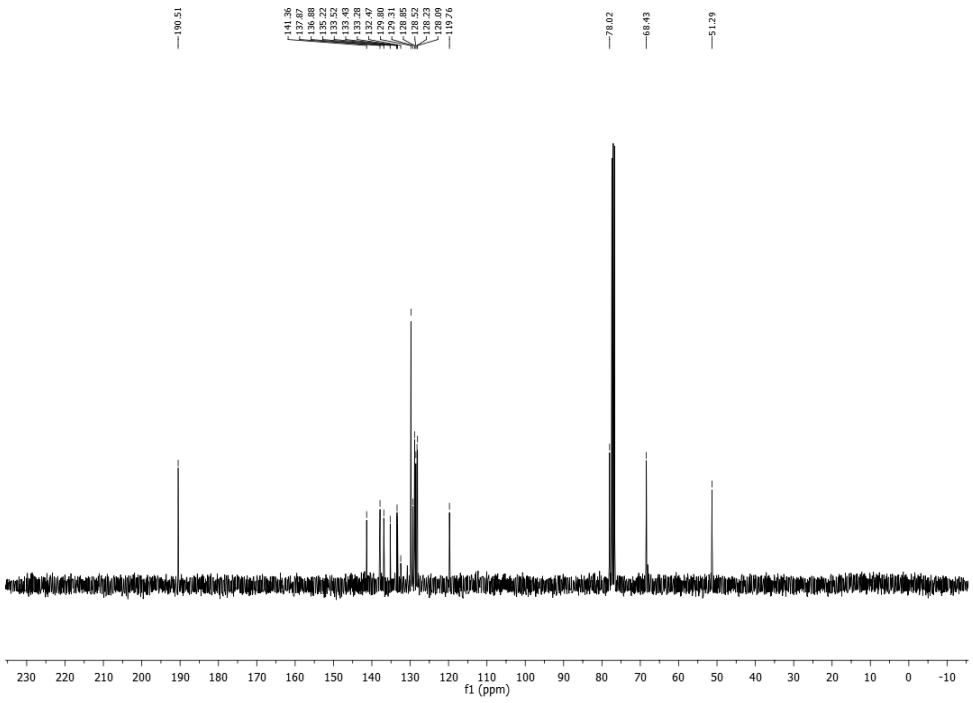

Annex: collection of spectra and characterization data

IR (ATR)

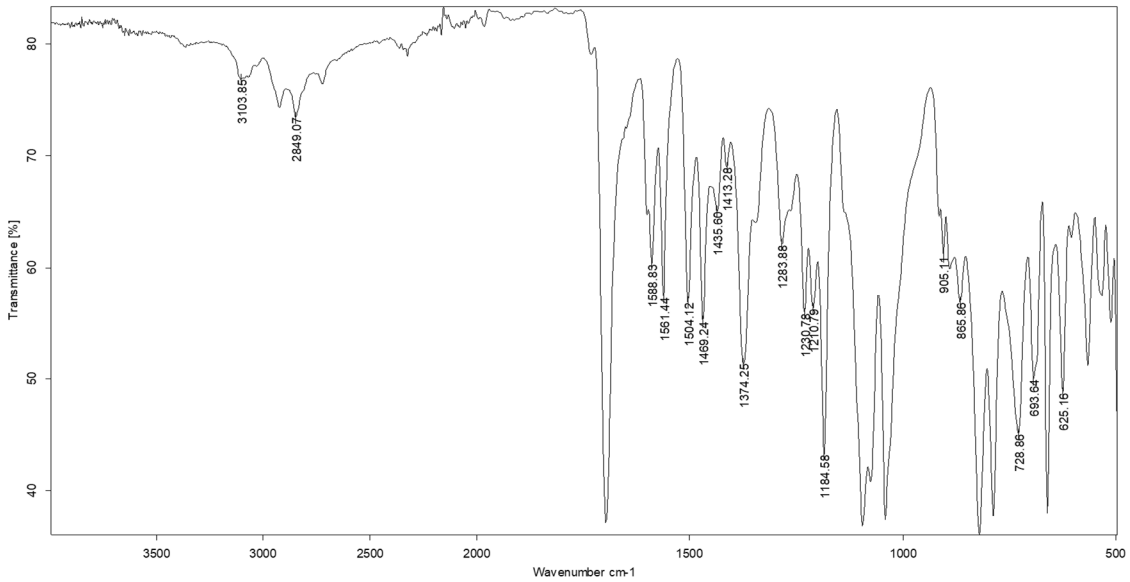

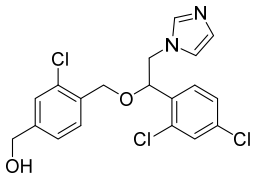

13

^{1}H NMR (360 MHz, $CDCl_3$)

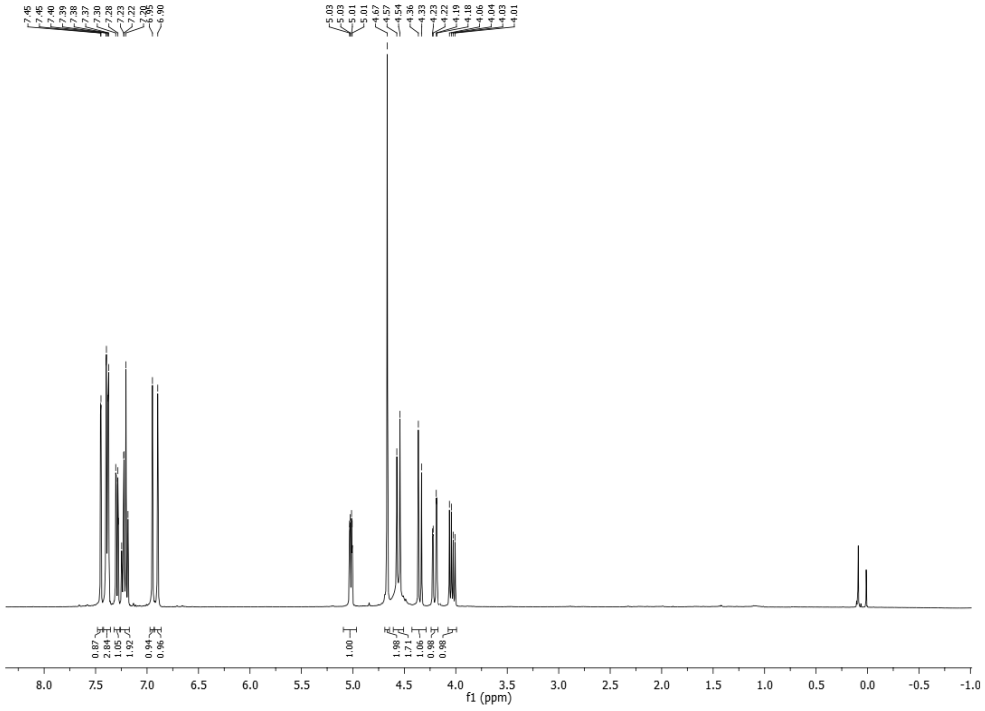

^{13}C NMR (91 MHz, $CDCl_3$)

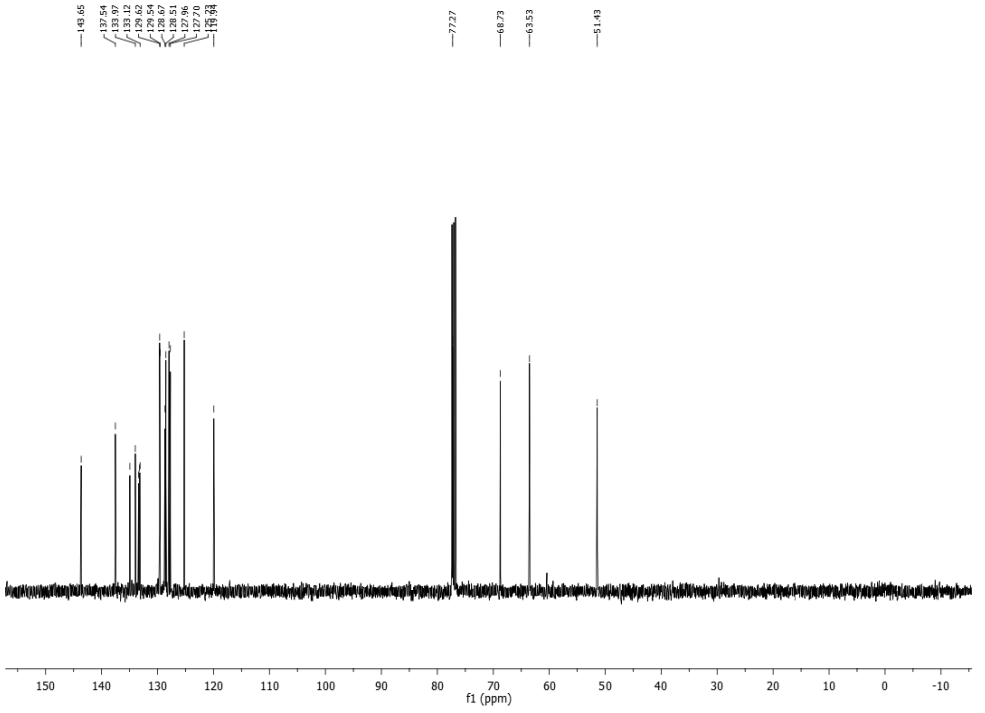

Annex: collection of spectra and characterization data

IR (ATR)

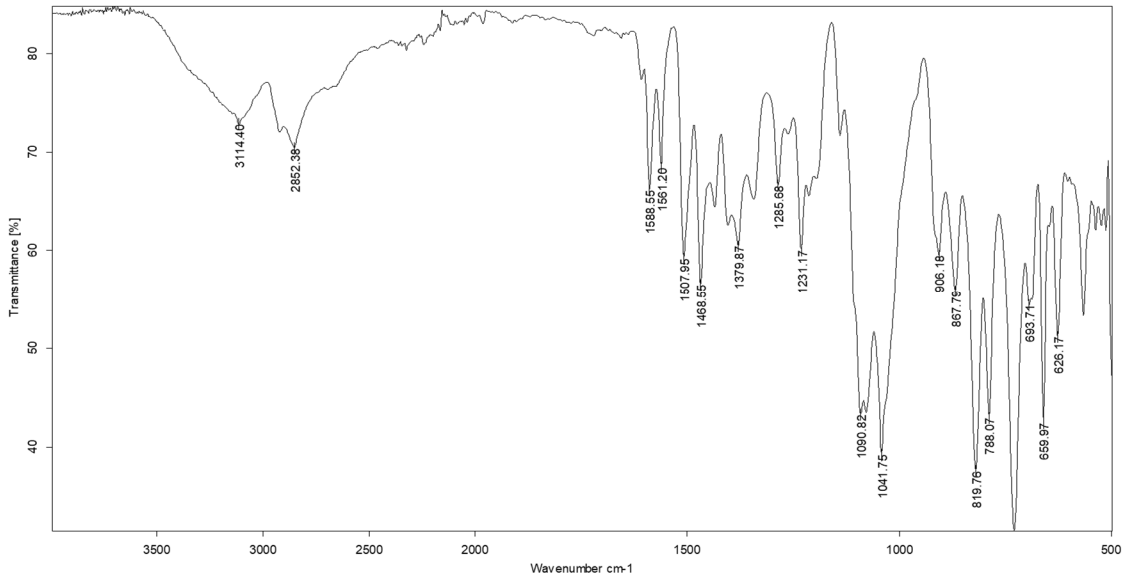

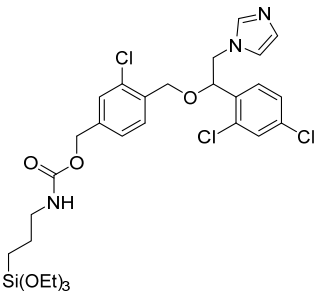

14

^{1}H NMR (360 MHz, $CDCl_3$)

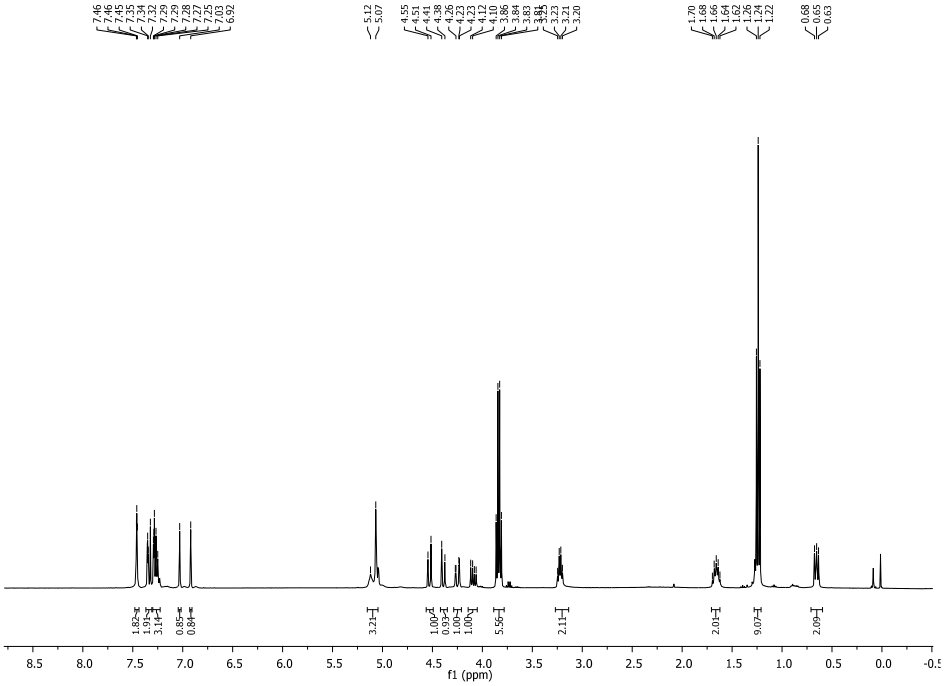

^{13}C NMR (91 MHz, $CDCl_3$)

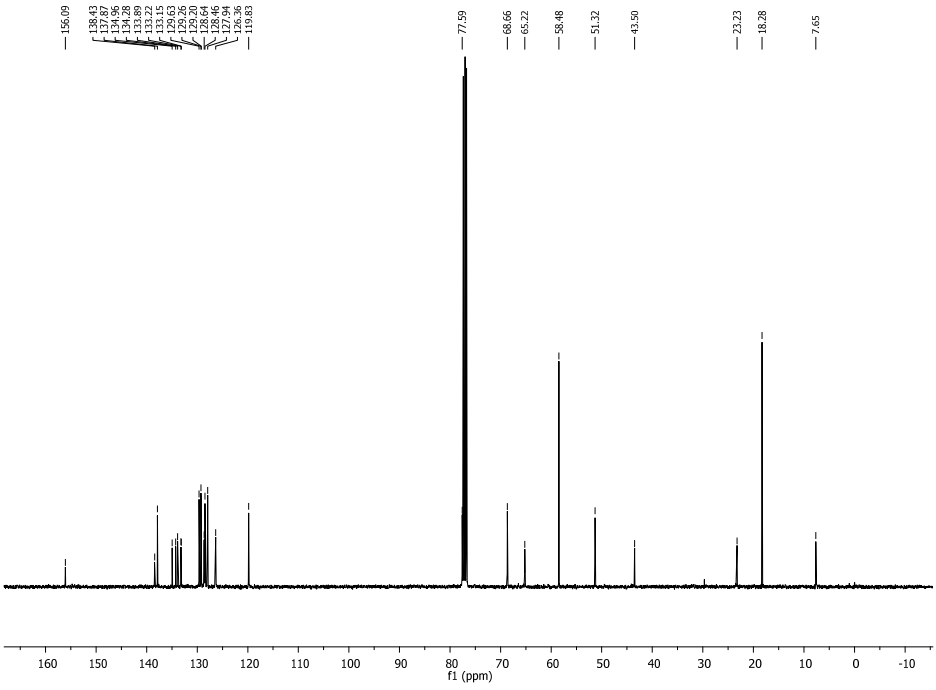

IR (ATR)

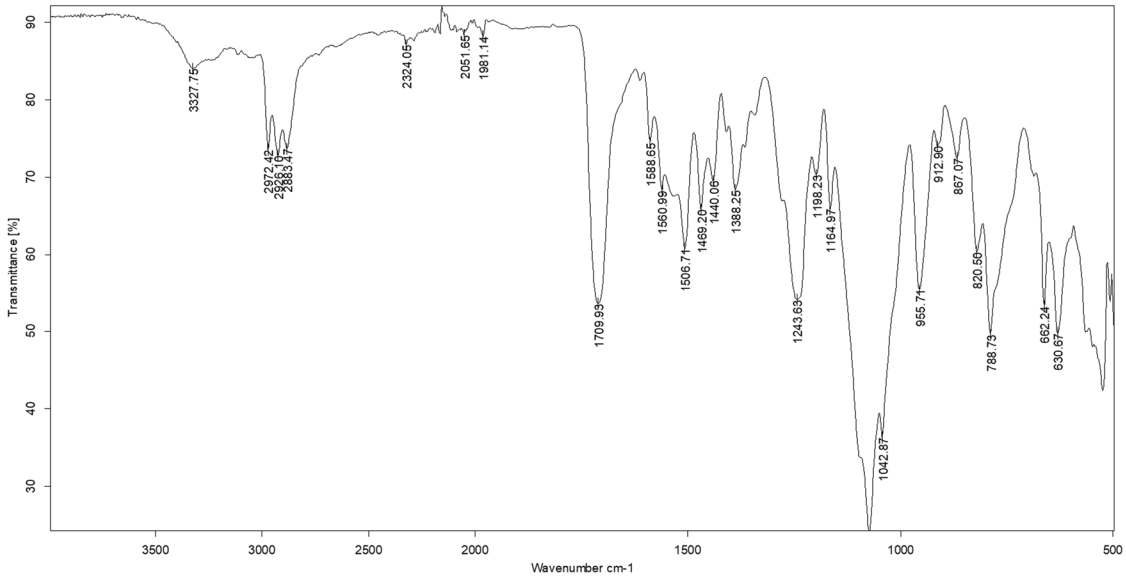
Transmittance [%]
Wavenumber cm-1
3327.75
2927.42
2888.01
2853.47
2324.05
2051.65
1981.14
1709.99
1588.65
1560.99
1506.71
1469.20
1440.06
1388.25
1243.63
1198.23
1164.97
1042.87
955.71
912.90
867.07
820.50
788.73
662.24
630.67

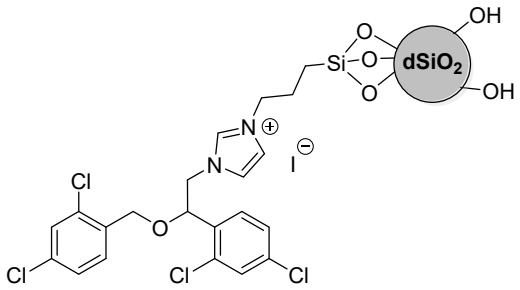

dN1

DLS

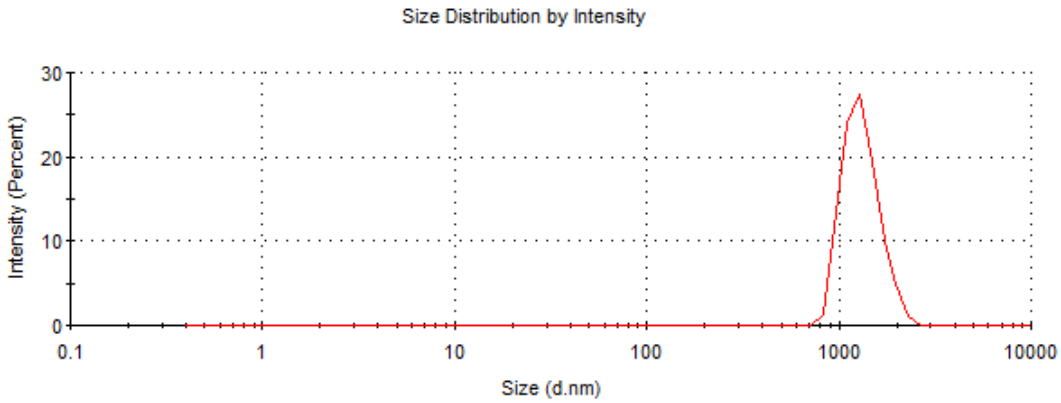

Zeta-potential

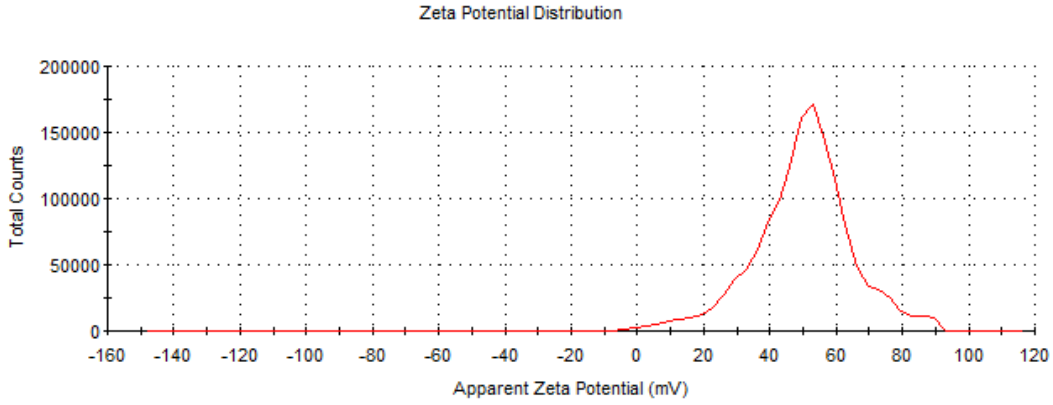

TEM

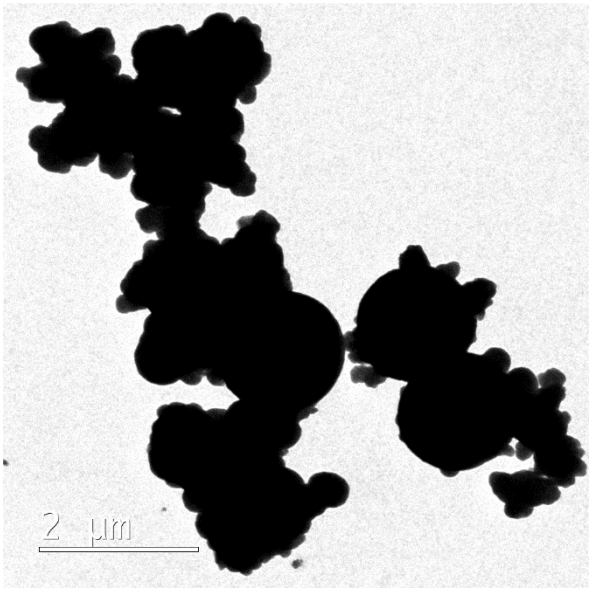
2 µm

IR (ATR)

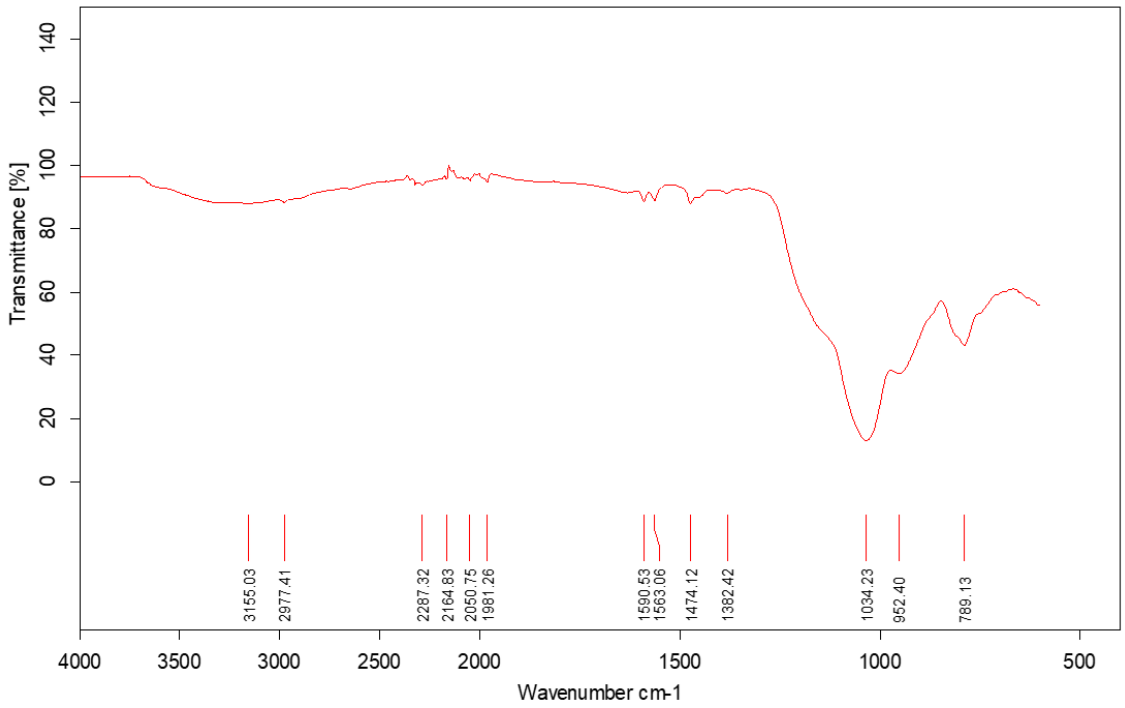
Transmittance [%]
0
20
40
60
80
100
120
140
3155.03
2977.41
2287.32
2164.83
2050.75
1981.26
1590.53
1563.06
1474.12
1382.42
1034.23
952.40
789.13
4000
3500
3000
2500
2000
1500
1000
500
Wavenumber cm-1

^{13}C CP MAS NMR

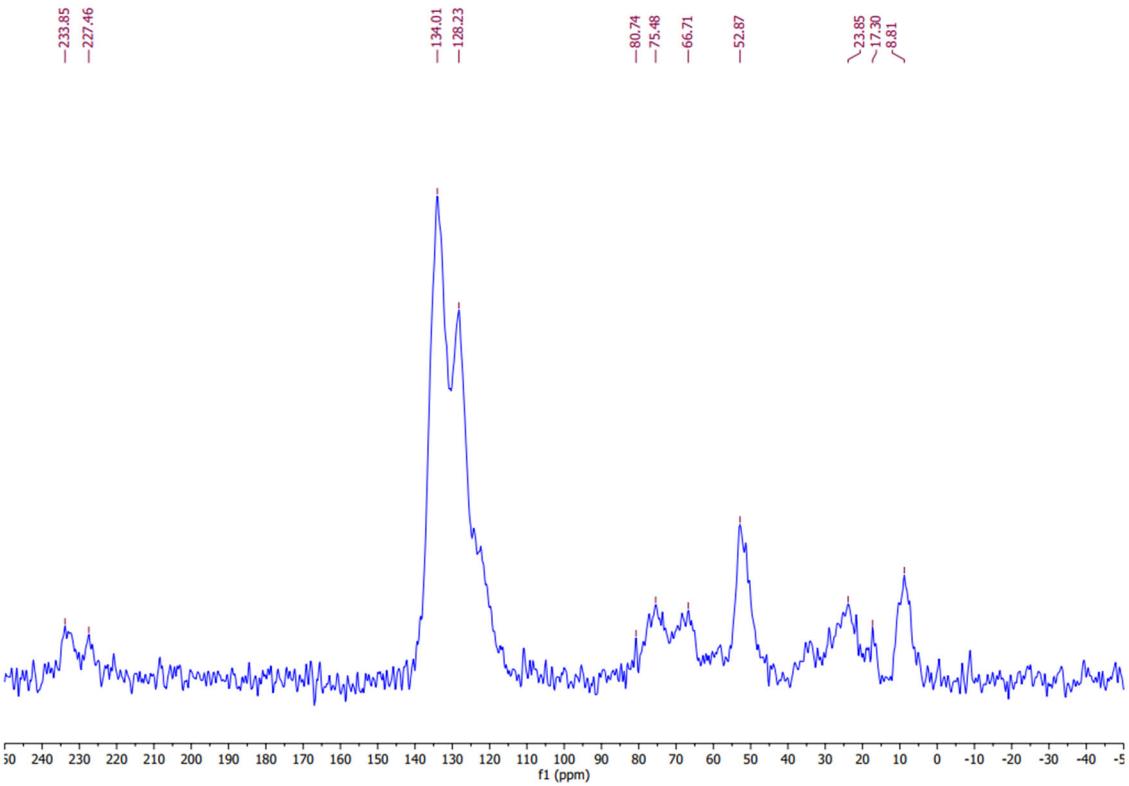

^{29}Si CP MAS NMR

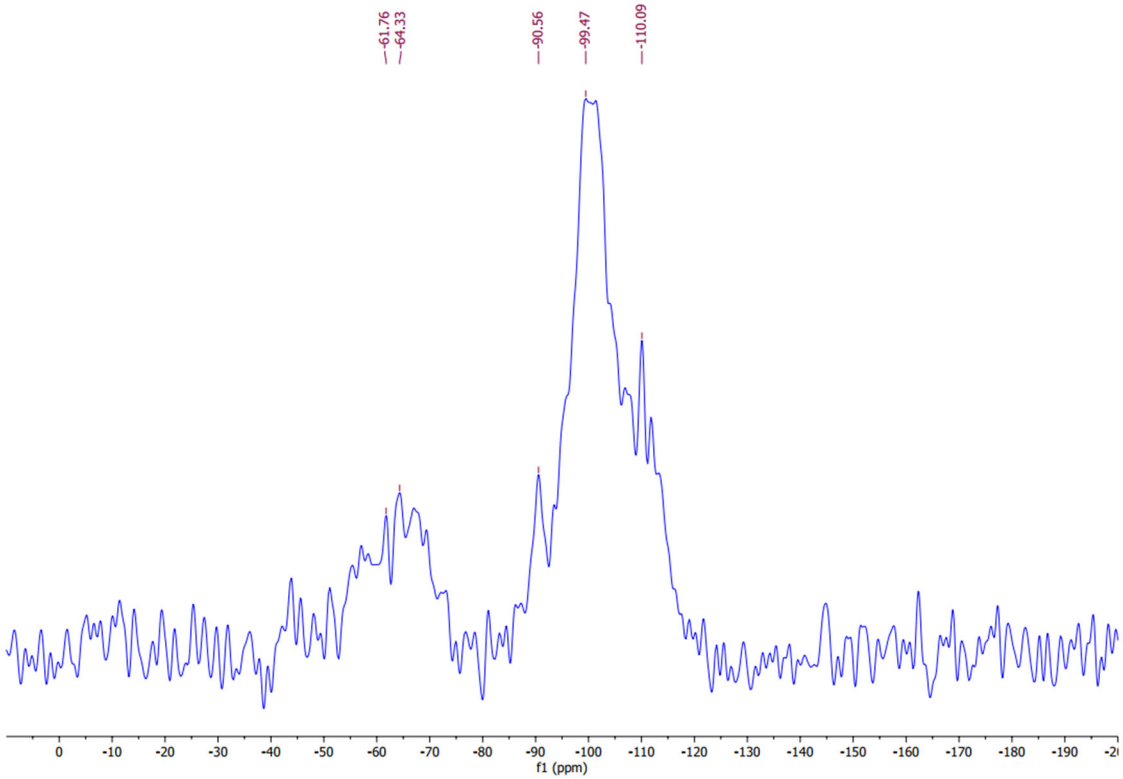

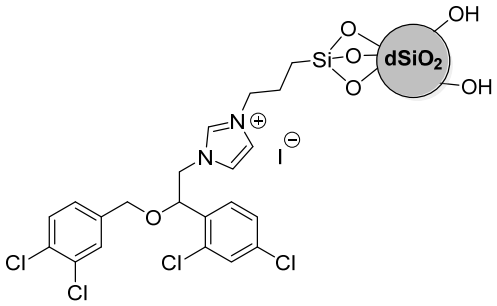

dN2

DLS

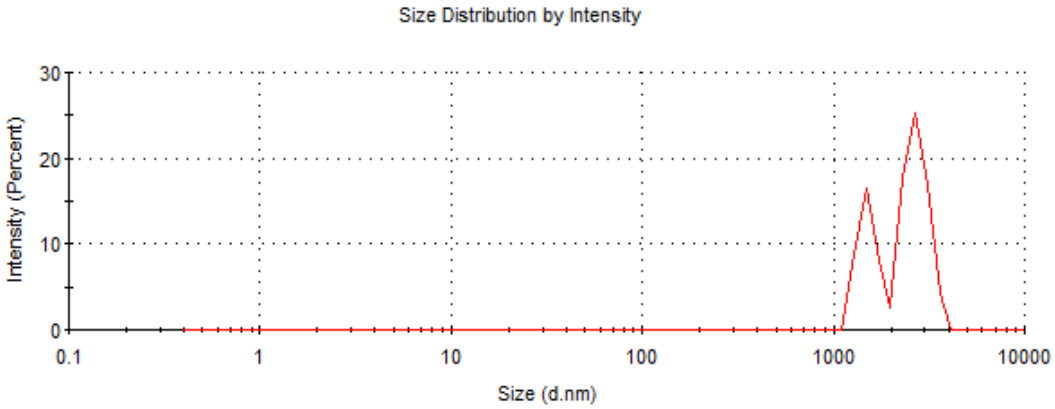

High polydispersity

Zeta-potential

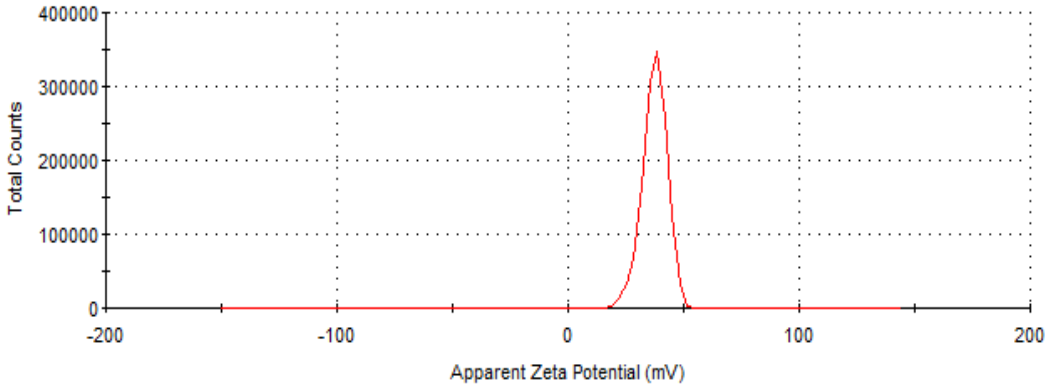

TEM

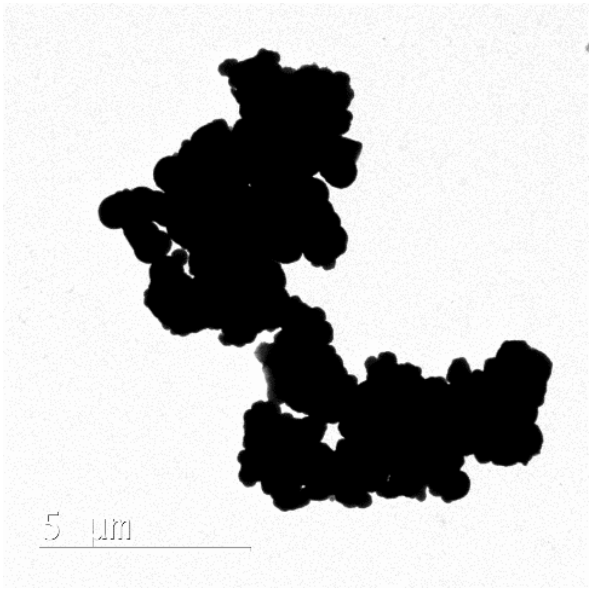
5 µm

IR (ATR)

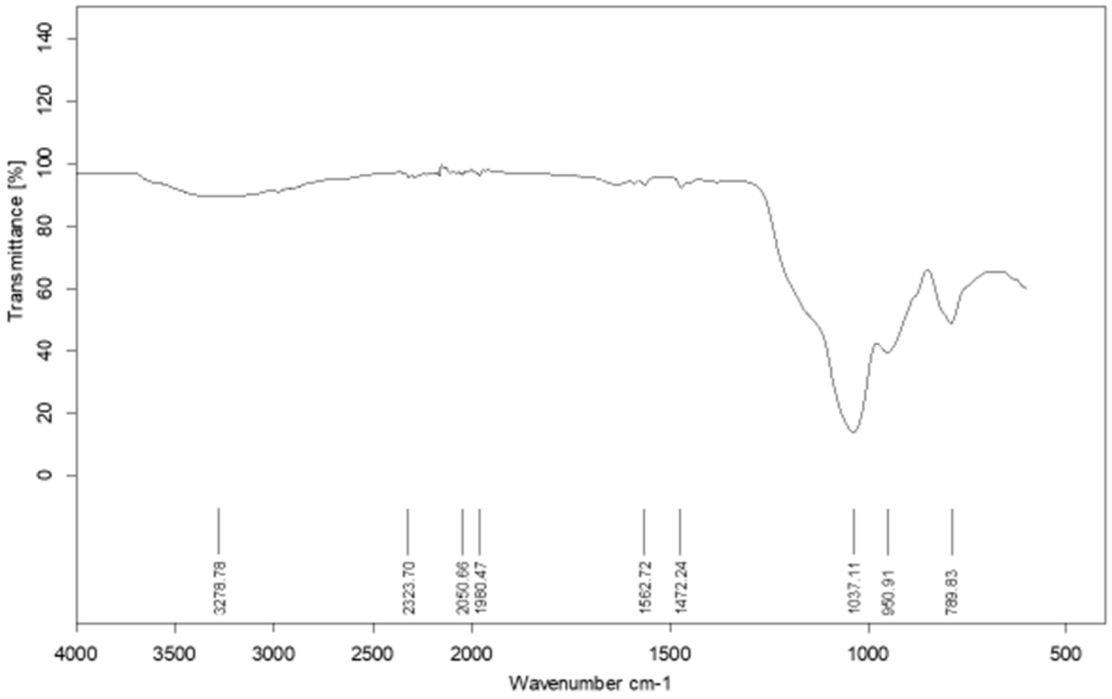
Transmittance [%]
0
20
40
60
80
100
120
140
3278.78
2323.70
2050.66
1980.47
1562.72
1472.24
1037.11
950.91
789.83
4000
3500
3000
2500
2000
1500
1000
500
Wavenumber cm-1

Annex: collection of spectra and characterization data

^{13}C CP MAS NMR

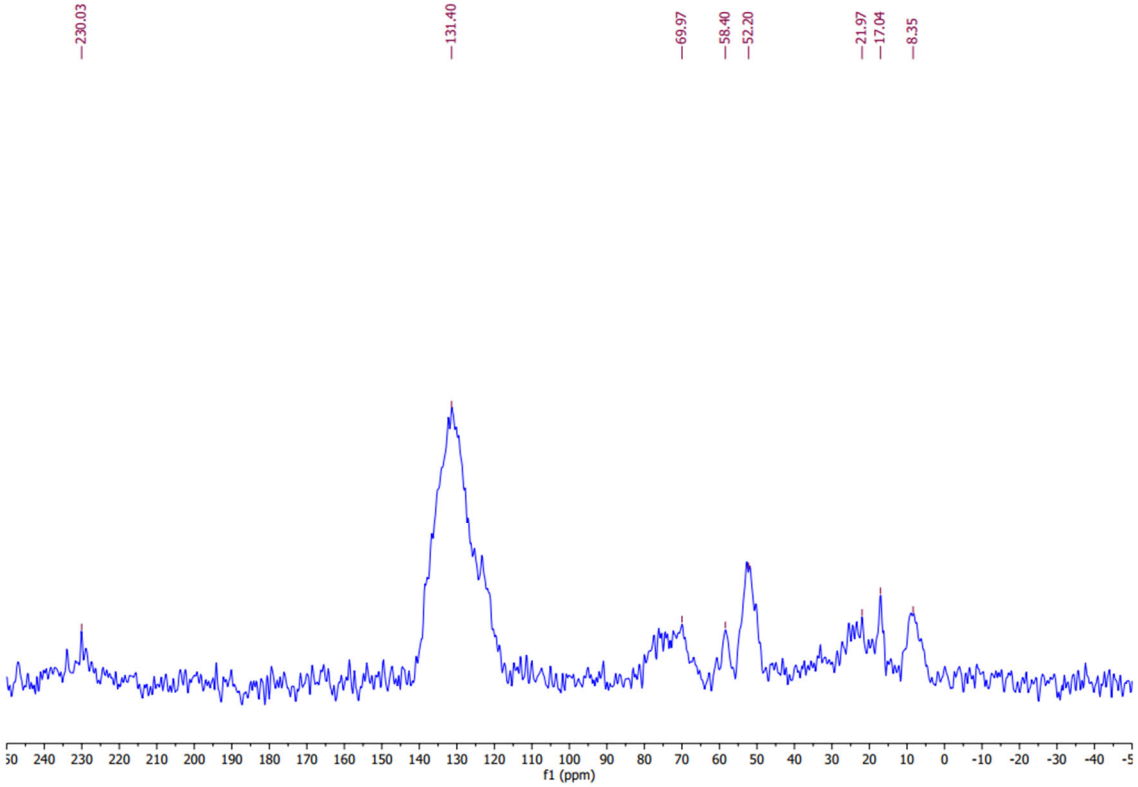

^{29}Si CP MAS NMR

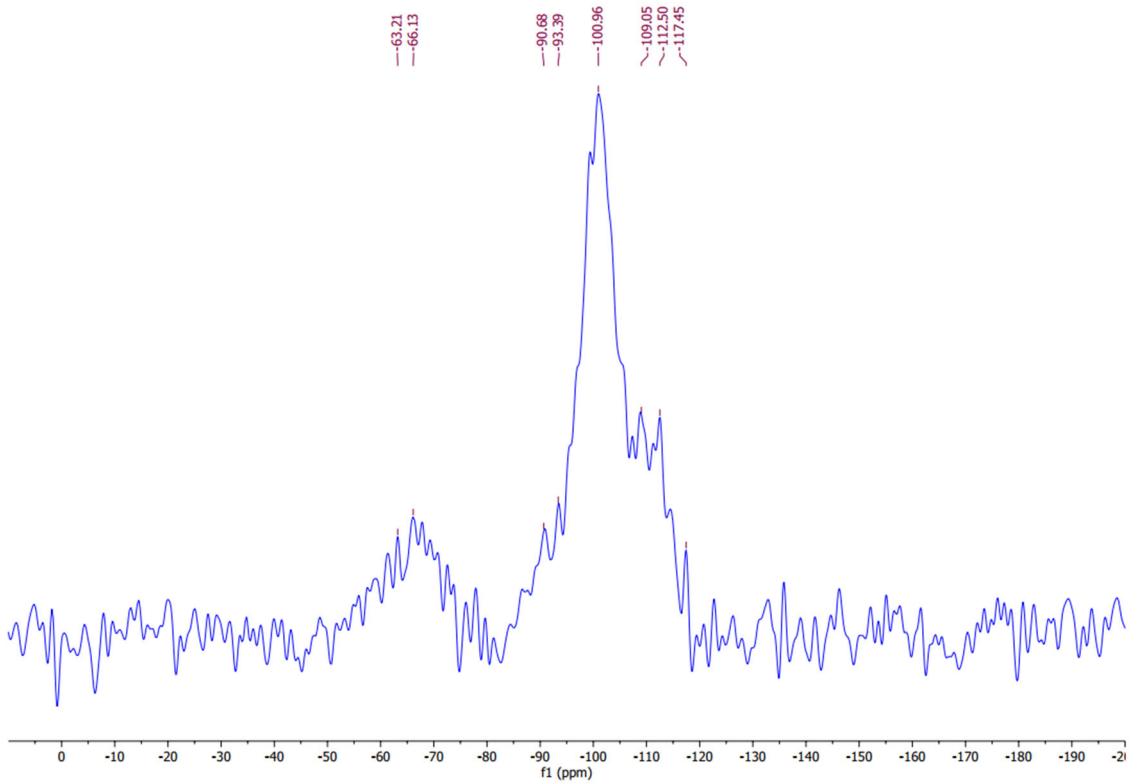

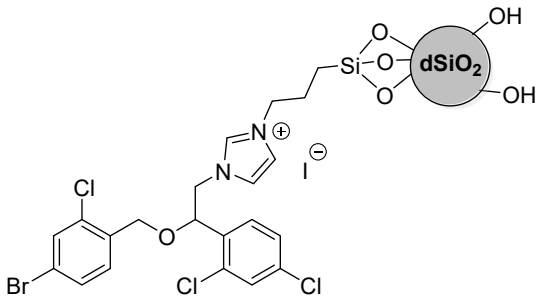

dN3

DLS

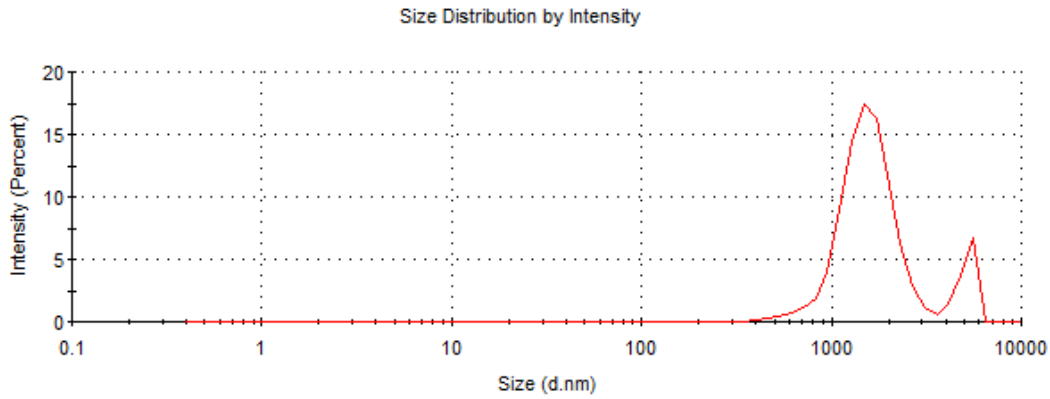

High polydispersity

Zeta-potential

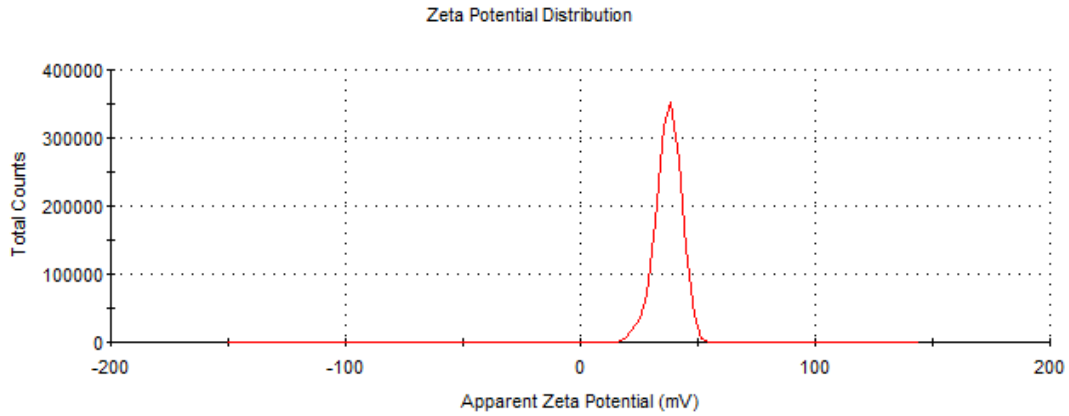

TEM

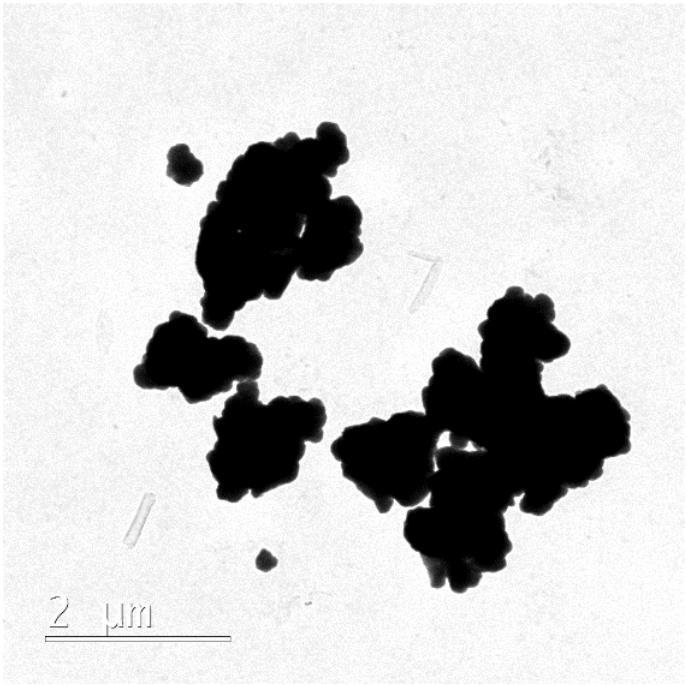
2 µm

IR (ATR)

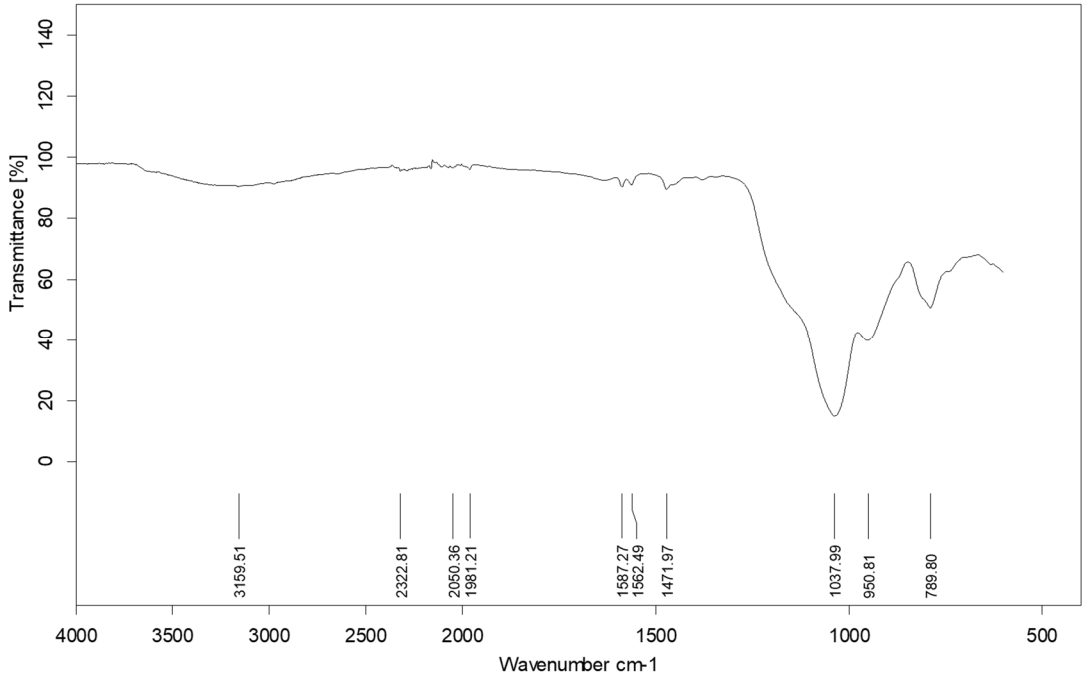
Transmittance [%]
0
20
40
60
80
100
120
140
3159.51
2322.81
2050.36
1981.21
1587.27
1562.49
1471.97
1037.99
950.81
789.80
4000
3500
3000
2500
2000
1500
1000
500
Wavenumber cm-1

^{13}C CP MAS NMR

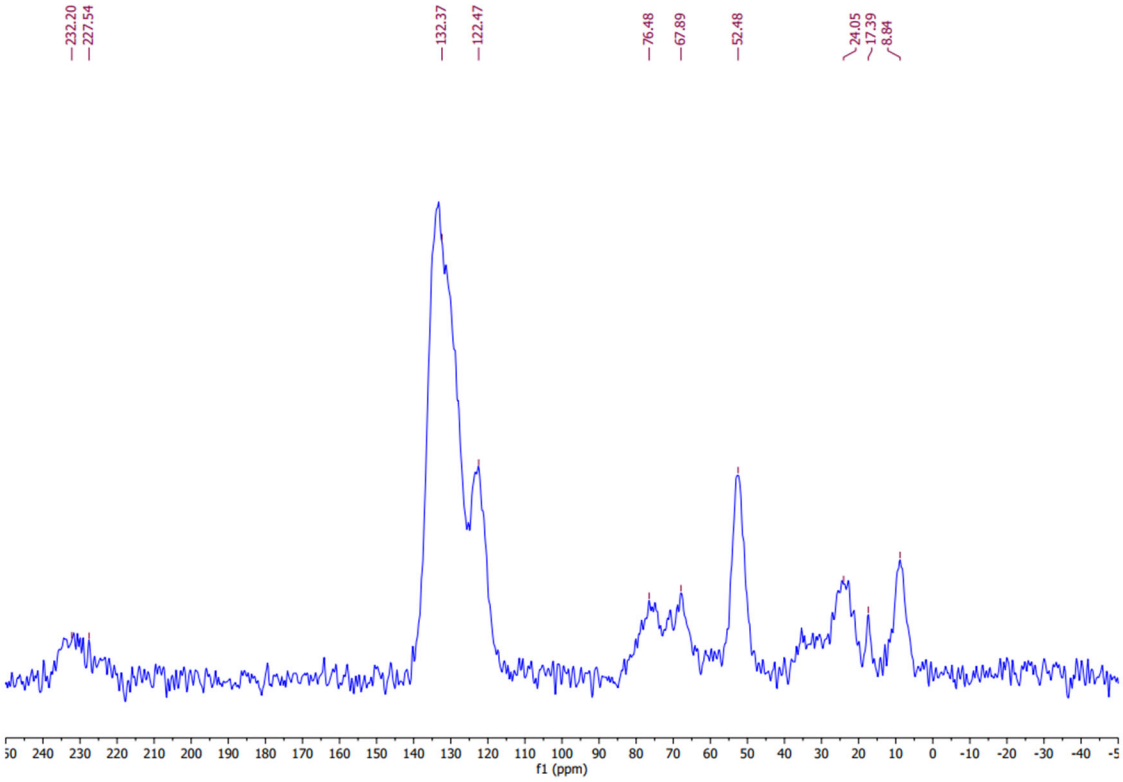

^{29}Si CP MAS NMR

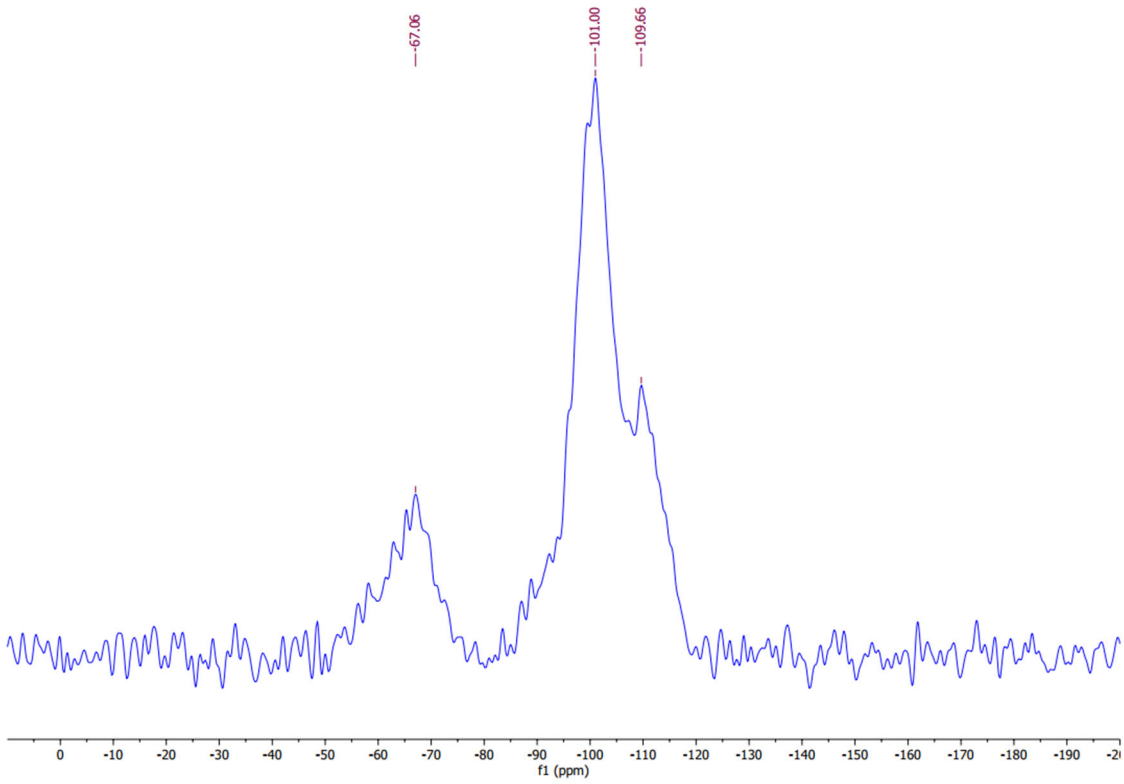

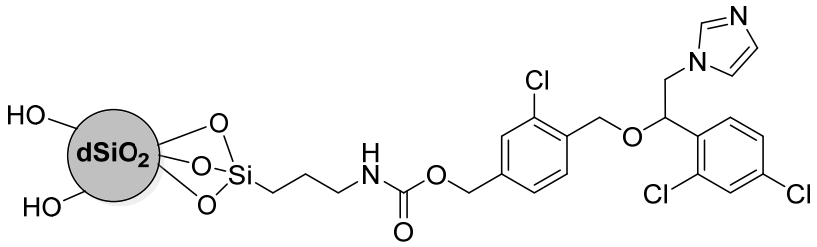

dN4

DLS

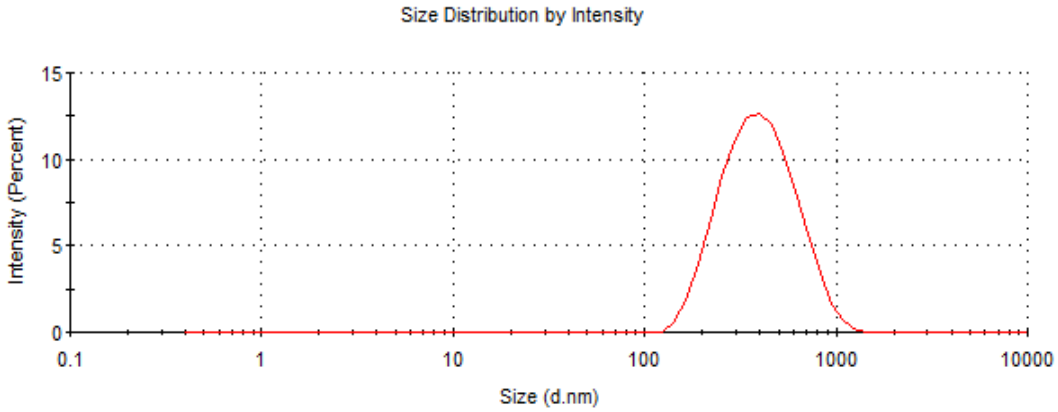

Zeta-potential

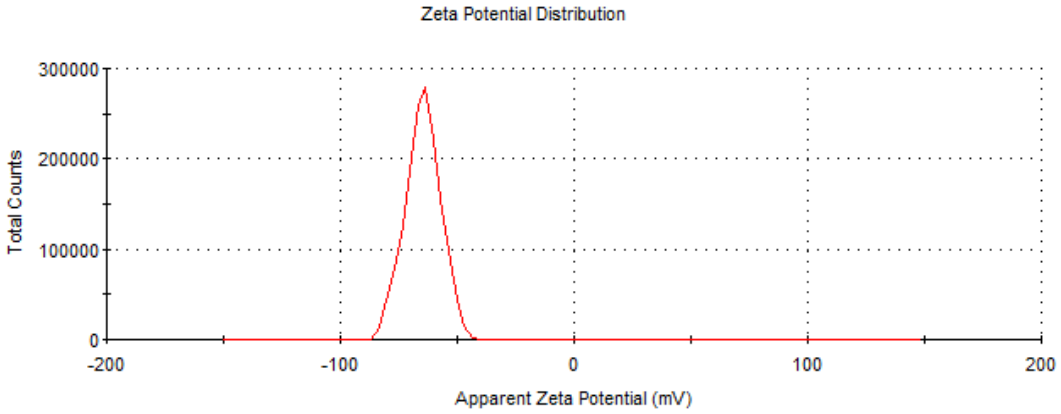

TEM

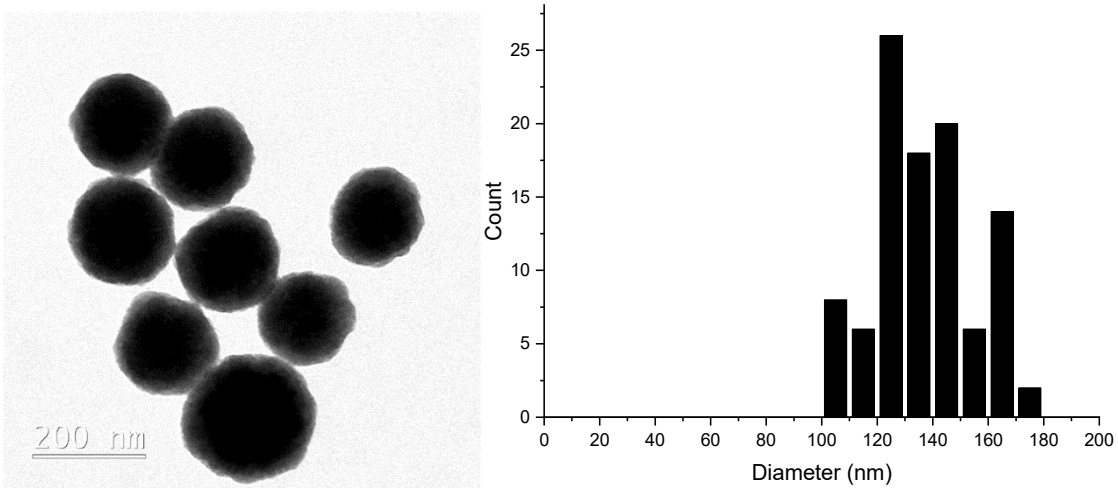
200 nm
Count
Diameter (nm)
0
5
10
15
20
25
0
20
40
60
80
100
120
140
160
180
200

IR (ATR)

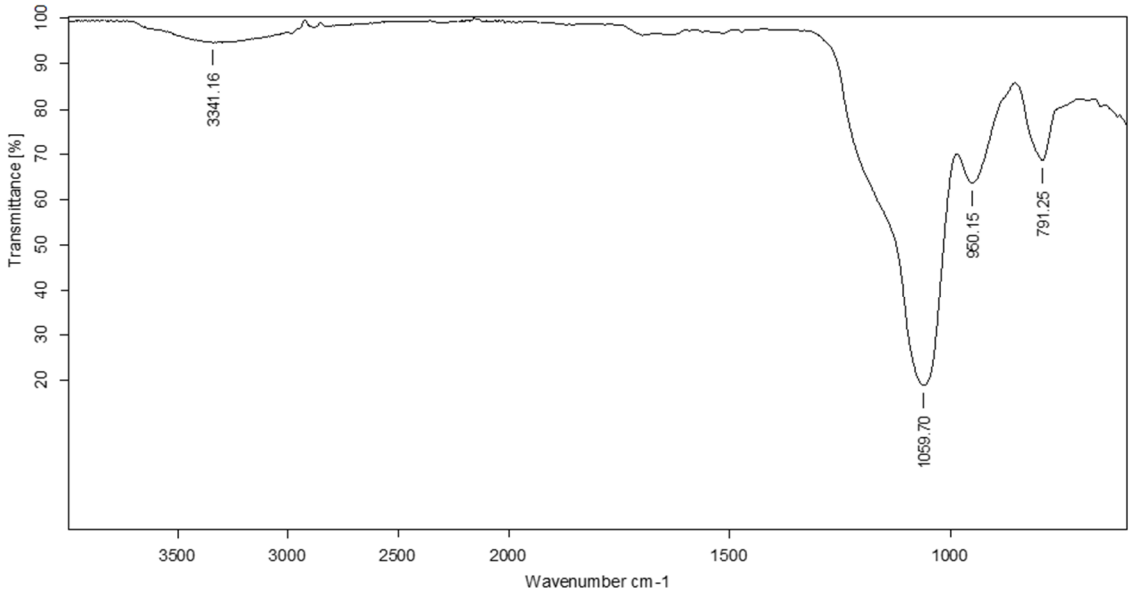
Transmittance [%]
Wavenumber cm-1
3341.16
1059.70
950.15
791.25
100
90
80
70
60
50
40
30
20
3500
3000
2500
2000
1500
1000

^{13}C CP MAS NMR

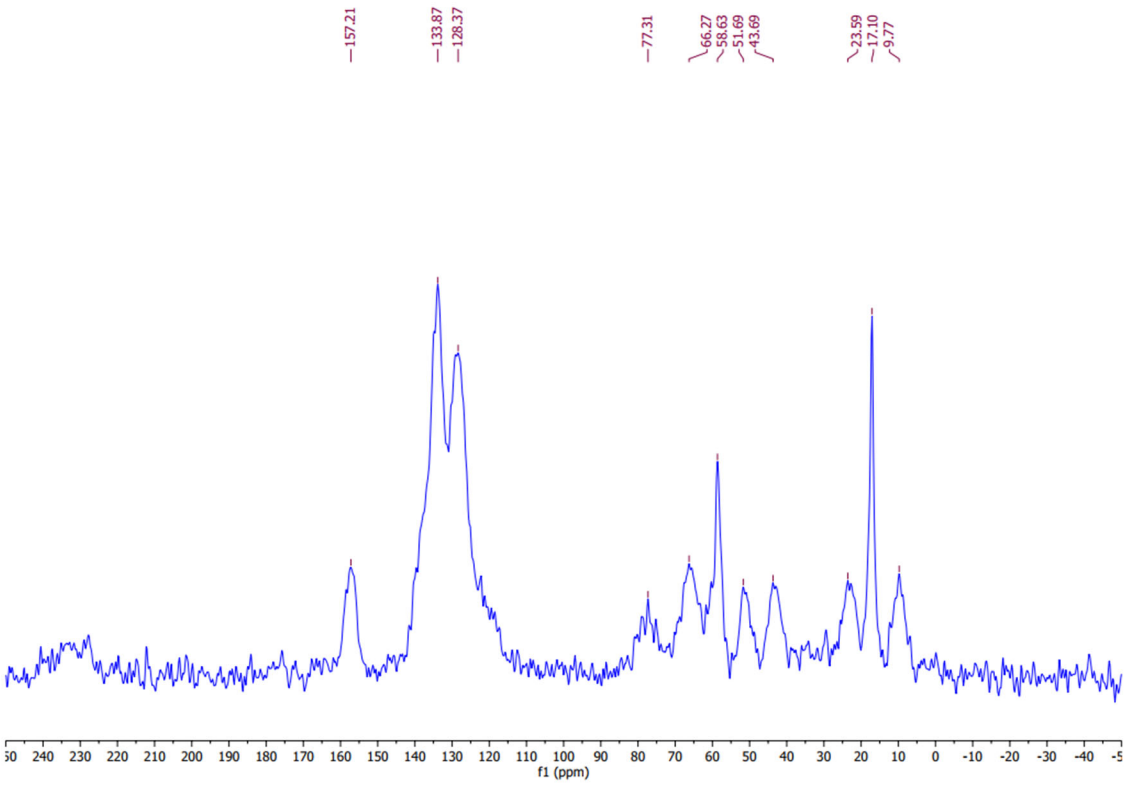

^{29}Si CP MAS NMR

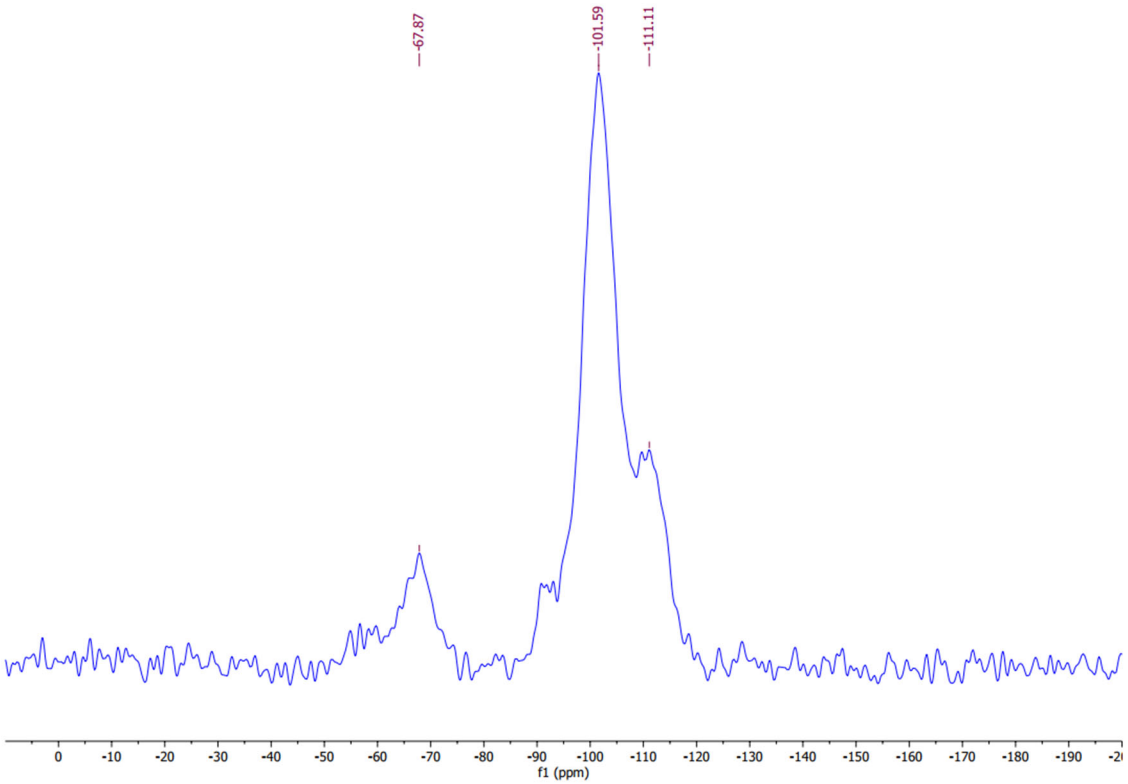

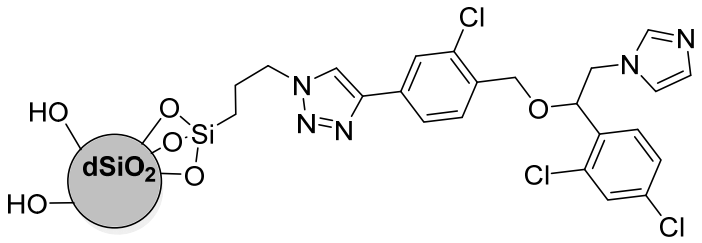

dN5

DLS

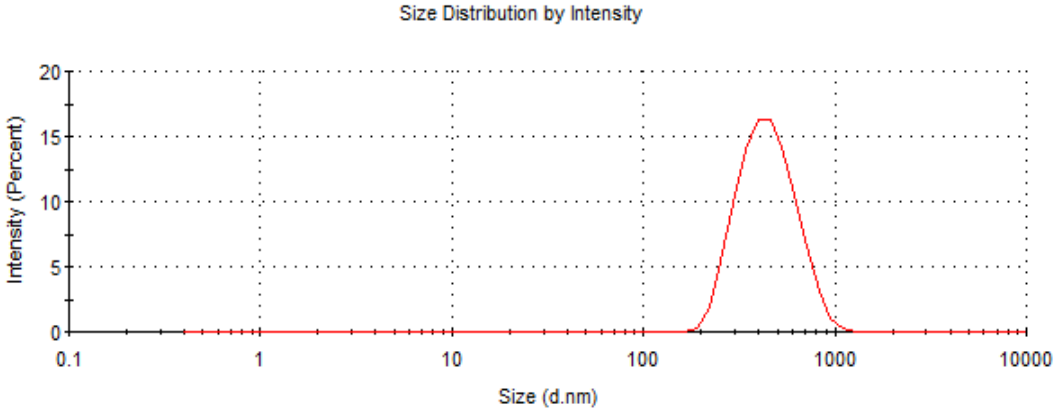

Zeta-potential

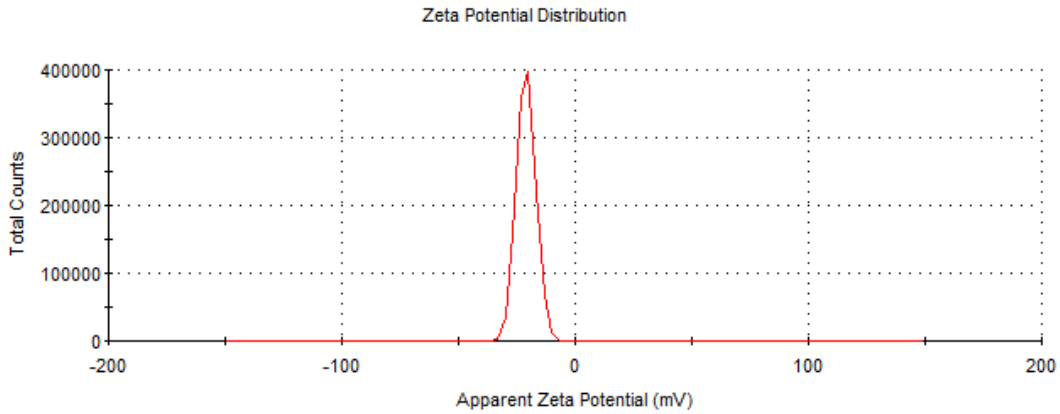

TEM

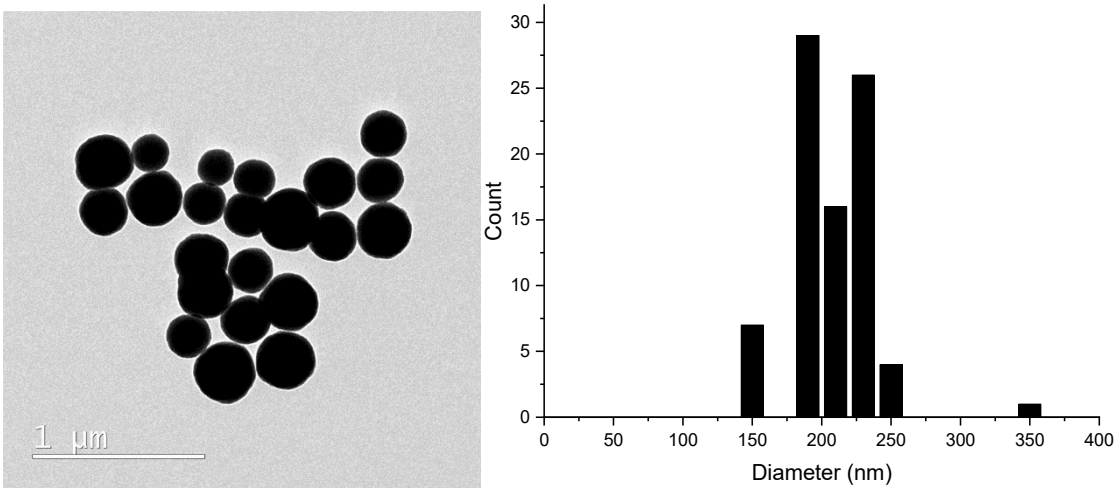
1 µm
Count
Diameter (nm)
0
5
10
15
20
25
30
0
50
100
150
200
250
300
350
400

IR (ATR)

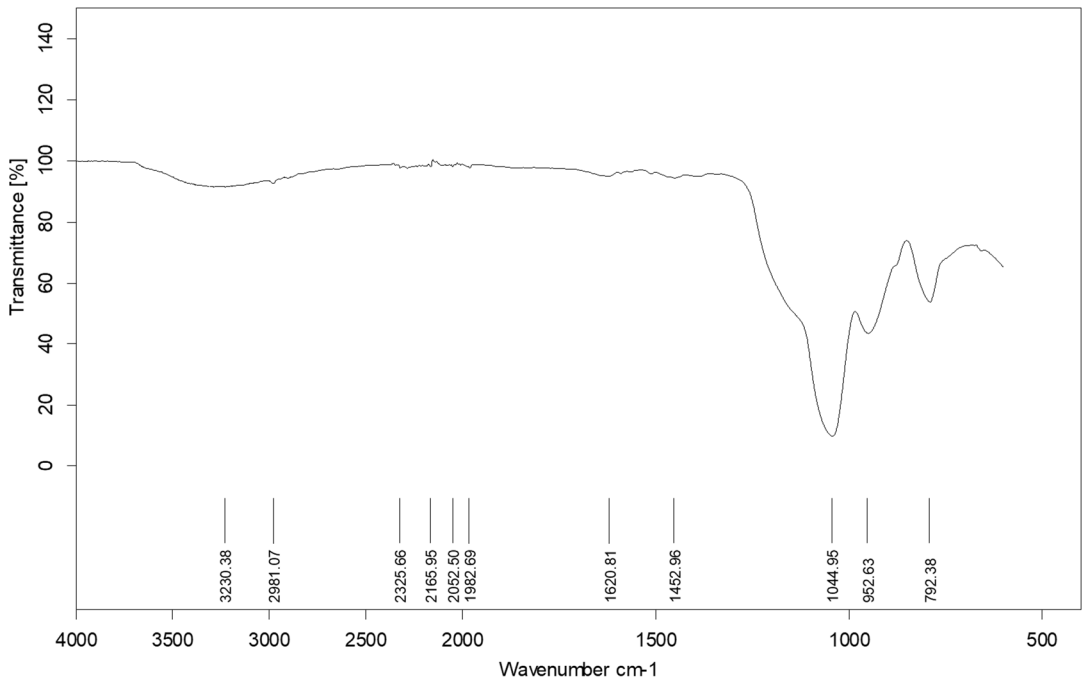
Transmittance [%]
Wavenumber cm-1
3230.38
2981.07
2325.66
2165.95
2052.50
1982.69
1620.81
1452.96
1044.95
952.63
792.38

^{13}C CP MAS NMR

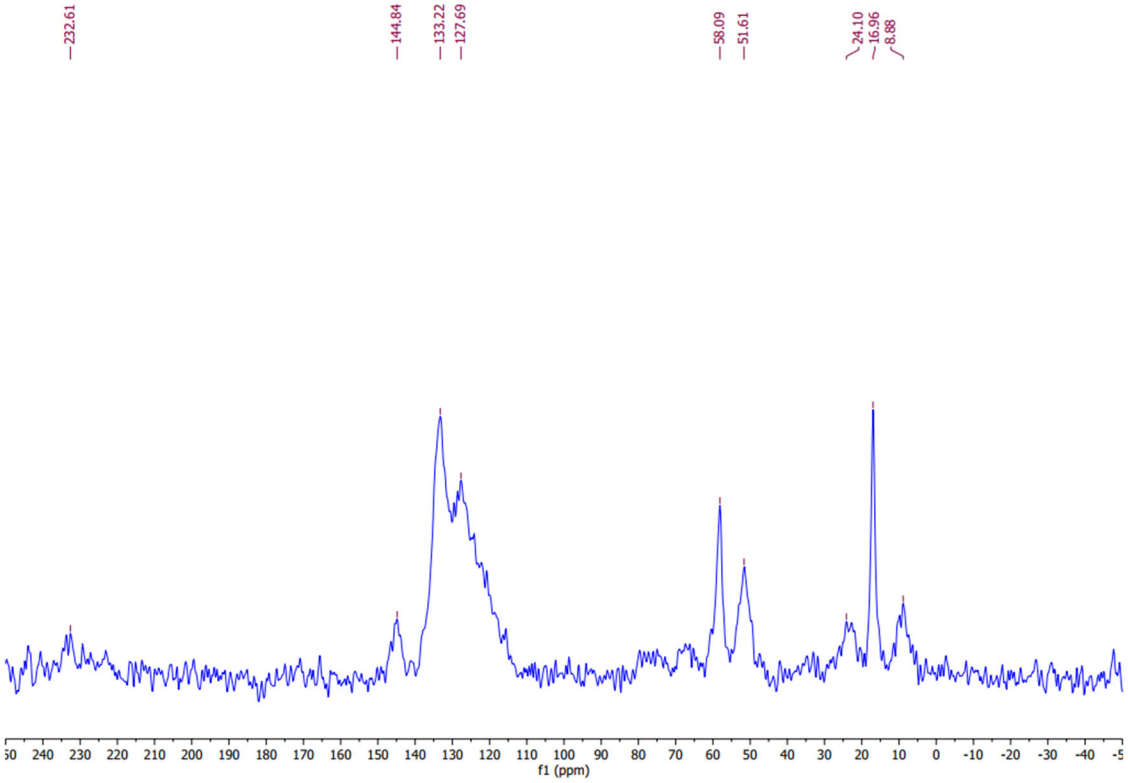

^{29}Si CP MAS NMR

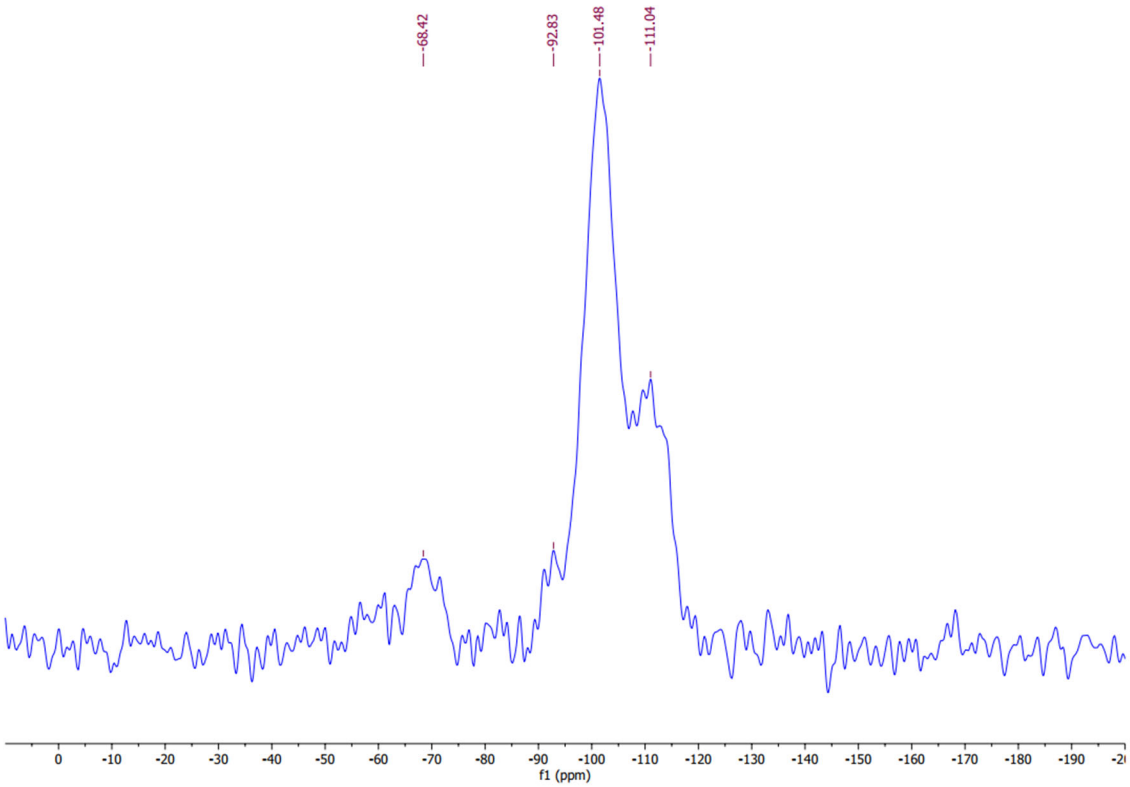

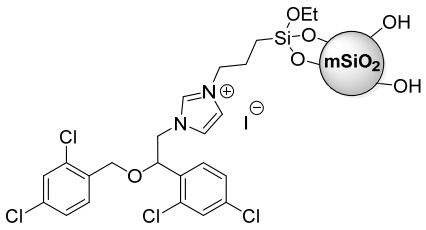

mN6

p-XRD

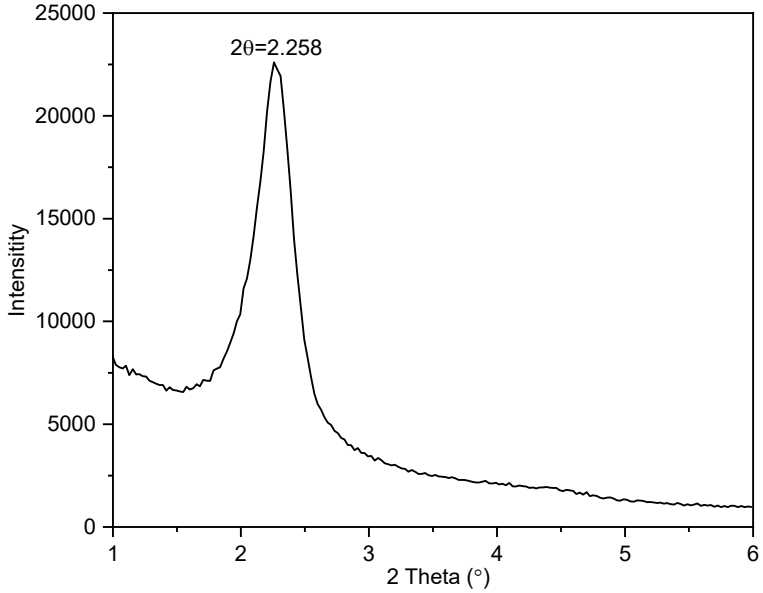

DLS

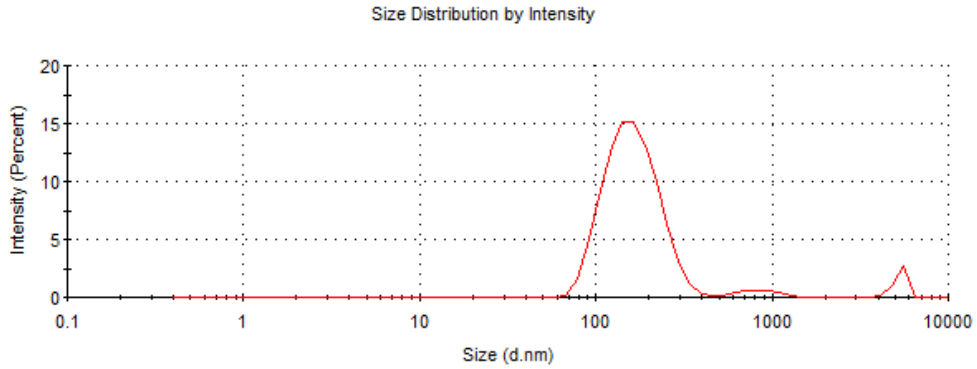

Zeta-potential

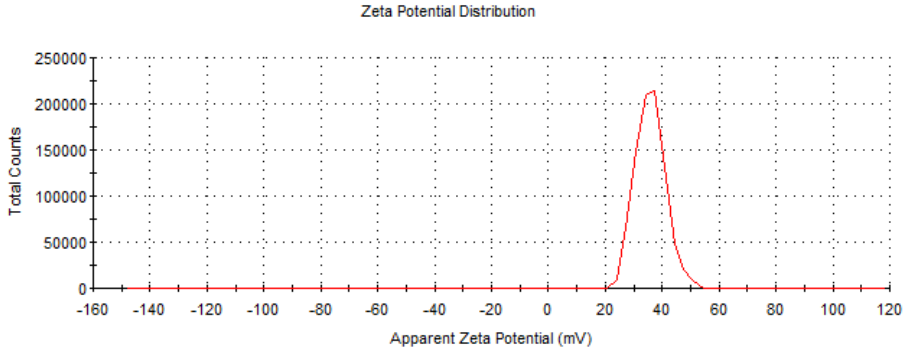

TEM

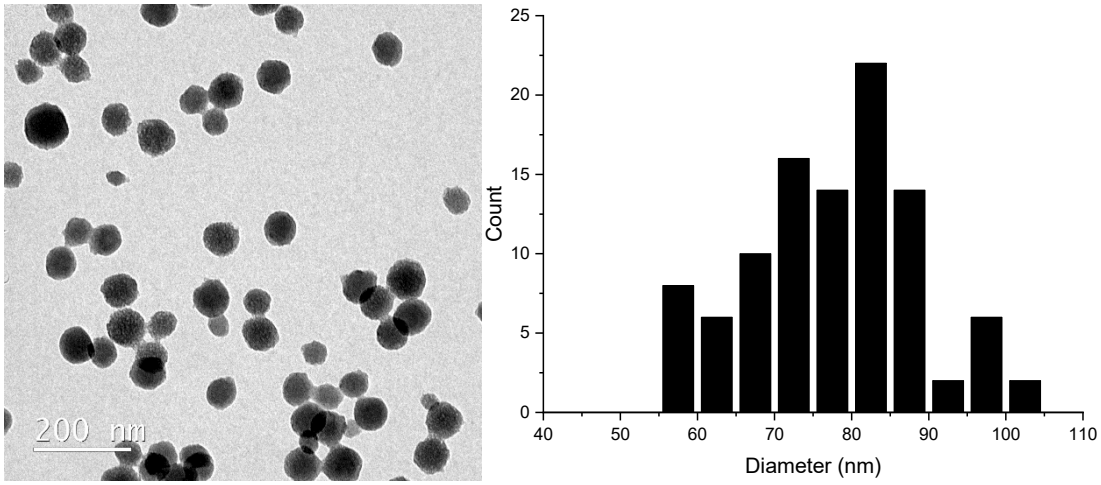
200 nm
Count
Diameter (nm)
0
5
10
15
20
25
40
50
60
70
80
90
100
110

IR (ATR)

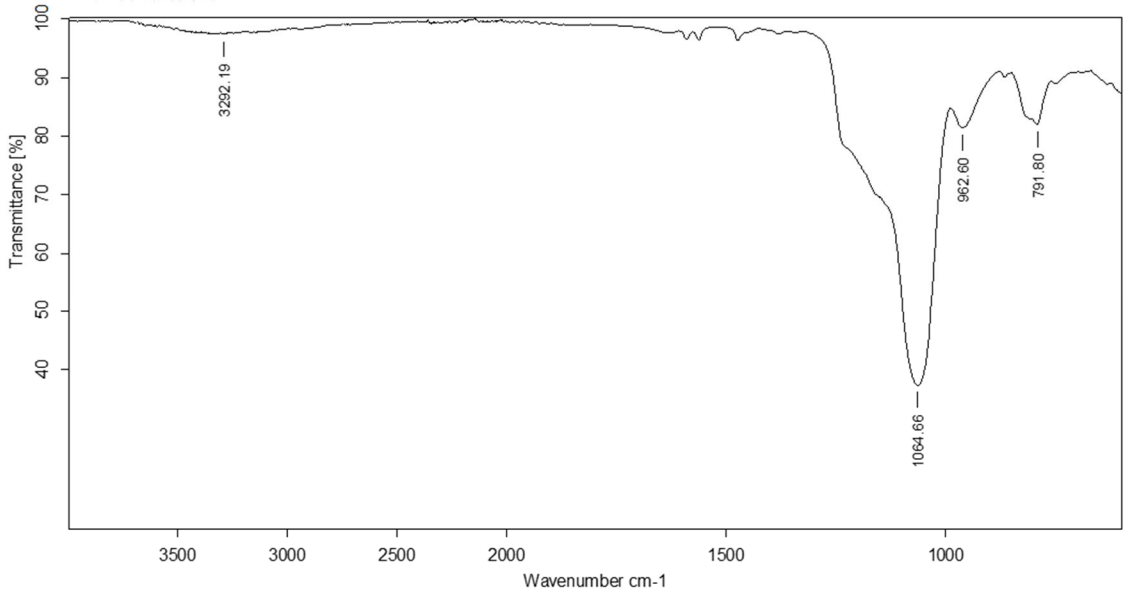
Transmittance [%]
100
90
80
70
60
50
40
3292.19
1064.66
962.60
791.80
3500
3000
2500
2000
1500
1000
Wavenumber cm-1

^{13}C CP MAS NMR

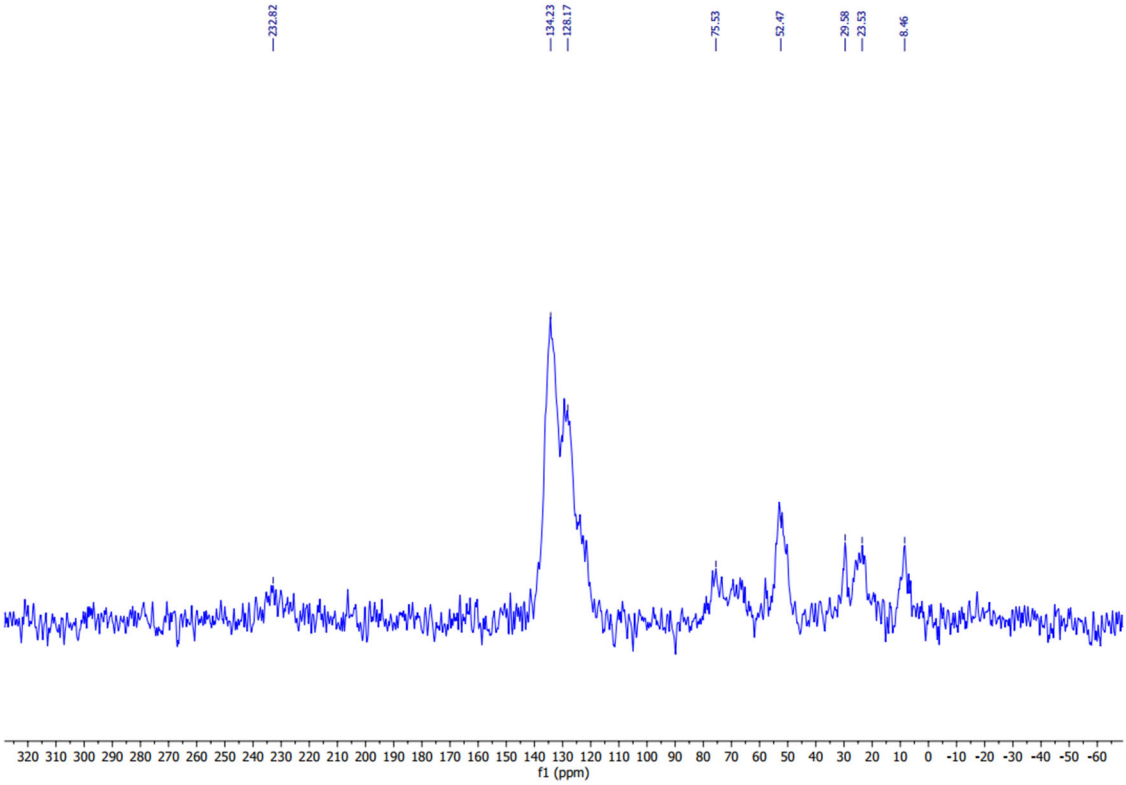

^{29}Si CP MAS NMR

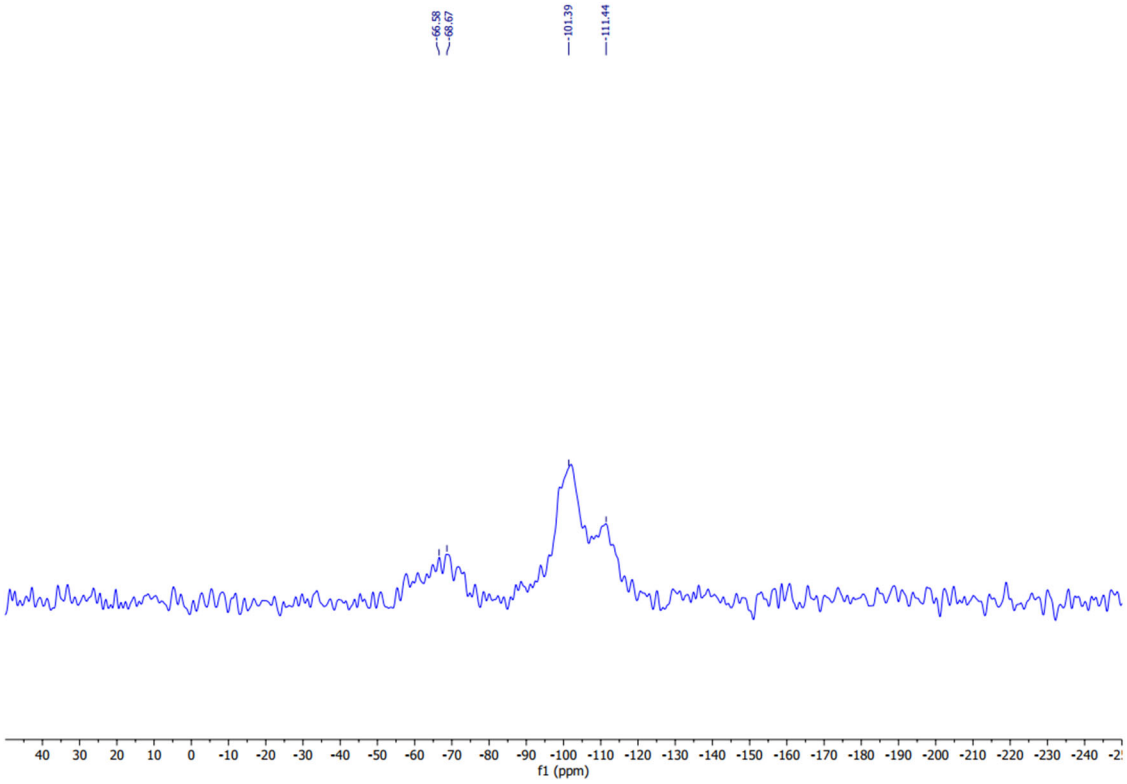

BET

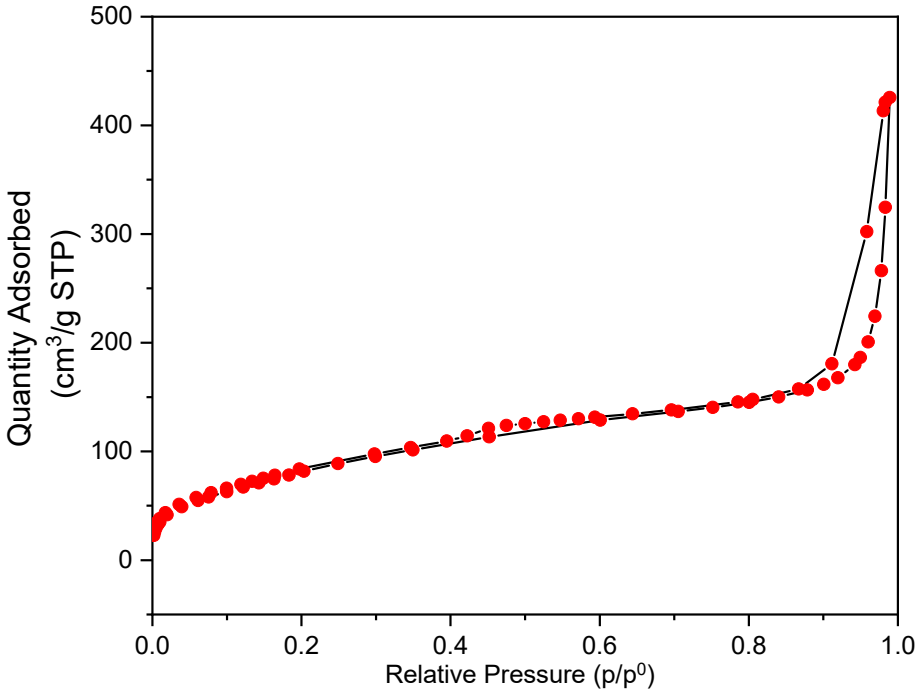
Quantity Adsorbed
(cm3/g STP)
500
400
300
200
100
0
0.0
0.2
0.4
0.6
0.8
1.0
Relative Pressure (p/p0)

Annex: collection of spectra and characterization data

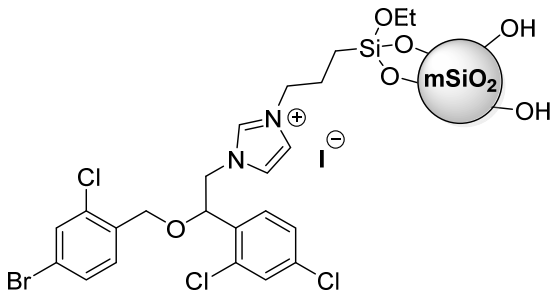

mN7

DLS

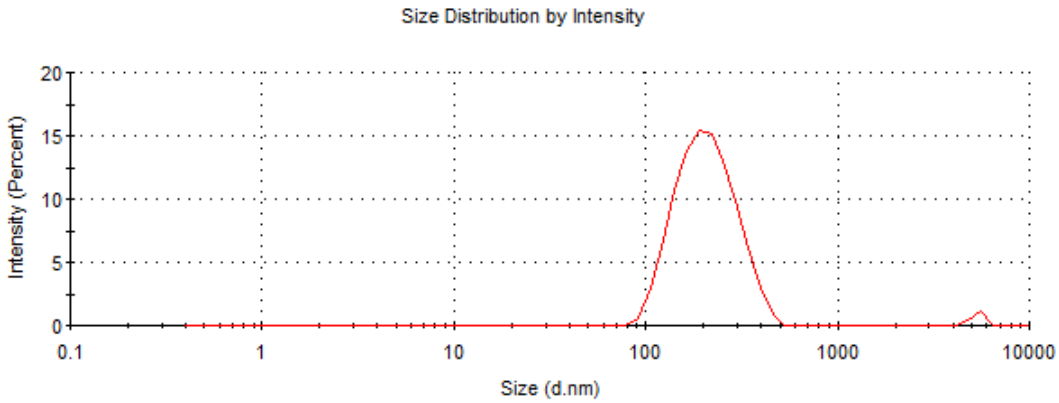

Zeta-potential

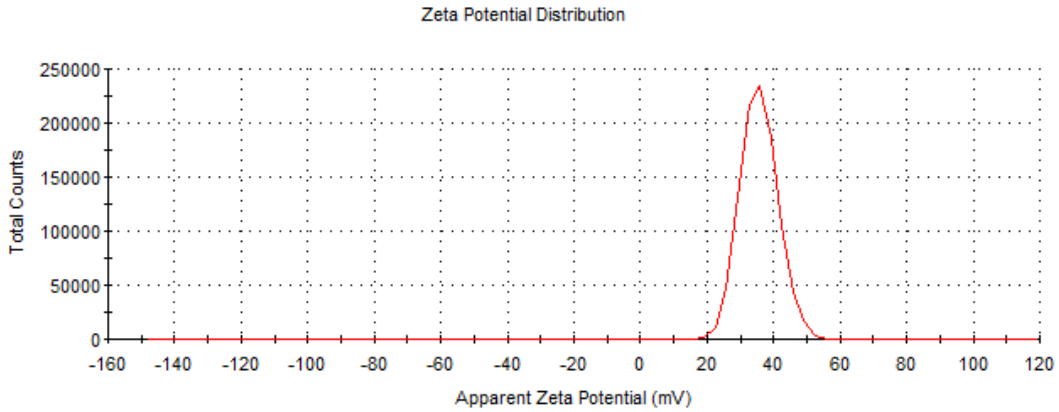

TEM

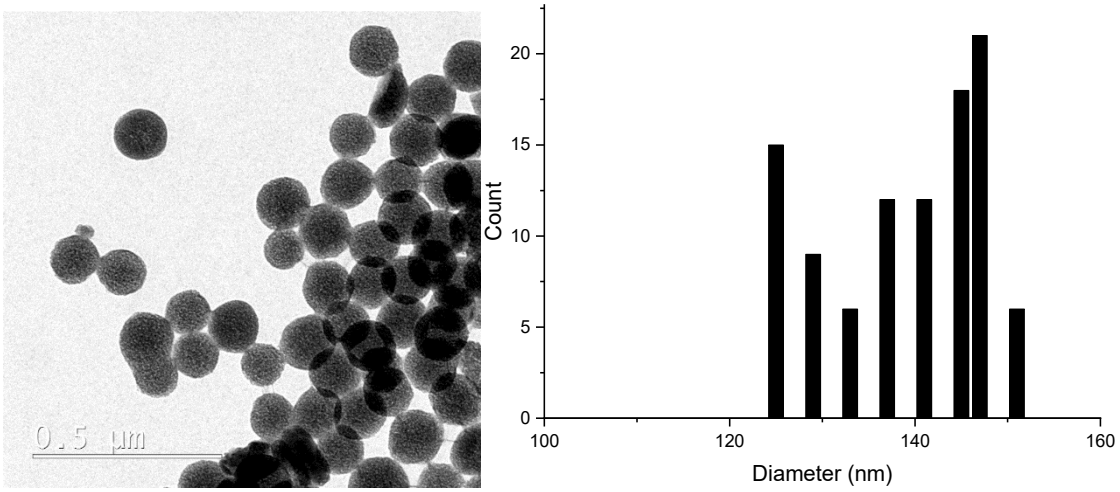
0.5 µm
Count
Diameter (nm)
0
5
10
15
20
100
120
140
160

IR (ATR)

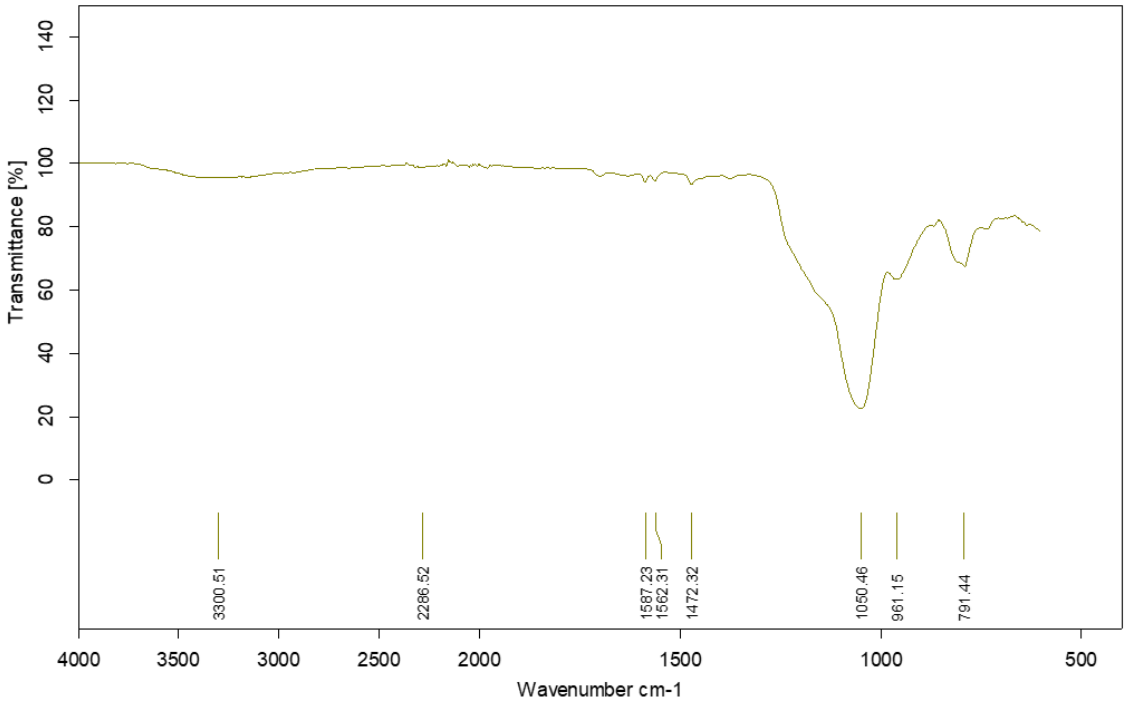
Transmittance [%]
Wavenumber cm-1
3300.51
2286.52
1587.23
1562.31
1472.32
1050.46
961.15
791.44

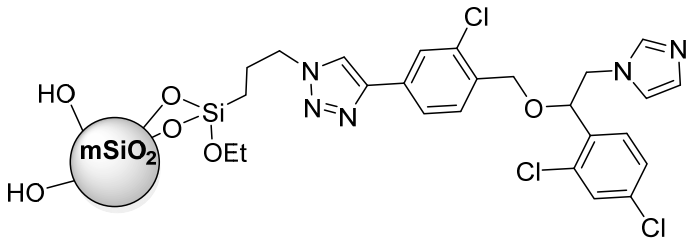

mN8

p-XRD

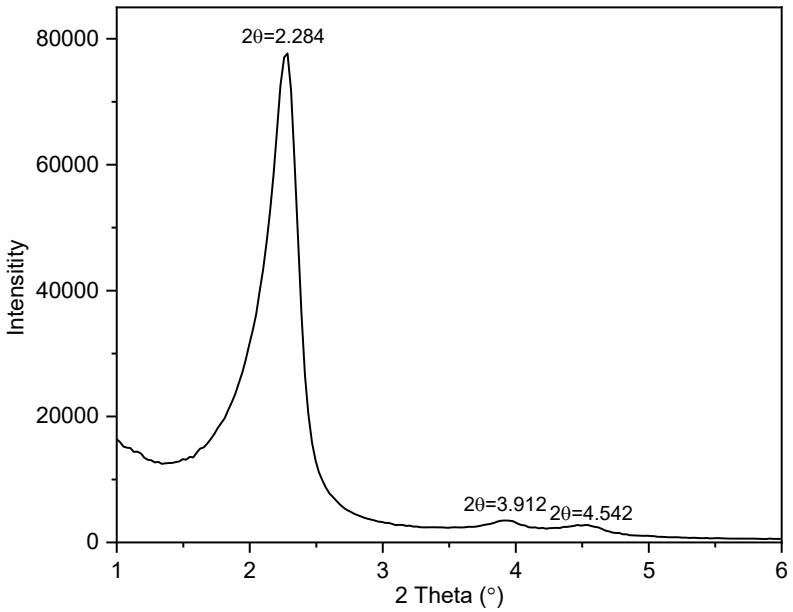

DLS

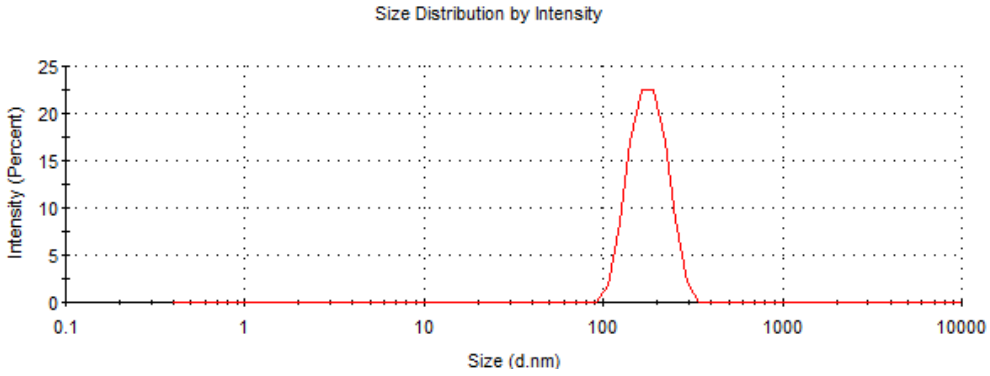

Zeta-potential

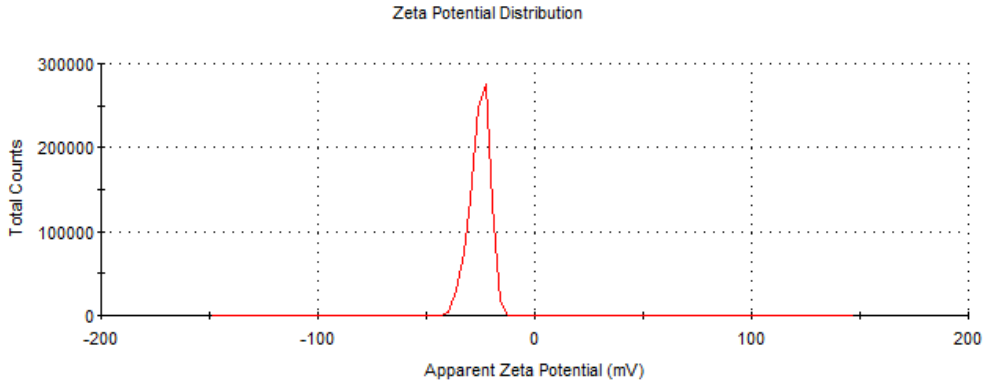

TEM

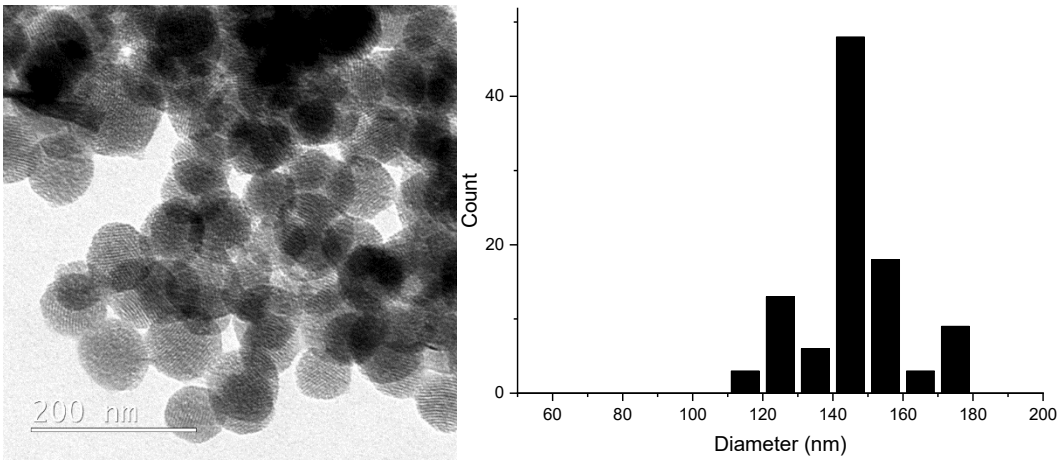
200 nm
Count
Diameter (nm)
0
20
40
60
80
100
120
140
160
180
200

IR (ATR)

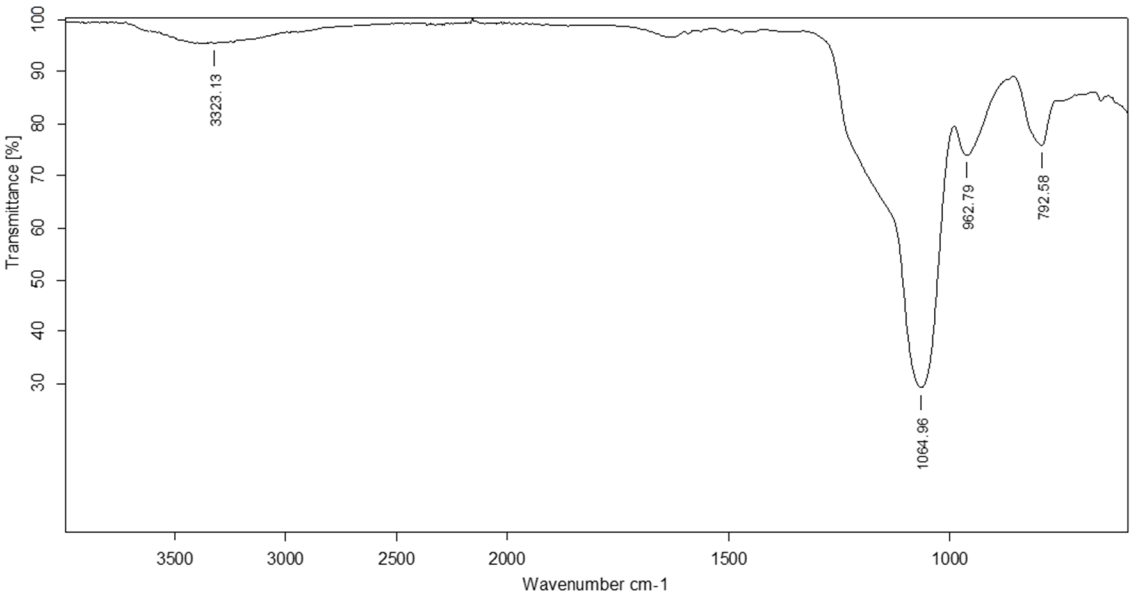
Transmittance [%]
Wavenumber cm-1
3323.13
1064.96
962.79
792.58
100
90
80
70
60
50
40
30
3500
3000
2500
2000
1500
1000

^{13}C CP MAS NMR

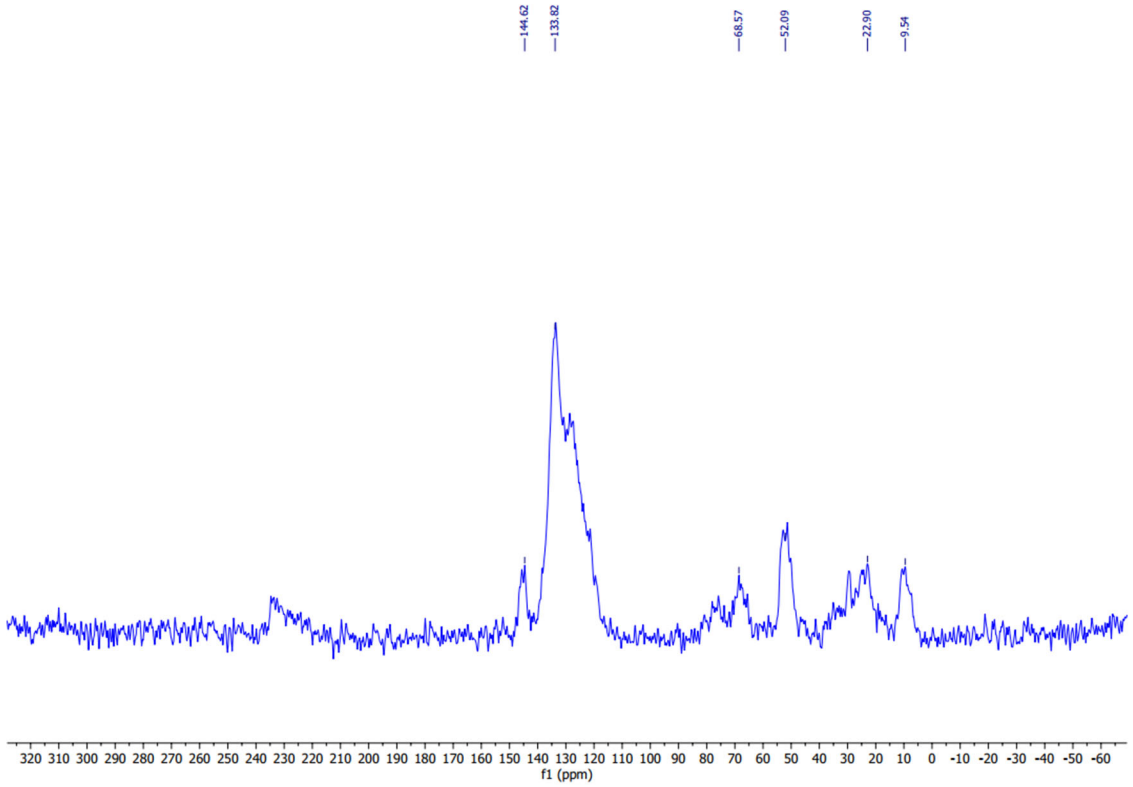

^{29}Si CP MAS NMR

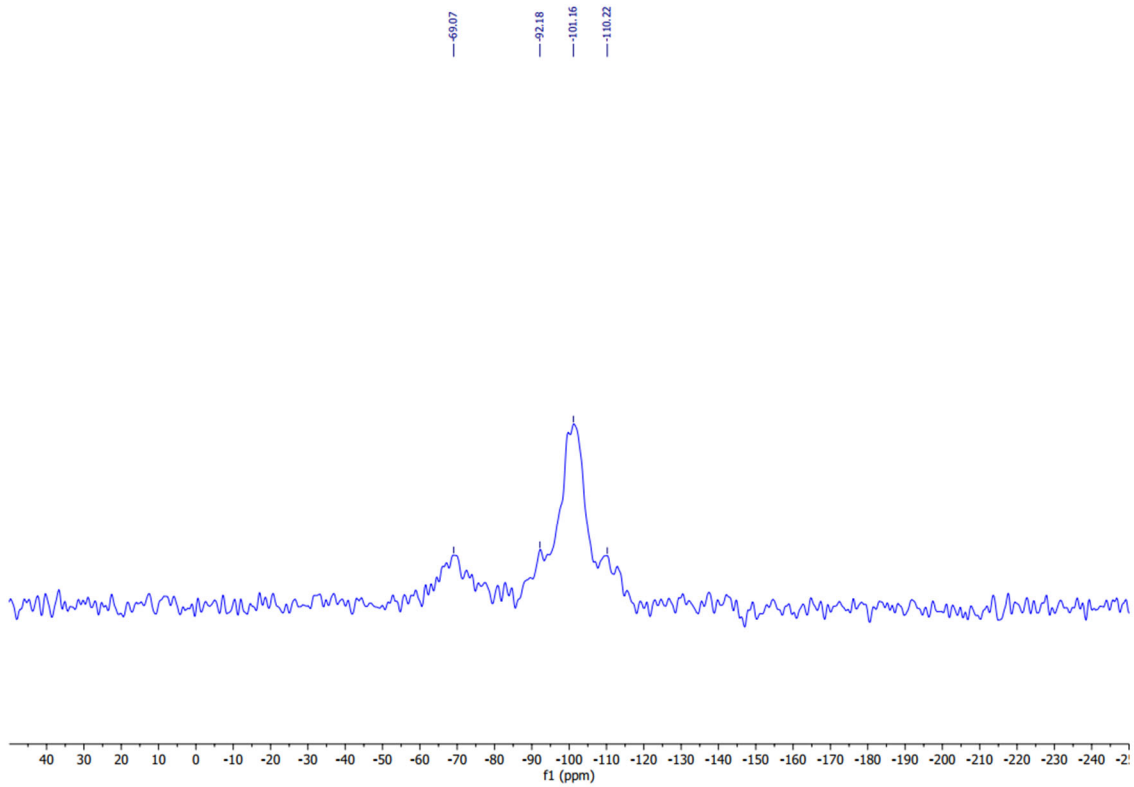

BET

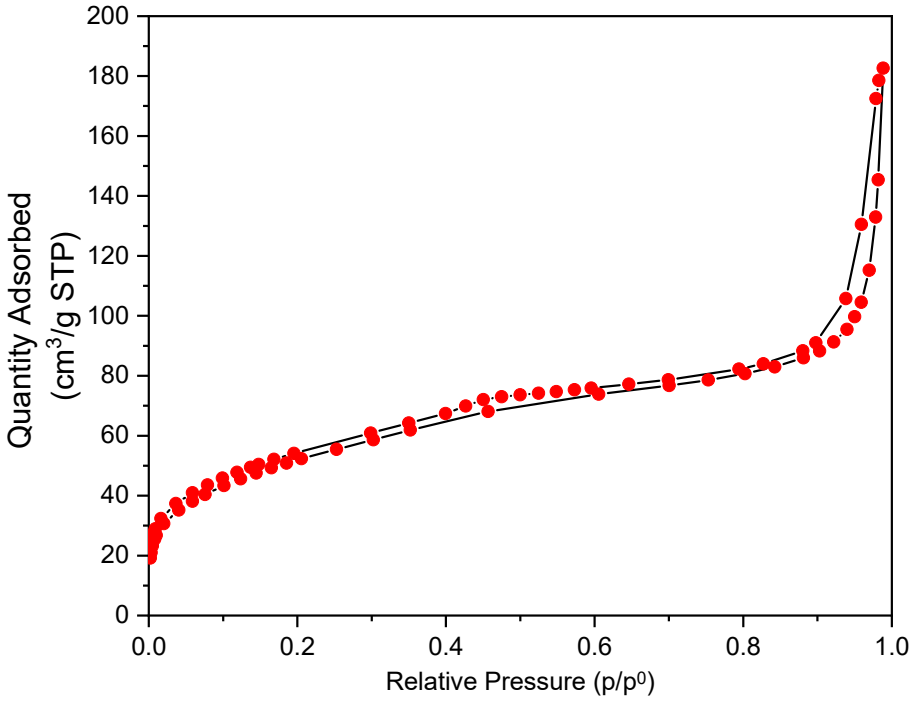
Quantity Adsorbed
(cm3/g STP)
Relative Pressure (p/p0)
0
20
40
60
80
100
120
140
160
180
200
0.0
0.2
0.4
0.6
0.8
1.0

Fabric-dN1

SEM

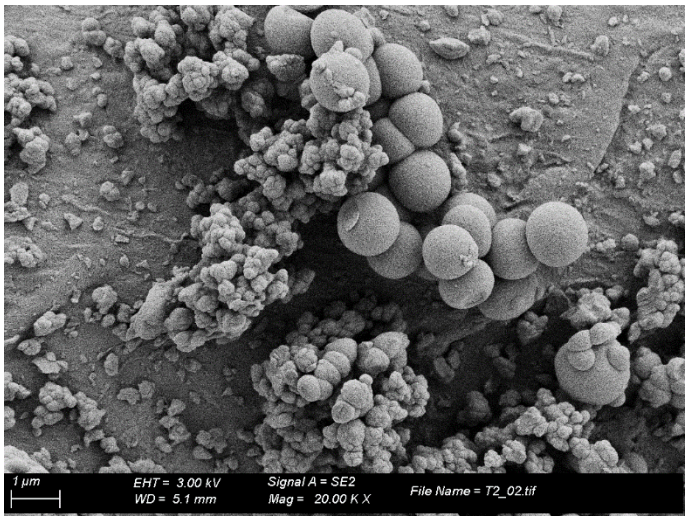

EDX/Mapping

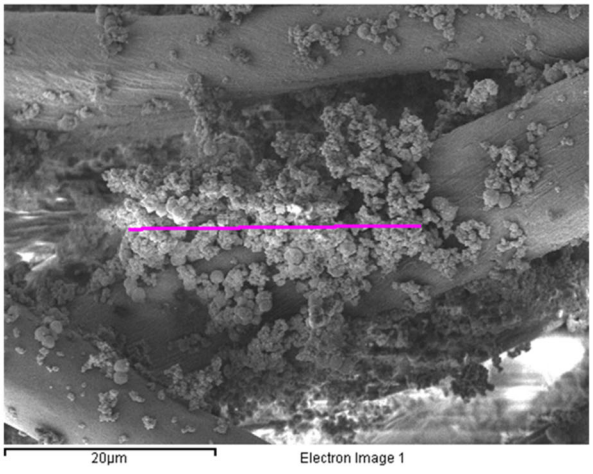

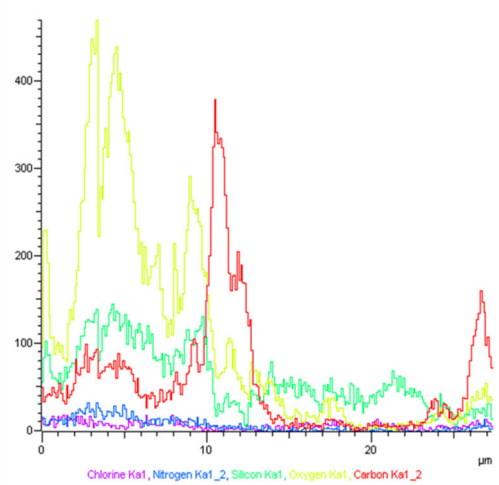

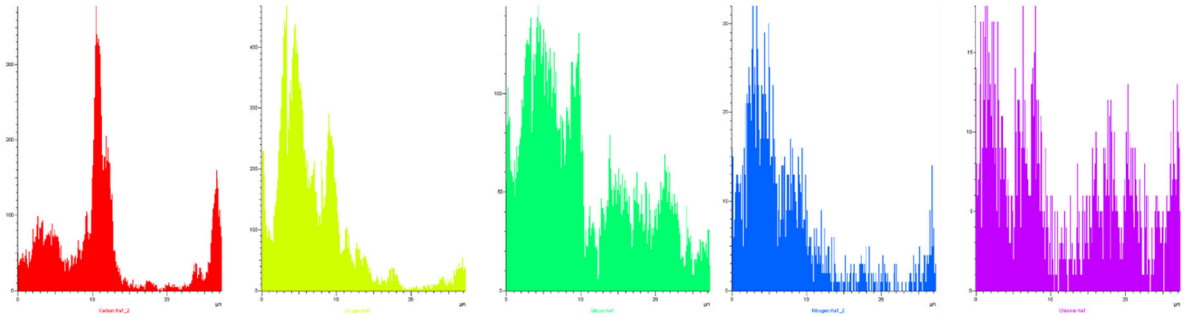

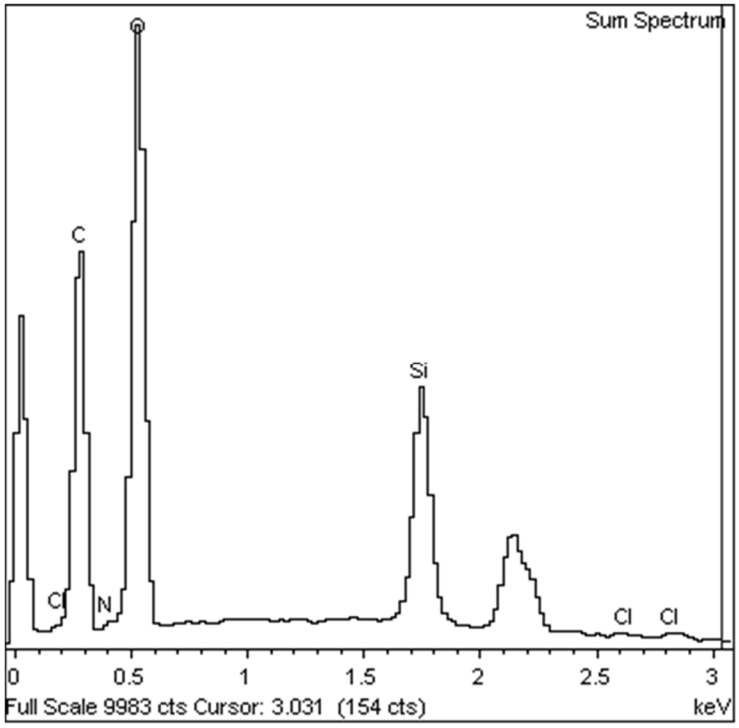
Sum Spectrum
C
O
Si
Cl
N
Cl
Cl
0
0.5
1
1.5
2
2.5
3
Full Scale 9983 cts Cursor: 3.031 (154 cts)
keV

Fabric-dN2

SEM

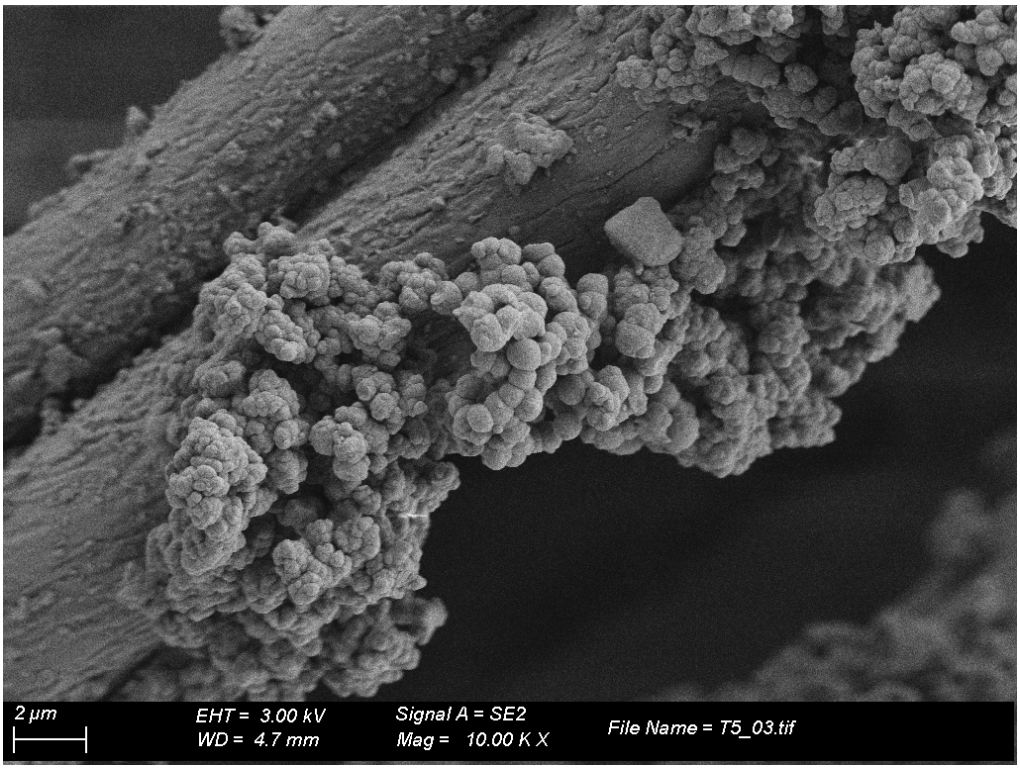

EDX/Mapping

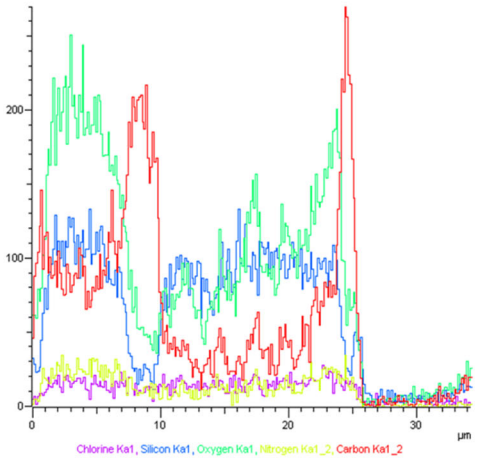

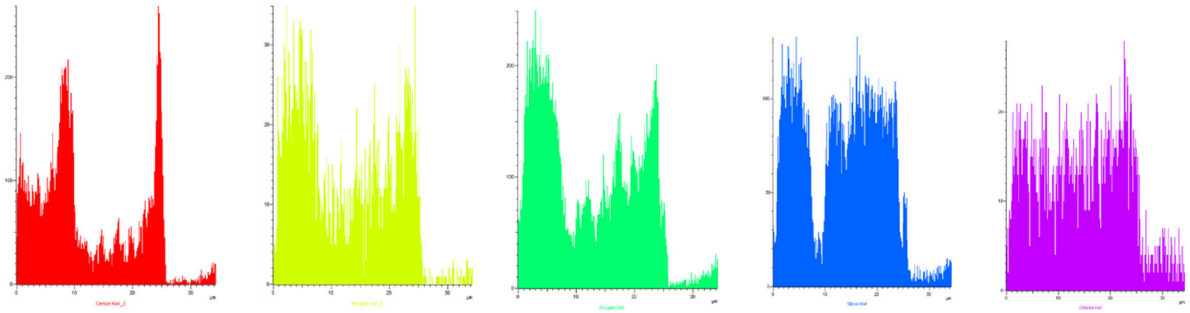

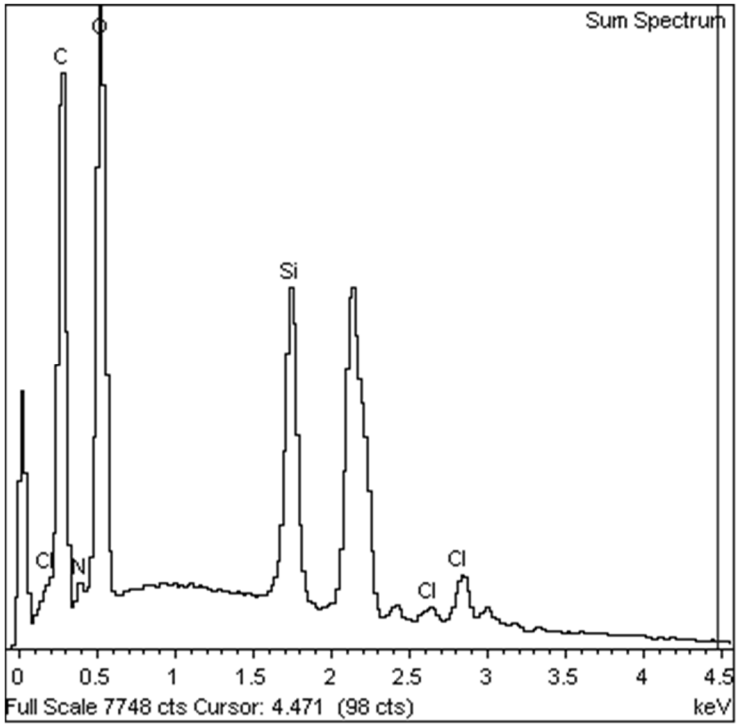
Sum Spectrum
O
C
Si
Cl
N
Cl
Cl
0
0.5
1
1.5
2
2.5
3
3.5
4
4.5
Full Scale 7748 cts Cursor: 4.471 (98 cts)
keV

Fabric-dN3

SEM

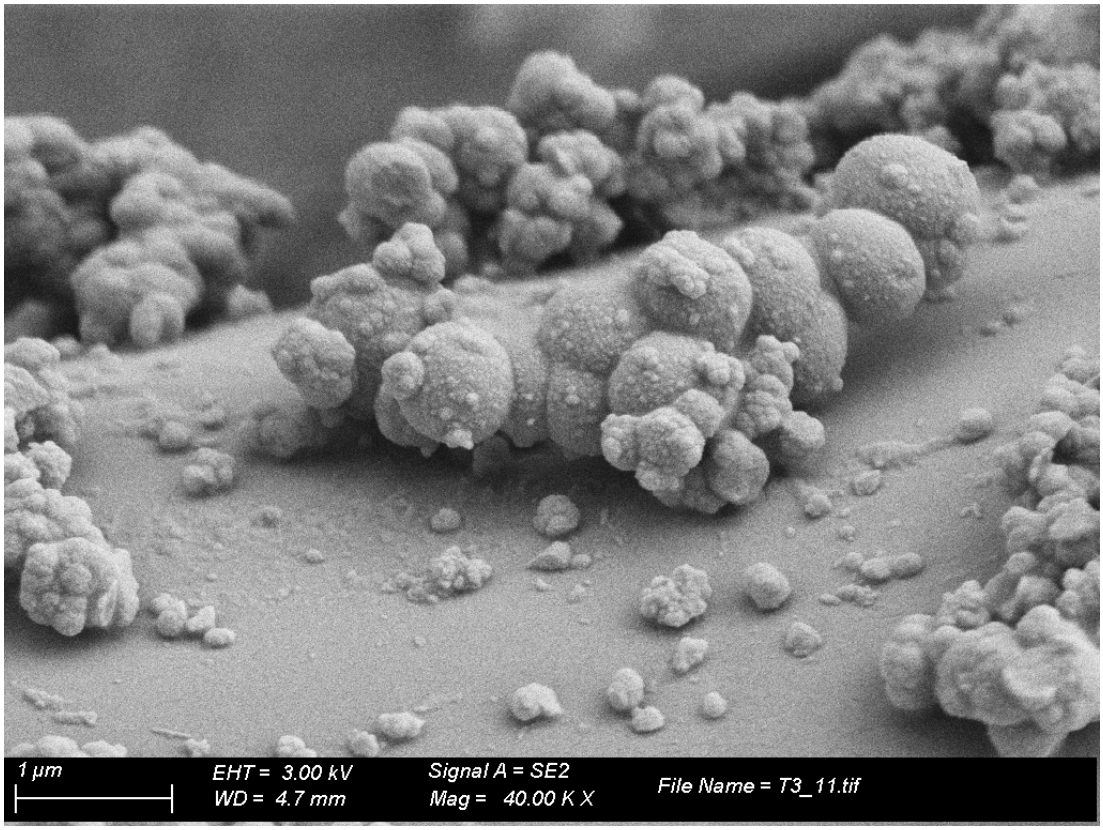

Contact angle

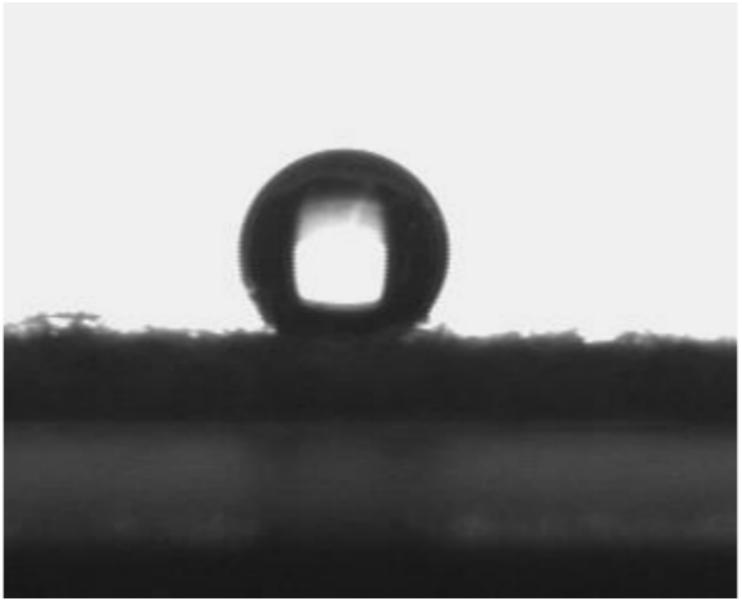

EDX/Mapping

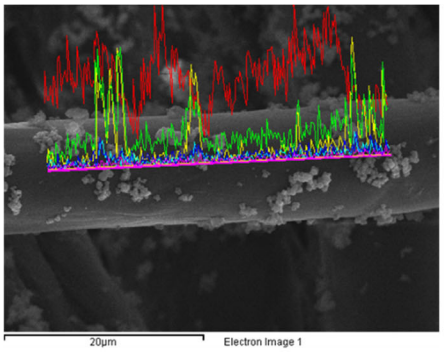
20µm
Electron Image 1

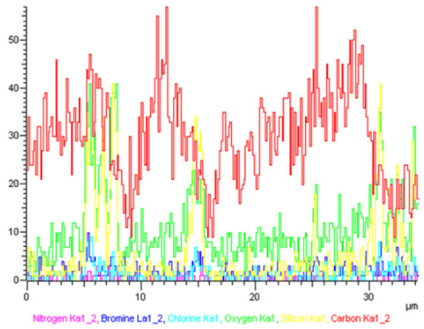
Nitrogen Ka1_2, Bromine La1_2, Chlorine Ka1, Oxygen Ka1, Silicon Ka1, Carbon Ka1_2

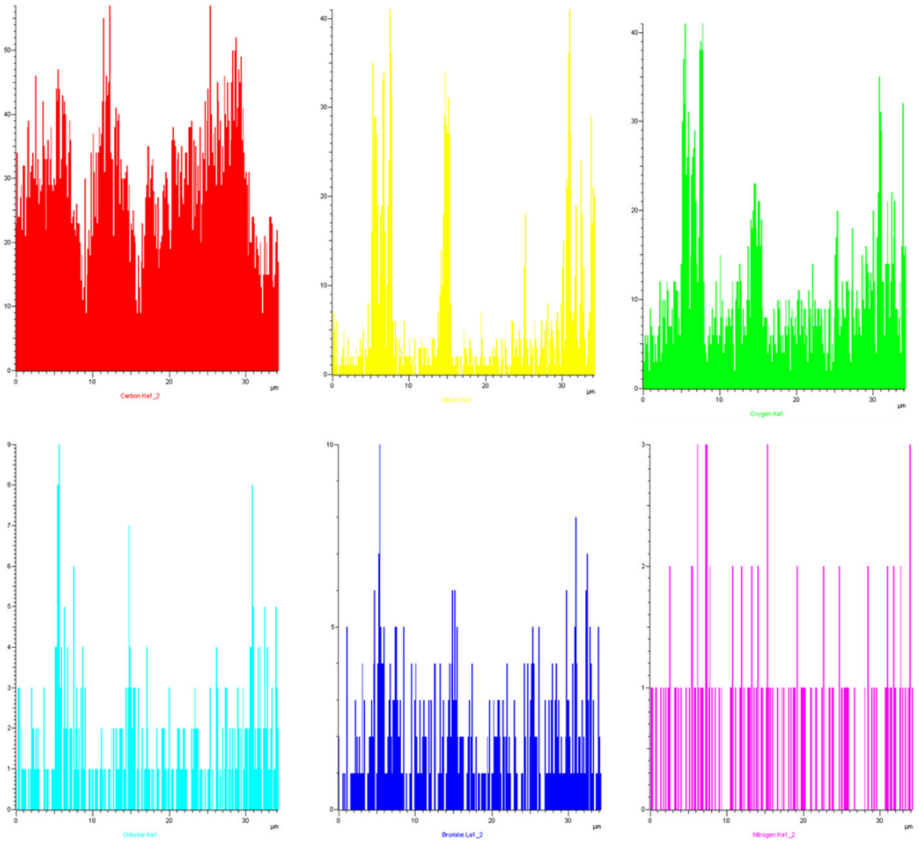

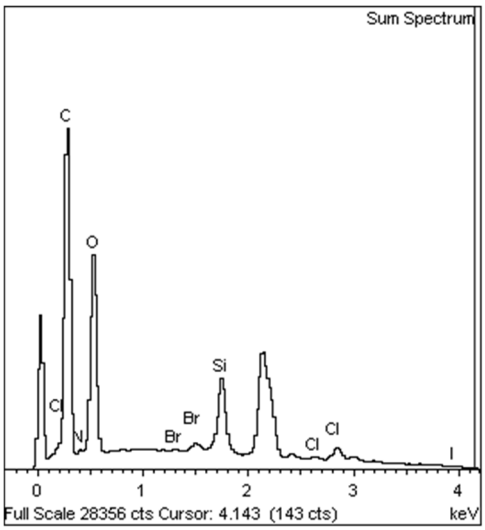
Sum Spectrum
C
O
Si
Cl
N
Br
Br
Cl
Cl
I
0
1
2
3
4
Full Scale 28356 cts Cursor: 4.143 (143 cts)
keV

Fabric-dN4

SEM

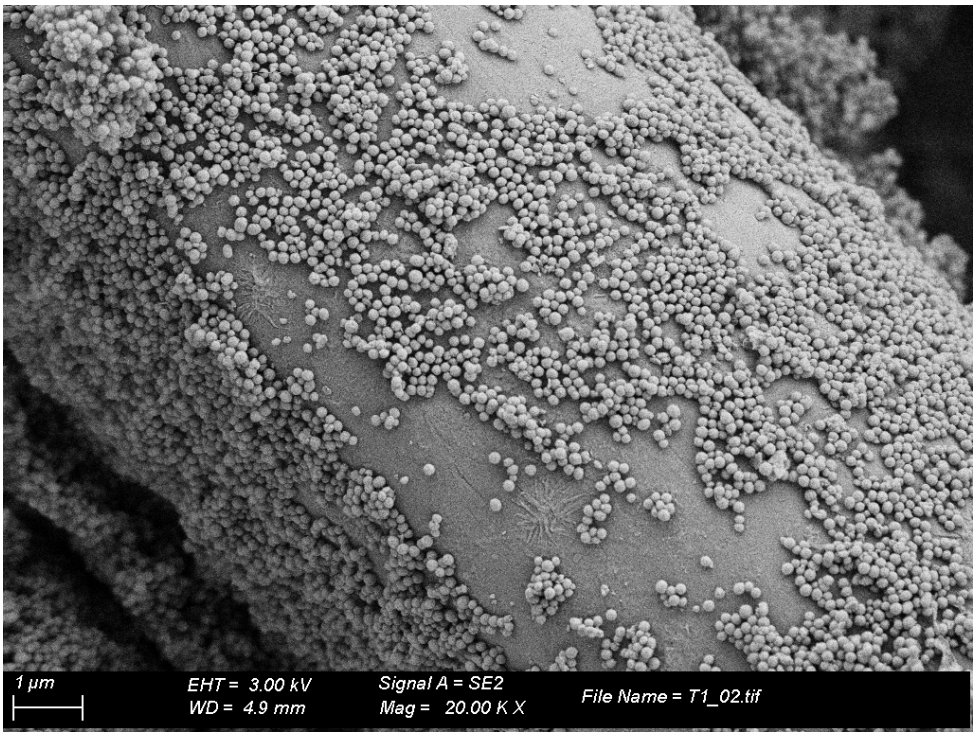

EDX/Mapping

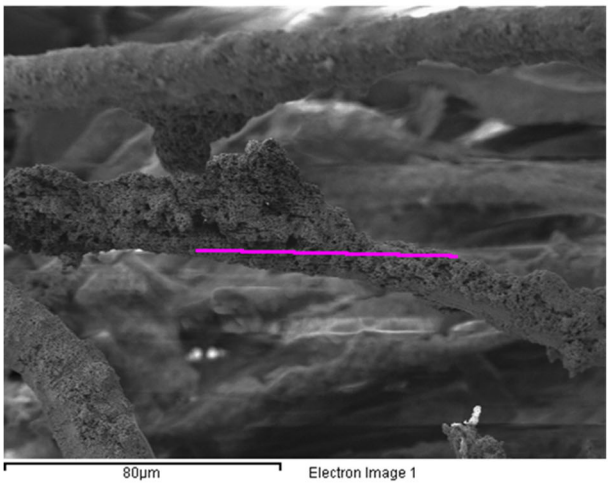

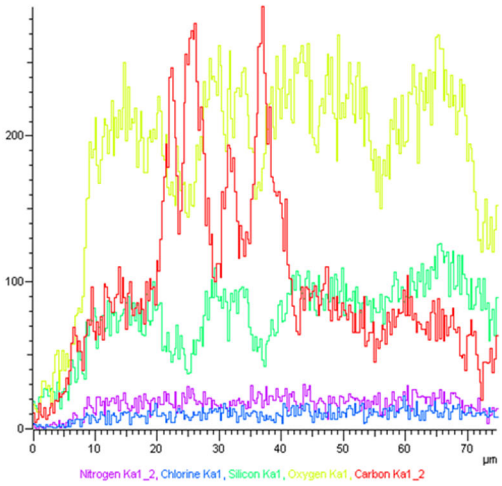

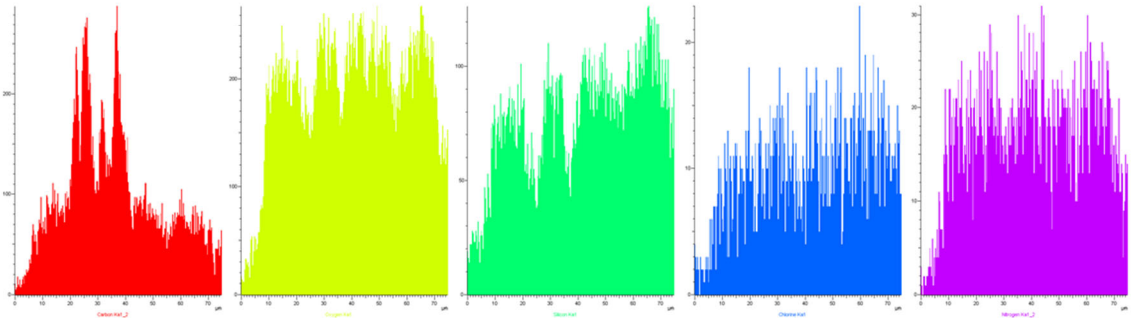

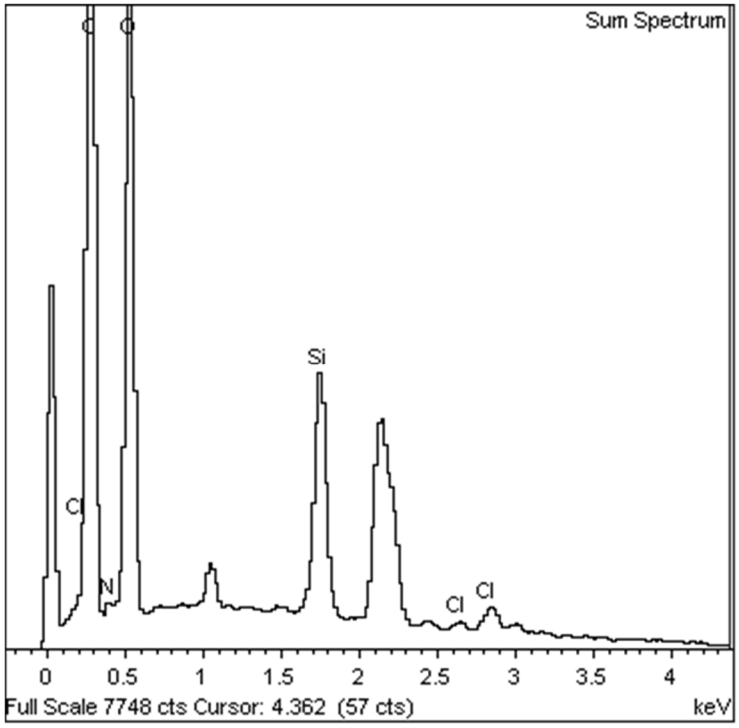
Sum Spectrum
O
O
Si
Cl
N
Cl
Cl
0
0.5
1
1.5
2
2.5
3
3.5
4
Full Scale 7748 cts Cursor: 4.362 (57 cts)
keV

Fabric-dN5

SEM

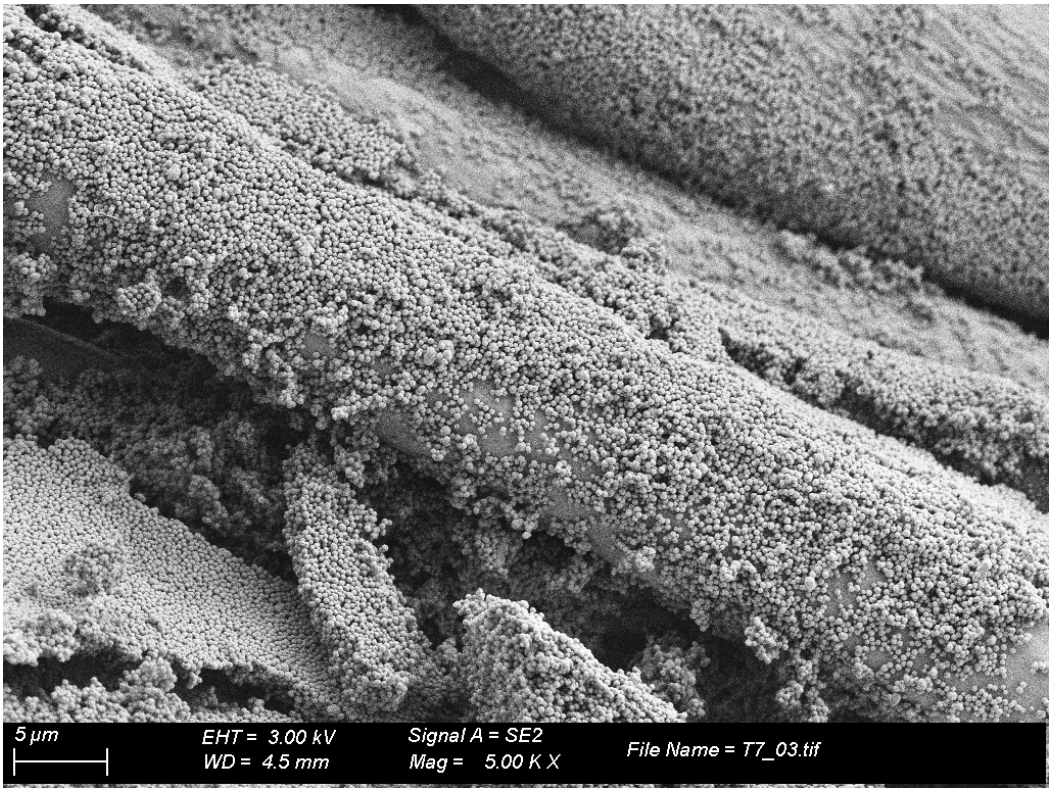

EDX/Mapping

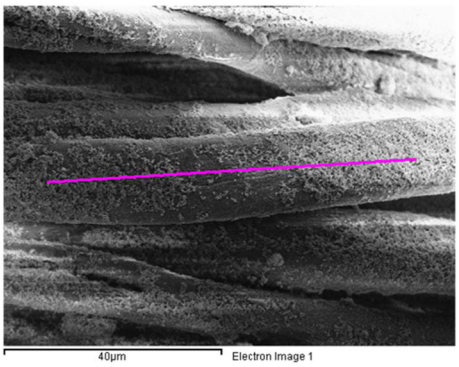

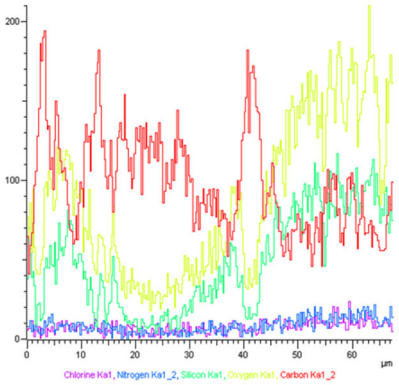

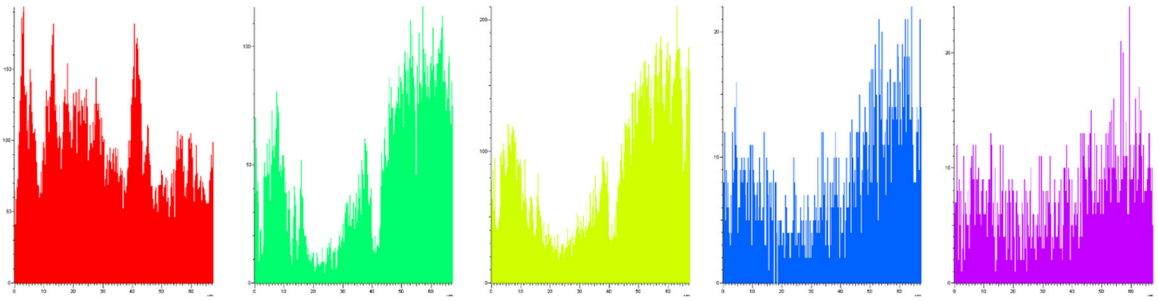

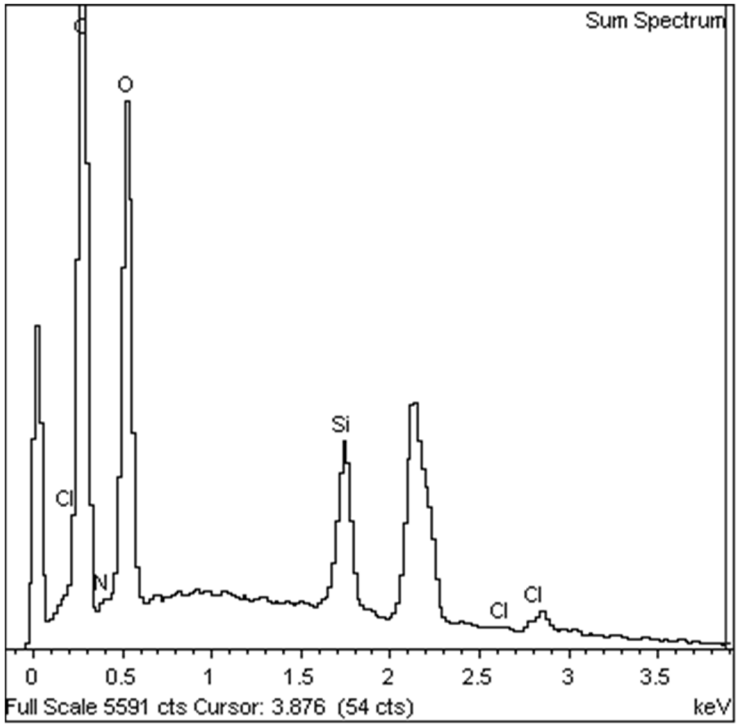

Contact angle

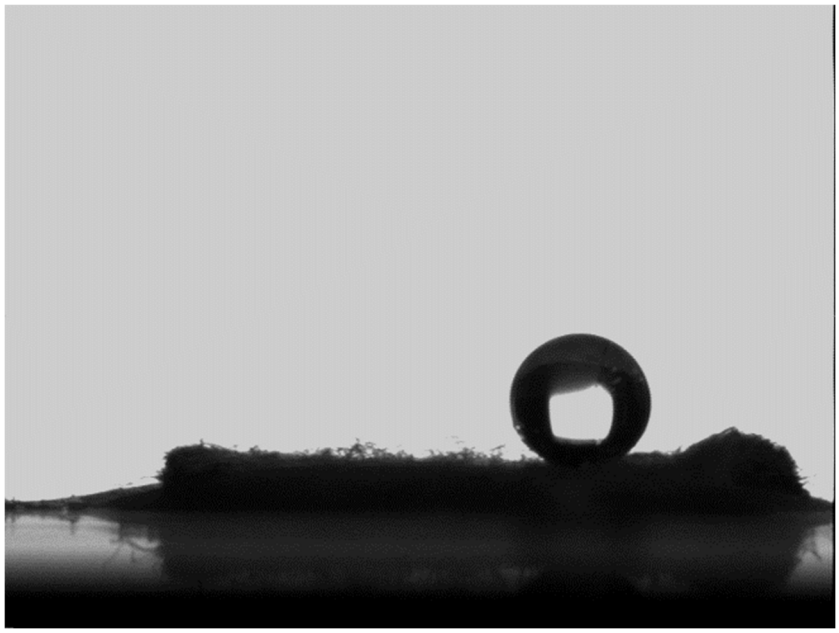

Fabric-mN6

SEM

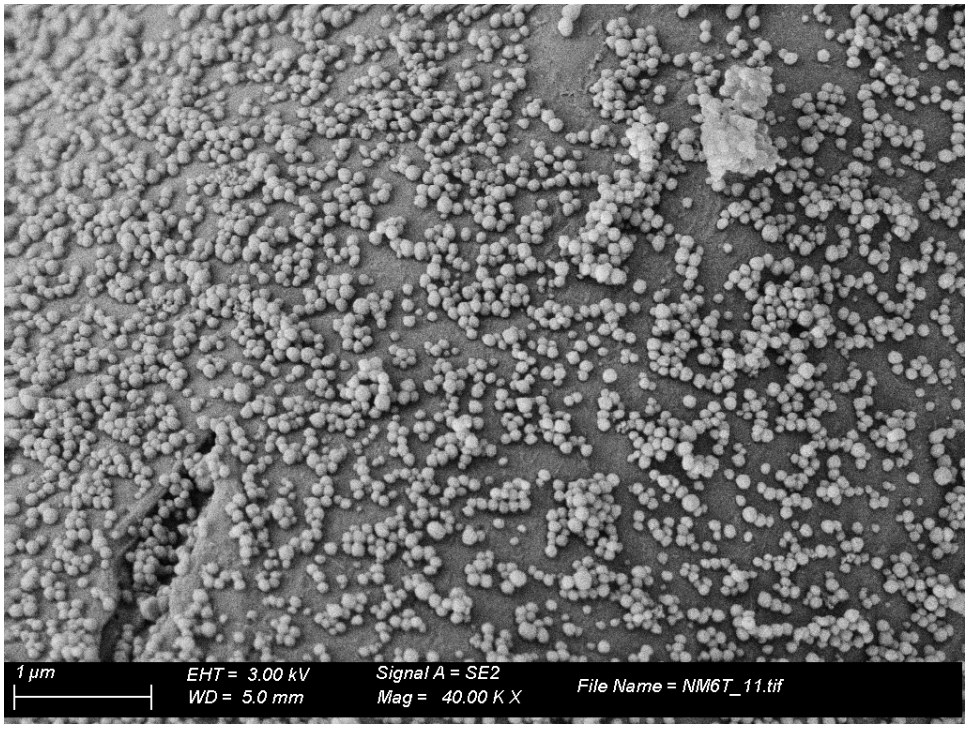

EDX/Mapping

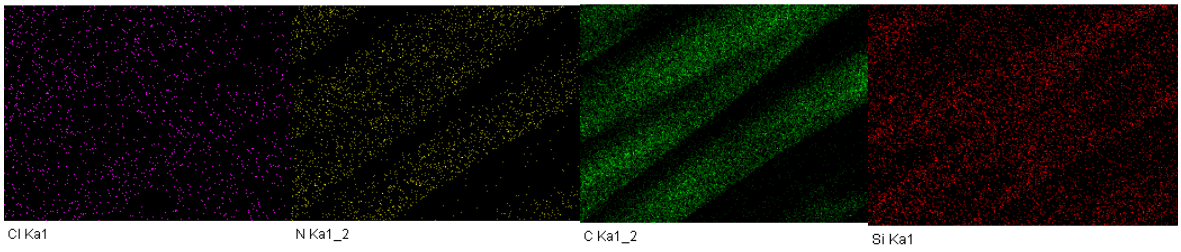

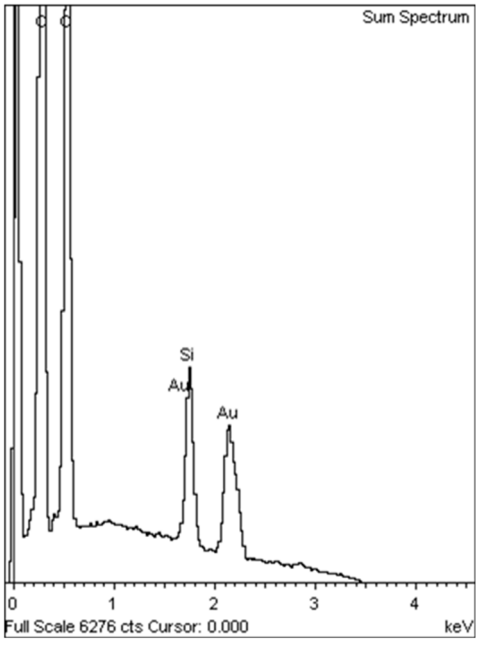

Fabric-mN7

SEM

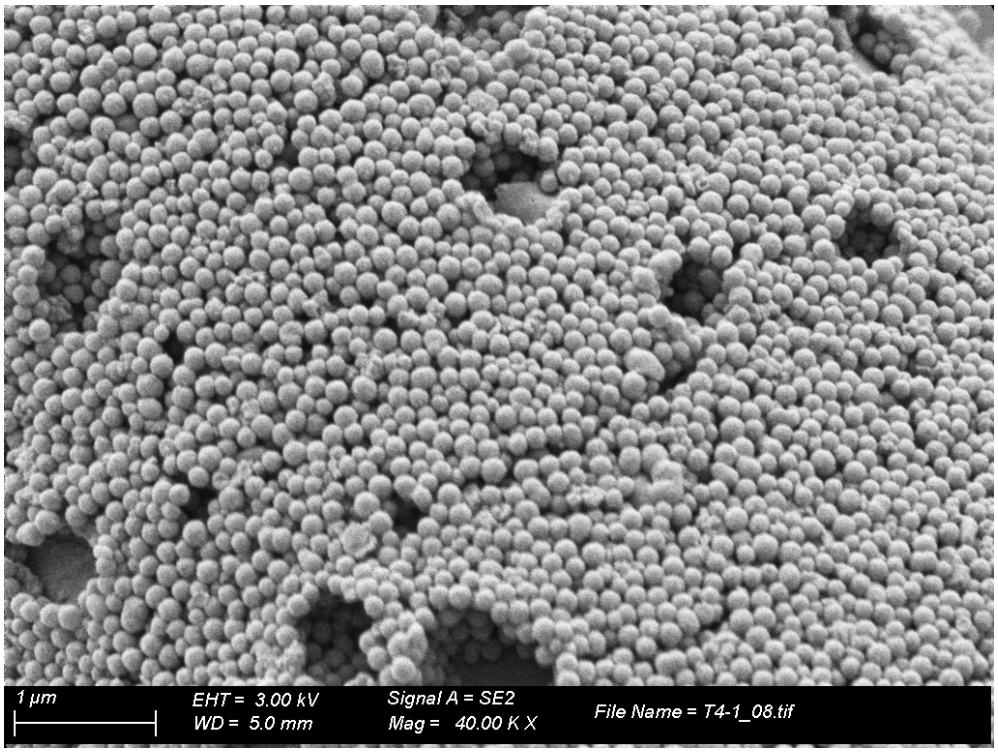

EDX/Mapping

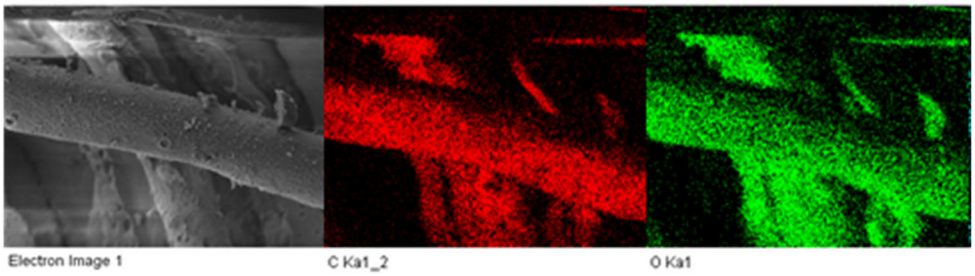

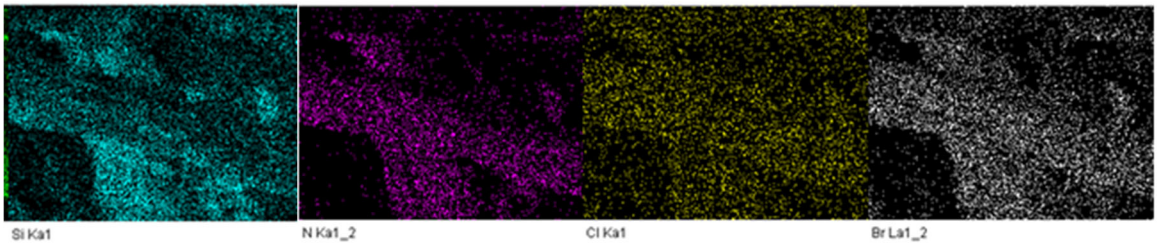

Annex: collection of spectra and characterization data

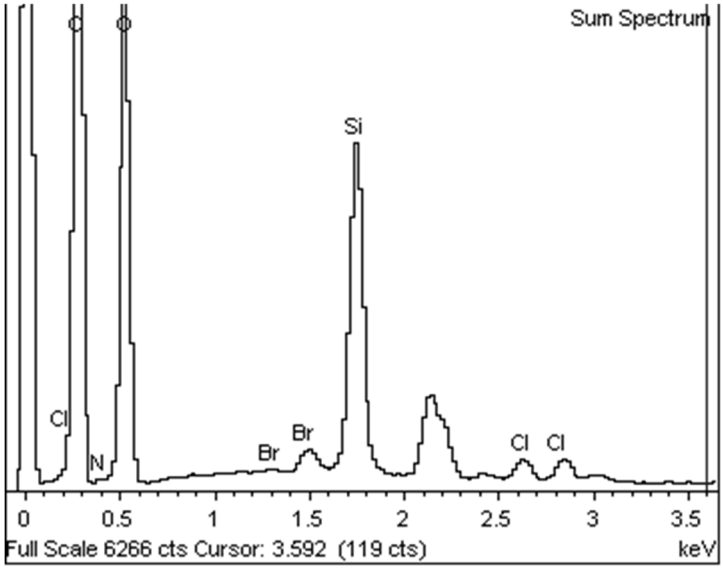

Fabric-mN8

SEM

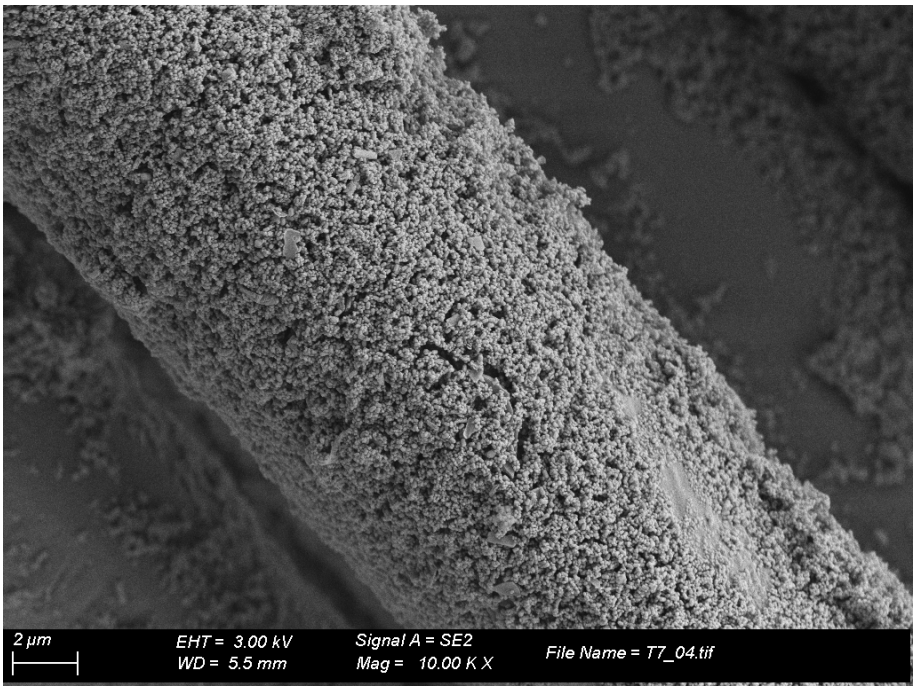

EDX/Mapping

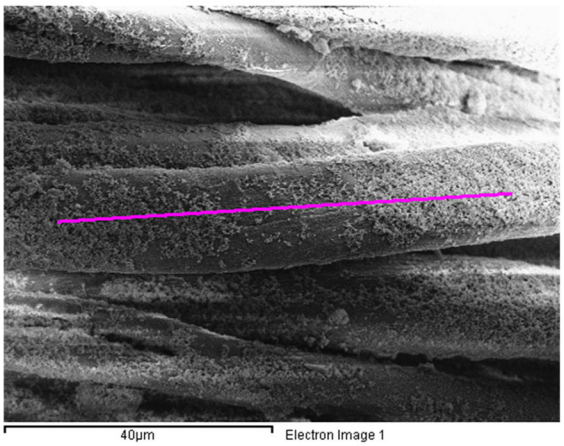

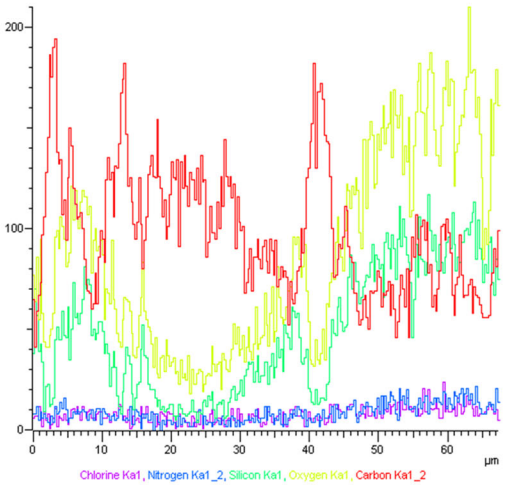

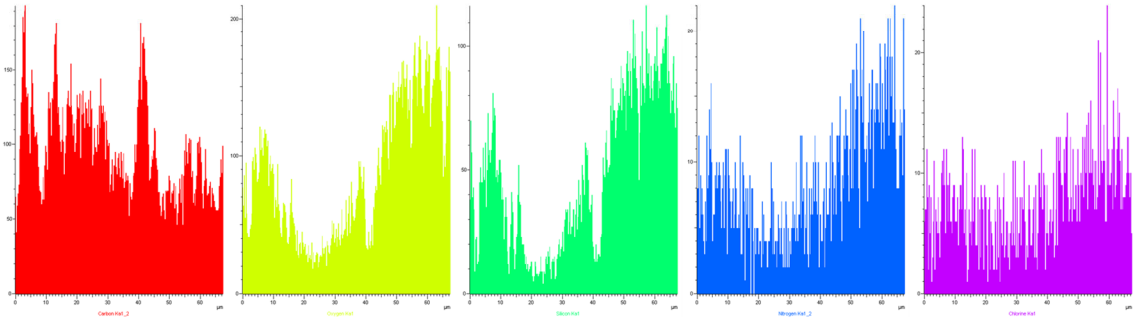

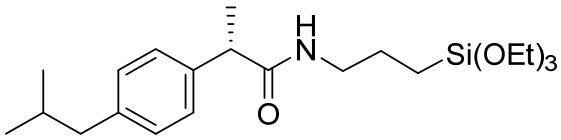

17

^{1}H NMR (400 MHz, $CDCl_3$)

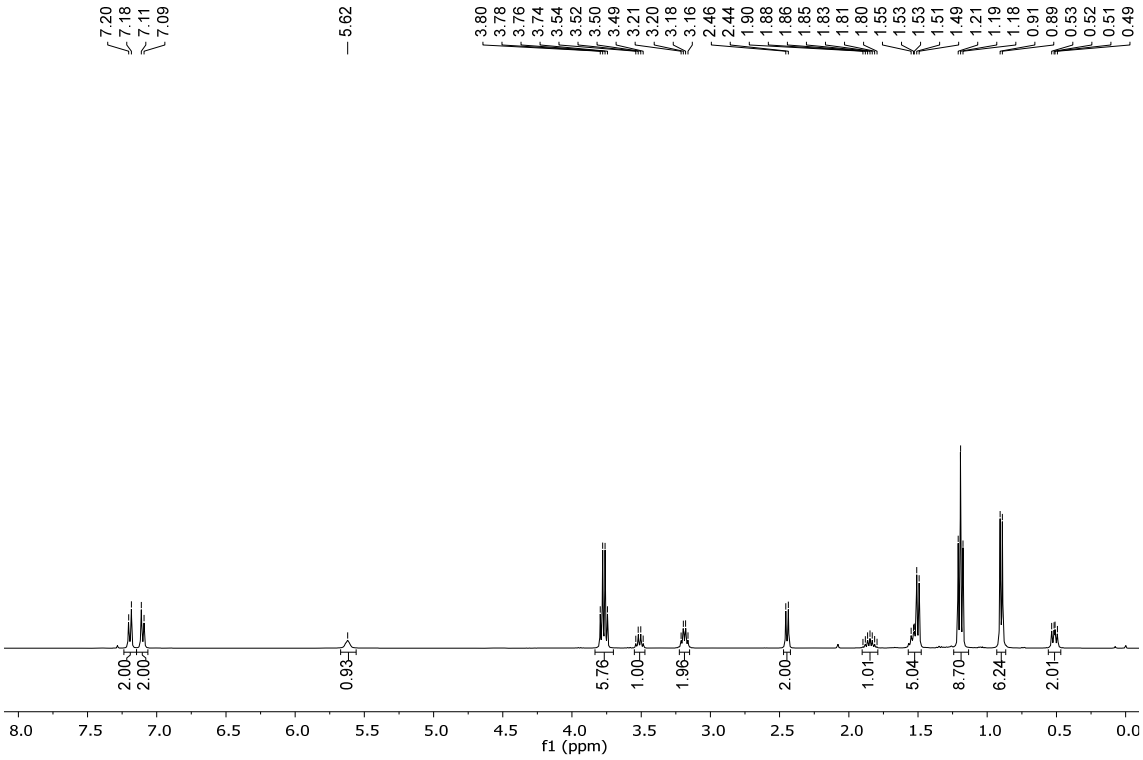

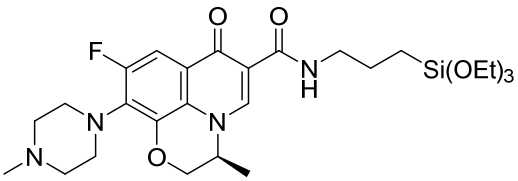

19

^{1}H NMR (400 MHz, $CDCl_3$)

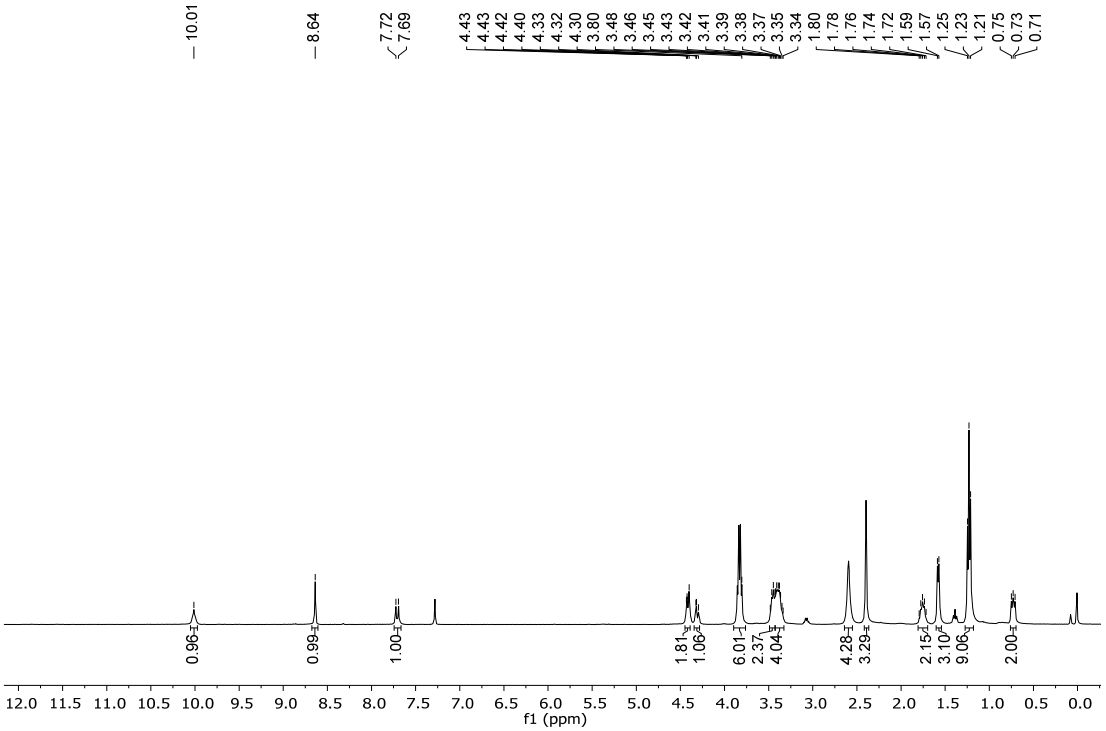

^{13}C NMR (101 MHz, $CDCl_3$)

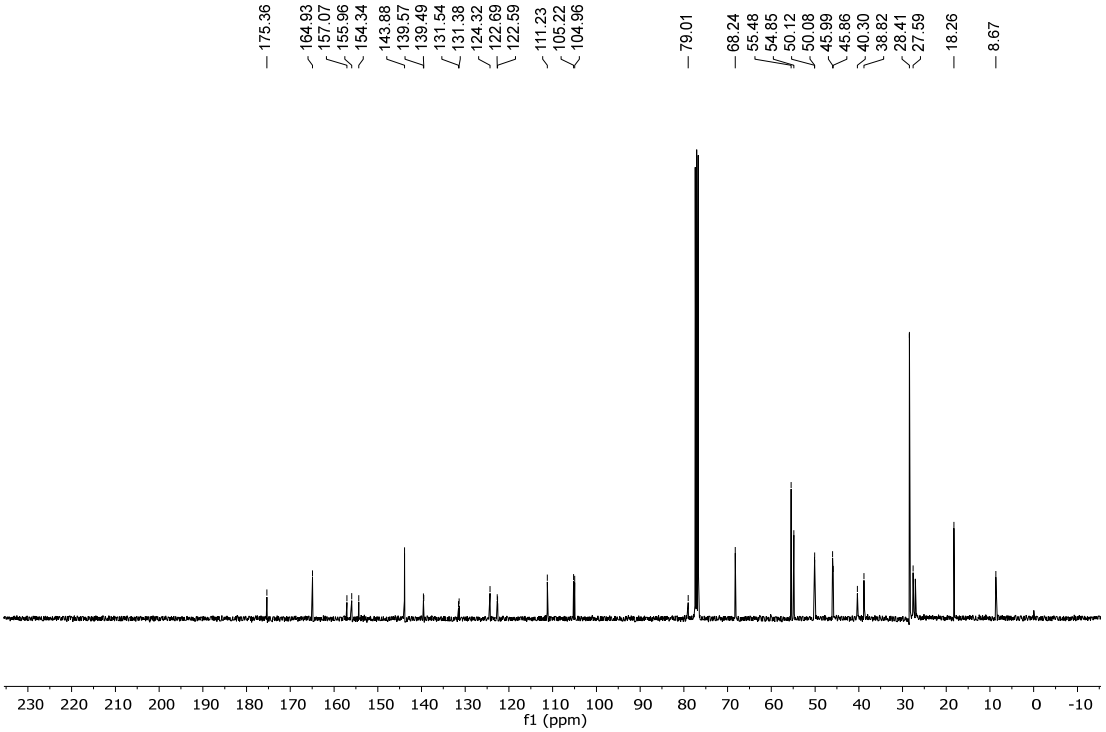

^{19}F NMR (376 MHz, $CDCl_3$)

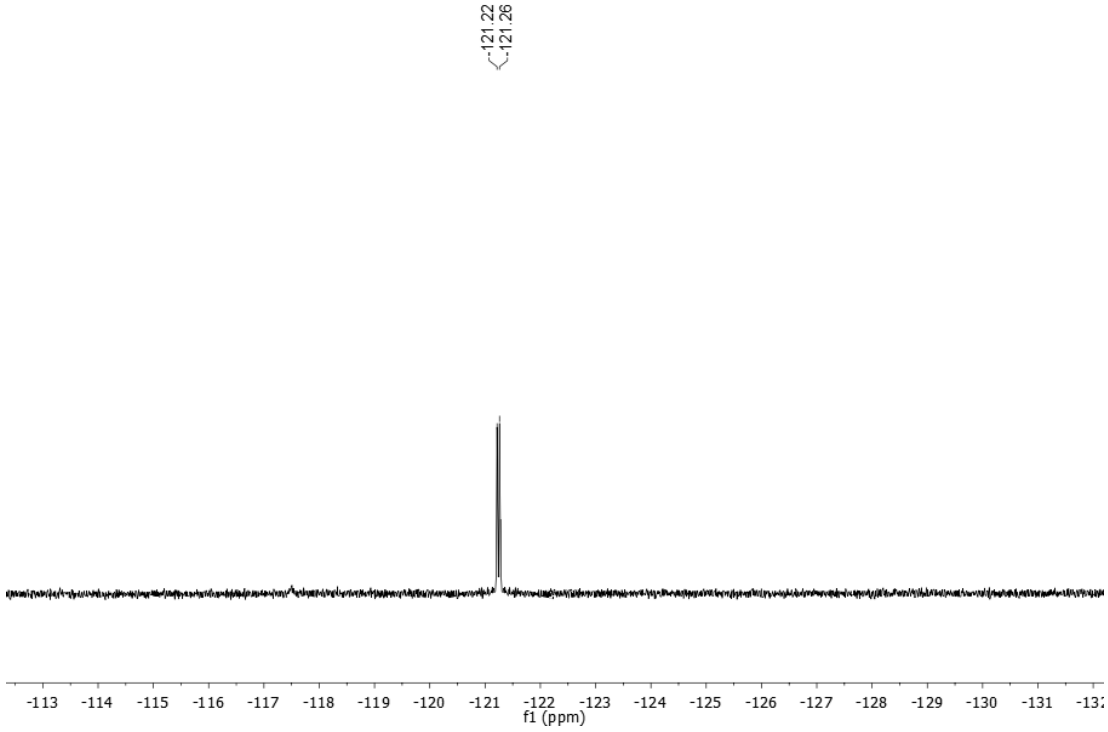

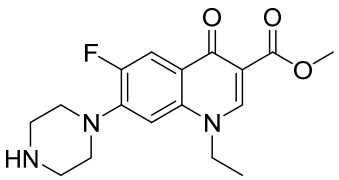

21

^{1}H NMR (400 MHz, $CDCl_3$)

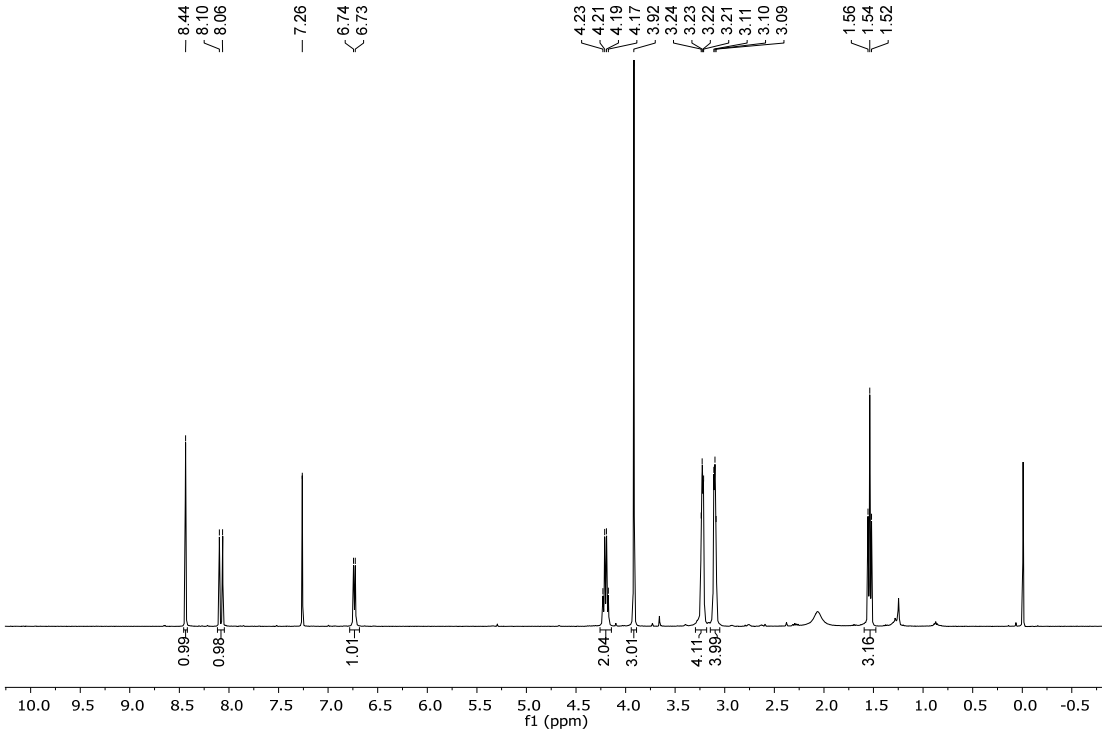

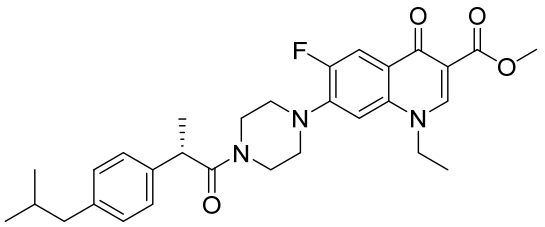

22

^{1}H NMR (400 MHz, $CDCl_3$)

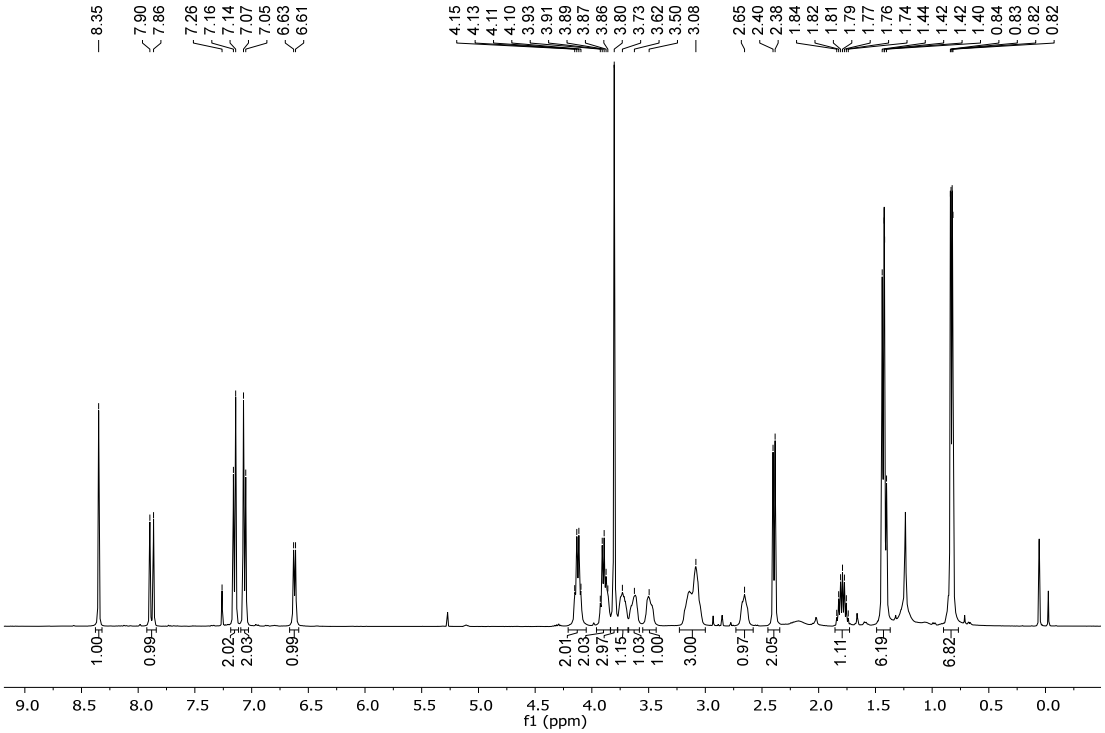

^{13}C NMR (101 MHz, $CDCl_3$)

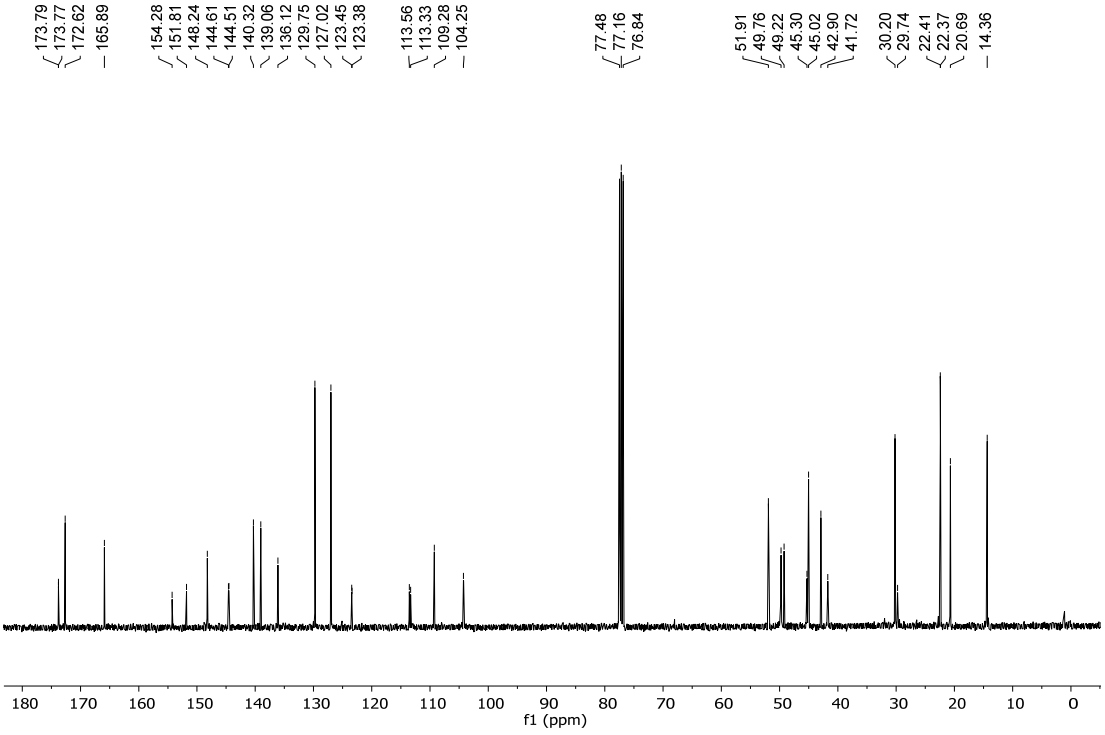

IR (ATR) of compound

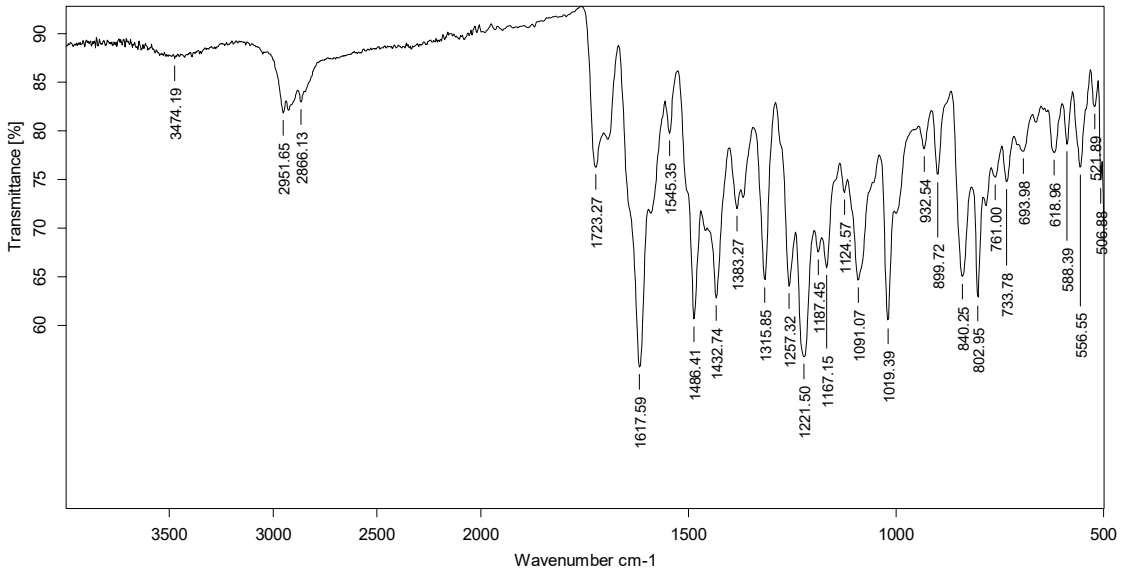

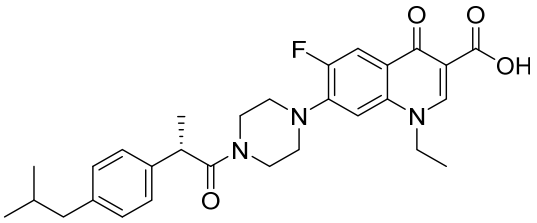

23

^{1}H NMR (400 MHz, $CDCl_3$)

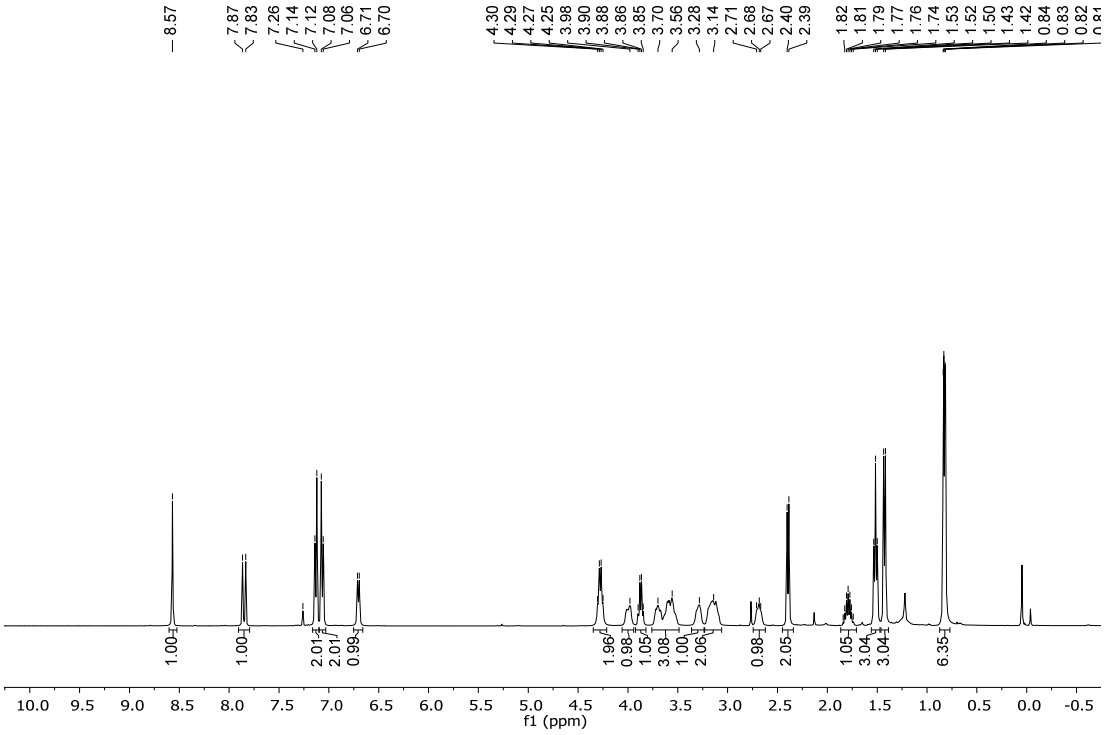

^{13}C NMR (101 MHz, $CDCl_3$)

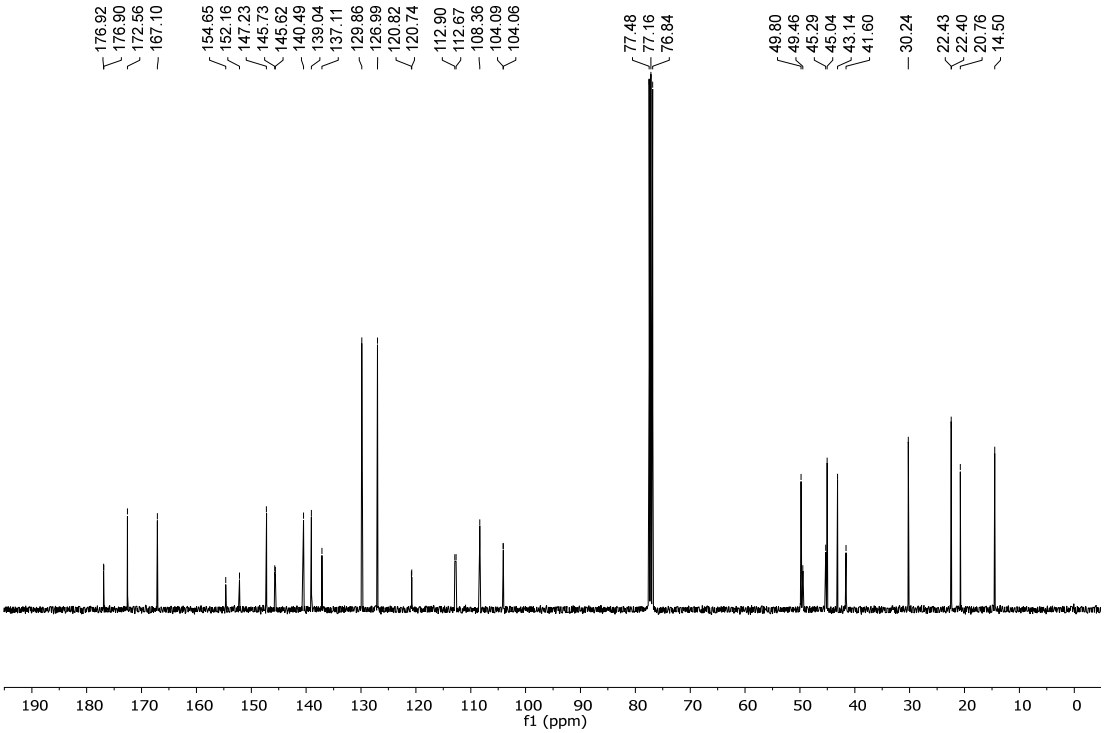

IR (ATR)

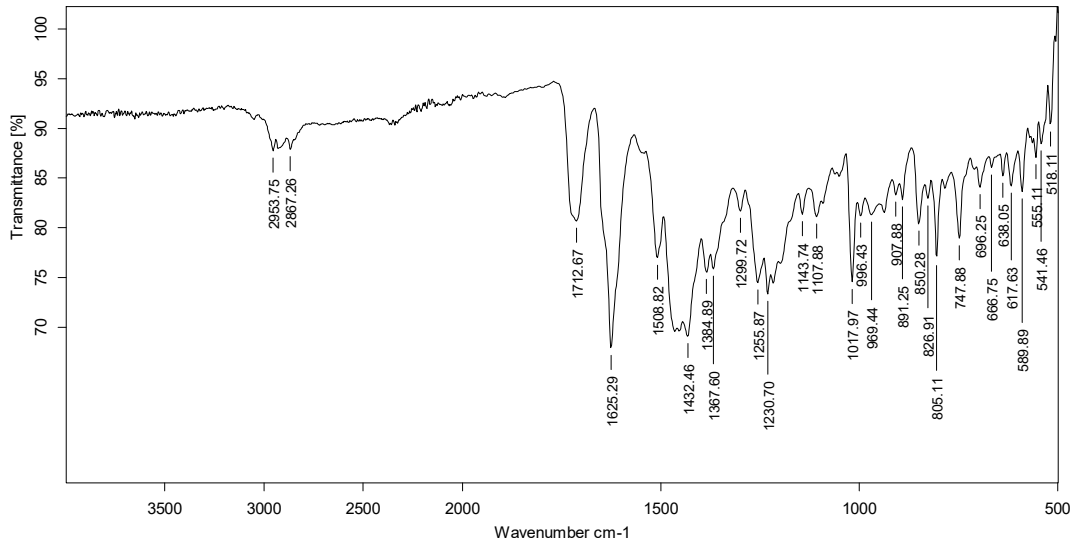
Transmittance [%]
100
95
90
85
80
75
70
2953.75
2867.26
1712.67
1625.29
1508.82
1432.46
1384.89
1367.60
1299.72
1255.87
1230.70
1143.74
1107.88
1017.97
996.43
969.44
907.88
891.25
850.28
826.91
805.11
747.88
696.25
666.75
638.05
617.63
589.89
555.11
541.46
518.11
3500
3000
2500
2000
1500
1000
500
Wavenumber cm-1

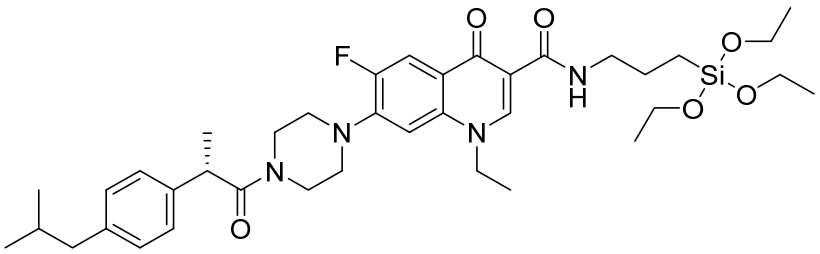

24

^{1}H NMR (400 MHz, $CDCl_3$)

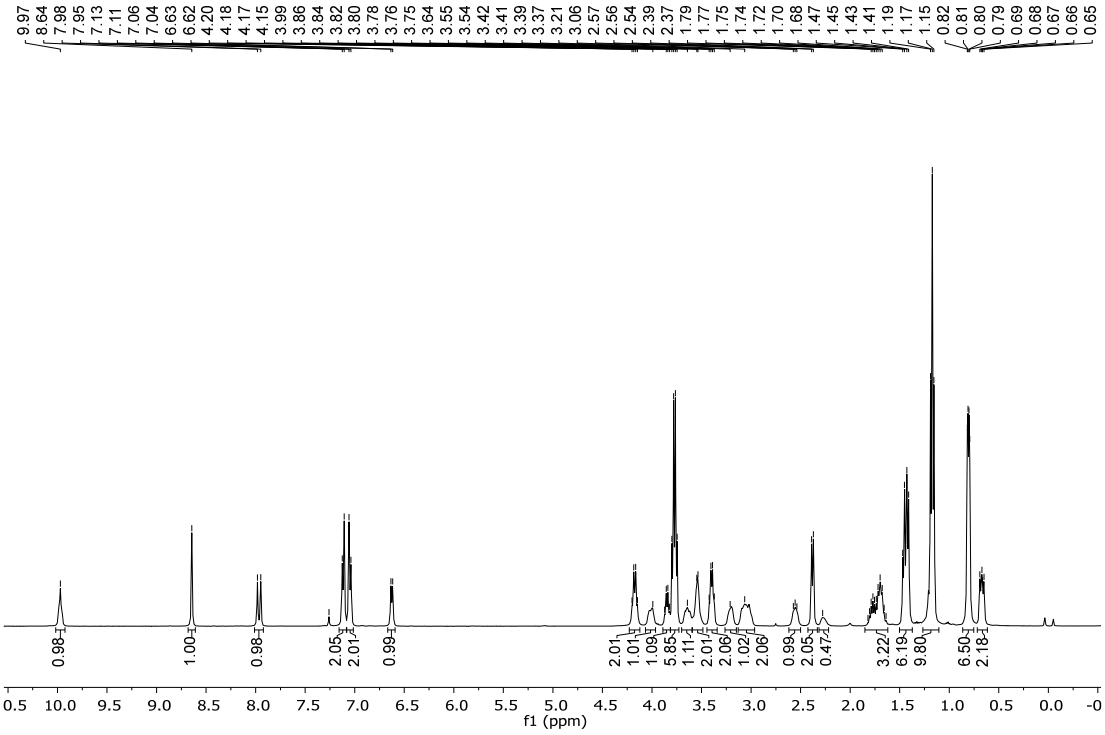

^{13}C NMR (101 MHz, $CDCl_3$)

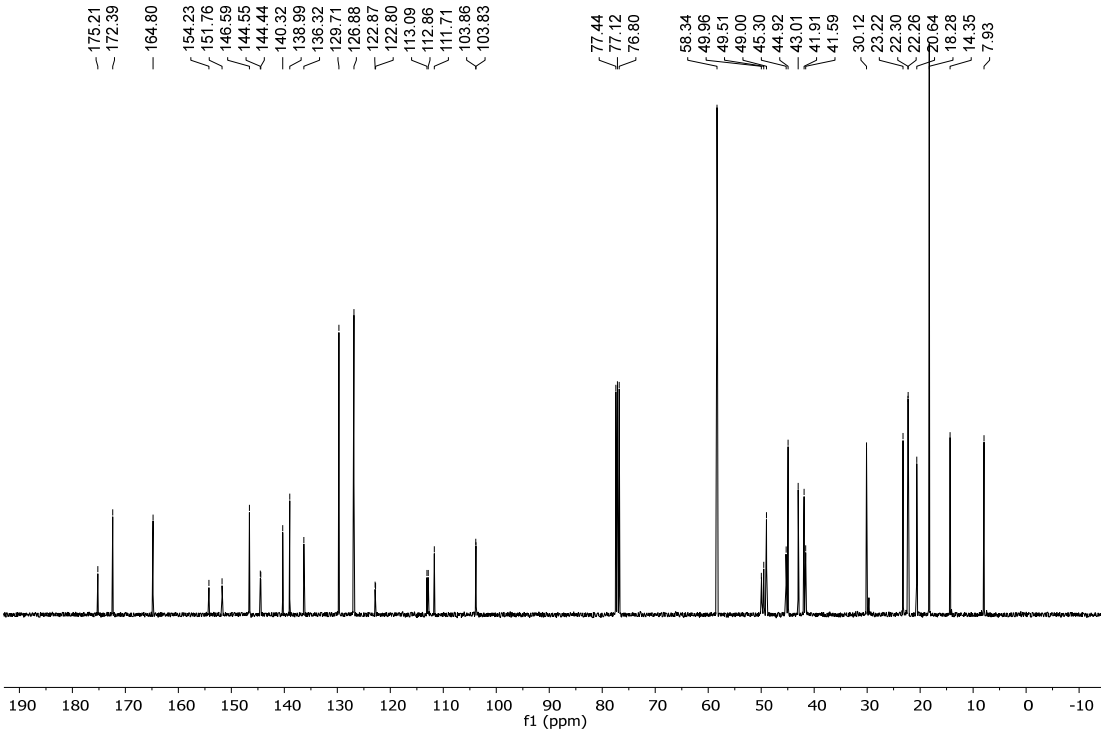

IR (ATR)

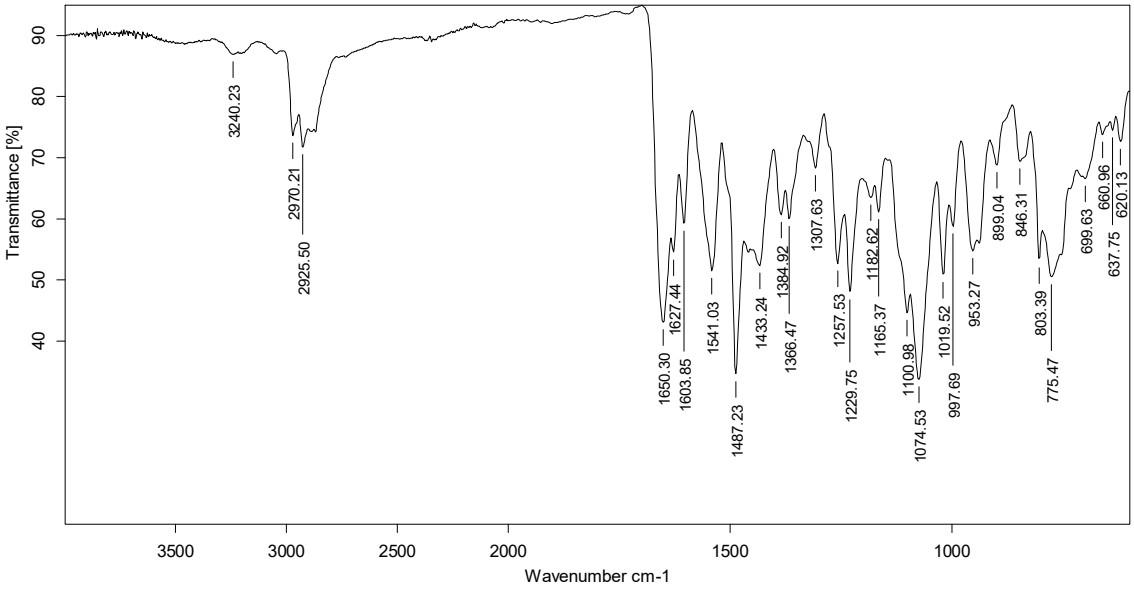
Transmittance [%]
90
80
70
60
50
40
3240.23
2970.21
2925.50
1650.30
1627.44
1603.85
1541.03
1487.23
1433.24
1384.92
1366.47
1307.63
1257.53
1229.75
1182.62
1165.37
1100.98
1074.53
1019.52
997.69
953.27
899.04
846.31
803.39
775.47
699.63
660.96
637.75
620.13
3500
3000
2500
2000
1500
1000
Wavenumber cm-1

SiO_2@Ibu+Leflox (20:0.5:0.5)

DLS

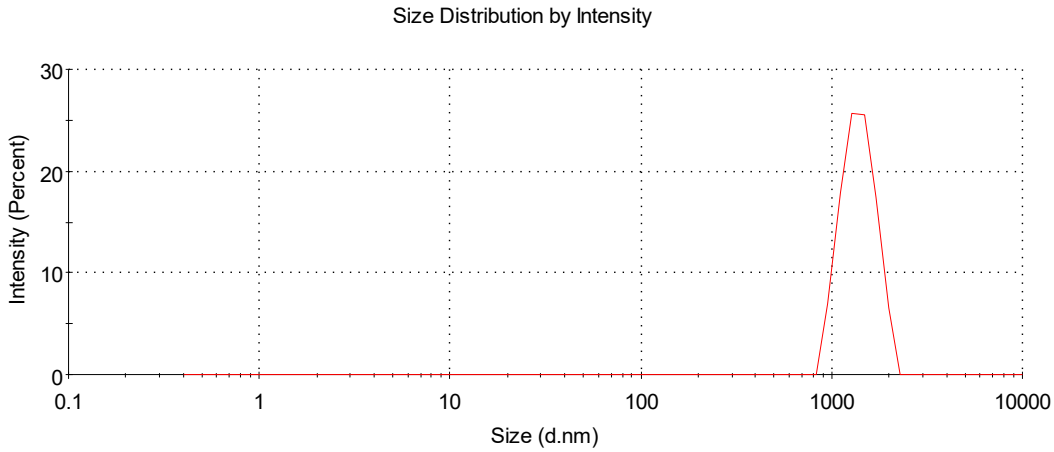

Zeta-potential

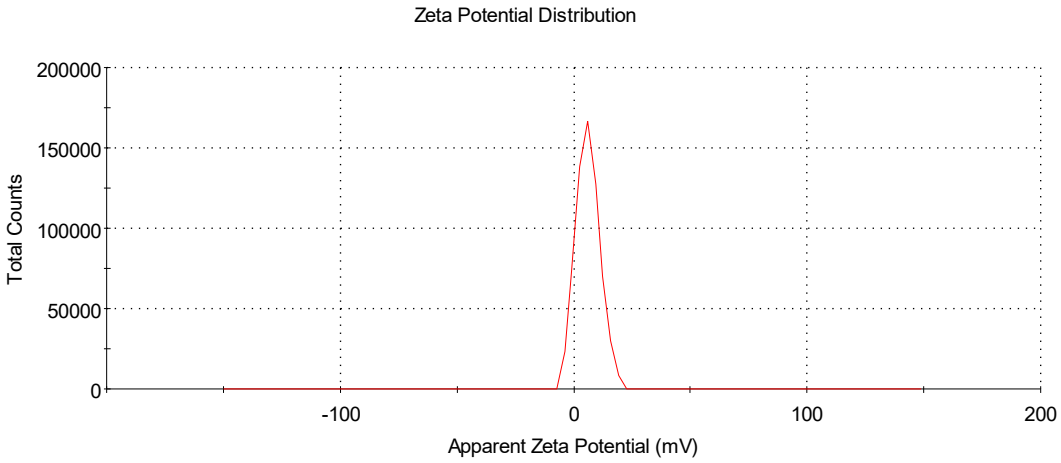

TEM

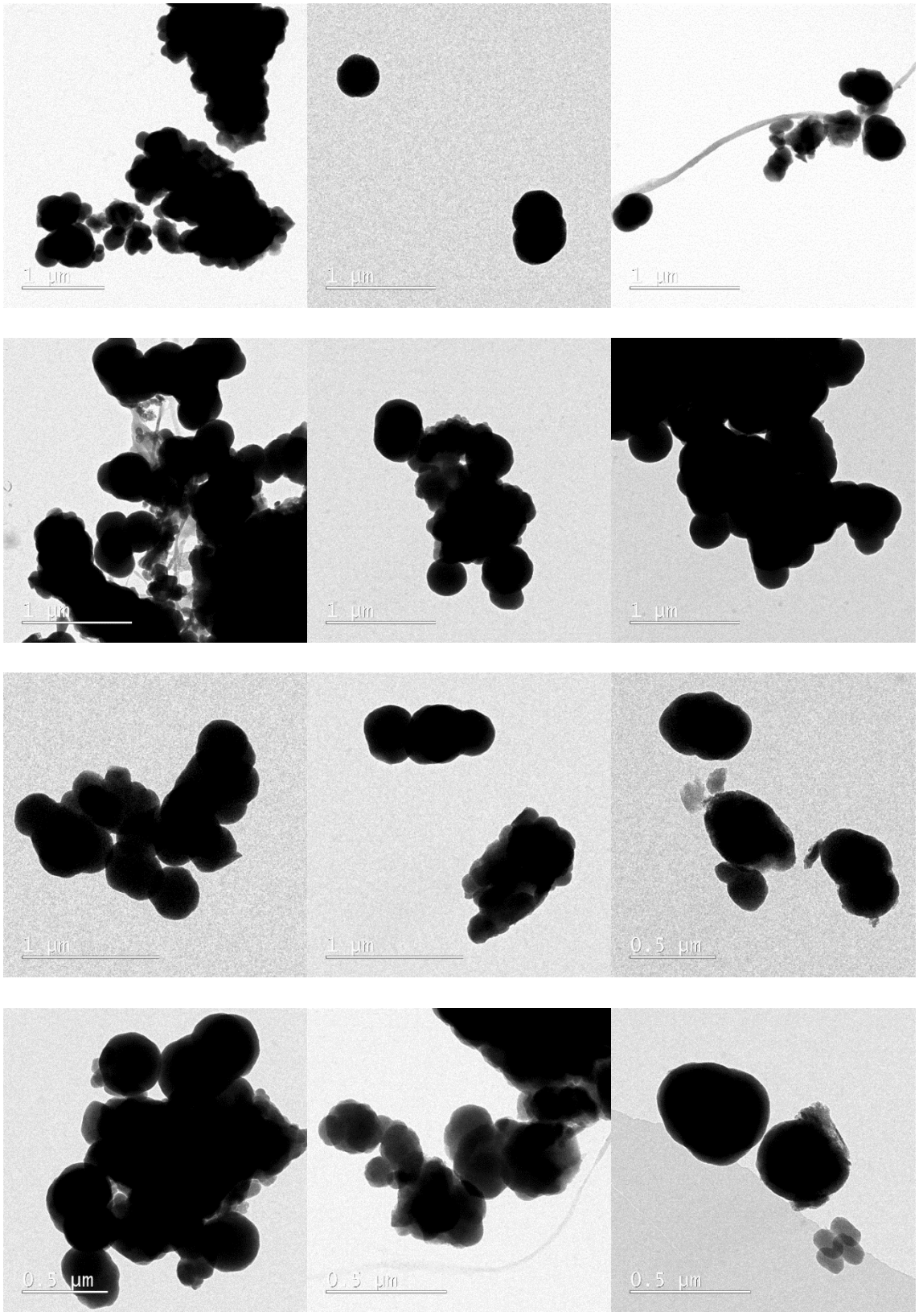

IR (ATR)

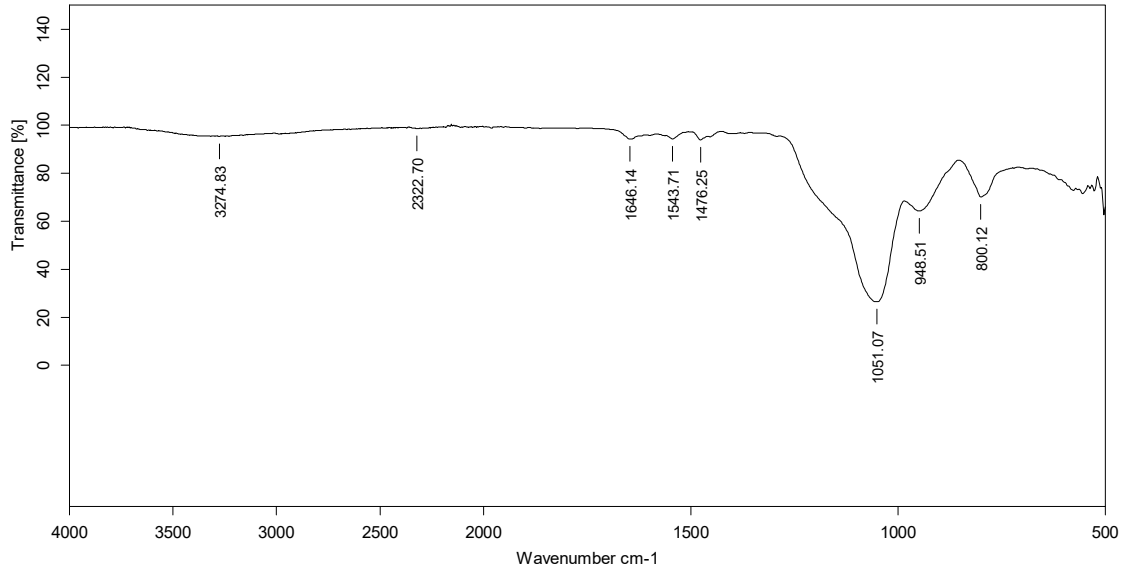
Transmittance [%]
0
20
40
60
80
100
120
140
3274.83
2322.70
1646.14
1543.71
1476.25
1051.07
948.51
800.12
4000
3500
3000
2500
2000
1500
1000
500
Wavenumber cm-1

SiO_2@Ibu+Leflox (20:0.75: 0.25)

DLS

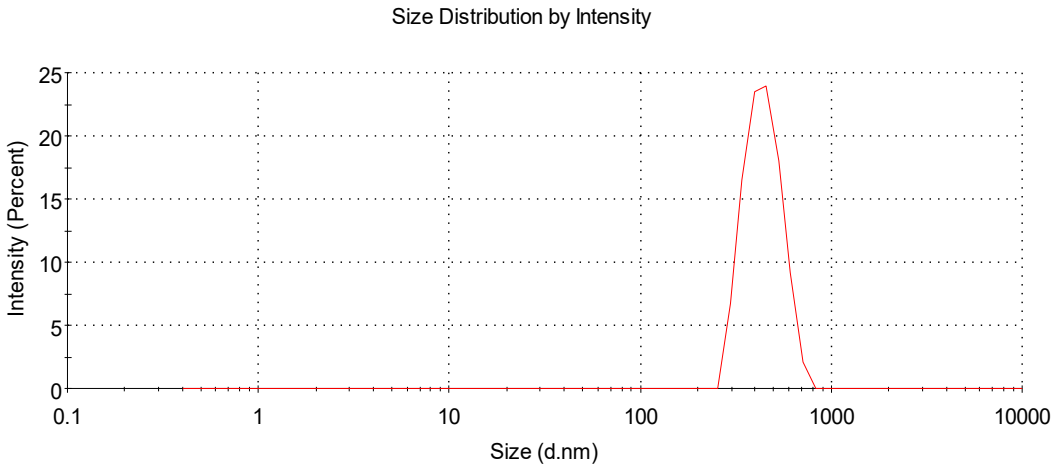

Zeta-potential

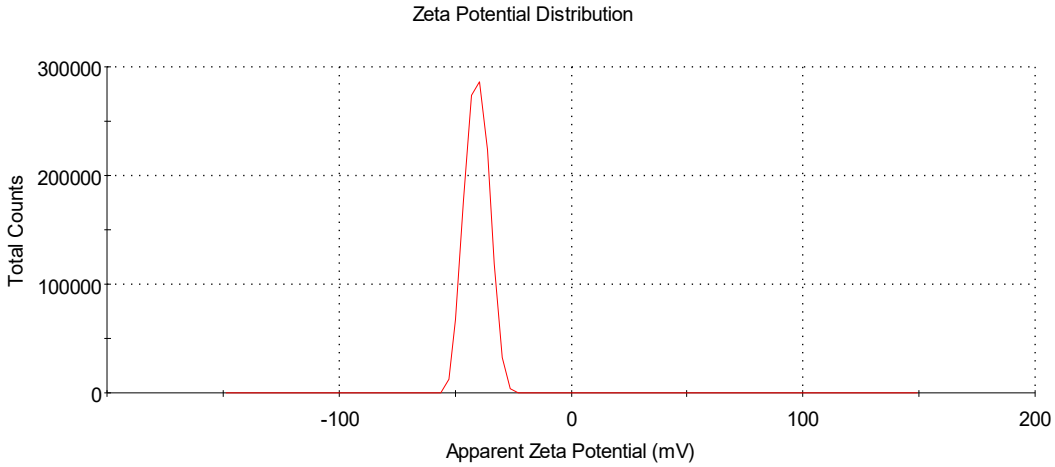

TEM

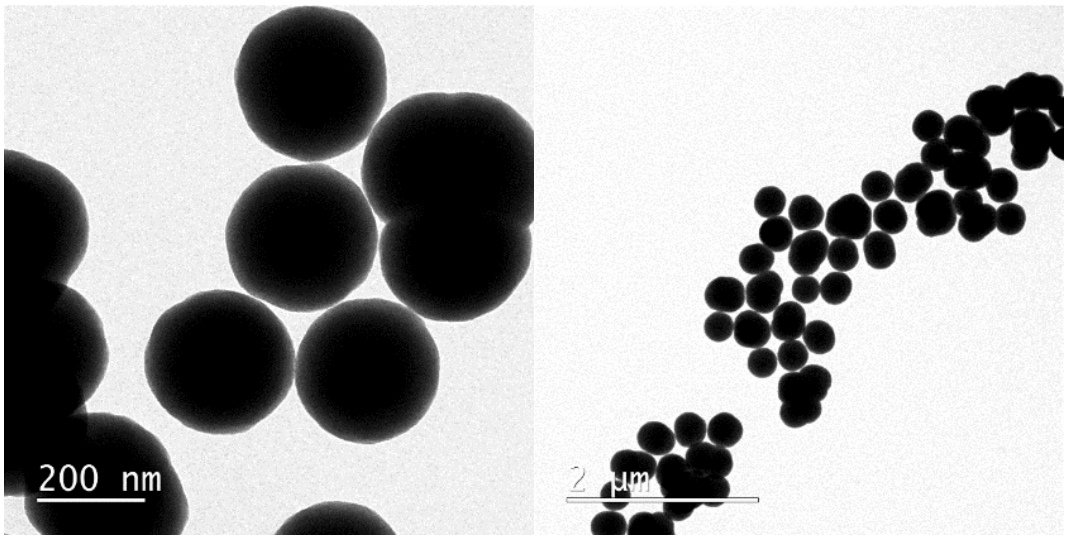

Annex: collection of spectra and characterization data

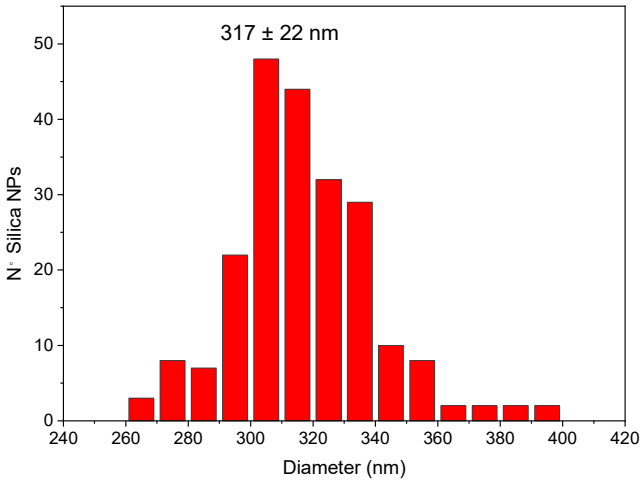

IR (ATR)

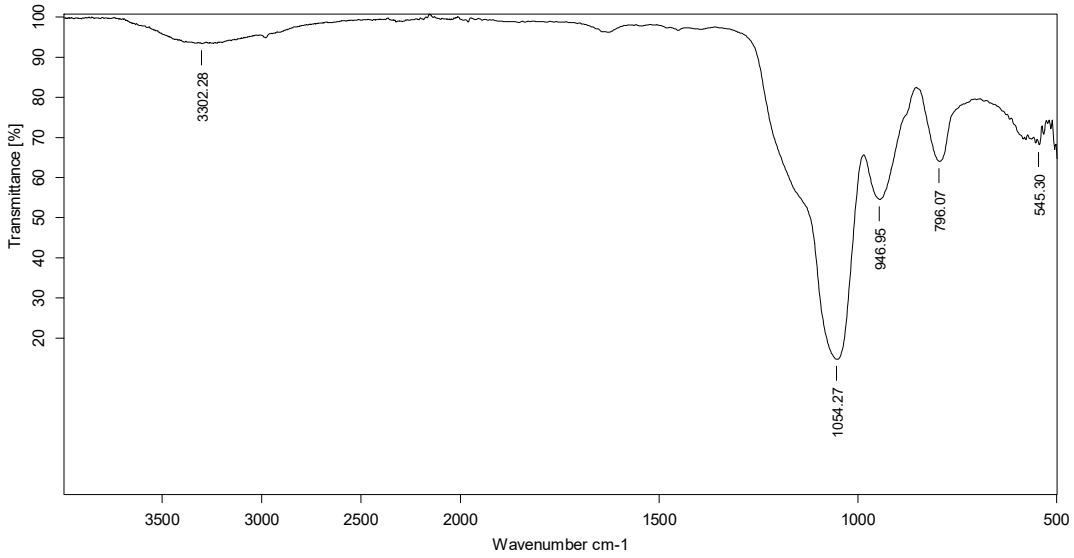

SiO_2@Norflox-Ibu (TEOS: 2c (20:1))

DLS

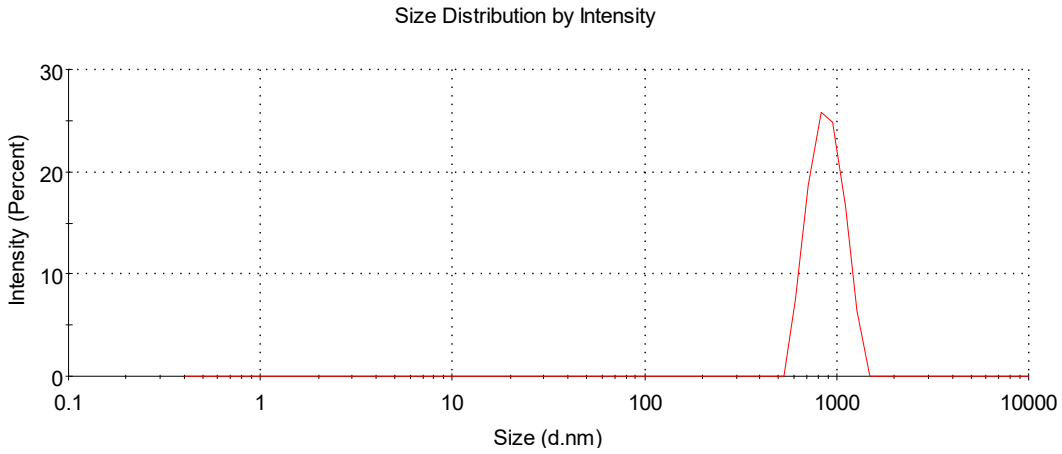

Zeta-potential

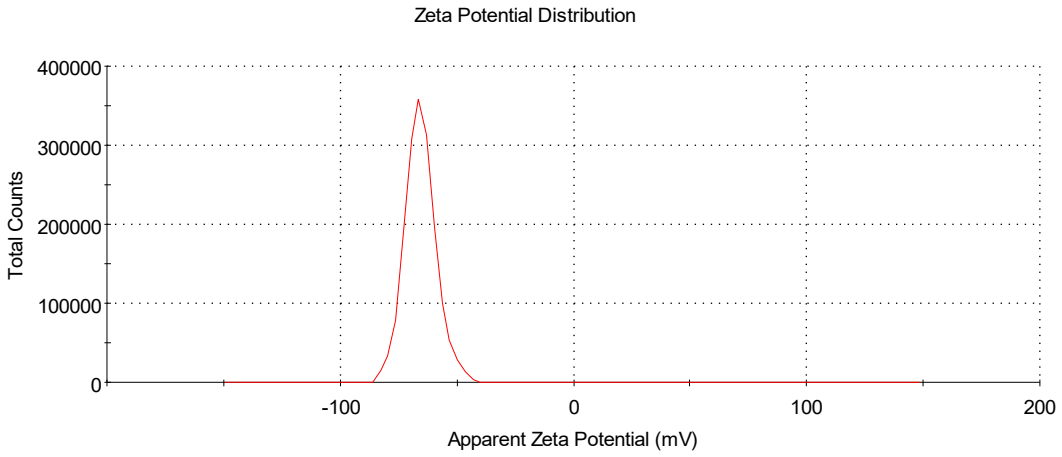

TEM

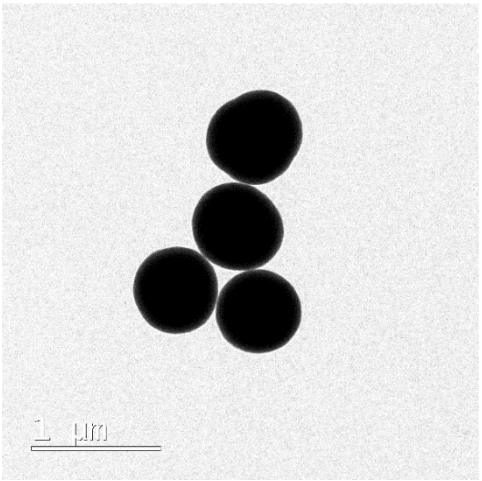

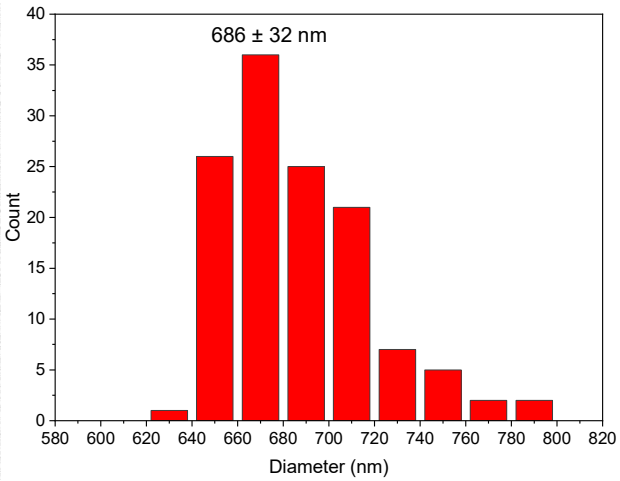

Solid state ^{13}C NMR^{29}Si NMR

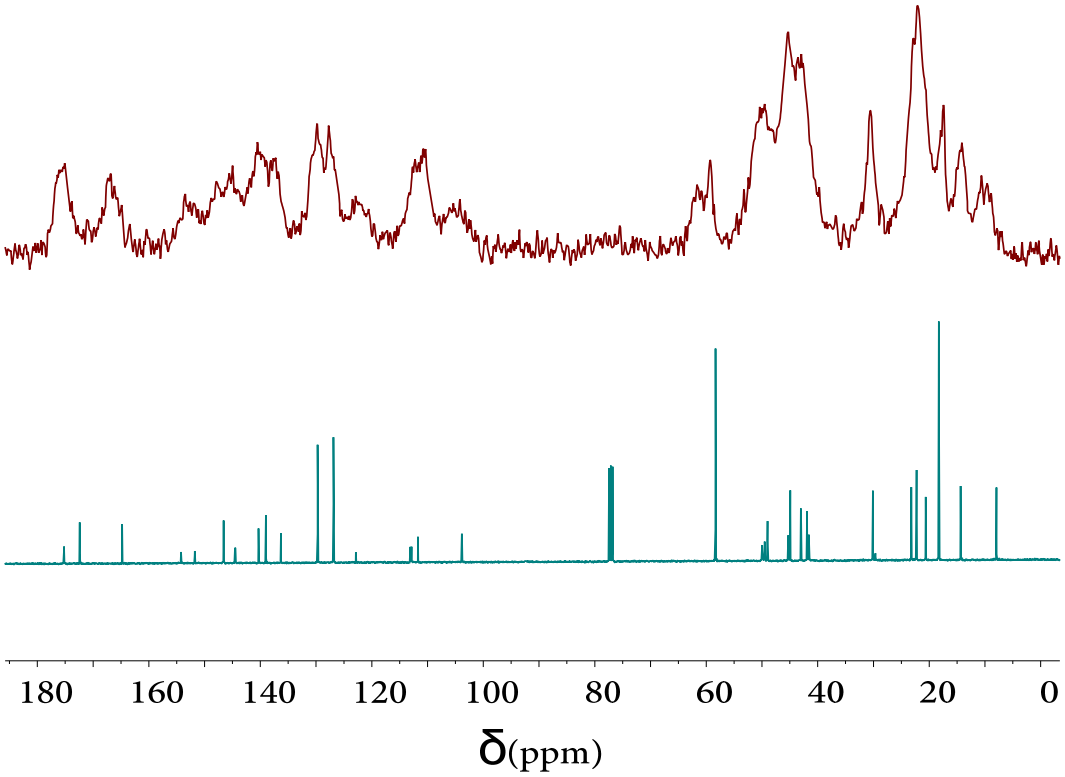

Solid state ^{29}Si NMR

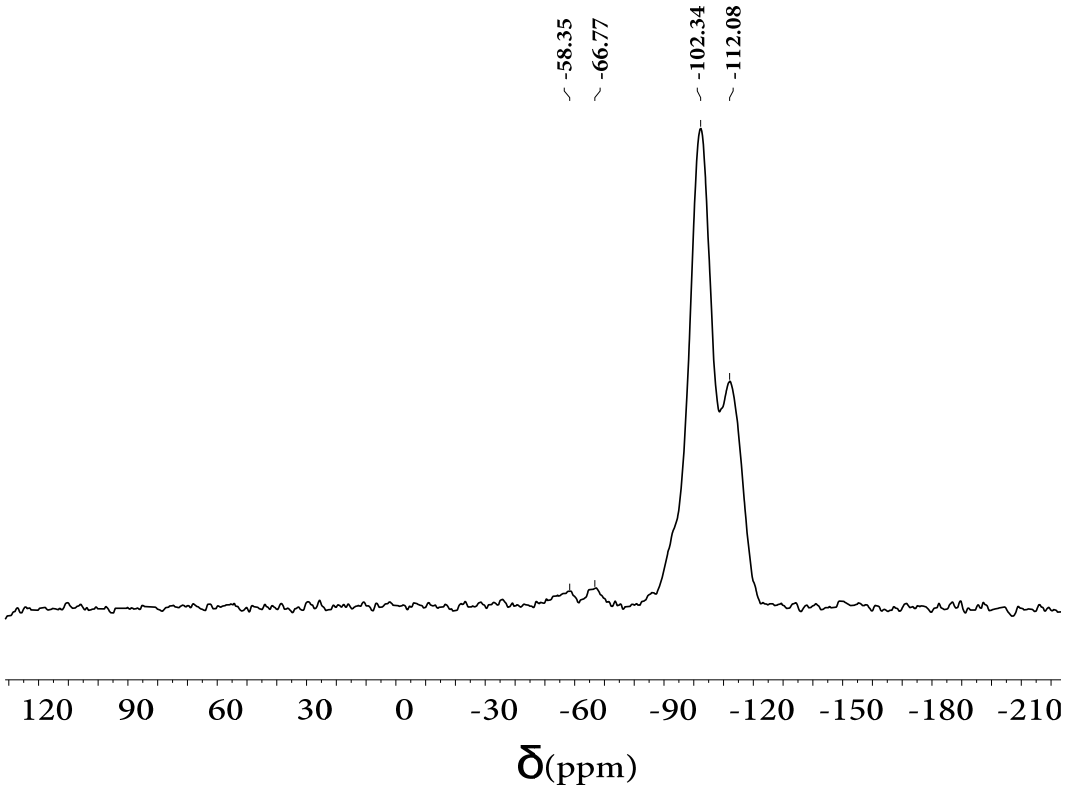

IR (ATR)

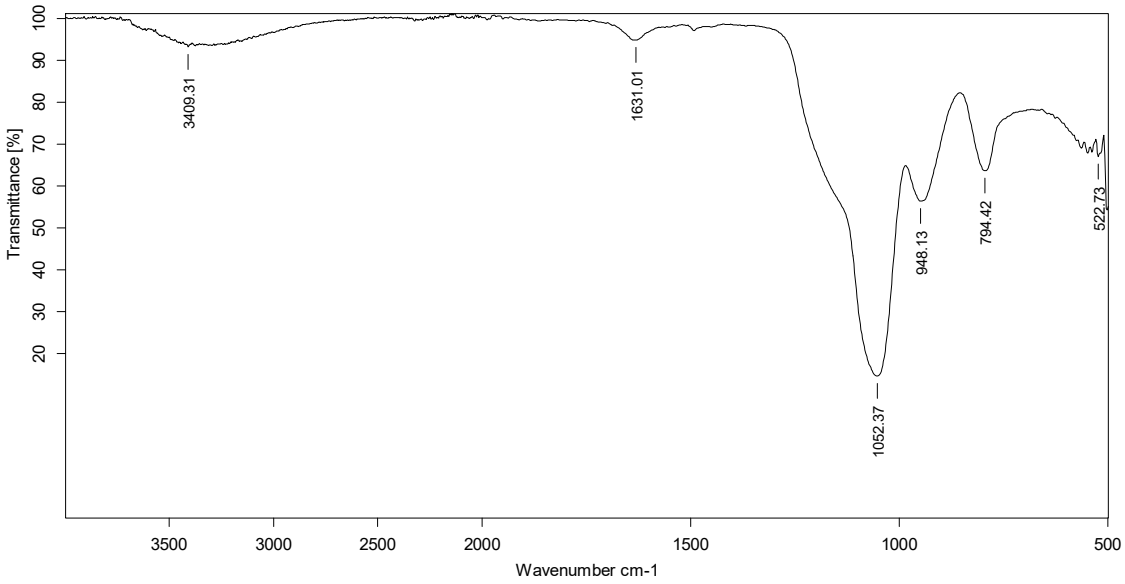
Transmittance [%]
100
90
80
70
60
50
40
30
20
3409.31
1631.01
1052.37
948.13
794.42
522.73
3500
3000
2500
2000
1500
1000
500
Wavenumber cm-1

SiO_2@Norflox-Ibu (TEOS: 2c (30:1))

DLS

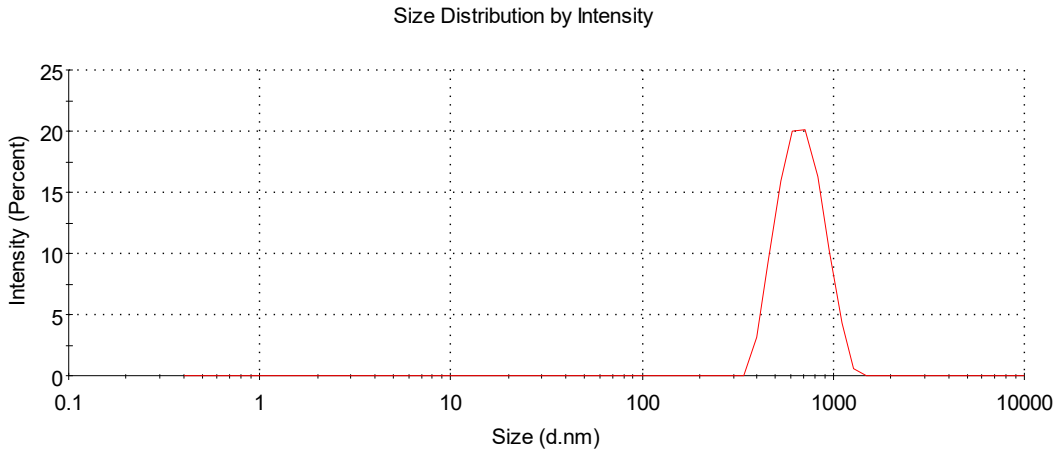

Zeta-potential

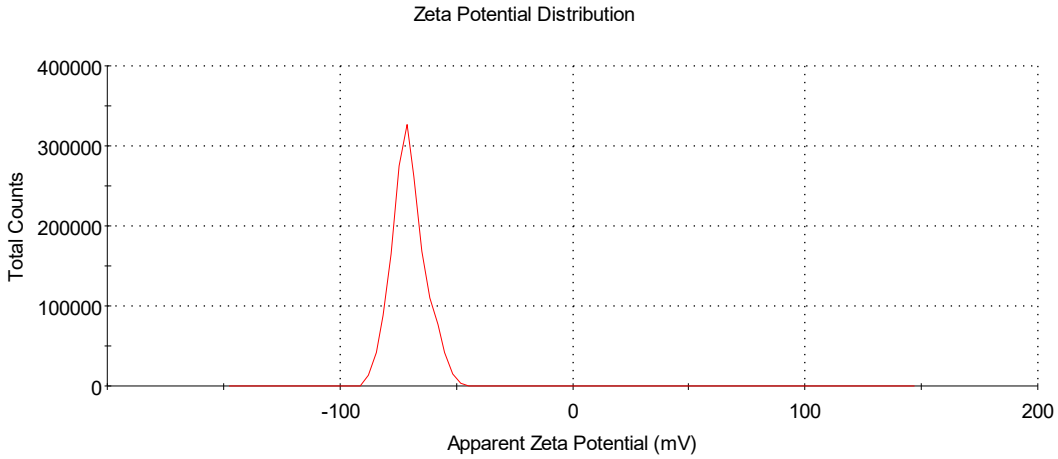

TEM

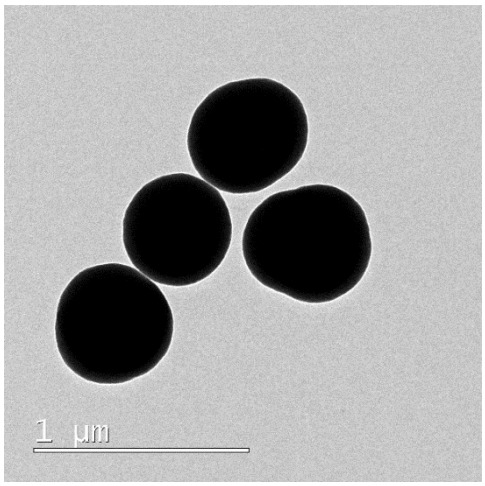

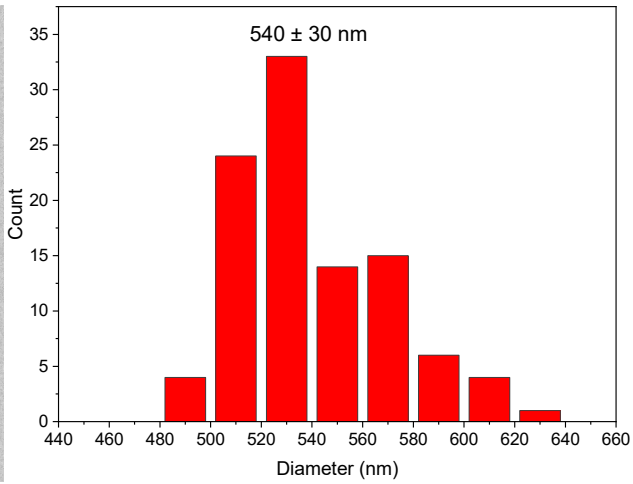

IR (ATR)

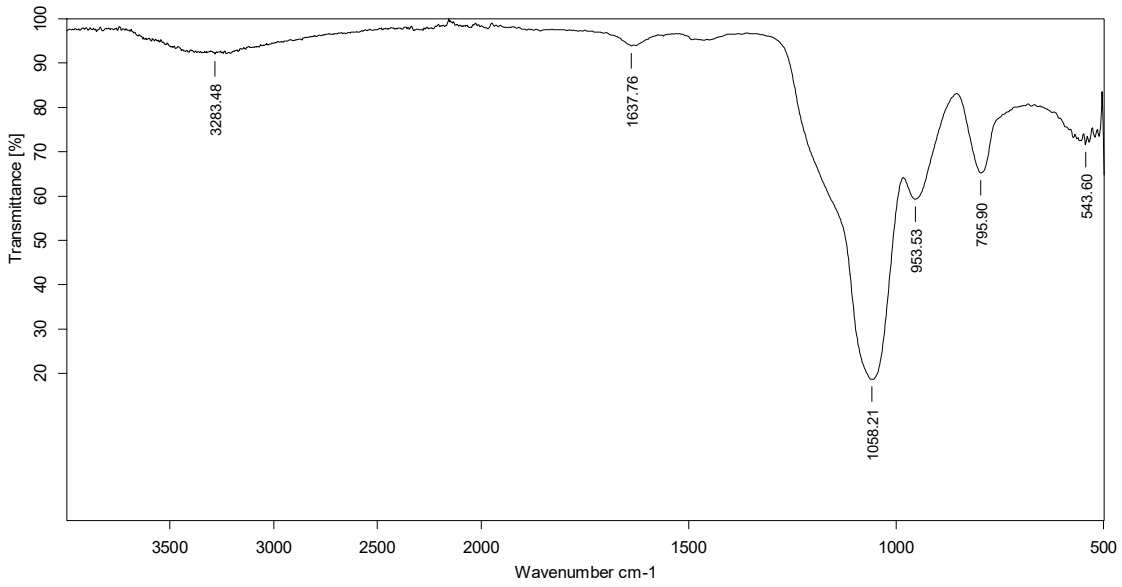
Transmittance [%]
100
90
80
70
60
50
40
30
20
3283.48
1637.76
1058.21
953.53
795.90
543.60
3500
3000
2500
2000
1500
1000
500
Wavenumber cm-1

SiO_2@Norflox-Ibu (TEOS: 2c (40:1))

DLS

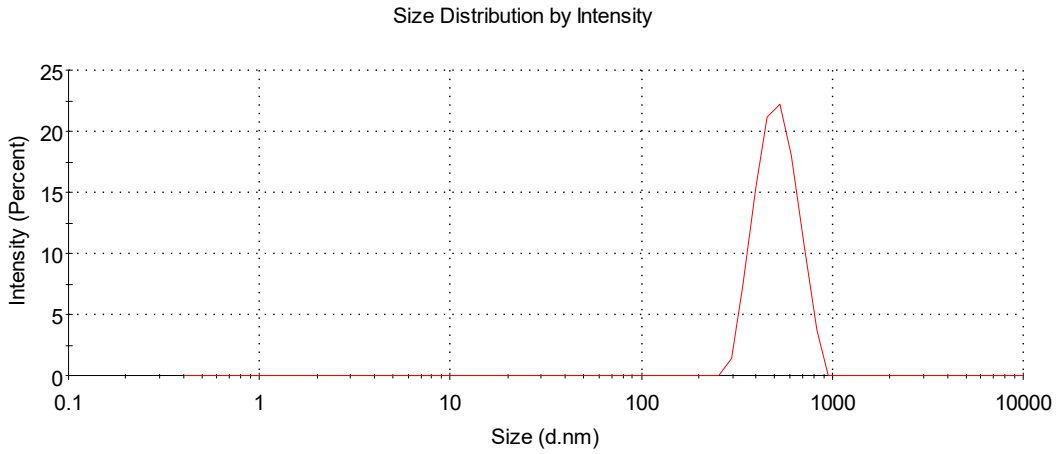

Zeta-potential

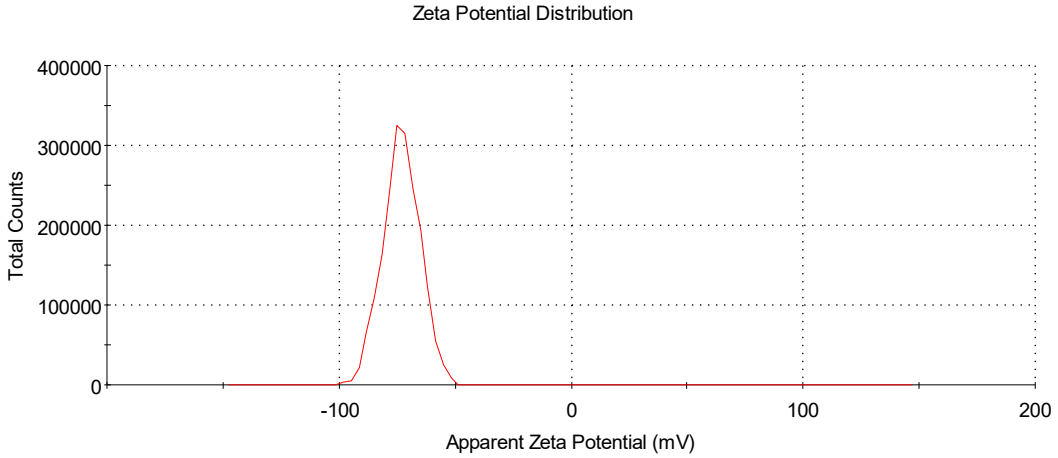

TEM

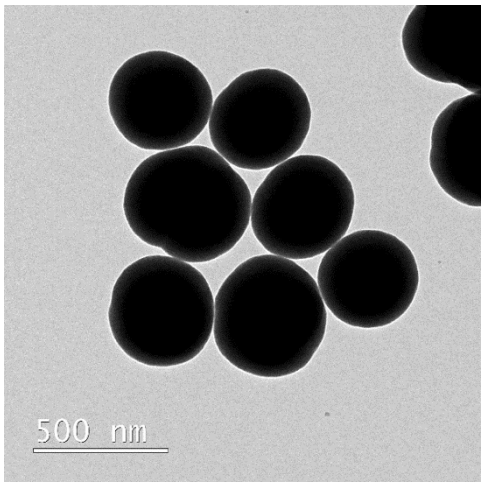

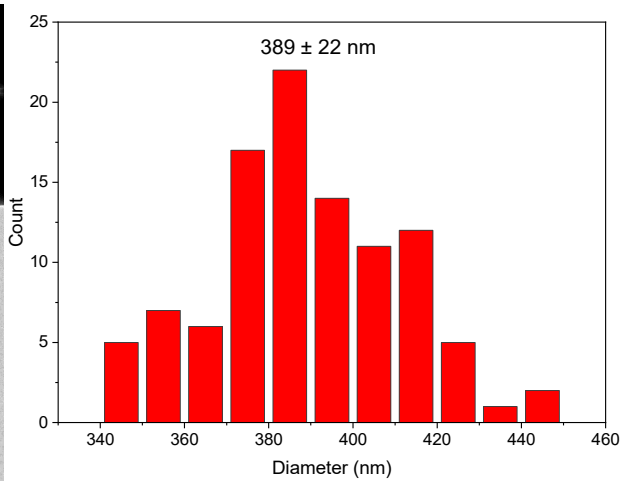

Solid state ^{29}Si NMR

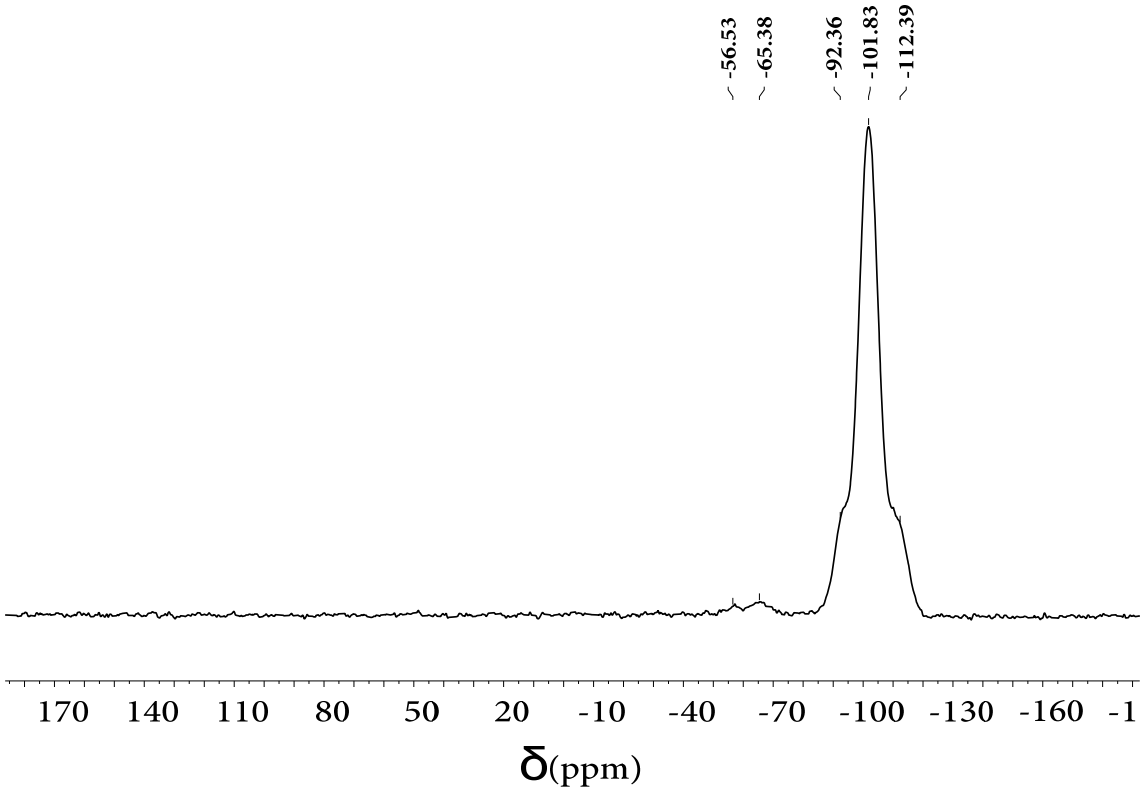

IR (ATR)

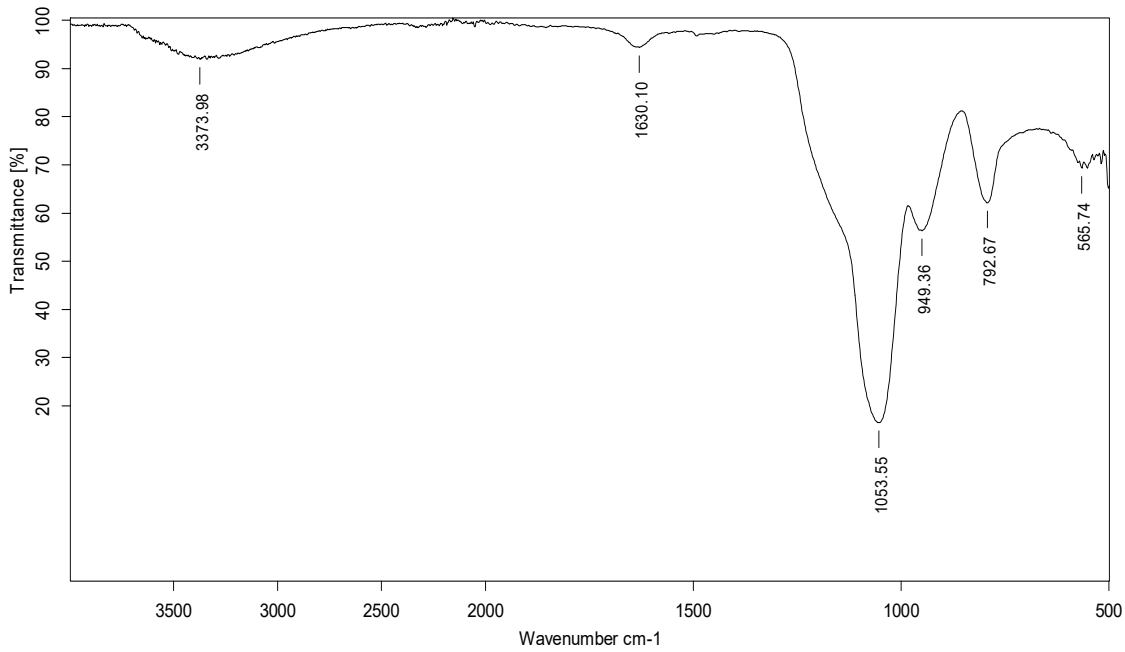

Fabric-SiO_2@Norflox-Ibu (40:1)

SEM

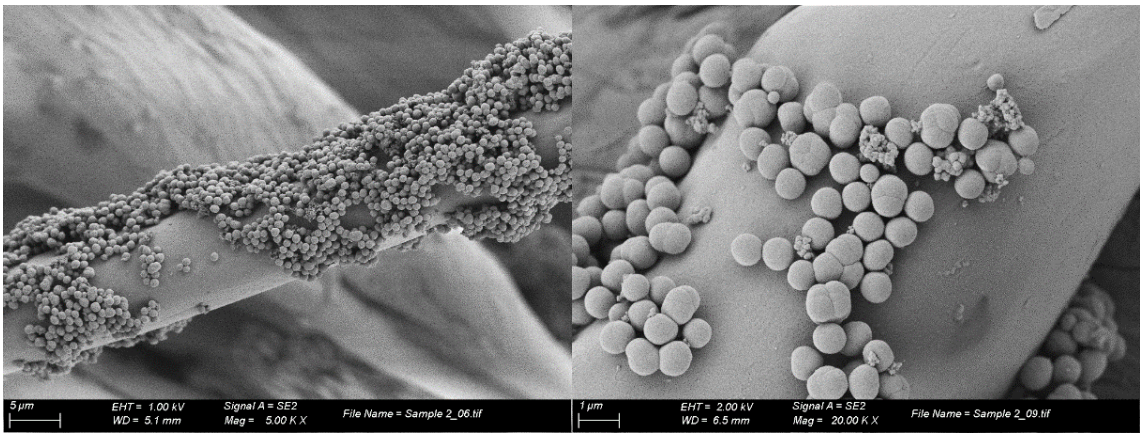

EDX mapping

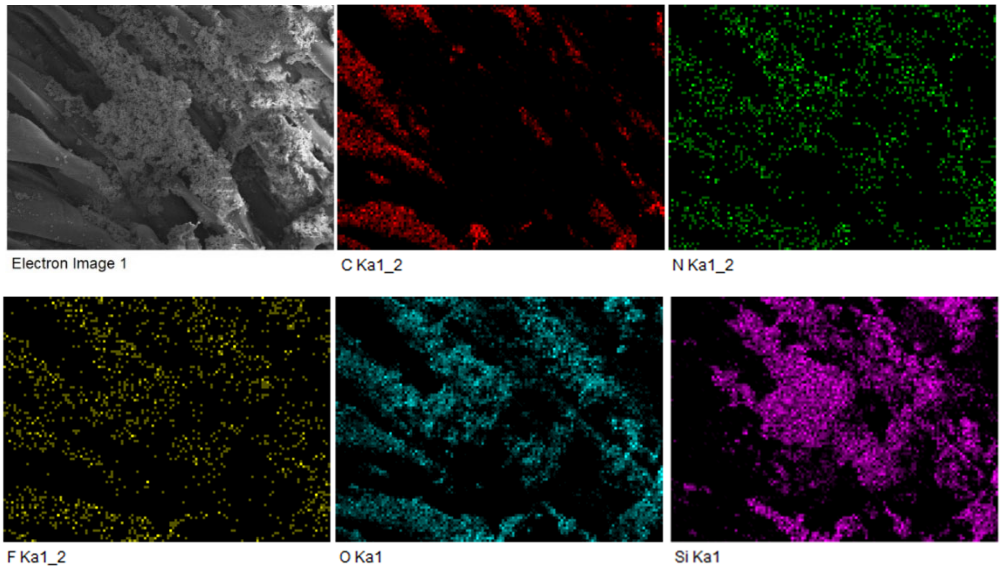

EDX linear scanning

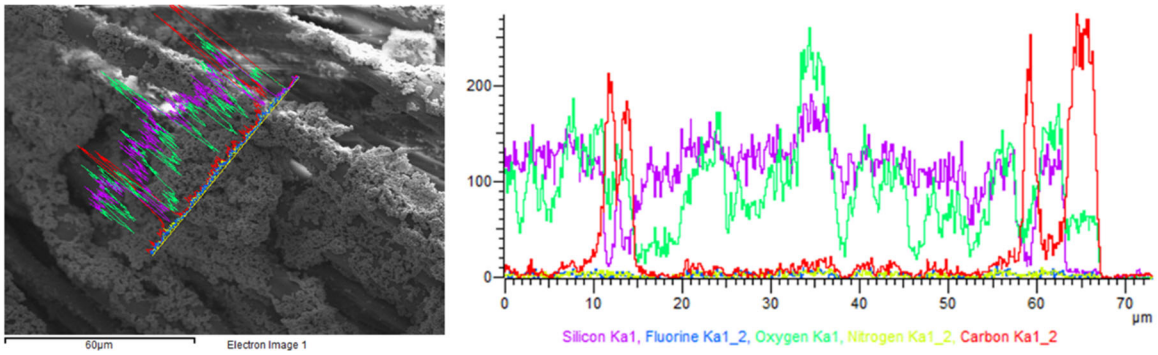

Element	App Conc.	Intensity Corrn.	Weight%	Weight% Sigma	Atomic%
C K	71.22	0.8193	24.23	0.29	34.07
N K	0.69	0.4052	0.47	0.29	0.57
O K	267.17	1.6888	44.09	0.29	46.55
F K	0.33	0.5990	0.15	0.14	0.14
Si K	121.39	1.0893	31.06	0.23	18.68
Totals			100.00		

IR (ATR)

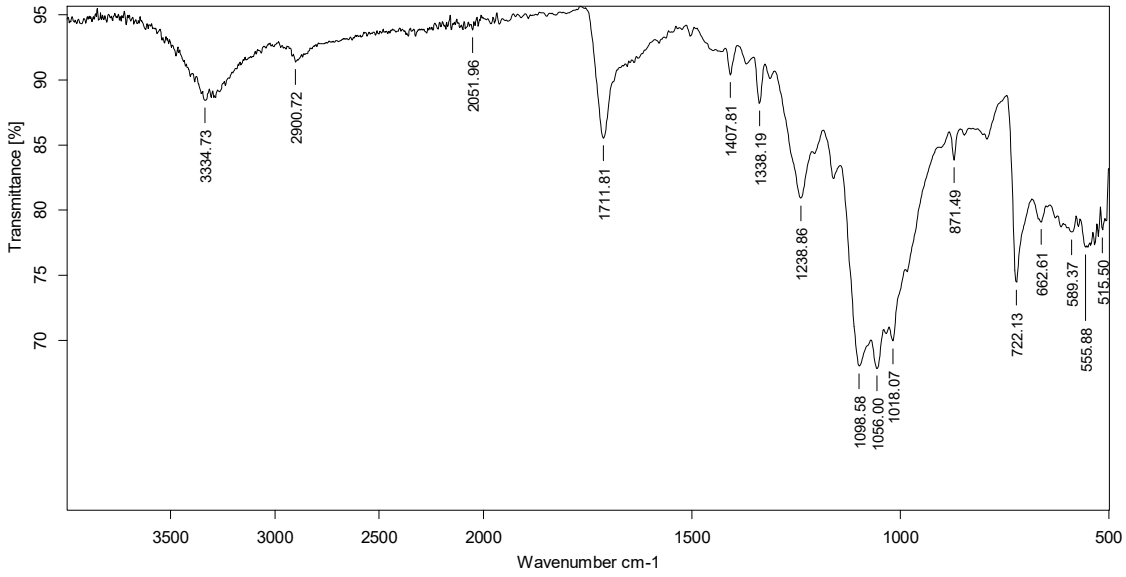

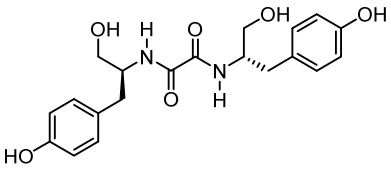

26

^{1}H NMR (400 MHz, DMSO)

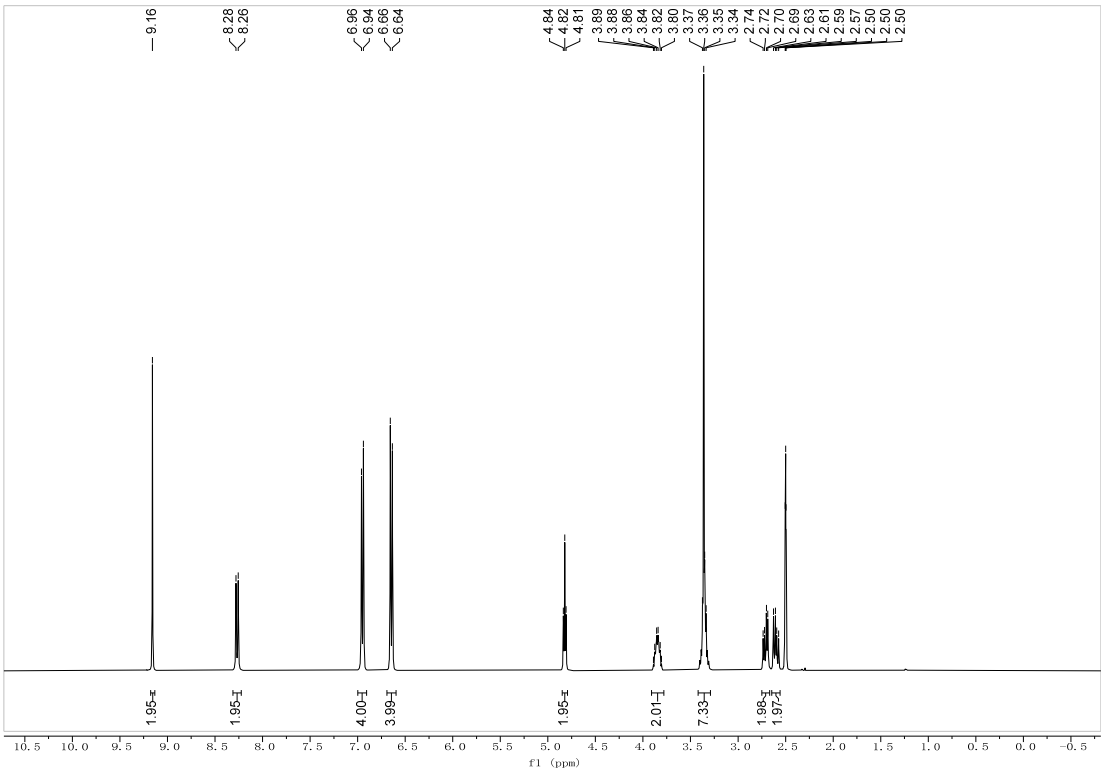

^{13}C NMR (101 MHz, DMSO)

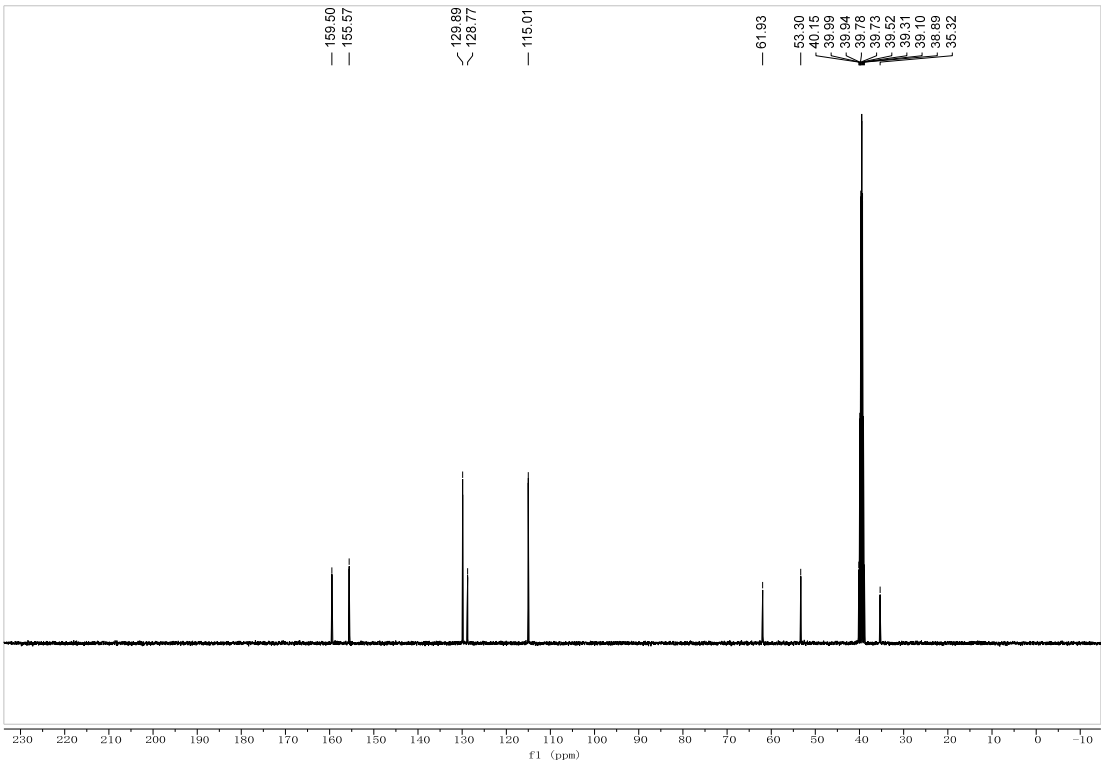

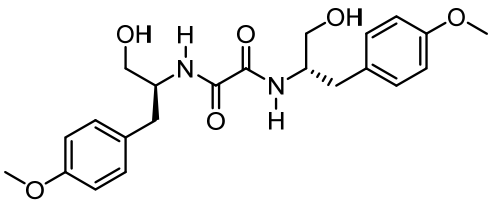

27

^{1}H NMR (300 MHz, DMSO)

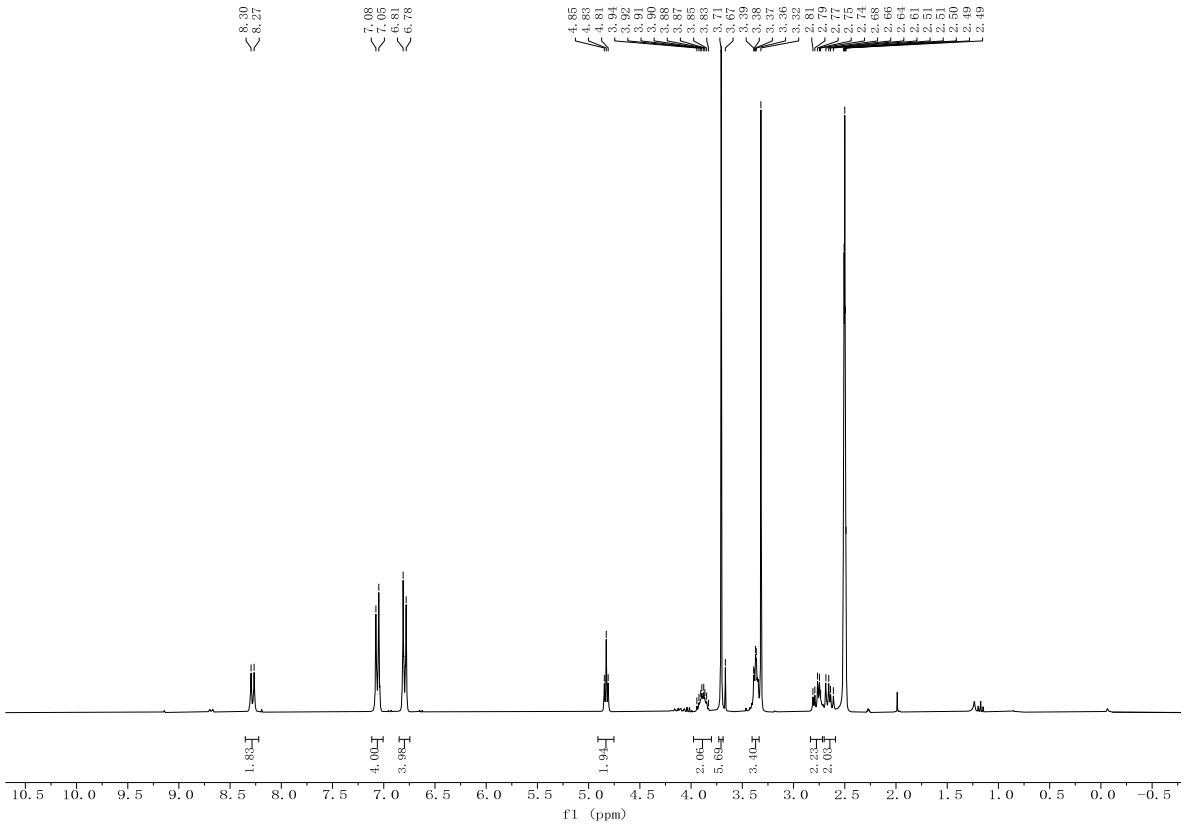

Annex: collection of spectra and characterization data

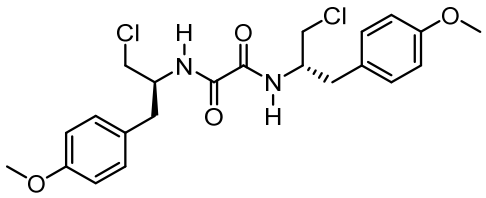

28

^{1}H NMR (400 MHz, $CDCl_3$)

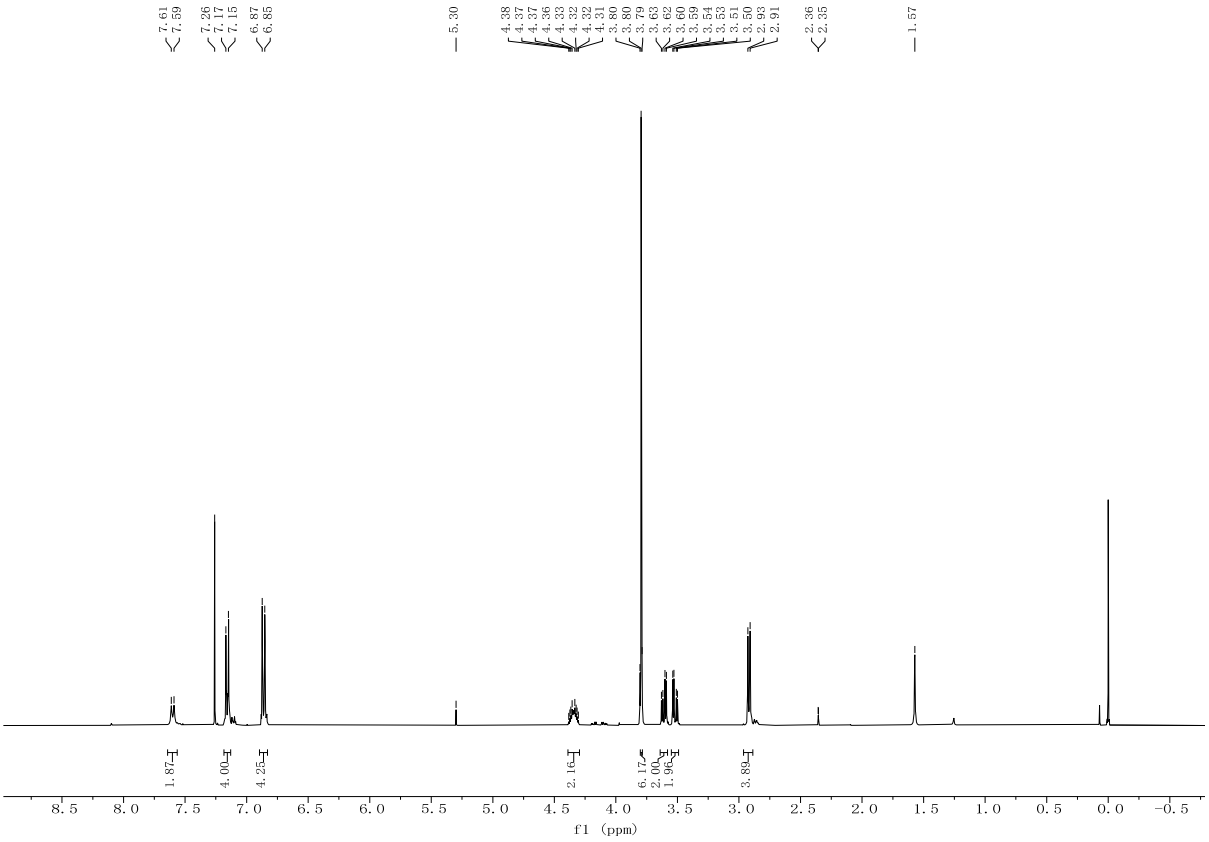

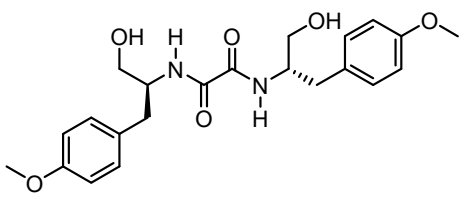

29

^{1}H NMR (400 MHz, $CDCl_3$)

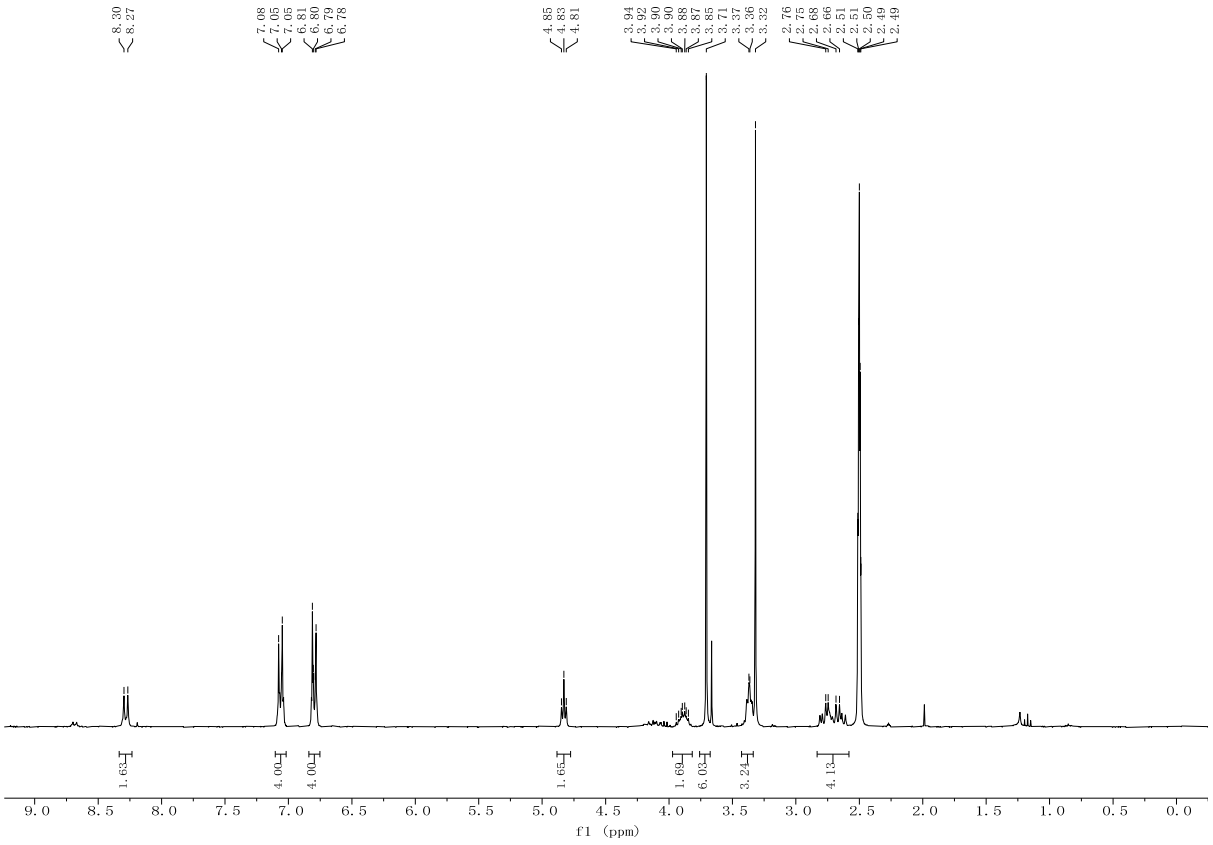

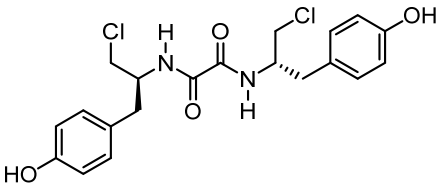

31

^{1}H NMR (300 MHz, DMSO)

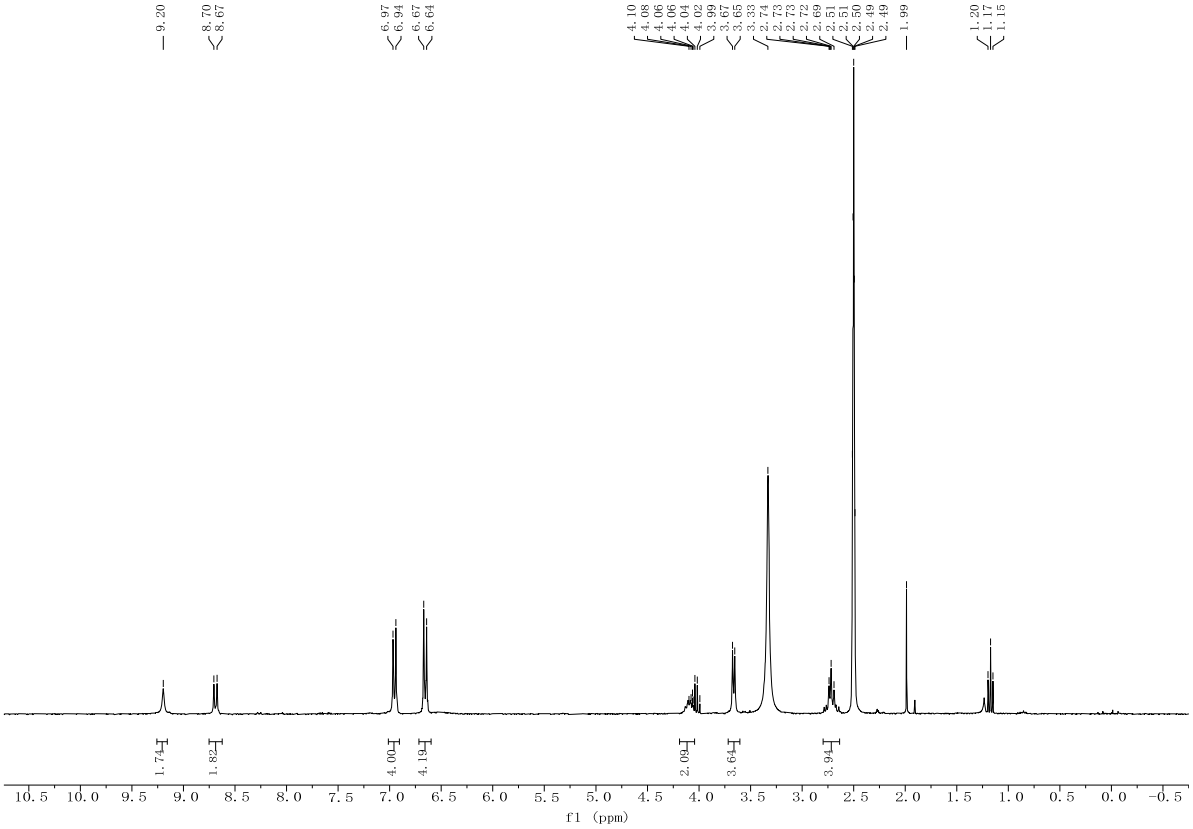

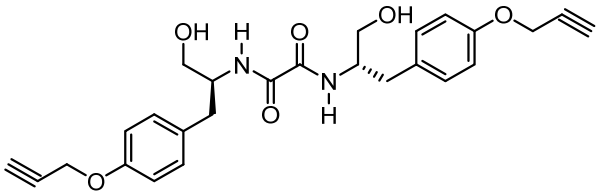

32

^{1}H NMR (400 MHz, DMSO)

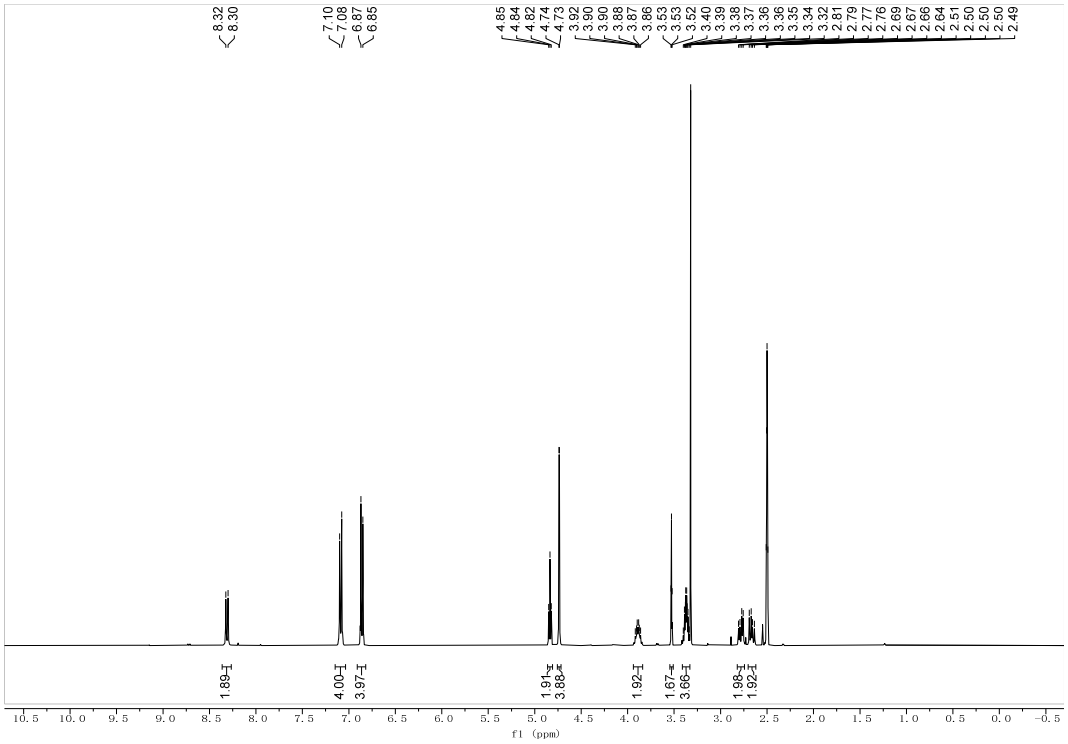

^{13}C NMR (76 MHz, DMSO)

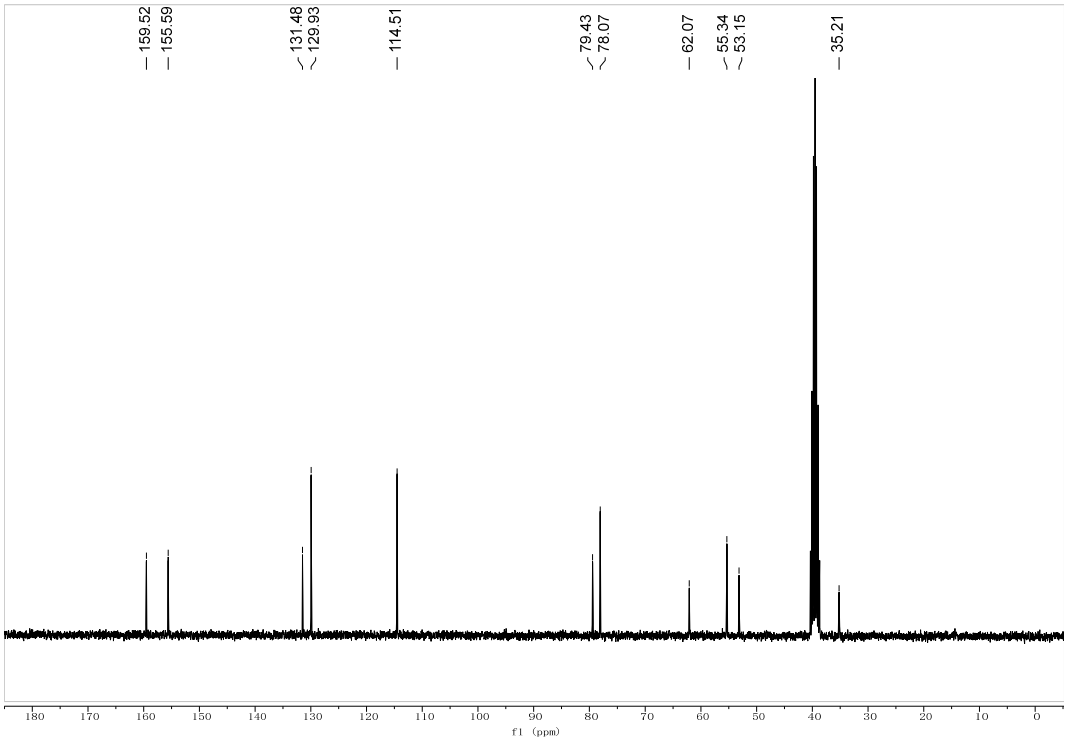

IR (ATR)

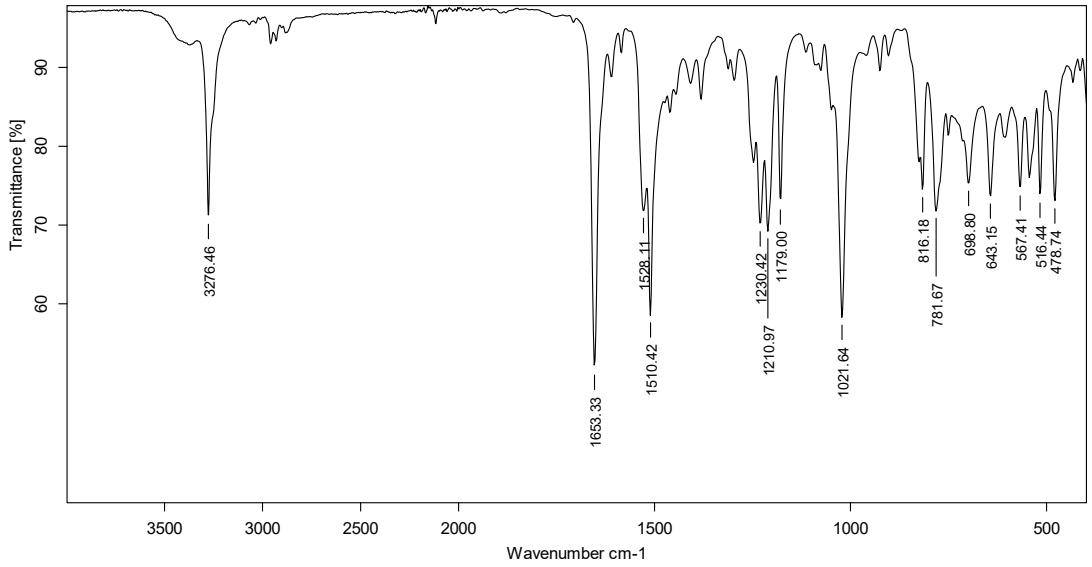
Transmittance [%]
90
80
70
60
3276.46
1653.33
1528.11
1510.42
1230.42
1210.97
1179.00
1021.64
816.18
781.67
698.80
643.15
567.41
516.44
478.74
3500
3000
2500
2000
1500
1000
500
Wavenumber cm-1

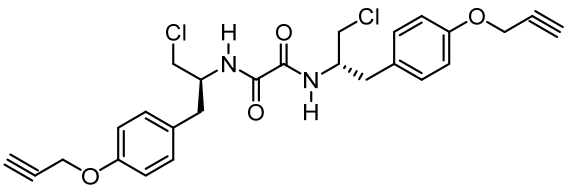

33

^{1}H NMR (400 MHz, $CDCl_3$)

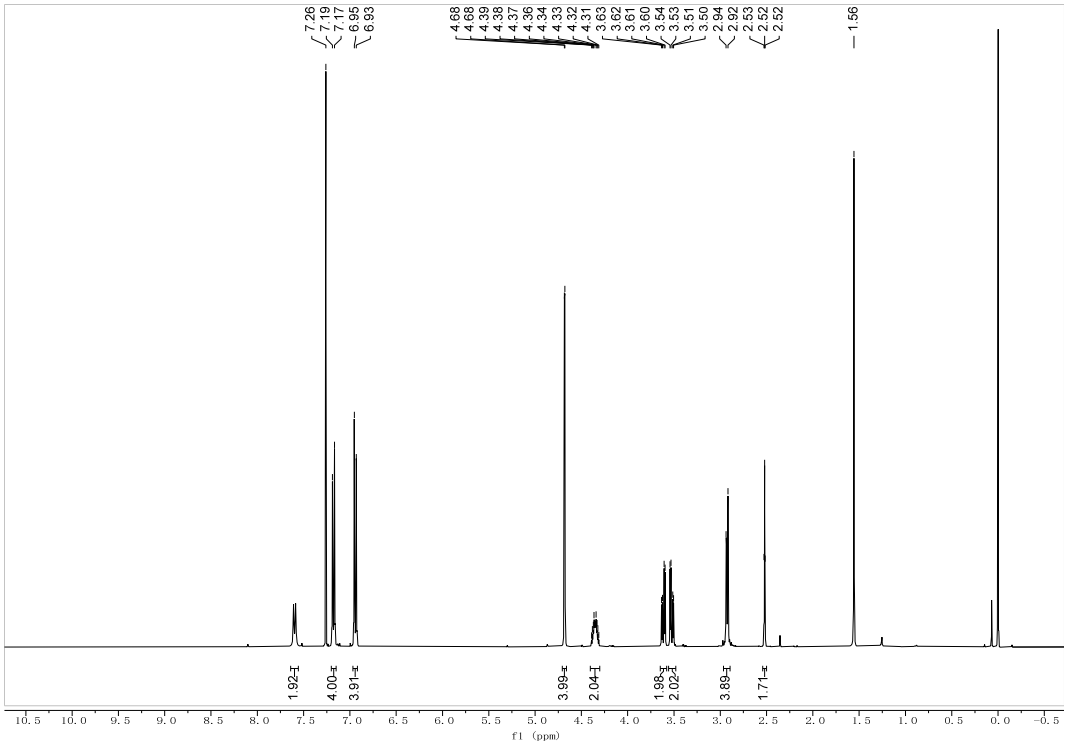

^{13}C NMR (101 MHz, $CDCl_3$)

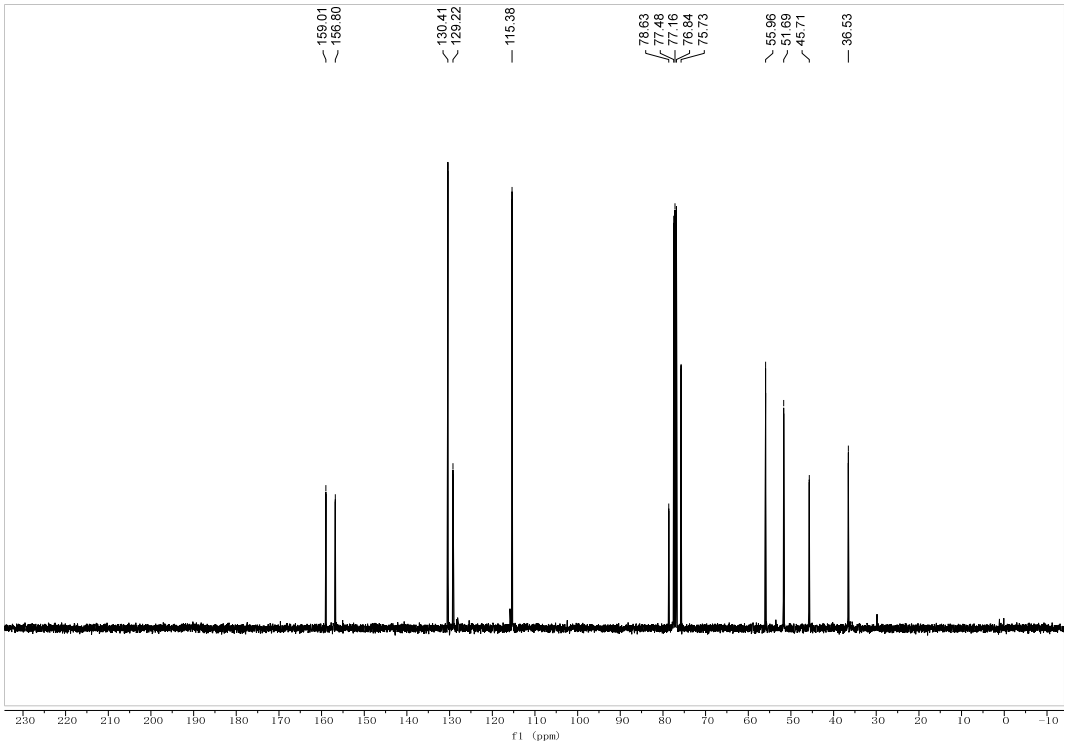

IR (ATR)

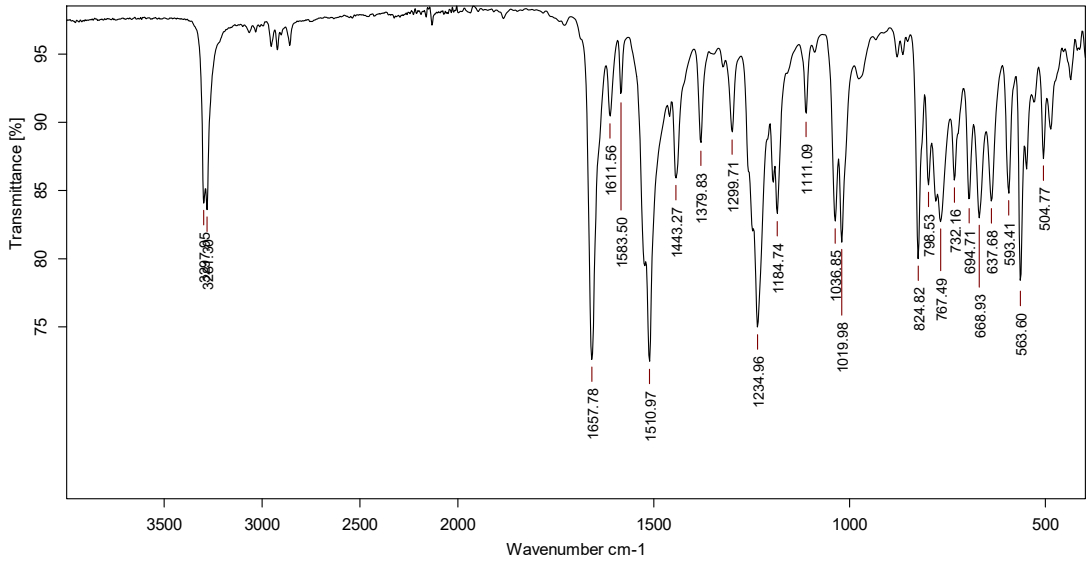
Transmittance [%]
95
90
85
80
75
3500
3000
2500
2000
1500
1000
500
Wavenumber cm-1
1657.78
1611.56
1583.50
1510.97
1443.27
1379.83
1299.71
1234.96
1184.74
1111.09
1036.85
1019.98
824.82
798.53
767.49
732.16
694.71
668.93
637.68
593.41
563.60
504.77

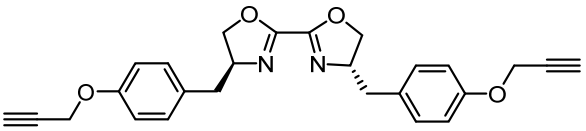

34

^{1}H NMR (400 MHz, $CDCl_3$)

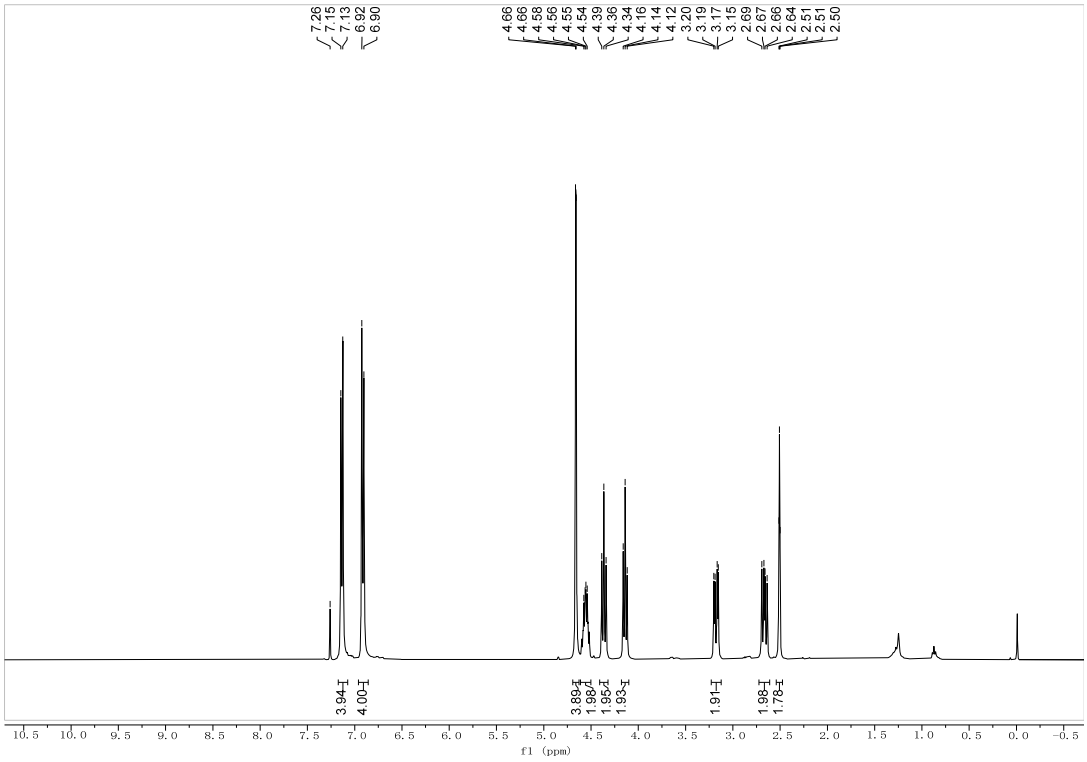

^{13}C NMR (101 MHz, $CDCl_3$)

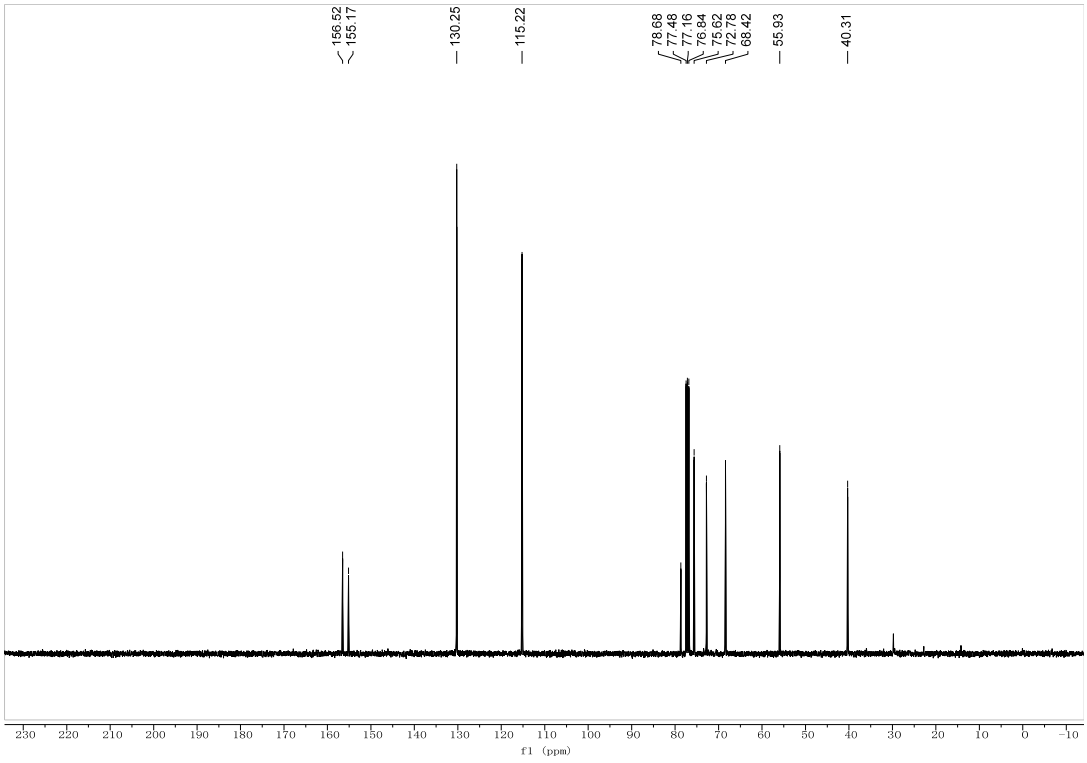

IR (ATR)

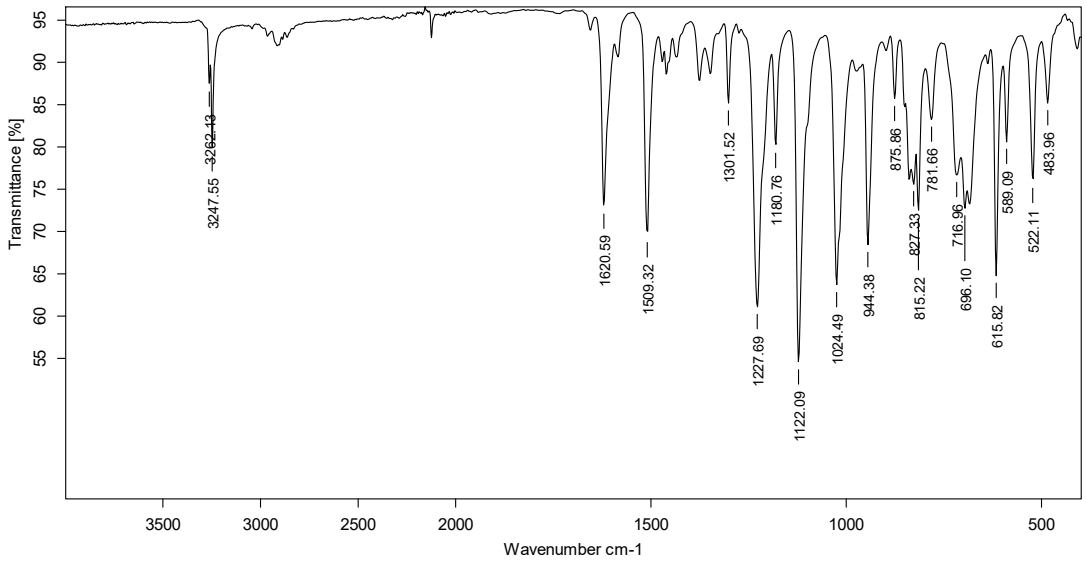
Transmittance [%]
95
90
85
80
75
70
65
60
55
3247.55
1620.59
1509.32
1301.52
1227.69
1180.76
1122.09
1024.49
944.38
875.86
827.33
815.22
781.66
716.96
696.10
615.82
589.09
522.11
483.96
3500
3000
2500
2000
1500
1000
500
Wavenumber cm-1

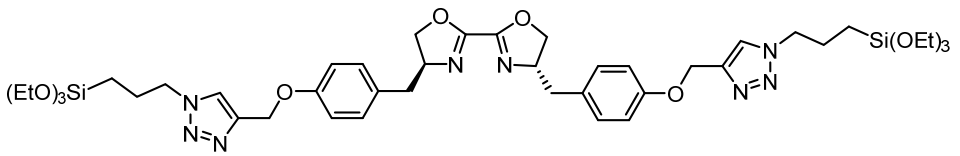

35

^{1}H NMR (300 MHz, $CDCl_3$)

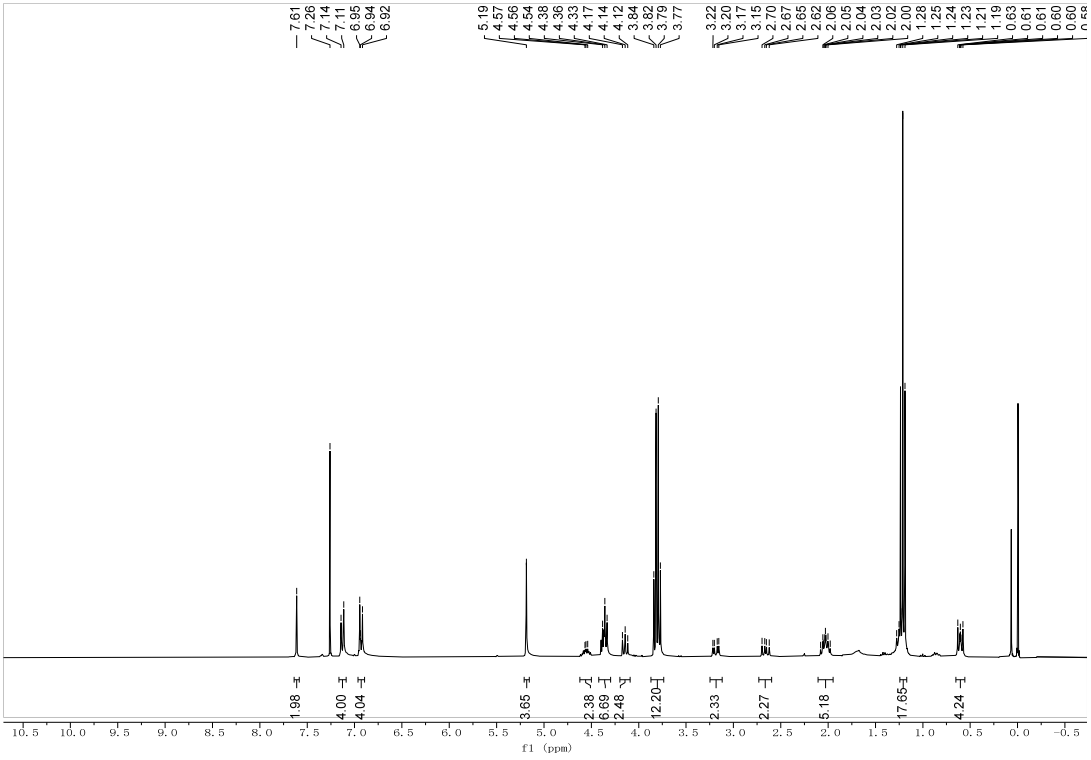

^{13}C NMR (76 MHz, $CDCl_3$)

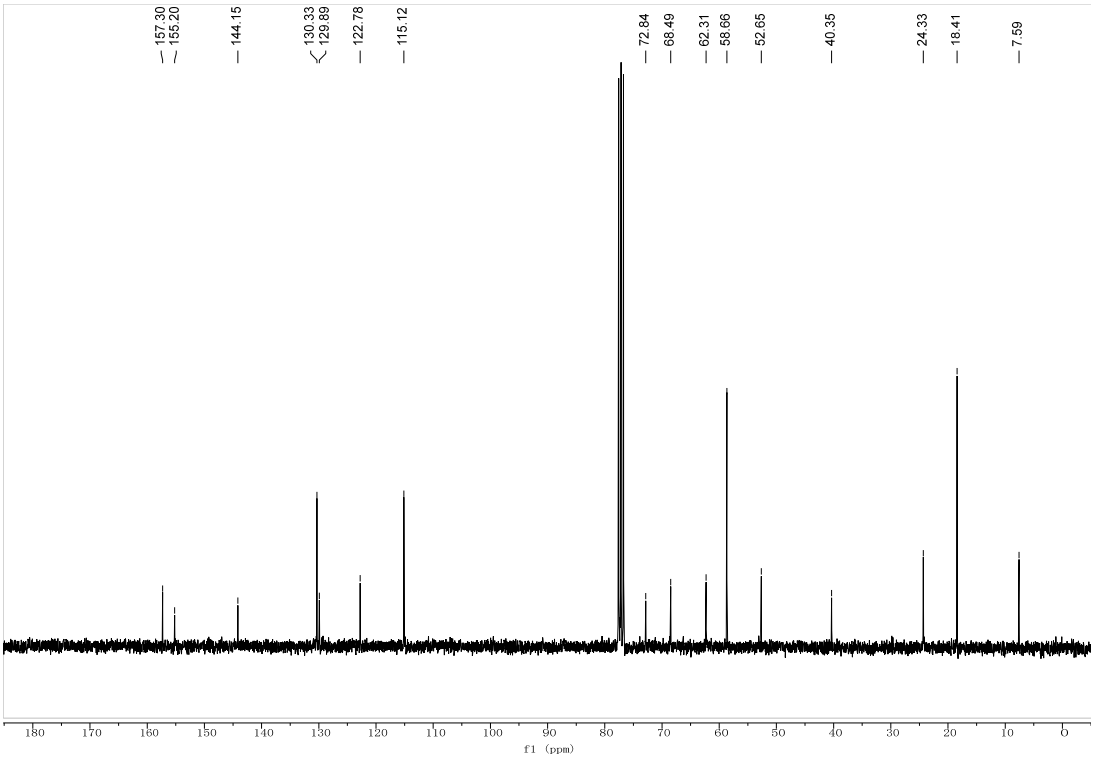

IR (ATR)

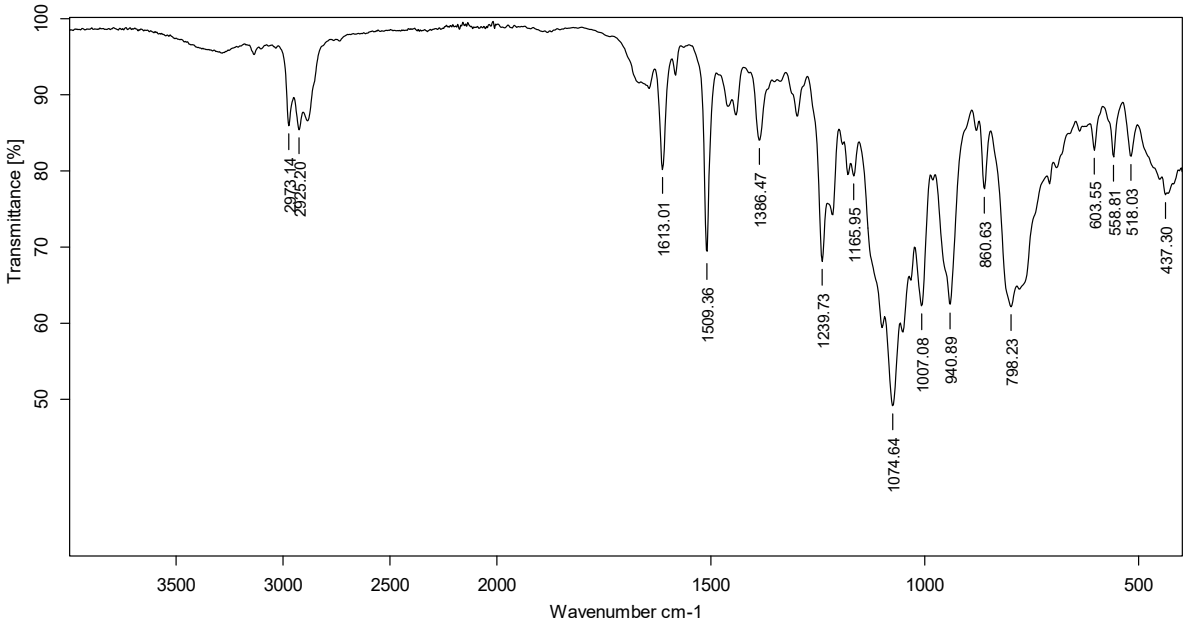
Transmittance [%]
100
90
80
70
60
50
2973.14
2925.20
1613.01
1509.36
1386.47
1239.73
1165.95
1074.64
1007.08
940.89
860.63
798.23
603.55
558.81
518.03
437.30
3500
3000
2500
2000
1500
1000
500
Wavenumber cm-1

M0 NPs

p-XRD

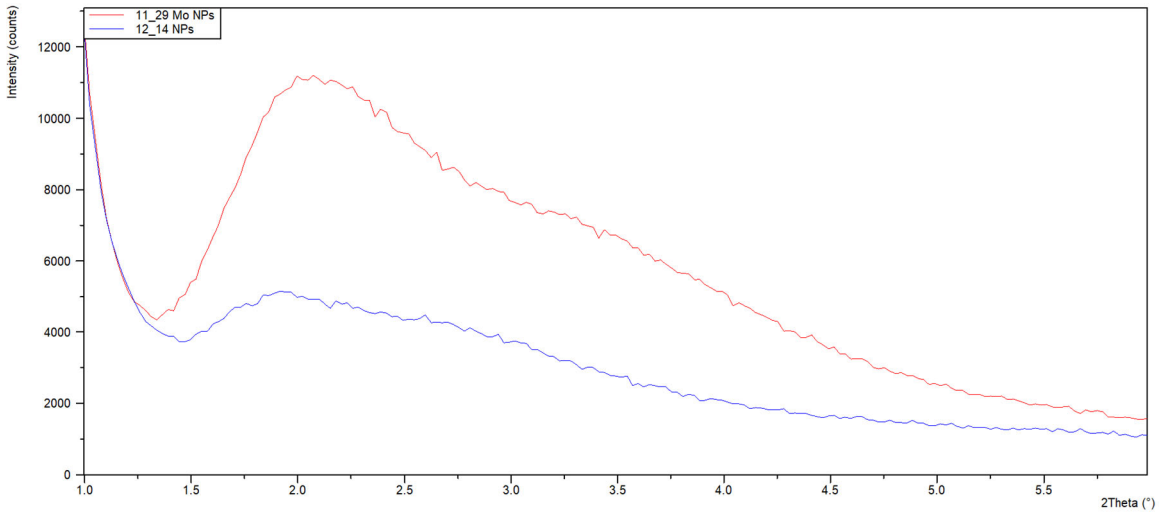

TEM

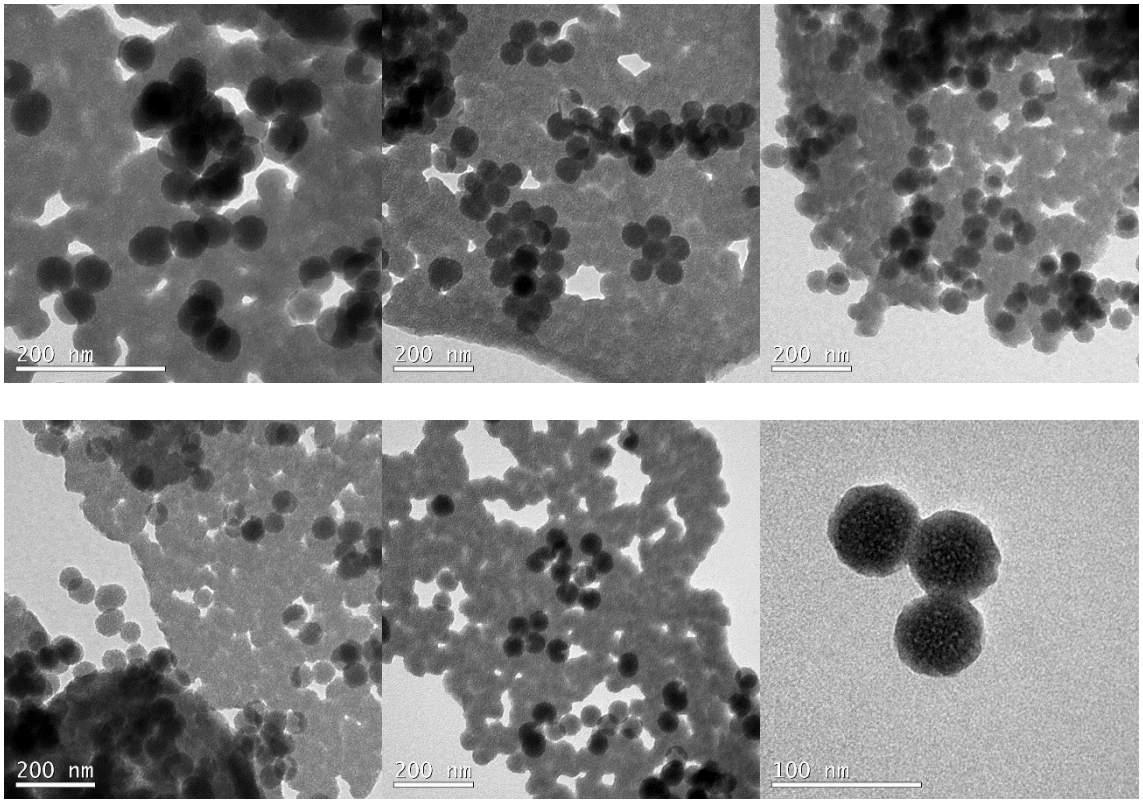

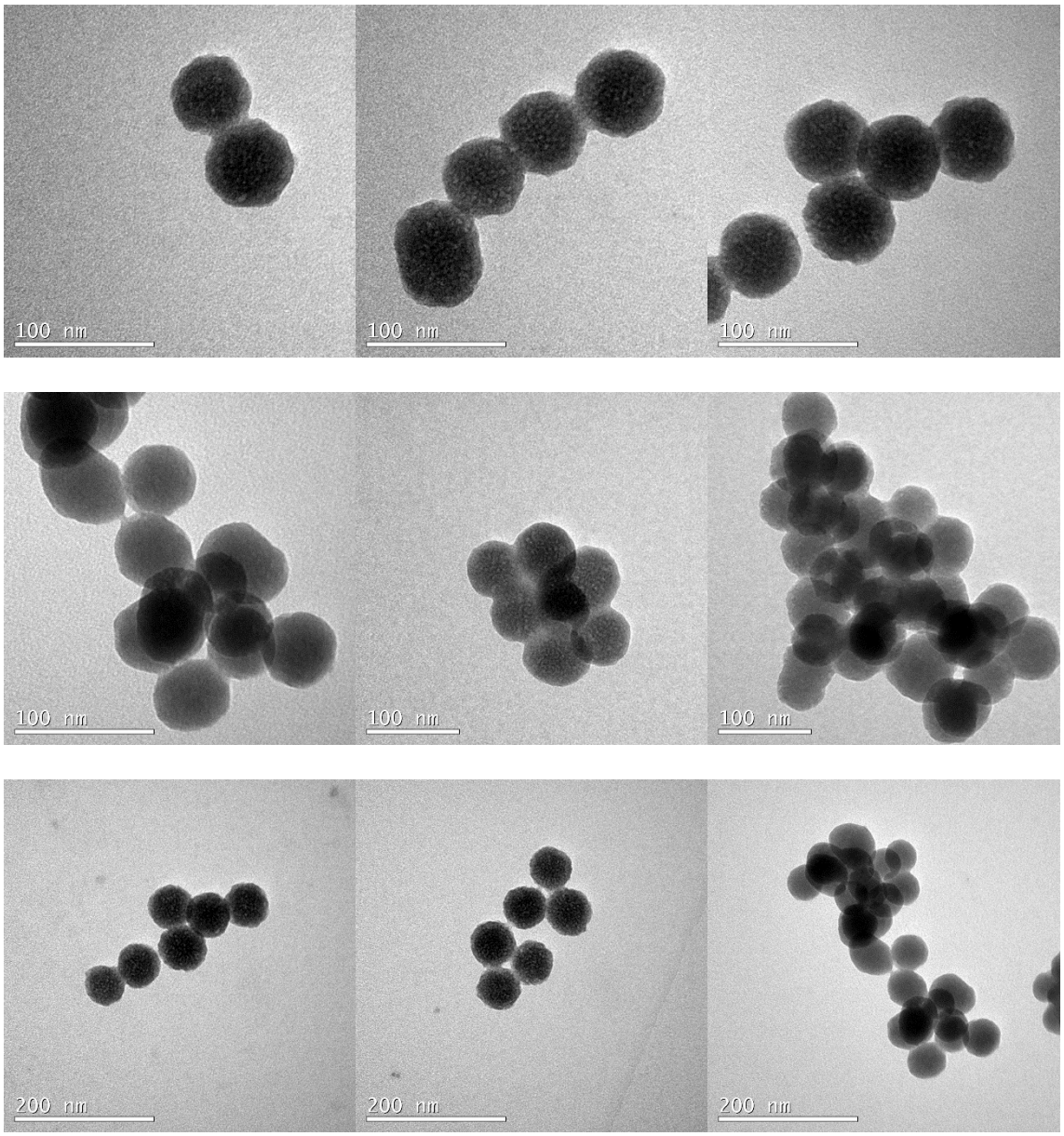
100 nm
100 nm
100 nm
100 nm
100 nm
100 nm
200 nm
200 nm
200 nm

mN9

TEM

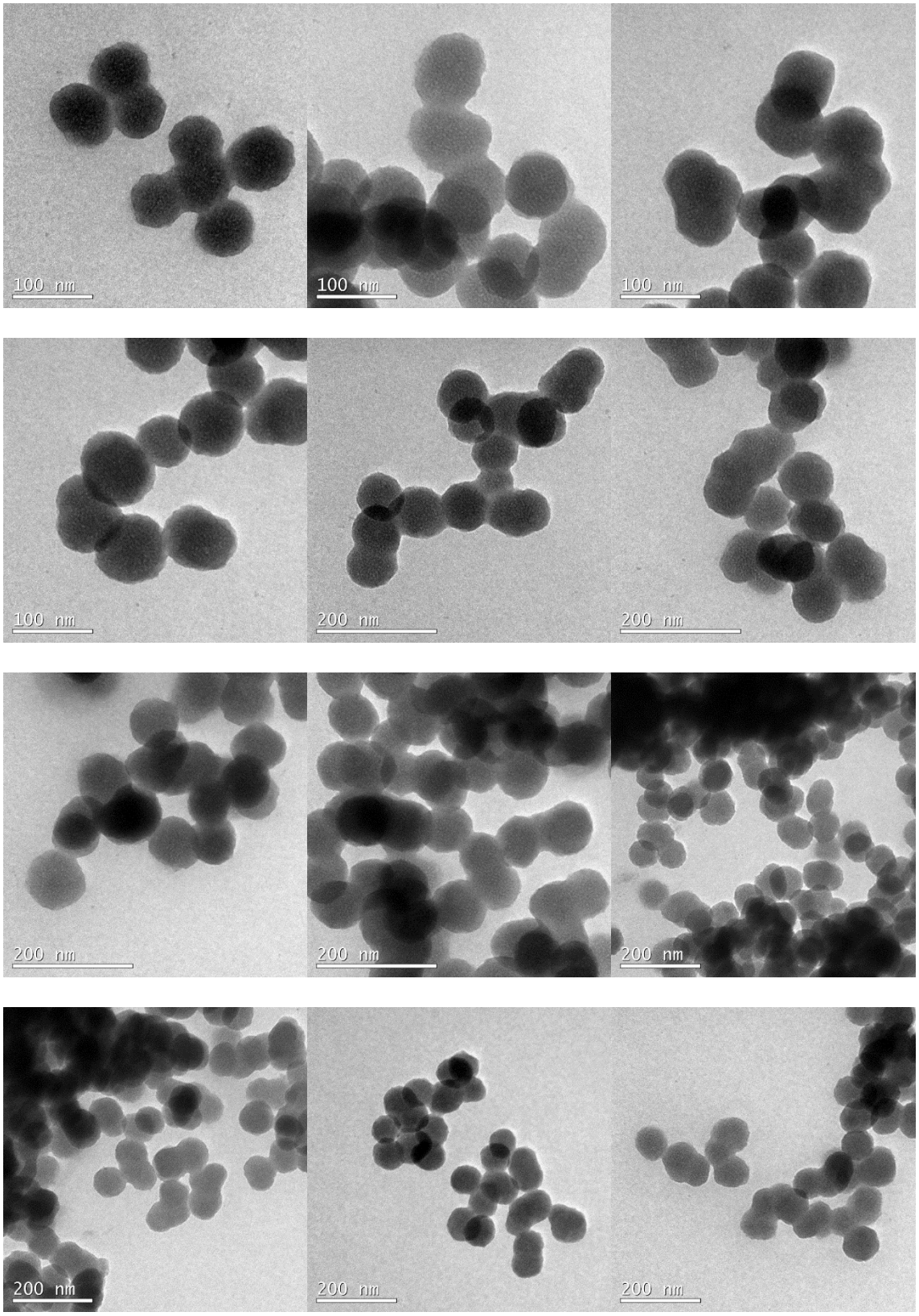
100 nm
100 nm
100 nm
100 nm
200 nm
200 nm
200 nm
200 nm
200 nm
200 nm
200 nm
200 nm

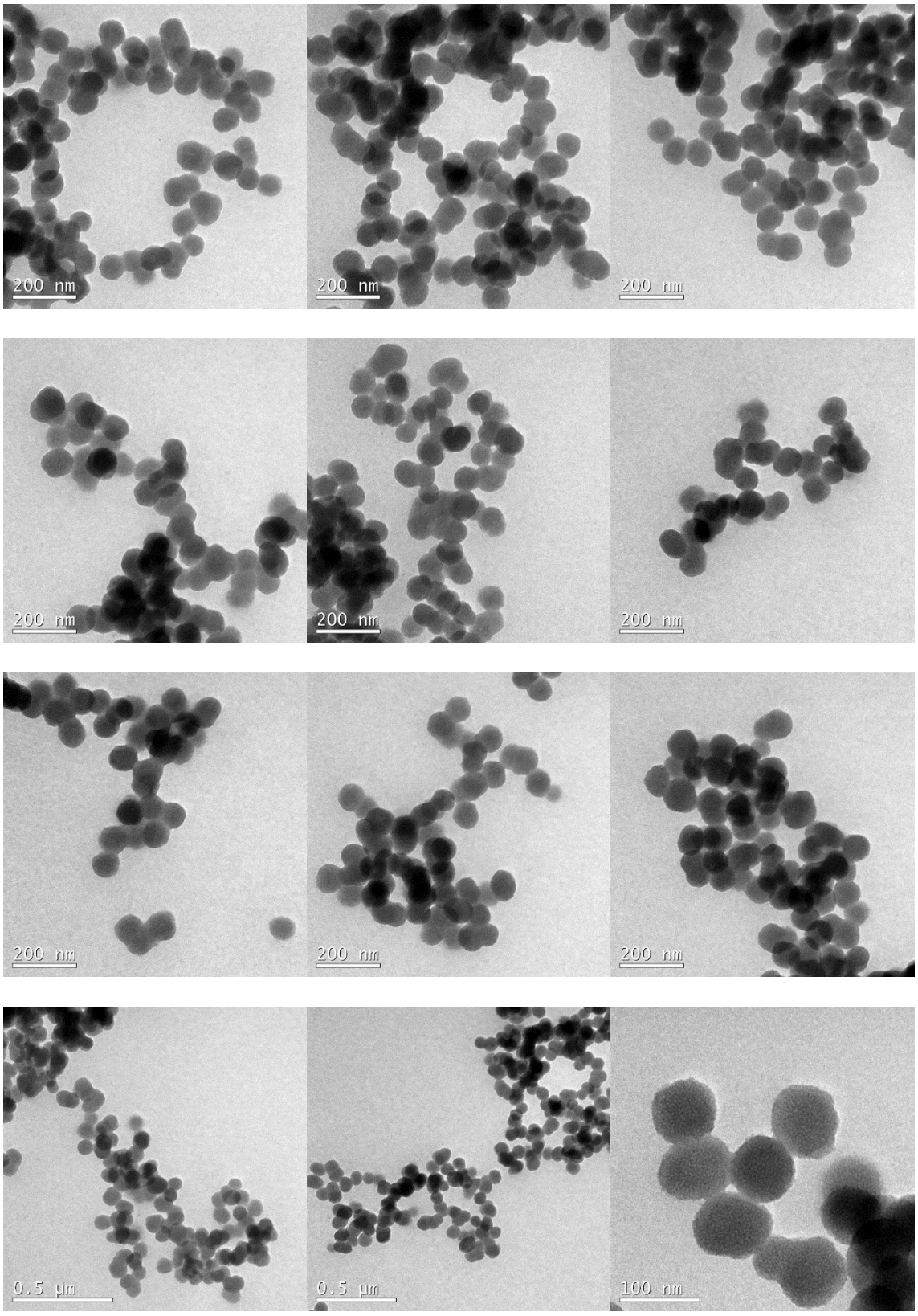
200 nm
200 nm
200 nm
200 nm
200 nm
200 nm
200 nm
200 nm
200 nm
0.5 µm
0.5 µm
100 nm

DLS

380.08 nm

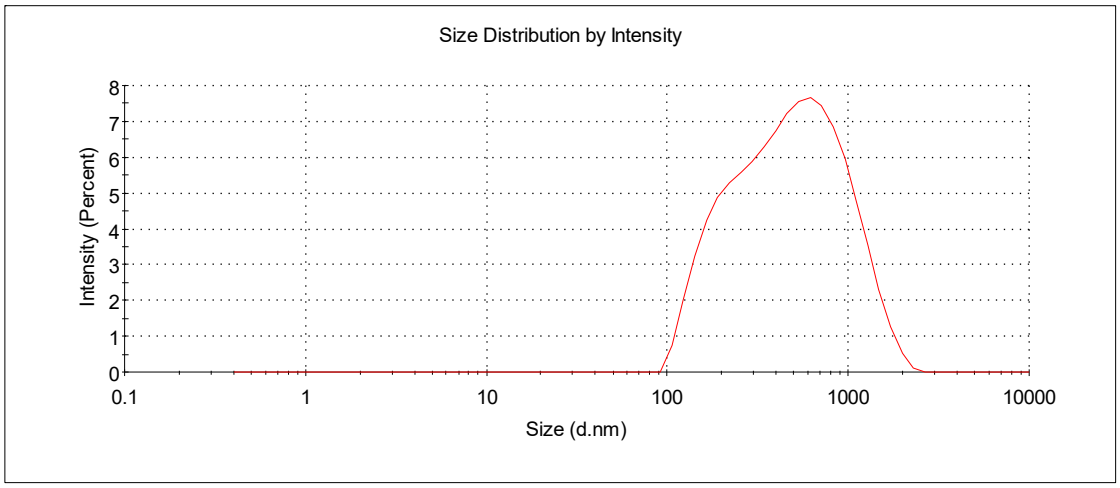

Zeta-potential

+7.59 mV

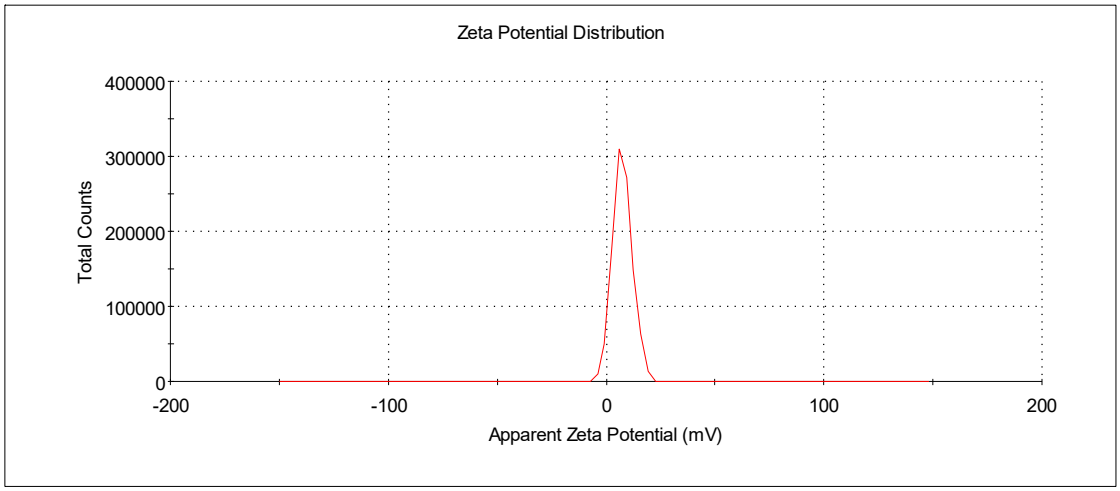

IR (ATR)

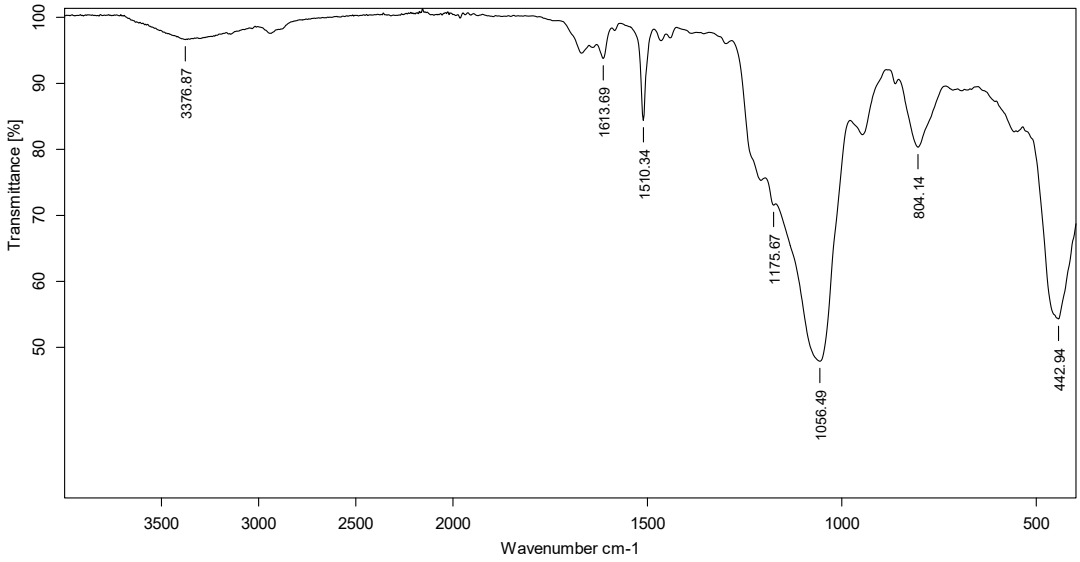
Transmittance [%]
100
90
80
70
60
50
3376.87
1613.69
1510.34
1175.67
1056.49
804.14
442.94
3500
3000
2500
2000
1500
1000
500
Wavenumber cm-1

^{13}C CP MAS NMR

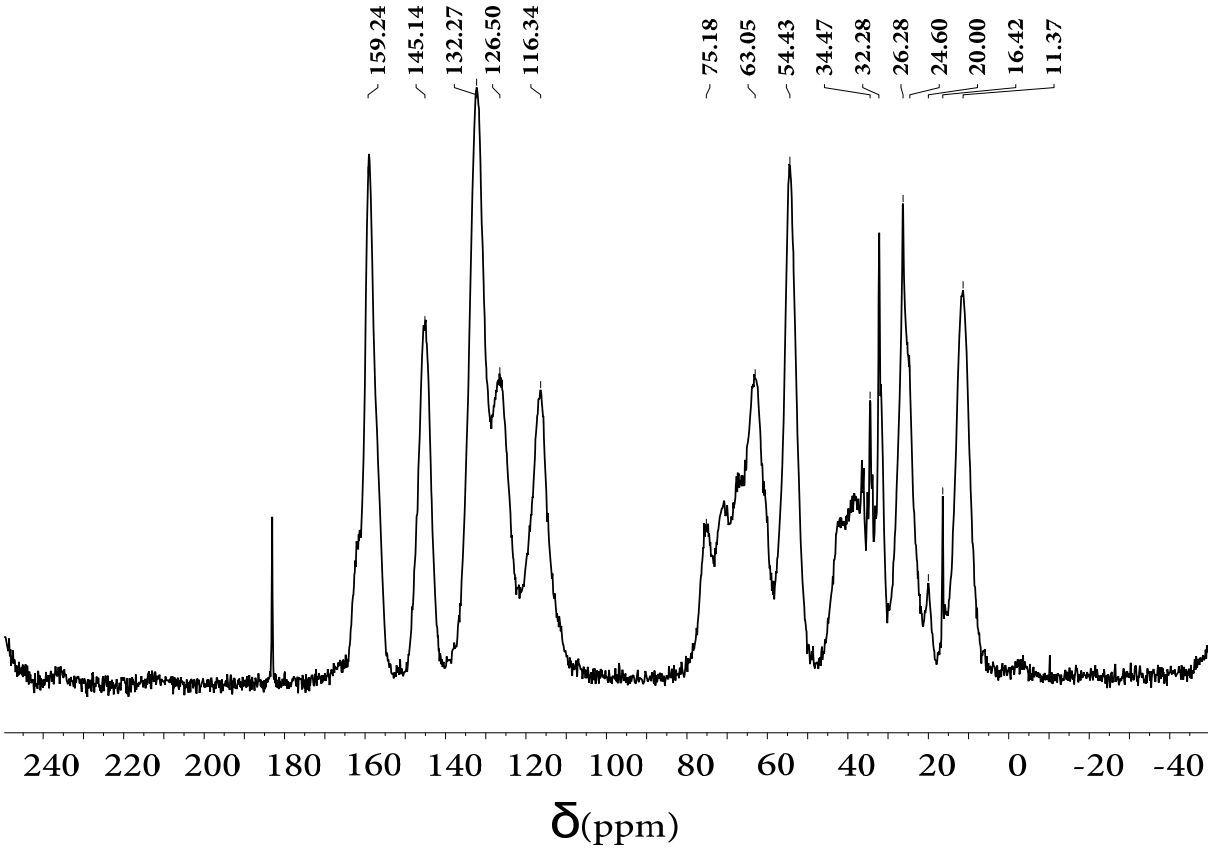

^{29}Si CP MAS NMR

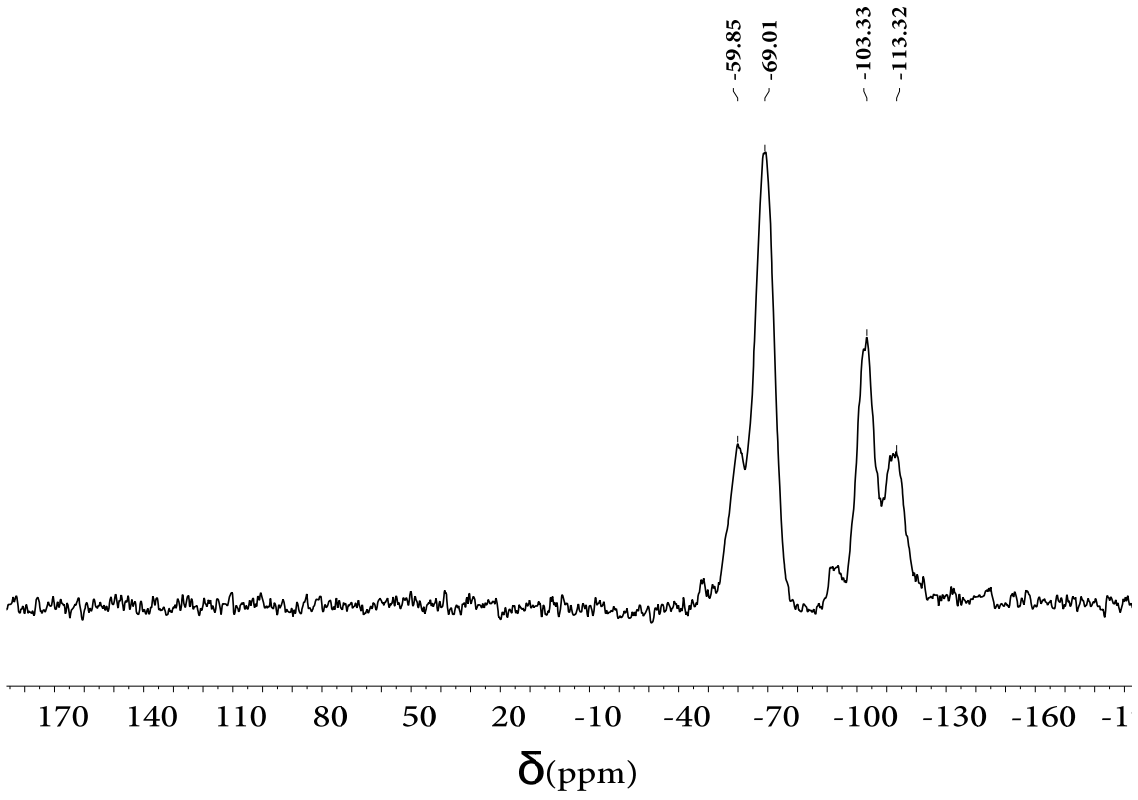

mN10

TEM

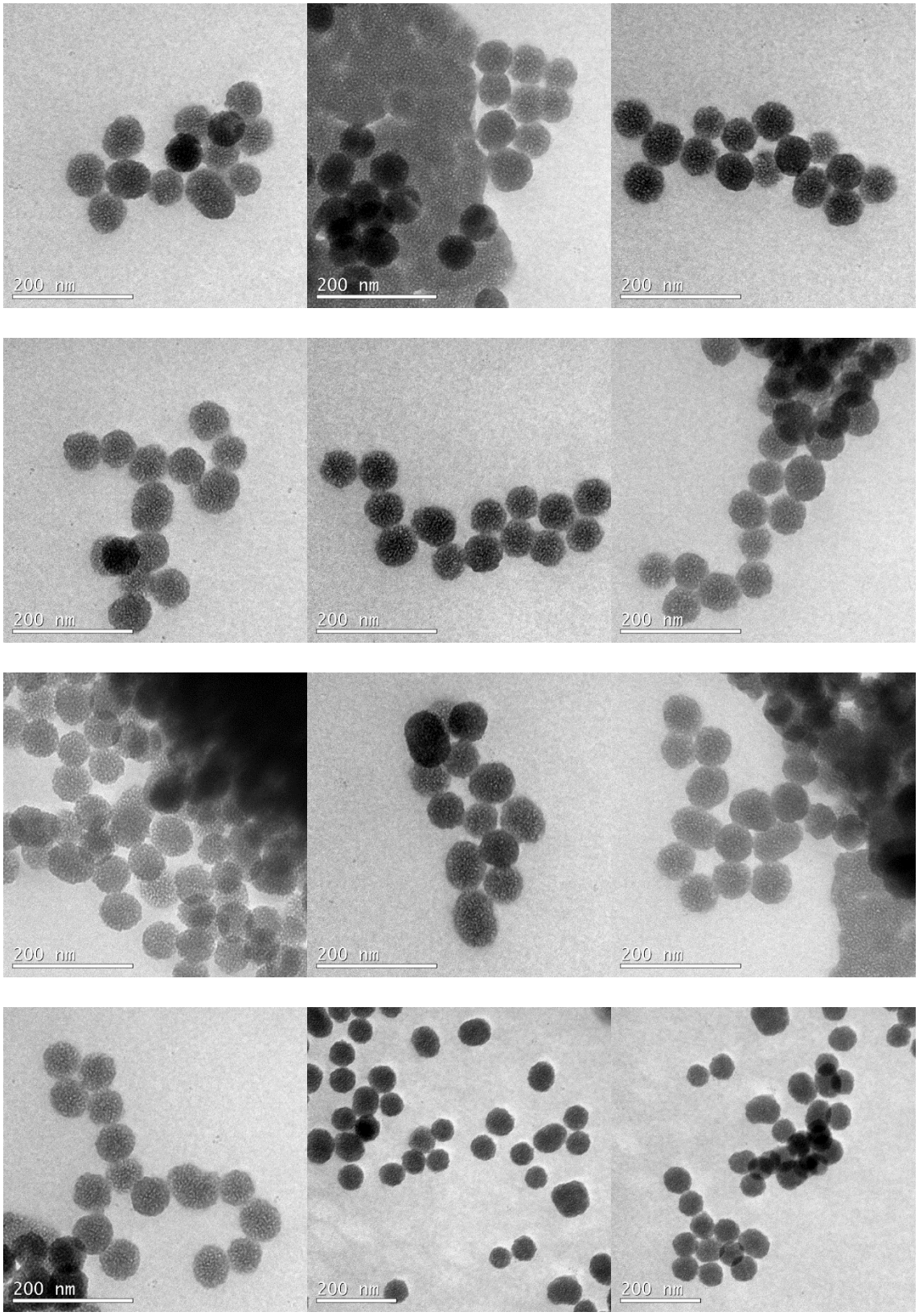
200 nm
200 nm
200 nm
200 nm
200 nm
200 nm
200 nm
200 nm
200 nm
200 nm
200 nm
200 nm

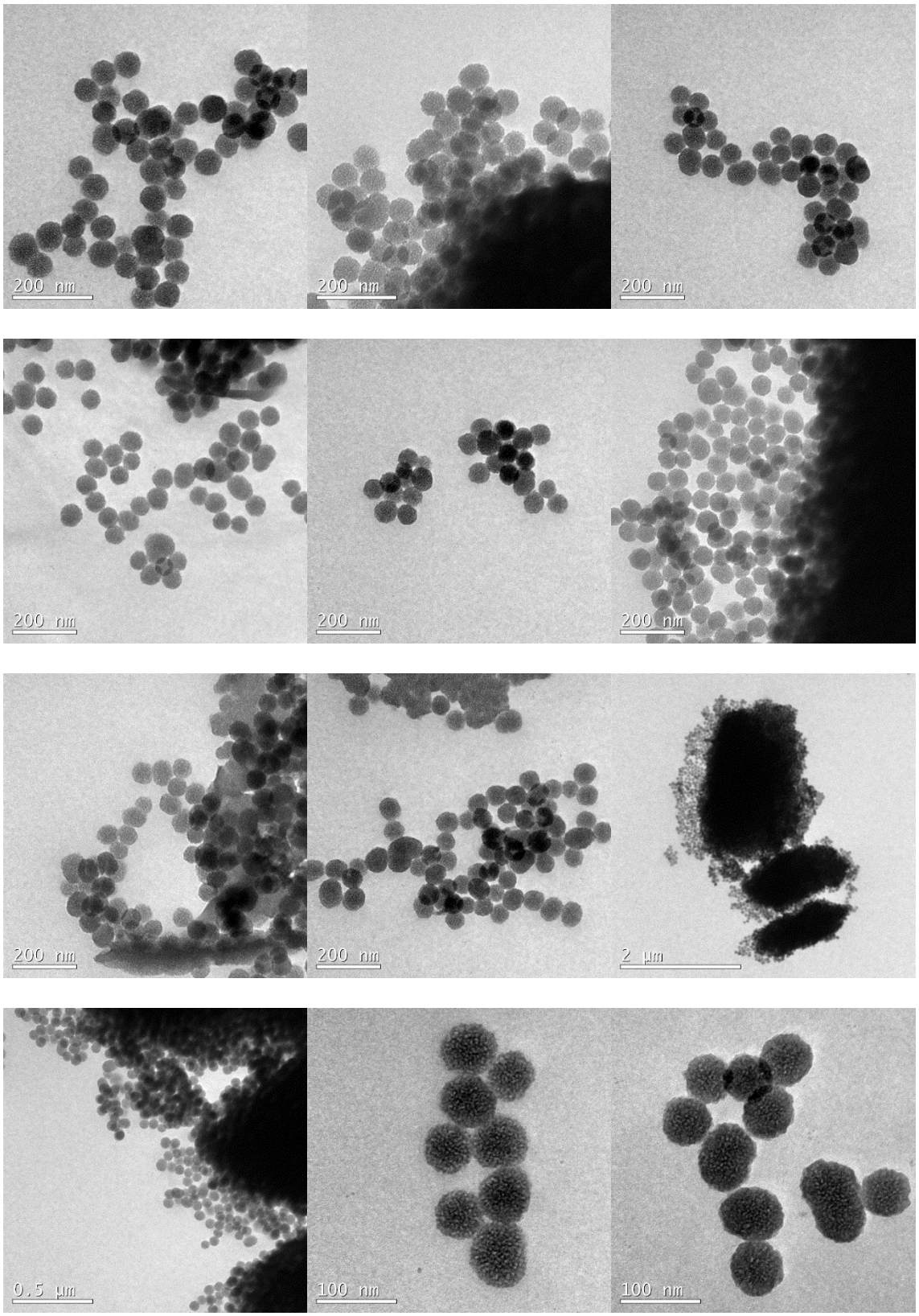
200 nm
200 nm
200 nm
200 nm
200 nm
200 nm
200 nm
200 nm
2 µm
0.5 µm
100 nm
100 nm

DLS

4191 nm

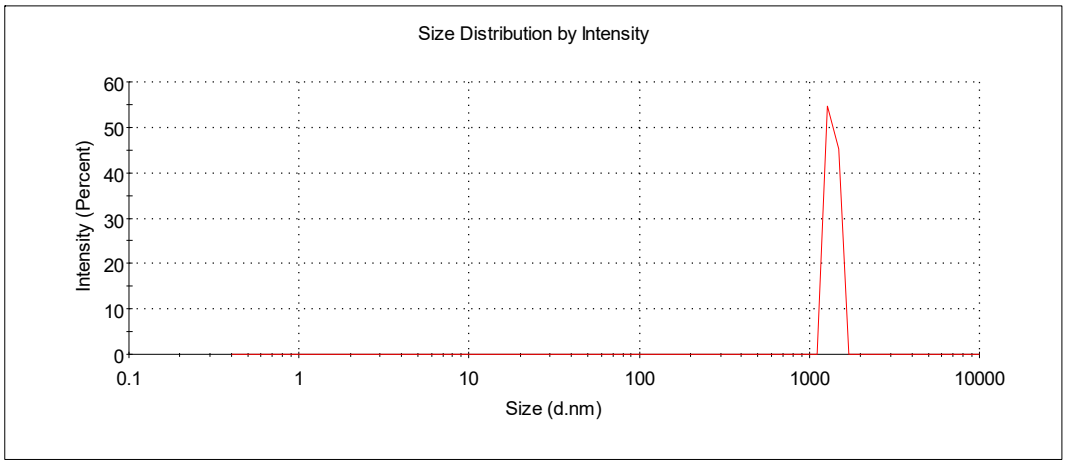

Zeta-potential

+5.90 mV

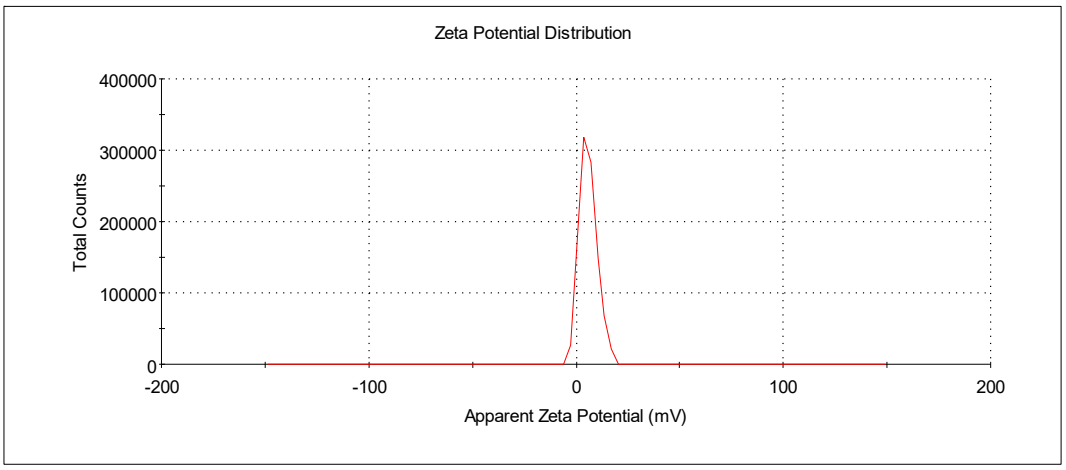

IR (ATR)

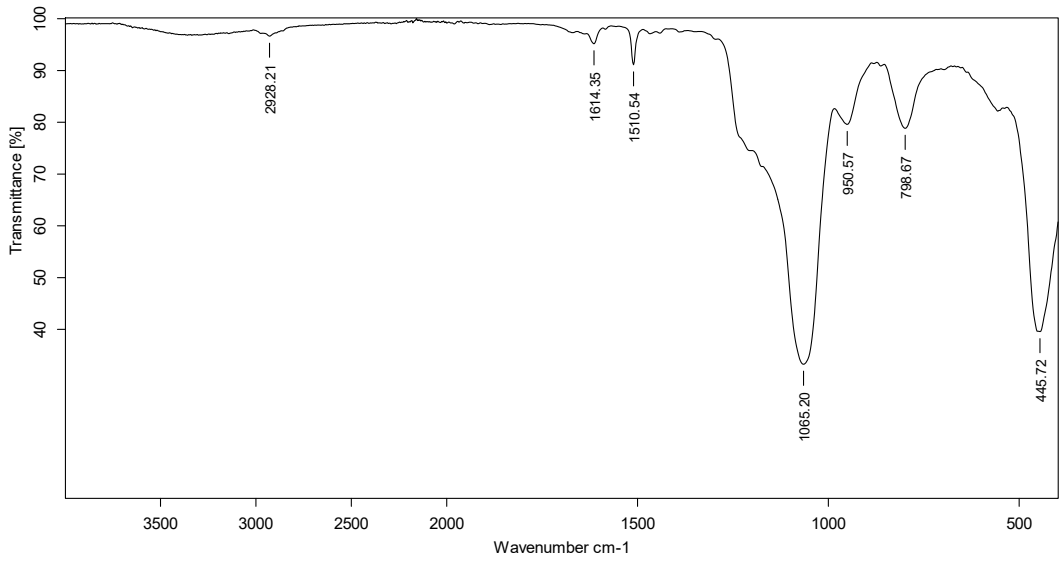

^{13}C CP MAS NMR

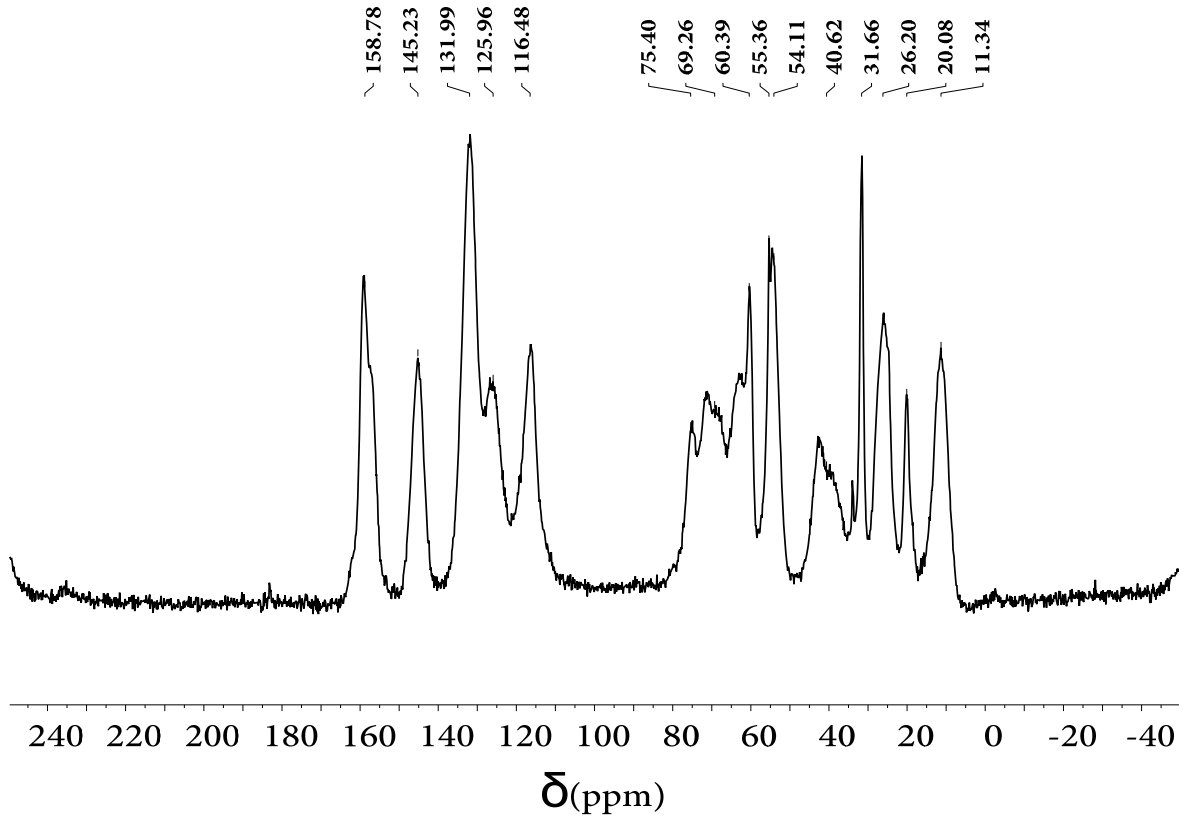

^{29}Si CP MAS NMR

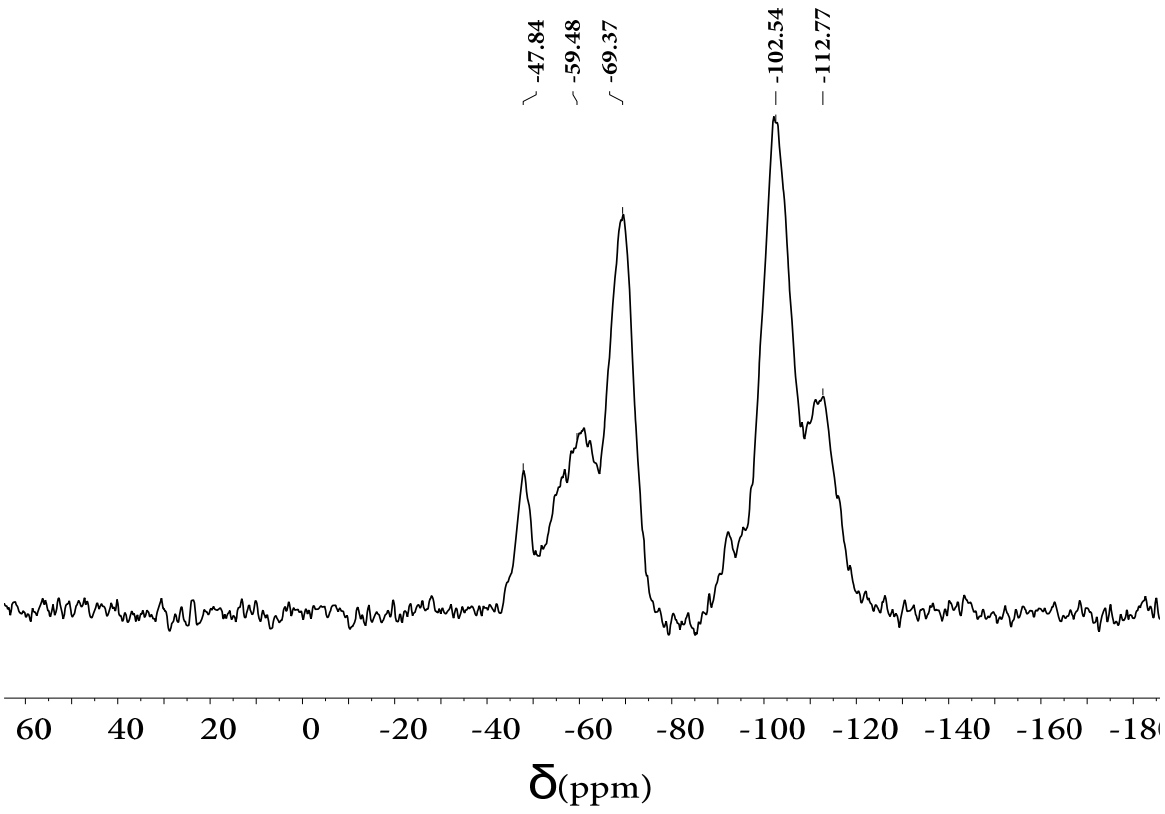

dN6

TEM

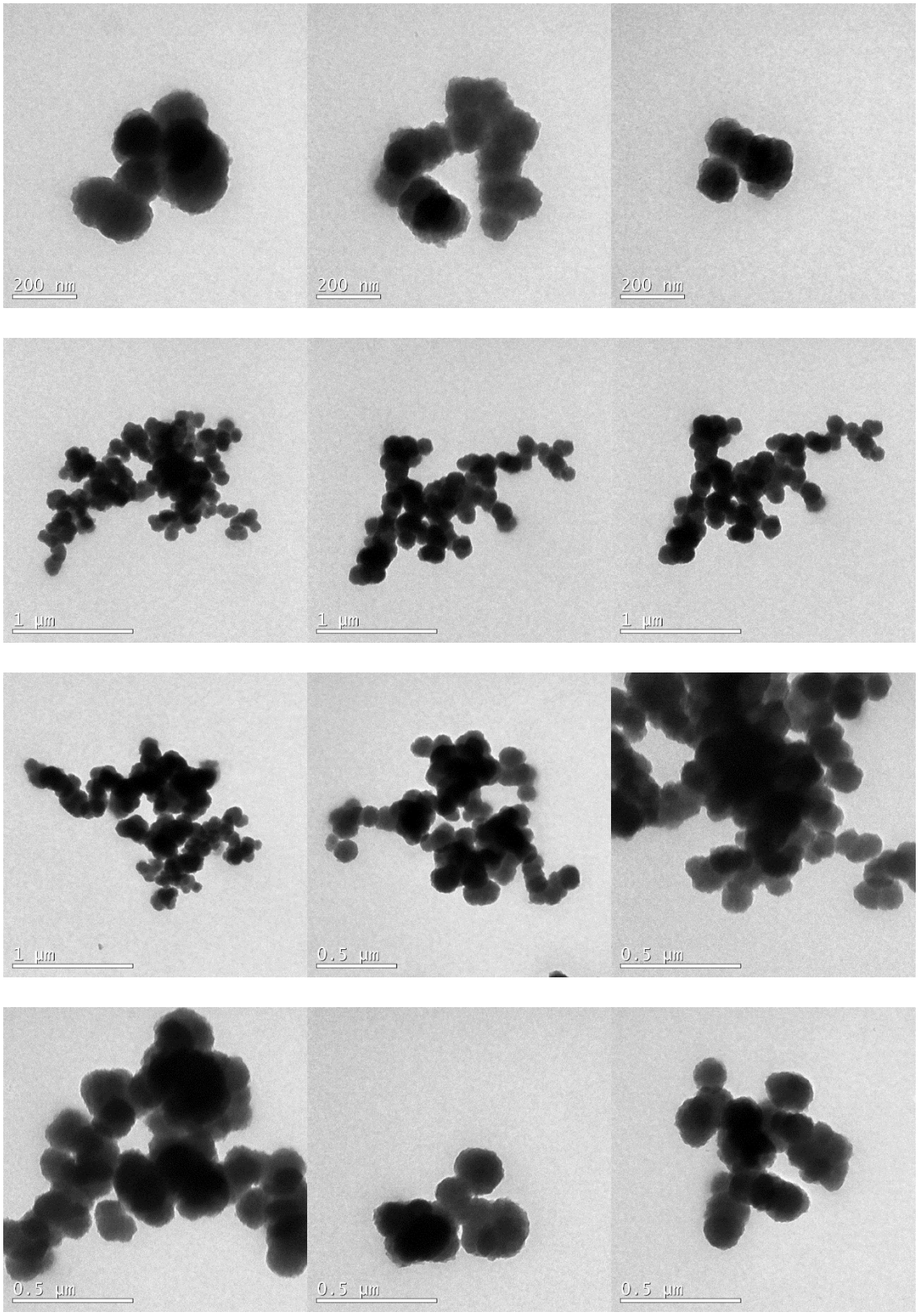

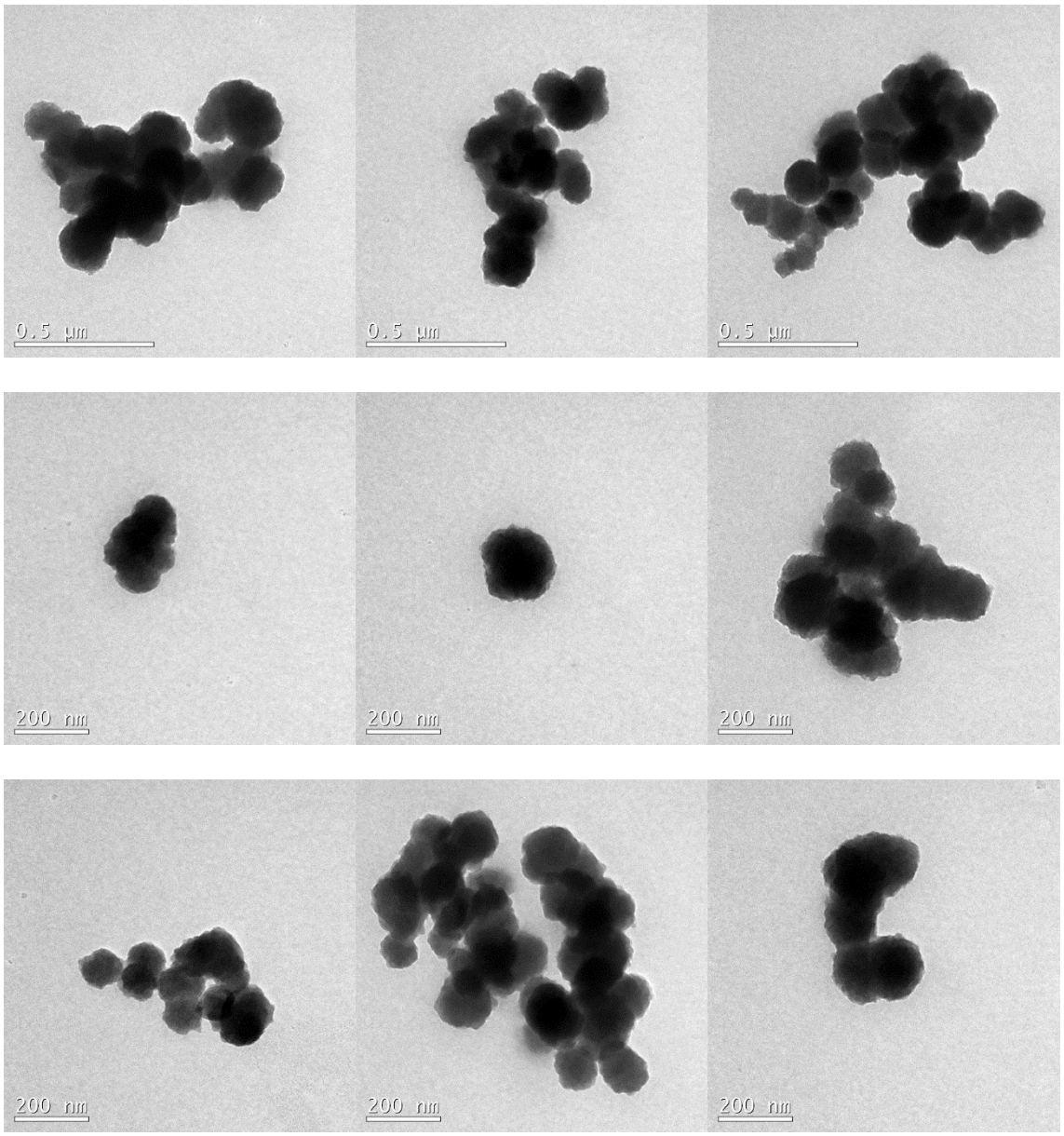
0.5 µm
0.5 µm
0.5 µm
200 nm
200 nm
200 nm
200 nm
200 nm
200 nm

DLS

728.5 nm

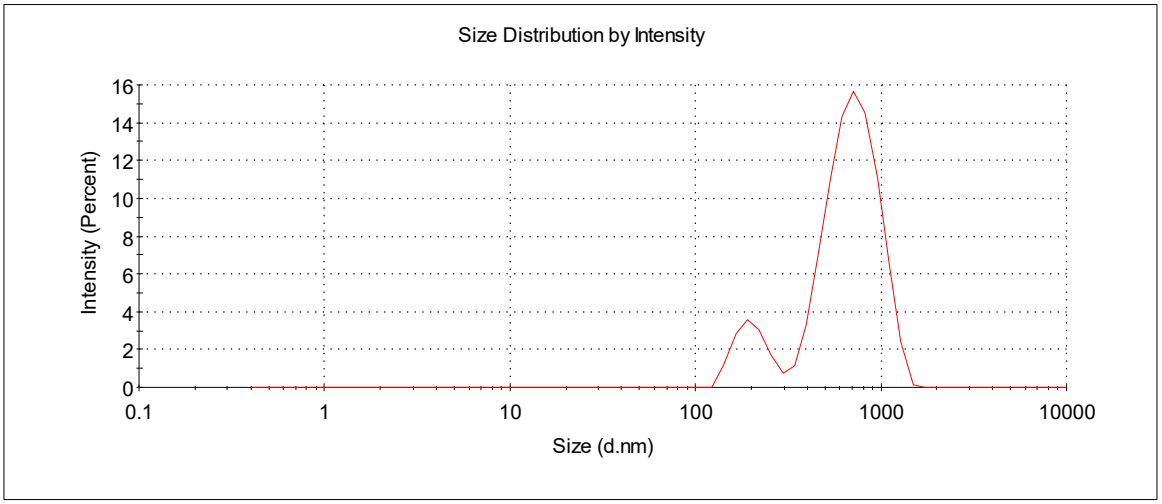

Zeta-potential

+17.8 mV

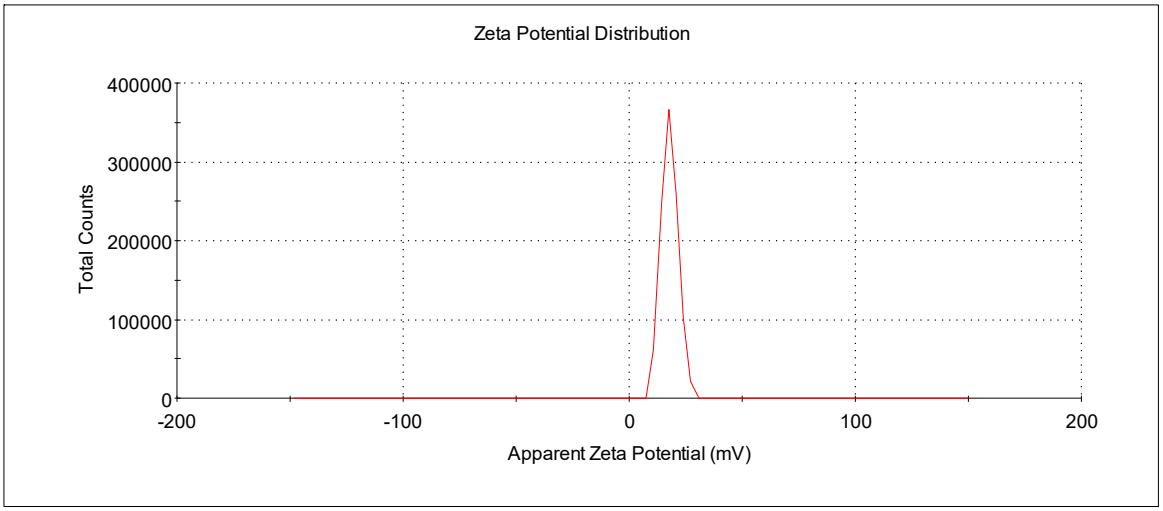

IR (ATR)

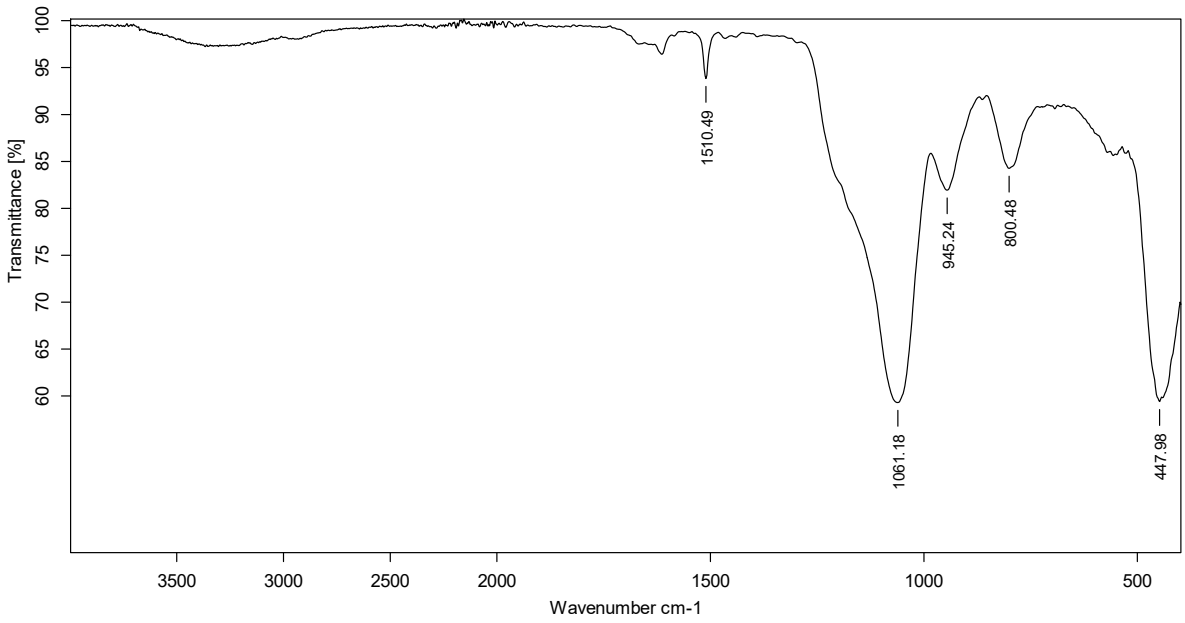
Transmittance [%]
100
95
90
85
80
75
70
65
60
1510.49
1061.18
945.24
800.48
447.98
3500
3000
2500
2000
1500
1000
500
Wavenumber cm-1

^{13}C CP MAS NMR

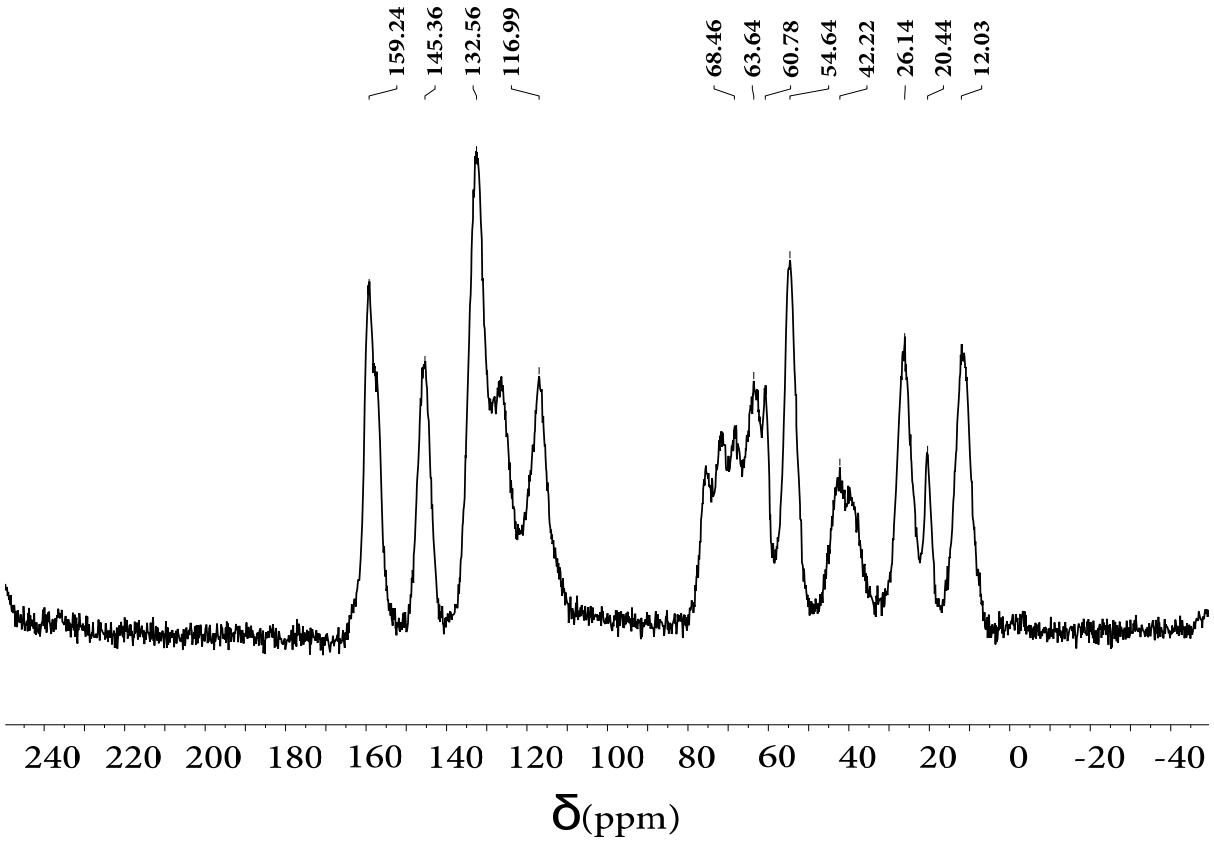

^{29}Si CP MAS NMR

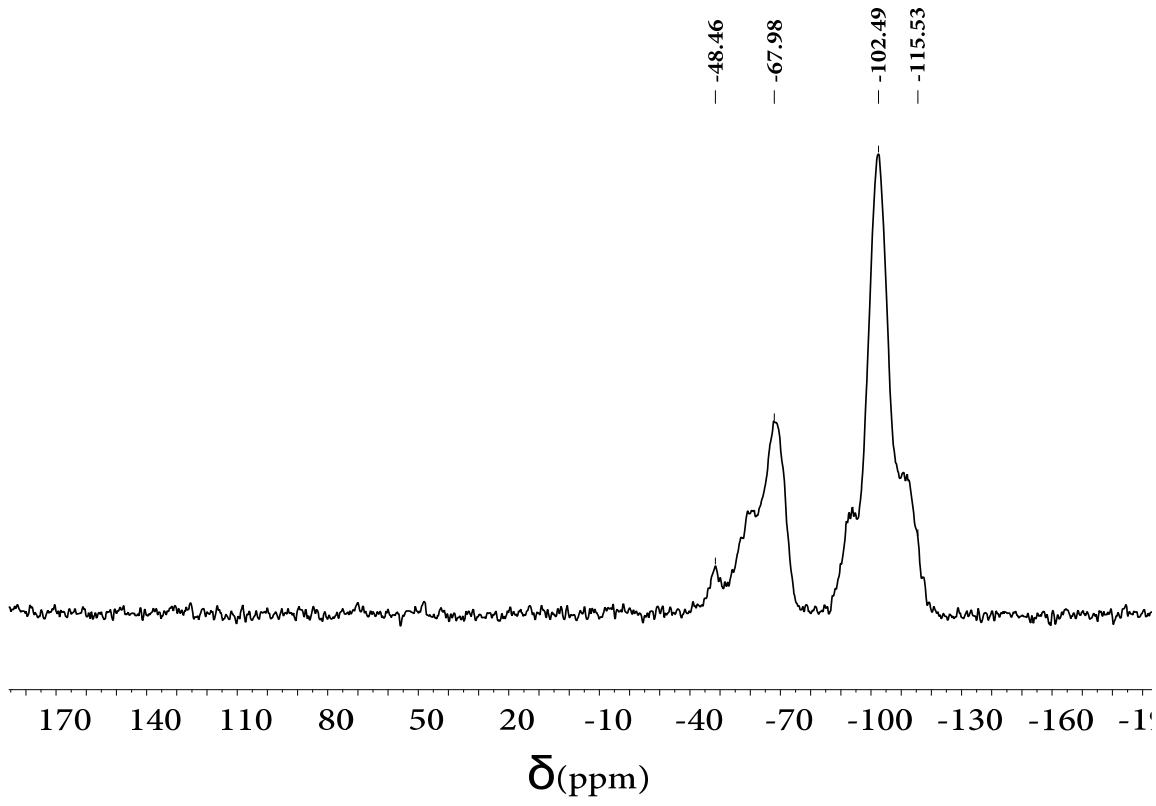

dN7

TEM

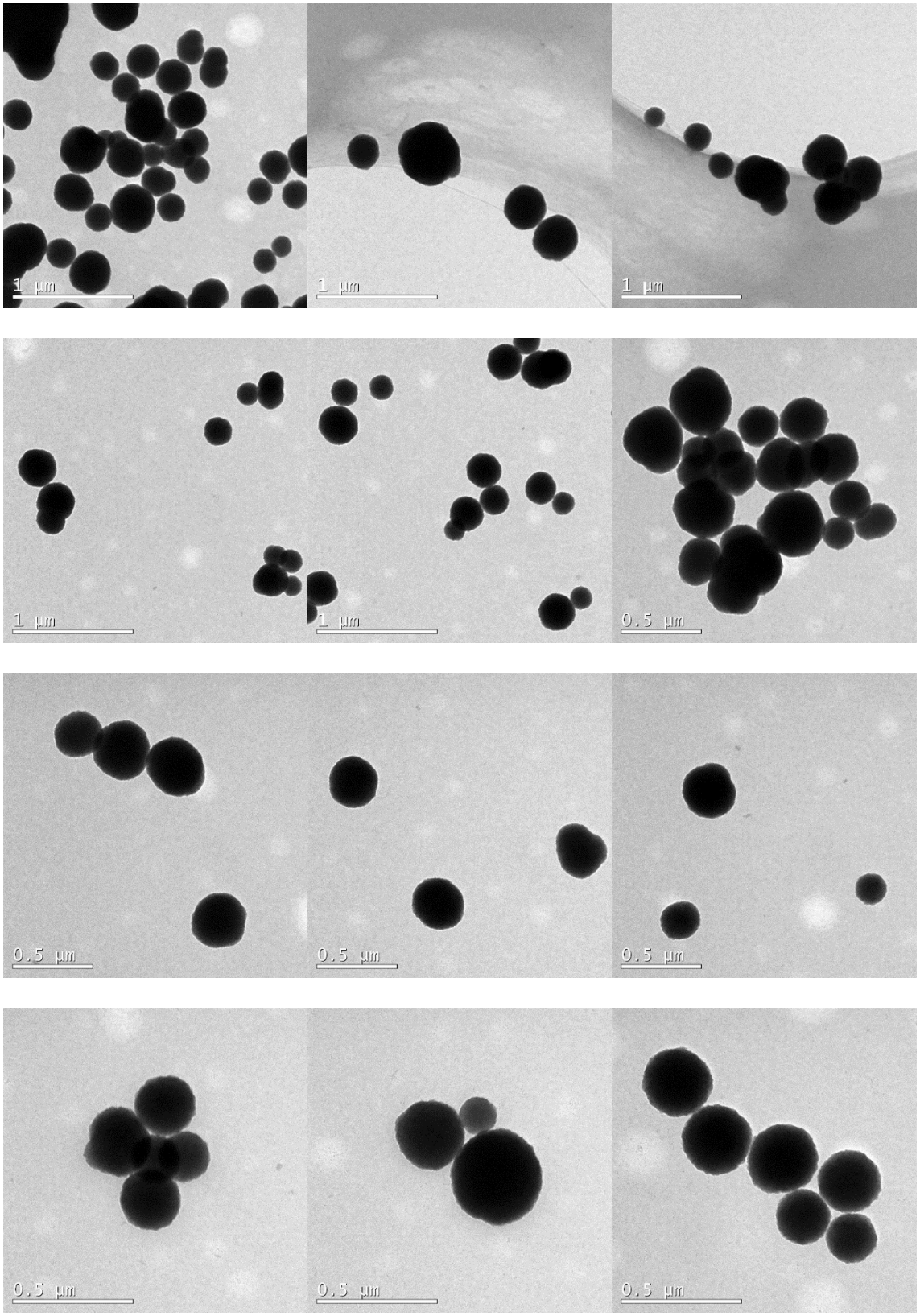

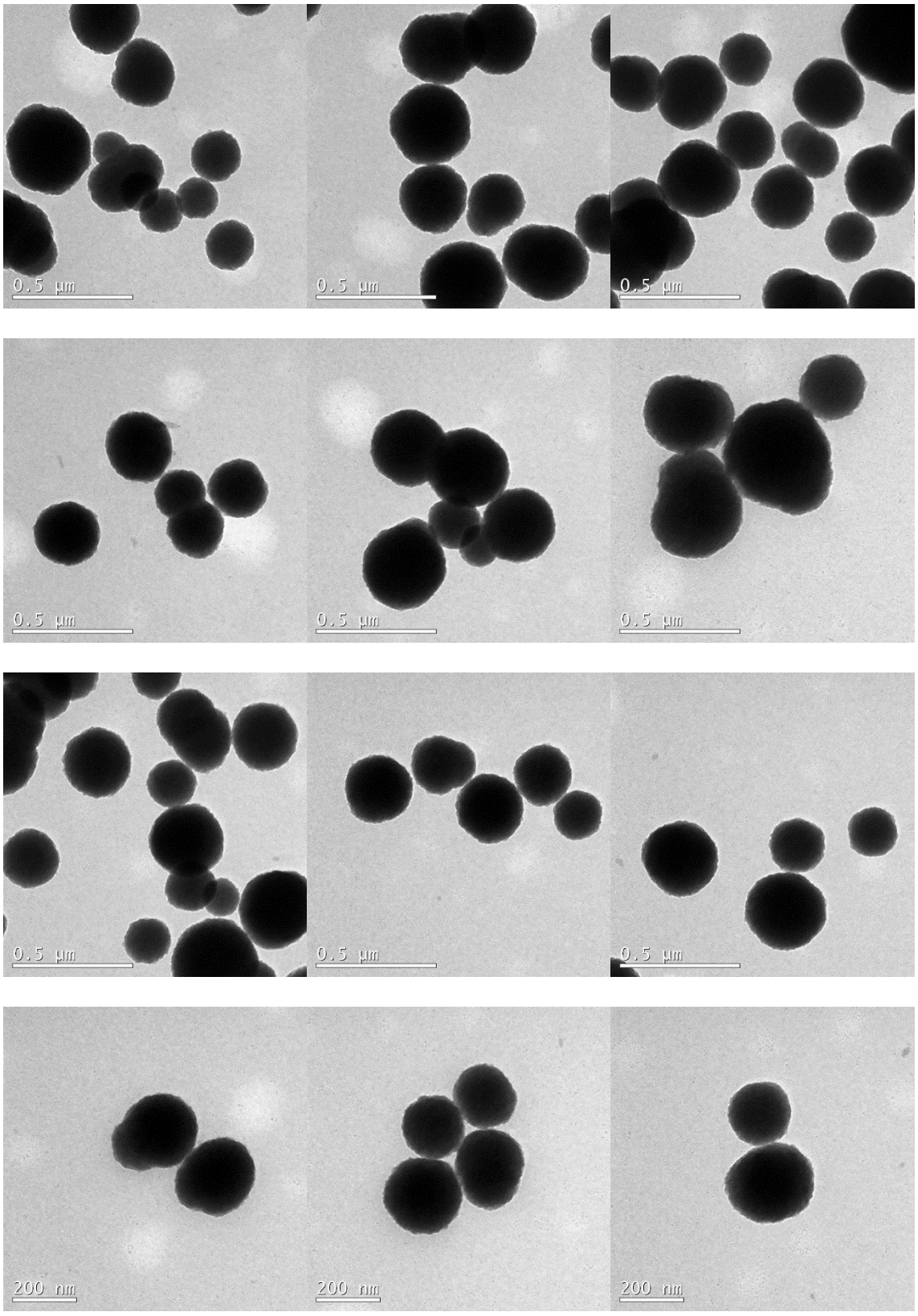
0.5 µm
0.5 µm
0.5 µm
0.5 µm
0.5 µm
0.5 µm
0.5 µm
0.5 µm
0.5 µm
200 nm
200 nm
200 nm

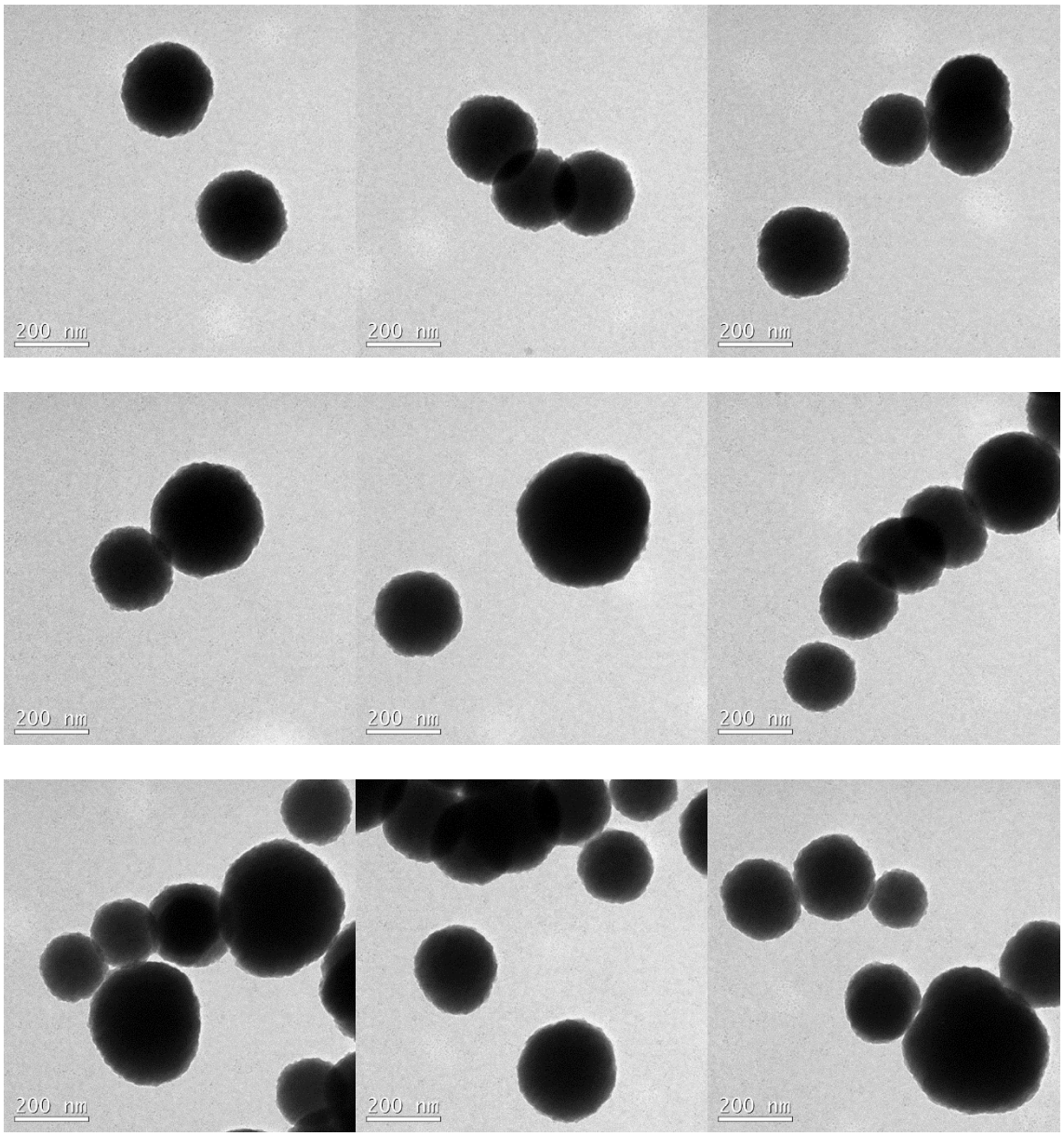
200 nm
200 nm
200 nm
200 nm
200 nm
200 nm
200 nm
200 nm
200 nm

DLS

352.7 nm

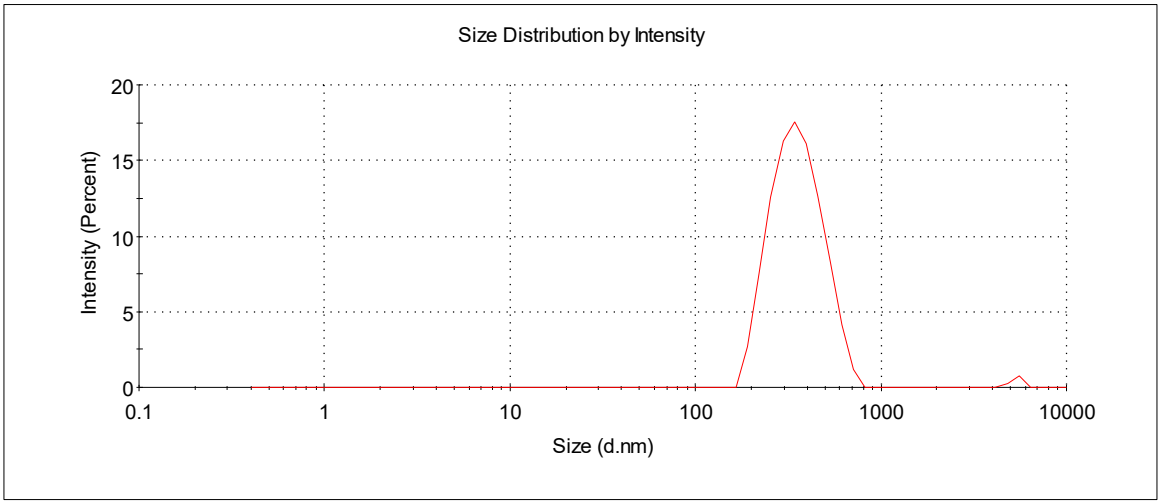

Zeta-potential

+25.1 mV

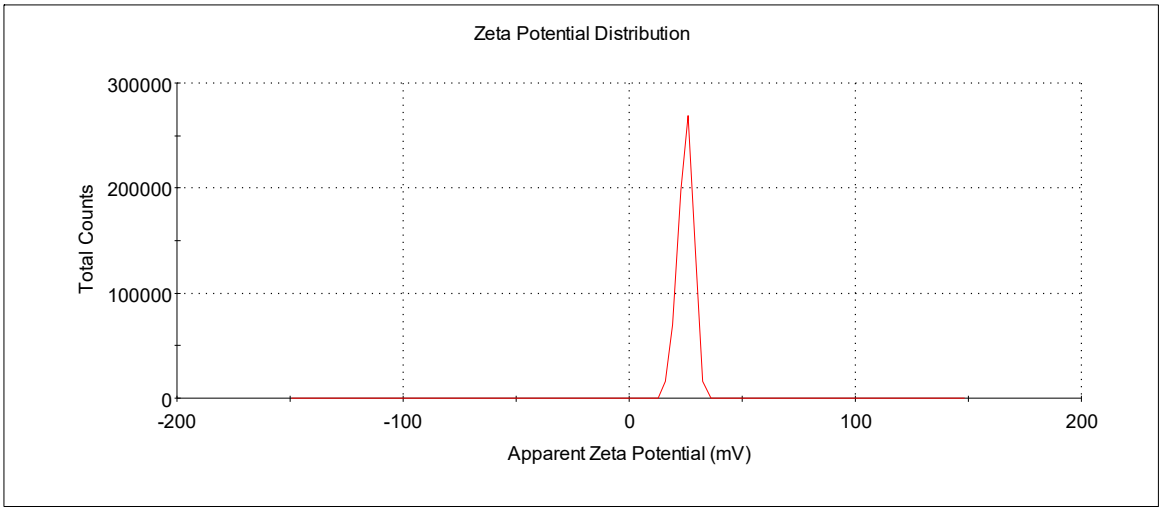

IR (ATR)

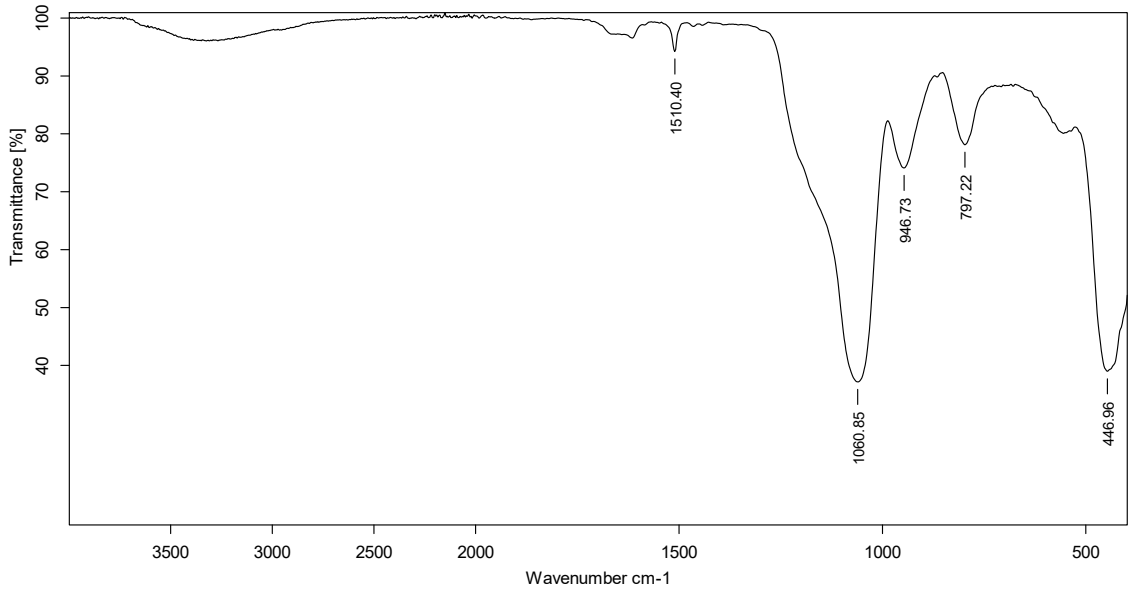
Transmittance [%]
100
90
80
70
60
50
40
1510.40
1060.85
946.73
797.22
446.96
3500
3000
2500
2000
1500
1000
500
Wavenumber cm-1

^{13}C CP MAS NMR

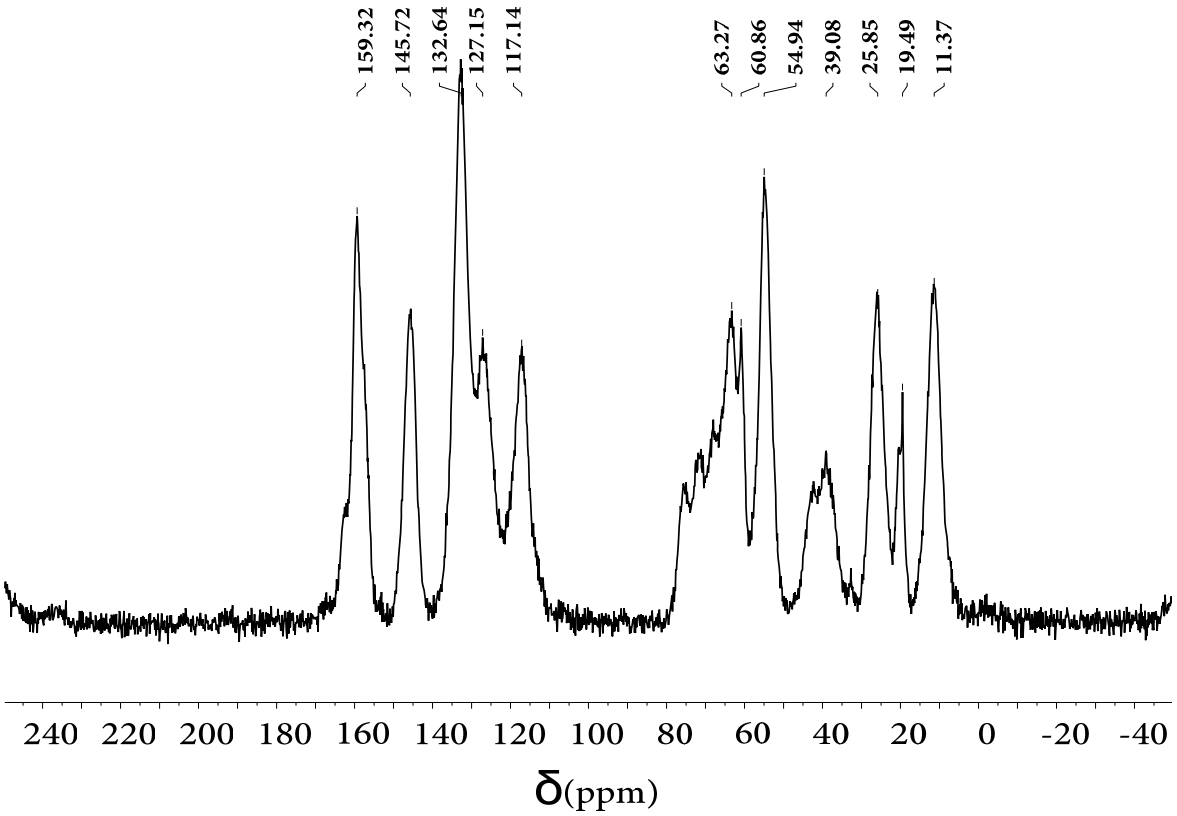

^{29}Si CP MAS NMR

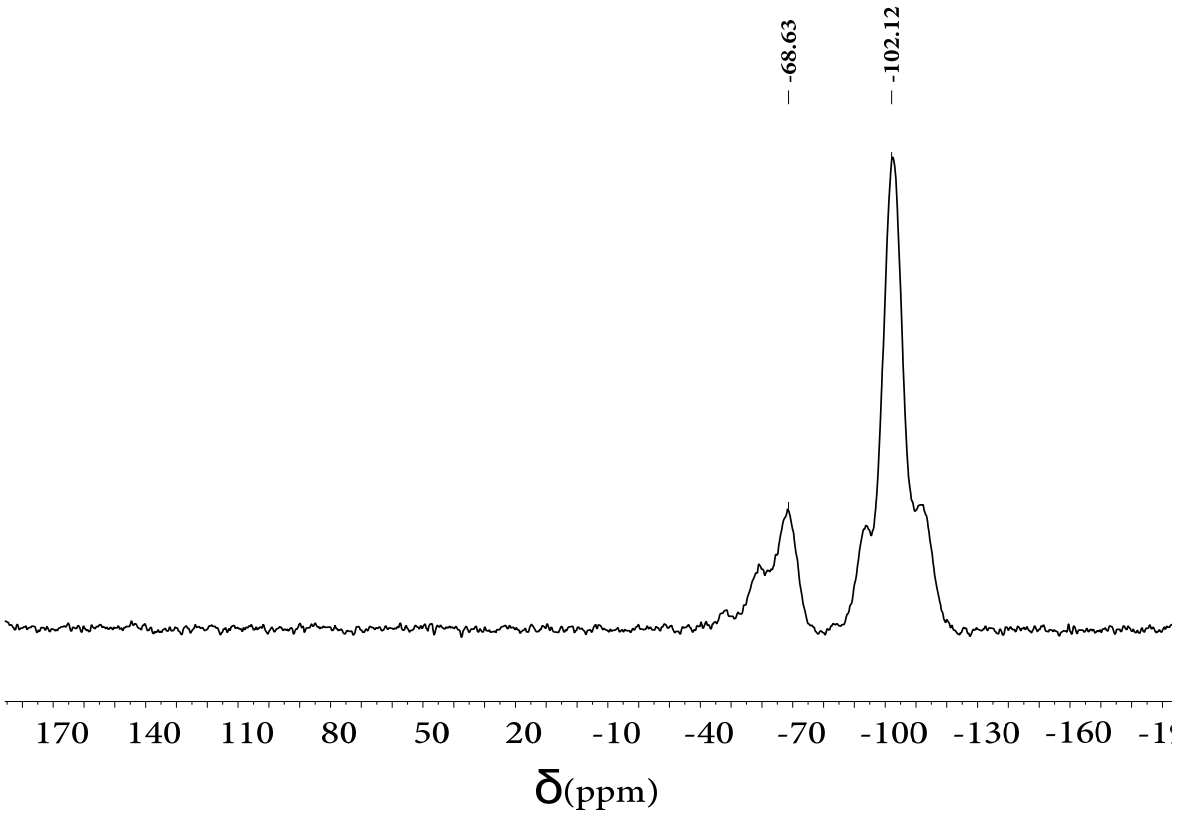

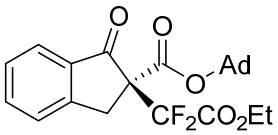

37

^{1}H NMR (300 MHz, $CDCl_3$)

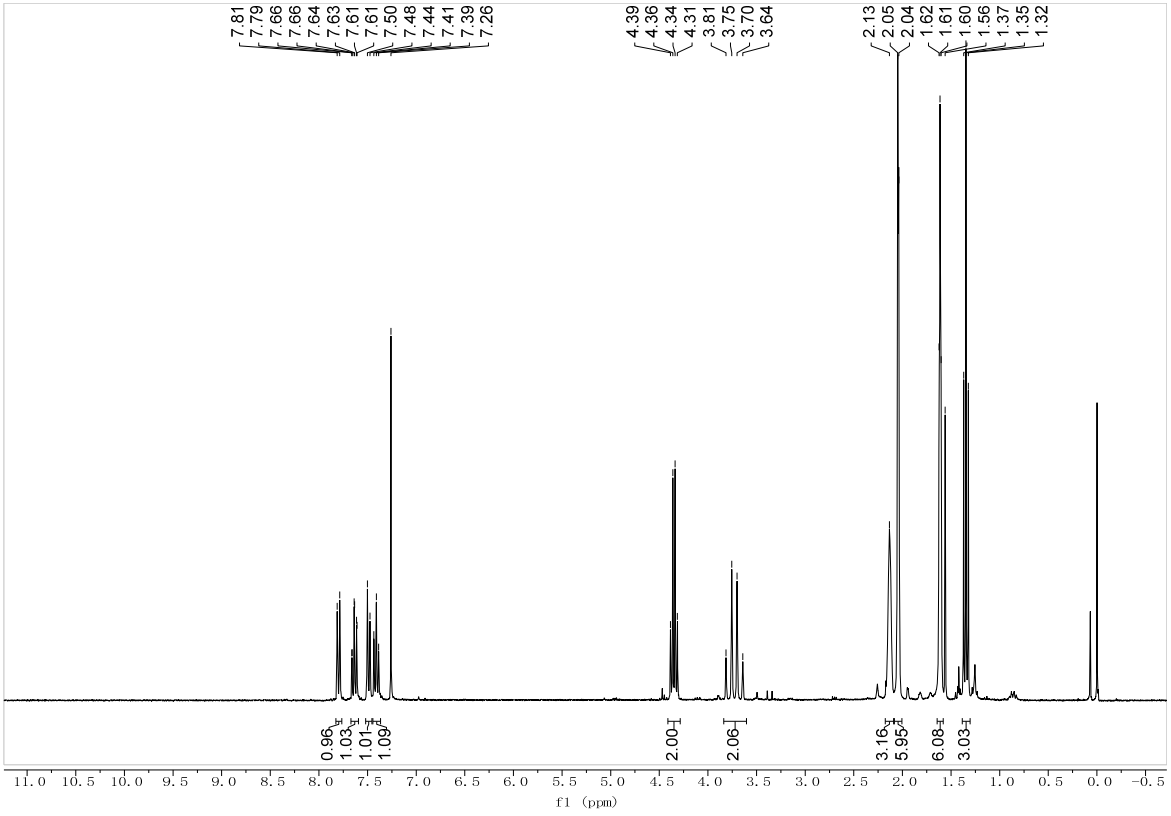

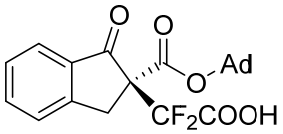

38

^{1}H NMR (300 MHz, $CDCl_3$)

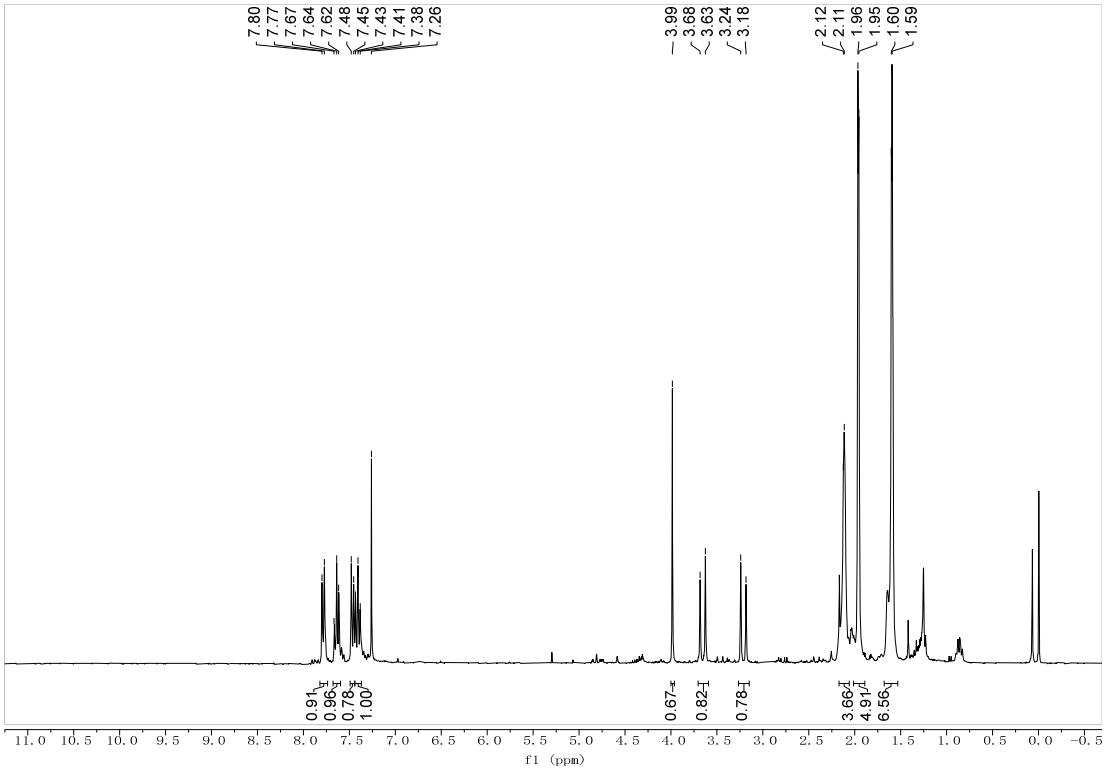

^{13}C NMR (75 MHz, $CDCl_3$)

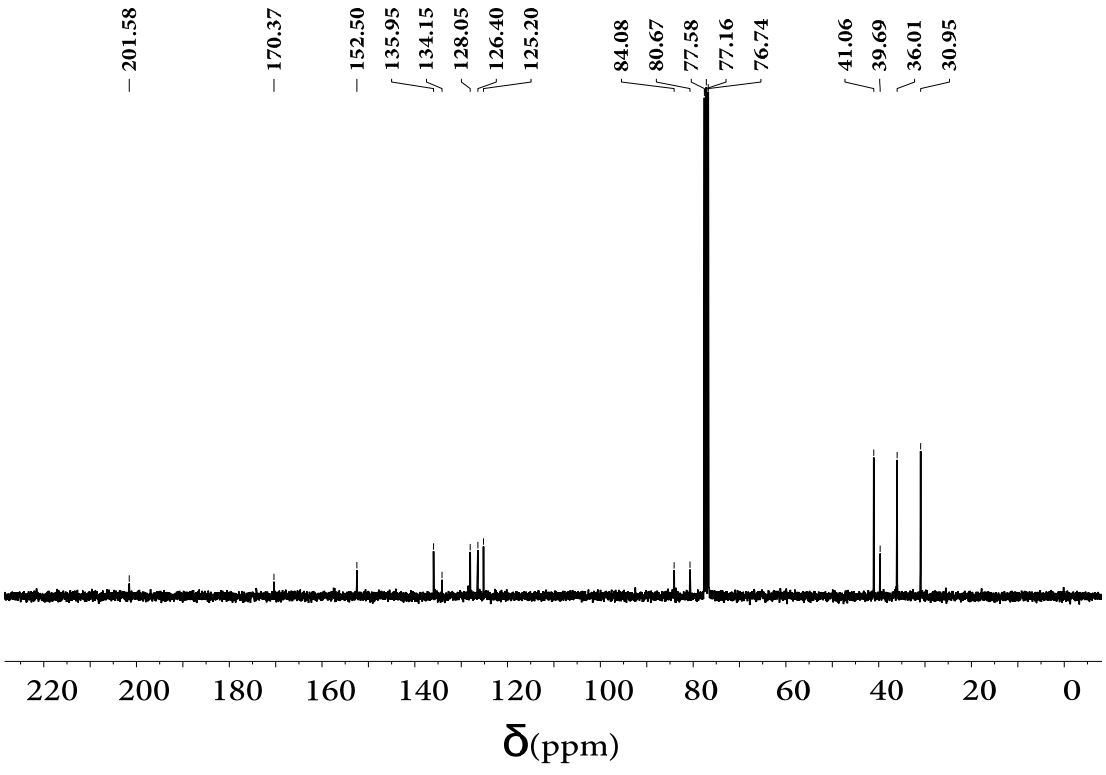

^{19}F NMR (377 MHz, $CDCl_3$)

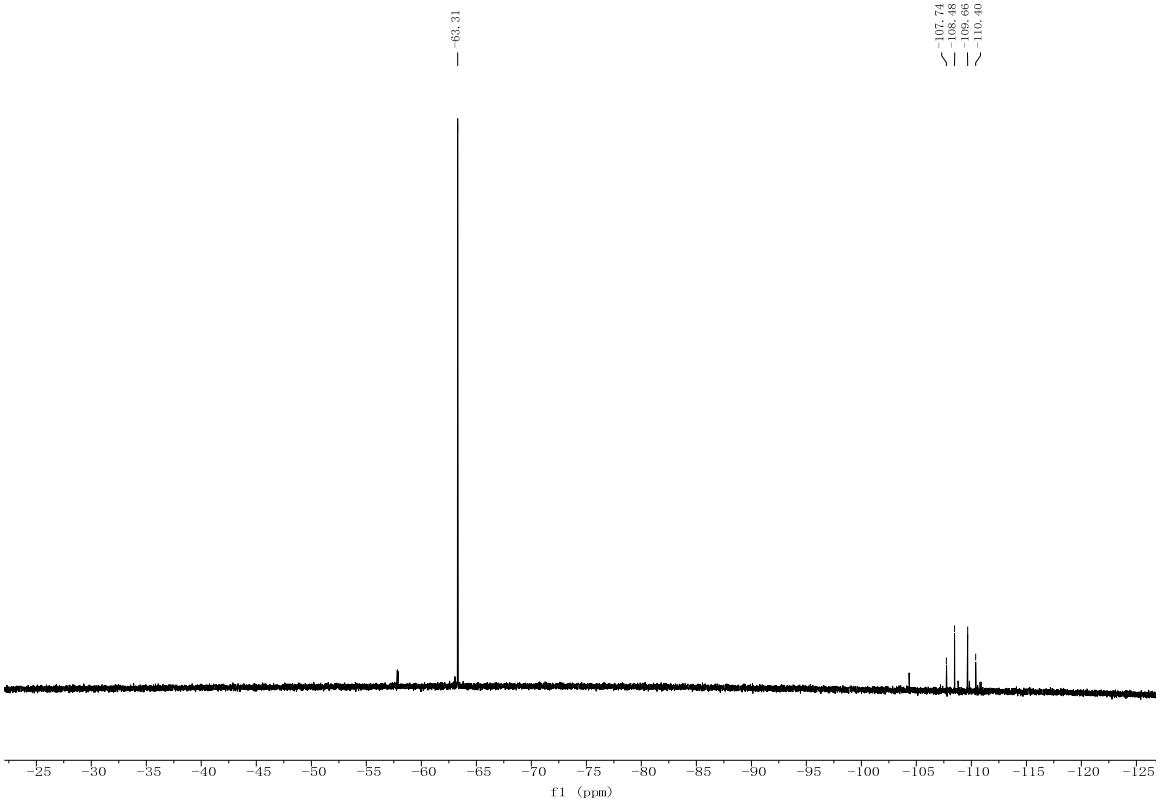

IR (ATR)